Author:
Buckland, Hannah M

Title:
Anticipating the formation, transport and deposition of ash from the next large volcanic eruption
lessons from the Mazama tephra

Anticipating the formation, transport and deposition of ash from the next large volcanic eruption: lessons from the Mazama tephra

Hannah Maeve Buckland

Supervisors: Katharine Cashman, Alison Rust & Samantha Engwell

A dissertation submitted to the University of Bristol in accordance with the requirements for award of the degree of Doctor of Philosophy in the Faculty of Science

School of Earth Sciences

Word Count: 45,580

ABSTRACT

Around once every millenium, a large magnitude explosive eruption occurs on Earth dispersing volcanic ash across millions of square kilometers. Volcanic ash uniquely poses a wide-range of hazards to human health, infrastructure and the environment, the impacts of which are felt close to source to >1000's of km from the volcano. Importantly for large eruptions, the removal of the ash is almost impossible, which means the material remains and is remobilised in the environment, posing secondary hazards for 100's of years after the initial eruption.

Here I present a study of the processes the produce, transport and deposit ash from large eruptions. I use the ~7.7 ka climactic eruption of Mount Mazama as a case study because the tephra was predominantly deposited on-land facilitating widespread data collection. I collate locations where the Mazama tephra has been recorded to produce a new isopach map and estimate of the total erupted volume (176 km^3 bulk or 61 km^3 Dense-Rock-Equivalent). The compilation of tephra thickness data also showed how the Mazama tephra deposit has been remobilised through time, exemplifying the uncertainties associated with field data. Remobilised deposits also provide insight into the types of secondary ash hazards that persist following large magnitude eruptions.

I also investigate the physical and chemical properties of Mazama ash to provide insight into eruptive processes such as co-PDC plumes and distal ash transport. I determine from the composition of Fe-Ti oxides, that the distal ash can be attributed to the later stages of the climactic Mazama eruption. I also observe that the Grain Size Distribution (GSD) of the distal Mazama tephra is remarkably stable, a trend that is observed for other large distal deposits.

This study also investigates the methods we use to analyse grain size in volcanology and outlines a new protocol for measuring the size and shape of volcanic ash using Dynamic Image Analysis (DIA). The benefits of DIA include the capacity for simultaneous particle size and shape characterisation, and the insight into particle density if used in parallel with sieve analysis.

The new estimate of the total erupted volume and distal GSD of the Mazama were integrated with Ash3D, a numerical model of volcanic ash transport and deposition, to simulate the eruption and test the sensitivity of Ash3D to uncertainty in the eruption source parameters. The results stress the need to integrate radial spreading in the umbrella cloud region with advection-diffusion models when simulating the ash transport during large magnitude eruptions. Furthermore, it highlights significant knowledge gaps regarding the deposition of very fine-ash during any scale of eruption. This underscores the benefits of studying fine-ash deposition using the deposits from large eruptions where significant depositional areas and ash volumes facilitate extensive data collection and model testing.

ACKNOWLEDGEMENTS

This PhD thesis would not have been possible without the unwavering support of my colleagues, partner, family and friends. Firstly, I would like to thank my supervisors, Kathy Cashman, Alison Rust and Sam Engwell, for believing in me and supporting me throughout my PhD. Not only have I learned so much from them as inspirational scientists and mentors, I feel I have gained colleagues and friends for life.

I was fortunate to be supported by a PhD studentship through the GW4+ DTP, funded by NERC (Grant - NE/L002434/1) with additional support from the British Geological Survey. I extend a huge thank you to the BGS Volcanology group (Julia Crummy, Mel Duncan, Fabio Dioguardi, Pablo Tierz, Sue Loughlin, Anna Hicks and John Stevenson) who made me feel so included in an amazing team of scientists during my visits to Edinburgh.

I am so grateful for the fieldwork opportunities I was afforded during my PhD. Special thanks go to the organisers and fellow attendees of the IAVCEI 2017 Crater Lake and Newberry Volcano field trip which first introduced me to the wonders of the Mazama eruption. Further thanks go to those who helped with my tephra fieldwork in Oregon and Washington, and the countless researchers who contributed to the vast database of Mazama localities. And thank you to the field assistant I never had a chance to meet, the North American badger, who really loves excavating Mazama ash.

Huge thanks to everyone at the University of Bristol who helped me throughout the PhD. Thank you to those in the research group (past and present): Julia Eychenne, Emma Liu, Keri McNamara, Ery Hughes, Sarah Brown, Frances Boreham, Jen Saxby, Ailsa Naismith, Fee Arens, Amelia Vale, Claudio Contreras, Byron Adams and my APM committee. Special thanks also go to Ben Buse, Stu Kearns, Hayley Goodes and Sam Mitchell for their support with laboratory facilities and tephra analysis. I am also grateful for the many students who worked with me during their undergraduate and Masters studies contributing valuable data and discussions to my project.

Thank you to my PhD cohort and friends: Sacha, Damaris, Rich, Chris, Ben, Jerome, Tom, and Josh. We made it through together with much needed coffee breaks, pub trips, laughter and support along the way. The list of friends and colleagues who made this experience so wonderful is endless, but special thanks also go to the VMSG and INTAV communities as well as the attendees of the CIDER 2019 summer school.

I could not have gone through this journey without an amazing group of non-volcanologists supporting me. Thank you to my parents, Lorna and Roger, my sister Ellen, her partner Ernesto and many friends including Corrie, Lizzie, Leanne, Luke, Clare, Anja, Rhona and Rachel. Thank you to my Oregon family who got to show me Mount Saint Helens for the first time. I am also grateful for my Clifton Running Club community and friends who helped me explore the city and surrounding trails. Thank you also to the O'Reilly family and the entertaining, and cuddly trio of Lola, The Bear and Reilly.

Last but certainly not least, I am so grateful for my wonderful partner Joe. Your belief in me over these four years has made me a better person and researcher. Without your R expertise, late night practise presentations and coffee making, I would not be where I am today. Thank you.

AUTHOR'S DECLARATION

I declare that the work in this dissertation was carried out in accordance with the requirements of the University's Regulations and Code of Practice for Research Degree Programmes and that it has not been submitted for any other academic award. Except where indicated by specific reference in the text, the work is the candidate's own work. Work done in collaboration with, or with the assistance of, others, is indicated as such. Any views expressed in the dissertation are those of the author.

25^{th} August 2021

SIGNED: ..... DATE: .....

"Always do your best."

Professor Lorna McKee

"So far so good."

Professor Roger Buckland

TABLE OF CONTENTS

List of Tables

List of Figures

List of Acronyms

AD Anno Domini
BC Before Christ
BP Before Present (1 January 1950 AD)
BGS British Geological Survey
BSE Backscattered Electron
CIDER Cooperative Institute for Dynamic Earth Research
CX2 Camsizer X2
DA Divider Ash
DEM Digital Elevation Model
DIA Dynamic Image Analysis
DRE Dense Rock Equivalent
DTP Doctoral Training Program
EARThD East African Rift Tephra Database
ECMWF European Centre for Medium-Range Weather Forecasts
EPMA Electron Probe Micro Analysis
ESP Eruption Source Parameter
FW Folk and Ward
GPS Global Positioning System
GSD Grain Size Distribution
GW4 Great Western Four
IAVCEI International Association of Volcanology and Chemistry of the Earth's Interior
INTAV International Focus Group on Tephrochronology and Volcanism
ISO International Organisation for Standardisation
IVESPA Independent Volcanic Eruption Source Parameter Archive
L-1-O Leave One Out
LaMEVE Large Magnitude Explosive Volcanic Eruptions
LD Laser Diffraction
LGM Lago Grande di Monticchio
LPU Lower Plinian Unit
MLDB Mazama Locality Database
MSH Mount Saint Helens
MWA Mass Weighted Average
NCEP National Centers for Environmental Prediction
NOAA National Oceanic and Atmospheric Administration
PDC Pyroclastic Density Current
PDF Probability Density Function
PND Particle Number Distribution
PSD Particle Size Distribution
QGIS Quantum Geographic Information Systems
RESET Response of Humans to Abrupt Environmental Transitions
RMSE Root Mean Squares Error
SE Secondary Electron
SEM Scanning Electron Microscope
SGM San Gregorio Magno
SPHT Sphericity
TGSD Total Grain Size Distribution
UPU Upper Plinian Unit
USA United States of America
USGS United States Geological Survey
UTC Universal Time Coordinated
UTM Universal Transverse Mercator
VAAC Volcanic Ash Advisory Centre
VATDM Volcanic Ash Transport and Deposition Model
VEI Volcanic Explosivity Index
VMSG Volcanic and Magmatic Studies Group
VOLCORE Volcanic Core Records
VOLGRIPA Volcanic Global Risk Identification and Analysis Project
WMO World Meteorological Organization
YTT Younger Toba Tuff

CHAPTER 1

INTRODUCTION

'Tephra' is the collective term for the products generated by the fragmentation of magma during a volcanic eruption. The physical and chemical properties of tephra provide unique insight into magmatic systems and the processes that drive eruptions. For example, the particle size distribution of tephra is related to the magma properties (e.g., composition, vesicularity and crystallinity) as well as the nature and efficiency of fragmentation (e.g., *Turcotte* 1986; *Barberi et al.* 1989; *Sparks et al.* 1992; *Gardner et al.* 1996; *Liu et al.* 2015; *Jones et al.* 2016). 'Tephrochronology' is the discipline that uses the unique physical and chemical properties of tephra, in addition to chronological constraints, to correlate tephra layers and produce eruptive histories that can span thousands of years (e.g., *Thorarinsson* 1968; *Kittleman* 1973; *Dugmore and Newton* 1992; *Larsen et al.* 2001; *Lowe* 2011). Tephra, however, is also associated with a series of hazards including ash fall (tephra <2 mm), Pyroclastic Density Currents (PDCs) and lahars (volcanic mudflows) as well as long-term environmental and climatic impacts. Every year, over 60 volcanoes erupt around the globe and around 800 million people live within 100 km of an active volcano (*Venzke*, 2013; *Brown et al.*, 2015). Therefore, understanding the processes that drive volcanic eruptions and the risk posed by tephra is a grand challenge in volcanology (see the ERUPT consensus study report from *The National Academies of Sciences, Engineering and Medicine* 2017).

Our understanding of volcanic activity is based on interpreting the tephra deposits of eruptions that have already occurred and observations made during on-going eruptions. Letters describing the 79 AD eruption of Vesuvius by Pliny the Younger are one of the earliest written accounts of volcanic activity and the letters have aided reconstructions of the eruptive phases and furthered our understanding of PDCs (*Sigurdsson et al.*, 1982; *Jashemski and Meyer*, 2002; *Gilman et al.*, 2007). However, volcanic activity was being observed for millennia prior to 79 AD, as evident

by the references to eruptions in oral legends and the folklore of many cultures (e.g., *Clark* 1953; *Blong* 1982; *Taylor* 1995; *Kauahikaua and Camara* 2000; *Cashman and Cronin* 2008). The tephra and geological records of volcanic activity extend further back in time than human records of eruptions. For example, eruptions predating the human settlement of Iceland in ~870 AD were identified by dating well-preserved tephra layers and linking their unique geochemistry to the source volcano (e.g., *Thorarinsson*, 1981; *Larsen and Eiríksson*, 2008; *Dugmore et al.*, 2013). Importantly, both historical and geological records of volcanic activity are affected by recording bias and uncertainties. For example, observations made during eruptions vary in detail and often reflect the scientific consensus and understanding of that time. The geological record, on the other hand, is impacted by the differential erosion and preservation of tephra deposits and these limitations are compounded the further back in time one goes (e.g., *Pierson and Major* 2014; *Pyle* 2016; *Panebianco et al.* 2017; *Blong et al.* 2017; *Dugmore et al.* 2018; *Cutler et al.* 2018). This means that our record of the frequency and size of volcanic eruptions through time is incomplete. It is only really since the beginning of the era of satellite remote sensing of volcanoes (past ~50 years, *Francis and Rothery* 2000) that we have a near continuous record of sub-aerial volcanism on Earth.

Eruptions with Magnitude ~7 ($M = log_{10}$(total erupted mass in kg)-7) typically occur once every ~1200 years (*Newhall et al.*, 2018; *Rougier et al.*, 2018) which means that our understanding of large eruptions is derived from interpreting tephra deposits and limited observational records. For example, *Stothers* (1984) reconstructed the phases of the 1815 AD eruption of Tambora, Indonesia (M=7) by combining contemporary accounts of the eruption with physical data gathered from the tephra deposit. No M≥7 eruption has occurred in the era of satellite remote sensing, but the satellite observations of smaller eruptions have helped improve models of volcanic activity. For example, thermal and visible satellite imagery of the M=6.1 eruption of Pinatubo in 1991 provided valuable information for numerical models of volcanic plumes (*Holasek et al.*, 1996; *Koyaguchi and Ohno*, 2001; *Dartevelle et al.*, 2002; *Fero et al.*, 2009). Similarly, remotely tracking the distal ash cloud of the 2010 eruption of Eyjafjallajökull, Iceland helped improve Volcanic Ash Transport and Deposition Models (VATDMs) as they could be calibrated against satellite retrievals, field data and ground-based observations (*Bonadonna et al.*, 2011; *Bursik et al.*, 2012; *Francis et al.*, 2012; *Gudmundsson et al.*, 2012; *Prata and Prata*, 2012). We can now use these improved models of volcanic activity to study larger eruptions. For example, we can run a VATDM to simulate the tephra deposit formed by a large eruption using a range of Eruption Source Parameters (ESPs) to compare against the real deposit. The differences between the modelled and simulated deposits then tell us something about the ash transport and deposition mechanisms. We might expect that VATDMs that have been calibrated on smaller eruptions will not accurately reproduce the deposits of large eruptions. Therefore, comparing models with field data provides insight into the relative importance of large plume dynamics, differences in the ESPs of large eruptions and the impact of uncertainty in field data collected from prehistoric deposits.

1.1 Thesis motivation

Predicting the likelihood of a volcanic eruption occurring at a specific location is one of the underlying goals of volcanology. This knowledge would revolutionise volcano hazard assessments and risk mitigation strategies. Anticipating the next large magnitude eruption (M≥7) is especially important because of the devastating impacts close to source and vast spatial footprint that is posed by eruptions on this scale (*Newhall et al.*, 2018). It is also paramount that the numerical models we use to forecast volcanic hazards are as accurate and precise as possible, which is achieved by rigorous model testing and senstivity analysis using appropriate input parameters. To work incrementally towards forecasting future catastrophic events, we must first further our understanding of the processes that produce, transport and deposit volcanic ash during large magnitude explosive eruptions.

Given the fundamental importance of the geological record for understanding large magnitude eruptions, this thesis investigates the efficacy of methods used to study prehistoric tephra deposits that have undergone modification since deposition. I use the extensive subaerial tephra deposit of the ~7.7 ka climactic Mazama eruption in Oregon, USA as a case study to investigate how tephra remobilisation can impact the thickness and grain size of tephra deposits as well as estimates of eruption volume and magnitude. This study expands the literature describing remobilised tephra deposits (*Gatti et al.*, 2013) which will improve our understanding of secondary tephra hazards that arise following large magnitude eruptions.

This thesis is also motivated by the need to forecast ash dispersion following or during any future large magnitude eruption. This requires an understanding of the mechanisms that produce the large volumes of fine volcanic ash (<125 μm, *Sparks and Walker* 1977; *Rose and Durant* 2009; *Engwell and Eychenne* 2016) and meaningful input parameters for VATDMs that describe the particle characteristics. To investigate the provenance of fine ash from the climactic Mazama eruption, I assess whether specific fragmentation processes, such as the secondary fragmentation of clasts within PDCs, can be reliably identified in distal tephra deposits using a combination of geochemical and granulometric techniques. This information will help determine which processes impact the Grain Size Distribution (GSD) of ash produced by large magnitude eruptions. Similarly, how we characterise the particle size and shape of volcanic ash is important for VATDMs (*Wilson and Huang*, 1979; *Beckett et al.*, 2015; *Bagheri et al.*, 2015; *Saxby et al.*, 2018) . Motivated by this, I interrogate the methods used to characterise the size and morphology of volcanic ash to determine how irregular particle shapes impact how we define particle size and whether this propagates as a systematic error to VATDMs and subsequent hazard assessments.

Finally, this thesis is also inspired by a recognition of the need to test VATDMS using the ESPs associated with large magnitude eruptions. Typically, VATDMs model the advection and diffusion of volcanic ash, however, the plumes from large eruptions typically require that such models

also account for umbrella cloud spreading close to source (*Costa et al.*, 2013; *Mastin et al.*, 2014; *Barker et al.*, 2019; *Webster et al.*, 2020). Given the extensive subaerial preservation of Mazama tephra, this context provides an excellent opportunity to investigate the calibration of a VATDM against field data for a M>7 eruption.

1.2 Thesis outline

This thesis consists of five science chapters (Chapters 2-6), each of which addresses the thesis aims outlined above.

In Chapter 2, I compile a database of localities where tephra from the ~7.7 ka climactic eruption of Mount Mazama, Oregon, USA has been reported. I collate tephra thickness data from the literature where it is available, and report data collected for this thesis during two field campaigns in August 2017 and July 2018. I then consider to what extent the tephra has been remobilised since deposition by assessing qualitatively the descriptions of tephra at each locality and comparing the observed thicknesses to the thickness predicted by empirical models of tephra deposit thinning. Finally, I use localities that likely record the unaltered tephra thickness to reconstruct isopachs (contours of equal deposit thickness) and estimate the total erupted volume of the climactic Mazama eruption.

The distal Mazama tephra deposit remains the focus of Chapter 3. Here I use granulometric and geochemical techniques to investigate whether the Plinian and co-PDC phases of the caldera forming eruption can be identified in the distal ash deposits.

In Chapter 4, I interrogate the methods used by volcanologists to characterise the size of volcanic tephra. This chapter also presents a relatively new method of size analysis in volcanology, Dynamic Image Analysis (DIA). I discuss the merits of DIA for characterising volcanic ash, for example, the ability to simultaneously measure particle size and shape.

Chapter 5 explores an application of particle size analysis in volcanology, reconstructing the Total Grain Size Distribution (TGSD) of a deposit. In this chapter I use the grain size data collated for the Mazama tephra in Chapters 2-4 to determine a TGSD whilst considering the sensitivity of the averaging methods used to determine this key ESP.

In Chapter 6, I compare and contrast simulations of the Mazama climactic eruption using Ash3d, a three-dimensional Eulerian VATDM, with the tephra deposit. This is a collaborative Chapter where I worked with Larry Mastin from the United States Geological Survey (USGS). Larry Mastin ran the Ash3D simulations, with simulation runs collaboratively designed using the ESPs I investigated in the previous chapters, including the eruption volume (Chapter 2) and the TGSD (Chapter 5). The widespread Mazama tephra deposit provides an excellent opportunity

to validate the Ash3D model using ESPs associated with a large magnitude eruption. Finally, in Chapter 7, I summarise the main outcomes of the thesis and suggest future work that would continue to advance our understanding of large magnitude eruptions.

1.3 Background

Here I present background information for the main thesis chapters and a brief review of the methods used to study large magnitude eruptions (section 1.3.3). Chapter 2 has been published in the Bulletin of Volcanology (*Buckland et al.*, 2020) and includes a thorough review of the Mazama tephra in section 2.2.2 that expands on section 1.3.4. Similarly, Chapter 3 reviews the geochemistry of the Mazama tephra products in more detail than section 1.3.4. Chapter 4 has been published in the Journal of Volcanology and Geothermal Research (*Buckland et al.*, 2021) and therefore sections 4.1 and 4.2 are written as standalone introductory and background information that is not repeated here. As Chapters 2 and 4 have been published, the supplementary material for each manuscript has been included as Appendices A and C respectively.

1.3.1 Large magnitude explosive eruptions

Three main indices are used to discriminate eruptions by size: (1) the Volcanic Explosivity Index (VEI), (2) eruption Magnitude (M) and (3) eruption Intensity (Fig. 1.1). The VEI is an integer scale that categorises volcanic eruptions according to the bulk erupted volume and plume height (Fig. 1.1a; *Newhall and Self* 1982; *Pyle* 2000). Despite its widespread use (e.g., *Venzke* 2013; *Newhall et al.* 2018) there are some disadvantages to using the VEI. For example, a long-lasting eruption with low mass eruption rate will be assigned the same VEI as a short-lived extremely explosive eruption if they have the same total erupted volume, even though the associated hazards of those eruptions would be dramatically different (*Pyle*, 2000). An alternative approach is to use the continuous scale of eruption Magnitude (a direct transformation of the erupted mass) and Intensity (Intensity = log_{10}(mass eruption rate) +3) in parallel (Fig. 1.1b; *Pyle* 2000). This allows eruptions with different mass eruption rates to be differentiated. For example, the violent Strombolian eruptions of Parícutin volcano (M=5.1, Intensity = 8.0) can easily be distinguished from the 1980 sub-Plinian eruption of Mount St. Helens (M=4.8, Intensity = 11.1) in Figure 1.1b. In the future, alternative measures of eruption size might be based on the total volatiles released (*Carn et al.*, 2017), or the disruption and damage caused by an eruption. Explosive eruptions where the bulk erupted volume exceeds ~100 km^3 typically rank high on all parameters used to quantify size because these cataclysmic events occur on short timescales leading to severe impacts (eruptions with M and VEI ≥7 in Fig. 1.1).

Determining the size of a volcanic eruption is important for assessing magnitude frequency relationships which indicate how often eruptions of a certain size are likely to occur. This is

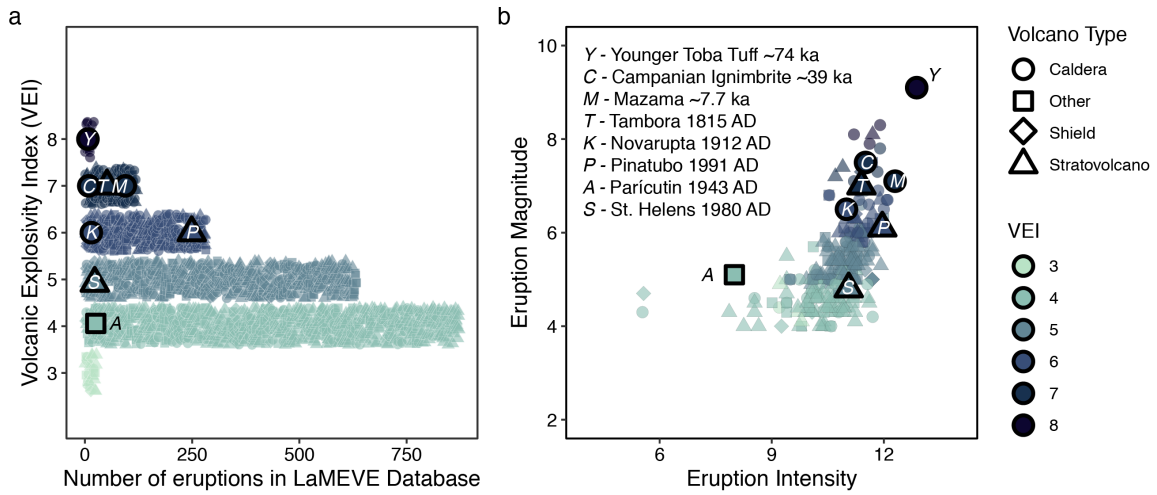

Figure 1.1: Comparison of different eruption size indices using data from the LaMEVE database. In both plots the point colour indicates the Volcanic Explosivity Index (VEI) and the shape is the volcano type according to the LaMEVE database. a) The discrete VEI scale where each individual point is an eruption in the LaMEVE database. The points have been offset above and below the central integer value to allow better visualisation of the number and shape of the individual points using the `geom_jitter` function in the `ggplot2` R package (*Wickham*, 2016). b) The same data as plot a) but the number of points has been reduced to only include eruptions where the magnitude and intensity is reported. In a) and b) eight key eruptions have been highlighted as large, bold markers where the letter corresponds to the specific eruption.

key for volcano monitoring and risk management; for example, we know small magnitude eruptions happen more frequently than large eruptions (*Pyle*, 2000; *Mason et al.*, 2004; *Rougier et al.*, 2018). Using the Large Magnitude Explosive Volcanic Eruptions database (LaMEVE; VOLGRIPA; www2.bgs.ac.uk/vogripa/view/controller.cfc?method=lameve; *Crosweller et al.* 2012; Fig. 1.2), *Rougier et al.* (2018) calculate that a M=7 eruption will occur every 680-2100 years (95% confidence interval). Uncertainty in these relationships comes from the under-recording of prehistoric eruptions (Fig. 1.2; *Rougier et al.* 2018) and uncertainties associated with calculating eruption magnitude and dating methods (*Biass and Bonadonna* 2011; *Bonadonna et al.* 2015, section 2.2.2). Importantly, such global magnitude frequency relationships are purely statistics-based and do not model the processes required to produce a large-magnitude eruption. Therefore, whilst we can estimate the time between large eruptions this approach does not predict where or why future large eruptions will occur.

To predict where future large magnitude eruptions might occur, we could use magnitude frequency relationships for individual volcanic systems where, in some cases, caldera-forming eruptions appear to be part of a magmatic cycle on the order of 10^4-10^6 years (e.g., *Smith* 1979; *Spera and Crisp* 1981; *Jellinek and DePaolo* 2003). However, it is also important to understand how large volumes of magma accumulate, are stored and exhumed, especially given the inaccuracies of the

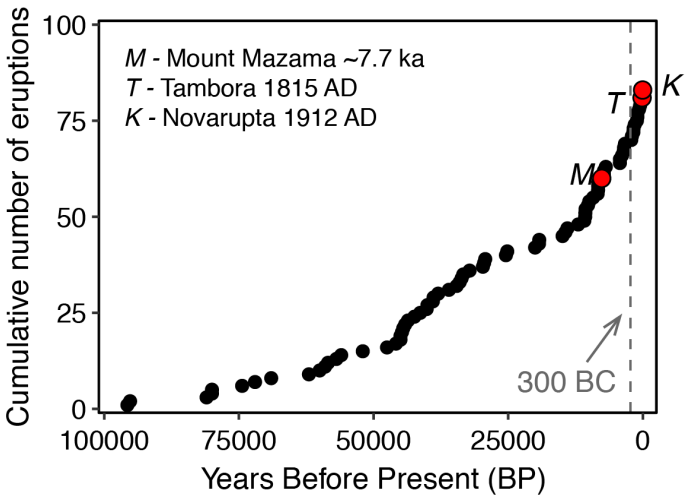

Figure 1.2: Cumulative number of eruptions through time for eruptions with 6.5≤M<7.5 in the LaMEVE database after *Rougier et al.* (2018). Key eruptions highlighted in red using the same letters as Fig. 1.1. The dashed line represents the time after which the recording probability is assumed to equal 1 (*Rougier et al.*, 2018).

volcanic record. A recent paradigm shift in our understanding of magma storage proposes that low melt-fraction 'mush reservoirs' exist below volcanic systems and that high-melt fraction 'magma-chamber' like bodies are ephemeral and only form close to the onset of eruption (e.g., *Annen et al.* 2006; *Bachmann and Bergantz* 2008; *Cashman et al.* 2017; *Jackson et al.* 2018). Incredibly, petrological evidence suggests that the final assimilation of eruptible magma can be rapid (~days to weeks) which is concerning for volcano monitoring (*Wilson et al.*, 2006; *Gelman et al.*, 2013; *Wotzlaw et al.*, 2015; *Sparks and Cashman*, 2017; *Cooper*, 2019; *Wilson et al.*, 2021). Where large volumes of eruptible magma can accumulate is related to the magma supply rate, plate tectonics, the regional stress regime, and the thermal state of the crust (e.g., *Annen* 2009; *Allan et al.* 2013, 2017; *Wilson and Charlier* 2016; *Cabaniss et al.* 2018). A database of settings that have or have the potential to produce a VEI 7 eruption (Fig. 1.3) suggests favourable conditions are present at continental hotspots and convergent plate boundaries (*Newhall et al.*, 2018). Whilst pre-eruptive conditions and magma storage are not the focus of this thesis, it is important to recognise that by studying the tephra record we are collecting valuable information, such as the total erupted mass and glass geochemistry, that can aid future studies interested in the processes that precede the eruption.

1.3.2 The impacts of large magnitude eruptions

Hazards associated with the dispersion and deposition of volcanic ash following a large magnitude eruption will be unlike anything experienced in modern times because of the high concentration of ash in the atmosphere (>>4 mgm^{-3}, the no-fly zone limit set by the European Commission;

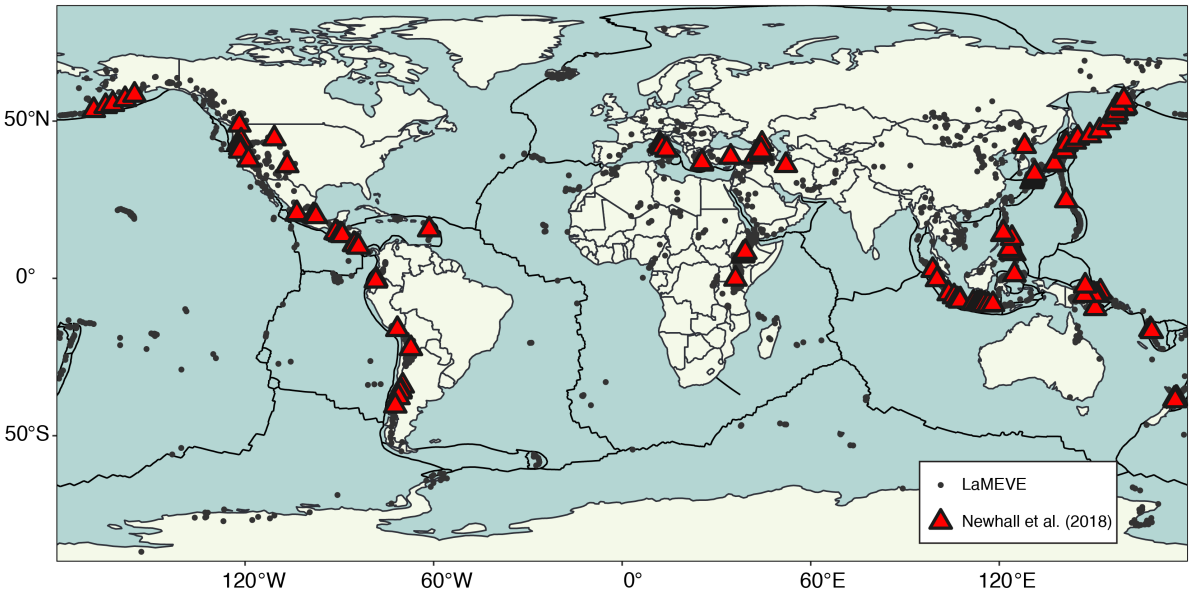

Figure 1.3: The global distribution of volcanoes with a history of or the potential to produce VEI 7 eruptions (red triangles) according to *Newhall et al.* (2018; their Table 1). Other volcanoes in the LaMEVE database are plotted as grey circles.

Stohl et al. 2011; *Gouhier et al.* 2019) and the very large areas impacted by ash fall (~millions of km^2). Ash in the atmosphere disrupts aviation, impacts local meteorology and can interfere with telecommunication signals (e.g., *Casadevall* 1994; *Durant et al.* 2009; *Prata and Tupper* 2009; *Wilson et al.* 2012; *Lechner et al.* 2018). Once the ash is deposited it can cause roof collapse and damage to other infrastructure such as electrical transmission networks and roads (e.g., *Wilson et al.* 2012; *Blake et al.* 2016, 2017; *Waitt* 2015). Volcanic ash also poses a health hazard and can contaminate water supplies (e.g., *Horwell et al.* 2003; *Horwell and Baxter* 2006; *Stewart et al.* 2006). For example, from geological and paleoecology records we know that the tephra from the climactic Mazama eruption devastated the proximal ecosystem (*Young*, 1990), affected flora species over 700 km from source (*Power et al.*, 2011), and the aerosols released caused short term changes in the climate of North America (*Zdanowicz et al.*, 1999).

Ash removal following a large eruption is likely to be nearly impossible so ash hazards will be long-lived, particularly as ash is continually remobilised by gravity, wind and water (e.g., *Hadley et al.* 2004; *Pierson and Major* 2014; *Panebianco et al.* 2017). The longevity of the ash hazards will amplify the societal impacts of a large eruption. For example, increased demand for limited resources, food shortages following contamination or cutoff imports can lead to civil unrest and even societal collapse (e.g., *Nel and Righarts* 2008; *Wilson et al.* 2012; *Newhall et al.* 2018). Indeed, archaeological evidence suggests that the Mazama eruption, combined with climate change, caused the inhabitants of the Northern Plains to abandon their homelands for 500-600 years (*Oetelaar and Beaudoin*, 2016). Therefore, it is paramount for hazard prediction

and risk mitigation efforts that VATDMs can produce meaningful forecasts of ash dispersal for M ≥7 eruption scenarios. These simulations can then be combined with magnitude frequency distributions for volcanic eruptions into probabilistic hazard assessments at volcanoes that have the potential to produce large eruptions (e.g., *Connor et al.* 2001; *Jenkins et al.* 2012; *Sheldrake* 2014; *Rougier et al.* 2018).

1.3.3 A volcanologist's toolkit

Volcanology is a multidisciplinary science that began as a sub-discipline of geology but has since gathered knowledge and methodologies from the atmospheric sciences, engineering, the humanities, and many other specialties. As a result, the tools used by volcanologists are extremely diverse and constantly evolving. Here I briefly review two broad categories of methods used to study explosive eruptions.

1.3.3.1 Field data and tephra sampling

Traditional geological mapping has been fundamental to studies of explosive volcanism. For example, studies of Italian volcanoes in the 1700-1800's identified layers of pyroclastic (tephra) deposits even in a time when the genesis of those rocks was debated by Vulcanists (who believed rocks were by intrusive magmatic activity from deep within the Earth) and Neptunists (who believed rocks precipitated out from matter dissolved in vast oceans on the Earth's surface, *Sigurdsson* 2015). Field studies of tephra deposits have become increasingly quantitative. For example, techniques from the wider field of sedimentology, such as sieving, were adopted which facilitated the distinction of nuée ardente or PDC deposits from fall deposits based on the relative sorting (*Lacroix* 1904; *Moore* 1934; *Fenner* 1937, section 4.2.2). The discipline of tephrochronology developed through studies of Icelandic volcanoes furthered our understanding of eruption frequencies and tephra dispersal (*Thorarinsson*, 1981; *Larsen et al.*, 2001). Similarly, systematic mapping of the thickness of tephra deposits led to reconstructions of the total erupted volume (e.g., *Williams* 1942; *Fries* 1953; *Williams and Goles* 1968; *Bond and Sparks* 1976, section 2.2.2). Measurements of particle size were also integrated with experimental and theoretical studies of fragmentation and fractal behaviour which helped us understand the way magma is broken up during eruptions (*Turcotte* 1986; *Wohletz et al.* 1989; *Gardner et al.* 1996, section 5.1).

Recent field studies of volcanism (past ~10 years) have focused on considering the uncertainties in field data (e.g., *Biass and Bonadonna* 2011; *Bonadonna et al.* 2013; *Engwell et al.* 2013, 2015; *Cutler et al.* 2018; section 2.2.3). For example, studies documenting the transformation of the May 1980 Mount St. Helens tephra deposit through time help assess the reliability of thickness and grain size measurements from older deposits (*Dugmore et al.*, 2018; *Cutler et al.*, 2018, 2020). Field and geochemical data are also increasingly being collated and shared via online journals and data repositories to ensure data preservation and avoid valuable field data only being reported in

field notebooks (e.g., TephraBase, *Newton et al.* 2007; LaMEVE, *Crosweller et al.* 2012; RESET, *Bronk Ramsey et al.* 2015; EARThD, *Mana et al.* 2018; VOLCORE, *Mahony et al.* 2020; IVESPA, *Aubry et al.* 2021). It must be noted, however, that there is no database dedicated to collating physical field data from tephra deposits, such as thickness and grain size information. These data, if reported at all, are still most commonly shared as an appendix to the main manuscript or in theses. The increased availability and quality of personal GPS equipment and photography is also improving the quality of field data as well as data sharing and reproducibility. These new approaches to field data collection and storage also mean that in the future field data can easily be reanalysed when new interpretation techniques become available.

1.3.3.2 Analytical and numerical models

Empirical and numerical models are required to relate the data collected from deposits to eruption parameters. For example, statistical models of deposit thinning have been computed so that thickness data can be used to calculate the deposit volume (e.g., *Pyle* 1989; *Fierstein and Nathenson* 1992; *Bonadonna and Costa* 2013; *Scarpati et al.* 2014). Similarly, the plume height of unobserved eruptions has been related to maximum clast size data using models of buoyant eruption columns (*Carey and Sparks*, 1986; *Burden et al.*, 2011; *Rossi et al.*, 2019). Laboratory models are then crucial for calibrating models of eruptive processes. For example, models of buoyant plumes require entrainment coefficients that have been investigated experimentally (*Kaminski et al.*, 2005; *Carazzo et al.*, 2006; *Kavanagh et al.*, 2018). Similarly, experiments analysing the settling of volcanic ash particles in fluids of known density and viscosity have produced functions for particle drag coefficient and terminal settling velocity that are used in VATDMs (e.g., *Wilson and Huang* 1979; *Dioguardi and Mele* 2015; *Saxby et al.* 2018).

Modelling of the transport and deposition of volcanic ash is fundamental for hazard assessments at volcanoes. VADTMs require ESPs, meteorological data and a model of tephra transport which is commonly the advection and diffusion of particles by atmospheric winds and turbulence (*Folch*, 2012; *Kavanagh et al.*, 2018). Purely advection diffusion models, however, are less appropriate for modelling large magnitude (M≥7) eruptions for multiple reasons which I discuss in detail in section 6.2.2. Briefly, these reasons are: (1) the absence of plume spreading in the umbrella cloud region, (2) poor characterisation of the Grain Size Distribution of distal ash clouds, (3) model simplifications and assumptions made to invoke the settling of fine particles (<125 μm) and (4) introduction of significant uncertainties when estimating the ESPs and meteorological data for prehistoric large eruptions. One way to deal with the challenge of constraining ESPs is to use a computational inversion approach where you solve the VATDM in reverse to produce a best-fit set of input parameters that would simulate the observed field data (e.g., *Connor and Connor* 2006; *Magill et al.* 2015; *Marti et al.* 2016; *White et al.* 2017, Appendix E). However, this approach still propagates uncertainties in the field data and can overfit the model parameters to spurious data.

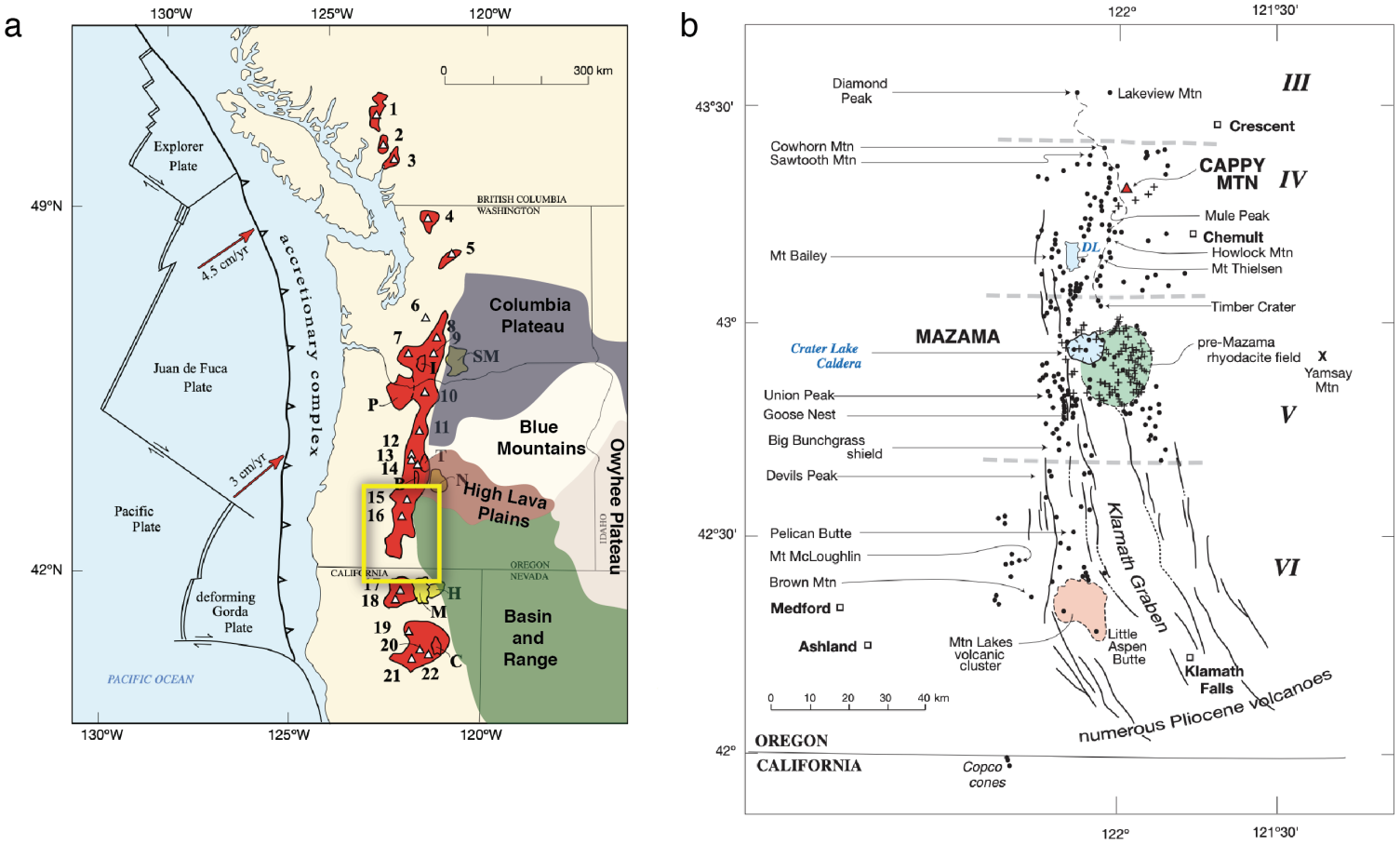

Figure 1.4: Tectonic setting of the Cascades Arc and Mazama volcanic centre. a) Quaternary Cascades arc with pre-Quaternary geological providences from *Ford et al.* (2013) highlighted in filled coloured shapes. The red arrows offshore indicate the direction of plate motion. The shaded red area encompasses the >2000 volcanic centres identified by *Hildreth* (2007). The main evolved volcanic centres are shown as numbered white triangles with number 16 = Mount Mazama. The yellow box illustrates the extent of panel b. This figure was adapted from Figure 1 in *Hildreth* (2007). b) The southern Oregon segment of the Cascades showing Quaternary vents and Mount Mazama. Please see Figure 15 in *Hildreth* (2007) for the symbology key and full figure caption.

1.3.4 The Cascades Volcanic Arc and Mount Mazama (Crater Lake or Giiwas)

Throughout this thesis, when referring to locations in North America, I use the volcano and places names used by the United States Geological Survey (USGS). However, in this section, where possible I also refer to the original Native American names. For example, the Cascades range is also known as Yamakiasham Yaina (*Klemetti*, 2021). The Cascade Volcanic Arc, is the result of NE subduction of the Gorda and Juan de Fuca plates beneath the North American plate (Fig. 1.4a). The arc stretches from northern California, along the Pacific Northwest coast of the USA and into British Columbia, Canada. The Cascade arc has been magmatically active since the Eocene (~55 Ma, e.g., *Hooper et al.* 2002; *Ford et al.* 2013; *Wells and McCaffrey* 2013), but, here I focus on Quaternary (~2 Ma) volcanism. *Hildreth* (2007) identified over 2000 Quaternary volcanoes along the Cascades arc of which 22 are stratovolcanoes and calderas (Fig. 1.4a). The arc has erupted products that range from basalt to rhyolite, and the volcanic vents are located on (e.g., Crater Lake or Giiwas) and off the arc axis (e.g., Mount St. Helens or Lawetlat'la). In this thesis, I focus on the Mazama volcanic centre which is located at the north end of the Klamath graben, a mildly extensional tectonic environment at the west edge of the Basin and Range Province (Fig. 1.4b, *Bacon* 1983; *Bacon and Lanphere* 2006; *Hildreth* 2007).

Mount Mazama, was a ~3700 m high stratovolcano in the Cascade Range built primarily of successive andesite and dacite lavas (*Bacon*, 1983; *Bacon and Lanphere*, 2006). It is one of the most voluminous silicic volcanic centres in the Cascades arc, but interestingly there is an absence of pure rhyolite (>73 wt% SiO_2); rather rhyodacite (68 to 73 wt% SiO_2) is the dominant silicic eruptive product. Prior to the climactic eruption, four distinctive lava flows and associated tephras were erupted: the Redcloud (oldest), Grouse Hill, Llao Rock and the Cleetwood (youngest; Fig. 1.5). These units are now well exposed in the caldera walls and were precursors to the much larger caldera-forming eruption (Fig. 1.6; Bacon, 1983).

The climactic eruption of Mount Mazama occurred ~7.7 ka and formed modern day Crater Lake, also named Giiwas, Oregon, USA (Fig. 1.6). More than 60 km^3 Dense-Rock-Equivalent (DRE) of rhyodacite magma was erupted and tephra was deposited across >1 million km^2 of north-western North America (*Williams*, 1942; *Lidstrom*, 1971; *Bacon*, 1983; *Young*, 1990). Studies of the proximal (<100 km from source) eruption sequence has substantially advanced our understanding of caldera collapse and the evolution of complex magmatic systems (e.g., *Williams* 1942; *Williams and Goles* 1968; *Bacon* 1983; *Bacon and Druitt* 1988; *Druitt and Bacon* 1989; *Young* 1990; *Klug et al.* 2002; *Wright et al.* 2012; *Karlstrom et al.* 2015). The dominant tephra dispersal direction towards the east and north-east of the vent means that the widespread distal Mazama forms an important Holocene isochron across much of the north-western conterminous USA and Canada, which has aided correlation and dating of countless sedimentary sequences, archaeological finds and palaeoseismic events (e.g., *Cressman et al.* 1960; *Abella* 1988; *Long et al.* 1998; *Goldfinger et al.* 2012; *Oetelaar and Beaudoin* 2016). I compile records of the Mazama

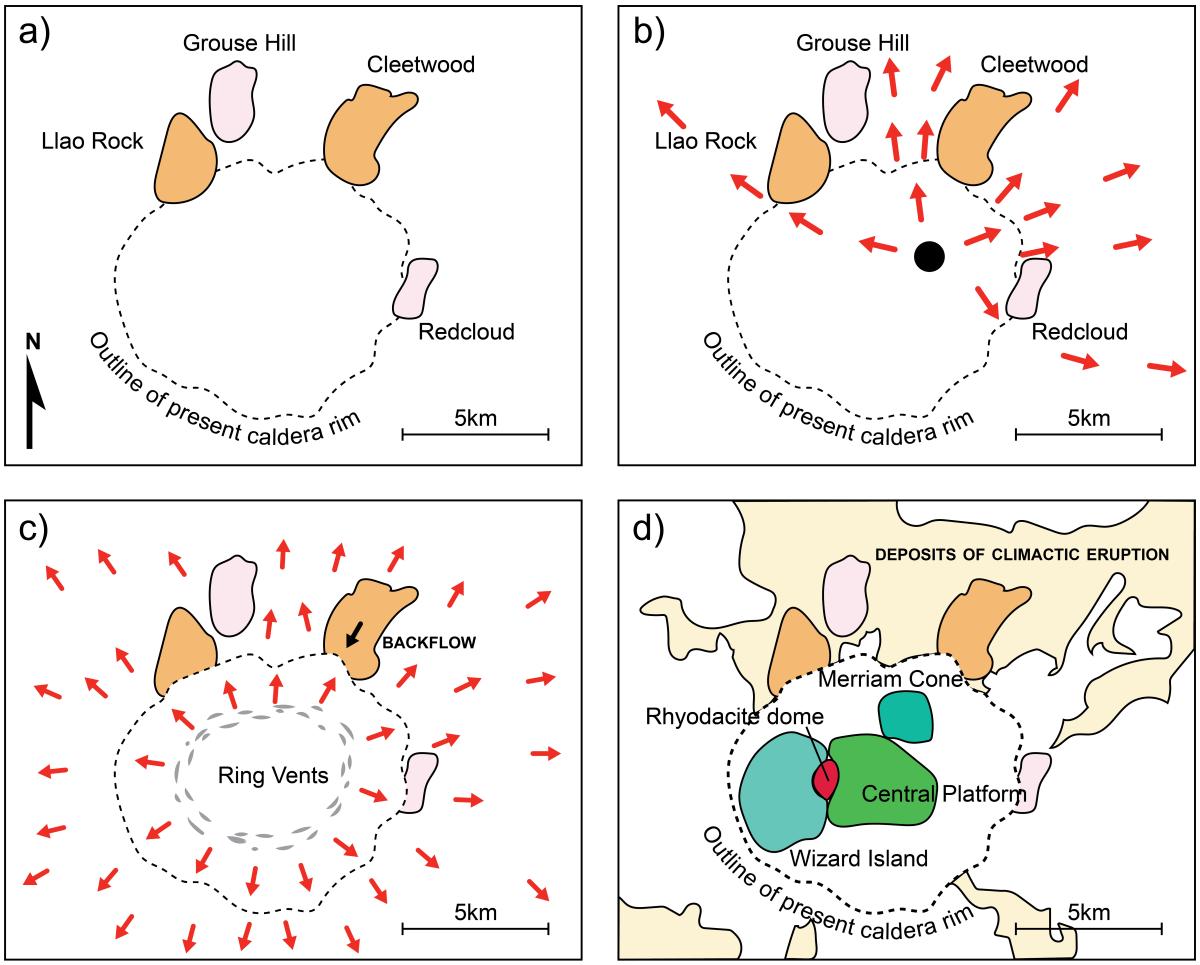

Figure 1.5: The eruptive history of Mount Mazama from the Pleistocene to present. a) Four prominent pre-climactic lava flows. b) The Plinian phase of the climactic eruption and c) the caldera collapse or ring-vent phase. Red arrows indicate the direction of the PDCs which were small and topographically confined in the Plinian phase (b) compared to the caldera collapse phase where PDCs surmounted topography and were erupted radially around the caldera (c). d) Pre-climactic eruptive activity confined to within the caldera walls. This figure has been adapted from *Bacon* (1983).

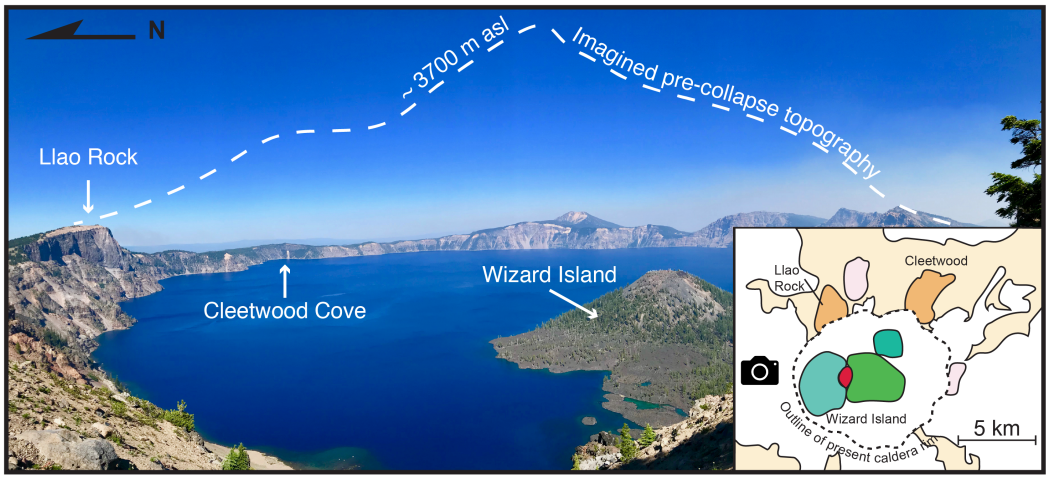

Figure 1.6: Photograph of Crater Lake caldera, also named Giiwas, with pre-climactic lava flows exposed in the caldera walls and post-climactic central cones. Inset panel shows the location where the photograph was taken.

tephra from these diverse sources in Chapter 2 and revisit estimates of the total eruptive volume taking into account sources of uncertainty in the field data and models used to estimate volume. The widespread subaerial tephra deposit also provides an excellent opportunity to validate the outputs of VATDMs against field observations which is the focus of Chapter 6.

The climactic Mazama eruption had two main eruptive phases (Fig. 1.5). Thick and well sorted fall deposits record an initial Plinian phase (*Williams*, 1942; *Bacon*, 1983; *Young*, 1990) that was followed by an ignimbrite forming phase and accompanying caldera collapse (*Bacon*, 1983; *Druitt and Bacon*, 1986). The latter phase produced a proximal lithic lag breccia and large (~16 km^3 DRE) PDCs that reached >70 km from source (*Williams*, 1942; *Druitt and Bacon*, 1986). Both phases erupted magma of similar composition except for the last pyroclastic density currents, which were more mafic (*Bacon*, 1983; *Druitt and Bacon*, 1989). I examine whether contributions from these phases can be differentiated in distal deposits in Chapter 3.

All eruptive activity at Mount Mazama since the climactic eruption has occurred within the caldera (Fig. 1.5). The interpretations of the deposits are the result of bathymetric data and sample dredging (*Bacon*, 1983). There are three distinguishable features: the Merriam Cone and Wizard Island which are broadly andesitic magmas, and the Central Platform, a collection of more silicic lavas with remnants of rhyodacite like the climactic eruption (Fig. 1.6; *Bacon and Druitt* 1988). There is no evidence of tephra from any post-caldera eruptions suggesting little to no explosive activity.

CHAPTER 2

SOURCES OF UNCERTAINTY IN THE MAZAMA ISOPACHS AND THE IMPLICATIONS FOR INTERPRETING DEPOSITS FROM LARGE MAGNITUDE ERUPTIONS

Buckland HM , Cashman KV, Engwell SL, Rust AC (2020) Sources of uncertainty in the Mazama isopachs and the implications for interpreting distal tephra deposits from large magnitude eruptions. *Bulletin of Volcanology* 82:23. https://doi.org/10.1007/s00445-020-1362-1

Author Contributions and declaration: H. Buckland carried out the data collection (literature review, fieldwork, particle size analysis) and analysis (GIS, spline fitted isopachs, volume calculations), and wrote the manuscript. Supervision and manuscript editing was provided by K. Cashman, A. Rust and S. Engwell. J. Egan and J. Westgate shared their databases of Mazama tephra localities with H. Buckland and similarly, C. Long, B.Jensen, M. Shapley and J. Oviatt shared their knowledge of Mazama tephra localities directly. Fieldwork was carried out with help from B. Carson, K. Nicolyasen, D. McKay and E. Gottesfeld. D. Pyle and S. Self provided useful reviews of the manuscript, which improved the final paper, and associate editor P.-S. Ross provided helpful copy-editing and manuscript handling.

Abstract

Estimating the area of tephra fallout and volume of large magnitude eruptions is fundamental to interpretations of the hazards posed by eruptions of this scale. This study uses the tephra from the caldera forming eruption of Mount Mazama (Crater Lake, Oregon, USA) to demonstrate the challenges faced when working with large prehistoric tephra deposits and outlines the methodologies required to determine eruption volume and Magnitude. We combine >250 Mazama tephra occurrences, reported by a range of disciplines (including archaeology, paleoclimatology and volcanology), with new field studies to better understand the extent of the distal tephra. We find that the Mazama tephra has been remobilised to varying degrees over the past 7000 years, so each tephra locality was appraised for the likelihood that it records primary tephra fallout. We designated 45 of the distal (>100 km from source) tephra sites as suitable for use in the production of isopachs using a spline fitting method. The new distal isopachs were then integrated with proximal fallout data and estimates of the ignimbrite volume from previous studies to revise the estimated bulk erupted volume from the climactic Mazama eruption to ~176 km^3 (~61 km^3 Dense-Rock Equivalent; DRE). This study demonstrates the importance of collating tephra localities from a range of disciplines and that even remobilised deposits, provide valuable information about the extent of the deposit. Interpreting remobilised deposits can provide insight into post-eruptive processes that could potentially pose secondary hazards following large magnitude eruptions. We also show that in some circumstances, remobilised deposits preserve important physical properties such as grain size.

2.1 Introduction

Large, caldera-forming eruptions pose a potentially devastating hazard to human populations and the environment. For example, the tephra generated by a Magnitude (M) 7 or greater eruption can be dispersed across millions of square kilometres, posing immediate and long-term hazards (e.g., Tambora, 1815; *Gertisser and Self*, 2015). In this Chapter, the term 'tephra' is used to refer only to fallout, deposits associated with PDCs (ignimbrites) are discussed separately. Deducing the nature and scale of the hazards from large eruptions is challenging as their long repose period means eruptions of this scale have not been observed in modern times. Therefore, we are reliant on tephra deposits from prehistoric eruptions to inform our interpretations. Past eruptions are typically studied by mapping the tephra deposit in terms of thickness and grain size, and then fitting the data using a range of models to approximate deposit extent, erupted volume, plume height and eruption Magnitude (e.g., *Carey and Sparks*, 1986; *Pyle*, 1989, 2000; *Bonadonna and Costa*, 2013). However, these methods often have limitations for large prehistoric eruptions that have dispersed fine ash over vast areas (e.g., *Biass and Bonadonna*, 2011; *Burden et al.*, 2013; *Engwell et al.*, 2013).

Estimating the volume of prehistoric eruptions is key to assessing the magnitude-frequency relationships which may provide insight into the driving forces of volcanism and inform future risk mitigation strategies (*Mason et al.*, 2004; *Self*, 2006; *Rougier et al.*, 2018; *Newhall et al.*, 2018). However, eruptive volume estimates of unobserved eruptions require detailed interpretations of tephra deposits (*Froggatt*, 1982; *Pyle*, 1989; *Fierstein and Nathenson*, 1992). This is challenging for large eruptions where the distal tephra is often deposited offshore (e.g., Tambora, 1815; *Kandlbauer and Sparks*, 2014) limiting our interpretive power unless an extensive offshore record is available to supplement the terrestrial record (e.g., the Campanian Ignimbrite tephra, 1815; *Engwell et al.*, 2014). Owing to its widespread, on-land distal tephra deposit (Fig. 2.1), the ~7.7 ka eruption of Mount Mazama in Oregon, USA, is an ideal, large (M > 7; *Crosweller et al.*, 2012, the LaMEVE database, VOLGRIPA; www.bgs.ac.uk/vogripa/view/controller.cfc?method=lamev) caldera forming eruption to study from this perspective (*Williams*, 1942; *Bacon*, 1983; *Young*, 1990). Pacific deep-sea cores only record the Mazama tephra in turbidite deposits, not as a primary layer, supporting predominantly on-land tephra deposition (Fig. 2.2, *Adams*, 1990). However, whilst the terrestrial Mazama tephra provides a unique opportunity to study a large prehistoric eruption, interpretation of the deposit is complicated by post-eruptive processes such as tephra remobilisation.

Remobilisation processes occur in the distal tephra deposits of large eruptions because of their wide spatial coverage and varied depositional environments. Tephra remobilisation is a secondary hazard acting over longer timescales than the primary hazards of the eruption. The remobilisation of tephra deposits is observed at a number of scales and can be initiated by fluvial, aeolian and

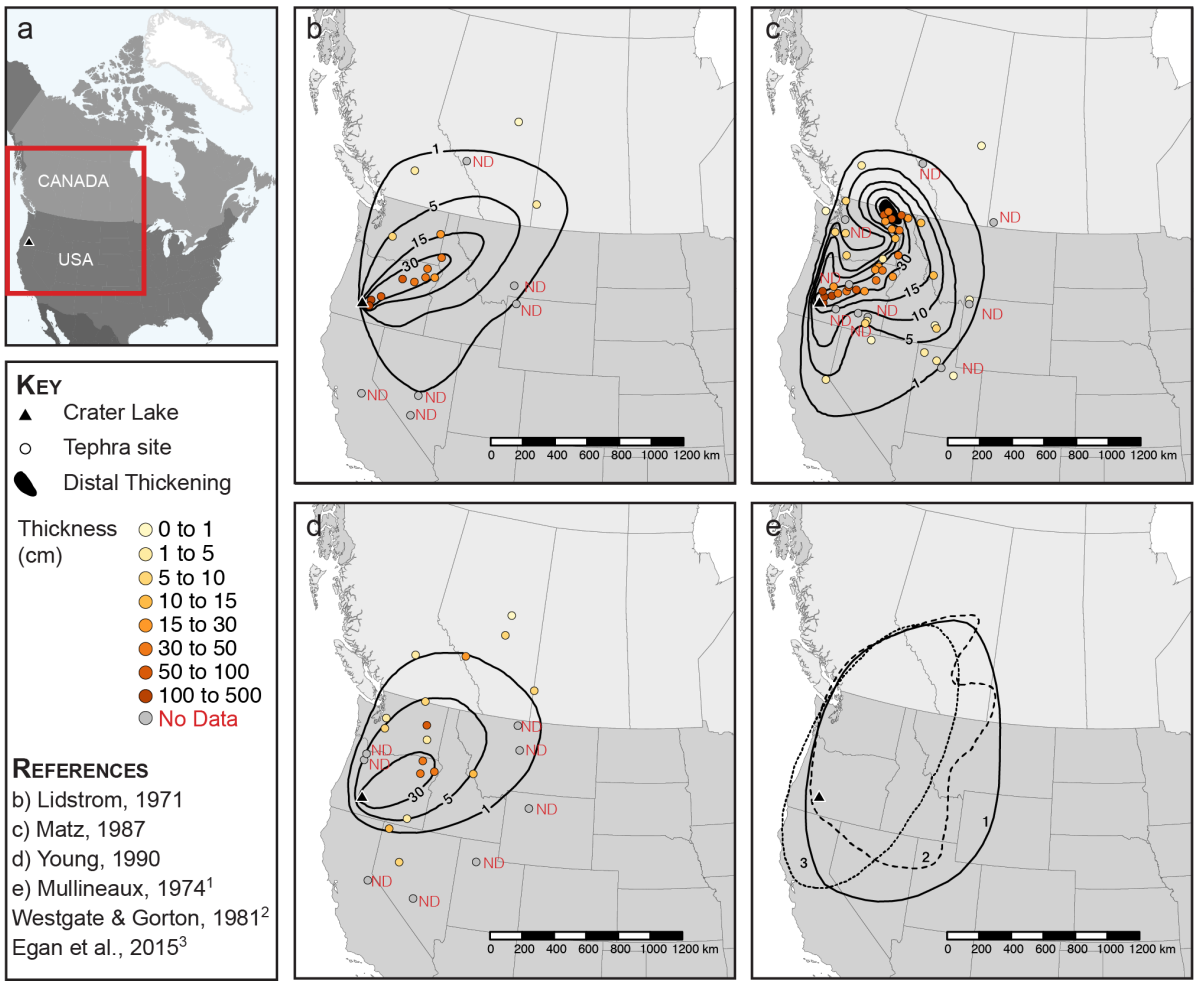

Figure 2.1: Compilation of Mazama isopach maps. a) Location map. Red rectangle outlines the extent of maps b-e. b). Isopach map from *Lidstrom* (1971), tephra thicknesses shown in centimetres. c) Isopach map from *Matz* (1987), with zone of 'Distal Thickening' in black. d) Isopach map by *Young* (1990). For the published isopachs (b-c) some thicknesses are not clearly stated in the relevant thesis and have been marked as 'ND'. e) Minimum extent maps of the Mazama tephra from 1. *Mullineaux* (1974), 2. *Westgate and Gorton* (1981) and 3. *Egan et al.* (2015).

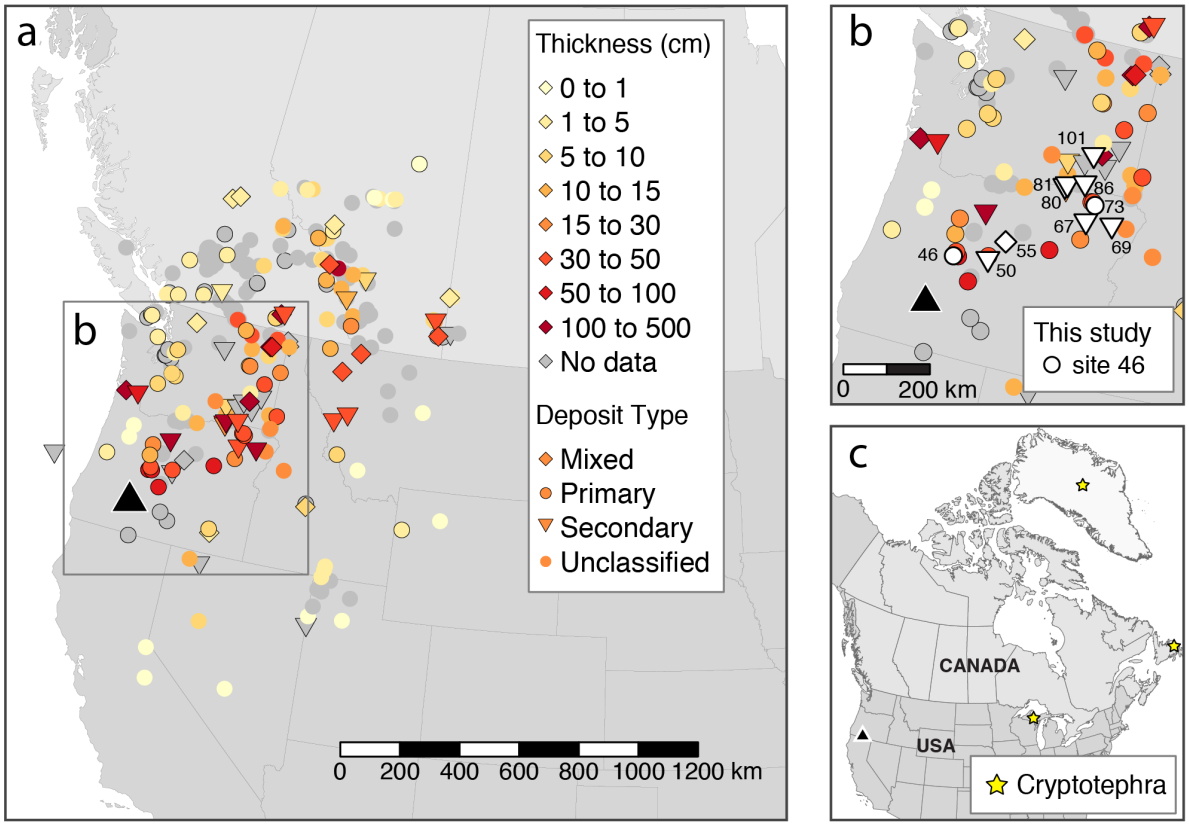

Figure 2.2: Distal Mazama tephra sites compiled for this study. a) Map of the western USA and Canada with sites of Mazama tephra >100 km from source. b) Inset map with field sites from this study highlighted in white symbols with the site number adjacent. c) Map of USA, Canada and Greenland with sites of Mazama cryptotephra (*Hammer et al.*, 1980; *Zdanowicz et al.*, 1999; *Pyne-O'Donnell et al.*, 2012; *Spano et al.*, 2017)

gravitational processes. Documenting and studying sites where these processes are observed is key to enhancing our understanding of the processes and resulting hazards (*Manville et al.*, 2000; *Hadley et al.*, 2004; *Lowe*, 2011; *Gatti et al.*, 2013; *Shapley and Finney*, 2015). For example, in the Younger Toba Tuff (YTT, M ~9.1) tephra there is evidence of fluvial reworking and slumping at a number of distal sites in Malaysia and India >350 km from source which altered the thickness and grain size (*Gatti et al.*, 2011, 2013). Here we combine new field data with the extensive published data available for the distal Mazama tephra to better constrain the deposit extent and erupted volume. We identify and account for post-eruptive processes before producing new isopach maps and eruptive volume estimates.

2.2 Background

2.2.1 The Mazama tephra

During the Holocene, the climactic eruption of Mount Mazama formed modern day Crater Lake in Oregon, USA (see section 1.3.4; *Bacon*, 1983; *Bacon and Druitt*, 1988; *Bacon and Lanphere*, 2006). The eruption began with an increasingly violent Plinian phase before the onset of caldera collapse that produced large volume PDCs (*Williams*, 1942; *Bacon*, 1983; *Young*, 1990). The tephra from the climactic eruption is found as a visible layer across the western USA and Canada and as cryptotephra (a non-visible tephra layer) in Greenland (*Hammer et al.*, 1980; *Zdanowicz et al.*, 1999), Newfoundland (*Pyne-O'Donnell et al.*, 2012), and the Great Lakes (*Spano et al.*, 2017, Fig.2.2c). Despite the extensive record of Mazama tephra and the importance of the tephra layers as an isochron, considerable uncertainty remains about the thickness distribution of the deposit.

Isopach maps are the most common way to represent the thickness of a tephra deposit and calculate erupted volume (*Pyle*, 1989; *Fierstein and Nathenson*, 1992; *Bonadonna et al.*, 1998). However, constructing isopachs is challenging when there is insufficient and unreliable field data (*Engwell et al.*, 2013). Therefore, for prehistoric eruptions such as the Mazama, the isopach maps contain a high degree of often unquantified uncertainty (*Engwell et al.*, 2015), the effect of which is amplified when isopachs are hand drawn (*Klawonn et al.*, 2014). The hand-drawn isopachs of the distal Mazama tephra in Figure 2.1 demonstrate considerable variability reflecting the subjective interpretation by each of the authors. Additionally, all the isopach maps (Fig. 2.1) use a relatively small number of ash thickness measurements (less than 55) to reconstruct the deposit over an area that is >1 million km^2, equivalent to ~1 measurement per 20 000 km^2 (*Lidstrom*, 1971; *Matz*, 1987; *Young*, 1990).

The challenges of interpreting the distal Mazama tephra have long been recognised and as a result, the better-preserved deposits closer to source have been favoured for mapping and compositional studies (*Williams*, 1942; *Young*, 1990). In this Chapter, we define distal as >100 km from source and proximal as ≤100 km from the volcano. Mapping of the Plinian fall deposit by *Williams* (1942), *Lidstrom* (1971) and *Young* (1990) produced a high density of proximal tephra localities. Two distinct units were identified within the fall deposit, which is then capped by a fine ash layer, interpreted to be of co-PDC (also known as co-ignimbrite) origin (Fig.2.3a *Young*, 1990). Here we integrate the proximal data collected by *Young* (1990) with previously reported and new distal localities to enhance our understanding of the primary tephra transport and deposition. Assimilating data sets from multiple disciplines, such as archaeology, paleoclimatology and volcanology, requires an assessment of data quality and compatibility (see *Lowe*, 2011). For example, a paleoclimate study may only require that the tephra layer be identified for dating purposes and will therefore record limited physical information such as thickness (*Heusser*, 1974). However, the observation that distal tephra exists at a given location, even without further

Table 2.1: Erupted volume estimates from the literature.

Reference	Volume estimate of caldera and Mount Mazama (km^3)	Bulk volume estimate (km^3)	Method used to calculate bulk volume	Ignimbrite included	DRE volume estimate (km^3)
Williams (1942)	71	44	Estimated from the thickness of deposits within 100 km from source	Y	27
Williams and Goles (1968)	62	55-71	Exponential fit to plot of thickness versus distance with 3 distal thicknesses	Y	42
Lidstrom (1971)	-	100-125[b]	Volume of arcuate segments distal isopachs (Fig.2.1b)	N	57-64
Bacon (1983)[a]	46-58	120	-	-	51-9
Druitt and Bacon (1986)[a]	-	-	-	-	47±7
Young (1990)	-	122	Exponential fit to log thickness versus square root area plot using proximal and distal isopachs (Fig.2.1d)	N	45
Machida (2002)[a]	-	78	-	-	-
Bacon and Lanphere (2006)	112	-	-	-	50
Geyer and Martí (2008)[a]	50-60	-	-	-	42
Johnston et al. (2014)[a]	-	153	-	-	~75
LaMEVE (2019)[a]	-	120	-	-	50

(a) Method of volume estimation not stated, they are only in text values

(b) This value was estimated for the volume >100 km from source

details, is useful information.

2.2.2 The volume of the Mazama eruption

The challenge of quantifying the volume of the climactic Mazama eruption has been approached in a number of ways and has produced a range of volume estimates (Table 2.1). Some of the first estimates of DRE volume were based on the volume of the caldera and reconstructed edifice. For example, *Williams* (1942) used the caldera depth to calculate an approximate caldera volume of ~50 km^3. Adding this to the assumed ~30 km^3 edifice, Williams estimated that >70 km^3 of material must have been ejected or removed by the climactic eruption. *Williams and Goles* (1968) and later *Bacon* (1983) revised those estimates to ~60 km^3. However, more recently *Bacon and Lanphere* (2006) reconstructed the Mount Mazama edifice and estimated a volume of ~112 km^3. They attribute the discrepancy between the edifice and erupted volume to an

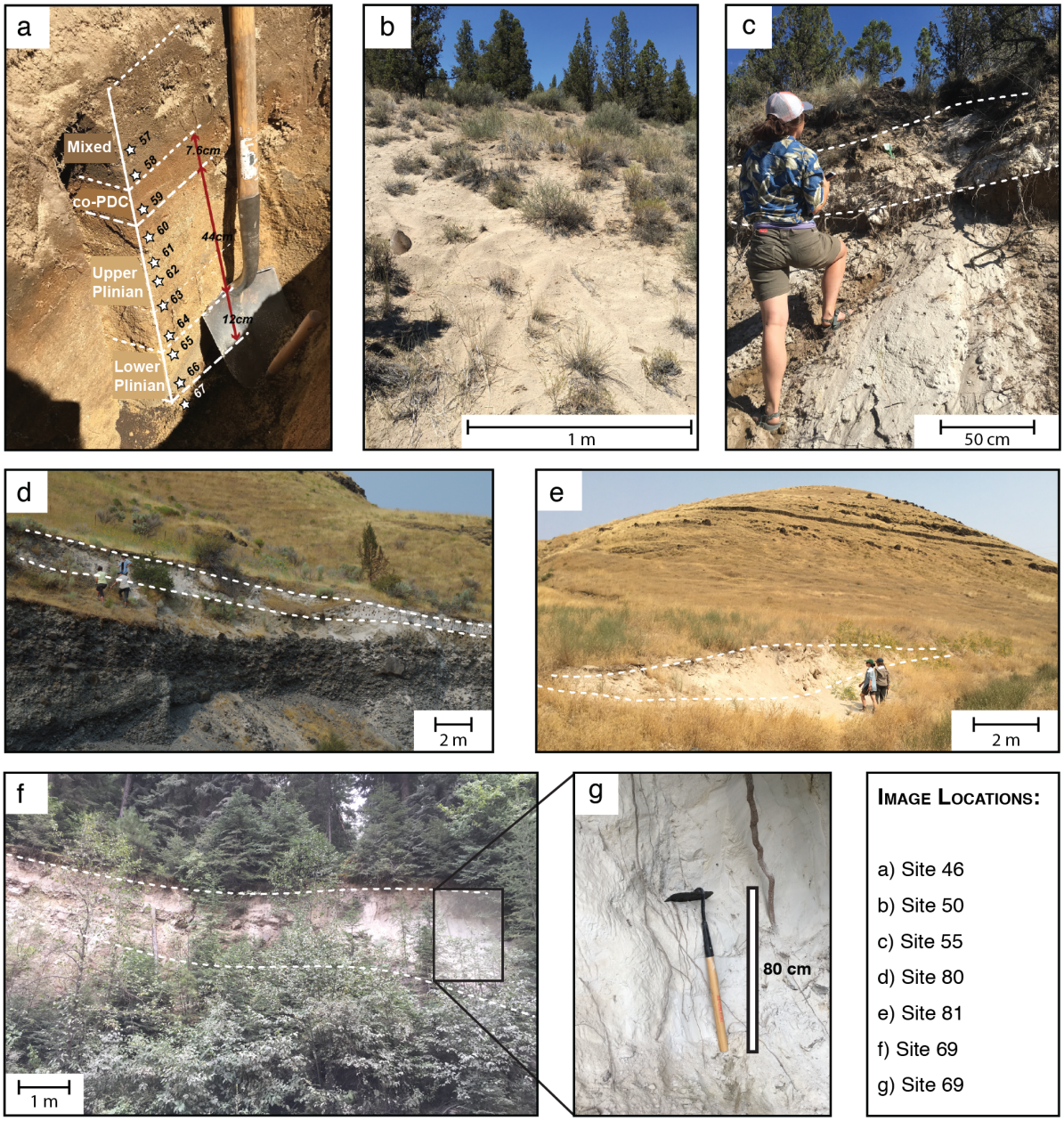

Figure 2.3: Field photographs of selected sites described in this Chapter. a) Tephra pit at Mount Bachelor (site 46). Star symbols reflect sampling sites. The tephra sequence records the climactic pumice fall and an upper fine-grained unit which has been interpreted as fine fallout associated with the ignimbrite phase (co-PDC ash). The top mixed layer was dominantly soil but contained occasional pumice clasts. b) Mazama tephra reworked at the surface near Prineville reservoir (site 50). c) A reversely graded, discontinuous layer of Mazama tephra near Mitchell, Oregon (site 55). d) 70cm thick layer of Mazama tephra at Juniper Canyon (site 80) on top of alluvial fan deposits. e) Dune like discontinuous deposit of Mazama tephra at Spring Gulch (site 81). f) 3m lens of remobilised Mazama tephra at Pole Bridge on top of alluvial deposits (site 69). g) Zoom on remobilised Mazama at site 69 showing absence of sedimentary structures

incomplete knowledge of the collapse deposits in the caldera and the additional volume erupted by pre-climactic eruptions such as the Llao Rock and Cleetwood eruptions (*Bacon and Lanphere*, 2006).

To estimate the bulk volume of the Mazama tephra deposit, multiple authors have used tephra thickness data (*Williams*, 1942; *Williams and Goles*, 1968; *Lidstrom*, 1971; *Young*, 1990, Table 2.1). *Williams* (1942) first estimate of ~15 km^3 was based on the thickness of the proximal fall deposit (<100 km from source). The estimate was revised by *Williams and Goles* (1968) who included three distal thickness measurements which increased the estimate by ~30 km^3 (Table 2.1). The first estimate that used distal isopachs was ~120 km^3 by *Lidstrom* (1971, Fig. 2.1b). Using different isopachs, and incorporating the thick proximal fallout, *Young* (1990, Fig.2.1d) also calculated a volume of ~120 km^3. However, we would expect a discrepancy between these estimates because *Lidstrom* (1971) did not include the proximal fallout. This highlights the inconsistencies in volume estimates made from different isopach data (Fig. 2.1).

Converting the bulk erupted volume to a DRE volume requires assumptions of deposit density, which in turn depends on packing density and the vesicularity and composition of the clasts. The conversion to DRE volumes for deposits such as the Mazama tephra are complicated further by variations in the deposits. The Mazama tephra is composed of pumice, lithics and crystals, which have unique densities, morphologies and vesicularites, and the proportion of each component changes throughout the eruption (*Lidstrom*, 1971; *Bacon and Druitt*, 1988; *Young*, 1990). The degree of deposit compaction also changes with grain size, depositional environment and time since deposition (*Lidstrom*, 1971). These caveats for DRE calculations may explain some of the variability in DRE estimates found in Table 2.1.

Another source of variability in the bulk deposit volume estimates relates to the inclusion or exclusion of the ignimbrite volume (Table 2.1). Early work by *Williams* (1942) mapped the extent of the ignimbrite ("glowing avalanches") and estimated a bulk ignimbrite volume ~29 km^3, which he included in his bulk erupted volume (total ~44 km^3). More recent estimates of total erupted volume, by *Young* (1990), consider only the Plinian fall and distal tephra, or they are unclear as to whether the ignimbrite volume has been included (*Bacon and Lanphere*, 2006; *Johnston et al.*, 2014). It is likely that a significant proportion (>10%) of the total erupted volume is contained in the ignimbrite, as flows reached over 70 km from source and are >80 m thick around the caldera (*Williams*, 1942). For this reason, the inclusion of this volume is important when calculating eruption Magnitude (M).

2.2.3 Tephra remobilisation

A major challenge of using tephra layers to understand prehistoric eruptions is recognising modifications that occurred after the initial deposition. Processes that can remobilise primary

tephra range from small scale bioturbation (*Griggs et al.*, 2015), local slumping and grain flow down slopes (*Boygle*, 1999); to large scale debris flows (*Manville et al.*, 2000) and resuspension by surface winds (*Wilson et al.*, 2011). Even if a tephra layer is not remobilised, varied depositional settings lead to differential preservation and compaction that result in variations in the tephra thickness preserved (*Blong et al.*, 2017). The effectiveness of transferring a tephra deposit to the stratigraphic record will depend on the background sedimentation, vegetation cover and slope angle (*Cutler et al.*, 2018; *Dugmore et al.*, 2018). For this reason, peat bogs and lakes are often favoured depositional settings for studying tephra stratigraphy (*Watson et al.*, 2016; *McNamara et al.*, 2019). The Mazama tephra is recorded in peat bogs (*Harward and Youngberg*, 1969) and lakes (*Long et al.*, 2014), but also in dry land sections (*Young*, 1990, *this study*) and aeolian sediments (*Sweeney et al.*, 2005). This means that each tephra locality will have experienced different preservation mechanisms and compaction, as well as being exposed to a variety of remobilisation processes. Furthermore, the effectiveness of preservation and remobilisation processes vary with the physical tephra properties (thickness, grain size, density; *Cutler et al.*, 2018; *Dugmore et al.*, 2018).

2.3 Methods

We implemented a variety of methods to constrain the distribution of the Mazama tephra and estimate the total bulk erupted volume. We compiled a database of distal tephra localities containing data from multi-disciplinary sources and new field sites. Each tephra locality was assessed for evidence of tephra mobilisation based on information in the original publication, field observation or what is implied for the location in relation to surrounding topography. Finally, we used thickness data from the newly optimised locality database to generate a reproducible isopach map using a cubic B-spline method. The new isopachs were then used for erupted volume calculations.

2.3.1 Compiling Mazama tephra localities

We have amalgamated and extended several existing databases of Mazama tephra localities to produce a single database that records >250 occurrences of Mazama tephra (*Lidstrom*, 1971; *Matz*, 1987; *Young*, 1990; *Hallett et al.*, 1997; *Egan et al.*, 2015; *Jensen et al.*, 2019, *J A Westgate*, pers. commun.). The database records physical information about the tephra layer at each locality, which complements that of *Egan et al.* (2015), whose focus was radiocarbon dating. The information used was gathered from scientific literature, Masters and PhD theses, geological maps and field guides, as well as new field sites outlined in this Chapter. The coordinates, locality name, reference(s), sampling method and research discipline of the original paper are provided for each locality. Where available, the thickness, grain size and the degree of remobilisation are reported with the accompanying metadata. If separate studies report different thicknesses at

the same locality, an average thickness is used. Similarly, if an author 'corrected' the thickness without explaining the rationale or method, the original thickness is used rather than the corrected value (*Matz*, 1987). Key field observations are included for terrestrial sites and for lake core localities, the depth of the tephra in the core is reported. If multiple cores were taken from the same site, only one locality is entered into the database, but the number of cores at each locality and any variability in thickness and grain size is documented in the metadata.

2.3.2 New field localities

This study includes new observations from ten field localities (all >100 km from source; Appendix A.1). The Mount Bachelor locality (site 46; Fig. 2.2b) is approximately equivalent to a site mapped by *Young* (1990). The site required a tephra pit 1.5 m deep to expose the Mazama tephra stratigraphy (Fig.2.3a). The total thickness and thickness of different horizons were measured, and samples were taken in 5 cm intervals from the top down. The stratigraphy was split according to the units in *Young* (1990) with a lower and upper pumice unit and final fine co-PDC ash.

At the Prineville Reservoir locality (site 50; Fig. 2.2b) the Mazama tephra had been reworked at the surface (Fig. 2.3b). This area was targeted based on previous studies (*Harward and Youngberg*, 1969; *Lidstrom*, 1971) that recorded Mazama ash in the area but provided no measurements of thickness or grain size. The Mazama tephra at the Mitchell locality (site 55; Fig.2.2b) outcrops as a discontinuous layer which is interpreted as evidence of remobilisation (Fig. 2.3c). However, the presence of reverse grading in places may reflect the original stratigraphy.

We also examined seven sites >450 km from Crater Lake (Fig. 2.2b). Some localities were previously documented in field guides (*Carson and Pogue*, 1996) and Quaternary studies of the region (*Waitt*, 1980). The sample sites were typically from riverbank, valley cut and roadcut exposures that required little excavation (Fig. 2.3d-g). No stratigraphic horizons could be identified in these deposits; therefore, only the total thickness was measured, and bulk samples taken.

The Grain Size Distributions (GSDs) of the tephra from the new field sites were measured by dry sieving from -3 ϕ to 3 ϕ (8 mm to 125 µm) in half ϕ intervals. The fine material was then measured using the Mastersizer 3000™ by Malvern Instruments Ltd in the School of Geographical Sciences at the University of Bristol. We recombined the 3 ϕ sieve fraction with the fine material (< 125 µm) prior to laser diffraction so the two methods of measuring grain size can be combined using the overlap in the 3 ϕ fraction (*Eychenne et al.*, 2012; *McNamara et al.*, 2018). For sites >450 km from source, only laser diffraction was required due to the fine grain size. The grain size statistics - mode, median (Md), sorting (σ), skewness (Sk) and kurtosis (K) - were calculated using GRADISTAT (*Folk and Ward*, 1957; *Blott and Pye*, 2001).

2.3.3 Interpolated isopachs

We used a method of spline interpolation to interpret the thickness data collated in the database. Following the method outlined in *Engwell et al.* (2015), a cubic B-spline under tension was used to fit a model surface to the log thickness data (*Inoue*, 1986, Appendix A.4). The FORTRAN code, developed by *Inoue* (1986) and modified by *Engwell et al.* (2015), outputs a gridded dataset across a specified x-y domain. This dataset was then processed in R using the 'raster', 'ggplot2' and 'rgdal' packages to produce contoured plots of thickness (isopach maps).

2.3.4 Erupted volume calculations

From the spline fitted isopachs, the volume of distal Mazama tephra deposit was determined by fitting an exponential thickness decay to a plot of thickness versus square root isopach area (*Pyle*, 1989). The same method was applied to previously published isopachs for comparison (Fig. 2.1).

The resulting log thickness versus square root area data was fit using 'AshCalc', a python tool for calculating erupted volumes (*Daggitt et al.*, 2014). The exponential model assumes that tephra thickness can be described as a simple exponential decay away from the point of maximum thickness (*Pyle*, 1989). For large and/or complex deposits, this exponential relationship breaks down and typically log thickness versus square root area plots are better described by multi-segment exponential decays (*Pyle*, 1989; *Fierstein and Nathenson*, 1992). In this work, we combine the distal isopachs with the spline isopachs of the proximal data (*Young*, 1990) and fit multi-segment exponential decays using 'AshCalc' (*Daggitt et al.*, 2014).

2.4 Results

The information amassed for each Mazama tephra locality and new field site is available in the database of tephra localities (see Appendix A.1, Table A.1). The map in Figure 2.2 shows all distal (>100 km) localities in the database. Each thickness measurement has been classed as either 'primary', 'secondary' or 'mixed' based on the information available in the original reference, field observations and drainage analysis. Where there was no description or insufficient data, the locality was left as 'unclassified'.

2.4.1 Identifying remobilisation

Thicknesses were classified as 'primary' where the measured thickness likely records the initial tephra thickness immediately after deposition. For example, site 46 (Fig. 2.3a) has been confidently classified as primary due to the well-preserved internal stratigraphy and topsoil development. Another primary site visited, site 73, preserves 30 cm of fine Mazama tephra with a sharp basal contact and well-developed topsoil. The locality is situated on a major drainage divide between the Snake River to the east and the John Day and Columbia Rivers to the west;

therefore we infer that the deposit at this site provides a minimum estimate of the primary fall deposit thickness, as no tephra has been remobilised from upslope (see Appendix A.3).

Thicknesses are considered 'secondary' if there is evidence for remobilisation such as slumping or bioturbation. An example from the literature is the 30 cm of Mazama tephra at site 174, Rockslide Lake in British Columbia, which contains multiple layers of Mazama tephra and has surrounding radiocarbon dates considerably younger than the eruptive date (*Foit et al.*, 2004). A number of the sites are classed as secondary based on their field characteristics (Fig. 2.3b-g). Observations at site 80 (Fig. 2.3d) suggest that the 70 cm of the Mazama tephra overlying alluvial deposits has been remobilised (*Sweeney et al.*, 2005, *this study*). Similarly, site 69 (Fig. 2.3f) records >3 m of overthickened Mazama tephra (*Carson and Pogue*, 1996, *this study*). Analysis of the upstream drainage (Appendix A.3) shows that, unlike site 73, there is substantial upstream drainage area for sites 69 and 80 which likely explains the overthickening.

'Mixed' thickness localities include both primary and secondary ash deposits. For example, the Mazama tephra at site 230 along the South Saskatchewan River has a sharp basal contact but is overlain by remobilised tephra that grades into the overlying sediment, which was included in the thickness reported (*David*, 1970). Some sites where no thickness has been recorded were still classified based on the description of the stratigraphy.

Plotting log thickness against distance from source (Fig. 2.4) highlights the anomalous thickness values that have been classed as secondary and mixed. Typically, non-primary deposits tend to be thicker than the primary deposits at the same distance from source. The scatter in the thickness measurements with distance also reflects the scarcity of measurements that are on-axis, particularly >500 km from source.

The GSDs of the ash samples collected for this study (Fig. 2.5) show that all the ash analysed from sites >450 km from source is finer than 1 mm. All the samples display a unimodal distribution with a mode between 38 and 54 μm (4.8–4.3 ϕ) and median (Md) grain size of 33–49 μm (4.9–4.4 ϕ). The sorting (σ) of all samples is ~1.5 and the distributions are fine (negatively) skewed. The coarsest sample, with a median grain size of 49 μm, is from site 101 where the tephra had been excavated by a badger, which likely caused the fines to be lofted away explaining the fines depletion. The GSD from site 73, a primary tephra locality, overlaps with all other (remobilised) deposits.

2.4.2 Cubic B-spline isopachs

The cubic B-spline method was applied to the primary thickness data (n=45, where n is the number of measurements; Fig. 2.6a). Visually, the isopachs generated for the modelled thickness surface are similar to the published isopachs in terms of the dominant dispersal direction (Figs.

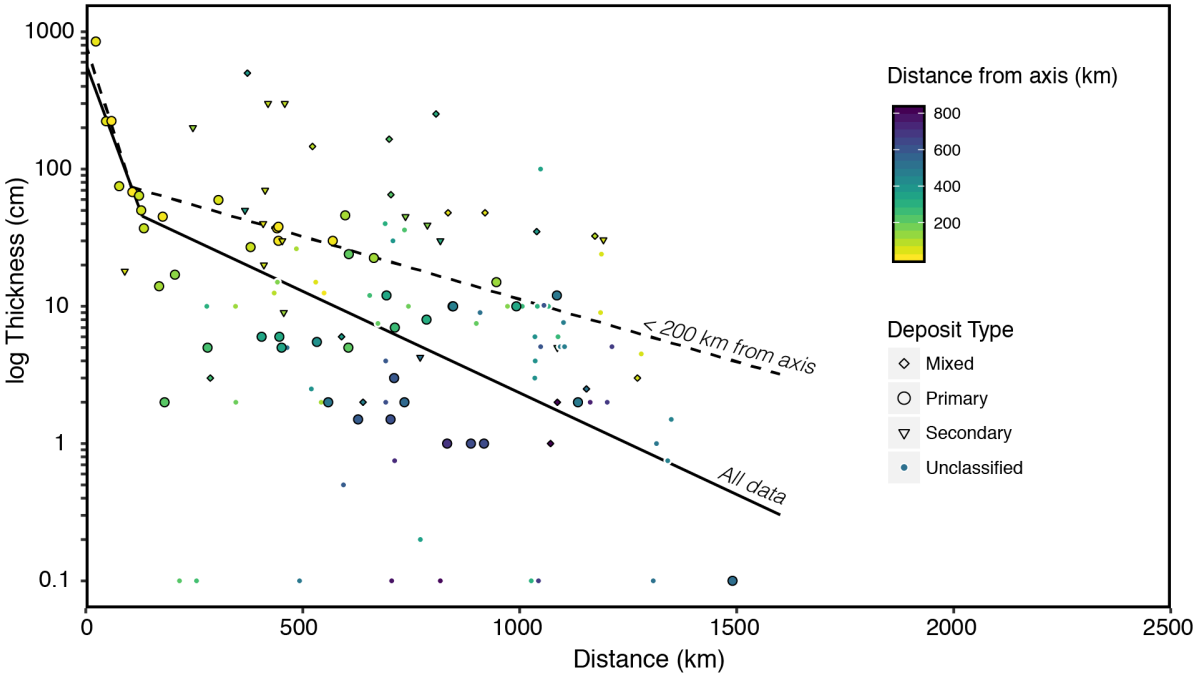

Figure 2.4: Log tephra thickness (cm) versus true distance from source (km). The solid line is a two-segment exponential fit to all the primary data and the dashed line is a two-segment fit to primary data <200 km off-axis.

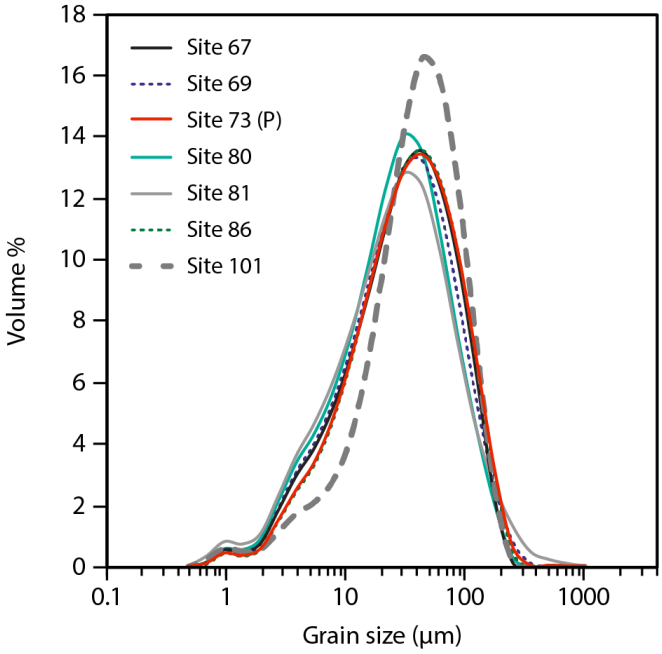

Figure 2.5: Grain Size Distribution of distal samples. Site 73 (red) is the only primary (not remobilised) sample.

2.1 & 2.6), as forced by the inferred upwind thicknesses (Appendix A.4). However, even with the (inferred) upwind thicknesses, the spline isopachs do not match the tightness of the published upwind isopachs. Based on the lack of real upwind thickness data (SE of Crater Lake), we cannot assess whether the spline or published isopachs best represent the decay of thickness with distance in the upwind direction. Another difference between the spline and published isopachs is the extent and value of the thickest isopach. Specifically, the published isopachs show 30 cm of tephra reaching ~500 km downwind (Fig. 2.1b-d), but this is not reflected in the cubic B-spline isopachs (Fig. 2.6a). The spline isopach that best matches the published 30cm isopachs is 20 cm thick. Whilst there are some important differences between the published and spline isopachs, the overall shape agrees with *Lidstrom* (1971) and *Young* (1990). In particular, along the main dispersal axis the extent of the 5 cm isopach is in close agreement.

The cubic B-spline method was also applied to all the thickness data (n=138) recorded in the database (Fig. 2.6b), including thickness measurements that have been classed as secondary, mixed and unclassified. The resulting isopachs record a more complex and convolute distribution of tephra thickness. In particular, the spline isopachs highlight an area of overthickening in north-eastern Washington, which broadly overlaps with the area designated as 'distal thickening' by *Matz* (1987). Another key difference between the published and spline isopachs is the 1 cm isopach. All of the published isopach maps include a 1 cm limit. However, the spline interpolation method had insufficient data to draw a closed contour of 1 cm.

The cubic B-spline isopachs of the proximal data from *Young* (1990) are shown in Figure 2.6c. The overall distribution of thickness is close to his hand-drawn isopachs, although, as with the distal spline isopachs, the upwind decay of thickness is much tighter in the hand-drawn isopachs. A south-east lobe in the cubic spline isopachs (Fig. 2.6c) corresponds to a mapped SE lobe in the lower pumice unit of the Plinian fall that was observed and interpreted by *Williams* (1942), *Lidstrom* (1971) and *Young* (1990) to correspond to a different wind direction and or plume height at the onset of the eruption.

The goodness of fit of the spline surface to the thickness data is output as a Root Mean Squares (RMS) residual (see Table 2.2). Although the RMS value quantifies the fit of the whole spline surface, we are interested in the difference between the modelled and measured thicknesses at individual localities. To assess this difference, we calculate a percentage error between the measured thickness and modelled thickness at each locality:

$$\%\ error = \frac{|modelled\ thickness - measured\ thickness|}{(modelled\ thickness)} \times 100 \tag{2.1}$$

Importantly, in equation 2.1 we divide the absolute difference by the modelled thickness because we want to highlight localities where the measured value deviates strongly from the spline

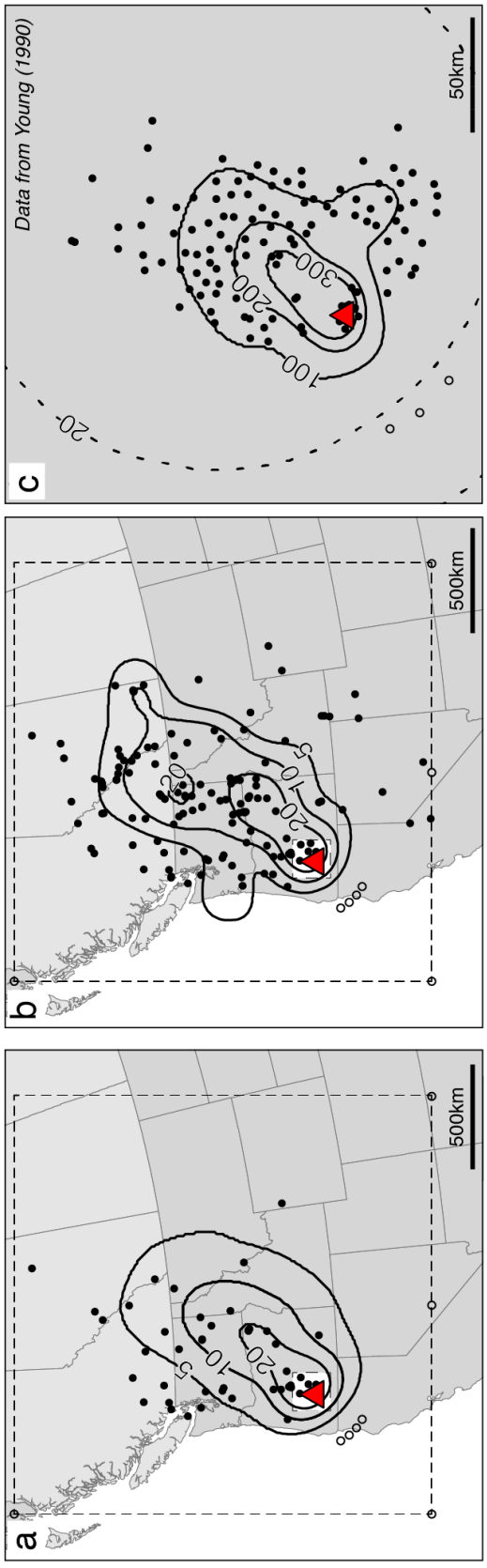

Figure 2.6: Cubic B-spline isopachs. The thickness measurements used to generate each isopach are shown as filled black circles, the inferred thicknesses are plotted as open circles and the isopach thickness is in cm. a) Primary thickness data and spline isopachs. b) All thickness data and (mixed) spline isopachs. c) Spline isopachs of proximal *Young* (1990) data. In a & b the domain over which the spline interpolation was performed is shown by the dashed box and the proximal domain is a filled white square.

Table 2.2: Calculated volumes from spline and published isopachs.

Isopachs	Number of measurements (n)	Number of distal isopachs (thicknesses in cm)	Distal volume only (km^3)[a]	RMS residual of spline fit	One-segment fit volume (km^3)[b]	Two-segment fit volume (km^3)[b]	Three-segment fit volume ($km3^3$)[b]
Primary spline	45	3 (5, 10, 20)	134	0.417	163	148	163
Mixed spline	138	3 (5, 10, 20)	161	0.542	202	172	183
Lidstrom (1971)	20	4 (1, 5, 15, 30)	153	-	227	163	170
Young (1990)	25	3 (1, 5, 30)	131	-	195	139	144
Matz (1987)	54	5 (1, 5, 10, 15, 30)	242	-	336	252	249

(a) Using only distal isopach data.
(b) Combining distal and proximal (*Young*, 1990) isopach data.

predicted value. We expect the spline surface to poorly match thick proximal sites due to the majority of the data fitted with the cubic B-splines being thinner distal data. For example, at a proximal locality (site 26) the measured tephra thickness is 233 cm, but the spline surface predicts 38 cm which we calculate as a 486% error. Whilst the fit appears poor to these few proximal sites, they were necessary to include in the fitting of the cubic B-spline model to locate the area of maximum thickness (Fig. 2.7a). For the mixed spline isopachs (Fig. 2.7b) the RMS residual and number of points with >400% difference between the spline and measured thickness is greater than in Figure 2.7a because the spline fitting has smoothed highly irregular data. Comparing the measured thicknesses of secondary and mixed sites to the primary spline surface (Fig. 2.7c) clearly highlights areas of overthickening (secondary and mixed deposits), where the percentage difference is typically >400%. Comparing the unclassified thicknesses to the primary spline surface (Fig. 2.7d) shows that 43 unclassified thicknesses are within 100% of the value predicted by the spline surface.

2.4.3 Volume calculations

The volume of the distal Mazama tephra calculated from the individual isopach maps in Figures 2.1 and 2.6 are shown in Table 2.2. For Figure 2.6b, the total area enclosed by the thickest isopach

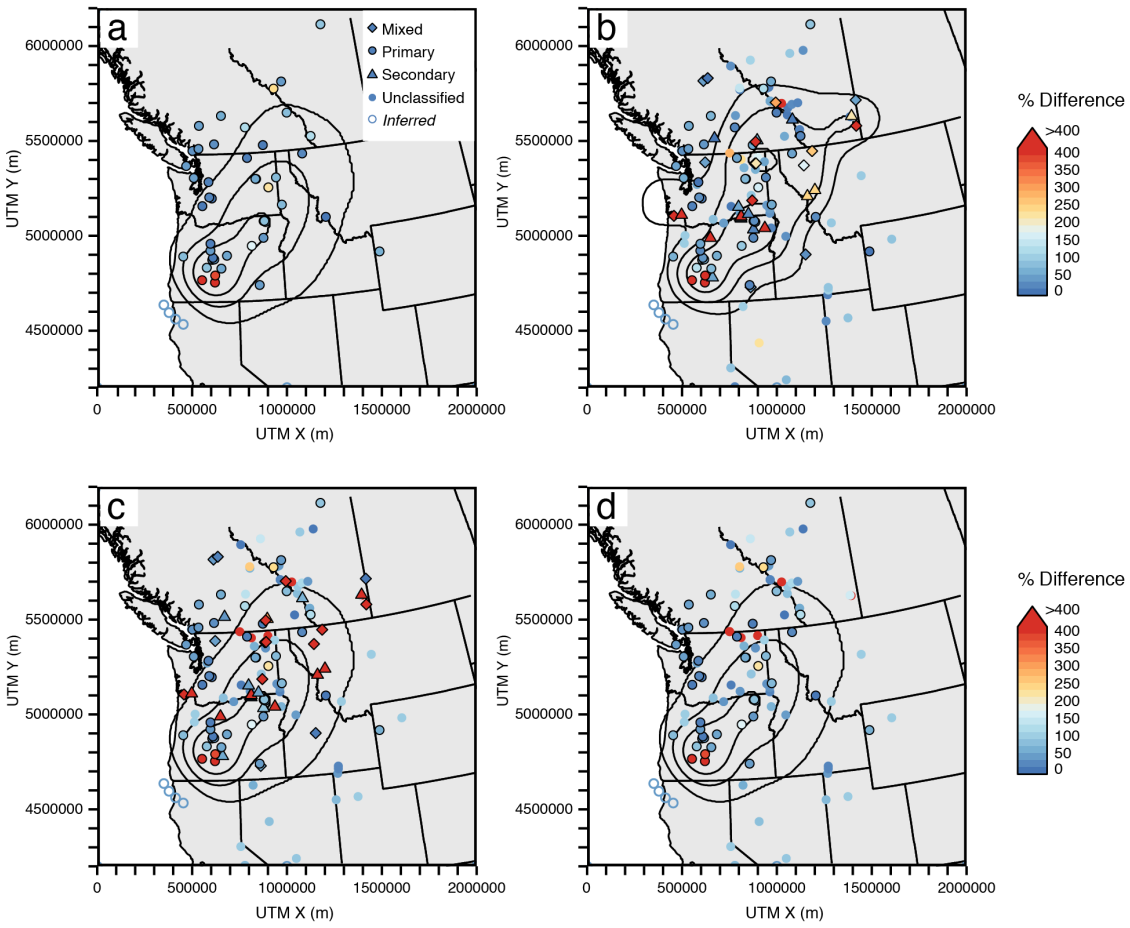

Figure 2.7: Percentage difference between the actual thickness measurements and the spline interpolated thicknesses. Isopach thicknesses are 20, 10 and 5cm. a) Primary thickness only; b) Mixed spline thicknesses; c) Difference between mixed thicknesses and primary spline surface; d) Difference between primary and unclassified thicknesses and primary spline surface.

is the summation of the areas enclosed by the two closed 20 cm contours. The volumes calculated from the primary and mixed spline isopachs are 134 km^3 and 161 km^3 respectively. The mixed spline isopachs thus suggest a ~30 km^3 increase in volume compared to the isopachs drawn using only the primary data. The largest calculated volume is 242 km^3, which includes the isopachs that show a zone of distal thickening and a large 1 cm isopach (Fig.2.1c, *Matz*, 1987). The smallest volume (131 km^3) was calculated from the distal *Young* (1990) isopachs. Importantly, all of the volumes calculated using the distal data alone are minima, as they do not include the volume in the thick proximal fallout.

The volumes in Table 2.2 calculated using both the proximal (*Young*, 1990) and distal data were fit using one, two and three segment exponential fits, as shown in Figure 2.8. Using two exponential

segments produces a better fit to the proximal and medial data for all of the isopach combinations compared to the single segment exponential decay which underestimates the thickness close to the vent and overestimates intermediate thicknesses. We also tested three-segment exponential fits, but conclude that they 'overfit' the data, as in most cases there are only two points controlling each exponential segment.

2.5 Discussion

2.5.1 Sources of variability in tephra thickness measurements

The amalgamation of >250 Mazama tephra occurrences highlights the wide range of disciplines that make use of the tephra layer from volcanology (*Westgate and Dreimanis*, 1967; *Mullineaux*, 1974) to archaeology (*Kittleman*, 1973; *McFarland*, 1989). The multidisciplinary use of the Mazama tephra has resulted in different methods of data collection and variable data quality. However, this alone cannot explain the extreme variations in tephra thickness data (Figs. 2.2 & 2.4). The large variability of tephra thickness across the deposit also reflects the extensive remobilisation of the distal Mazama tephra, as the material has been eroded and redeposited over the past ~7700 years. Despite the paucity of primary distal Mazama tephra localities, detailed reporting and publication of all tephra sites is important as remobilised localities provide a record of tephra deposition close to that location.

Direct field observations of remobilised deposits identify common features of non-primary Mazama tephra, such as discontinuous beds, lens and fan-shaped outcrops and the co-occurrence with alluvial deposits (Fig. 2.3). Where we observed remobilised Mazama tephra, however, there were no obvious sedimentary structures; this differs from the remobilised YTT deposits which contain fine scale cross-beds (*Gatti et al.*, 2013). The remobilised YTT also exhibits different GSDs compared to the primary YTT (*Gatti et al.*, 2011, 2013); in contrast, the GSD of the remobilised and primary Mazama tephra are nearly identical, at least ~150-500 km from source (Fig. 2.5). Therefore, without broad deposit context, distinguishing the remobilised Mazama tephra deposits from primary Mazama tephra is difficult. The lack of sedimentary structures, and seemingly unaltered GSD, suggests that the remobilised distal samples have not experienced significant contamination from background sediments, or hydrodynamic sorting, even when found on top of alluvial deposits, implicating water in the remobilisation process. This is in contrast to the prominent sedimentary structures in remobilised YTT that are clearly the result of transport by water (*Gatti et al.*, 2013). We hypothesise that downslope remobilisation of Mazama tephra occurred en-masse with minimal water entrainment, and shortly after the primary deposition, such that little foreign material was incorporated, and no sedimentary structures were developed.

During the mid-Holocene (~8–5 ka) North America was slightly warmer and drier than present (*Dean et al.*, 1996; *Thompson et al.*, 2016) and reconstructions of the vegetation cover (Fig. 2.9,

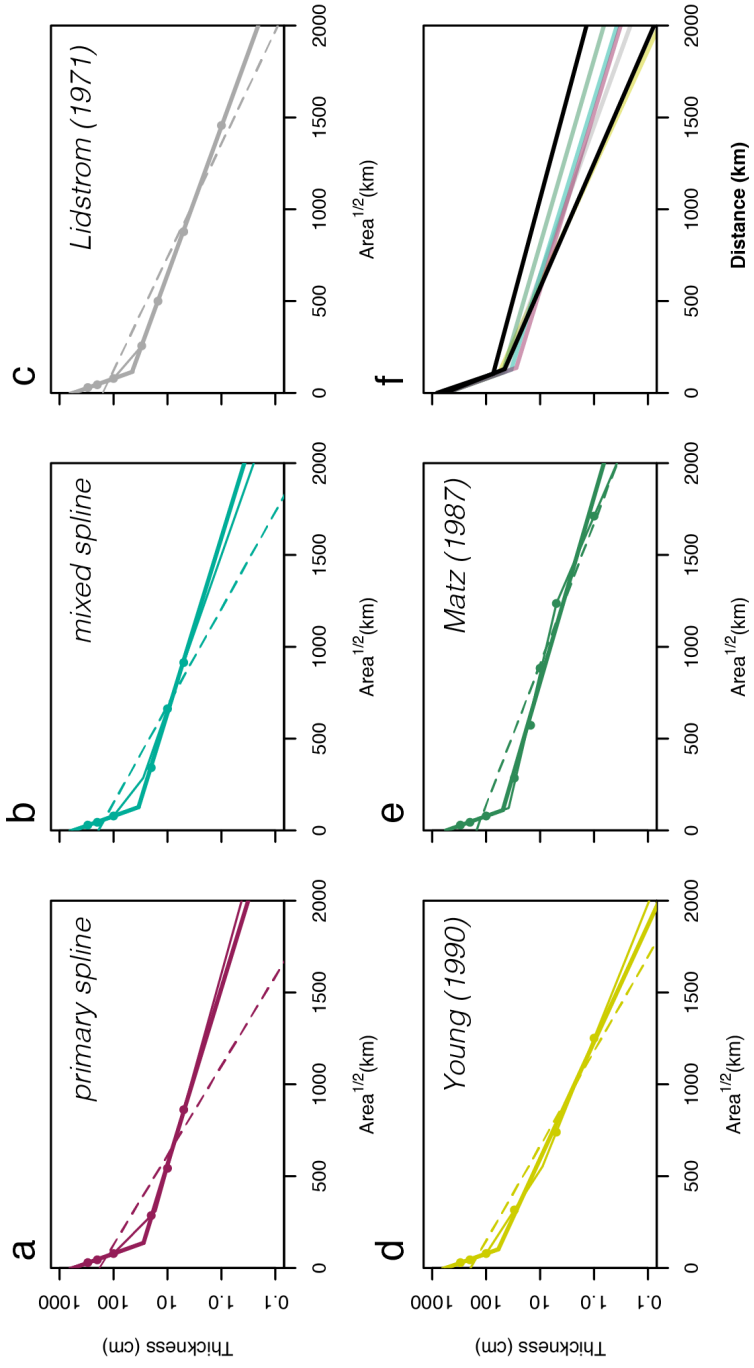

Figure 2.8: Square root area versus log thickness plots for proximal and distal Mazama isopachs. a-e) Dashed line shows single segment fit, thick line shows two-segment fit and thin line shows three-segment fit. Corresponding volume estimates can be found in Table 2.2. All proximal data corresponds to cubic B-spline fit of *Young* (1990) data (Fig. 2.6c). a) Primary spline isopachs; b) Mixed spline isopachs; c) *Lidstrom* (1971); d) *Young* (1990); e) *Matz* (1987). f) Two-segment exponential fits to log thickness versus true distance data from Figure 2.4 overlain on two-segment fits from a-e.

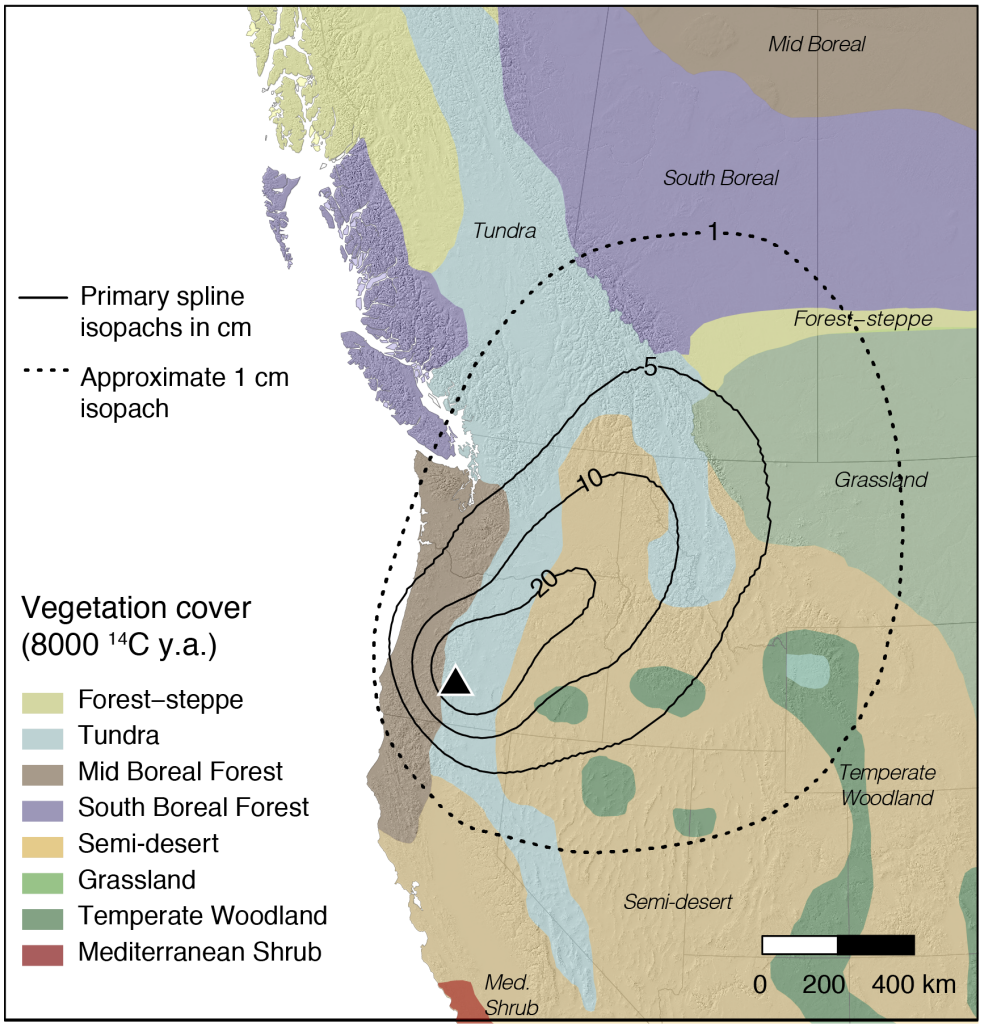

Figure 2.9: Mazama tephra distribution in relation to paleo-vegetation cover. Vegetation zone limits are from *Adams et al.* (1997).

Adams et al., 1997) suggest that most of the Mazama tephra was deposited in a semi-desert to tundra dominated environment. This supports our interpretation that the downslope processes that led to the substantially overthickened deposits (Fig. 2.3) could have been relatively dry. However, pollen suggest that the Mazama eruption occurred in northern hemisphere autumn (*Mehringer et al.*, 1977a). This could have resulted in snow melt the following spring remobilising the deposits in some areas (*Manville et al.*, 2000) and the unimodal GSD of the distal tephra (Fig. 2.5) may be the reason for the absence of obvious sedimentary structures. As such, the processes that lead to extreme overthickening (3 m from ~30 cm primary fall at site 69) require further study.

To avoid the challenges of redeposited terrestrial tephra deposits, numerous studies have used lake sediments to reconstruct volcanic histories as lake cores can provide excellent records of tephra stratigraphy (e.g., *Lowe et al.*, 1980; *Hopkins et al.*, 2015; *Fontijn et al.*, 2016; *McNamara et al.*, 2019). However, we find that lake cores, as with land sections, do not always provide reliable records of tephra thickness. Remobilised tephra in lake cores can be identified by diffuse upper or lower contacts with the background sediments, altered GSDs and anomalous radiocarbon dates surrounding the layer (*Hopkins et al.*, 2015). For example, Swiftcurrent Lake (site 150) in Montana contains 48 cm of Mazama tephra but with up to 25% clastic contamination (*MacGregor et al.*, 2011), suggesting the layer measured was a mixture of primary and reworked material. Unfortunately, many of the lake core localities lack detailed observations of the tephra layer making it difficult to confidently classify the tephra as remobilised or primary.

A number of factors can affect the thickness of tephra recorded in lake cores, including the vegetation and steepness of the surrounding hillslopes (*Dugmore et al.*, 2018), catchment size (Appendix A.3), lake depth, aeolian transport, the position of major inlets relative to the coring sites, and the background sedimentation (*McNamara et al.*, 2018). Factors independent of the lake setting may also influence the preservation of tephra in lake cores. For example, the rate of tephra deposition and the quantity of accumulated tephra will influence how the tephra is transported from the lake surface to the lake bottom (*Engwell et al.*, 2014; *McNamara et al.*, 2019). The density and grain size of the tephra could be another external factor affecting tephra preservation in lakes. The distal Mazama tephra is fines dominated (~32–63 μm; Fig. 2.5) which may make it more susceptible to syn-deposition remobilisation as the slower settling velocities will mean it has a longer residence time in the water column. Furthermore, once it has reached the lake bottom, the fine grained tephra might experience additional remobilisation by lake bottom currents and bioturbation (*Dashtgard et al.*, 2008).

Tephra thicknesses recorded in both lake and terrestrial settings may also have been influenced by wind remobilisation. The modal grain size of the distal Mazama tephra (Fig. 2.5) falls within the range measured for resuspended modern ash in Iceland and Argentina (*Liu et al.*, 2014; *Panebianco et al.*, 2017) and is also similar to (wind-transported) loess (*Sun et al.*, 2004). Semi-desert and tundra environments, which we infer a substantial proportion of the tephra was deposited in (Fig. 2.9), provide the ideal dry and windy conditions for tephra resuspension. Wind remobilisation could thin the deposit in some places but could also explain overthickening in other sites. For example, at Marys Pond, Montana (site 102, *Foit et al.*, 1993), the small glacial lake must have had an input of Mazama tephra other than purely upstream to explain the accumulation of 9-90 cm of tephra >700 km from source. Other windblown particulates, such as loess, are known to accumulate in lakes (*Pye*, 1995), therefore, wind-blown tephra may help explain some overthickened lake deposits.

Understanding mechanisms that remobilise tephra after a large eruption are crucial for anticipating post-eruptive hazards. Ash resuspension for example, has closed airports (*Hadley et al.*, 2004) and could pose hazards to human health (*Horwell and Baxter*, 2006; *Thorsteinsson et al.*, 2012). Resuspension events are a persistent hazard in Alaska over 100 years after the M=6.5 Novarupta (Katmai) eruption in 1912 (*Hadley et al.*, 2004) and it is likely that the Mazama tephra (M>7) posed resuspension hazards over similar time scales or longer. Archaeological records provide evidence for long term ash remobilisation, revealing that communities abandoned parts of the north-western Plains (modern Wyoming, Montana, North and South Dakota, southern Alberta Saskatchewan and Manitoba) following the Mazama eruption and only returned permanently after 500 years (*Oetelaar and Beaudoin*, 2016).

2.5.2 Validity of isopachs for large eruptions

The published isopachs for the distal Mazama tephra (Fig. 2.1) show the challenges in creating isopachs for large and older tephra deposits. Our study shows that the isopach variability derives from overthickening, sparse coverage and different environments of deposition (Figs. 2.2-2.4). This raises the question of whether isopach maps are an appropriate way to present thickness data for large deposits, or if the uncertainties and limitations invalidate this approach. The disadvantages of hand-drawn isopachs have been discussed (*Klawonn et al.*, 2014; *Engwell et al.*, 2015), while acknowledging the value of intrinsic knowledge of the authors, which may not be possible to quantify or transfer by means other than hand-drawn isopachs. However, it is still important to clearly document the data used to construct the isopachs in a best effort to transfer this knowledge. As Figure 2.1 shows, often the data are poorly documented, and are therefore unusable except to determine the areal extent of tephra coverage.

Alternatively, studies of large and poorly documented deposits may report thickness against true distance from source (e.g., the Campanian Ignimbrite tephra, *Engwell et al.* 2014; Toba, *Gatti and Oppenheimer* 2012; Taupo, *Matthews et al.* 2012). The equivalent plot of the Mazama thickness data in Figure 2.4 shows the value of this approach. Here the large scatter of thickness data at the same distance from source reflects both the distance from the main dispersal axis and the inclusion of non-primary thickness measurements. Using the data in this form for volume calculations comes with caveats (see below and Appendix A.5), however, qualitatively comparing the decay of thickness with distance between large tephra deposits provides a means of contrasting the Magnitudes of different eruptions without the need to draw isopachs. We demonstrate this in Figure 2.10, where we compare exponential fits to the distal thickness data for the Campanian Ignimbrite tephra (*Engwell et al.*, 2014), Rangitawa (Taupo, *Matthews et al.*, 2012), YTT (*Matthews et al.*, 2012) and Mazama eruptions. Whilst the data exhibit substantial scatter due to the reasons previously discussed, the simple exponential fits highlight the different thinning trends of 'super-eruptions' (M>8) and M~7 eruptions such as the Mazama and the

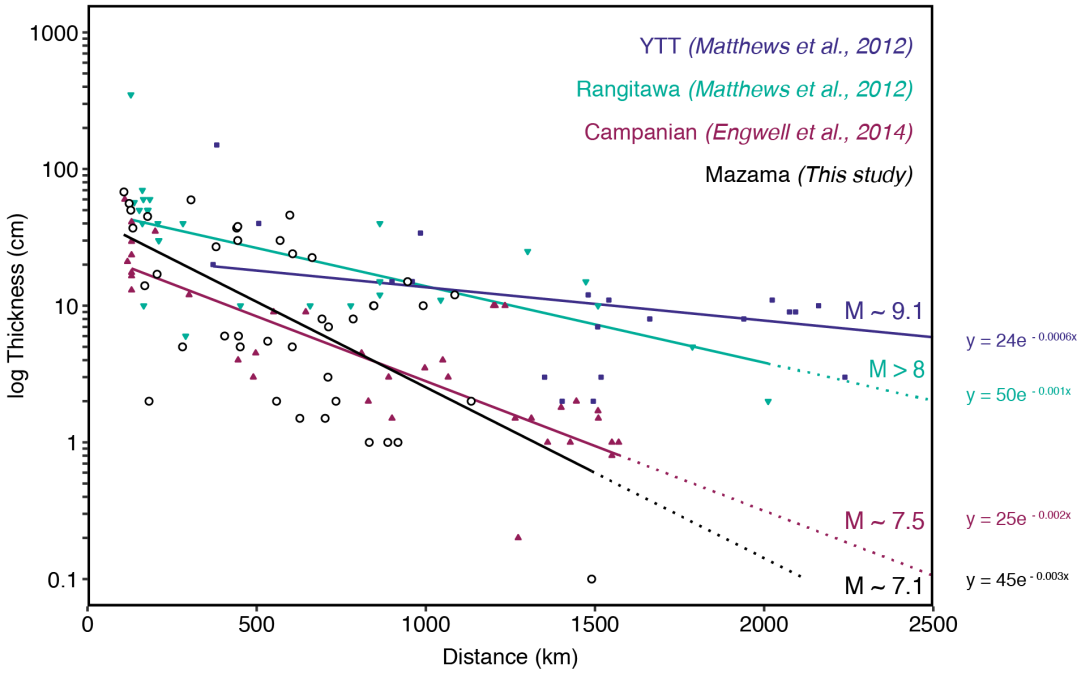

Figure 2.10: Comparing the exponential decay of distal tephra thickness with distance from large magnitude eruptions. Younger Toba Tuff (YTT), Campanian and Mazama Magnitude values (M) are taken from the LaMEVE database, (VOLGRIPA; www2.bgs.ac.uk/vogripa/view/controller.cfc?method=lameve) and Rangitawa M is assuming DRE >1500 km^3 (*Matthews et al.*, 2012).

Campanian Ignimbrite.

2.5.3 Spline fitted isopachs

To overcome the disadvantages of hand-drawn isopachs, we applied a spline interpolation method (*Engwell et al.*, 2015) to the distal and proximal thickness data (Fig. 2.6). This method generates reproducible isopachs of the distal Mazama tephra with reduced subjectivity. However, the spline fitting still requires user input, therefore necessitating prior knowledge of the deposit. For example, fitting the cubic B-spline to the raw primary thickness data required inferred upwind thicknesses to characterise the asymmetry of the deposit (Appendix A.4). This user input can only be avoided entirely when the thickness dataset is spatially dense, with zero values delimiting the edge of the deposit (e.g. Mount Saint Helens, 1980; *Sarna-Wojcicki et al.*, 1981; *Engwell et al.*, 2015). Fitting the cubic-B spline model also requires a choice of the fitting parameters: roughness, tension, area divisions and weightings (Appendix A.4). For this study we followed the guidelines of *Engwell et al.* (2015) and found the values that best visually recreated the expected dispersal, however this introduces another area of subjectivity.

Irrespective of the limitations of the spline method, there are benefits to using models to generate

isopachs. Notably, the same isopachs can now be reproduced given the same thickness dataset and model parameters regardless of user bias or experience which cannot be said for hand-drawn isopachs (*Klawonn et al.*, 2014). The spline fit does not recreate the exact fallout of the Mazama tephra, as it involves no physical processes relating to ash dispersal and transport, but it generates a 'model' tephra surface from which anomalous thicknesses and unusual deposition can be highlighted (Fig. 2.7). Figure 2.7c shows the correlation between the percentage difference and the thickness classification. Additionally, Figure 2.7d shows that this approach could be used to make best estimates of otherwise 'unclassified' localities which could inform future field studies of primary tephra localities. Another benefit of using the spline fitting approach is the capacity to include non-primary thicknesses to explore the sensitivity of isopach construction to these measurements (Fig. 2.6b).

2.5.4 Estimating the erupted volume from large tephra deposits

The bulk erupted volumes of the distal Mazama tephra calculated from published and spline isopachs using an exponential fit range from 131 to 242 km^3 (Table 2.2). The range in estimates arises from the inclusion of non-primary thicknesses (Fig. 2.6b) and convolute published isopachs (Fig. 2.1c; *Matz* 1987). Including non-primary, overthickened thickness measurements in isopach construction is useful for highlighting areas of tephra remobilisation. However, using isopachs that include overthickened data to estimate erupted volumes is problematic as this negates the assumption of deposit thinning with increasing distance from source, which is fundamental to the methods used to estimate volumes from isopach maps (*Pyle*, 1989; *Fierstein and Nathenson*, 1992). For this reason, direct integration of the volume below the spline surface may provide a better way to estimate volume from non-primary isopachs (Appendix A.5). However, the spline fit underestimates the thickness at source and the integration range is limited by the thinnest isopach, this method provides only volume minima. For these reasons, we do not use the convolute (*Matz* 1987, Fig. 2.1c) and mixed spline isopachs (Fig. 2.6b) to estimate the total erupted volume of the Mazama tephra. Whilst the range in estimates remains significant (distal only 131–153 km^3; Table 2.2), large uncertainties on erupted volumes are expected for large eruptions.

Combining the primary distal spline isopachs (Fig. 2.6a) and the proximal spline isopachs (Fig. 2.6c) gives the best estimate of 148 km^3 bulk erupted volume. When added to the ~29 km^3 assumed to be in the ignimbrite (Williams 1942), we estimate a total erupted volume of ~176 km^3 which is ~20 km^3 greater than the estimates in Table 2.1. To convert this to a DRE volume we assign average densities to the three portions of the deposit and use 2200 kgm^{-3} as the bulk density of the magma (*Lidstrom*, 1971; *Young*, 1990). For the proximal deposit, we use an average deposit density of 500 kgm^{-3}, taking into account average pumice densities (Young 1990) and packing density. We measured a bulk density of 700 kgm^{-3} for the distal ash, which is in agreement with the value used by *Lidstrom* (1971), *Bacon* (1983) and *Young* (1990), with the low

density likely reflecting the micro-vesicularity of the fine ash. For the ignimbrite we use 1200 kgm^{-3}, the higher density reflecting the large lithic component in the ignimbrite flows (*Bacon*, 1983). Using this density distribution and the relative proportion of volume in the proximal (19 km^3) and distal (129 km^3) segments, we calculate a DRE volume of ~61 km^3 and calculate an eruption Magnitude of 7.1 ($M = log_{10}(DRE \times 2200) - 7$; *Pyle* 2000). This value is in agreement with DRE estimates by *Lidstrom* (1971) and *Bacon* (1983) and is less than the caldera and edifice volume estimate by *Bacon and Lanphere* (2006) allowing for the volume contained in collapse deposits and pre-caldera forming eruptions (Table 2.1).

2.6 Conclusions

Estimating the eruptive volume and Magnitude of prehistoric large magnitude eruptions is vital to interpreting the hazards posed by these eruptions. However, the tephra deposits required to estimate parameters such as eruptive volume, are often poorly preserved and exhibit low sampling density and diverse data quality, especially at large distances from source (>100 km). These limitations are encountered when interpreting the distal Mazama tephra. We combined an extensive literature search, field observations and new methods of interpolation and data manipulation, to develop an extensive record of Mazama tephra occurrences (Table A.1). Using the compilation of primary tephra sites, we constructed new reproducible isopachs of the deposit and revised the bulk erupted volume estimate to ~176 km^3, including the ignimbrite volume. The new isopach map (Fig. 2.9) provides a modelled thickness distribution which broadly agrees with past hand-drawn isopachs and are a resource that can be used to inform future field studies. Specifically, further work is needed to constrain the upwind deposit and the limits of the distal tephra, for example the limit of the 1 cm isopach which has only been approximated (Fig. 2.9). This will improve our volume estimates as well as our understanding of the spatial footprint of hazards from the primary tephra fallout during large caldera forming eruptions.

We use our compilation of Mazama tephra occurrences and isopach maps to highlight areas where the Mazama tephra has been remobilised and overthickened, and show that incorporating non-primary thicknesses dramatically influences the isopachs and the bulk erupted volume estimates. However, we emphasise that the reporting of all tephra sites is important as they are still a record of deposition at a specific location, even if the thickness cannot be used in isopach construction. Furthermore, understanding the mechanisms and conditions that encourage tephra remobilisation is crucial for interpreting the post-eruptive hazards posed by a Mazama like eruption as they have the potential to have long lasting effects (100+ years) over large areas (millions of km^2).

CHAPTER 3

THE CONTRIBUTION OF CO-PDC ASH TO THE DISTAL MAZAMA TEPHRA

Author Contributions and declaration: H. Buckland carried out the data collection (field sampling, grain size, SEM, EPMA) and analysis (geothermobarometry), created the figures and wrote the main text of this Chapter. The componentry analyses were repeated and corroborated by L. Day and J. Rawlings. Supervision and Chapter edits were provided by K. Cashman, A. Rust and S. Engwell. B. Buse and S. Kearns assisted H. Buckland with setting up and running the major element analyses on the JEOL JXA8530F Hyperprobe at the University of Bristol. C. Long kindly shared samples from the Tumalo Lake core for grain size and geochemical analysis.

Abstract

Fine grained (<100 μm) volcanic ash is commonly produced in propagating Pyroclastic Density Currents (PDCs) and can travel long distances if elutriated into the atmosphere. Such ash is typically referred to as co-PDC ash and is thought to represent a large proportion of distal deposits from large magnitude explosive eruptions. Detailed geological mapping and tephrostratigraphy have established that the ~7.7 ka Mazama eruption had two phases: a single-vent Plinian phase, followed by a ring-vent phase coincident with the onset of caldera collapse. Here, we examine whether the distal ash from the climactic Mazama eruption can be attributed to a co-PDC source using granulometric and geochemical fingerprinting. We analyse the grain size and geochemistry of known Plinian and co-PDC ash from a land section and lake core 130 km from source and perform the same analyses on distal tephra sampled >130 km from source. Two bimodal deposits are recorded in a zone of poor tephra preservation, but it is unclear if the coarse and fine modes represent different eruptive units. The GSD of the samples >400 km from source is unimodal and cannot be used identify the eruptive phase or associated fragmentation mechanism. The major element geochemistry of the rhyodacitic glass is homogeneous throughout all phases of the eruption, meaning it does not differ between the eruptive phases. However, there is evidence of the FeTi oxide composition changing throughout the eruptive sequence which associates the distal deposits to the late stage Plinian and co-PDC deposits. However, approximating the volume contribution of co-PDC ash to the distal ash is not possible from these analyses. Future trace element geochemistry and further analysis of the bimodal deposits could help determine the co-PDC contribution to the total ash volume which is crucial for understanding the mechanisms of ash generation dispersal from large magnitude eruptions.

3.1 Introduction

Large magnitude eruptions are closely associated with voluminous Pyroclastic Density Currents (PDCs) and significant co-PDC plumes (e.g., Santorini 3.6 ka, *Sparks et al.* 1983; Tambora 1815, *Sigurdsson and Carey* 1989; the Campanian Ignimbrite ~39 ka , *Perrotta and Scarpati* 2003; *Engwell et al.* 2014). Co-PDC plumes (sometimes referred to as co-ignimbrite plumes) form as fine material is elutriated and entrained into a buoyant turbulent cloud above a dense basal current (*Sparks and Walker*, 1977; *Sparks et al.*, 1978) and can act as a significant source of fine ash. Co-PDC plumes contain fine material produced by the initial fragmentation processes; ash can also be generated within PDCs by the comminution of particles during transport (*Woods and Wohletz*, 1991; *Marti et al.*, 2015; *Jones et al.*, 2016; *Mueller et al.*, 2017; *Buckland et al.*, 2018). Understanding how co-PDC ash contributes to the total ash budget of large magnitude eruptions is therefore important for recognising the significance of secondary fragmentation processes and the processes that form co-PDC plumes. Furthermore, this knowledge might be used to modify Volcanic Ash Transport and Deposition Models (VATDMs) to better represent a co-PDC source, including the shape of the source (area or point) and the Grain Size Distribution (GSD).

Very large eruptions (M≥7) are rare and none have occurred during the modern era of volcano monitoring (past several decades). For this reason, studies of large eruptions require the interpretation of pre-historic tephra deposits, preferably deposits that are extensively preserved on land. An example is the climactic Mazama eruption ~7.7 ka in Oregon, USA (*Bacon* 1983, Chapter 2, section 2.2.1). Field studies of proximal Mazama tephra deposits (<100 km from source) have found that the Mazama eruption had two main phases: a Plinian or 'single-vent' phase followed by an ignimbrite forming or 'ring-vent' phase (*Williams*, 1942; *Williams and Goles*, 1968; *Bacon*, 1983; *Young*, 1990). The second phase of the eruption was characterised by large volume PDCs that have been mapped to 70 km from source (*Williams*, 1942; *Bacon and Druitt*, 1988) and account for at least 16 km^3 of the total DRE volume (~61 km^3; Chapter 2, section 2.5.4). The distal ash deposit covers an area greater than 1 million km^2 and cryptotephra has been recorded in the Greenland ice core records (*Zdanowicz et al.* 1999; *Hammer et al.* 1980, Fig. 2.2). The relative contribution of co-PDC ash to the total distal ash volume, however, is poorly constrained. In this Chapter we investigate whether physical and geochemical signatures can be used to determine the provenance of the distal Mazama tephra and, by extension, whether co-PDC plumes were the dominant source of fine ash during the eruption.

3.2 Background

There is strong evidence to support the hypothesis that significant co-PDC plumes were formed during the climactic Mazama eruption. Firstly, smaller volume PDCs observed during modern eruptions have been accompanied by co-PDC plumes (e.g., Pinatubo 1991, *Koyaguchi and Tokuno*

1993; *Scott et al.* 1996; Montserrat, *Horwell et al.* 2001; Mount St. Helens 1980, *Eychenne et al.* 2015; *Engwell and Eychenne* 2016). Therefore, the large-volume co-PDCs during the Mazama eruption probably also produced co-PDC plumes. Conversely, not all large explosive eruptions are associated with significant co-PDC ash deposits. For example, the Quilotoa 800 yr BP and the 1912 Novarupta eruptions produced fine ash layers that are attributed to co-Plinian rather than co-PDC sources (*Fierstein and Hildreth*, 1992; *Mothes and Hall*, 2008). However, in both eruptions the proportion of the total erupted volume contained in the PDCs was small and the PDC material was crystal-rich meaning that the production and elutriation of fine ash from the flows was limited (*Fierstein and Hildreth*, 1992; *Mothes and Hall*, 2008). Due to the significant volume contained in the Mazama PDCs and the highly vesicularity and low crystalinity of the PDC components, we infer these were prime conditions for co-PDC ash and plume formation.

Here we review how co-PDC ash can be recognised in tephra deposits. We also consider unique geochemical aspects of the Mazama eruption that could be used to attribute distal deposits to distinct eruptive phases.

3.2.1 Identifying co-PDC ash

Ash associated with co-PDC plumes can be identified in the field based on stratigraphic relationships and the eruption sequence. For example, the ~39 ka Campanian Ignimbrite eruption produced two proximal fall deposits followed by a major ignimbrite unit (*Rosi et al.*, 1999; *Scarpati and Perrotta*, 2016). This is reflected in lake core records analysed by *Engwell et al.* (2014) where co-PDC ash overlies Plinian fall deposits (Fig. 3.1a). Here, the grain size of the ash was also used to distinguish the two populations (Fig. 3.1; *Engwell et al.*, 2014).

Co-PDC plumes preferentially contain small particles (<125 μm) that are susceptible to elutriation (*Engwell and Eychenne*, 2016). Fine-grained ash can be deposited at the same distance from source as coarser particles thanks to enhanced sedimentation processes (e.g., *Carazzo and Jellinek*, 2013; *Manzella et al.*, 2015; *Engwell and Eychenne*, 2016; *Eychenne et al.*, 2017). This size difference can then be related to the provenance of the ash, for example, where coarse Plinian ash and fine-grained co-PDC ash have been co-deposited (Fig. 3.1a; *Engwell et al.*, 2014). However, as the distance from source increases, the grain size of the Plinian ash converges on the grain size of co-PDC material and grain size is no longer a unique identifier of ash origin (Fig.3.1b; *Engwell and Eychenne*, 2016).

The fine material preferentially elutriated and dispersed by co-PDC plumes is typically glassy (vitric), consistent with the increased proportion of dense components - crystals, crystalline matrix fragments and lithics preserved in PDC deposits (*Sparks and Walker*, 1977). In contrast, the componentry of ash from a Plinian source more closely matches the crystallinity of the erupting magma (*Jones et al.*, 2016; *Paredes-Mariño et al.*, 2019; *Mele et al.*, 2020). In theory, differences

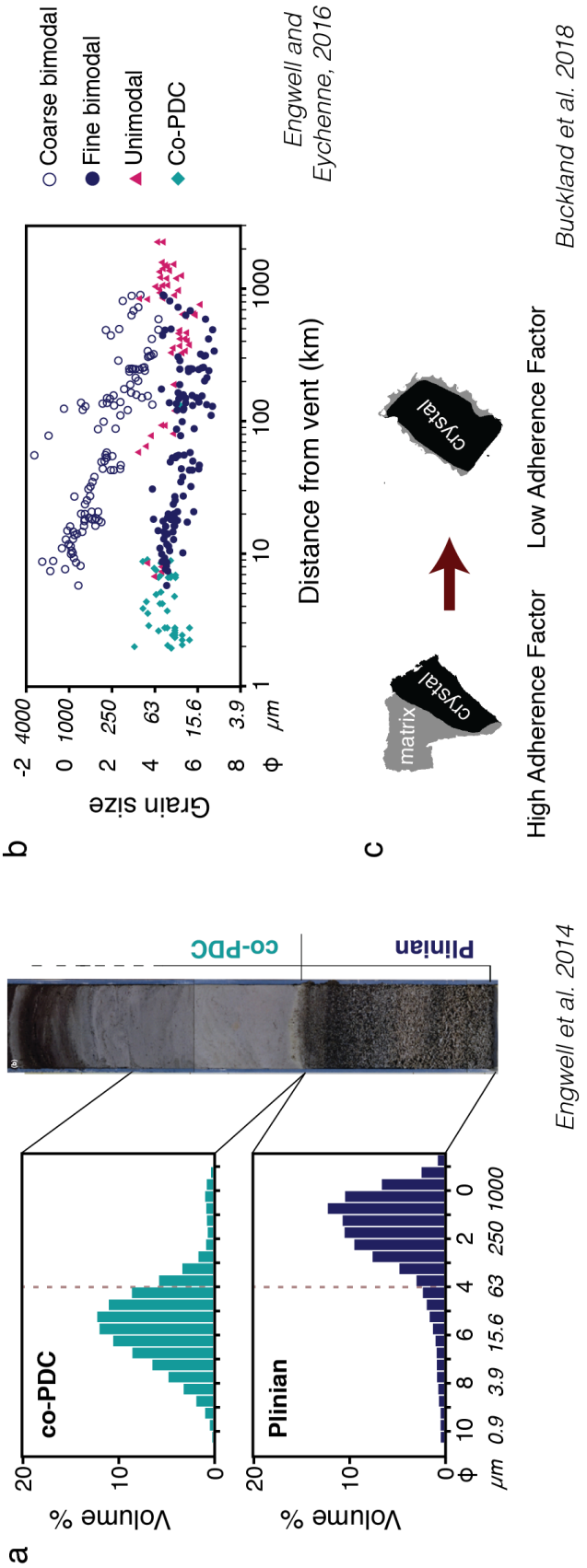

Figure 3.1: Summary of the physical characteristics of co-PDC ash. a) Lake core record of ~39 ka Campanian Ignimbrite tephra from Lago Grande di Monticchio with average Grain Size Distributions for each unit (image and GSDs from *Engwell et al.* 2014). b) Variations in median grain size of co-PDC and mixed fallout deposits (figure adapted from *Engwell and Eychenne* 2016) c) Schematic of the adherence factor parameter to quantify the amount of adhered matrix to crystals (images from *Buckland et al.* 2018).

in the relative componentry of ash deposits could then be used to discriminate between co-PDC and Plinian ash. However, the componentry of Plinian ash becomes increasingly glass dominated with greater distance from source as dense components are deposited closer to source and form crystal concentrations in fall deposits (*Walker* 1981a; *Scarpati et al.* 2014; *Cashman and Rust* 2016, see Chapter 4).

The abrasion of particles in PDCs can produce fine-ash and, in some cases, affect the shape of PDC constituents (*Manga et al.*, 2011; *Mueller et al.*, 2015; *Buckland et al.*, 2018). For example, coarse pumice clasts (>2 mm) in PDCs are typically rounded (*Wilson and Hildreth*, 1998; *Calder et al.*, 2000); co-PDC ash (<2 mm) may also have more rounded morphologies compared to Plinian ash from the same eruption (Fig. 3.1 *Liu et al.*, 2015; *Jones et al.*, 2016; *Buckland et al.*, 2018). Furthermore, crystals in co-PDC ash characteristically have less adhered matrix glass (low adherence factor) as the result of efficient matrix stripping by abrasion processes during PDC emplacement (Fig. 3.1c *Jones et al.*, 2016; *Buckland et al.*, 2018). However, unique shape properties of co-PDC ash may not be recorded in distal ash deposits. For example, not all the ash in co-PDC plumes are rounded, particularly when the erupted material is highly vesicular (*Buckland et al.*, 2018). Similarly, whilst the adherence factor is a good identifier of co-PDC ash (*Jones et al.*, 2016; *Buckland et al.*, 2018), it is only observable if the ash contains crystals. As previously discussed, the distal ash from large magnitude eruptions is often dominated by highly vesicular particles or platy glass shards, which present a challenge to using shape and adherence factor to determine ash provenance.

In summary, the physical characteristics used to discriminate ash provenance might be best suited to regions close to source where there are observable differences in eruptive stratigraphy, grain size, componentry and ash shape. In this study we add geochemical properties to the characterisation of physical characteristics of the distal Mazama ash.

3.2.2 Geochemistry of the Mount Mazama eruptive products

The climactic Mount Mazama eruption is an example of the rapid exhumation of a large, compositionally zoned magma reservoir (*Bacon*, 1983; *Bacon and Druitt*, 1988). The explosive products are predominantly homogenous rhyodacitic pumice (~70.5 wt% SiO_2; *Bacon and Druitt* 1988) which contain ~10-15 wt% phenocrysts of plagioclase, orthopyroxene, augite, hornblende and FeTi oxides (*Bacon and Druitt*, 1988; *Bacon and Lanphere*, 2006). During the ring-vent phase of the eruption an increasing proportion of crystal-rich (30-70 wt% crystals) andesite to basaltic-andesite scoria was erupted (48-61% wt% SiO_2; *Bacon and Druitt* 1988), as recognised in proximal sections of the flow units at 9.3–30.9 km from the vent (Fig. 3.2; *Druitt and Bacon*, 1986). In detail, the basal flows are primarily silicic; there is a gradual change to more mafic material up section, although no abrupt changes in the relative proportion of clasts are observed (*Druitt and Bacon*, 1986). Interestingly, the PDCs sections logged furthest from source do not record the

more mafic unit, suggesting that the later mafic flows were either more channelised or smaller in volume (Fig. 3.2b; *Druitt and Bacon* 1986). Whilst the compositional zoning of the PDCs is strongly evident in the proximal sections, it is not known whether the compositional zoning is observable in the co-PDC or distal ash.

Previous efforts to determine the contribution of co-PDC ash to the distal Mazama deposit have suggested that the geochemistry of titanomagnetites can be used to correlate ash to the eruptive phase (*Osborn*, 1985; *Young*, 1990). *Osborn* (1985) documented a sub-population of titanomagnetites with elevated TiO_2 in distal Mazama ash deposited in Canada. The anomalous compositions, and the range of titanomagnetite compositions, was inferred to reflect the zonation of the primary magma reservoir. *Young* (1990) associated the evidence of zoning in the distal deposits more specifically with the ring-vent phase of the eruption where the zonation is most evident in the proximal deposits (*Druitt and Bacon*, 1986; *Bacon and Druitt*, 1988). However, there are no published studies of titanomagnetite composition throughout the proximal Mazama products and eruption sequence to support this interpretation.

3.3 Methods

Here we outline the physical and geochemical methods used to characterise explosive products from the climactic Mazama eruption. The samples analysed include fall deposits and co-PDC ash in addition to distal samples where the association with eruptive phase is unknown.

3.3.1 Tephra sampling

The tephra localities chosen for physical and geochemical characterisation come from sites ~100–900 km from source (Fig. 3.3). Site 46 is a key locality in this study. At this locality we observe two well-sorted fall deposit units which are overlain by a fine-grained unit that grades into a mixture of tephra and topsoil (Fig. 3.3c). A lake core sampled ~10 km from site 46 (site 47; *Long et al.* 2014) records the same fall deposit sequence. The top of the Mazama deposit in the lake core is also very fine-grained and interpreted as co-PDC ash.

Two of the tephra sections in this study (sites 50 & 55) were sampled in a zone where the preservation of the Mazama deposit is poor (~130–400 km from source). Across this zone, the stratigraphy changes from having clearly distinguishable fall deposit units and an overlying fine-grained unit (sites 46 & 47) to a purely fine-grained and massive unit (site 73; >400 km). The tephra at site 55 did record some evidence of reverse grading, however, the lateral continuity was limited.

The sites studied 230-600 km from source either preserve the primary tephra thickness (e.g., site 73) or the tephra has undergone remobilisation since deposition (e.g., site 67; Fig. 3.3d; Chapter

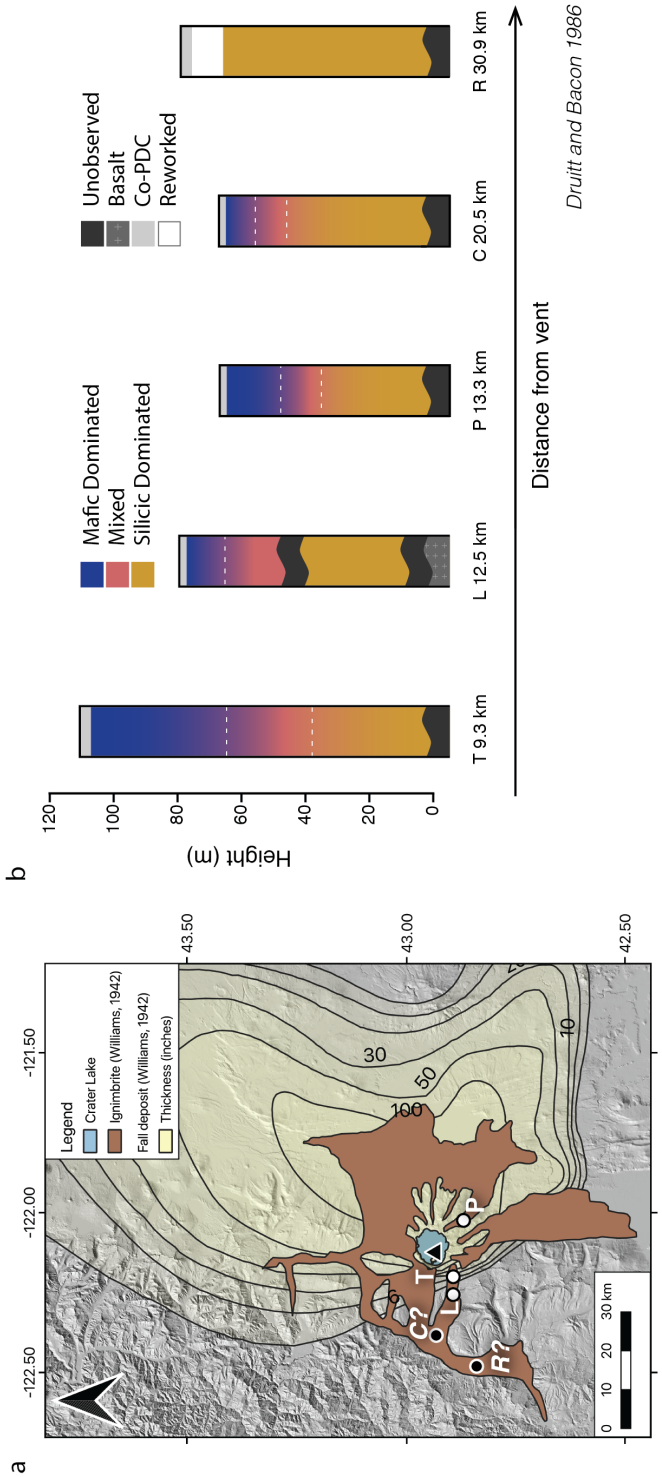

Figure 3.2: Distribution of fall deposit and PDCs from climactic Mazama eruption. a) Map of Plinian fall and PDC deposits (ignimbrite) adapted from *Williams* (1942). The location of sections C and R have been approximated based on the distance from source and letter assignment used by *Druitt and Bacon* (1986; C – Castle Creek and R – Rogue River). b) Schematic of PDC zonation from silicic dominated at the base that grades into mafic dominated at the top (figure adapted from *Druitt and Bacon* 1986).

2, section 2.4.1). When sampling remobilised deposits, care was taken to avoid areas that showed clear mixing with the surrounding sediments. We later confirmed from SEM imaging that the remobilised tephra analysed in this study had no significant contamination from background sediments.

We also include additional sites >600 km Mazama samples for grain size analysis (Fig. 3.3b). The sites include both locations where the primary tephra thickness has been preserved and locations where the deposit has been overthickened by secondary processes (see Chapter 2). The samples were collected by J.Westgate (*pers. comm*) and *Jensen et al.* (2019), who also collected the major element glass geochemical data. Four additional sites in Figure 3.3b correspond to the sampling sites of *Osborn* (1985), who collected major element geochemical data on FeTi oxides in the Mazama tephra found at these localities.

3.3.2 Physical ash characterisation

Grain Size Distributions (GSDs) for all the tephra samples were acquired using a combination of sieving and Dynamic Image Analysis (DIA). The samples were dried in a 60° oven overnight prior to analysis and then were split at least once to obtain an aliquot for size analysis. Sieving was required for 4 samples that contained material >2 mm (sites 46, 47, 50 & 55). The samples were manually dry-sieved from -3 to 3 ϕ (8 mm to 125 µm) in half- ϕ intervals and the coarse GSD was quantified according to the mass in each sieve fraction. The 3 ϕ sieve fraction was then recombined with the material >3 ϕ (<125 µm) prior to the characterisation of the fine material.

The fine material from the sieved samples and the remaining un-sieved samples were analysed using the X-jet dispersion mechanism of the Camsizer X2 (CX2) from Microtrac MRB (*MRB*, 2020). The GSDs were quantified according to three size parameters – $x_c$min (shortest dimension), xarea (equivalent circle diameter) and xFemax (longest caliper diameter) – to facilitate comparisons with other techniques and to provide insight into particle shape. GSDs that were quantified according to $x_c$min were combined with the sieve analysis data (*Freret-Lorgeril et al.*, 2019). Particle shape is also directly measured by the CX2, which calculates the aspect ratio $\frac{x_c min}{x_{Fe} max}$) and sphericity $\frac{4\pi A_P}{U^2}$) of each particle. An in depth review of DIA and a protocol for using the CX2 to measure the size and shape of volcanic ash is found in Chapter 4.

The unsieved tephra samples were mounted in epoxy and polished to expose particle interiors. Mounts of the sieved samples were prepared for each sieve fraction from 1-3 ϕ. The magnetic fraction was isolated for mounting from sub-samples of the 2.5 ϕ sieve fraction using a hand-held magnet. All the polished mounts were then carbon coated and imaged using a Hitachi S-3500N Scanning Electron Microscope (SEM) at the University of Bristol in backscattered electron (BSE) mode. Grid images of the ash mounts were collected for quantitative componentry assessments.

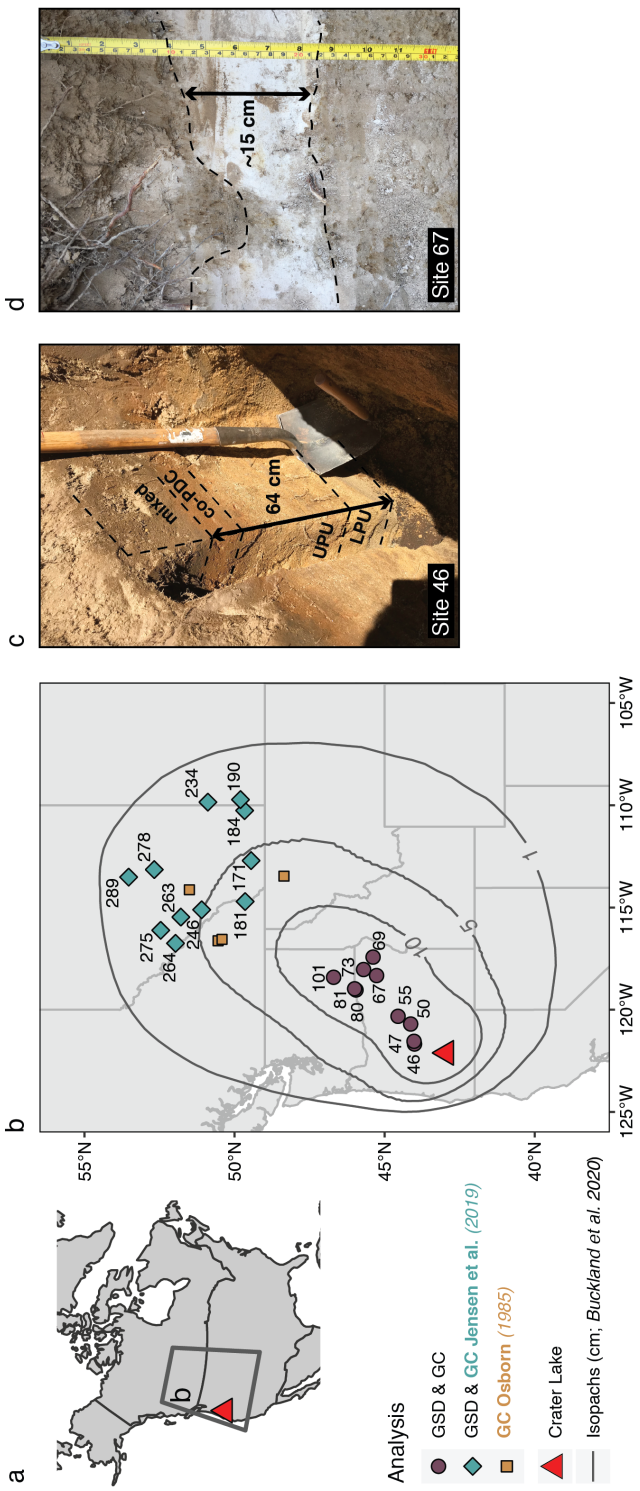

Figure 3.3: Tephra sampling sites for granulometric and geochemical analysis. a) Map of North America with location of map b outlined. b) Map of localities with site number according to the database of Mazama localities developed in Chapter 2 (Appendix A.1). The colour and shape of the symbol corresponds to the analysis carried out on the samples from that site. GSD & GC = grain size analysis and geochemistry, GSD & GC Jensen et al. (2019) = grain size analysis in this study, geochemical analysis by *Jensen et al.* (2019) and GC Osborn (1985) = location of FeTi oxides analysed by *Osborn* (1985; sites not in Appendix A.1). c) Mazama stratigraphy as recorded at terrestrial tephra pit dug at site 46 (near Mount Bachelor). d) Example of remobilised distal Mazama tephra at site 67. Main features are bright white colour and unimodal fine-grained texture.

The imaging conditions used a working distance of ~16 mm, an accelerating voltage of 15 or 20 kV; typically 100-250 x magnification gave optimal resolution for component identification. When imaging the magnetic fractions, the brightness and contrast were optimised to differentiate between ilmenite (dark) and magnetite (light) based on the BSE greyscale. The componentry of the grain mounts was quantified from the grid images by point counting grains in five categories: plagioclase, pyroxene and FeTi oxide crystals, holocrystalline material, and vesicular glassy material.

3.3.3 Geochemical characterisation

Major element glass geochemistry data was collected for all samples by electron probe microanalysis (EPMA) using a JEOL JXA8530F Hyperprobe at the University of Bristol. The conditions for analysis used a 5 nA beam current with a 10 µm spot size and an accelerating voltage of 15 kV. All elements were counted on-peak and the count times were adjusted for each element to minimise beam damage. K, Ca, Si, Na and Al were analysed first for 10s, Ti and Mg (60s), and Fe, Mn P, Cl (50s). Secondary standards KN18 and Lipari were regularly analysed at the start and end of each analytical session with no drift or deviation in the analyses observed. Only analyses with totals >97% have been retained and all data has been normalised to 100%. 20-30 individual analyses were collected per sample. Totals below 100% are attributed to secondary hydration, which is common in older tephra deposits (*Fontijn et al.*, 2016; *McNamara et al.*, 2018). Each analysis spot was carefully checked for microlites or voids and where possible large glass areas were targeted. The full major element data is available in Appendix B including the secondary standard analyses.

FeTi oxides were analysed using the same JEOL Hyperprobe at the University of Bristol. The conditions for analysis used a 10 nA beam, a 5 µm spot size and an accelerating voltage of 15 kV. The elements Ca, Ti, Mg, Al, Si (60s), Fe (30s), Mn and Cr (80s) were counted on-peak. K22 ilmenite, two hematite and magnetite secondary standards were analysed throughout the duration of data acquisition with no variability or drift observed. The EPMA results were output as total FeO* and then the mineral stoichiometry and iron oxidation state was calculated using the SPINCALC and ILMCALC spreadsheets (*GabbroSoft*, 2011). At least 25 FeTi oxides were analysed per sample (approximately 10 ilmenites and 15 titanomagnetites as identified from differences in greyscale on the SEM) and, where possible, 5 touching pairs of titanomagnetite and ilmenite. We then applied the FeTi-oxide geothermometer/oxygen as formulated by *Ghiorso and Evans* (2008) using the 'Fe-Ti-Oxide-Geotherm' app (*Ghiorso and Prissel*, 2020). The full major element data is available in Appendix B including the secondary standard analyses.

3.4 Results

3.4.1 Granulometry - grain size, shape and componentry

The grain size of the Plinian fall units at sites 46 and 47 can be correlated with each other and the changes in grain size correspond to the trends originally described by *Young* (1990; Fig. 3.4). Qualitative assessment of the units at the hand sample scale similarly match the descriptions of the lower and upper pumice units (*Young*, 1990). The lower pumice has a high proportion of lithics and mafic crystals giving it a salt and pepper appearance compared to upper pumice that is dominated by pumice clasts and plagioclase. The overall grain size of the co-PDC unit at site 46 has a median grain size (Md) of 1.5 ϕ (354 µm) and is coarser than expected for pure co-PDC ash. However, the unit does have a fine-grained sub-population with a Md=4.9 ϕ (33.5 µm; Fig. 3.4c). Interestingly the fine population material of the co-PDC material from site 47 is finer with Md=6.4 ϕ (~12 µm; Fig. 3.4c).

The GSDs of the samples from the zone of poor preservation are bimodal (Fig. 3.4d). The Md of fine-grained sub-populations is 5.8-5.6 ϕ (18-21 µm; $x_c$min). Samples from >400 km from source are all unimodal with a narrow range in Md of 5.5-4.8 ϕ (22-37 µm; $x_c$min), 5.3-4.4 ϕ (26–48 µm; xarea) and 4.8-4.1 ϕ (36-59 µm; x_{Fe}max; Fig. 3.4f). The differences in GSDs quantified according to different size parameters (Fig. 3.4e) reflect the irregularity of particle shape also seen in SEM images, particularly in the distal samples which are dominated by vesicular glass fragments.

The 2.5 ϕ sieve fractions of sieved samples contain range of components (Fig. 3.5a). At site 46, the lower pumice contains a diverse range of crystals (~60%), holocrystalline (34%) and vesicular particles (6%; Fig. 3.5c). The upper pumice is dominated by plagioclase crystals, which account for >65% of the particles analysed (Fig. 3.5c). The samples from the zone of poor preservation (170-230 km) contain a mixture of holocrystalline particles (20%), free crystals (60%) and vesicular particles (20%; Fig. 3.5c). All the crystal phases found in the Plinian units correspond to the expected crystal population of explosive Mazama products (*Bacon and Druitt*, 1988; *Bacon and Lanphere*, 2006). Unimodal distal samples (>400 km) contain >90% volcanic glass with only minor FeTi oxides, plagioclase, and pyroxene crystals (Fig. 3.5c). The glassy particles are highly vesicular and some have shard morphologies (Fig. 3.5b).

The differences in componentry of the Mazama tephra (Fig. 3.5) are reflected in the shape parameters measured by the CX2. At sites 46 and 47, the 1-3 ϕ sieve fractions have average particle sphericities (SPHT) ~0.82 and an average aspect ratio (b/l) ~0.64. The material >3 ϕ (<125 µm), however, has average SPHT ~0.77 and b/l ~ 0.63. The higher SPHT of the coarse sieve fractions is caused by the high proportion of crystals which have smooth particle perimeters compared to the micro-vesicular particles that dominate the material <125 µm. The unimodal distal samples have an average SPHT ~0.76 and average b/l ~0.6 because of the abundance of

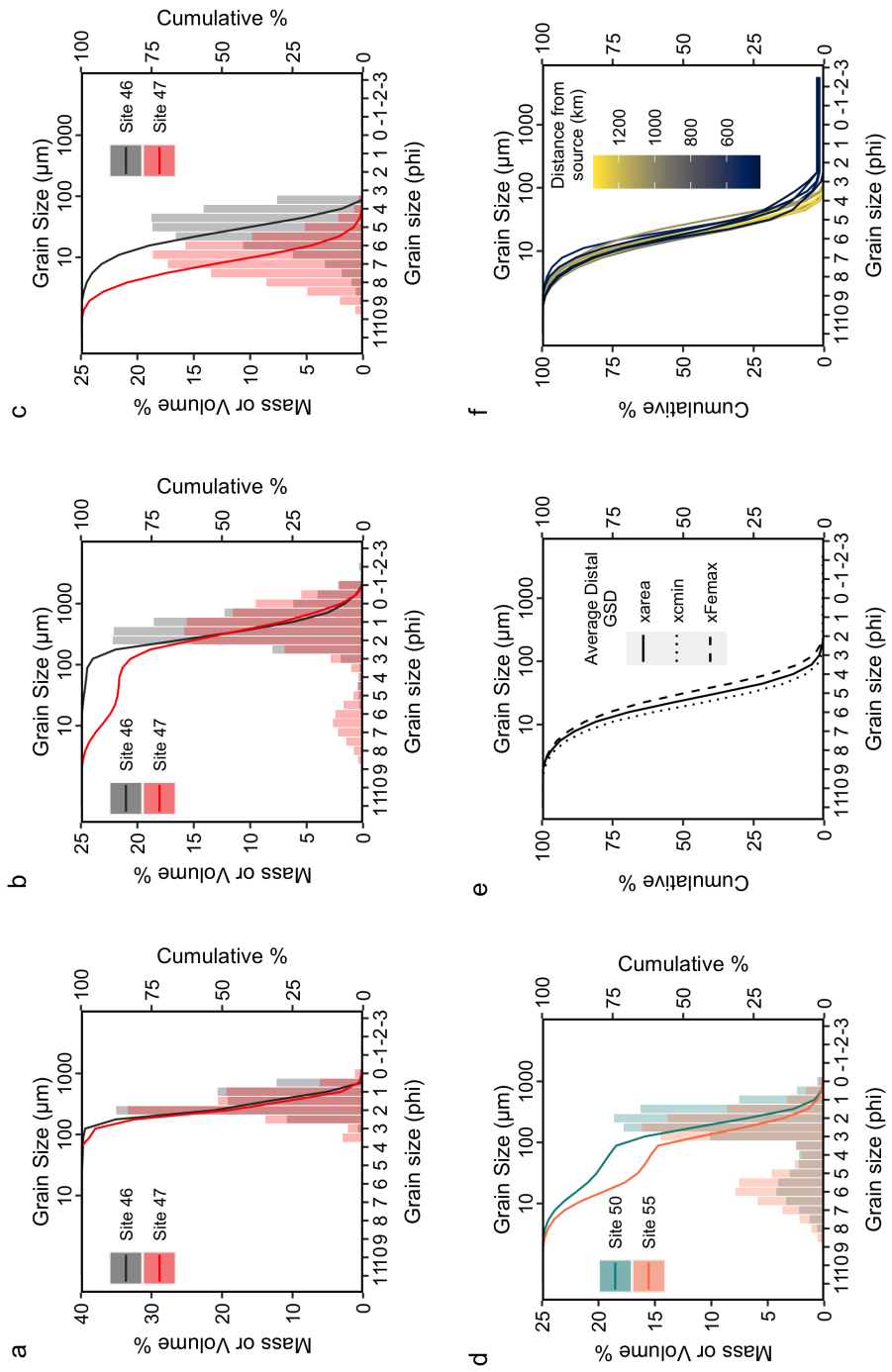

Figure 3.4: Grain Size Distributions of Mazama tephra at difference distances from source. a) Lower pumice unit GSD for equivalent terrestrial (site 46) and lake (site 47) records. b) Upper pumice unit GSD for equivalent terrestrial and lake records. c) Fine-grained GSDs for co-PDC samples. Renormalised for material >3 ϕ (<125 µm). d) GSDs of two bimodal samples sampled in the zone of poor preservation. e) Average GSD of all unimodal distal samples quantified according to different size parameters and f) all distal unimodal sample GSDs ($x_c$min) coloured according to the distance from source.

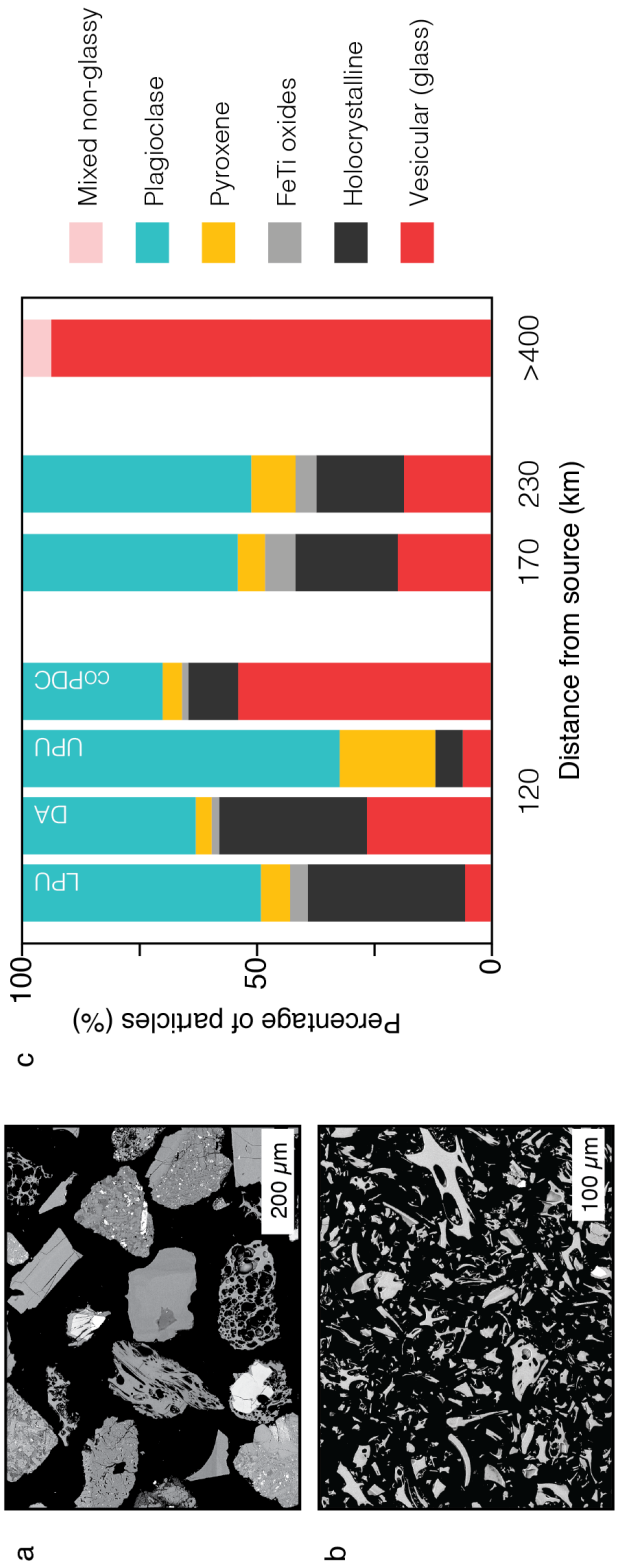

Figure 3.5: Relationship between ash componentry, eruptive unit and distance from source. a) BSE-SEM image of 2.5 ϕ sieve fraction from site 50 (170 km from source). b) BSE-SEM image of un-sieved distal sample from site 73 (440 km from source). c) Stacked bar plots showing relative proportion of each component type with distance from source.

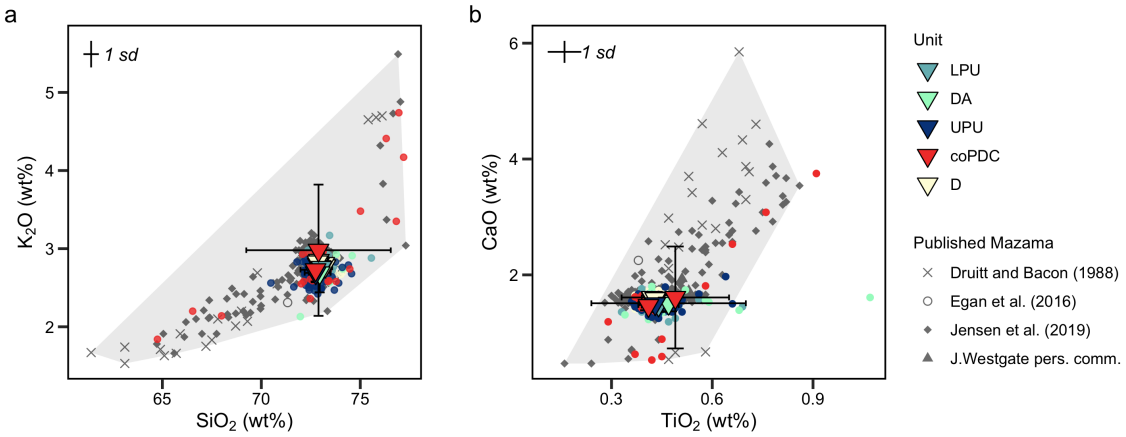

Figure 3.6: Major glass geochemical data for all samples analysed in this study. Average per sample plotted as triangles with the error bars showing the standard deviation within the sample. Individual analyses plotted in coloured circles. Averages and individual analyses are colour coded by the eruptive unit. The standard deviation of the secondary standard analyses is shown in the top left corner or each plot. Reference Mazama geochemistry is plotted as grey symbols and the filled area is a filled convex across the compositional range. a). SiO_2 wt% versus K_2O wt%. b) TiO_2 wt% versus CaO wt%.

vesicular and glass shard particle morphologies. It also suggests that distal Mazama ash exhibits significant particle elongation (see Chapter 4, Fig. 4.12). Finally, there is no apparent change in the shape of the unimodal (>400 km) Mazama ash with distance.

3.4.2 Major element geochemistry of Mazama glass and oxides

The average major element geochemical data for each sample is reported in Table 3.1. All samples >130 km from source have been classified as 'distal' because no stratigraphic units were identified for separate geochemical analysis. All measured glass compositions correspond to published analyses of climactic Mazama rhyodacite (Fig. 3.6) and there is very little variability within or between all samples. For example, excluding the co-PDC samples, the average glass SiO_2 is 72.94 wt% with a standard deviation of ±0.94. The most variable analyses are associated with the upper fine-grained unit of the lake core sample (site 47) where some particles record SiO_2 >75% and others have dacitic glass composition (SiO_2 ~66 wt%; Fig 3.6 and Table B.1). However, these compositions still lie within the expected range of climactic Mazama products according to published data (Fig. 3.6; *Egan et al.*, 2016; *Bacon and Druitt*, 1988; *Jensen et al.*, 2019). Interestingly, the low and high SiO_2 analyses seem to correspond with scoriae and granitoid glass analyses from *Bacon and Druitt* (1988; Fig. 3.7).

Table 3.1: Average and standard deviation of glass major element composition of Mazama tephras analysed in this study. Full data including secondary glass standards are presented in Tables B.1&B.2. Units correspond to D – distal, LPU – lower pumice unit, DA – divider ash, UPU – upper pumice unit, coPDC – upper fine-grained units at site 46 and 47.

Site	Unit	n		SiO_2	TiO_2	Al_2O_3	FeO	MnO	MgO	CaO	Na_2O	K_2O	P_2O_5	Cl	Total
50	D	30	Av.	73.07	0.44	14.34	1.97	0.05	0.45	1.56	5.1	2.79	0.06	0.17	98.88
			St.Dev	*0.34*	*0.02*	*0.24*	*0.04*	*0.01*	*0.01*	*0.09*	*0.14*	*0.09*	*0.01*	*0.01*	*0.79*
55	D	32	Av.	73.24	0.44	14.2	1.97	0.05	0.44	1.54	5.08	2.78	0.07	0.18	98.63
			St.Dev	*0.33*	*0.02*	*0.26*	*0.06*	*0.01*	*0.02*	*0.11*	*0.11*	*0.08*	*0.02*	*0.04*	*0.9*
80	D	10	Av.	73.18	0.42	14.13	1.91	0.04	0.44	1.59	5.24	2.81	0.06	0.17	98.32
			St.Dev	*0.2*	*0.02*	*0.17*	*0.03*	*0.01*	*0.03*	*0.06*	*0.13*	*0.08*	*0.02*	*0.01*	*0.67*
81	D	7	Av.	72.93	0.43	14.31	1.92	0.04	0.45	1.55	5.3	2.81	0.08	0.18	98.89
			St.Dev	*0.18*	*0.02*	*0.13*	*0.02*	*0.02*	*0.02*	*0.05*	*0.11*	*0.04*	*0.03*	*0.01*	*0.72*
101	D	9	Av.	72.91	0.42	14.25	1.92	0.04	0.44	1.61	5.29	2.85	0.08	0.18	98.93
			St.Dev	*0.2*	*0.02*	*0.17*	*0.03*	*0.01*	*0.03*	*0.06*	*0.13*	*0.08*	*0.02*	*0.01*	*0.67*
67	D	10	Av.	72.85	0.43	14.31	1.93	0.05	0.45	1.6	5.33	2.8	0.07	0.17	98.96
			St.Dev	*0.24*	*0.02*	*0.14*	*0.04*	*0.01*	*0.03*	*0.08*	*0.15*	*0.05*	*0.02*	*0.01*	*0.82*
69	D	10	Av.	72.99	0.42	14.26	1.92	0.05	0.45	1.61	5.3	2.77	0.07	0.18	100.23
			St.Dev	*0.25*	*0.03*	*0.14*	*0.04*	*0.02*	*0.02*	*0.09*	*0.14*	*0.07*	*0.02*	*0.01*	*0.52*
73	D	23	Av.	72.84	0.43	14.26	1.92	0.05	0.44	1.59	5.39	2.83	0.07	0.18	98.39
			St.Dev	*0.28*	*0.02*	*0.17*	*0.04*	*0.01*	*0.03*	*0.08*	*0.15*	*0.06*	*0.02*	*0.01*	*0.61*
46	LPU	41	Av.	73.04	0.44	14.05	2.37	0.03	0.4	1.48	5.21	2.76	0.06	0.17	97.98
			St.Dev	*0.54*	*0.06*	*0.23*	*0.21*	*0.02*	*0.04*	*0.12*	*0.37*	*0.13*	*0.02*	*0.02*	*0.65*
46	DA	28	Av.	72.95	0.47	14.12	2.42	0.04	0.39	1.51	5.18	2.69	0.06	0.18	98.94
			St.Dev	*0.55*	*0.23*	*0.27*	*0.4*	*0.02*	*0.03*	*0.14*	*0.13*	*0.25*	*0.02*	*0.05*	*0.88*
46	UPU	81	Av.	72.75	0.43	14.16	2.49	0.04	0.42	1.5	5.29	2.69	0.06	0.18	98.61
			St.Dev	*0.56*	*0.05*	*0.28*	*0.28*	*0.02*	*0.04*	*0.12*	*0.37*	*0.12*	*0.02*	*0.03*	*0.99*
46	co-PDC	9	Av.	72.74	0.41	14.22	2.41	0.05	0.41	1.47	5.32	2.73	0.08	0.17	98.67
			St.Dev	*0.76*	*0.02*	*0.37*	*0.21*	*0.02*	*0.04*	*0.08*	*0.23*	*0.15*	*0.02*	*0.01*	*0.87*
47	co-PDC	16	Av.	72.89	0.49	13.74	2.51	0.03	0.54	1.61	4.93	2.98	0.1	0.18	99.02
			St.Dev	*3.65*	*0.16*	*1.49*	*0.97*	*0.03*	*0.44*	*0.88*	*0.68*	*0.84*	*0.1*	*0.06*	*0.94*

The major element geochemical data and stoichiometric calculations for the FeTi oxides are reported in Table 3.2. Titanomagnetite compositions for the Plinian, co-PDC and distal samples are shown in Figure 3.8. The marginal density plots (Fig. 3.8b) highlight the presence of titanomagnetites with elevated TiO_2 in all samples except the lower pumice unit (LPU). From this we define $TiO_2 > 9.22$ wt% as the criteria to classify each titanomagnetites as a high- or low-Ti.

Titanomagnetite-ilmenite geothermobarometry results are reported in Table 3.3. Calculated temperatures range from 856–942°C with a mean temperature of 893°C. Corresponding oxygen fugacities are 0.67–1.18 ΔNNO with an average value of 1.07. The seven touching pairs that contained high-Ti titanomagnetites gave an average equilibrium temperature of 921°C. Different temperature and oxygen fugacity formulations were used for comparison, and each gave slightly

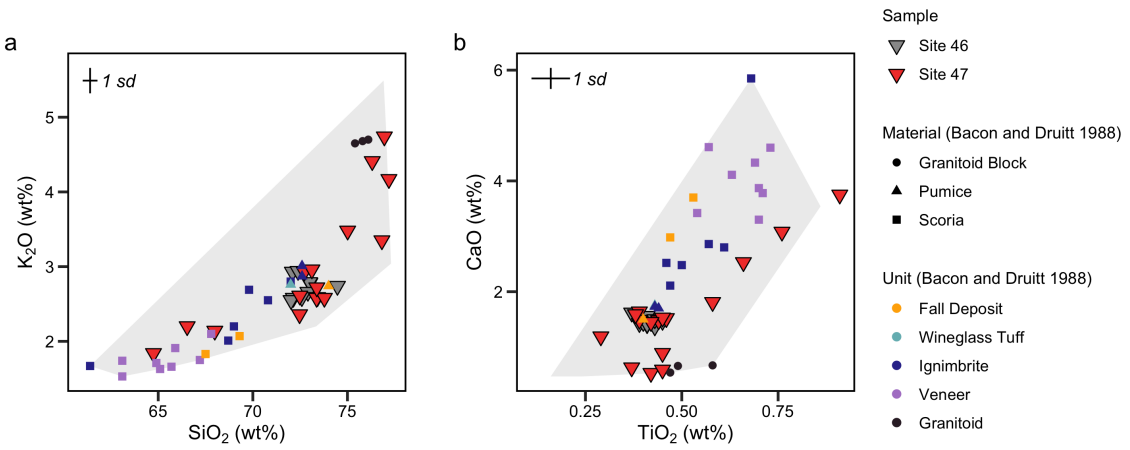

Figure 3.7: Glass composition of co-PDC samples. Bivariant plots of a) SiO_2 versus K_2O (wt%) and b) TiO_2 versus CaO (wt%). The colour of the triangles indicates the sampling site (46 – terrestrial, 47 – lake core). The compositional range of all published data is shown by are within the grey filled convex hull. Glass data from *Bacon and Druitt* (1988) has been plotted for comparison. The shape of the *Bacon and Druitt* (1988) points corresponds to the material analysed and the colour corresponds to the eruptive unit.

different absolute values of temperature and ΔNNO. However, all yield higher temperatures for the small number of high-Ti titanomagnetite pairs; the spread of absolute values for all the analyses was the same (range of ~100 °C).

3.5 Discussion

Do new geochemical and physical data collected for Plinian, co-PDC and distal Mazama samples provide new insight into the relative contribution of co-PDC ash to the distal ash budget? To answer this question, we first assess whether the characterisation of tephra sections that preserve distinct Plinian and co-PDC units has provided unique physical or geochemical identifiers that can be traced to distal ash deposits. We then explore whether these characteristics could be used to approximate a relative volume of Plinian and co-PDC ash. Finally, we outline future work that could further elucidate the provenance of fine-grained ash during large magnitude eruptions.

3.5.1 Evidence of co-PDC ash contribution to distal Mazama deposits

The physical characteristics of the distal Mazama ash are consistent with ash associated with co-PDC plumes. In particular, the distal ash is dominated by fine-grained (<125 μm) glassy, material (Figs. 3.4 & 3.5) which is typical of ash elutriated from PDCs (Fig. 3.1). However, the

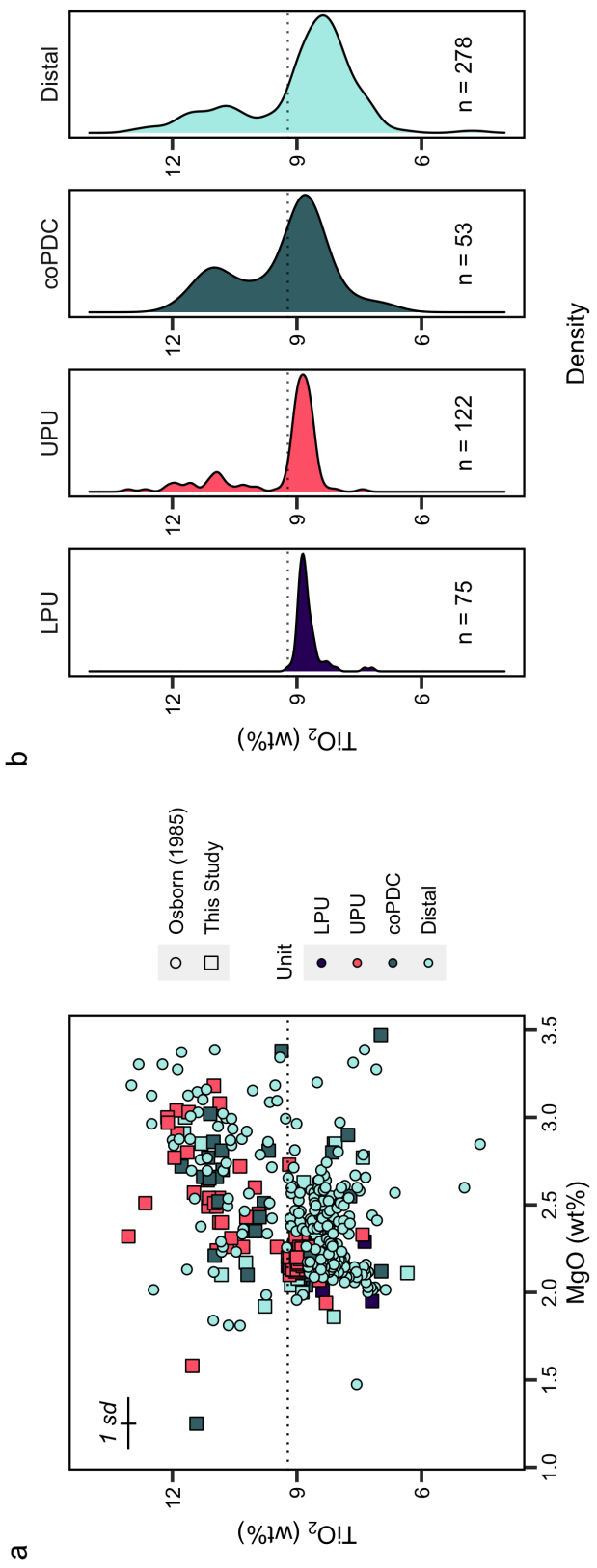

Figure 3.8: Major element geochemistry of Mazama titanomagnetites. a) MgO (wt%) versus TiO_2 (wt%) of oxides analysed in this study compared to geochemistry of distal grains analysed by *Osborn* (1985). b) Marginal density plots of TiO_2 content split by the eruptive unit and distance from source. n is the number of grains analysed per plot. The dashed line in a and b is the upper limit of TiO_2 measured in the LPU oxides.

Table 3.2: Average and standard deviation of FeTi oxide major element composition of Mazama tephras analysed in this study. Full data including secondary standards are presented in Tables B.3&B.4. Units correspond to D – distal, LPU – lower pumice unit, DA – divider ash, UPU – upper pumice unit. Mineral codes are TM – titanomagnetite and ILM – ilmenite.

Site	Mineral	Unit	n		TiO_2	Al_2O_3	FeO_t	FeO*	Fe_2O_3*	MnO	MgO	SiO_2	Cr_2O_3	$Total_t$	Total*
50	TM	D	20	Av.	9.06	2.2	81.07	35.98	50.11	0.48	2.29	0.07		95.16	100.18
				St.Dev	*0.99*	*0.33*	*1.29*	*0.79*	*2.18*	*0.03*	*0.27*	*0.02*		*0.34*	*0.33*
55	TM	D	20	Av.	8.92	2.25	81.42	35.98	50.51	0.47	2.28	0.07		95.41	100.47
				St.Dev	*0.84*	*0.5*	*0.99*	*0.79*	*1.67*	*0.06*	*0.28*	*0.02*		*0.39*	*0.36*
46	TM	LPU	50	Av.	8.73	2.07	81.41	35.9	50.57	0.49	2.14	0.05	0.03	94.92	99.98
				St.Dev	*0.35*	*0.11*	*0.37*	*0.37*	*0.64*	*0.02*	*0.07*	*0.01*	*0.02*	*0.36*	*0.36*
46	TM	DA	25	Av.	8.78	2.07	81.44	35.99	50.51	0.49	2.15	0.06	0.03	95.01	100.07
				St.Dev	*0.24*	*0.05*	*0.35*	*0.26*	*0.48*	*0.02*	*0.04*	*0.02*	*0.01*	*0.34*	*0.36*
46	TM	UPU	122	Av.	9.39	2.23	80.65	36.38	49.2	0.47	2.29	0.06	0.04	95.12	100.05
				St.Dev	*1.1*	*0.35*	*1.37*	*0.92*	*2.45*	*0.04*	*0.24*	*0.01*	*0.03*	*0.37*	*0.3*
46	TM	co-PDC	37	Av.	8.99	2.32	80.98	36.1	49.87	0.46	2.27	0.06	0.04	95.12	100.12
				St.Dev	*0.93*	*0.49*	*1.27*	*0.9*	*2.12*	*0.05*	*0.31*	*0.01*	*0.05*	*0.36*	*0.36*
47	TM	co-PDC	16	Av.	10.07	2.85	79.08	37.04	46.72	0.4	2.51	0.07	0.14	95.11	99.79
				St.Dev	*1.21*	*0.7*	*1.28*	*1.34*	*2.38*	*0.08*	*0.47*	*0.01*	*0.14*	*0.38*	*0.4*
Mult.[a]	TM	D	8	Av.	8.45	2.02	80.83	35.62	50.25	0.49	2.09	0.1	0.05	94.03	99.06
				St.Dev	*0.99*	*0.1*	*1.05*	*1.02*	*2.04*	*0.03*	*0.1*	*0.04*	*0.03*	*0.82*	*0.86*
50	ILM	D	20	Av.	40.32	0.29	53.2	30.19	25.57	0.48	3.14	0.02		97.44	100
				St.Dev	*0.87*	*0.03*	*0.87*	*0.69*	*1.68*	*0.04*	*0.12*	*0.01*		*0.31*	*0.32*
55	ILM	D	20	Av.	40.13	0.28	53.51	30.07	26.04	0.49	3.12	0.02		97.55	100.15
				St.Dev	*0.23*	*0.01*	*0.33*	*0.21*	*0.41*	*0.02*	*0.09*	*0.01*		*0.24*	*0.26*
46	ILM	LPU	25	Av.	40.36	0.27	53.37	30.54	25.36	0.51	2.97	0.01		97.49	100.02
				St.Dev	*0.32*	*0.04*	*0.34*	*0.67*	*0.8*	*0.13*	*0.32*	*0.01*		*0.33*	*0.35*
46	ILM	DA	10	Av.	40.31	0.28	53.45	30.49	25.52	0.49	2.99	0.02		97.52	100.08
				St.Dev	*0.39*	*0.03*	*0.39*	*0.3*	*0.69*	*0.02*	*0.07*	*0.01*		*0.23*	*0.21*
46	ILM	UPU	39	Av.	41.12	0.3	52.81	30.91	24.34	0.48	3.17	0.02		97.89	100.33
				St.Dev	*1.43*	*0.04*	*1.44*	*0.92*	*2.49*	*0.04*	*0.32*	*0.02*		*0.54*	*0.47*
46	ILM	co-PDC	10	Av.	40.22	0.29	53.37	30.25	25.7	0.49	3.07	0.02		97.45	100.02
				St.Dev	*0.28*	*0.02*	*0.31*	*0.31*	*0.59*	*0.02*	*0.06*	*0.01*		*0.23*	*0.24*
47	ILM	co-PDC	4	Av.	41.97	0.31	52.25	31.56	22.99	0.48	3.24	0.02		98.26	100.56
				St.Dev	*1.4*	*0.03*	*1.54*	*0.81*	*2.61*	*0.04*	*0.27*	*0*		*0.4*	*0.43*

(a) Data for 8 distal titanomagnetite crystals sampled >400 km from source in crystal poor samples.

Table 3.3: Results of FeTi-oxide geothermometer/oxygen barometer (*Ghiorso and Evans*, 2008). n indicates the number of analyses per grouping.

Touching pairs group	n	Average temperature (T°C)	*St.Dev (T°C)*	Average oxygen fugacity (ΔNNO)	*St.Dev (ΔNNO)*
All	76	893	*12.6*	1.07	*0.12*
High-Ti TM (TiO_2 >9.22 wt%)	7	921	*15.2*	0.78	*0.13*
Low-Ti TM	69	890	*7.0*	1.10	*0.05*

shape of distal ash remains highly irregular due to the vesicular nature of the Mazama tephra (Fig. 3.5b) and the proportion of crystals was too low in the distal deposits to assess the adherence factor. Moreover, other studies (*Moore*, 1991; *Perrotta and Scarpati*, 2003; *Matthews et al.*, 2012; *Engwell et al.*, 2014) have shown that the physical characteristics of co-PDC and Plinian ash can converge on the same grain size and componentry as the distance from source increases. From this we conclude that the size and componentry cannot be used to uniquely identify ash source for the distal Mazama tephra, although the data allow a substantial contribution of co-PDC ash.

The parallel geochemical characterisation of the Mazama tephra provides evidence to associate at least some of the fine ash with the later stages of the climactic eruption. For example, the fine-grained (inferred co-PDC) ash at site 47 (lake core) contains several particles with dacitic (~65 wt% SiO_2) glass compositions that may record the mafic enrichment observed by *Bacon and Druitt* (1988) in the PDCs (Fig. 3.7b). The range of glass compositions recorded in the lake core co-PDC sample is also similar to the range recorded by *Jensen et al.* (2019) in distal Mazama tephra samples from Canada (Figs. 3.3 & 3.6), which again supports the hypothesis that at least some portion of the distal ash is associated with the ignimbrite forming phase.

The composition of the titanomagnetites in the stratigraphic section at site 46 (Fig. 3.8b) show that high-Ti magnetites are only associated with later stages of the Plinian phase and are then present throughout the ignimbrite forming phase. This data supports the hypothesis of *Osborn* (1985) that distal high-Ti titanomagnetites are associated with the later stages of the Mazama eruption and that their presence in distal Mazama tephra could indicate a co-PDC source. Furthermore, the Fe-Ti oxide geothermometry suggests higher temperatures are associated with the high-Ti titanomagnetites. *Druitt and Bacon* (1989) similarly measured higher magmatic temperatures from Fe-Ti oxides in climactic scoria samples (892–929°C) further supporting the association of the high-Ti titanomagnetites with the later stages of the eruption.

3.5.2 Relative contribution of fine ash from different fragmentation processes

The physical and geochemical characterisation of distal Mazama tephra provide evidence to suggest that co-PDC ash contributed to the total volume of fine ash produced and dispersed during the climactic eruption. However, estimating the proportion of the total ash volume attributed to a co-PDC source ash is more challenging. Firstly, the physical characteristics cannot alone determine the ash source. Similarly, whilst the range of glass compositions in the co-PDC and distal samples does parallel the range of glass compositions recorded in the ignimbrite forming phase, small amounts of scoria were erupted during the Plinian phase of the eruption (*Bacon and Druitt*, 1988; *Druitt and Bacon*, 1989) and we show that high-Ti magnetites are not exclusive to the co-PDC phase (Fig. 3.8).

One reason that the Mazama co-PDC ash is not fully geochemically distinct from the co-Plinian ash, is that rhyodacite pumice was the principle major component of the PDCs and the major element geochemistry of the climactic rhyodacite pumice remains homogenous across all phases of the eruption (3.6; *Bacon*, 1983; *Bacon and Druitt*, 1988). Equally, the mafic enriched flows were smaller in volume and the farthest travelled PDCs were rhyodacite (*Druitt and Bacon*, 1986). Moreover, the mafic scoria has a high crystal content (21–51 vol% crystals, *Druitt and Bacon* 1989) making it less susceptible to secondary fragmentation processes within PDCs such as abrasion that can produce co-PDC ash (*Buckland et al.*, 2018). This means that it is unlikely that significant portions of the co-PDC ash would reflect the mafic components.

Interestingly, the upper fine-grained unit at site 46 (Fig. 3.3) did not record the same range of glass compositions as the parallel lake core (site 47). Similarly, the fine-grained subpopulation (Fig. 3.5) was coarser than the lake core. This could suggest that very fine-grained tephras from co-PDC sources are poorly preserved in the terrestrial record, particularly close to source. This is supported by the field evidence of weathering in the terrestrial record and minor contaminant particles found in the uppermost unit (see Table B.1). This is an important interpretation as it suggests that our record is biased against preserving co-PDC ashes close to source and thus we could underestimate their significance when forecasting future eruptions.

To determine an approximate volume contribution from a co-PDC source for the distal Mazama tephra, we cannot use the geochemical or physical characteristics of the ash alone. Other studies have used proximal deposit volumes in addition to granulometric and geochemical data to estimate the contribution of co-PDC ash. For example, for the Campanian Ignimbrite tephra, the ratio of co-Plinian to co-PDC ash volume is estimated as 1:5 (*Perrotta and Scarpati*, 2003). This comes from volume estimates of the proximal Plinian and PDC volumes close to source. Following this approach, we would suggest that the ratio of co-Plinian to co-PDC in the distal Mazama tephra could be 1:4 because the proximal fall out volume is ~4 km^3 (see Chapter 2) compared to

the 16 km^3 volume of the PDCs (*Williams*, 1942). This would equate to 30 km^3 DRE of distal ash from a co-PDC source.

3.6 Conclusions

Detailed physical and geochemical characterisation of Plinian, co-PDC and distal Mazama tephra has provided new evidence that the distal ash can be related to the late Plinian and ignimbrite forming phases of the climactic eruption. A definitive identifier of co-PDC ash was not provided by the analysis because of the non-unique physical attributes of distal co-Plinian and co-PDC ash in addition to the homogenous nature of the rhyodacite that is the dominant erupted product. However, the range of glass compositions recorded in a proximal lake core that recorded a fine-grained co-PDC unit has been linked to glass compositions from the ignimbrite forming phase (*Bacon and Druitt*, 1988) which is paralleled by distal Mazama tephras (*Westgate and Gorton*, 1981; *Jensen et al.*, 2019).

Combining the new insight with volume estimates provides a rough estimate of the ratio of co-Plinian to co-PDC ash of around 1:4, which is within the range determined for other large explosive eruptions (*Sigurdsson and Carey*, 1989; *Dartevelle et al.*, 2002; *Perrotta and Scarpati*, 2003). To improve our understanding of the significance of co-PDC ash from the Mazama eruption a number of research questions could be investigated further. Firstly, analysing the trace element geochemistry of the erupted products across the well-constrained stratigraphic sections at sites 46 & 47 would provide insight into any small deviations in the rhyodacite composition. This was useful for distinguishing the Plinian and ignimbrite phases in the Campanian Ignimbrite tephra which can be separated on a plot of Zr-Th (*Tomlinson et al.*, 2012). Of particular interest for Mazama products is the Sr content in the glass which should be lower towards the end of the ignimbrite forming phase. Finally, more extensive work on the proximal PDCs and data collection in the zone of poor preservation could prove useful. For example, assessing the relative componentry of the PDCs would determine the degree of crystal enrichment due to the lofting of fine ash lost in co-PDC plumes.

CHAPTER 4

MEASURING THE SIZE OF NON-SPHERICAL PARTICLES AND THE IMPLICATIONS FOR GRAIN SIZE ANALYSIS IN VOLCANOLOGY

Buckland HM, Saxby J, Roche M, Meredith P, Rust AC, Cashmam KC, Engwell SL (2021) Measuring the size of non-spherical particles and the implications for grain size analysis in volcanology. *Journal of Volcanology and Geothermal Research.*

Author Contributions and declaration: H. Buckland carried out the conceptualization, method testing and development, data analysis and writing of the manuscript. J. Saxby contributed 3D data collected on extreme ash shapes and manuscript edits. M. Roche ran the glass sphere analyses and preliminary comparisons of sieving and CX2 as part of an undergraduate summer research program. P. Meredith collected the grain size data for the new MSH samples as part of her MSc dissertation and carried out preliminnary comparisons of the different size parameters. K. Cashman, A. Rust and S. Engwell provided supervision and helped with manuscript editing. Samples were provided by E. Liu; U. Mueller, W. Ferrand, D. Pyle, D. Veres; B. Carson and B. Jensen. Grain size data and distribution analyses of the MSH samples was shared by A. Durant and J. Eychenne. H. Goodes helped setup and run the CX2 in the School of Earth Sciences at the University of Bristol. T. Giachetti and J. Castro provided insightful reviews that improved the published manuscript and K. Russell provided quick and helpful editorial handling.

Abstract

To quantify the size of tephra, two practical challenges must be addressed: the wide range of particle sizes (10^{-8} to 10^{1} m) and the diversity of particle shape, density and optical properties. Here we use Dynamic Image Analysis (DIA) to simultaneously characterise the size and shape of tephra samples from Mount Mazama, Krafla, Mount St. Helens and Campi Flegrei. The Camsizer X2 instrument used in this study, which has a measurement range of 0.8 µm to 8 mm, avoids the need to overlap different measurement methods and principles for fine (<125 µm) and coarse (>125 µm) particle sizes. Importantly, DIA does not require an assumption of particle properties. DIA also allows the measurement of Grain Size Distributions (GSDs) using multiple size definitions. Quantification by particle long axis and the area equivalent sphere diameter, for example, make DIA GSDs compatible with the outputs of other methods such as laser diffraction and sieving. Parallel mass-based (sieving) and volume-based (DIA) GSDs highlight the effects of particle density variations on methods of size analysis; concentrations of dense crystals within a narrow size range, in particular, can affect mass-based GSDs and their interpretations. We also show that particle shape has an important effect on the apparent grain size of distal tephra. Extreme particle shapes, such as the platy glass shards typical of the distal Campanian Ignimbrite deposits, can appear coarser than other distal tephras if size is quantified according to the particle long axis. These results have important implications for ash dispersion models, where input GSDs assume that reported measurements are for volume-equivalent sphere diameters. We conclude that DIA methods are not only suitable for characterising, simultaneously, the size and shape of ash particles but also provide new insights into particle properties that are useful for both ash dispersion modelling and studies of explosive volcanism.

4.1 Introduction

Particles with highly irregular shapes, such as the products of explosive volcanic eruptions (tephra), present a particular challenge when quantifying particle size. The 'size' of non-spherical particles can be quantified in multiple ways depending on the method of measurement and definition of 'size'. For example, size can be measured as the longest particle dimension using callipers, or the diameter of a volume equivalent sphere calculated from 3D data (*Bagheri et al.*, 2015; *Saxby et al.*, 2020). A clear and consistent definition of size is important because the 'size' of tephra is used to predict the dispersal of the particles in the atmosphere (*Rose and Durant*, 2009; *Mele et al.*, 2011; *Engwell and Eychenne*, 2016; *Saxby et al.*, 2018). The Grain Size Distribution (GSD) of tephra also provides insight into fragmentation mechanisms (e.g., *Barberi et al.*, 1989; *Wohletz et al.*, 1989; *Jones et al.*, 2016; *Mele et al.*, 2020) and estimates of eruption column heights for unobserved eruptions (e.g., *Carey and Sparks*, 1986; *Burden et al.*, 2011; *Rossi et al.*, 2019). Additionally, accurate measurements of the GSD of volcanic ash (tephra <2 mm) are important for understanding the risks posed to human health and infrastructure (*Horwell and Baxter*, 2006; *Horwell*, 2007; *Bebbington et al.*, 2008; *Wilson et al.*, 2012; *Blake et al.*, 2017) and the efficiency of wind-driven remobilisation (*Hadley et al.*, 2004; *Leadbetter et al.*, 2012; *Liu et al.*, 2014; *Panebianco et al.*, 2017). Finally, quantitative measurements of particle shape complement size analysis and are equally important for interpreting eruptive processes and forecasting tephra transport and sedimentation (*Heiken*, 1972; *Riley et al.*, 2003; *Cioni et al.*, 2014; *Bagheri et al.*, 2015; *Liu et al.*, 2015; *Saxby et al.*, 2018; *Dürig et al.*, 2020).

One of the main challenges faced when characterising a tephra deposit is the large range of particle sizes produced by an eruption (from 10^{-8} to 10^{1} m). This has required the use of a variety of methods to measure size, often requiring an overlap of two or more methods to analyse the coarse and fine components of a single sample. Numerous size and shape parameters are associated with different methods and the choice of parameter has implications for data interpretation and comparison. Furthermore, particle size and shape are typically analysed separately using different methods, leading to slow data collection and processing as noted by several authors who have investigated the range of shape parameters and size characterisation methods for volcanic ash (*Riley et al.*, 2003; *Leibrandt and Le Pennec*, 2015; *Liu et al.*, 2015). Thus, despite the importance of grain size and shape characterisation, data compilation and comparison across different studies is hindered by the range of methods used.

Tephra from a single eruption is a mixture of components (e.g., lithics, free-crystals and juvenile fragments such as pumice) and each component can have unique optical and physical properties (e.g., refractive index, density, porosity and permeability) which can limit the efficacy of grain size methods initially developed for analysing more homogeneous materials. The different components within a single sample can have individual GSDs that overlap to produce the GSD of the whole

sample (*Moore*, 1934; *Walker*, 1971; *Sparks*, 1976; *Mele et al.*, 2020). A further complication is that the relative proportion of each component can vary spatially in a deposit due to emplacement and transport processes (*Sparks and Walker*, 1977; *Carey and Sigurdsson*, 1982; *Williams and Self*, 1983; *Eychenne et al.*, 2015). For example, crystal concentrations observed in fall deposits reflect a narrow crystal size and density distribution that causes deposition over a limited transport distance. Grain size procedures that do not account for variations in particle density or componentry with size (e.g., sieving) could therefore produce inaccurate interpretations of GSDs.

Here we outline an analytical protocol for simultaneous size and shape characterisation using a fast and flexible method that employs Dynamic Image Analysis (DIA). Methods of size measurement that use image analysis do not need to assume particle shape, which is analysed simultaneously. Imaging individual particles also means that multiple size parameters (e.g., particle long axis and equivalent circle diameter) are measured concurrently. This provides both adaptability and consistency when reporting size measurements. First, we discuss the significance of grain size measurement in studies of explosive volcanism (Section 4.2) and review grain size analysis methods with emphasis on how 'size' is quantified (Table 4.1; Appendix C.1). We then outline a methodology for size analysis using DIA with example analyses using spherical and non-spherical particles (Section 4.3). We follow this by discussing the benefits of DIA for measuring the grain size of tephra and examine the implications of using different size measurements in volcanological applications (Sections 4.4-4.5). We conclude by showing ways in which inconsistencies in size definitions for non-spherical particles affect studies of explosive volcanism, particularly when particle shapes are extreme, as is common for glass shards.

4.2 Background

Analysing the grain size of tephra is a long-established practise in volcanology and the standard methodologies applied were adopted from the wider field of sedimentology (*Wentworth*, 1922; *Krumbein*, 1934; *Pettijohn*, 1949). For example, early work characterising the grain size of field deposits helped distinguish poorly sorted pyroclastic density current deposits (nuée ardente or ignimbrite deposits) from well sorted airfall deposits (*Lacroix*, 1904; *Moore*, 1934; *Fenner*, 1937). Standard statistical procedures from sedimentology were also adopted, such as characterising GSDs using the maximum clast size, median diameter (Md) and sorting (σ; *Fisher*, 1964). Also adapted from sedimentology is the practise of deconvolving multi-modal GSDs into sub-populations. Studies of sands attribute sub-populations in multi-modal GSDs to the genesis of the material (*Visher*, 1969) and when applied to volcanic GSDs, grain size sub-populations can be related to eruptive processes (*Sheridan*, 1971; *Wohletz et al.*, 1989; *Engwell et al.*, 2014; *Eychenne et al.*, 2015). Whilst these procedures have merit and can provide insight into volcanic processes, the complex and heterogeneous physical properties of tephra as a result of the mixture of components suggests that volcanic GSDs measured using traditional grain size methods may

need additional scrutiny.

4.2.1 Why is grain size important for volcanology?

Grain size data are used to interpret two key Eruption Source Parameters (ESPs), the eruption column height (*Carey and Sparks*, 1986; *Woods and Wohletz*, 1991; *Sparks et al.*, 1992; *Burden et al.*, 2011) and the Total Grain Size Distribution (TGSD; *Carey and Sigurdsson*, 1982; *Bonadonna et al.*, 2005a). Both parameters are used to interpret the nature of eruptive activity from field deposits. Eruption column height can be inferred from modelled clast support envelopes within the eruption column (*Carey and Sparks*, 1986) and requires maximum clast size data that are typically measured in the field on a sub-sample of the largest clasts (*Bonadonna et al.*, 2013). TGSDs are produced by combining GSDs from multiple sampling sites across the tephra deposit and weighting them according to the mass accumulation of tephra (*Carey and Sparks*, 1986; *Bonadonna et al.*, 2005a).

ESPs are a key requirement for ash dispersion models, which can be used to reconstruct past eruptions or to forecast tephra dispersal from future eruptions (*Mastin et al.*, 2009; *Webley et al.*, 2009; *Bonadonna et al.*, 2012; *Beckett et al.*, 2015). Most operational and research-based ash dispersion models use an input Particle Size Distribution (PSD), where PSD is used in reference to tephra in the atmosphere (*Mastin et al.*, 2009; *Bonadonna et al.*, 2012; *Beckett et al.*, 2015; *WMO*, 2018). TGSDs determined from tephra deposits (on the ground) can be used to inform PSDs but there are several challenges to relating the two measures. First, TGSD estimates are sensitive to both the spatial coverage and number of individual GSDs measured (*Bonadonna et al.*, 2005a; *Alfano et al.*, 2016; *Pioli et al.*, 2019), which can propagate as uncertainty in the outputs of dispersion models if TGSDs are used as input PSDs (*Beckett et al.*, 2015). Second, most ash dispersion model PSDs describe a distribution of spherical particles (or particles with a fixed shape factor; *Beckett et al.*, 2015; *Saxby et al.*, 2018). Therefore, equating measured TGSDs directly to PSDs is not appropriate where particle shapes are not constant and 'size' measurements vary with particle shape and/or other physical properties such as density or refractive index.

An alternative to using TGSDs for ash dispersion modelling is to use PSDs that have been measured in situ from an active plume. In situ PSDs have been measured following aircraft encounters with ash clouds (*Hobbs et al.*, 1991; *Casadevall*, 1994; *Pieri et al.*, 2002), by flying sampling devices through plumes (e.g., *Johnson et al.*, 2012; *Petäjä et al.*, 2012; *Mori et al.*, 2016; *Schellenberg et al.*, 2019), from satellite retrievals (e.g., *Prata and Grant*, 2001; *Bonadonna et al.*, 2011; *Pavolonis et al.*, 2013; *Gouhier et al.*, 2019) and using ground based sensors (*Scollo et al.*, 2005; *Bonadonna et al.*, 2011; *Kozono et al.*, 2019). However, in situ measurements are limited to a small number of modern eruptions and the range of grain sizes is never fully covered by one technique. Furthermore, how 'size' is quantified is not consistent across ground-based or in situ

techniques, which makes the combination and comparison of in situ PSDs and GSDs challenging (*Bonadonna et al.*, 2011; *Stevenson et al.*, 2015).

4.2.2 Grain size methods in volcanology

A wide variety of methods are used to quantify the size of tephra, including laboratory-based protocols such as sieve analysis, laser diffraction, electrozone sensing, particle sedimentation and image analysis, and in situ methods such as ground-based radar and satellite remote sensing (see Appendix C.1 for details). Importantly, each method of size analysis measures the size of non-spherical particles according to a different definition of 'size' and several methods require an assumption or simplification of particle properties such as shape, density and refractive index (Appendix C.1; Table 4.1). For example, sieve analysis sorts irregular particles by both size and shape (*Komar and Cui*, 1984); GSDs measured by sieving, however, are reported as the mass fraction within grain size or sieve increments with no consideration of which particle dimension the sieve aperture refers to. Similarly, laser diffraction and electrozone sensing methods require an assumption of particle shape which means that the resulting GSDs are quantified according to unspecified particle dimensions (Table 4.1; Appendix C.1). Quantifying grain size using image analysis can ensure consistency in the size parameter measured and simultaneous shape quantification. However, some image analysis methods require pre-analysis sample preparation, such as sieving, and substantial analysis time (~hours to days) to collect and process the images, particularly when fine material necessitates high resolution images. For this reason, these methods can be time-consuming or burdensome when analysing large sample suites (>10's samples).

After measurement the convention is to report GSD statistics that facilitate comparison with other distributions. The most common parameters reported for volcanic GSDs are based on the *Inman* (1952) or *Folk and Ward* (1957) graphical methods which determine the mean (μ), median (Md), standard deviation or sorting (σ), skewness (Sk) and Kurtosis (K; *Blott and Pye*, 2001). These methods were designed for grain size data on the ϕ-scale and require very little data manipulation (Appendix C.2). This method, however, assumes that the GSD follows a log-normal distribution, in other words the GSD is normally distributed on the ϕ-scale. Alternatively, the GSD can be described using a Weibull or Rosin-Rammler distribution (*Rosin and Rammler*, 1933; *Weibull*, 1951; *Brown and Wohletz*, 1995) from which shape and scale parameters can be described (Appendix C.2). Log-normal and Weibull distributions can be fit as mixture models to account for the multimodal form of many volcanic GSDs (Appendix C.2; *Eychenne et al.*, 2012, 2015; *Costa et al.*, 2016; *Pioli et al.*, 2019; *Mele et al.*, 2020). The number and proportion of subpopulations provide additional parameters that can be compared between different samples; in some cases subpopulations can be related to distinct eruptive processes (e.g., *Sheridan*, 1971; *Eychenne et al.*, 2012, 2015; *Engwell et al.*, 2014).

Common themes found when reviewing grain size methodologies (Appendix C.1; Table 4.1) are the lack of quantified shape characterisation, the need to assume particle properties such as density and refractive index (sieving, sedimentation, laser diffraction and electrozone sensing), and the requirement of pre-analysis sample preparation (image analysis methods). Furthermore, the amount of material analysed varies between methods. Notably, methods and instruments commonly used in volcanology such as the Mastersizer 3000, Morphologi G3 and SEM image analysis use <10 mg of material per analysis, which can cause undercounting of large grains. Hence the rationale for developing approaches to particle size analysis that no do not require assumptions of shape and the pertinence of methods that can measure multiple size parameters for non-spherical particles.

4.3 Methods

4.3.1 Instrumentation

Here we present a relatively new analytical approach to characterise the size and shape of tephra which addresses some of the limitations of other techniques. The protocol involves the CAMSIZER® X2 (CX2), a particle analyser manufactured by Microtrac MRB (formerly Retsch Technology) that utilises Dynamic Image Analysis (DIA; ISO 13322-2) to characterise the grain size of particulate materials. *Castro and Andronico* (2008) published a detailed INGV report outlining similar procedures using an earlier CAMSIZER model, although the CX2 model described in this study has capabilities to work with much finer material (>0.8 µm) thanks to the multiple particle dispersion modules.

4.3.1.1 Basic principles of the CAMSIZER X2

The CX2 is a compact particle analyser that consists of three key components: the sample feeder and particle dispersal module, the imaging module, and a desktop computer running the CX2 software (Fig. 4.1). The DIA principle requires that particles are dispersed past the field of view of two high resolution digital cameras to image the moving particles that are back lit by an LED (Fig. 4.1). The combination of two cameras (one basic and one zoom) ensures that a range of particle sizes (0.8 µm to 8 mm) can be imaged at an optimum resolution. These images are processed in real-time by the CX2 software to generate shape and size distributions and compute grain size statistics.

The particles are dispersed past the cameras' field of view by one of three mechanisms: wet dispersion (X-flow), compressed air (X-jet) or as free-falling particles (X-fall). Each dispersion mechanism has an optimum grain size range. The X-fall dispersion is best for coarse material (10 µm to 8 mm), X-jet covers 0.8 µm to 5 mm and X-flow is suited to fine material (0.8 µm to 1 mm). The choice between X-jet and X-flow for fine material (0.8 µm to 1 mm) depends on the maximum

Table 4.1: Summary of grain size methods discussed in this chapter with measurement range and the assumptions required to quantify size. See Appendix C.1 for more details.

Method name	Measurement range (μm)	Method assumptions	Size measure	Mass or volume distribution
Sieving	20-125000	Sieve aperture only equal to particle size if spherical	Diameter for spheres, minimum to intermediate dimension for non-spherical particles	M
Pipette method	50-5000	Constant density spheres	Equivalent settling velocity sphere diameter	V
Roller apparatus	1-100	Settling velocity classes of constant density spheres	Equivalent settling velocity sphere diameter	V
Laser diffraction (Mie theory)	0.01-3500	Spherical particles, constant refractive index	Volume equivalent sphere diameter	V
Laser diffraction (Fraunhofer approximation)	10-3500 μm	Flat disc particles, particles only cause diffraction	Maximum width	V
Electrozone sensing (e.g., Coulter counter)	0.4-1600	Spherical particles	Volume equivalent sphere diameter	V
Image analysis (SEM)	~0.01-200	Conversion from 2D area to 3D volume	2D Miscellaneous	V
Image analysis (Morphologi)	0.5-1300	Conversion from 2D area to 3D volume	2D Miscellaneous	V
Image analysis (cryptotephra)	20-250	Conversion from 2D area to 3D volume, material <20 μm removed	2D Miscellaneous	V
Radar disdrometer (e.g., PLUDIX)	1000-10000	Dense spherical particles	Volume equivalent sphere diameter	V
Laser disdrometer (e.g., Parsivel2)	200-25000	Dense spherical particles	Volume equivalent sphere diameter or maximum width	V
High resolution video	62-2000	Conversion from 2D area to 3D volume	2D Miscellaneous	V
Satellite infrared retrievals	~0-100	Spherical particles, constant refractive index	Volume equivalent sphere diameter	V
Dynamic Image Analysis (e.g., Camsizer X2)	0.8-8000	Conversion from 2D area to 3D volume	2D Miscellaneous	V

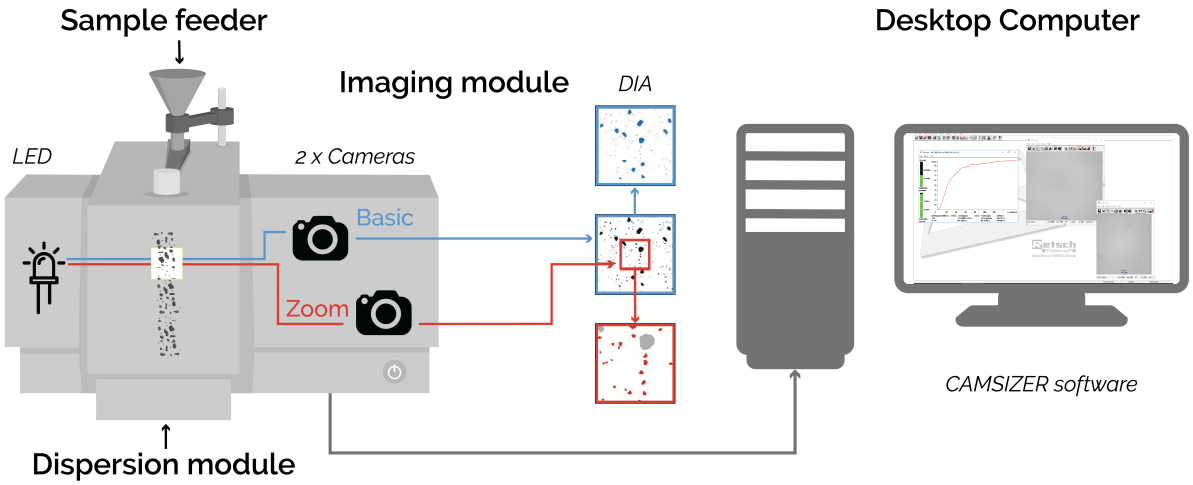

Figure 4.1: Modular set up of CAMSIZER® X2 modified from *MRB* (2020)

grain size and amount of material available to be analysed. The X-flow uses only a very small amount (<10 mg) of material for analysis so is best suited to volume-limited fine-grained samples. The choice of dispersion method for coarse material (1 to 8 mm) depends on whether sample recovery is required, which is only possible for the X-fall.

For every analysis, the CX2 requires a 'task file' (*Castro and Andronico*, 2008) that informs the software of the analytical conditions to use and allows the user to customise the data acquisition. For example, particles with certain characteristics (e.g., related to size or shape parameters) can be excluded; this is useful for eliminating contaminating fibres which have extreme values of shape parameters such as compactness and convexity (Table 4.2). One important feature of the task file is whether a 'velocity adaption' is required. When using the X-fall module (free falling particles), large particles fall faster than small particles under gravity, which causes them to be under-counted as they remain in the field of view of the camera for less time. In contrast, when using the X-jet dispersion mechanism, small particles move faster in the stream of compressed air relative to large particles, therefore, large particles are over-counted. To account for this, the CX2 images the dispersed particles twice in quick succession to produce double exposure images where the time interval between the two images has been specified by the user. Then from the double exposure images the CX2 software calculates the distance travelled by each particle and using the time interval calculates a velocity per particle. Fitting a curve to the particle velocity and particle size data then allows the software to correct for the over- or under-counting of particles based on their size (Fig. C.5). Best practise is to produce a new velocity adaption for samples

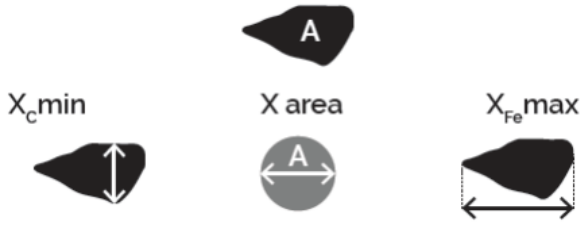

Figure 4.2: Schematic of three key size parameters; x$_c$min the minimum chord diameter, xarea the equivalent circle diameter and x$_{Fe}$max the maximum Feret diameter.

where there is a broad GSD, and for samples that have not been analysed using the CX2 before (i.e., where there no pre-existing task file).

4.3.1.2 Principles of Dynamic Image Analysis

The raw images captured by the basic and zoom cameras are converted to binary images (particle versus no particle). The size and shape of the particles in each image are measured by the CX2 software using an algorithm that combines the results from the basic and zoom cameras (Appendix C.3). Every particle imaged above a minimum size threshold is measured, with the minimum size determined by the limit of image resolution or the limit set in the task file. The software has the capacity to measure 100's of millions of particles at >300 images per second and can measure multiple size and shape parameters per particle (Table 4.2; *MRB*, 2020). Three key size parameters are equivalent circle diameter (xarea), minimum chord diameter (x$_c$min) and maximum Feret diameter (x$_{Fe}$max; Table 4.2; Fig. 4.2). These parameters are not identical for irregular particles and therefore yield different information about the particle distribution. Importantly, computing all three size parameters allows CX2 outputs to be compared with different grain size measurement methods. For example, laser diffraction using Mie theory outputs equivalent sphere diameters (~xarea) while cryptotephra data report the long axis (x$_{Fe}$max) and the retaining sieve aperture should be greater than or equal to the minimum diameter of a particle (x$_c$min; *Freret-Lorgeril et al.*, 2019).

To obtain a GSD using the CX2, the results of the 2D image analysis are converted to 3D by calculating an apparent volume per particle. The conversion from area to volume depends on the size parameters chosen. Using xarea, the conversion to volume assumes spherical particles, whereas using x$_{Fe}$max and x$_c$min assumes ellipses where the long and short axes are represented by x$_{Fe}$max and x$_c$min respectively (*Castro and Andronico*, 2008). The data can be output as a GSD in terms of volume fraction or as a particle number distribution (PND; number of particles in each size fraction).

Table 4.2: Size and shape parameters used by the CAMSIZER® X2 software.

Notation or symbol	Name	Definition or formula	Alternative nomenclature
A_P	Area of particle		
A_{CH}	Area of bounding convex hull		
U	Perimeter		
r_1 and r_2	Particle radii	Minimum and maximum radii of a particle from the centre of the particle area	
xarea	Equivalent circle diameter	Diameter of the circle having the same projection area of the particle	
x_{Fe}	Feret diameter	The perpendicular distance between parallel tangents touching opposite sides of the profile	Length, caliper diameter
$x_c$min	Chord diameter	Minimum width of the particle	Width, minimum rope
x_{Ma}	Martin diameter	Line bisecting the area of the particle	
SPHT	Sphericity	$\frac{4\pi A_P}{U^2}$	Form factor (*Liu et al.*, 2015)
b/l	Aspect ratio	$\frac{x_c min}{x_{Fe} max}$	Width to length ratio, axial ratio (*Liu et al.*, 2015)
CVX	Convexity	$\frac{A_P}{A_{CH}}$	Solidity (*Liu et al.*, 2015), roughness
CPT	Compactness	$\frac{\sqrt{\frac{A_P}{\pi}}}{x_{Fe} max}$	Roundness (*Liu et al.*, 2015)
Symm	Symmetry	$\frac{1}{2}\left[1 + min\left(\frac{r_1}{r_2}\right)\right]$	

4.3.1.3 Post-processing and data analysis

The CX2 software has flexible data processing that allows adjustable binning of raw data (logarithmic or arithmetic). This means that there are no restrictions equivalent to those that arise from fixed sieve intervals. The software outputs the GSD as a Probability Density Function and Cumulative Distribution Function (PDF and CDF), and has customisable data visualisation options. The output of the CX2 software is a 'resource description framework' file (`.rdf`), that can be output as a Microsoft Excel compatible file (`.xle`) for user-specific data processing and analysis. Images can also be saved.

Another useful feature in the CX2 software is the 'particle wizard' tool, which crops the saved images to allow visualisation of individual particles. This can be helpful for ensuring the task file has been designed correctly. For example, particles with specific shape and size characteristics can be displayed to confirm that contaminants (such as fibres) are identified and eliminated from the GSD. The particle wizard is also useful for qualitatively characterising particle shapes in different size fractions.

To facilitate flexible and reproducible data processing and visualisation, we analyse sample GSDs in Microsoft Excel and R. We output each GSD from the CX2 in two grain size bin configurations, one equivalent to a half-ϕ scale for compatibility with sieve data, and one on the linear scale with a bin width of 5 µm. For all GSDs we compute the *Folk and Ward* (1957) graphical parameters of mean (μ_{FW}), standard deviation or sorting (σ_{FW}), skewness (Sk) and Kurtosis (K). We also fit log-normal and Weibull distributions directly to the GSDs using the '`fitdistrplus`' package in R (*Delignette-Muller and Dutang*, 2015). Mixture models of log-normal and Weibull distributions were fit to multimodal GSDs using the '`mixfit`' function from the '`mixR`' R package (*Yu*, 2018). The probability density functions, and distribution fitting methods are reported in Appendix C.2.

4.3.2 Test samples and method comparison

4.3.2.1 Sample preparation and data collection

To test the capabilities and performance of the CX2, we conducted a series of preliminary analyses with fixed shape samples including glass spheres (ballotini), sub-spherical, disc- and rod-shaped particles. We also analysed natural samples that had been characterised using other techniques. Prior to analysis, some sample preparation was required. To gauge the approximate size, the ballotini were dry sieved into 6 sieve fractions using disposable nylon sieve meshes to ensure no contamination: >500 µm, 355–500 µm, 100-250 µm, 65-110 µm, 50-65 µm and 20-50 µm. The natural samples include Mazama tephra (~7.7 ka eruption of Crater Lake, OR, USA) sampled at different distances from source (see Chapter 2 and Appendix A.1), hydromagmatic fallout samples from the Hverfjall Fires (~2.5 ka eruptive episode of Krafla Volcanic System, Iceland) sampled by *Liu et al.* (2017), distal Campanian Ignimbrite tephra (~39 ka eruption from Phlegrean

Fields, Italy) sampled by *Engwell et al.* (2014) and references therein, and tephra from the 1980 eruption of Mount St. Helens (MSH), Washington, USA sampled via multiple sources (*Meredith*, 2019). Some of the MSH samples are assumed to be equivalent to samples analysed by other authors (*Sarna-Wojcicki et al.*, 1983; *Durant et al.*, 2009) based on comparable sampling locations (Appendix C.4). The tephra was dried to eliminate particle cohesion (*Castro and Andronico*, 2008) and dry sieved into half-ϕ intervals from 8 mm to 125 µm (-3 to 3 ϕ) where necessary. Further information on the natural samples can be found in Appendix C.4.

4.3.2.2 Choice of size parameters

To explore the reliability of the different size parameters calculated by the CX2, we measured the ballotini sieve fractions using xarea, x_{Fe}max and $x_c$min (Fig. 4.2). As expected, the choice of size parameter for the ballotini did not significantly alter the GSD in any sieve fraction (Fig. 4.3a) because xarea, x_{Fe}max and $x_c$min are equal for spherical particles (equivalent to circular in 2D images; Fig. 4.3c). The near vertical cumulative distributions reflect the manufacturing of the ballotini to achieve narrow GSDs and the efficacy of pre-analysis sieving. There is a slight fine tail in two of the analyses (Fig. 4.3a) that could indicate imperfect sieving where the finer material had not fully segregated into the correct sieve fraction. The largest variability in size parameter is observed in the x_{Fe}max data. This is attributed to the presence of slightly elongated spheres which we observed with optical microscope images (Fig. 4.3b). Similarly, the coarsest sieve fraction contained some irregular particles (Fig. 4.3c), which are likely a manufacturing fault.

We repeated this analysis on non-spherical fixed shape particles and sieved natural samples to further explore the sensitivity of GSDs to size parameter (Figs. 4.4 & 4.5; Appendix C.5). Non-spherical particles, including volcanic tephra, have GSDs that vary according to the size parameter as reflected in the grain size statistics. For example, the Md $x_c$min of the rod-shaped particles is 1800 µm compared to 6400 µm when size is measured as x_{Fe}max. Similarly, the Md size of the disc-shaped particles ranges from 3200 µm ($x_c$min) to 3700 µm (x_{Fe}max, see Table C.3 and Fig.C.7). The sensitivity of GSDs to size parameter is also observed within the individual sieve fractions of tephra. Interestingly, GSDs quantified by $x_c$min are closest to the expected sieve range according to sieve diameter d. Extending the sieve range so that the maximum grain size is equal to the hypotenuse of the sieve aperture shows better agreement with the xarea GSD (Fig. 4.4b), consistent with comparisons between optical image analysis (Morphologi GS3) and sieving (*Freret-Lorgeril et al.*, 2019). In contrast, the coarse tail on the x_{Fe}max GSD extends well beyond both sieve ranges, indicating that elongated particles can pass through the sieves on their intermediate or short axes. The xarea and x_{Fe}max distributions within a size fraction also vary between samples (Fig. 4.4). For example, the Md x_{Fe}max of the Campanian Ignimbrite 2 ϕ sieve fraction is 512 µm, compared to a Md x_{Fe}max of 427 µm for the same sieve fraction of Mazama

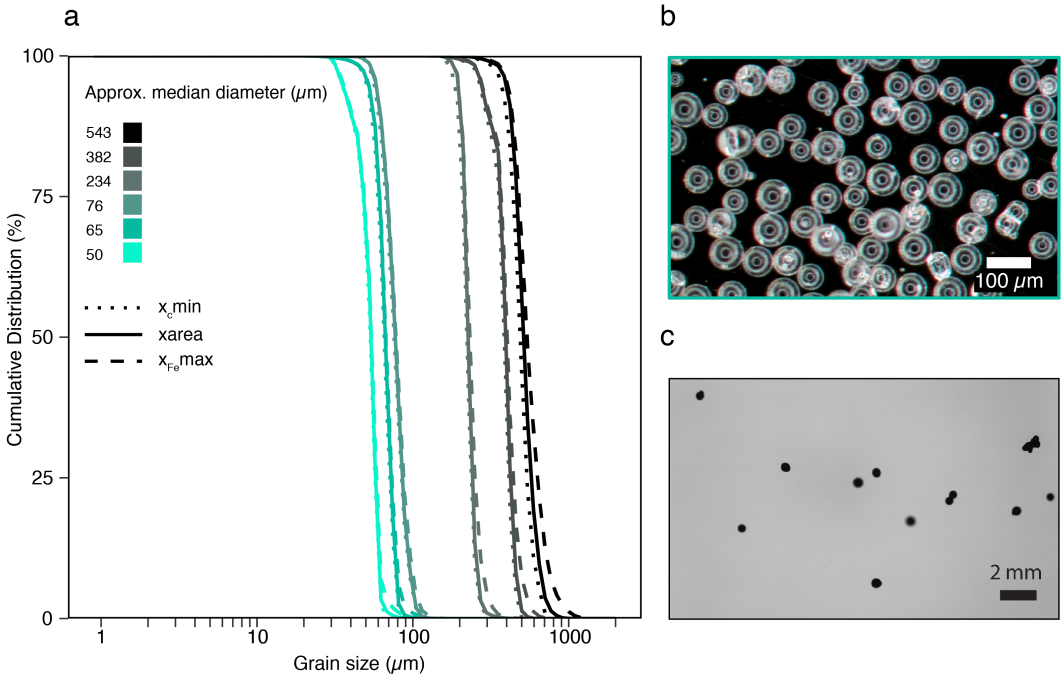

Figure 4.3: Comparing the size parameters for six ballotini size fractions. a) Cumulative GSDs showing that the three size parameters (differentiated by the line pattern) plot close to on top of each other for each size fraction (differentiated by the line colour). b) Optical microscope image of the 65-110 µm sieve fraction. c) CX2 image from the DIA of the >500 µm sieve fraction.

tephra. Similar to the ballotini analyses (Fig. 4.3), the observation that all GSDs of the natural samples have fine tails below the sieve range signifies that fine material is often retained in coarse sieves due to imperfect segregation as a result of the aggregation of fines or the adhesion of fine material to larger particles.

4.3.2.3 Shape parameters and distributions

The CX2 measures multiple shape parameters. Three shape parameters measured on the fixed shape particles and natural samples were sphericity (SPHT; $(\frac{4\pi A_P}{U^2})$, symmetry (Symm; $\frac{1}{2}\left[1+min\left(\frac{r_1}{r_2}\right)\right]$) and aspect ratio (b/l; Table 4.2). For perfectly spherical particles these parameters should equal 1 for all grain sizes. However, small imperfections and deviations from perfect spheres will reduce these shape parameters to <1 and each has a different sensitivity. For example, the interpretation that the x_{Fe}max results for the coarser ballotini contained a larger proportion of non-spherical particles (Fig. 4.3) is supported by the lower mean values of both symmetry (0.95) and aspect ratio (0.87) compared to the finer ballotini (Symm = 0.97, b/l = 0.96). In contrast, there is no significant change in the range of SPHT, a parameter that is sensitive to particle perimeter (roughness), with grain size for the ballotini, suggesting that the deviations

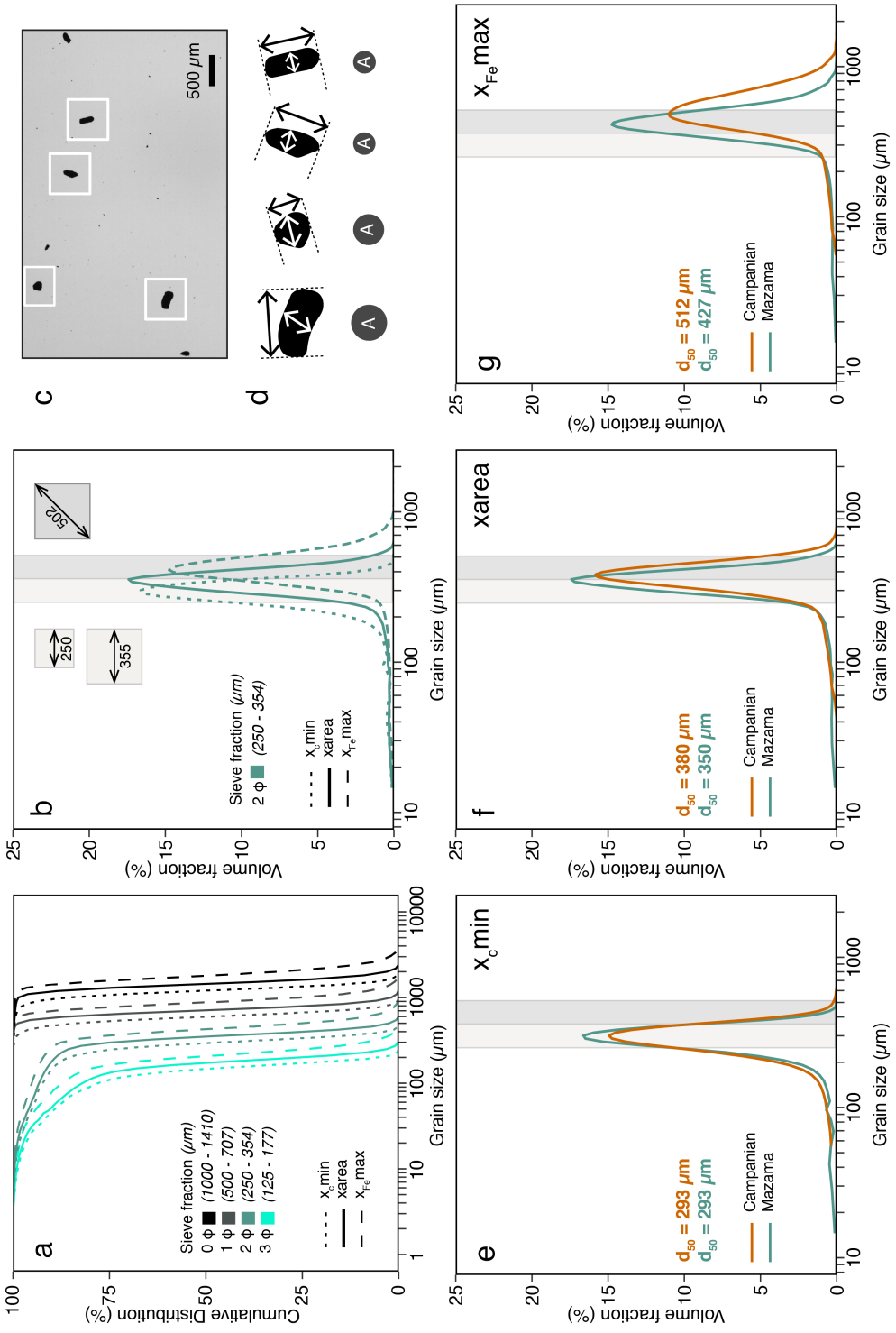

Figure 4.4: Comparing different size parameters for natural sieved tephras. a) Cumulative GSDs for Mazama tephra showing the three size parameters (differentiated by the line pattern) for each half-ϕ sieve fraction (differentiated by the line colour). b) GSDs of the 2 ϕ (250-354 μm) sieve fraction for each size parameter. The light grey box indicates the size range expected from sieving according to sieve diameter, d; the dark grey box extends this range to the length of the sieve aperture hypotenuse. c) CX2 image from the DIA (using X-Jet) of the 2 ϕ sieve fraction of Mazama tephra. d) Binary images of irregular Mazama tephra particles from c) with x_{Fe}max, $x_c$min and xarea indicated. e-g) Comparing GSDs within a sieve fraction according to the size parameter for the Mazama and Campanian Ignimbrite tephras.

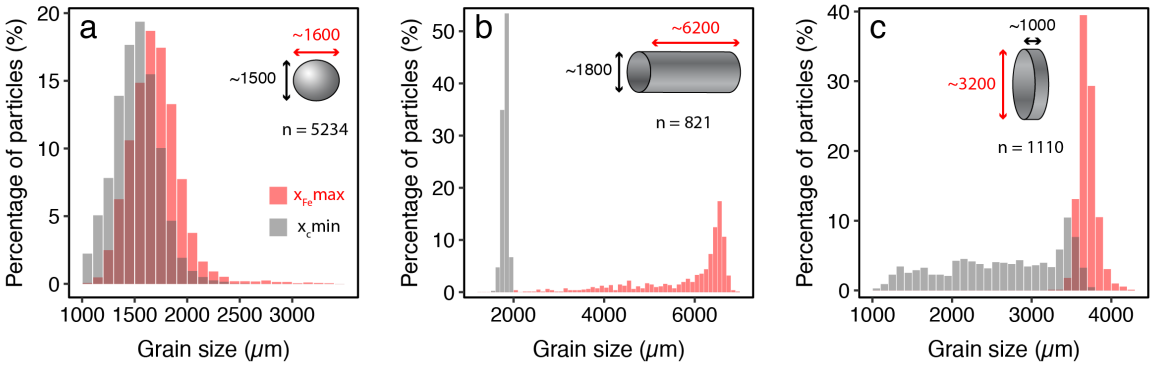

Figure 4.5: The impact of particle shape on size and shape parameters. Particle number distributions according to x_{Fe}max and $x_c$min for a) sub-spherical particles, b) cylindrical particles and c) disc shaped particles. The diagrams show the 3D shapes and approximate dimensions with n equal to the number of particles analysed.

from perfect spheres arise primarily from elongation and surface protrusions rather than surface roughness (Fig. 4.3c; Appendix C.5).

Shape data are also susceptible to differences in image resolution, which becomes a problem when samples span a wide size range (e.g., *Saxby et al.*, 2020). For example, the large number of pixels per particle for coarse particles could increase the particle perimeter measurement relative to the particle area, which would artificially lower the SPHT. Nevertheless, our data on ballotini show little relation between particle size and the SPHT (Appendix C.5) and we attribute the changes in Symm and b/l with grain size to imperfections in the ballotini rather than differences in image resolution.

Shape distributions measured for the non-spherical test particles and the natural tephra samples show that the CX2 can be used to differentiate samples according to particle shape (Figs. 4.5 & 4.6). For example, analysis of rod-shaped glass beads generated an average aspect ratio (b/l) of 0.32, which is close to the value expected from the manufacturer size specifications (~0.3). Due to the varied orientation of the particles relative to the imaging module, however, the CX2 method can underestimate the size and shape of some particles. This is particularly evident in the analyses of disc-shaped particles where the shortest dimension is rarely perpendicular to the imaging module; this means that $x_c$min and thus the aspect ratio, is overestimated (Fig. 4.5c; CX2 b/l ~ 0.7 versus real b/l ~ 0.3). However, the large number of particles measured by the CX2 means that the shape parameters and distributions still reflect the non-sphericity of particles which is evident in the shape distributions for natural samples (Fig. 4.6; n ~ 10^8 particles per tephra analysis; see supplementary data)

Compared to the ballotini, the sieved Campanian Ignimbrite, Hverfjall and Mazama tephras

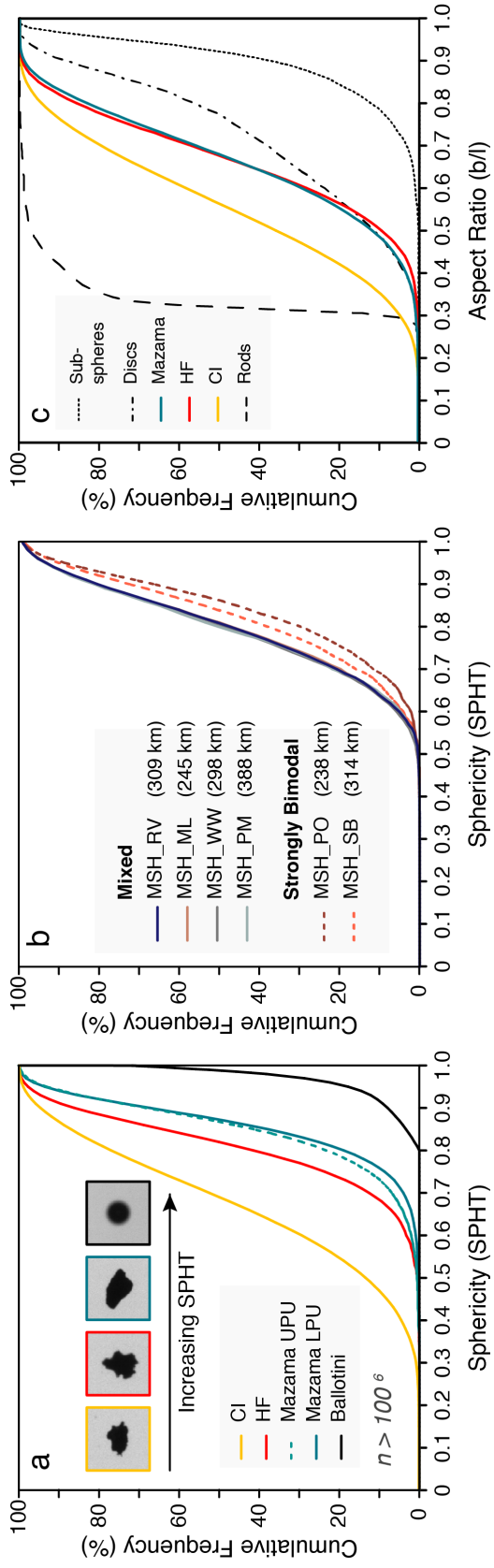

Figure 4.6: Cumulative shape distributions for ballotini and natural samples: Campanian Ignimbrite (CI), Hverfjall Fires (HF), Mazama Upper and Lower Pumice Units (UPU, LPU) and Mount St. Helens (MSH). a) Comparing SPHT for individual sieve fractions of ballotini and natural tephra samples. The 2.5 ϕ sieve fraction (180-250 µm) is shown for the natural samples, and the ballotini data is for the sieve fraction with Md=234 µm. b) SPHT distributions for distal MSH samples. c) Comparing b/l distributions for the 2.5 ϕ sieve fraction of natural tephra samples and fixed shape.

show a wide range of SPHT values as a result of the irregular particle morphology (Fig. 4.6a). The Mazama distribution shows the highest SPHT values as it contains a high proportion of free crystals with smooth surface textures compared to the basaltic Hverfjall and micro-pumice rich Campanian Ignimbrite tephras (Fig. 4.6a). Interestingly, bimodal and unimodal MSH samples display different SPHT distributions (Fig. 4.6b); here bimodal samples have been interpreted to record particles produced by different phases of the eruption (*Eychenne et al.*, 2015). The aspect ratio (b/l), which reflects the elongation of particles, is lowest for the Campanian Ignimbrite tephra but shows no real difference between the Hverfjall and Mazama tephras (Fig. 4.6c).

4.3.2.4 Comparison of CAMSIZER X2 results with other methods

The GSD of the natural samples has been previously characterised using a combination of sieving and laser diffraction (Mount St. Helens *Durant et al.* 2009; Campanian Ignimbrite, *Engwell et al.* 2014; Hverfjall Fires, *Liu et al.* 2017; Mazama, Chapter 2, Fig. 2.5). Here we compare the GSDs of fine-grained tephras measured using laser diffraction with GSDs measured using DIA with X-jet and X-flow dispersion mechanisms (Fig. 4.7). We expect the xarea CX2 GSDs to be the most comparable to GSDs from laser diffraction if Mie scattering theory (Appendix C.1) is used (Fig. 4.7a-b). The Campanian Ignimbrite GSD measured by laser diffraction used the Fraunhofer approximation (Appendix C.1) and appears to be best matched by $x_{Fe}max$ in the CX2 GSD (Fig. 4.7c). The laser diffraction GSDs consistently have a broader fine-grained tail than the CX2 results (Fig. 4.7). For example, laser diffraction suggests that 10% of the volume of the MSH tephra is <4 µm whereas the X-jet GSD quantified as xarea suggests that 10% of the sample is <8 µm (Fig. 4.7b). The X-jet and X-flow GSDs also differ slightly at the coarse end of the distribution with the X-flow distribution showing that <5% of the Mazama tephra is coarser than 100 µm while the laser diffraction and X-jet distributions show that >10% of the sample is coarser than 100 µm (Fig. 4.7a).

In Fig. 4.7, the differences between the CX2 and laser diffraction at the <10 µm end of the scale are due to the different minimum particle sizes measured by the instruments. Laser diffraction detects particles >0.01 µm, whereas the lower size limit of the CX2 is 0.8 µm. For very fine-grained material (<10 µm) there are also some limitations of laser diffraction. For example, fine material can cause multiple scatterings of the laser beam, and some authors have attributed an overestimation of fine particles to the presence of non-spherical grains (*Vriend and Prins*, 2005; *Jonkers et al.*, 2009). The differences in the GSDs >100 µm are likely the result of the amount of material analysed. The X-jet method analyses the largest volume of material; this ensures representative sampling of coarse particles, unlike the wet dispersion methods which uses a small amount of material per analysis and are thus more likely to underrepresent coarse particles. Importantly, small differences in the number of large particles can translate to considerable variability in volume-based GSDs because of the large contribution of coarse particles to the total

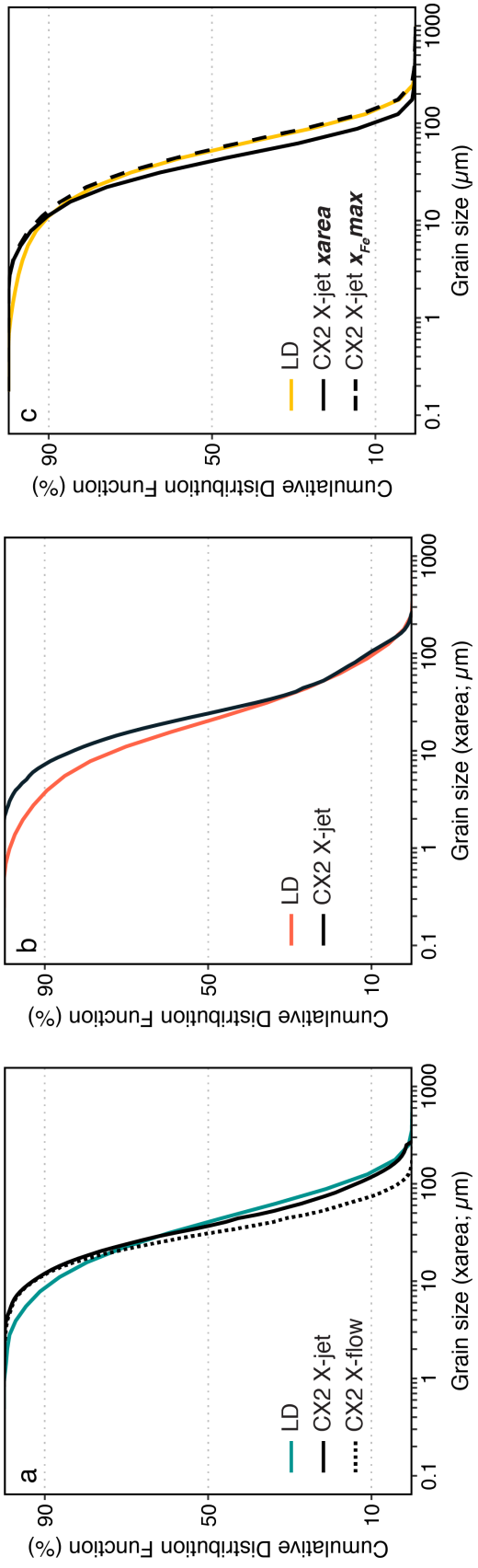

Figure 4.7: Comparing GSDs from laser diffraction (LD) with CX2 GSDs for fine-grained distal tephras. a) GSDs for distal Mazama sample from site 73. b) GSDs for distal MSH sample. Laser diffraction analysis carried out on sample DAVIS11 by *Durant et al.* (2009), corresponding sample MSH_RV analysed using CX2 for this study (see Appendix C.4). c) GSDs for ultra-distal Campanian Ignimbrite tephra. Laser diffraction analysis from *Engwell et al.* (2014) compared to X-jet GSDs according to size parameter.

sample volume.

For the coarser Mazama tephra, we compare GSDs measured using a combination of sieving and CX2 (X-jet) with GSDs produced using the CX2 alone, where the X-fall (>125 μm) and X-jet (<125 μm) analyses are combined (Fig. 4.8). The sieve and CX2 data were combined using the overlap between the methods at 125-250 μm by assuming a constant particle density and therefore converting the volumetric size distribution (CX2) to a mass distribution (e.g., *Eychenne et al.*, 2012). The X-fall and X-jet data were combined by weighting the coarse and fine distributions according to the mass percentage that was greater than and less than 125 μm. For the sake of comparison, all data were processed in half-ϕ intervals to match the limits of data manipulation imposed by sieving.

The difference between the GSDs in Fig. 4.8 results from the distinction between coarse GSDs that are quantified as weight percent (mass%; sieving & CX2) versus volume percent (vol%; CX2). The GSDs obtained from sieving have a strong mode at 2-1.5 ϕ (250-354 μm), which corresponds to the sieve fraction that contains a large proportion of dense phenocrysts (magnetite and pyroxene); this mode remains constant throughout the Mazama tephra section (upper and lower pumice fallout units). The modes in the CX2-only distributions (Figs. 4.8a-b) do not align with the GSDs from sieving because they are represented in terms of the vol% (rather than mass%) in each size class. This means that although the X-fall and X-jet analyses are combined by the relative mass% > and < 125 μm, dense individual size fractions (crystal concentrations) do not manifest as the mode of the GSDs.

4.4 Results

The method development and testing reviewed in section 4.3 show that the CX2 provides an appropriate analytical protocol for characterising the grain size and morphology of volcanic tephra up to 8 mm (≥ -3 ϕ). Here we explore the unique capabilities of DIA for determining GSDs of samples with non-uniform density distributions and then examine the sensitivity of grain size statistics to the choice of size parameter and method of grain size measurement.

4.4.1 Non-uniform density distributions

The CX2 and sieve analyses of the coarse Mazama tephra differ because of the non-uniform density of the pyroclasts across the GSD (Fig. 4.8). In contrast, parallel sieve and CX2 analyses of natural tephras with less significant changes in clast density show similar GSDs when quantified by either mass or volume (Appendix C.5). This contrast suggests we can use simultaneous measurements of GSDs by mass and volume to invert for density distributions.

To obtain independent measurements of density, we used a water pycnometer (e.g., *Eychenne*

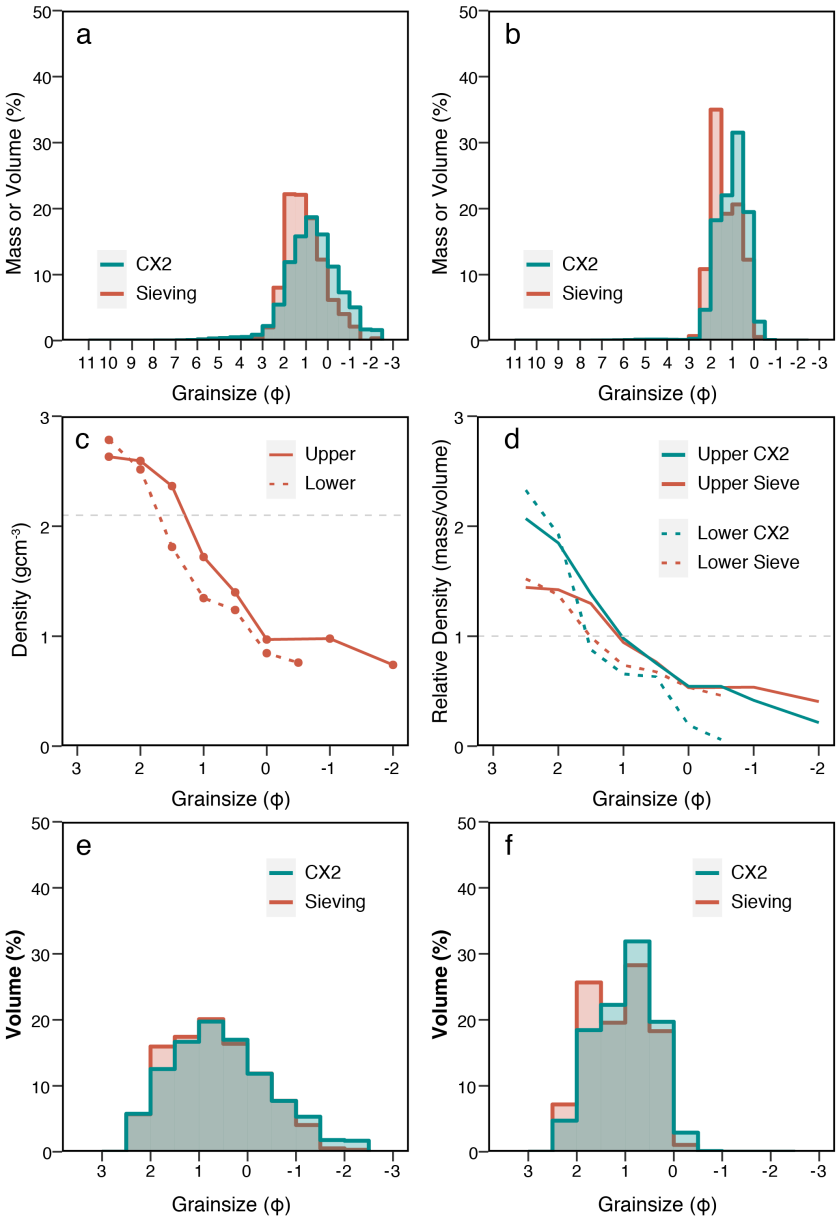

Figure 4.8: Comparing GSDs of Mazama tephra measured by sieving & CX2, with CX2 alone. All samples are from a fallout section located at site 46 ~120 km from source (see Appendix C.4). a) Sample from the upper pumice unit, b) sample from the lower pumice unit. c) Measured densities (gcm^{-3}) of individual sieve fractions for the upper and lower unit with the dashed line indicating the density of Mazama glass ~2.1 gcm^{-3}. d) The relative density of half-ϕ sieve fractions calculated using the sieve data (red) and the CX2 & sieve data (blue). e) and f) Comparing the volume distributions measured using the CX2 with calculated volume distributions from sieve data for the upper (e) and lower (f) units between 2.5 and -2.5 ϕ.

and Le Pennec, 2012; *Liu et al.*, 2017) to analyse the -2 to 2.5 ϕ sieved size fractions of Mazama samples from the upper and lower pumice units (Fig. 4.8c). These data show the expected increase in particle density with decreasing size (*Bonadonna and Phillips*, 2003; *Eychenne and Le Pennec*, 2012) but also highlight the high density ($\rho \sim 2.6$ gcm^{-3}) of the 2 and 2.5 ϕ sieve fractions where pyroxene and magnetite crystals are concentrated, a density that greatly exceeds that of the matrix glass (~2.1 gcm^{-3}). We used the sieved mass and measured density of each size class to calculate a volume-based GSD to compare with the CX2 GSD (Fig. 4.8e-f). This comparison shows that relative to the sieve data, the CX2 underestimates the volume in the sieve fractions (1.5-2.5 ϕ) that contain the dense crystals and overestimates the volume of the coarse pumice clasts. For example, sieve data shows that 16% of Mazama upper pumice sample is in the 2 ϕ sieve fraction compared to 12% according to the CX2 GSD (Fig. 4.8e). This difference is reflected in the relative density calculated by dividing the mass % by the volume % in each class (Fig. 4.8d). Importantly, whilst the resulting absolute values of relative density diverge, for sieve and CX2 data, the relative density profiles derived from the CX2 data clearly show the presence of dense crystal-rich grain size fractions (3-1.5 ϕ) compared to the coarse low-density pumice clasts (<1.5 ϕ). These data illustrate the important information about the particle population that can be determined from a direct comparison of mass and volume.

4.4.2 Grain Size Distribution statistics

Grain size statistics provide a way to quantitatively compare GSDs that arise from different measurement methods. For example, the *Folk and Ward* (1957) mean grain size (μ_{FW}) calculated for the Mazama upper pumice is 1.07 ϕ (476 µm) for sieve data compared to 0.38 ϕ (768 µm) for the CX2 GSD (Table 4.3). Similarly, for fine-grained Mazama samples (Fig. 4.7), μ_{FW} varies from 4.73-5.38 ϕ (38-24 µm) depending on the size parameter ($x_c$min or xarea) and method of grain size analysis used (laser diffraction or CX2; Table 4.3). The FW sorting (σ_{FW}; measure of spread) and skewness (Sk; measure of symmetry) also depend on the method used (Table 4.2). For example, the Sk of the lower pumice is -0.20 when measured by sieving but +0.15 when measured with the CX2. This difference affects the qualitative classification from finely skewed (sieving) to coarsely skewed (CX2; Table B1). Another important parameter is the proportion of fine (<125 µm) and very fine (<15 µm) ash. Here the proportion of very fine ash (<15 µm) in sample MZ73 ranges from 16% (xarea; X-jet) to 26% ($x_c$min; X-flow) of the total volume.

The statistics and interpretation of multimodal GSDs are similarly sensitive to the method used to characterise the distribution (Fig. 4.9; Table 4.4). The distal MSH ash has previously been shown to contain at least two grain size sub-populations (*Durant et al.*, 2009; *Eychenne et al.*, 2015). Deconvolution of GSDs into subpopulations, however, is sensitive to differences in both the starting GSD and the distribution chosen (log-normal or Weibull; Appendix C.2). We illustrate this difference using PDFs deconvolved for the laser diffraction GSD compared to the CX2 GSD

Table 4.3: Grain size statistics calculated for different methods of grain size analysis.[a]

Sample	Method	Binning	μ_{FW}	σ_{FW}	Sk_{FW}	<125 µm (%)	<15 µm (%)
MZ46 Upper Pumice (Fig. 4.8a)	Sieving & CX2	$\frac{1}{2}\phi$	1.07	0.92	-0.15 *(coarse skewed)*	2.4	0.2
	CX2 ($x_c$min)	$\frac{1}{2}\phi$	0.66	1.15	-0.04 *(symmetrical)*	2.4	0.2
MZ46 Lower Pumice (Fig. 4.8b)	Sieving & CX2	$\frac{1}{2}\phi$	1.32	0.67	-0.25 *(coarse skewed)*	0.82	0.01
	CX2 ($x_c$min)	$\frac{1}{2}\phi$	1.00	0.65	0.13 *(fine skewed)*	0.84	0.01
MZ73	CX2 X-jet ($x_c$min)	$\frac{1}{4}\phi$	5.11	1.24	-0.01 *(symmetrical)*	95	23
	CX2 X-jet (xarea)	$\frac{1}{4}\phi$	4.74	1.27	-0.01 *(symmetrical)*	91	16
	CX2 X-flow ($x_c$min)	$\frac{1}{4}\phi$	5.38	1.01	0.06 *(symmetrical)*	99	26
	CX2 X-flow (xarea)	$\frac{1}{4}\phi$	5.03	1.04	0.05 *(symmetrical)*	99	17
	LD (xarea)	$\frac{1}{2}\phi$	4.73	1.53	0.14 *(fine skewed)*	89	20

(a) FW = *Folk and Ward* (1957) graphical method of calculating GSD statistics.

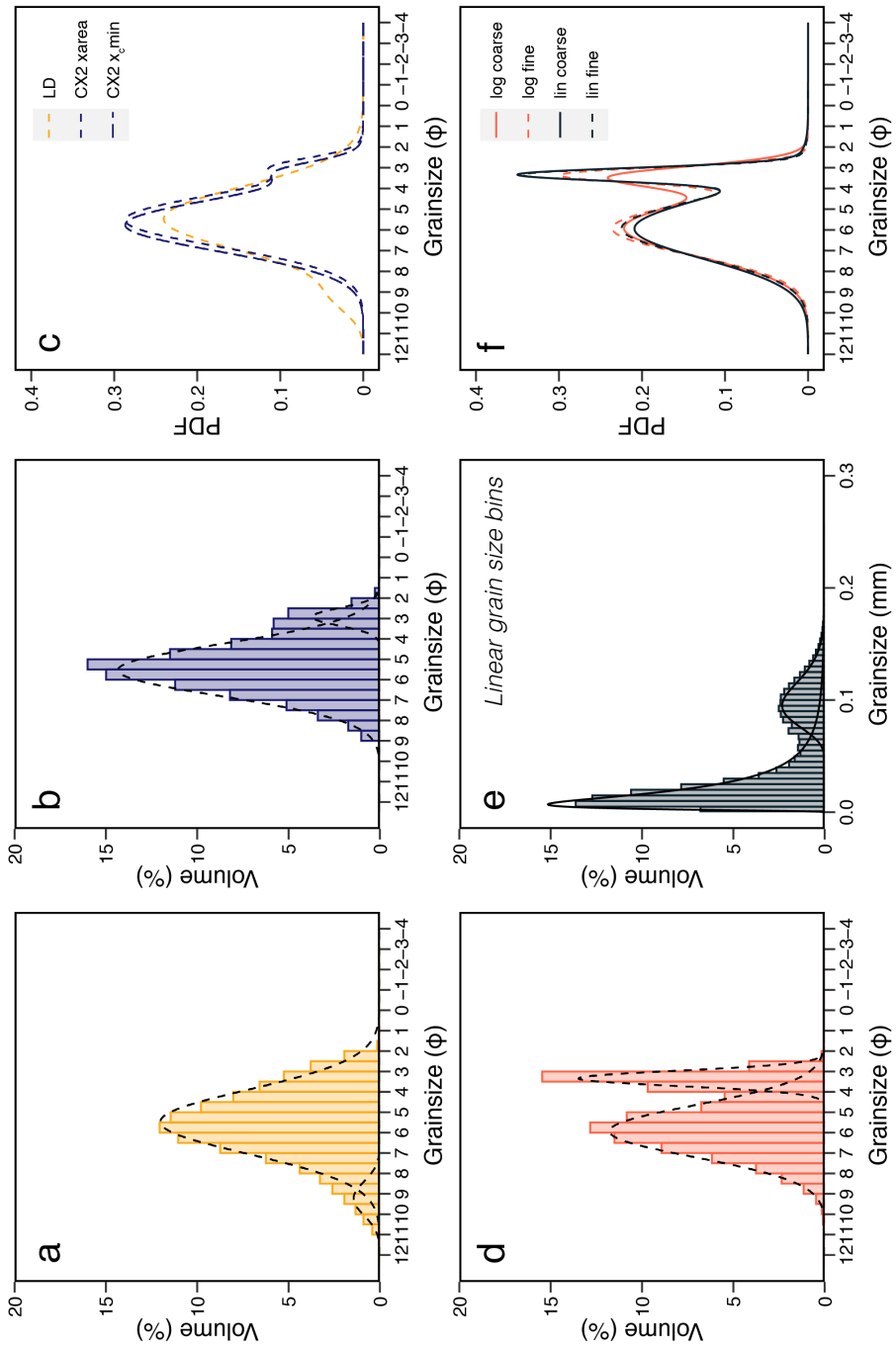

Figure 4.9: Bimodal log-normal distributions fit to MSH GSDs. a) GSD of DAVIS11 measured with laser diffraction (*Durant et al.*, 2009) fit with two log-normal subpopulations. b) GSD of MSH_RV measured by X-jet (xarea) fit with two log-normal subpopulations. c) Comparison between bimodal distributions according to method and CX2 size parameter. d) GSD of MSH_SB sample in half-ϕ bins with two log-normal subpopulations. e) GSD of MSH_SB sample binned on the linear scale (5 µm) fitted with two log-normal subpopulations. f) Comparison between distributions fit on the ϕ and linear scales, as well as coarse (full-ϕ; 10 µm) and fine bins (half-ϕ; 5 µm).

Table 4.4: Main parameters of bi-modal MSH samples calculated using different methods of grain size analysis and different bin configurations. $\mu_{\phi 1}$, $\mu_{\phi 2}$ = log-mean, $\sigma_{\phi 1}$, $\sigma_{\phi 2}$ = log-standard deviation, p_1, p_2 = proportion of the total GSD of the fine- and coarse-grained subpopulations respectively.

Sample	Method	Binning	$\mu_{\phi 1}$	$\mu_{\phi 2}$	$\sigma_{\phi 1}$	$\sigma_{\phi 2}$	p_1	p_2
DAVIS11[a] (Fig. 4.9a&c)	LD	$\frac{1}{2}\phi$	9.23	5.47	0.83	1.56	0.06	0.94
MSH_RV (Fig. 4.9b-c)	CX2 (xarea)	$\frac{1}{2}\phi$	5.53	2.92	1.28	0.43	0.92	0.08
	CX2 ($x_c$min)	$\frac{1}{2}\phi$	5.76	3.13	1.28	0.46	0.92	0.08
MSH_SB (Fig. 4.9d-f)	CX2 ($x_c$min)	1ϕ	5.92	3.42	1.35	0.50	0.75	0.25
		$\frac{1}{2}\phi$	5.93	3.34	1.27	0.37	0.75	0.25
		$\frac{1}{4}\phi$	5.93	3.34	1.25	0.32	0.74	0.26
		1 µm	5.94	3.36	1.25	0.32	0.75	0.25
		5 µm	5.92	3.33	1.35	0.31	0.76	0.24
		10 µm	5.94	3.32	1.45	0.31	0.76	0.24

(a) DAVIS 11 sample was sampled very close to MSH_SB (*Sarna-Wojcicki et al.*, 1981; *Durant et al.*, 2009; *Meredith*, 2019).

(Figs. 4.9c&f). When the number of log-normal subpopulations is fixed at 2, the laser diffraction GSD (Fig. 4.9a) is resolved into distributions with means of 9.23 ϕ (2 µm) and 5.47 ϕ (26 µm). The same fitting algorithm applied to the CX2 GSD resolves two sub-populations with means of ~5.6 and 3.0 ϕ (21 and 125 µm) respectively (Fig. 4.9b; Table 4.4). This comparison shows that two samples from the same deposit, taken from the same location, can have GSDs that can be interpreted differently simply because of measurement method

It is well known that grain size statistics are also sensitive to bin size. To explore this sensitivity, we processed the data in multiple bin configurations (Table 4.4). We find that fitting of unimodal and bimodal distributions is not strongly affected by the type of binning used, particularly when working with fine-grained material (Fig. 4.9d-f). However, coarse bins are still problematic for particles >500 µm when using the ϕ-scale, which translates into a wide range on the linear scale and poor resolution of the distribution within the sieve intervals (*Hails et al.*, 1973). Similarly,

coarse linear binning (>5 μm) can obscure the GSD in the fine grain sizes and places too much emphasis on the coarse particles (*Blott and Pye*, 2001).

4.5 Discussion

The CX2 is a valuable tool for simultaneously analysing the size and shape of non-spherical particles, such as tephra, thanks to the DIA principle. Here we discuss some of the benefits of DIA relative to more widely used methods of grain size analysis (see section 4.2; Table 4.1; Appendix C.1). We also consider the limitations of grain size analysis methods, in particular, for studying ultra-fine (<10 μm) particles. Finally, we discuss the implications of different grain size methods for using and interpreting grain size data for the purposes of studying explosive volcanism.

4.5.1 Appraisal of Dynamic Image Analysis for measuring non-spherical particles

DIA facilitates rapid and simultaneous quantification of the size and shape of tephra whilst other particle analysis techniques compromise on either particle shape information or analysis time. For example, laser diffraction contains no shape information but is fast (~minutes), whereas SEM image analysis provides excellent particle shape data but can require pre-analysis sample preparation (sieving) and substantial image processing (~hours to days). DIA has the added benefit of automatically measuring multiple size descriptors (Figs. 4.2-4.5). Comparing GSDs quantified by different size parameters supplements shape parameterisation as the disparities between the GSDs can be used to infer the presence of extreme particle shapes (Figs. 4.4-4.5).

Quantifying different size parameters can also explain some of the grain size anomalies described in the literature. For example, the large grains reported in cryptotephra studies (*Stevenson et al.*, 2015; *Saxby et al.*, 2019) are quantified according to their $x_{Fe}max$ size. Our data show that within individual sieve classes particles can have $x_{Fe}max$ values that extend well beyond the range predicted by the sieve aperture (Fig. 4.4). In other words, sieve data can mask extreme particle sizes if the maximum particle dimension is assumed equal to the passing sieve aperture. Furthermore, we have confirmed that the size parameter measured by sieving depends on particle shape. For example, elongated particles are most commonly sorted according to their minimum dimension ($x_c min$), however, platy particles such as found in the Campanian Ignimbrite tephra, are sorted by their intermediate dimension. This has implications for converting from sieve aperture to particle volume as it will lead to the overestimation of particle volume for most non-spherical particles.

Collection of multiple size parameters allows comparison of DIA GSDs with other widely used grain size measurement methods. The $x_c min$ parameter closely matches the expected sieve range (Fig. 4.4), meaning that there is limited data loss and manipulation required to combine coarse

and fine-grained measurement methods. Laser diffraction (LD) estimates xarea when using Mie theory and x_{Fe}max when using the Fraunhofer approximation (Fig. 4.7). Aside from differences in the finest grain sizes (<10 µm,) CX2 and LD GSDs are comparable, which is advantageous for comparisons with established grain size datasets (*Durant et al.*, 2009; *Engwell et al.*, 2014; *Liu et al.*, 2017).

An additional benefit of DIA is that it quantifies GSDs in terms of volume percent, such that coarse (>125 µm) GSDs can be compared directly with other volume-based methods of grain size analysis (laser diffraction, image analysis). This means there is no need to convert between volume and mass which requires an assumption of particle density. The effect of variable particle density on GSDs is illustrated in Fig. 4.8, which shows that mass-based GSDs can be influenced by dense grain size fractions that arise from crystal concentrations. Fig. 4.8d also clearly highlights an abrupt increase in particle density that can be related to crystal concentration in the 2-3 ϕ size range. Importantly, disparities between the volumetric GSDs calculated from direct mass and density measurements and those measured using the CX2 (Fig. 4.8e-f) can be explained by the propagation of uncertainty in the density measurements (+/- 10%) as well as a limitation of the CX2 velocity adaption when a wide range of particle densities exist in a narrow size range (see Appendix C.3). Whilst the relative density distributions calculated cannot be used quantitatively (Fig. 4.8d), this approach provides a fast way to qualitatively investigate changes in particle density and can be used to identify size classes that require direct density measurements, which whilst more accurate are more time consuming.

Although DIA has clear advantages for characterising tephra it also has limitations. Firstly, the minimum grain size measured by the CX2 is 0.8 µm, which is coarser than laser diffraction techniques (e.g., the Mastersizer 3000 minimum size is 0.01 µm). Sub-micron and nano scale particles are important for understanding satellite retrievals of volcanic ash in the atmosphere (e.g., *Prata*, 1989; *Muñoz et al.*, 2004; *Miffre et al.*, 2012; *Prata and Prata*, 2012), the health impacts of volcanic ash (*Horwell*, 2007; *Horwell and Baxter*, 2006), the electrification of volcanic plumes (e.g., *James et al.*, 2000; *Miura et al.*, 2002; *Cimarelli et al.*, 2014) and the meteorological (*Durant et al.*, 2008; *Gibbs et al.*, 2015) and climatic effects of volcanic eruptions (*Rampino and Self*, 1993; *Dartevelle et al.*, 2002). As the proportion of particles <0.8 µm cannot be determined with the CX2, characterisation of the ultra-fine GSD is incomplete.

The minimum grain size and image resolution limits of the CX2 also have consequences for the shape measurements. As the DIA approaches the limit of image resolution, the edge detection for particles will be increasingly affected by image pixelation. This could lead to over smoothed or imprecise particle outlines, which will be particularly significant for shape parameters that include particle perimeter (e.g., SPHT; Fig. 4.5; *Liu et al.*, 2015). Additionally, the shape parameter formulae are not always consistent with other studies, for example, the convexity formulation

used by the CX2 software is equivalent to the 'solidity' parameter used by *Cioni et al.* (2014) and *Liu et al.* (2015). The CX2 is also limited to 2D shape characterisation whereas some studies of volcanic ash compute 3D shape parameters (e.g., *Ganser*, 1993; *Dioguardi et al.*, 2017; *Saxby et al.*, 2018). Whilst it is common that shape parameters have different definitions and formulations, it is not possible to modify the shape parameter formulations in the CX2 software, meaning that not all shape parameters and formulations can be computed and compared with other shape studies without reanalysing the saved images using other methods.

4.5.2 Significance of comprehensive grain size characterisation

DIA is a valuable method for scrutinising the size and shape of distal ash samples simultaneously. The median grain size of distal ash deposits is known to stabilise at large distances from source (Fig. 4.10 *Engwell et al.*, 2014; *Engwell and Eychenne*, 2016; *Cashman and Rust*, 2020). The transition to the stable distal grain size occurs when the sedimentation of particles is no longer governed by Stokes' settling law (*Engwell and Eychenne*, 2016). However, analysis of distal MSH, Mazama and Campanian Ignimbrite tephra shows that the median grain size of distal ash is not uniform across different eruptions, meaning particle 'size' alone cannot explain this phenomenon (Fig. 4.10). We propose that differences in how particle size is quantified can partly explain the dissimilar distal grain sizes. For example, the laser diffraction method used to measure the GSD of the Campanian Ignimbrite tephra (Fraunhofer theory; *Engwell et al.*, 2014) produces the equivalent of an x_{Fe}max distribution (particle long axis), which may explain the apparent coarse distal grain size when compared to GSDs quantified as $x_c$min (sieving) or xarea (laser diffraction using Mie theory).

The inputs used by ash dispersion models, moreover, use a different measure of size than used by physical ash samples. Particle Size Distributions (PSDs) used by ash dispersion models are specified in terms of equivalent volume sphere diameter (D_V; *Beckett et al.*, 2015; *Saxby et al.*, 2020). *Saxby et al.* (2020) used 3D data of ash volumes to demonstrate the divergence between volume-equivalent sphere diameters and long axis (x_{Fe}max) measurements that result from extreme ash morphologies. The 3D data show that for extreme ash shapes the volume equivalent sphere diameter (D_V) is consistently less than the particle long axis (L) as the data plots above the 1:1 line in Fig. 4.11. For example, for a Campanian Ignimbrite ash shard with an average shard thickness of ~10 µm, the resulting difference between the maximum length (L or x_{Fe}max) and volume equivalent sphere diameter (D_V) is more than 5-fold. Importantly, to quantify particle size as an equivalent volume sphere diameter, 2D image analysis techniques assume that the equivalent area circle diameter (xarea) can be converted directly to D_V, although the relation between xarea and D_V varies with the 3D shape. These differences partly explain the mismatch between physical measurements of ash shape (GSDs) and the PSDs used in ash dispersion models.

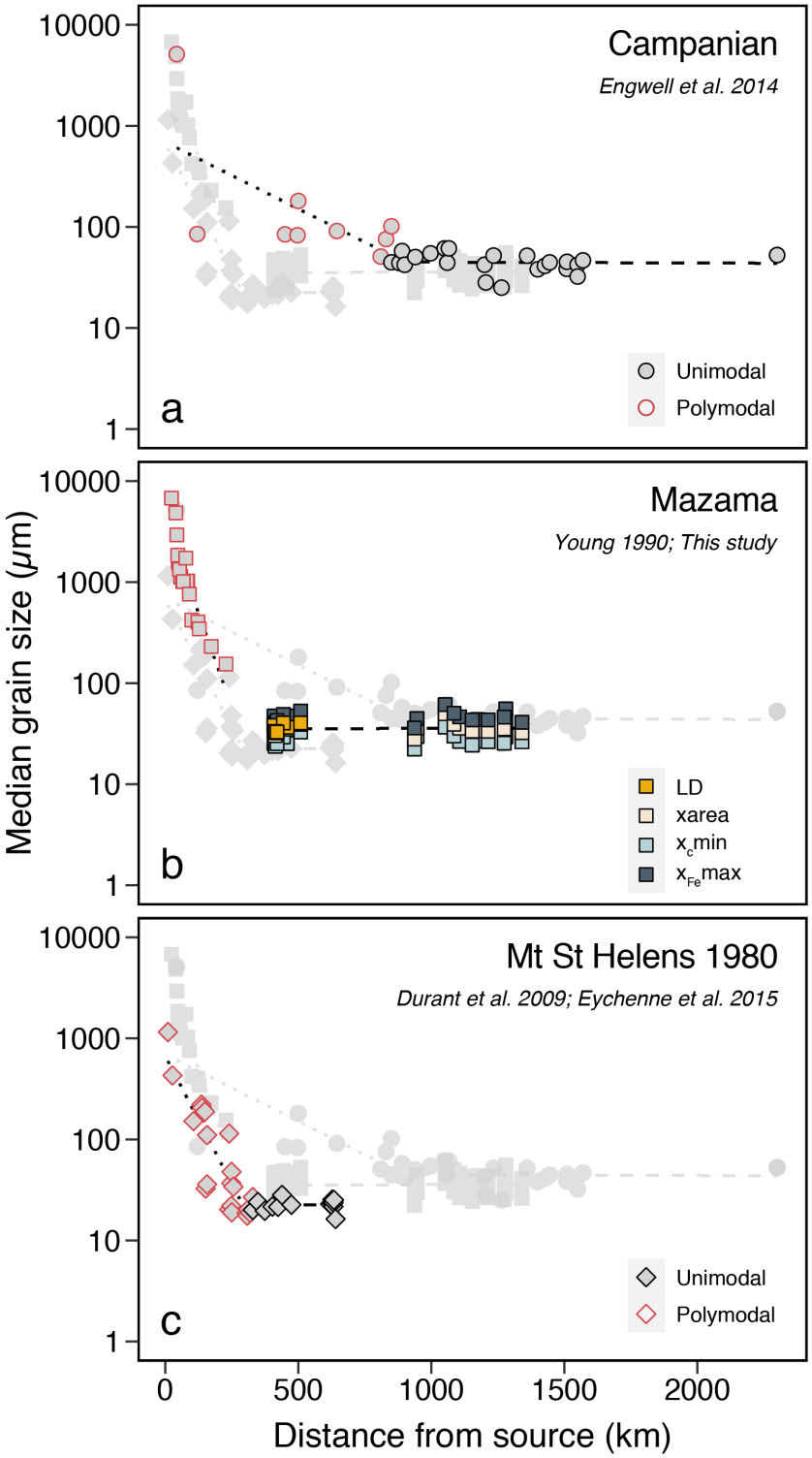

Figure 4.10: Grain size of distal tephras with distance from source. a) Campanian tephra with GSDs and sub-populations from *Engwell et al.* (2014). b) Mazama tephra with data from *Young* (1990), Chapter 2 and this study. c) Mount St. Helens 1980 data from *Durant et al.* (2009) and deconvolution by *Engwell et al.* (2014).

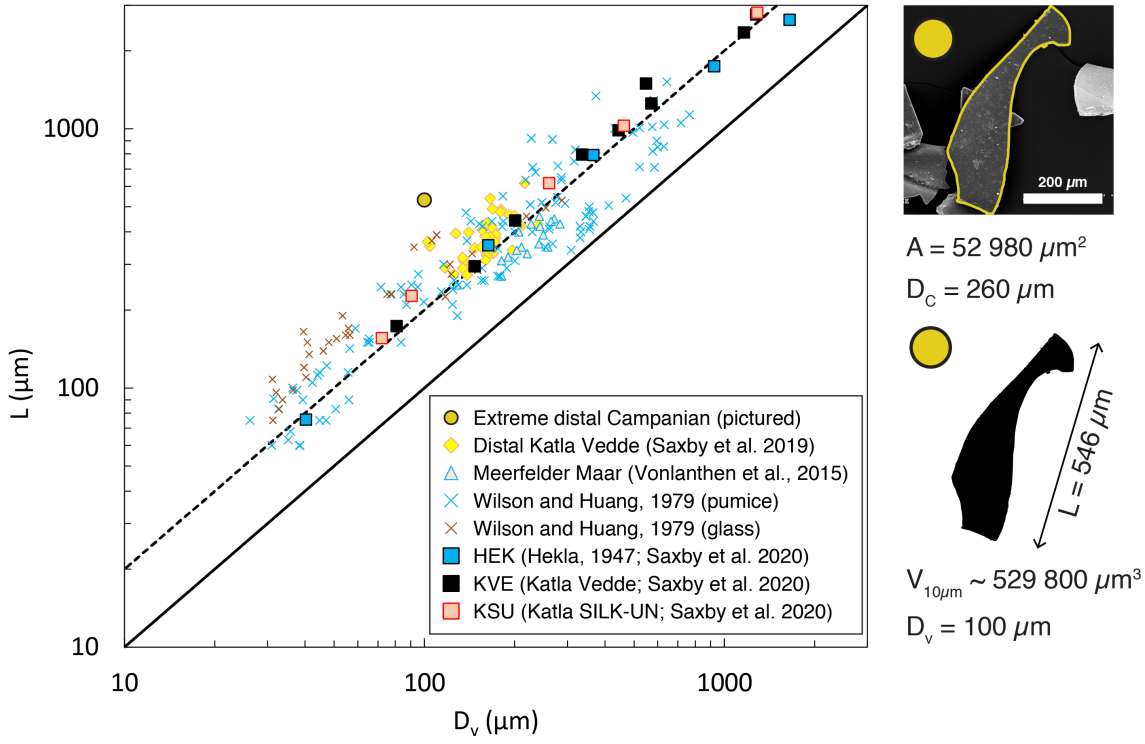

Figure 4.11: Volume-equivalent sphere diameter Dv vs long axis length L with example extreme Campanian Ignimbrite ash shard (circle symbol). A is the 2D area of the particle and Dc is the equivalent circle diameter. Square symbols show means (from X-ray CT data; *Saxby et al.*, 2020); diamond symbols are from optical measurements (*Saxby et al.*, 2019) and all other symbols are individual particle measurements collated in *Saxby et al.* (2020). Solid line: y = x, dashed line: y = 2x. The SE image (top right) and binary image (bottom right) illustrate how the long axis (L) and equivalent circle diameter (Dc) is determined from 2D image analysis.

Another explanation for the coarse grain size of the distal Campanian Ignimbrite and Mazama samples relative to the MSH distal tephra is related to particle shape (Fig. 4.12). Non-spherical particles have higher drag coefficients and lower settling velocities than volume-equivalent spherical particles (*Mele et al.*, 2011; *Dioguardi et al.*, 2017; *Saxby et al.*, 2018, 2019). The low values of SPHT for distal Campanian Ignimbrite ash, for example, reflect the high proportion of glass shards and plates seen in SEM images (Fig. 4.12b). The higher SPHT values of MSH 1980 tephra, on the other hand, are consistent with SEM images that show particles that are more elliptical in shape (Fig. 4.12d). Therefore, it is likely that the differences in the distal grain sizes (Fig. 4.10) reflect both different parameterisations of size and the impact of particle shape on terminal settling velocities. It is also possible that the differences in distal median grain size reflect the initial fragmentation processes. For instance, the fine-grained MSH ash (Md ~20 µm)

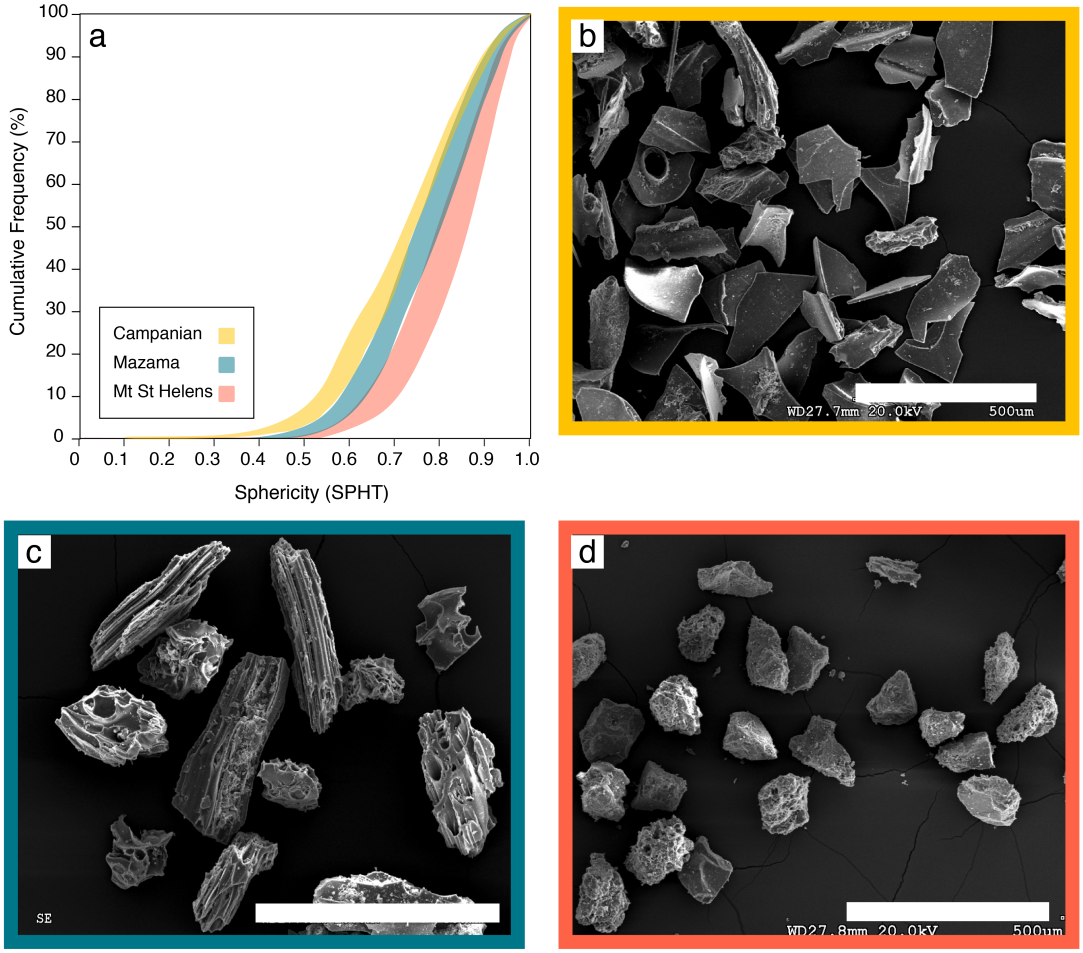

Figure 4.12: Sphericity distributions and SE images of distal tephras. Sampling distance ranges: Campanian Ignimbrite ~600-2300 km, Mazama tephra ~400-1350, Mount St. Helens ~150-400 km from source. a) Ranges of multiple individual SPHT distributions for each distal tephra suite. b-d) Images collected on the Hitachi S-3500 N SEM at the University of Bristol in secondary electron mode. Samples were sieved between 90 and 125 µm, mounted on carbon stubs gold coated. Images were collected at 20 kV using a working distance of ~27.7 mm. White bars are 500 µm in all images. Sample name and distance from source: b) Borschevo ~2300 km; c) Andies Prairie (MZ73) 444 km and d) Starbuck (MSH_SB) 314 km (Appendix C.4).

has been attributed to the co-PDC plume formed as a result of the lateral blast (*Eychenne et al.*, 2015).

Particle density also governs the settling velocity of tephra. Parallel sieve and CX2 analyses, paired with density measurements, highlight the non-uniform density distribution in coarse Mazama tephras (Fig. 4.8); and provide a qualitative assessment of density across the size array. Importantly, the density distribution measured for the coarse Mazama samples (Fig. 4.8c) differs from the sigmoidal distributions of clast density that have been measured and modelled in other tephra deposits (e.g., *Barberi et al.*, 1989; *Koyaguchi and Ohno*, 2001; *Bonadonna et al.*, 2013; *Eychenne and Le Pennec*, 2012). The main difference is that the maximum measured density (~2.6 gcm^{-3}) exceeds the glass density (~2.1 gcm^{-3}), which is often used to approximate the density of the very fine ash that is typically dominated by glass fragments. Whilst the high proportion of lithics and iron titanium oxides in the Mazama tephra contribute to this extreme density value, crystal concentrations are frequently observed in fallout deposits (Taupo, *Walker* 1981b; MSH, *Carey and Sigurdsson* 1982; Santa Maria, *Williams and Self* 1983) and it is likely that their occurrence could influence interpretations of GSDs, especially when quantified as mass distributions without reference to parallel componentry analyses. Moreover, componentry is often determined from SEM images (*Liu et al.*, 2017; *Buckland et al.*, 2018; *McNamara et al.*, 2018); without consideration of particle density, the componentry proportions from SEM images do not map directly to the proportion of the sample mass. This has implications for methods that use the proportion of crystals in deposits to calculate erupted volumes (*Walker*, 1980; *Pyle*, 1989; *Fierstein and Nathenson*, 1992; *Scarpati et al.*, 2014). Whilst crystal and lithic concentrations pose a challenge for grain size analysis methods, sample density does converge on the glass density at small grain sizes (distal ash). Understanding where the transition to stable ash density occurs is important for ash dispersion modelling and likely relates to the eruption intensity and properties of the parent magma.

4.6 Conclusions

Quantifying the size of an irregular shaped particle can be ambiguous and the range of methods available to analyse grain size adds another source of variability to the definition of particle 'size' (*Bagheri et al.*, 2015). The heterogeneous nature of tephra, which is often a mixture of components with varied particle densities and shapes, also complicates size analysis. We have shown, however, that DIA methods can provide a useful protocol for characterising the size and shape of irregular particles. For example, sieving, which is often considered to sort by size, actually sorts non-spherical particles by size and shape and the size range within a sieve fraction depends on the size parameter used (*Sanford and Swift*, 1971). In contrast, DIA can measure continuously over a large size range and GSDs can be quantified according to multiple size measures. DIA also quantifies GSDs as volume distributions which the facilitates comparisons between DIA

methods and other techniques such as laser diffraction. Using grain size statistics, we show that both GSDs and the interpretation of GSDs are sensitive to the method of particle size analysis. For example, different sub-populations may be deconvolved from multi-modal deposits that have been analysed in different ways. This suggests that caution should be used when comparing GSDs and their statistics for samples that have been analysed using different methods. Similarly, associating eruptive processes to grain size sub-populations could be influenced by the starting GSD and the method of deconvolution.

Our analysis shows that the observed discrepancy between PSDs used in volcanic ash dispersion models and ground-based GSDs (*Bonadonna et al.*, 2011; *Stevenson et al.*, 2015) can be explained by a combination of different analysis methods, different size parameterisations, different size ranges and the impact of non-spherical particles. For instance, large distal ash grains often exhibit extreme shapes, that when described using $x_{Fe}max$ or their long axis appear oversized compared to their volume-equivalent sphere diameter (*Saxby et al.*, 2020). Importantly, the disparity in size definitions needs to be considered when comparing model results to deposit data and when using deposit data (GSDs) as the basis for model PSDs. Characterising the 3D morphology of volcanic particles and their density is impractical on a large scale, although this would provide the necessary information to fully resolve the aerodynamic properties of tephra. We have shown however, that 2D methods of size analysis such as DIA can provide insight into the properties of distal ash and that careful consideration of size methods and the impact of non-spherical particles have in part explained the differences between the grain size of distal tephras. This information could be used to inform the PSDs used by ash dispersion models, especially if predicting long range ash dispersal is the main goal.

CHAPTER 5

RECONSTRUCTING THE TOTAL GRAIN SIZE DISTRIBUTION OF THE CLIMACTIC MAZAMA ERUPTION, OREGON, USA

Author Contributions and declaration: H. Buckland carried out the data collection (field sampling, grain size) and analysis (jack-knife resampling, Voronoi tesselation, mass weighted averages), created the figures and wrote the main text of this Chapter. Supervision and Chapter edits were provided by K. Cashman, A. Rust and S. Engwell. B. Jensen and J. Westgate kindly shared the Mazama samples from Alberta and British Columbia for grain size analysis. Preliminary results from this Chapter were presented at the virtual Volcanic and Magmatic Studies Group, 2021.

Abstract

The Total Grain Size Distribution (TGSD) of a tephra deposit provides insight into the fragmentation processes associated with explosive eruptions, and the TGSD is a key Eruption Source Parameter (ESP) for models of tephra dispersal and sedimentation. TGSDs are produced by combining multiple GSDs from individual sites according to the mass accumulation of tephra at that location and hence are sensitive to the spatial distribution of sampling sites as well as the method used to combine the data. In this study, we derive a TGSD for the ~7.7 ka climactic eruption of Mount Mazama (Crater Lake, Oregon, USA) by combining data amassed from the literature with new distal grain size data. We show that the TGSD is extremely sensitive to the data used and this is particularly evident when proximal data from within ~130 km from source is excluded. TGSDs are contingent on the sampling distribution and TGSDs calculated without sufficient proximal data are not representative of the whole deposit. Therefore, we encourage caution when interpreting fragmentation mechanisms and eruptive dynamics from the TGSDs of large, prehistoric tephra deposits especially when the sampling distribution is uneven and the deposits represent multiple eruptive phases. However, we show using the distal Mazama deposit that if sufficient distal grain size data is available, thanks to the stability of the GSD over large distances from source we can determine useful inputs for VATDMs by excluding the more complex proximal deposits.

5.1 Introduction and Background

The Total Grain Size Distribution (TGSD) of a tephra deposit provides insight into fragmentation and eruptive processes (*Turcotte*, 1986; *Kaminski and Jaupart*, 1998; *Costa et al.*, 2016). Owing to the association of large magnitude eruptions (M≥7) with explosive fragmentation mechanisms (*Gardner et al.*, 1998; *Papale*, 1999; *Kueppers et al.*, 2006) and the occurrence of large volume Pyroclastic Density Currents (PDCs), which can increase the fine ash fraction (<125 μm; *Sparks and Walker* 1977; *Sigurdsson and Carey* 1989; *Engwell and Eychenne* 2016), we might expect that the TGSDs of M≥7 eruptions may differ from those of smaller eruptions. However, reconstructing and comparing TGSDs can be challenging as this requires multiple GSDs to be analysed across the tephra deposits. Furthermore, TGSDs are extremely sensitive to the distribution of the field data, particularly in areas of the deposit that contain a significant proportion of the total erupted mass (*Bonadonna et al.*, 2015; *Costa et al.*, 2016; *Pioli et al.*, 2019).

Since 1980, following smaller magnitude (M≤5.1) eruptions, TGSDs have been constructed from field data that was systematically sampled soon after the tephra was deposited meaning that the deposits had not undergone significant remobilisation (e.g., Mount St. Helens May 1980, *Sarna-Wojcicki et al.* 1981; *Carey and Sigurdsson* 1982; Ruapehu 1996, *Bonadonna et al.* 2005a; Chaiten 2008, *Alfano et al.* 2011a; *Durant et al.* 2012). The TGSDs reconstructed for these eruptions are highly varied (*Costa et al.*, 2016; *Pioli et al.*, 2019; *Aubry et al.*, 2021), indicating that the TGSD is an eruption-specific parameter affected by distinct fragmentation mechanisms and magma properties (e.g., composition, vesicularity and crystallinity). Rapid data collection and systematic sampling is impossible when dealing with the tephra deposits from large magnitude eruptions because no M≥7 eruptions have occurred in historical times and have therefore not been studied using modern scientific techniques (past ~50 years). Often the tephra deposits of M≥7 eruptions have been remobilised (see Chapter 2) and portions of the deposit are poorly preserved or difficult to access, as seen when tephra has been deposited offshore (e.g., Askja 1875, *Sparks et al.* 1981 and multiple eruptions of Campi Flegrei, *Costa et al.* 2016; *Mele et al.* 2020). However, the tephra deposit of the climactic Mazama eruption ~7.7 ka, Oregon, USA, has tephra deposited mostly on land, which has allowed extensive field observations and sampling (*Bacon* 1983; *Young* 1990, see Chapter 2, Fig. 2.2). This offers the opportunity to reconstruct the TGSD of a M=7.1 eruption and determine the sensitivity of this Eruption Source Parameter (ESP) to the field data.

Reconstructing the TGSD of a tephra deposit is sensitive to the method used to average the individual GSDs as well as the raw data used (*Durant et al.*, 2009; *Volentik et al.*, 2010; *Bonadonna et al.*, 2015; *Pioli et al.*, 2019). Three main methods are used to determine TSGDs: (1) a weighted average where the GSD at each location is weighted according to the mass per unit area of tephra (e.g., *Brazier et al.* 1982; *Parfitt* 1998; *Bonadonna et al.* 2002); (2) isopach maps are divided into sectors where each sector relates to a sampling site, and then each GSD is weighted according

to the sector area and the mass accumulation (e.g., *Sparks et al.* 1981; *Carey and Sigurdsson* 1982; *Durant et al.* 2012); (3) Voronoi tessellation, a spatial interpolation technique, is used to split the deposit into sectors before each GSD is weighted according to the mass accumulation and area of the Voronoi cell (e.g., *Bonadonna et al.* 2005a; *Biass and Bonadonna* 2014; *Alfano et al.* 2016). Each method introduces subjectivity into TGSD reconstructions, in addition to the variability that arises from different sampling distributions, as shown by studies where different TGSDs are produced for the same deposit by using different methods and datasets (e.g., Chaiten 2008; *Durant et al.* 2012; *Osores et al.* 2013; *Alfano et al.* 2016). In this Chapter, we compare the sensitivity of the Voronoi tesselation and weighted average methods to data from the Mazama tephra deposit.

Once reconstructed from field data, TGSDs can be used to determine the Particle Number Distribution (PND) of a tephra deposit (*Kaminski and Jaupart*, 1998; *Costa et al.*, 2016; *Pioli et al.*, 2019). Theoretical and laboratory studies have found that the PND of products generated by explosive fragmentation exhibits fractal behaviour which can be described by a power-law relationship. The power-law exponent (or fractal dimension) is then used to infer fragmentation efficiency (*Turcotte*, 1986; *Wohletz et al.*, 1989; *Gardner et al.*, 1996). However, this analysis of PNDs is problematic for large explosive eruptions because the TGSDs can represent multiple fragmentation mechanisms (*Bonadonna et al.*, 2015; *Costa et al.*, 2016) and include PDC and fall deposits. We know from Chapter 3 that we cannot discriminate the different eruptive phases in the distal Mazama deposits which is why we do not evaluate PNDs in this Chapter.

TGSDs are a common input of Volcanic Ash Transport and Deposition Models (VATDMs; *Osores et al.* 2013; *Beckett et al.* 2015). Volcanic Ash Advisory Centres (VAACs), however, that use VATDMs operationally, typically model the far-travelled distal ash to forecast potential disruption to aviation (*Webley and Mastin*, 2009; *Bonadonna et al.*, 2012; *Beckett et al.*, 2015; *WMO*, 2018; *Saxby et al.*, 2018). Therefore, most important for distal ash hazard assessments are accurate GSDs (or Particle Size Distributions, PSDs) of the distal ash fraction rather than the full particle size range produced by the eruption. The default PSDs used by VAACs typically ignore particles >100 μm (*WMO*, 2018), a convention based on in situ measurements of active volcanic plumes (*Hobbs et al.*, 1991; *Johnson et al.*, 2012), and the assumption that larger particles are deposited close to the source (<200 km) and are therefore a negligible component of distal ash clouds (*Rose et al.*, 2001). However, an explicit upper size limit for VATDM PSDs is poorly constrained, particularly when ground-based GSDs record particles >100 μm that have travelled 1000's of km from source (*Dugmore et al.*, 1992; *Wastegård et al.*, 2000; *Pyle et al.*, 2006; *Engwell et al.*, 2014; *Stevenson et al.*, 2015; *Cashman and Rust*, 2016; *Saxby et al.*, 2019). Importantly, evidence for substantial long-distance transport of larger ash particles derives primarily from deposits of very large (unobserved) eruptions and raises questions about PSDs appropriate for modelling large volcanic plumes. Here we address this question using grain size data from the distal Mazama

deposit (see Chapters 2-4).

5.2 Grain size data for the Mazama tephra

The grain size of the climactic Mazama tephra has been measured from proximal deposits (<130 km; *Young* 1990, Chapters 2-4) to ultra-distal cryptotephra (non-visible tephra) records >1000 km from source (Fig. 5.1a; *Zdanowicz et al.* 1999; *Pyne-O'Donnell et al.* 2012; *Spano et al.* 2017, Chapters 2-4). However, methods used to analyse grain size are inconsistent across the sampling sites. For example, sieved data (*Young*, 1990) quantify GSDs by the mass in each sieve interval. The grain size of cryptotephra, however, is measured by averaging the long axis of individual glass shards (e.g., *Pyne-O'Donnell et al.* 2012; *Spano et al.* 2017). To ensure consistency in the size data used to reconstruct the TGSD, we have filtered our database of Mazama grain size data (Fig. 5.1a) to include only the 36 sites where the full GSD has been measured and reported either by sieving or Dynamic Image Analysis (DIA; Chapters 2-4; Fig. 5.1b-c).

We reprocess all GSDs in full-ϕ size fractions to match the sieve interval used by *Young* (1990) for proximal to medial deposits. GSDs measured using DIA are quantified according to the minimum particle dimension ($x_c$min) for compatibility with sieve data (see Chapter 4, section 4.3.1.2, Fig. 4.4). Bimodal GSDs are described using mixture models of two normal distributions (with the data in ϕ units, see Appendix C.2, Eq. C.7). We use 130 km to delimit the proximal sites (Fig. 5.1c) because at distances >130 km from source the deposit is massive with no distinct stratigraphic units; <130 km from source, in contrast, two individual fall units and an overlying fine-grained unit can be identified in the stratigraphy (e.g., sites 46 & 47).

TGSD reconstruction requires the mass accumulation of tephra at each locality. This has either been measured directly in the field (*Young*, 1990) or calculated from the deposit thickness and average deposit density. Where the thickness has not been reported, or the deposit has been remobilised, we use an interpolated thickness according to the isopachs produced in Chapter 2 (Fig. 5.2). Also, we use a 100 km buffer around the 1 cm isopach from Chapter 2 (Fig. 2.9) for the line of zero mass required for the Voronoi tessellation method of TGSD approximation (Fig. 5.2b).

The distribution of sampling localities is not uniform across the Mazama deposit but instead has two main sampling gaps, as highlighted in Figure 5.2a. The first zone of missing data (Z1 230-400 km) is significant because the median grain size (Md) changes across this gap from decreasing with distance to reaching stability. Unfortunately, Z1 corresponds to an area where the preservation of the tephra is poor, and no Z1 sites reported in the literature (e.g., Forty Day Creek; *Rai* 1971) include grain size data.

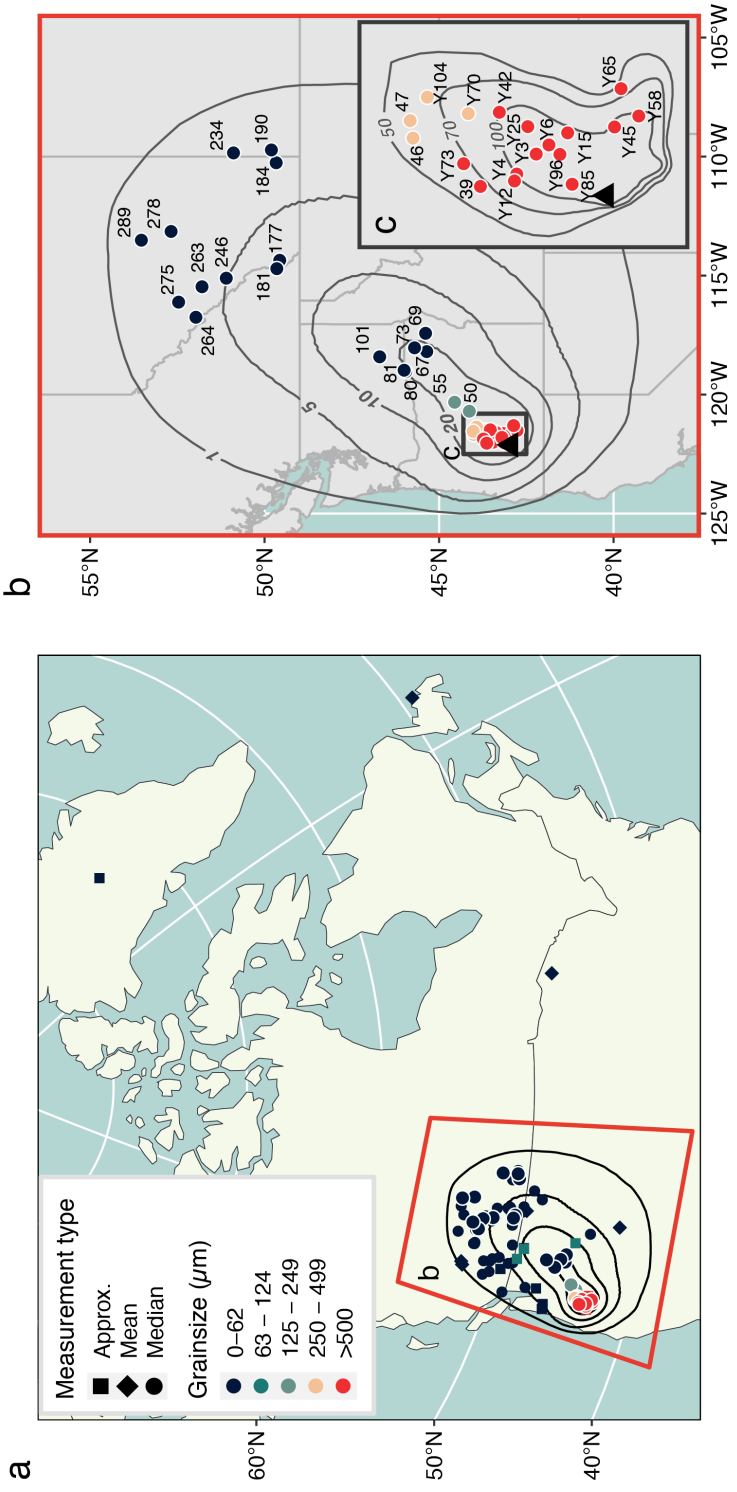

Figure 5.1: Locations of grain size measurements for the climactic Mazama tephra. a) Map with grain size data from the Mazama Locality Database (Chapter 2 and Appendix A.1) and *Young* (1990). The colour of the symbol corresponds to the grain size reported and the symbol shape represents the type of measurement (approximate, mean, or median). b) Map of localities where the full GSD has been measured or reported. Locality numbers and isopachs from Chapter 2 and Appendix A.1. Isopach thicknesses in cm. c) Inset plot of localities from *Young* (1990; symbol number preceded by 'Y') and Appendix A.1. Isopachs of the proximal fall deposit from *Williams* (1942) and re-labelled with approximate thicknesses in cm.

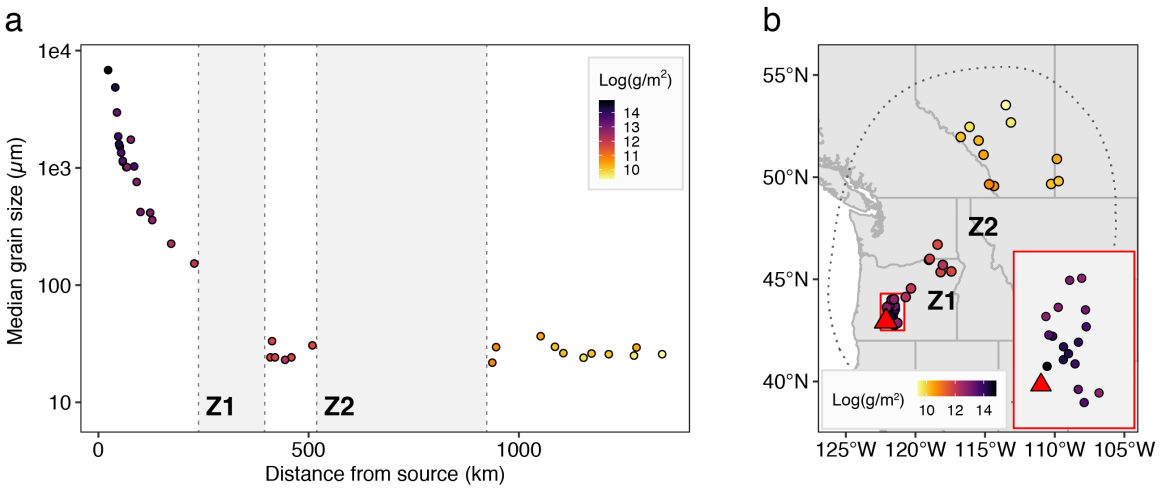

Figure 5.2: Median grain size with distance from source and mass accumulation of tephra. In both panels the points colour represents the mass accumulation of tephra at that locality. a) Median grain size with distance from source with sampling gaps highlighted. Z1 – zone 1 (230-400 km), Z2- zone 2 (510-950 km). b) Location map with line of zero mass shown as dotted line.

5.3 TGSD sensitivity analysis

In this chapter, we investigate the sensitivity of the TGSD calculations to the exclusion of single data point. This is motivated by *Meredith* (2019) observing variability in the Mount St. Helens 1980 TGSD during preliminary analyses when an incomplete GSD dataset was downloaded and analysed that didn't include the GSD measured closest to the volcano (see Appendix D). The Mazama grain size data is spread across a larger area and the mass accumulation and GSDs span up to three orders of magnitude (Fig. 5.2) thus providing a unique opportunity to investigate the relative importance of a single data point.

5.3.1 Full deposit TGSD

To reconstruct the TGSD of the Mazama tephra, we applied the Voronoi tessellation method (*Bonadonna et al.*, 2005a) to the GSDs collated from the sites (Figure 5.3, Dataset A, n=36). We then investigated the sensitivity of this calculation using jack-knife resampling, that is, we repeated the TGSD computation 36 times, leaving out one GSD in each iteration. For comparison, we also calculated the TGSD using a simple weighted average where the individual GSDs are weighted according to the mass accumulation at that locality (Fig. 5.4a) and repeated the leave-one-out analysis.

The complete TGSD reconstructed for the Mazama tephra is shown in Figure 5.3a (Table 5.1). The distribution is strongly bimodal with modes of -0.78 ϕ (1720 µm) and 5.44 ϕ (23 µm) and Md 0.57 ϕ (674 µm). The coarsest and finest TGSDs produced by the leave-one-out analysis on

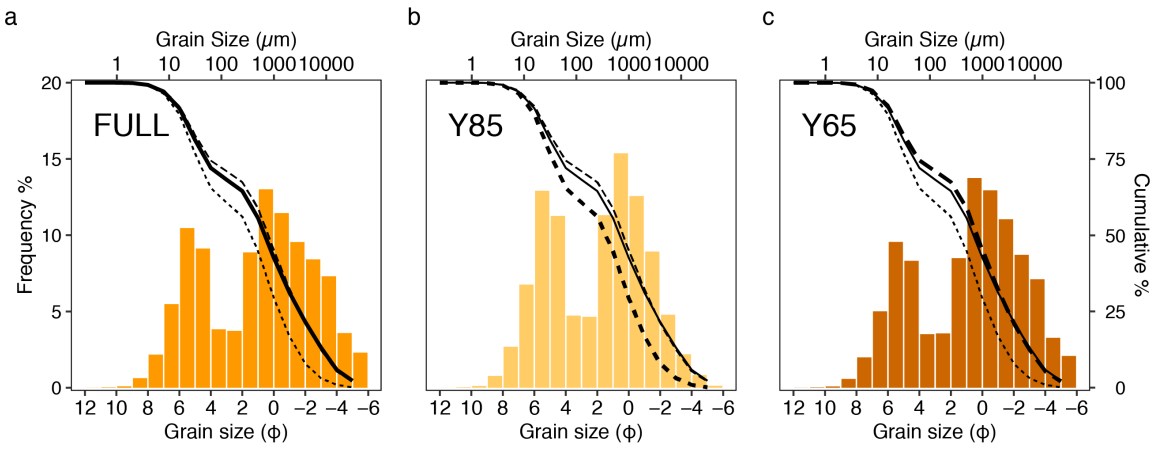

Figure 5.3: Results of TGSD reconstruction using the Voronoi tessellation method with Dataset A and jack-knife resampling. The bars in each panel represent the TGSD as the frequency in each size fraction. The three black lines represent the cumulative frequency distribution for each panel, with the bold line in each panel corresponding to the frequency plot per panel. a) TGSD from full Dataset A. b) Finest TGSD from jack-knife resampling of Dataset A; Y85 is the locality excluded. c) Coarsest TGSD from jack-knife resampling of Dataset A; Y65 is the locality excluded.

Dataset A are shown in Figure 5.3b & c with Md equal to 0.35 ϕ (785 µm) and 1.46 ϕ (364 µm) respectively (Table 5.1). The sensitivity testing shows that reconstruction of the coarse portion of the TGSD (<0 ϕ, >2 mm) is strongly dependent on the inclusion of the GSD measured at the most proximal locality (Y85; Fig. 5.3b), which has the highest mass accumulation of tephra and leaving it out from the calculation produces the finest TGSD (Md=1.46 ϕ, Fig. 5.2). The coarsest TGSD (Md=0.35 ϕ) is calculated when the locality closest to Y85 is excluded (Y65; Fig. 5.3c), because this increases the area of the Voronoi cell and subsequent weighting of Y85 in the TGSD calculation. Leaving out a single unimodal distal GSD, in contrast, does not have a significant effect on the TGSD (Fig. 5.4a).

5.3.2 Fine-ash fraction GSD (FGSD)

To investigate the sensitivity of "total" GSDs produced for use in VATDMs, the individual GSDs were normalised to include only material >2 ϕ (<250 µm; Dataset B) and > 3ϕ (<125 µm; Dataset C). We then resampled Dataset A for sites >130 km (Dataset D) and >400 km from source (Dataset E). For each dataset, we repeated both methods of TGSD calculation (Voronoi and simple weighted average) and the leave-one-out analysis. To distinguish the results of these calculations from the full deposit TGSD calculations, we shall use "FGSD" as a substitute for 'Fine-ash fraction Grain Size Distribution'.

The FGSDs vary according to the criteria used to filter the grain size data (Fig. 5.4). For example, excluding all mass <2 ϕ (>250 µm; Dataset B) and removing all sites <130 km (Dataset D)

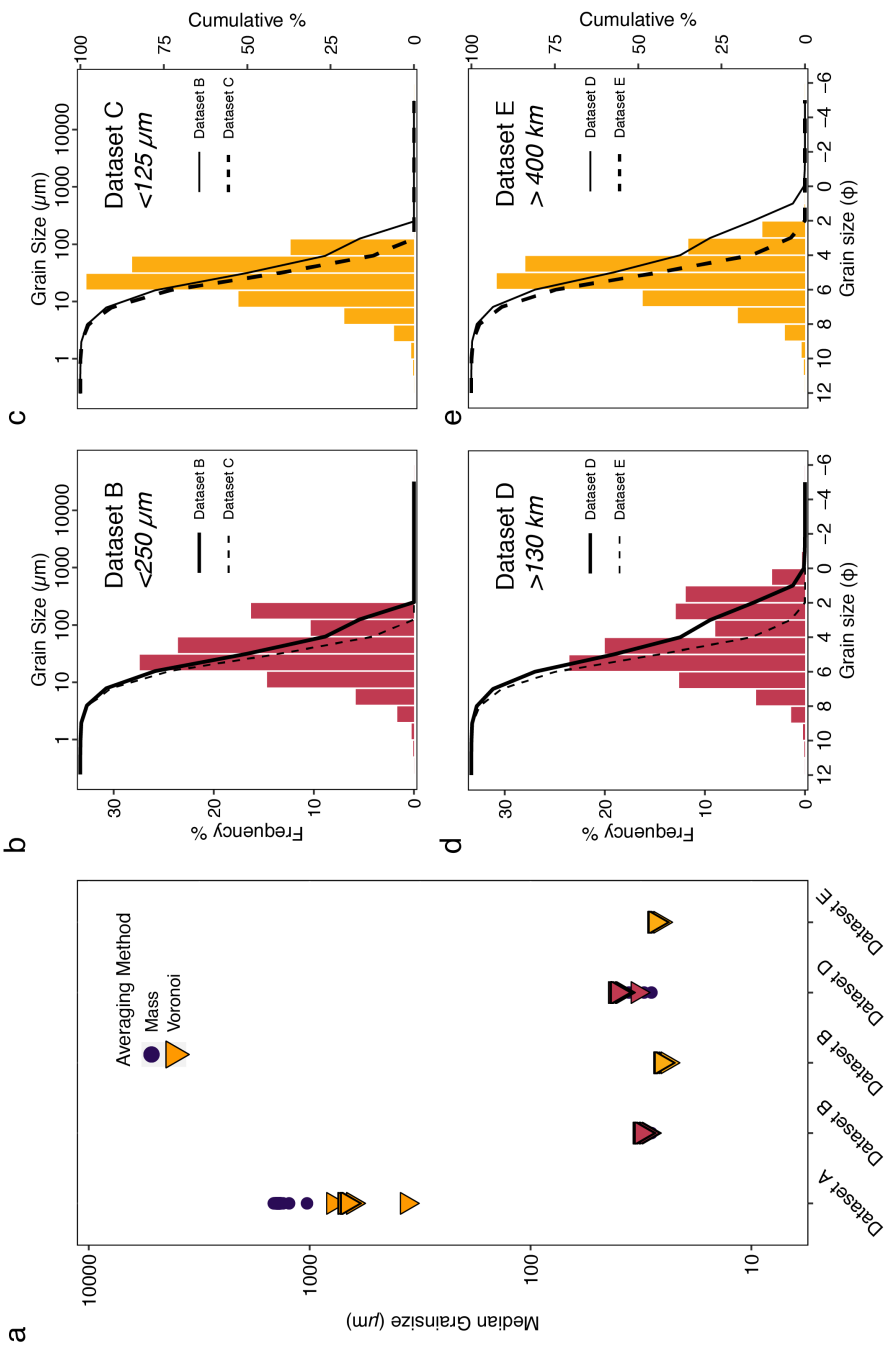

Figure 5.4: Sensitivity of FGSDs reconstructed for volcanic ash transport and deposition models. a) The results of the jack-knife resampling for all datasets using a mass weighted average (circles) and a Voronoi (mass and area) weighted average (triangles). b-e) Frequency and cumulative distributions of the FGSDs calculated using the Voronoi tessellation method. The datasets have been reduced to: b) exclude all mass >250 μm, c) exclude all mass >125 μm, d) exclude localities <130 km from source and e) exclude localities < 400 km from source.

Table 5.1: Grain size statistics of Mazama TGSD and FGSDs. Values are reported in ϕ and (μm).

	Data excluded	Voronoi Md	Bimodal (Y/N)	Coarse mode	Fine mode	Coarsest L-1-O[a] Voronoi (Md)	Finest L-1-O[a] Voronoi (Md)	MWA[b] (Md)
Dataset A	-	0.57 *(674)*	Y	-0.78 *(1720)*	5.44 *(23)*	0.35 *(785)*	1.46 *(363)*	-0.46 *(1376)*
Dataset B	Mass <2 ϕ *(>250 μm)*	4.99 *(31)*	Y	2.5 *(177)*	5.27 *(26)*	4.96 *(32)*	5.10 *(29)*	5.07 *(30)*
Dataset C	Mass <3 ϕ *(>125 μm)*	5.29 *(26)*	N	-	-	(5.27 *(26)*	5.38 *(24)*	5.37 *(24)*
Dataset D	Sites <130 km	4.63 *(40)*	Y	1.87 *(274)*	5.29 *(26)*	4.59 *(42)*	4.93 *(33)*	4.93 *(33)*
Dataset E	Sites <400 km	5.20 *(27)*	N	-	-	5.18 *(28)*	5.27 *(26)*	5.25 *(26)*

(a) Leave-one-out.

(b) Mass Weighted Average.

produces bimodal FGSDs (Fig. 5.4 b & d; Table 5.1). The FGSDs calculated from Datasets C (≥ 3 ϕ) and E (>400 km), however, are unimodal with Md ~5.2-5.3 ϕ (26-27 µm).

5.4 Discussion

Analysing grain size data from the climactic Mazama eruption has highlighted three limitations when reconstructing the TGSD of a large prehistoric eruption. Firstly, gathering representative data across the deposit area is challenging, especially when the tephra is unevenly preserved and remobilised (Fig. 5.2; Chapter 2). Secondly, comprehensive sampling of the proximal record is particularly challenging. The Mazama deposit <50 km from source is complex, with overlapping PDC and lithic breccia units that obscure the initial tephra fall deposits (*Bacon*, 1983; *Druitt and Bacon*, 1986; *Young*, 1990). Also, the final stage of the eruption involved caldera collapse; the material originally deposited within this (very proximal) area is unaccounted for in TGSD calculations (*Bacon and Lanphere*, 2006). Similarly, no grain size data from the PDC deposits has been collected or included in the TGSD reconstruction even though they contain a significant proportion of the total erupted mass (*Williams*, 1942; *Bacon*, 1983; *Bacon and Druitt*, 1988, Chapter 2). The final limitation is the sensitivity of methods used to reconstruct TGSDs. For example, excluding a single proximal point halves the median grain size of the Mazama TGSD (Fig. 5.3; Table 5.1) suggesting that additional proximal sites with substantial mass accumulation would similarly impact the output. Here we discuss the wider implications of these limitations on the interpretation of TGSDs and how to most effectively use field-based observations to produce PSDs for VATDMs.

5.4.1 Sensitivity of the coarse size fraction of TGSDs

The uneven sampling distribution of the Mazama tephra (Fig. 5.2) and incomplete proximal record means that the TGSD of Dataset A (Fig. 5.3a) does not represent the complete particle size distribution produced by the climactic Mazama eruption. We conclude, therefore, that the TGSD reconstructed from Dataset A is unsuitable for inferring fragmentation efficiency (*Kaminski and Jaupart*, 1998), eruptive column height or magma viscosity (*Costa et al.*, 2016). This is particularly true because field measurements of the Mazama deposits are the summation of multiple phases of explosive activity (*Bacon* 1983; *Young* 1990; Chapter 3), each of which may be associated with different fragmentation mechanisms and eruption dynamics.

The limitations associated with sample distribution and complex proximal deposits affect other TGSDs constructed from field deposits. For example, the TGSD of the May 1980 eruption of Mount St. Helens is extremely fine-grained when compared to other TGSDs collated in the Independent Volcanic ESP Archive (IVESPA; Fig. 5.5; *Aubry et al.* 2021). The very fine grain size of the deposit is commonly attributed to the lateral blast that enhanced the production of fine ash (*Eychenne et al.*, 2015). However, we suggest that it could also be explained, at least in part, by an underrepresentation of the proximal record. Although sampling of the deposit was extremely comprehensive and undertaken soon after the eruption (*Sarna-Wojcicki et al.*, 1981; *Waitt et al.*, 1981), only two GSDs from <50 km from source and within the 1 cm isopach are included in the TGSD calculations (Appendix D; *Carey and Sigurdsson* 1982; *Durant et al.* 2009; *Eychenne et al.* 2015). This suggests that the Mount St. Helens 1980 TGSD available in the IVESPA database (*Carey and Sparks*, 1986; *Durant et al.*, 2009; *Aubry et al.*, 2021) underrepresents the proximal record, perhaps substantially, and therefore inferring eruption dynamics and fragmentation efficiency using the published TGSD should be carefully considered (*Costa et al.*, 2016).

All methods of TGSD calculation use the mass accumulation of tephra to weight the individual GSDs. This is why proximal sites with high mass accumulation (gm^{-2}) are critical to reconstructing a representative TGSD (*Bonadonna et al.*, 2015; *Pioli et al.*, 2019). Similarly, in distal deposits if there is still variability in the GSD, individual sampling sites can significantly alter the FGSD. For example, two Mazama samples at 170 and 230 km from source (sites 50 & 55; Fig. 5.3b) have bimodal GSDs and, when included in the FGSD calculation (Dataset D), they produce a strongly bimodal FGSD (Fig. 5.4d). Furthermore, their significant mass accumulation relative to sites >400 km from source means that excluding either of the bimodal sites in the FGSD calculation causes pronounced variability in the leave-one-out analysis (Fig. 5.4a). Important for VATDMs is that grain size bimodality persists to >200 km, and with grain sizes >125 μm; this suggests caution in the application of default PSDs to VATDM models of large eruptions.

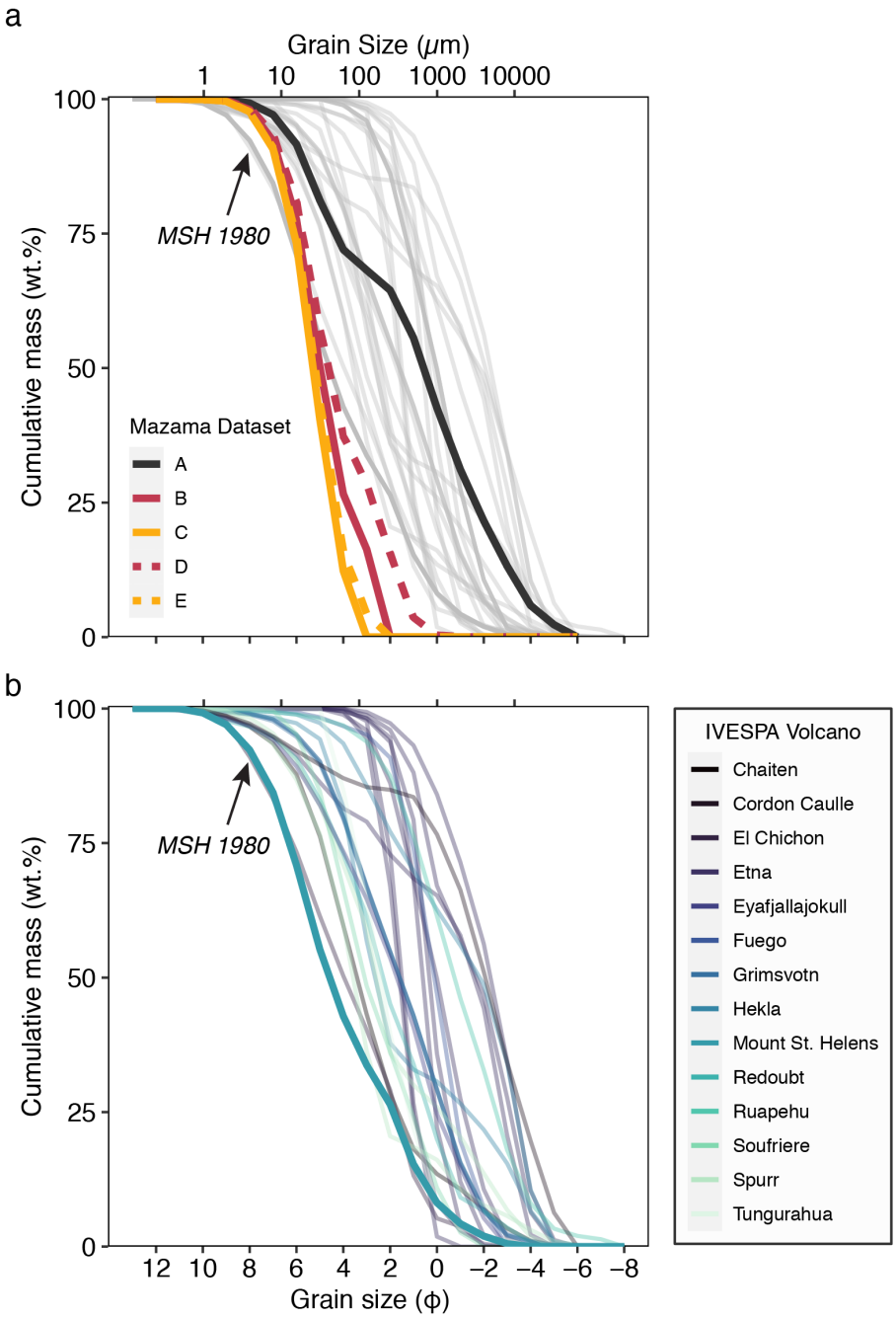

Figure 5.5: Comparing the Mazama TGSD and FGSDs to published TGSDs for other deposits. a) The GSDs reconstructed from Datasets A-E compared to the TGSDs in the IVESPA Eruption Source Parameter database (*Aubry et al.*, 2021). b) The IVESPA TGSDs colour coded according to the source volcano. The TGSD of the May 1980 eruption of Mount St. Helens is highlighted (*Carey and Sigurdsson*, 1982; *Durant et al.*, 2009).

5.4.2 Using field data to produce inputs for VATDMs

Irregular sample distributions, the limited characterisation of proximal deposits and the sensitivity of averaging techniques are most important when analysing the coarse fraction of the TGSD (>250 μm). However, VATDMs typically focus on the distal fine-ash fraction (≤125 μm). Different subsets of the Mazama data produce different GSDs for the fine-ash fraction (FGSD), however, excluding the mass >125 μm (Dataset C) and including only sites >400 km (Dataset E) produced very similar FGSDs when calculated using a simple weighted average of distal ash sites (Fig. 5.4c & e; Table 5.1). Importantly, mass-weighting eliminates the requirement of the zero-mass line used the Voronoi tessellation method, which can introduce subjectivity into the TGSD calculations (*Volentik et al.*, 2010; *Bonadonna et al.*, 2015). Eliminating this uncertainty is particularly beneficial for deposits such as the Mazama tephra where the zero mass line is not well constrained.

The stability of the distal Mazama GSD (Fig. 5.2) explains the stability of the FGSD; this phenomena has been observed in many other tephra deposits (Campanian Ignimbrite tephra; *Engwell et al.* 2014; Mount St. Helens 1980; *Eychenne et al.* 2015, Chapter 4, Fig. 4.10). Critically, this GSD stabilisation suggests that GSDs measured from the portion of tephra deposit where the GSD has stabilised can be input directly into VATDMs with little need for extensive sampling across the distal deposit.

5.5 Conclusions

Reconstructing the TGSD of the climactic Mazama eruption is impeded by the limited number of GSDs measured from the very proximal deposit (<50 km from source). Because of the very high tephra mass accumulation measured at the proximal sites (>2000 kgm^{-2}) compared to the distal sites (<20 kgm^{-2}), excluding a single very proximal GSD dramatically impacts the Md of the TGSD and proportion of the mass attributed to the coarse mode of the distribution (Fig. D.3 & Table 5.1). Significant sampling gaps, that correspond to regions where the grain size trend with distance is changing (Fig. D.2), also mean that the TGSD calculated for the Mazama tephra from Dataset A is likely not representative of the full range of particle sizes produced by the eruption. This suggests that caution should be applied when interpreting TGSDs reconstructed from large, eroded tephra deposits.

The GSD of the fine-ash fraction of the Mazama deposit (FGSD) is less susceptible to variability from sporadic field data thanks to the less significant changes in the mass accumulation >130 km from source (Fig. D.2). But, given there are only two GSDs measured between 130 and 400 km from source (Fig. D.2) and the sensitivity of TGSD methods to individual points, the reliability of the bimodal FGSDs (Datasets B and D) is limited. The stability of the Mazama GSD >400 km, however, means that the FGSD reconstructed from Dataset E (Fig. D.4e) is not sensitive to a

single data point or the averaging method (Fig. D.4a). The latter is beneficial because the Voronoi tesselation method is sensitive to the zero mass line which can be difficult to delineate, especially for old deposits that cover large areas (*Bonadonna et al.*, 2015). Now, we will investigate the suitability of using the bimodal and unimodal FGSDs as inputs to a VATDM in Chapter 6.

CHAPTER 6

MODELLING THE MAZAMA ERUPTION

Author Contributions and declaration: This Chapter is a collaboration with L. Mastin of the United States Geological Survey (USGS). H. Buckland produced the estimates of the Eruption Source Parameters and L. Mastin ran the Ash3D simulations on the USGS super-computer. This work is currently in preparation for publication. H. Buckland has written the main text and produced the figures, excluding Figures 6.1 and 6.5 which have been produced by L. Mastin. L. Mastin, S. Engwell and K. Cashman have contributed to the writing of the Chapter and discussion of the results. A. Van Eaton contributed discussion to the early stages of this project. A. Rust has also contributed to the discussion and copy editing of the text.

Abstract

Volcanic Ash Transport and Deposition Models (VATDMs) are necessary for forecasting the tephra dispersal during volcanic eruptions and are a useful tool for interpreting prehistoric tephra deposits. Here we use Ash3D, a Eulerian VATDM to simulate the tephra deposit from the ~7.7 ka climactic eruption of Mount Mazama in an effort to test and improve the accuracy of VATDMs using with the Eruption Source Parameters (ESPs) characteristic of a large magnitude eruption. We simplify the simulation to focus on the distal deposit as if it was formed by a single phase of Plinian activity using a total magmatic volume of 40 km^3. Our results firstly emphasise the importance of determining appropriate reanalysis meteorological data to recreate prehistoric deposits. Secondly, the off-axis spreading of the Mazama deposit is only reproduced when umbrella cloud spreading regimes are used in addition to advection-diffusion. Thirdly, we show the importance of using Grain Size Distributions based on field deposits. Overall, the Ash3D simulations were able to reproduce the thickness and grain size of the Mazama tephra deposit to a reasonable degree given the uncertainties inherent in using modern wind profiles for a prehistoric eruption. However, this endeavour highlighted the simplifications and assumptions required to simulate the deposition of fine-grained (<125 μm) volcanic ash that constitutes the distal Mazama tephra. To accurately predict where fine-ash will be concentrated in the air and on the ground during and following future eruptions of any scale, further research in needed into the atmospheric and particle processes that drive the deposition of fine-ash.

6.1 Introduction

Predicting the transport and deposition of volcanic ash following a large magnitude explosive volcanic eruption poses an unprecedented challenge for hazard mitigation (*Newhall et al.*, 2018). Whilst Volcanic Ash Transport and Deposition Models (VATDMs) have undergone increased testing and validation since the 2010 eruption of Eyjafjallajökull in Iceland (e.g., *Bonadonna and Costa* 2012; *Gudmundsson et al.* 2012; *WMO* 2018; *Beckett et al.* 2020), these advances have been informed by observations following recent, relatively small magnitude eruptions (e.g., *Dacre et al.* 2011; *Folch et al.* 2012; *Osores et al.* 2013; *Magill et al.* 2015; *Mastin et al.* 2016; *White et al.* 2017). Large eruptions, in contrast, can have multiple phases of activity (e.g., *Sigurdsson and Carey* 1989; *Rosi et al.* 2001; *Perrotta and Scarpati* 2003; *Marti et al.* 2015), a large fine-ash fraction (*Rose and Durant*, 2009; *Engwell and Eychenne*, 2016), extreme erupted volumes (*Froggatt*, 1982; *Matthews et al.*, 2012), and complex plume dynamics (*Baines and Sparks*, 2005; *Costa et al.*, 2014, 2018; *Barker et al.*, 2019) all of which pose a challenge for existing VATDMs (section 6.2.1). Furthermore, the Eruption Source Parameters (ESPs), such as plume height and mass eruption rate, must be based on the interpretation of field deposits, which can introduce significant uncertainty (*Bonadonna et al.* 2015, Chapters 2 & 5) compared to determining appropriate ESPs for smaller eruptions using satellite remote sensing methods (*Holasek et al.*, 1996; *Bonadonna et al.*, 2011; *Osores et al.*, 2013). Here we use the ESPs investigated in Chapters 2-5 to simulate the climactic Mazama eruption with the Eulerian ash dispersion model Ash3D (*Schwaiger et al.*, 2012). Our aim is to reproduce observed tephra deposit trends and to investigate the sensitivity of the Ash3D simulations to the volcanic input parameters. There are unavoidable sources of uncertainty when using a simplified model to reconstruct the ash dispersion of a prehistoric eruption. However, using the well characterised Mazama deposit offers an opportunity to validate the output of a VATDM against field data for a M≥7 eruption. Attributes of the Mazama tephra deposit that the Ash3D simulations cannot explain can be used to identify features that may be unique to large explosive eruptions that are not well captured by VATDMs largely based and tested on smaller eruptions. We then discuss reasons why Ash3D simulations differ from the field data from both the perspective of direct simplifications in VATDMs as well as uncertainty in the field data.

6.2 Background

The widespread subaerial tephra deposit formed by the climactic Mazama eruption provides an excellent opportunity to validate the outputs of VATDMs against field observations. In this section we discuss the limitations of existing VATDMs for modelling large eruptions and the governing equations used by the Ash3D model. Details on the Mazama eruption and tephra deposit are available in sections 1.3.4, 2.2.2, 3.2.2 and 5.2.

6.2.1 Modelling large volcanic eruptions

Modelling the dispersal of volcanic ash from a large magnitude (M≥7) eruption is considerably more complex than smaller magnitude (M≤5) events for multiple reasons. Firstly, the mass eruption rate into Plinian columns produced by large magnitude eruptions is such that gravity currents are commonly formed as the plume reaches neutral buoyancy in the atmosphere, meaning that the plume dominantly spreads by buoyancy forces close to source rather than advection-diffusion. This gravitational spreading in the umbrella cloud region impacts tephra dispersion but is typically not accounted for in VATDMs (*Woods and Wohletz*, 1991; *Sparks et al.*, 1997; *Suzuki and Koyaguchi*, 2009; *Costa et al.*, 2013; *Pouget et al.*, 2016). The distance from source that gravitational spreading will impact tephra transport during large eruptions is also poorly constrained and may be much greater than what has been witnessed during historical eruptions (*Houghton et al.*, 2004; *Costa et al.*, 2018; *Constantinescu et al.*, 2021).

Secondly, large explosive eruptions, especially those with significant co-Pyroclastic Density Current (co-PDC) phases, are associated with large volumes of fine ash. Analysis of trends of median grain size with distance (Figure 4.10 & 5.2; *Engwell and Eychenne* 2016) show that the grain size of deposits decays with distance from source, up to a distance beyond which it remains relatively stable, a trend particularly well identified for large eruptions. While there is some difference in the grain size of these distal deposits, the median grain size typically ranges between 30-60 μm (*Engwell and Eychenne*, 2016). The vertical component of air velocity (atmospheric turbulence) is often greater than the settling velocity of particles of this size, meaning that they do not fall as individuals and other mechanisms are required for their sedimentation, for example aggregation (*Brown et al.*, 2012; *Van Eaton et al.*, 2012; *Rossi et al.*, 2021) or the formation of convective instabilities (*Manzella et al.*, 2015; *Scollo et al.*, 2017; *Freret-Lorgeril et al.*, 2020). Because it is not trivial to simulate such processes in VATDMs, significant assumptions must be made to invoke the settling of these fine particles in numerical models.

Thirdly, as exemplified by the Mazama eruption, large eruptions typically have multiple phases often including a co-PDC phase (e.g., Santorini 3.6 ka, *Sparks et al.* 1983; Tambora 1815, *Sigurdsson and Carey* 1989; the Campanian Ignimbrite ~39 ka, *Perrotta and Scarpati* 2003; *Engwell et al.* 2014). This means that ESPs are highly variable and likely time dependent which is extremely challenging to reconstruct from field deposits, for example, shifting wind conditions, varying mass eruption rates and unsteady plume heights. Furthermore, the definition of ESPs for co-PDC plumes is less well studied than for Plinian plumes. For example, co-PDC plumes cannot be approximated as a point source and the relationship between mass eruption rate and the mass entering the plume may be significantly different from the Plinian phase (*Woods and Wohletz*, 1991; *Baines and Sparks*, 2005; *Marti et al.*, 2015; *Engwell and Eychenne*, 2016).

Fourth, ESPs are necessarily derived from field deposits for prehistoric eruptions and thus have

significant uncertainties associated with them due to lack of data, remobilisation of deposits, and the models used to approximate deposit trends (*Biass and Bonadonna* 2011; *Bonadonna et al.* 2015; Chapter 2). This can be particularly important when considering parameters such as the Total Grain Size Distribution (TGSD). Large eruptions can deposit tephra many thousands of kilometres from source and across a deposit, measurements of the deposit characteristics (such as deposit thickness and grain size) can be sparse. Additionally, in proximal regions, it may be possible to identify deposits from individual phases of an eruption (e.g., Plinian versus co-PDC) but in distal reaches (typically distances greater than several hundreds of kilometres for large explosive eruptions) deposits merge and it becomes impossible to separate these contributions (see Chapter 3). This results in the TGSD, and other field measurements such as deposit thickness, commonly representing multiple eruption phases.

Finally, simulation of volcanic plumes requires meteorological information. However, given the age of most large explosive eruptions, quantitative meteorological data for these times is not available. We therefore use modern meteorological information under the assumption that conditions have not changed significantly in the intervening time (*Johnston et al.*, 2012). Moreover, meteorological conditions vary seasonally, and for most pre-historic eruptions information on the seasonality of an eruption is limited, however, there is evidence from pollen records that the Mazama eruption occurred during the northern hemisphere autumn (*Mehringer et al.*, 1977a).

6.2.2 Ash3D model description and umbrella spreading regimes

Ash3D is an Eulerian dispersion model that computes tephra transport and deposition across a 3D grid using a time-dependent wind field (*Schwaiger et al.*, 2012; *Mastin et al.*, 2013). The model does not include the dynamics of a rising plume. Instead, the standard model setup, which works well for weak plumes and sub-Plinian eruptions, approximates a volcanic plume by adding tephra above the vent either as a point source, vertical line source or most commonly, some vertical distribution such as that of *Suzuki* (1983):

$$\frac{d\dot{M}}{dz} = \dot{M}\frac{k_s^2(1-z/H_T)exp(k_s(z/H_T-1))}{H_T[1-(1+k_s)exp(-k_s)]}. \tag{6.1}$$

Here $\dot{M}$ is the mass flow rate into the column of cells (approximate plume), H_T is the height of the plume top, z is the elevation at a particular point in the column and k_s is a constant that controls the mass distribution across cells (Figs. 6.1 & 6.2).

For modelling large eruptions, several dispersal models now consider the dynamics of a growing umbrella cloud. Ash3D calculates the radial spreading within an umbrella cloud at the neutral density elevation (H_u; Fig. 6.1b; *Mastin et al.* 2014) following the formula of *Costa et al.* (2013 and erratum), which assumes that the volume growth rate of the umbrella cloud (q) is proportional to

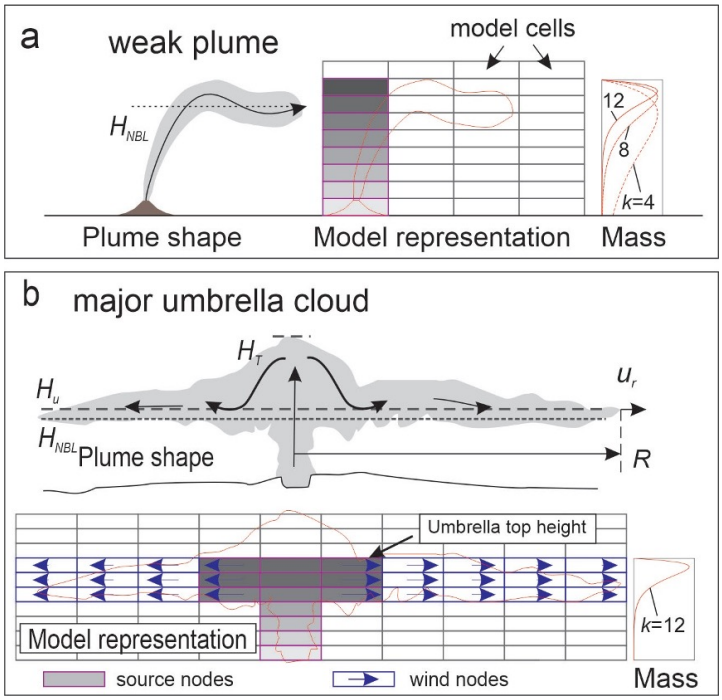

Figure 6.1: Model configuration for different plume regimes in Ash3D. a) A weak plume; and b) a major umbrella cloud. The grey cells are source nodes that show where the ash (mass) is added at each time step in the model. Plume a) is approximated by vertical column of model cells. Plume b) is approximated by a 3x3 matrix of source cells. The umbrella cloud wind field is shown by the nodes with blue arrows. The panels on the right-hand side represent the mass distribution in the plume with different values of the constant k_s (Eq.6.1) which are shown in detail in Figure 6.2. Figure from *Mastin et al.* (2014).

the mass eruption rate ($\dot{M}$):

$$q = C\sqrt{k_e}\frac{\dot{M}^{3/4}}{N^{5/4}} \tag{6.2}$$

where k_e is the radial entrainment coefficient, C is a constant of proportionality and N is the Brunt-Väisälä frequency. C has been determined empirically to be ~0.43 x 10^3 $m^3kg^{-3/4}s^{-3/2}$ for tropical eruptions and 0.87 x 10^3 $m^3kg^{-3/4}s^{-3/2}$ for polar and midlatitude eruptions (*Suzuki and Koyaguchi*, 2009; *Costa et al.*, 2013, erratum). We use C=0.87 x 10^3 $m^3kg^{-3/4}s^{-3/2}$, k_e=0.1 and N=0.02 s^{-1} for the simulations.

The velocity field within the umbrella cloud is then calculated using the volume growth rate (q) and the radial distance within the umbrella cloud (R; see Appendix E.1 for details). The appropriate formula for calculating radial winds is still the matter of some discussion (*Costa et al.*, 2013; *Pouget et al.*, 2016; *Webster et al.*, 2020). In this study, we use two formulas for calculating the radial winds. Firstly, the method of *Costa et al.* (2013, Eq. 11), implemented by *Mastin et al.*

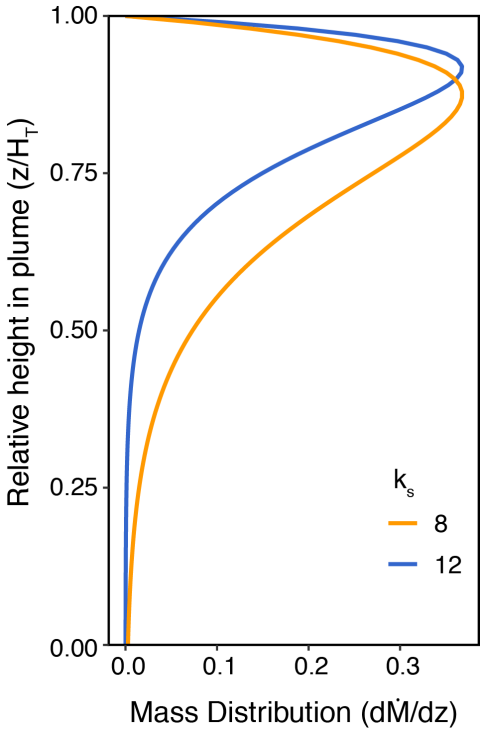

Figure 6.2: The Suzuki probability density function used to distribute mass in the plume (Eq. 6.1). Changing the k_s value (shown by the line colour) alters the mass distribution across the total plume height.

in Ash3D (2014, Eq. 7) where the radial velocity within the umbrella cloud u_r is governed by:

$$u_r = \frac{3}{4} u_R \frac{R}{r} \left(1 + \frac{1}{3}\frac{r^2}{R^2}\right) \tag{6.3}$$

where u_R is the velocity at the flow front ($u_r = dR/dt$) and r is the position in the umbrella cloud. Secondly, the formulation of *Webster et al.* (2020, Eq.7):

$$u_r \;=\; u_R \left(\frac{R}{r}\right)^{\frac{1}{2}}. \tag{6.4}$$

The difference between the two spreading regimes is shown in Figure 6.3. Both regimes meet the boundary condition that when r=R, u_r=u_R but Eq.6.3 (*Costa et al.*, 2013) gives stronger winds when $r << R$ (Fig. 6.3).

Once the mass is added to the cells, Ash3D computes the conservation of mass in each cell by tracking the mass concentration Q with time t:

$$\frac{\partial Q}{\partial t} + \nabla \bullet [(u_a + v_s)Q] - \nabla \bullet (K \nabla Q) = S, \tag{6.5}$$

where u_a is the 3D wind vector, v_s is the settling velocity, K is the diffusivity and S is the source term which is non-zero only in the column of nodes above the volcano. The second and third

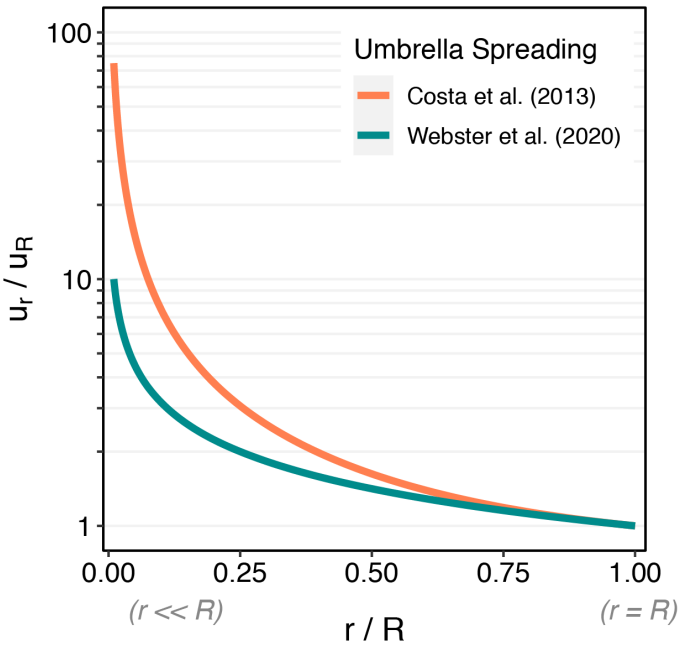

Figure 6.3: Different umbrella cloud radial wind formulations used in Ash3D. Ratio of position in umbrella cloud r to the radius of the umbrella cloud R plotted against the ratio of the radial wind velocity at position r (u_r) to the velocity at the cloud front (u_R). Two different formulations used are from *Costa et al.* (2013) and *Webster et al.* (2020).

terms in this equation represent (1) advection by wind and settling, and (2) turbulent diffusion, respectively.

Using the umbrella spreading scheme at the beginning of the simulation, the mass flow rate into the umbrella cloud (q) is calculated using Eq. 6.2. Ash is placed into the source nodes (grey nodes, Fig. 6.3b) and distributed vertically using a Suzuki distribution (Eq.6.1) with k_s=12. Then, at each time step during the eruption, radial winds are calculated using Eq.6.3 or Eq.6.4 and added to the ambient wind field u_a, and the movement of the ash across each cell is calculated using Eq. 6.5. After the end of the eruption, the advection and diffusion of ash continues to be calculated using Eq.6.5, but no ash is added to the source nodes and radial winds are no longer added to the ambient winds.

6.3 Ash3D model inputs

Here we summarise and explain the model inputs used to simulate the ~7.7 ka climactic Mazama eruption using Ash3D. We report the range of parameters used in Table 6.1.

6.3.1 Volcanic inputs - erupted volume, particle characteristics, eruption duration and plume height

The aim of this Chapter is to model the dispersion of distal tephra; therefore, we exclude the volume contained in deposits <130 km from source. Furthermore, the volume of the proximal deposits is poorly constrained because of overlapping eruptive units and the unknown volume contained within the caldera collapse deposits (*Bonadonna et al.*, 2015, see Chapter 2). Similarly, within ~100 km source for large eruptions the transport and deposition of material is controlled by a range of complex processes caused by plume and edifice instabilities (*Houghton et al.*, 2004; *Costa et al.*, 2018; *Constantinescu et al.*, 2021); therefore, by excluding the proximal deposit we aim to reduce uncertainty in Ash3D simulations.

To estimate the bulk volume of the distal Mazama deposit, we use isopachs constructed using distal ash thicknesses and then fit a single exponential function to the square root of the isopach area against tephra thickness (*Pyle*, 1989; *Fierstein and Nathenson*, 1992; *Daggitt et al.*, 2014, see Chapter 2). The bulk volume estimates range between 129 – 134 km^2 depending on whether you extrapolate the distal isopachs back to the source (Fig. 6.4a) or only include the volume beyond the proximal isopachs (Fig. 6.4b). The Dense-Rock Equivalent (DRE) volume is then determined using the average deposit density (700 kgm^{-3}) to give a minimum value of 40 km^3 DRE (Chapter 2, Section 2.5.4).

We use four different Grain Size Distributions (GSDs) in the Ash3D simulations (Fig. 6.5). (1) The GSD used by *Mastin et al.* (2014) when simulating a super-eruption from Yellowstone (GSD_M14). (2) A simplified version (*Mastin et al.*, 2016) of the TGSD of the May 1980 eruption of Mount St. Helens (*Durant et al.* 2009; GSD_M16). (3) A bimodal TGSD based on the grain size of Mazama tephra deposits >130 km from source (GSD_B21_B; Chapter 5) and (4) a unimodal TGSD that reflects the grain size of the Mazama tephra >400 km from source (GSD_B21_U; Chapter 5).

Aggregation is not a process directly modelled by Ash3D (*Mastin et al.*, 2016). For all GSDs the mass <125 μm has been amalgamated into an aggregate size class to simulate the aggregation of fine material (see Appendix E.4). Two aggregate size distributions were used with different median aggregate sizes and skew (Fig. 6.5b; *Mastin et al.* 2016).

The particle densities for GSD_M14 and GSD_M16 have been taken from the literature (*Mastin et al.*, 2014, 2016). For the simulations using GSD_B21 we use the densities measured for the individual sieve fractions >250 μm determined in Chapter 4 (see Fig. 4.8). For particles ≤250 μm, the particle density is equal to the glass density of the Mazama rhyodacite ~2200 kgm^{-3} (*Bacon*, 1983; *Druitt and Bacon*, 1989). The aggregate density is kept constant at 600 kgm^{-3} following *Mastin et al.* (2016).

We use a particle shape factor (F) value of 0.65 for the individual particles. This is based

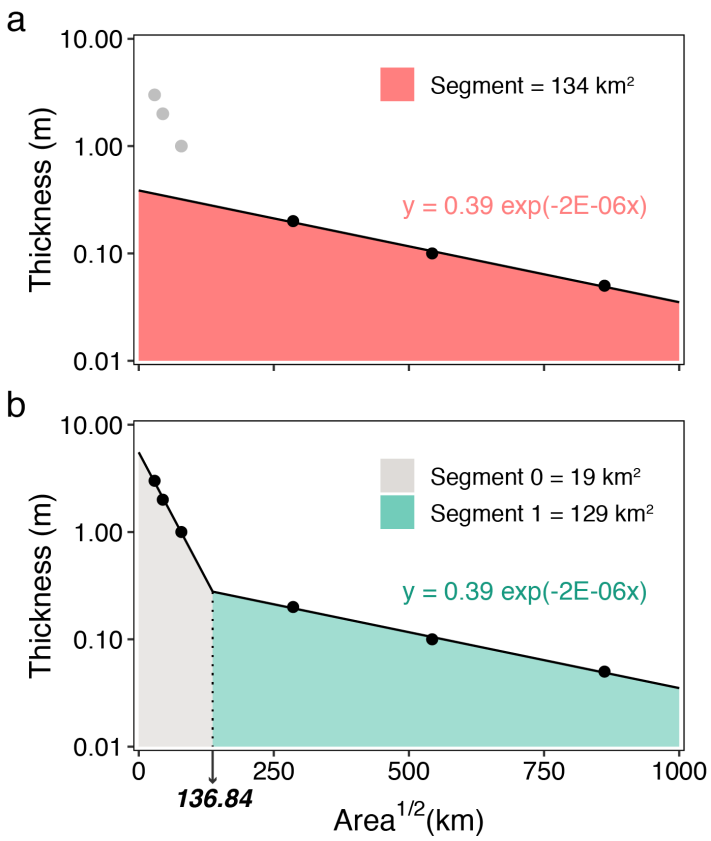

Figure 6.4: Exponential fits to square root area versus log thickness for Mazama isopachs. Isopachs estimated in Chapter 2. Bulk volume is calculated by finding the area under the exponential functions (*Pyle*, 1989; *Fierstein and Nathenson*, 1992). a) Exponential function fit to isopachs excluding the proximal isopachs. b) Two segment exponential fits including proximal isopachs from *Young* (1990). The limit of integration for each segment is x=136.84.

on measurements made using Dynamic Image Analysis (DIA; see Fig. 4.12, Chapter 4). DIA measures the aspect ratio of particles ($x_c$min/x_{Fe}max) which we equate to the 3D shape factor F used by Ash3D to calculate the particle drag coefficient according to the formulation of *Wilson and Huang* (1979). F=(b+c)/2a, where a, b and c are the maximum, intermediate and minimum diameters of the particle. All aggregates are assigned F = 1 (*Van Eaton et al.*, 2012; *Mastin et al.*, 2016).

We use an eruption duration of 24 hours in the Ash3D simulations. The actual duration of the climactic Mazama eruption is difficult to constrain without real-time observations using modern monitoring methods. Therefore, our estimate is based on the absence of evidence for an extended eruption duration. For example, there is no apparent erosion or soil development between the

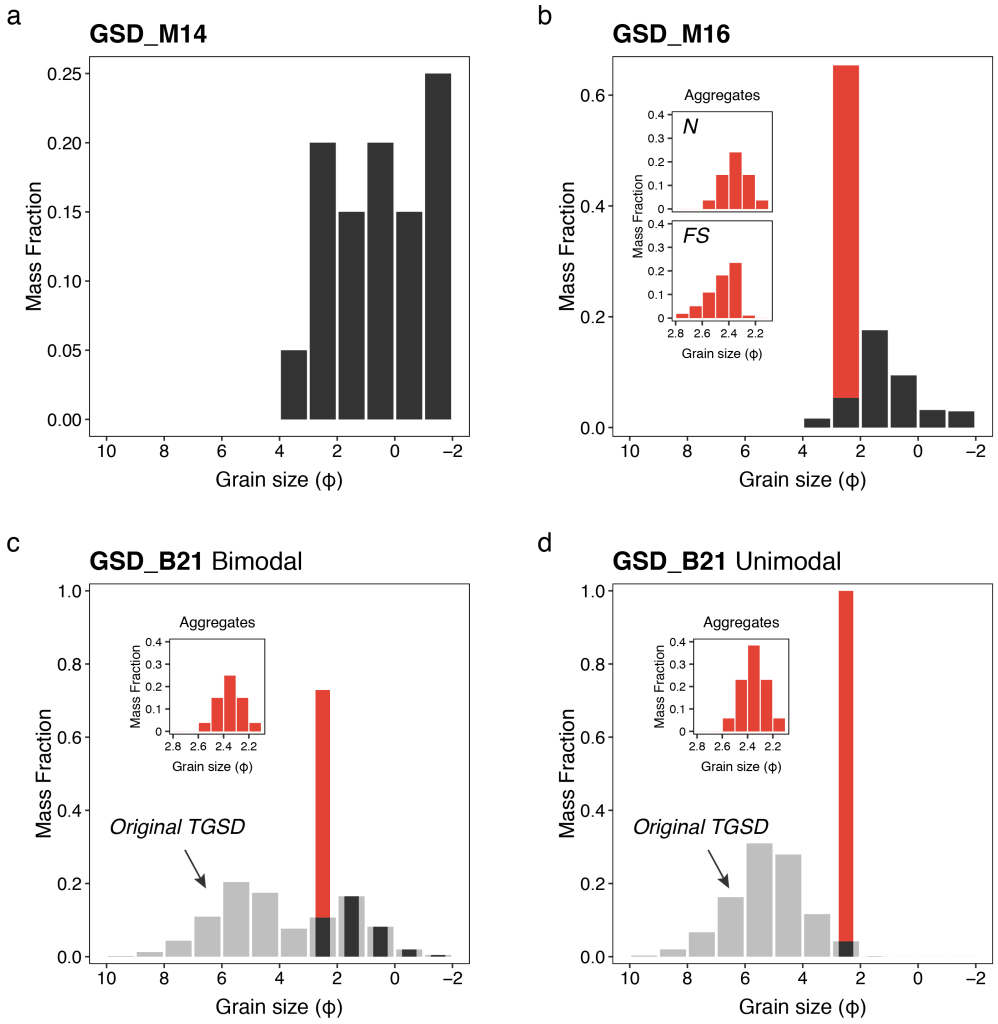

Figure 6.5: GSDs used in Ash3D simulations. a) GSD_M14 from *Mastin et al.* (2014). b) GSD_M16 from *Mastin et al.* (2016), with example of normal (N) and fine-skewed (FS) aggregate distributions. c) Bimodal TGSD of the Mazama ash >130 km from source reconstructed in Chapter 5 (Dataset D) compared to the aggregated GSD_B21 with 100% of material <125 µm aggregated. d) Unimodal TGSD of the Mazama ash >400 km from source reconstructed in Chapter 5 (Dataset E) compared to the aggregated GSD_B21 with 100% of material <125 µm aggregated.

Table 6.1: Model parameters used for all simulations after resolving the best-fit wind profile.

Parameter	Value(s)
Eruption start time[a]	2010 11 06 11:36 UTC
Duration	24 hours
Erupted volume	40 km^3
Height of the top of umbrella cloud (H_u)	15-40 km
Model domain	90 to 135°W longitude
	32.5 to 77.5°N latitude
Model resolution	0.5° horizontally
	2 km vertically
GSD	*Multiple* (see Fig. 6.5)
Diffusion constant (K)	0 and 1000 m^2s^{-1}
Umbrella spreading regime	*Multiple* (see Fig. 6.3)
Deposit density (ρ_d)	700 and 1000 kgm^{-3}
k_e	0.1
N	0.02 s^{-1}
C	0.87 x 10^3 $m^3kg^{-3/4}s^{-3/2}$
λ	0.2

(a) Refers to the best-fit wind profile determined using reanalysis data.

individual fall units or eruptive phases (*Young*, 1990; *Bacon and Lanphere*, 2006). The inferred duration of 24 hours and erupted volume of 40 km^3 DRE gives a mass eruptions rate of 1.46 x10^8 kgs^{-1} which is within the range inferred and reconstructed for other large eruptions ~ 10^8 – 10^{10} kgs^{-1} (e.g., Novarupta, 1912, *Fierstein and Nathenson* 1992; Pinatubo, 1991; *Koyaguchi and Ohno* 2001; Tambora, 1815, *Kandlbauer and Sparks* 2014). We note that this is not an estimate of the real mass eruption rate because we are using only the mass contained in the distal deposit rather than the total erupted mass.

In Ash3D simulations, the plume height used as model input is the top of the umbrella cloud rather than the top of the overshooting plume, under the assumption that the overshooting plume collapses gravitationally into the umbrella rather than being advected laterally with the ambient winds. Most of our simulations use an umbrella-top height of 30 km, but we experimented with values between 15 and 40 km asl based on the range of plume heights inferred for the 1991 eruption of Pinatubo (25-45 km; *Pyle* 2000; *Koyaguchi and Ohno* 2001; *Bonadonna and Costa* 2013). We try the lower value of 15 km asl to test the impact of strong stratospheric winds above the tropopause on the dispersion. Plume heights ~30-40 km were also resolved by inversion modelling of the proximal Mazama deposits using Tephra2 (Appendix E.2; *Suzuki* 1983; *Armienti et al.* 1988; *Bonadonna et al.* 2005a; *Connor and Connor* 2006; *Biass* 2018). *Young* (1990) estimated the plume height from isopleths using the *Carey and Sparks* (1986) model. This approach indicates plume heights >55 km above sea level which we suggest are implausible and exemplify the limitations of the *Carey and Sparks* (1986) model for large magnitude eruptions.

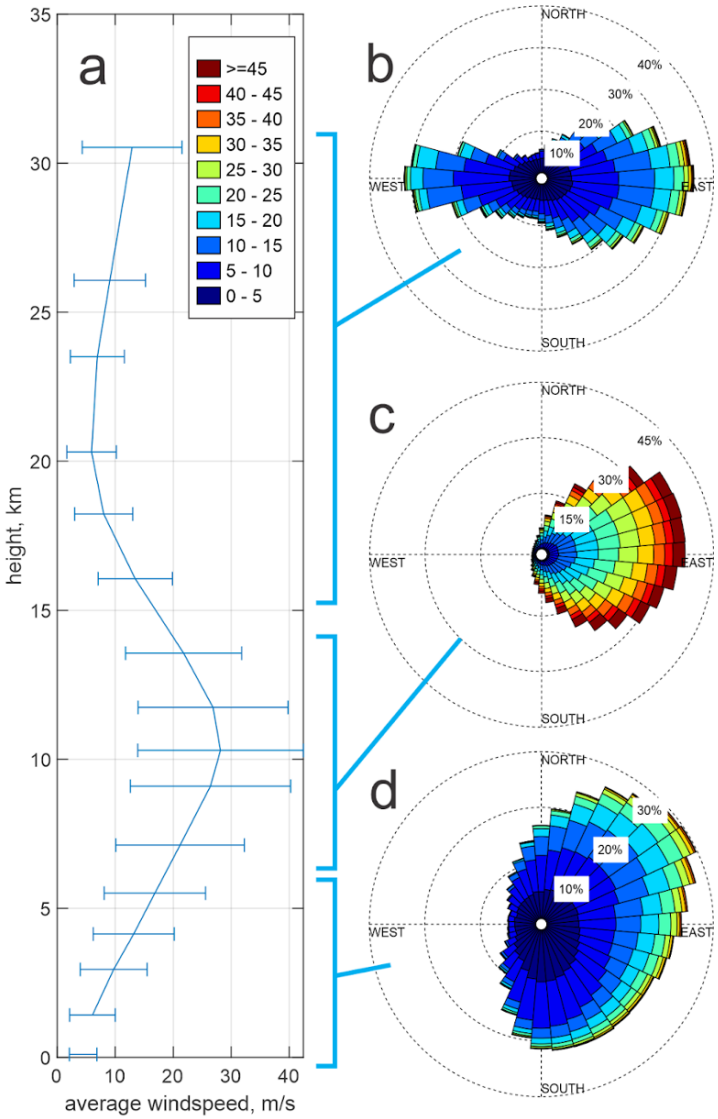

Figure 6.6: Reanalysis wind data for Crater Lake. (a) wind speed versus elevation above sea level at Crater Lake based on NCEP Reanalysis 1 data for 1990-2010. Pie segments depict the direction toward which the wind is blowing. Error bars are plus and minus one standard deviation. (b)-(d) wind rose plots for the elevation ranges indicated, based on the same dataset.

6.3.2 Meteorological data and model parameters

The meteorological data used for the simulations is from the NOAA NCEP/NCAR Reanalysis 1 (RE1) model (*Kalnay et al.*, 1996), a global meteorological model extending from 1948 to the present, with a horizontal resolution of 2.5 degrees latitude/longitude, temporal resolution of 6 hours, and 17 pressure levels from 1000 (sea level) to 10 millibars (~30 km asl). Ash3D uses wind vectors, geopotential height and temperature from these models to calculate advection and fall velocities. At elevations above ~30 km, Ash3D uses the wind vectors in the highest RE1 model node, and extrapolates pressure and temperature from the highest trends. Average wind data for Mount Mazama (Crater Lake) over the period from 1990-2010 are shown in Figure 6.6. Although winds below 5 km elevation are slow and variable in direction, at 6-14 km they are dominantly towards the East and are fastest, 28±16 ms^{-1} around the tropopause at 10-11 km (Fig. 6.6a). At higher elevation, velocities decrease and directions become bimodal, toward both the east and west (Fig. 6.6b).

Using the ESPs listed in Table 6.1 (with H_u=30 km, GSD_M16_N, umbrella spreading according to *Costa et al.* (2013) and K=0), we ran the Ash3D simulation 800 times with different wind profiles and output the tephra thicknesses at each sampling site (Fig. 6.7). Calculating the Root Mean Squares Error (RMSE) for each run using Eq.6.6 helped quantify the agreement between the model and observations for different wind fields:

$$RMSE = \sqrt{\frac{\sum_{i=1}^{n}(t_{o_i} - t_{m_i})^2}{n}}, \tag{6.6}$$

where $t_{o,i}$ is the thickness observed at each sample location i and $t_{m,i}$ is the modelled thickness at the same sample location i. We found, however, visual comparison of the location of the model isopachs against the measured thickness at the sample locations allowed for easier qualitative comparison (Fig. 6.7), for example of the direction and curvature of the dispersal axis, the deposit width, and downwind thickness decay. The simulation with a start time of 06 November 2010, 1135 UTC (Table 6.1), was chosen based on its good agreement in the direction of the dispersal axis and on thinning rate with distance. A comparison of this run with three others, randomly chosen from the 800, is shown in Figure 6.7.

The diffusion constant used in Ash3D (K in Eq. 6.5) accounts for complex and competing atmospheric processes, meaning that the value of K cannot be directly related to a single physical process. Ash3D calculates turbulent diffusion using an implicit Crank-Nicolson method (*Schwaiger et al.*, 2012). When diffusivity is set to zero, Ash3D simulations run about three times faster and produce realistic-looking results. Thus diffusivity is set to zero in operational simulations (at https://vsc-ash.wr.usgs.gov) when speed is important. But in systematic comparisons, diffusion-free simulations produce deposits that are slightly narrower than mapped ones, and underestimate thickness in distal areas, even when adjusted for finer grain sizes (e.g., *Mastin et al.* 2016; *Mastin and Van Eaton* 2020). We run the Mazama simulations using different values

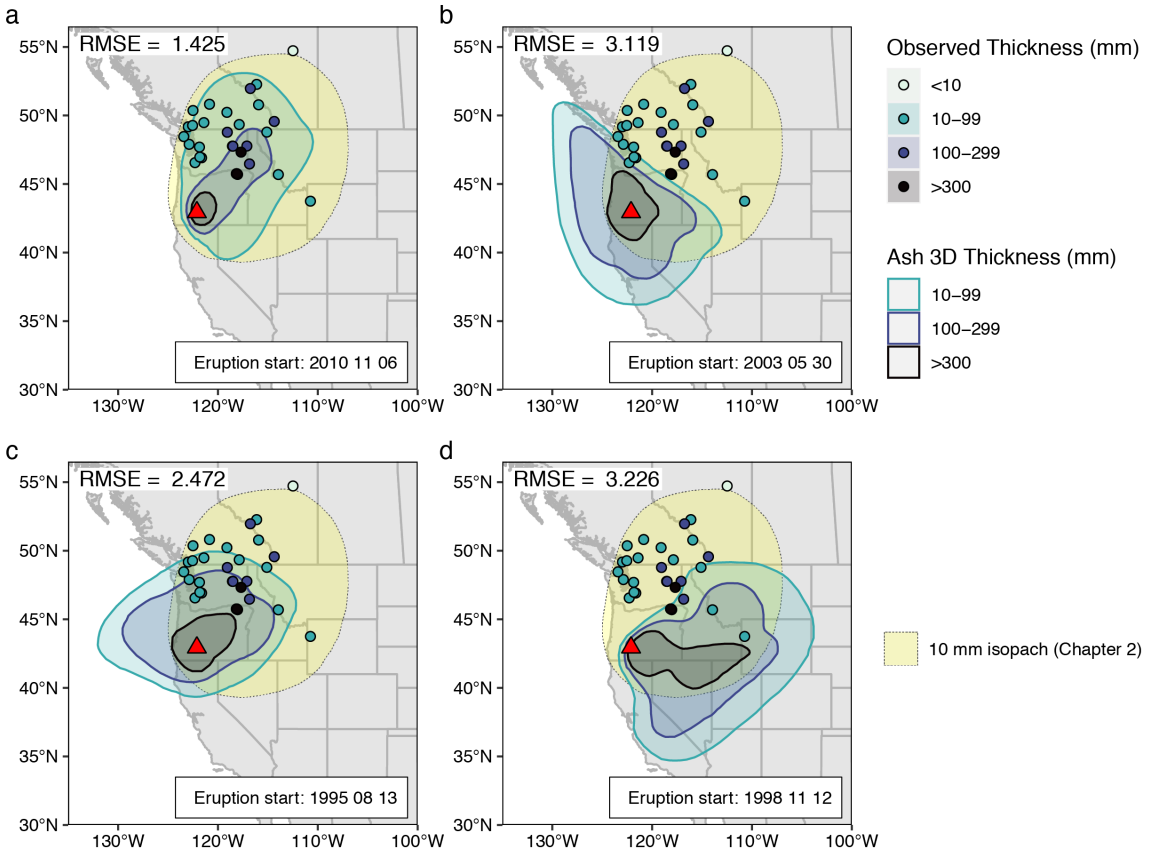

Figure 6.7: Sensitivity of Ash3D simulations to meteorological data. Maps of the simulated deposit (filled contours) compared to the observed thickness recorded (filled circles). The yellow filled contour indicates the overall direction of the deposit according to the compilation of localities in Chapter 2. The RMSE values have been calculated according to Eq. 6.6, where lower values indicates a better fit. The eruption start date is in the format YYYY MM DD and refers to the NCEP Reanalysis profile used for the simulation.

of K to account for the fact that K reflects multiple physical processes, such as entrainment into the plume, and that these processes are likely spatially varied and complex for large eruptions (Table 6.1).

6.4 Results

We ran 46 simulations of the climactic Mazama eruption using the best-fit wind profile to explore the sensitivity of Ash3D to five critical parameters: the diffusivity constant (K; Fig. 6.8), the deposit density (ρ_d, Fig. 6.9), the umbrella cloud spreading regime (Fig. 6.10), the height of the eruption column (H_u; Fig. 6.11) and the GSD (Fig. 6.12). The default model parameters are reported in Table 6.1 and the run specific inputs used in benchmark simulations are listed in

Table 6.2: Significant Ash3D simulations for model sensitivity testing.

	Height of umbrella cloud (H_u, km)	Umbrella spreading regime	GSD	Diffusion (m^2s^{-1})	Deposit density (kgm^{-3})	Figure
Run001	30	*Costa et al.* (2013)	GSD_M16_N	0	1000	6.8
Run004	30	*Costa et al.* (2013)	GSD_M16_N	1000	1000	6.8-6.14
Run057	30	*Costa et al.* (2013)	GSD_M16_N	1000	700	6.9
Run007	40[a]	None	GSD_M16_N	1000	1000	6.10
Run008	30	*Webster et al.* (2020)	GSD_M16_N	1000	1000	6.10
Run020	25	*Costa et al.* (2013)	GSD_M16_FS	1000	1000	6.11
Run021	15	*Costa et al.* (2013)	GSD_M16_FS	1000	1000	6.11
Run005	30	*Costa et al.* (2013)	GSD_M14	1000	1000	6.12-6.14
Run006	30	*Costa et al.* (2013)	GSD_M16_FS	1000	1000	6.12-6.14
Run054	30	*Costa et al.* (2013)	GSD_B21_B	1000	1000	6.12-6.14
Run014	30	*Costa et al.* (2013)	GSD_B21_U	1000	1000	6.12-6.14

(a) With no umbrella spreading this height is the top of the plume (H_T)

Table 6.2. A full inventory of the simulations can be found in Appendix E.3. Here we describe the impact of changing the individual input parameters (section 6.4.1) and comment on the ability of the model to replicate the deposit thickness and GSD at specific localities (section 6.4.2.).

6.4.1 Sensitivity to model inputs

To visualise the Ash3D outputs in this section, we plot a map of primary Mazama tephra localities (see Chapter 2) with an opaque isopach map of the simulated deposit (Figs. 6.8a-6.12a). The colour of each locality indicates the observed thickness and the same colour scheme is used for the shaded isopachs of the simulated deposit. In Figures 6.8-6.11, we also plot the square root of the isopach area against the isopach thickness and fit an exponential function to the data (*Pyle*, 1989). We refer to these as "Pyle plots" in the figure captions for brevity.

Increasing the diffusivity constant (K) from 0 to 1000 m^2s^{-1} increases the area enclosed by the thinnest isopach (Fig. 6.8). This supports what has been observed in simulations of other eruptions, where higher K increases off-axis spreading (*Schwaiger et al.*, 2012; *Mastin et al.*, 2016). Based on the expected width of the Mazama isopachs (see Fig. 2.9, Chapter 2), we use K=1000 m^2s^{-1} for most of the Ash3D simulations (see Table 6.2 and Appendix E.3).

Ash3D calculates the mass accumulation of tephra across the model domain which is then converted into deposit thickness using a fixed deposit density (ρ_d). We reduced ρ_d from 1000 to 700 kgm^{-3} to equal the ρ_d measured from distal Mazama tephra deposits (*Lidstrom*, 1971; *Bacon*, 1983; *Young*, 1990, Chapter 2) which extends the area enclosed by the thinnest isopach (1

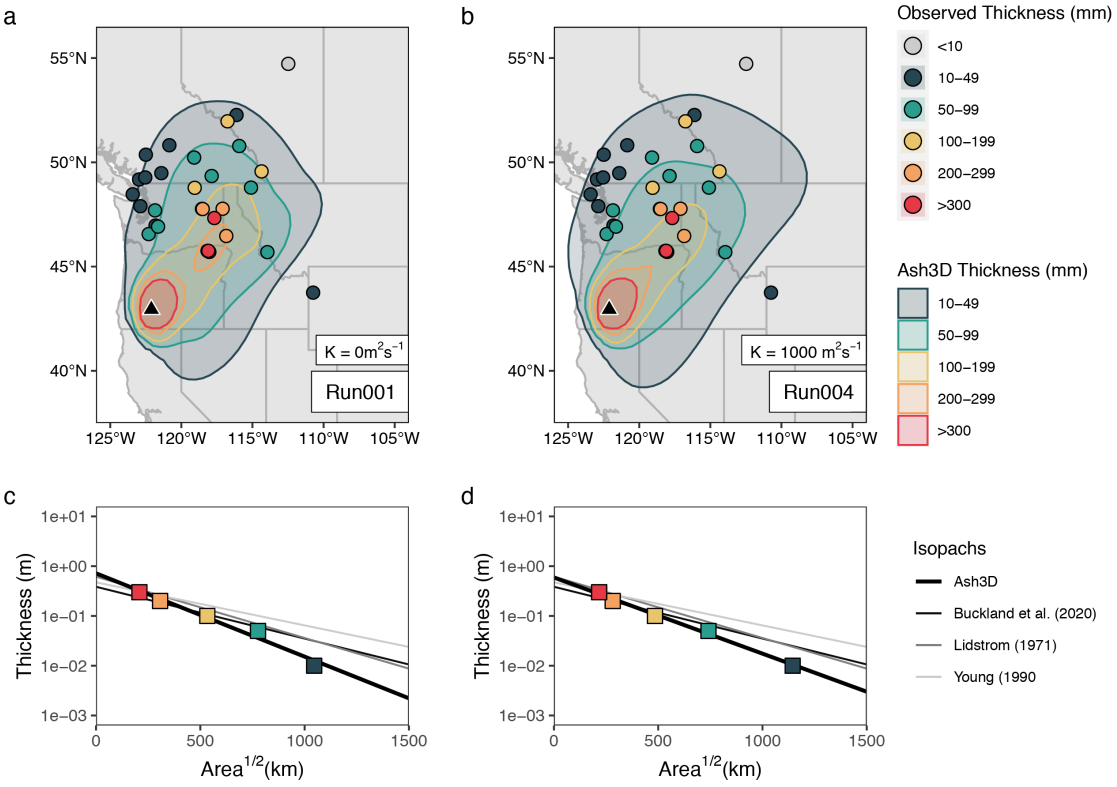

Figure 6.8: Ash3D sensitivity to diffusion constant. Maps of the simulated tephra fall from an eruption of Mount Mazama using a diffusion coefficient (K) of a) 0 m^2s^{-1} and b) 1000 m^2s^{-1}. The coloured points correspond to primary thickness data measured at the localities collated in Chapter 2 and Appendix A.1. The colour of the filled circles and shaded isopachs correspond to intervals of ash thickness in mm. c & d) Square root isopach area versus thickness plots showing data for the 300, 200, 100, 50 and 10 mm isopachs fitted with an exponential function (*Pyle*, 1989; *Daggitt et al.*, 2014). Also plotted are the exponential functions fit to the data for the isopachs reported in Chapter 2 and Figure 2.1 (*Lidstrom*, 1971; *Young*, 1990). These plots will be referred to as "Pyle plots" in the subsequent figure captions.

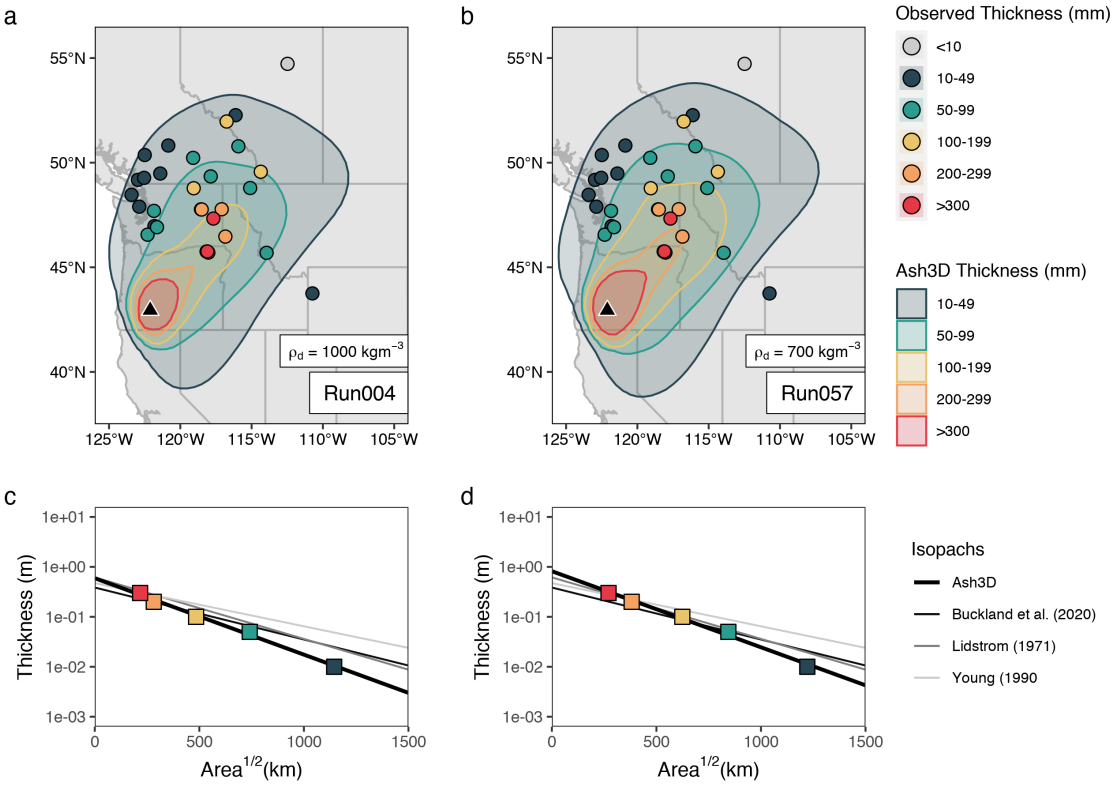

Figure 6.9: Ash3D sensitivity to deposit density. Maps of the simulated tephra fall from an eruption of Mount Mazama using a deposit density (ρ_d) of a) 1000 kgm^{-3} and b) 700 kgm^{-3}. c & d) Related Pyle plots for panels a & b. The colours and symbology are the same as Figure 6.8.

cm; Fig. 6.9). Furthermore, the exponential thinning trend in Figure 6.9d more closely matches that predicted by the isopachs constructed in Chapter 2 (Fig. 2.8).

The Mazama simulations are sensitive to the umbrella spreading regime used in Ash3D (Fig. 6.10). Running the simulations with no radial umbrella winds produces an elongated deposit (Fig. 6.10a). There is minimal off-axis spreading and the ash has been dispersed purely by advection diffusion coupled to the meteorological winds. Wider isopachs are produced when umbrella winds are added to the ambient wind field and the amount of off-axis spreading depends on the formulation used to calculate the radial wind speeds (Eq. 6.4; Fig. 6.10b and Eq. 6.3; Fig. 6.10c).

The height of the umbrella cloud also influences the Ash3D simulations (H_u; Fig. 6.11). Reducing the umbrella-top height from 30 km asl increases the proximal deposition and less ash reaches the localities in British Columbia, especially when H_u=15 km asl (Fig. 6.11c).

The GSD used significantly impacts the Ash3D simulations (Fig. 6.12). For example, simulations using GSD_M14 (the coarsest GSD from *Mastin et al.* 2014, Fig. 6.5a) produce the smallest area

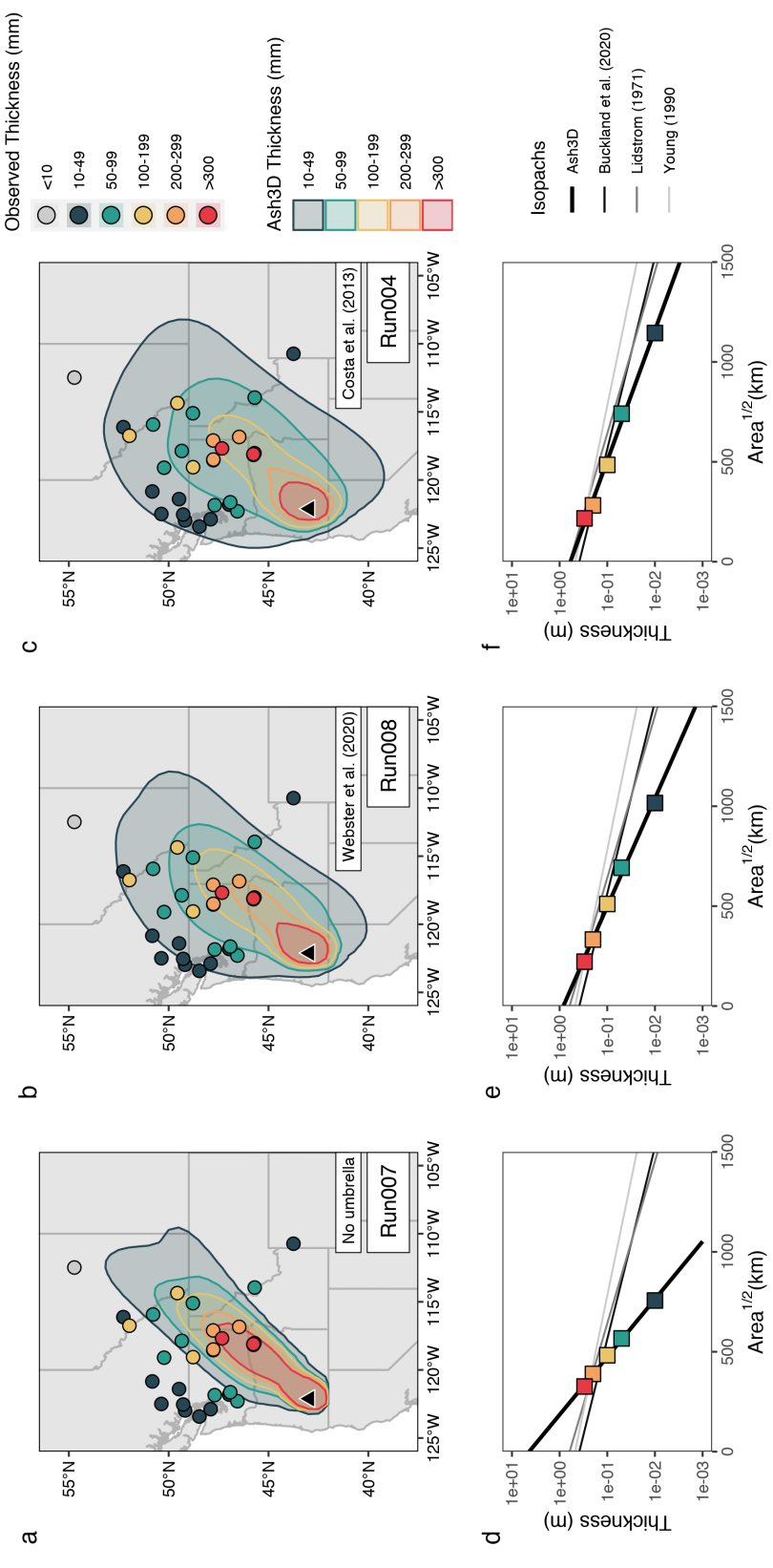

Figure 6.10: Ash3D sensitivity to radial umbrella spreading. Maps of the simulated tephra fall from an eruption of Mount Mazama using different umbrella spreading schemes a) no umbrella spreading, b) radial spreading using formulation from Webster et al. (2020) and c) radial spreading using formulation from Costa et al. (2013). d-f) Related Pyle plots for panels a-c. The colours and symbology are the same as Figure 6.8.

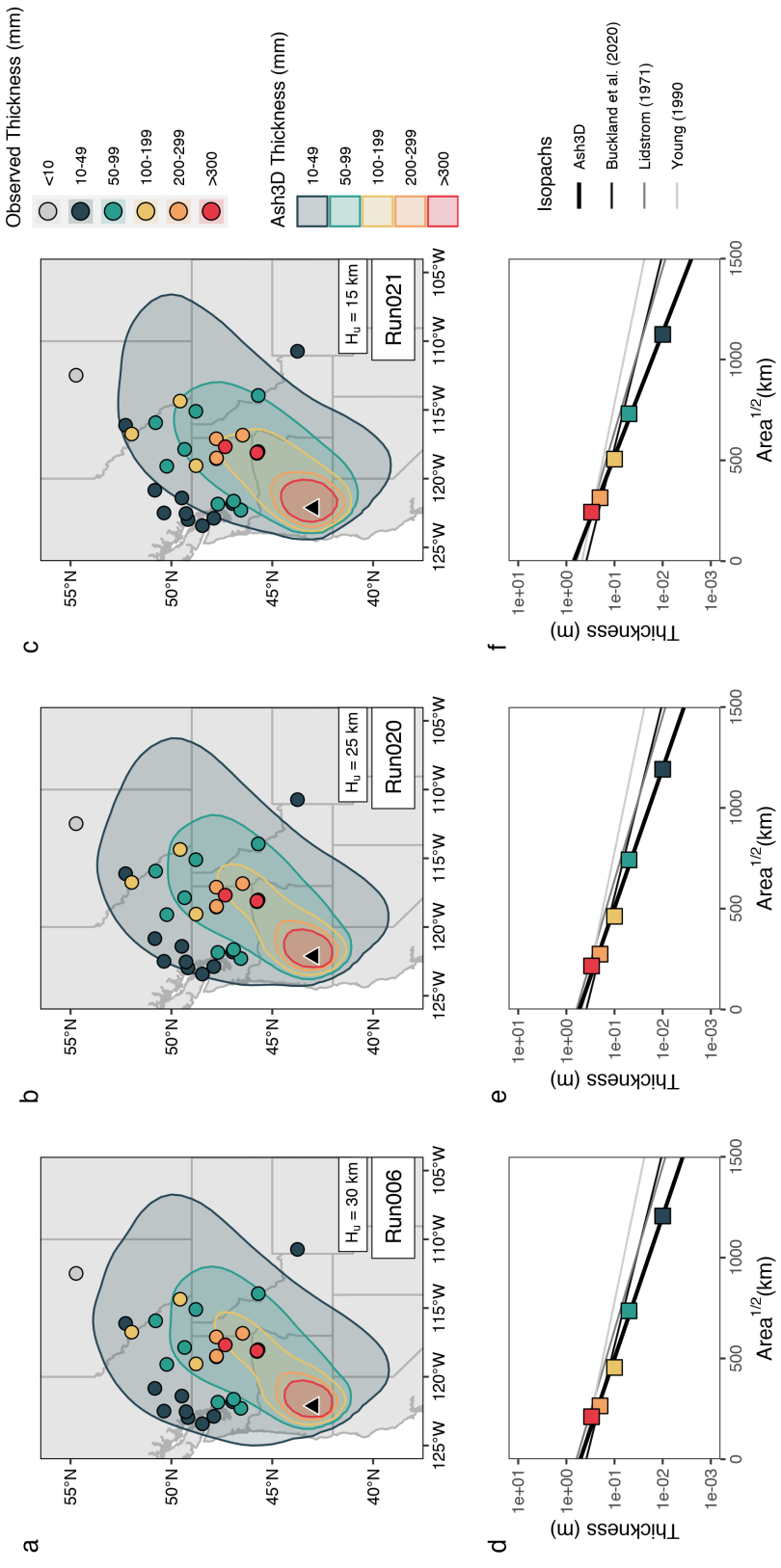

Figure 6.11: Ash3D sensitivity to plume height. Maps of the simulated tephra fall from an eruption of Mount Mazama using a plume height of a) 30 km, b) 25 km and c) 15 km. d-f) Related Pyle plots for panels a-c. The colours and symbology are the same as Figure 6.8.

of deposition because the GSD lacks fine particles or low density aggregates (Figs. 6.5a & 6.12a). Using GSD_M16 (Fig. 6.5b) increases the area enclosed by the 10 mm isopach (Figs. 6.12b & c) and the isopach area is largest when the fine-skewed aggregate size distribution is used (Figs. 6.5b & 6.12). Simulations using GSD_B21_B (Fig. 6.5c) produce similar 10 mm isopachs to runs using GSD_M16_N, but the 200 mm isopach (orange) extends further out to the NE of the vent (Fig. 6.12d). However, sites where the observed thickness >200 mm (red and orange filled circles) still lie outside of the simulated 200 mm isopach. GSD_B21_U is a strongly unimodal distribution (especially when aggregated) and is therefore effectively modelling the fallout of a single size class and Figure 6.12e shows that the size class does not deposit close to the vent. Interestingly, we see that the distance from source of the thickness maximum when simulating the deposition of GSD_B21_U corresponds to sites where the observed distal thicknesses >200 mm (Fig. 6.12e).

6.4.2 Comparing Ash3D outputs to the Mazama tephra deposit

Here we compare the thickness of the modelled deposit at localities where we have corresponding field measurements (see Chapters 2, Fig. 2.2). To visualise the differences, we plot the modelled and observed thickness at 30 localities on log-log plots. This ensures that differences in the thickness of distal, thinner deposits are evident (Fig. 6.13). However, we also include the equivalent plot using linear axes (Fig. 6.13), which helps visualise the differences in thicker, more proximal deposits as well as the differences between different simulations. For each run we also calculate the RMSE according to Eq.6.6.

Simulations that use the GSDs reconstructed from field data (Chapter 5) best replicate the thickness of deposits along the main dispersal axis as indicated by the lower fit values (Figs. 6.13 & 6.14). For example, at Site 73 we measured 30 cm of primary Mazama tephra (see Chapter 2, section. 2.4.1). Using GSD_B21_U, Ash3D forecasts 26-37 cm of ash deposition at Site 73 depending on the deposit density (ρ_d) used (Fig. 6.13e & 6.14e). In contrast, all the simulations using GSD_M14 and GSD_M16 predict <30 cm at Site 73 irrespective of the ρ_d.

Ash3D outputs the GSD at specified locations which we compare to the GSD measured at that locality (Fig. 6.15). Excluding the simulations using GSD_B21_U, all simulations predict coarser particles reaching further from source than observed in the field deposits. For example, using DIA and laser diffraction we know that at site 73 particles >250 µm account for < 1 % of the sample volume (Figs. 2.5, 3.4 & 4.7a). However, simulations using GSD_M14, GSD_M16 and GSD_B21_B predict that particles >250 µm are being deposited at that distance from source.

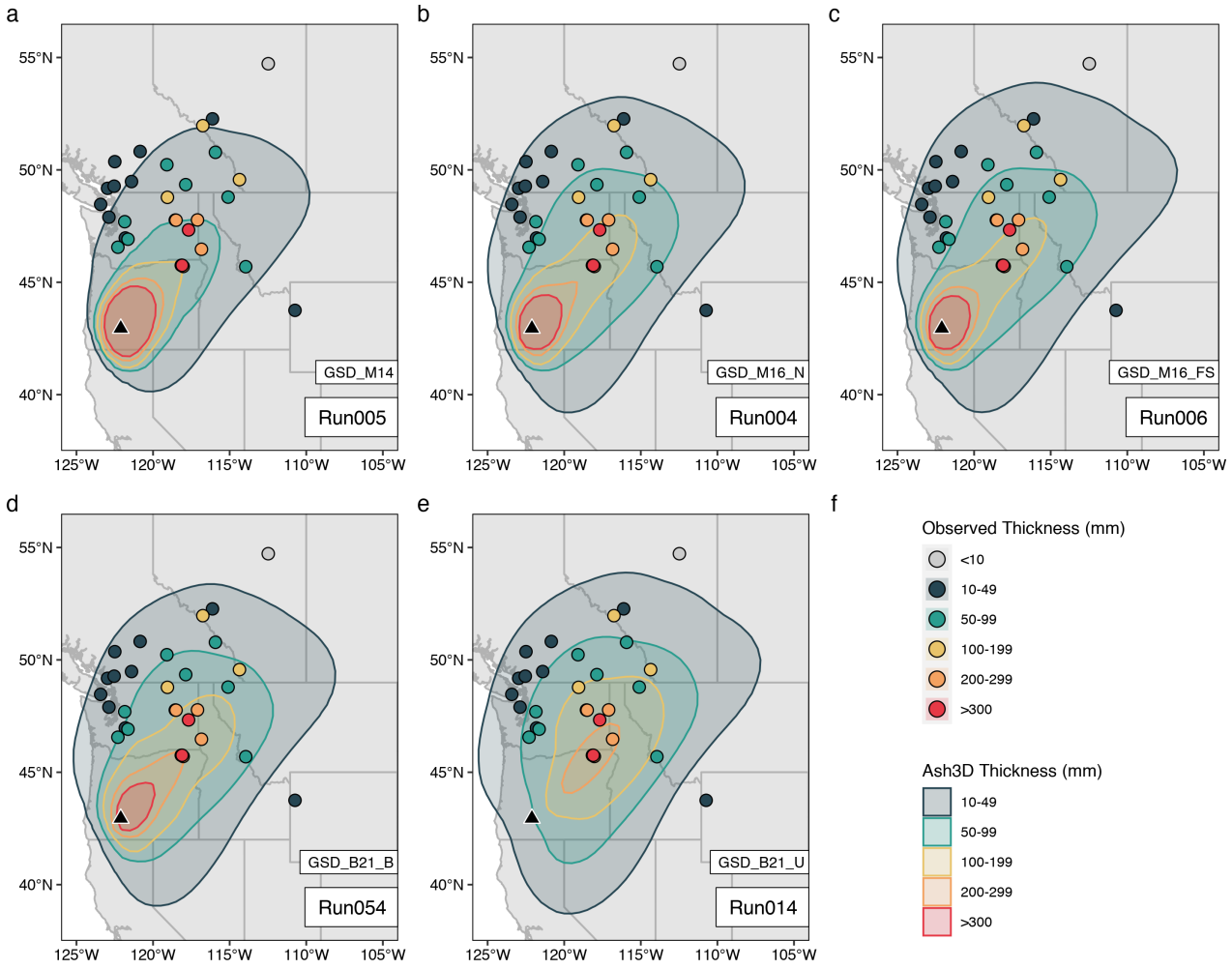

Figure 6.12: Ash3D sensitivity to the Grain Size Distribution. Maps of the simulated tephra fall from an eruption of Mount Mazama using a) GSD_M14 (Fig. 6.5a; *Mastin et al.* 2014), b) GSD_M16_N (Fig. 6.5b) and c) GSD_M16_FS from *Mastin et al.* (2016; Fig. 6.5b), d) GSD_B21_B (bimodal; Fig. 6.5c) and e) GSD_B21_U (unimodal; Fig. 6.5d) are TGSDs from field deposits of Mazama tephra reconstructed in Chapter 5 (see Fig. 5.4). The colours and symbology are the same as Figure 6.8.

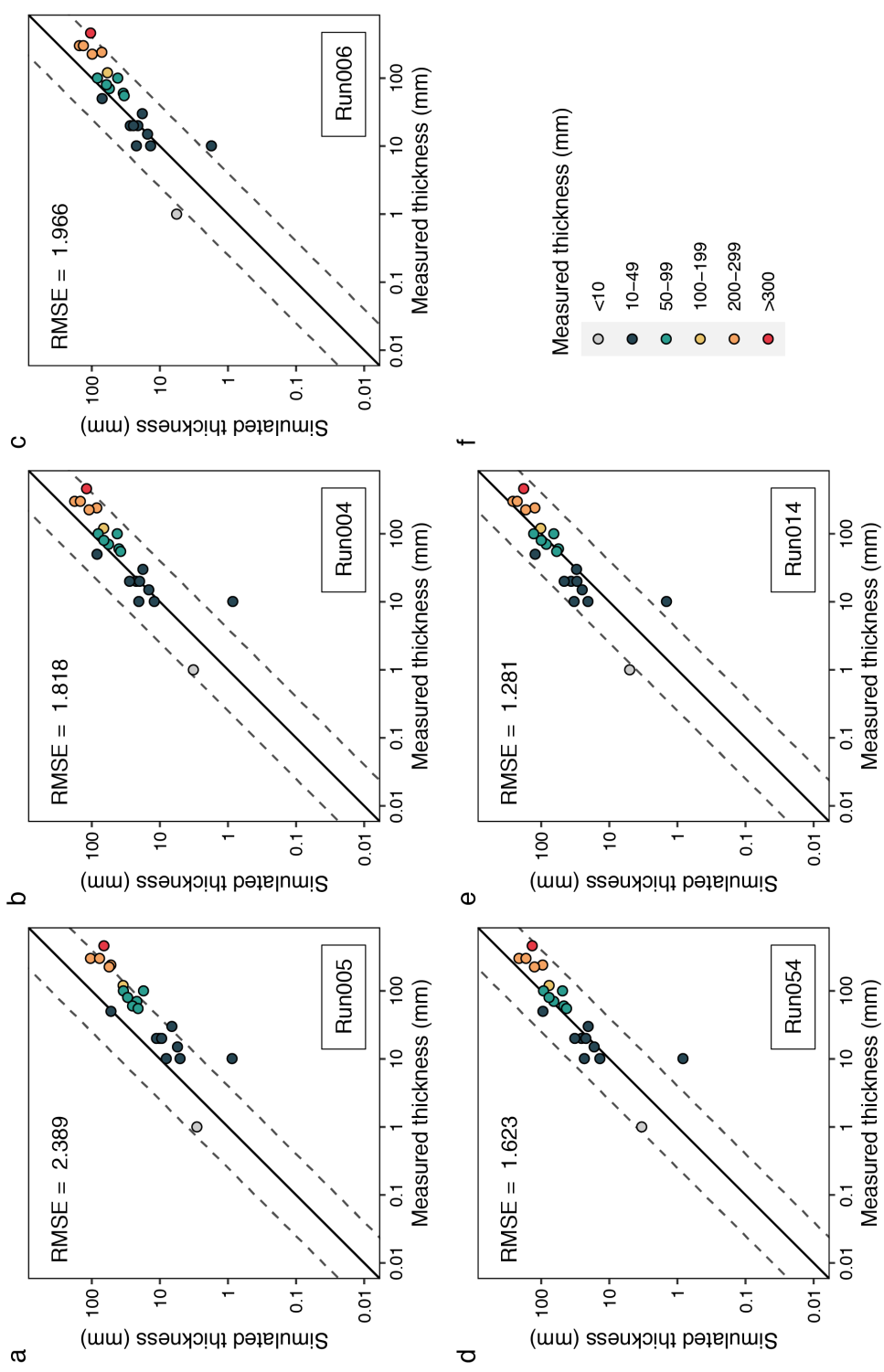

Figure 6.13: Measured versus simulated thicknesses for different GSD simulations on log scale. Upper and lower dashed lines show values of 4 (over-estimation) and 0.25 (underestimation) times the 1:1 ratio of measured to simulated (solid line). RMSE calculated using Eq. 6.6.

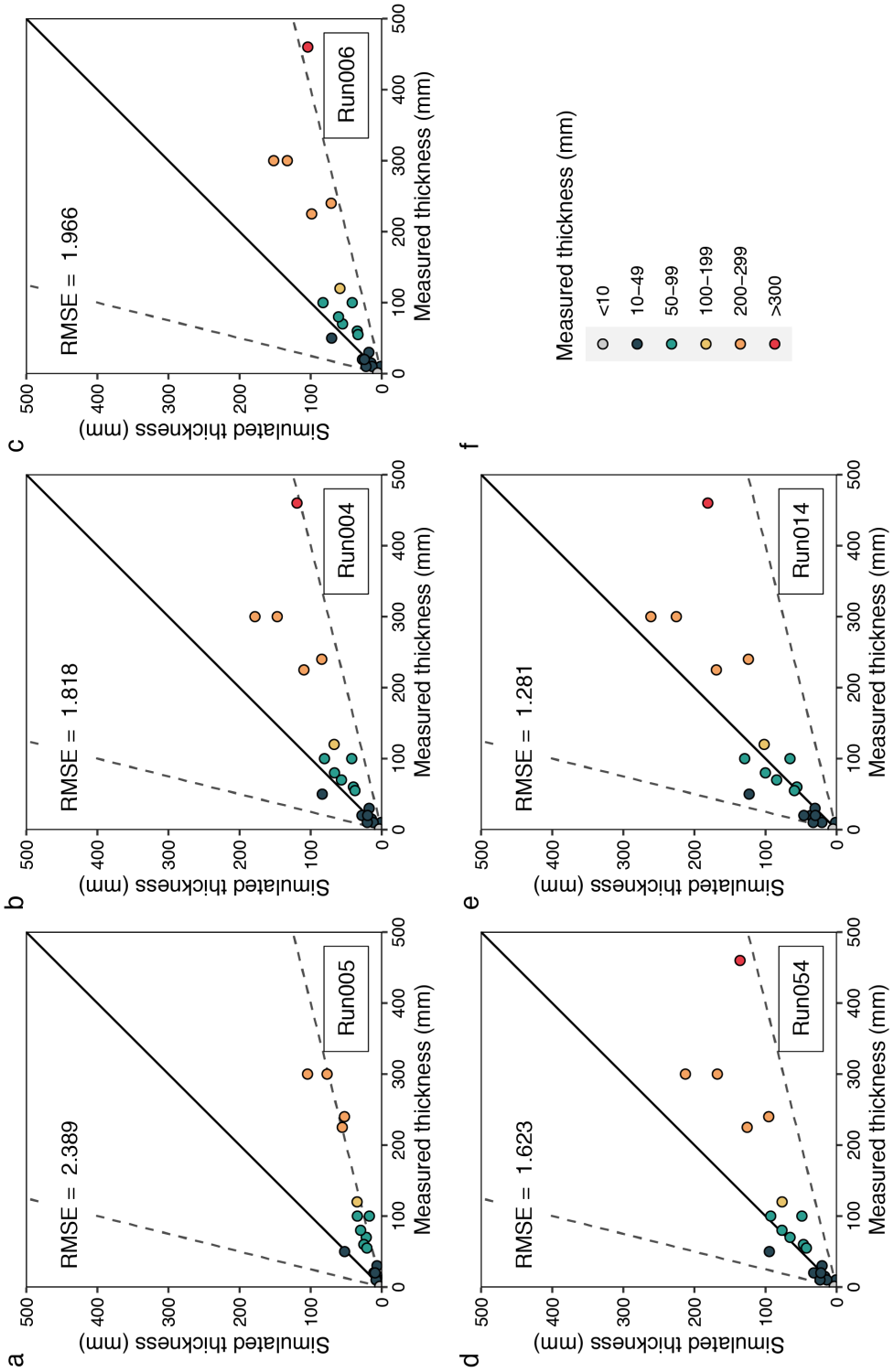

Figure 6.14: Measured versus simulated thicknesses for different GSD simulations. RMSE calculated using Eq. 6.6. Equivalent linear plot of Figure 12.

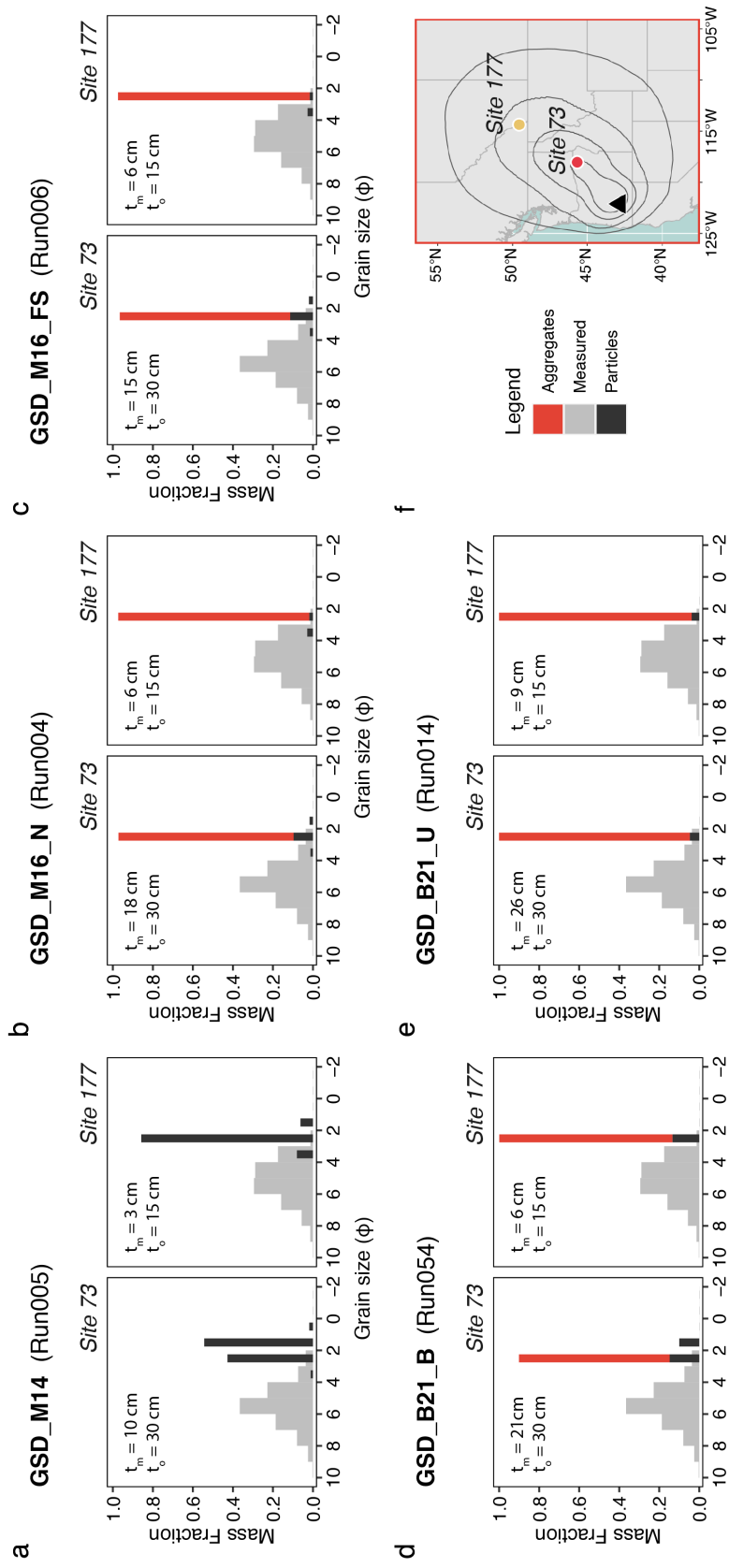

Figure 6.15: Measured versus Ash3D GSDs for different simulations. Two sites analysed 73 and 133. to is the observed thickness and tm is the modelled thickness at that site.

6.5 Discussion

Here we summarise the accuracy of the Ash3D simulations of the ~7.7 ka Mazama tephra deposit. We also consider potential reasons that the model is unable to reproduce all the features of the deposit and discuss the implications for using VATDMs to simulate large magnitude eruptions.

6.5.1 Comparing the Ash3D simulations with the Mazama deposit

Using appropriate meteorological reanalysis data is crucial for reproducing the overall dispersal direction of the tephra towards the northeast of Crater Lake (Fig. 6.7). Another key factor in replicating the Mazama deposit is to simulate umbrella spreading (Fig. 6.10) and increase the diffusion coefficient (Fig. 6.8) as both produce wide isopachs with significant off-axis spreading which is what is observed in the field (Figs. 2.1 & 2.9).

The simulated thicknesses are within 4 and 0.25 times the observed thickness at 35 of the 36 primary localities for all the simulations using the best-fit wind profile, excluding those that use GSD_M14 (Figs. 6.13-6.14). This suggests that the Ash3D simulations are reproducing the Mazama deposit reasonably well. For example, we know from lake core records that at Lofty Lake, in Alberta, Canada, >1500 km from source (site 291 in Table A.1, Appendix A.1) at least 0.1 cm was deposited at this locality (*Lichti-Federovich*, 1970; *Lidstrom*, 1971; *Young*, 1990). This is a conservative estimate given the occurrence of thick (>10 cm) remobilised Mazama deposits in nearby Edmonton, Alberta (*B. Jensen*, pers. commun.). The Ash3D simulations using GSD_B21_U (e.g., Run014; Fig. 6.12e) predict >0.5 cm of tephra at Lofty Lake which appears closer to the real thickness deposited at that location.

The primary locality where the simulated thickness is consistently underestimated by Ash3D compared to the field data, is Jenny Lake, Wyoming, USA (site 42 in Table A.1, Appendix A.1). Lake core records suggest ~1 cm of primary Mazama tephra was deposited at Jenny Lake (*Larsen et al.*, 2016), whereas a maximum 0.2 cm was estimated by the Ash3D simulations. One explanation for the poor fit at Jenny Lake is the uncertainty that arises from using modern reanalysis meteorological data for a prehistoric eruption. For instance, we know from the proximal deposits of the lower pumice (*Young* 1990, Figs. 2.6c & 3.2) that during the earlier stages of the Mazama eruption the deposit was dispersed more directly towards the east and southeast. We have not simulated this changing wind direction and is one potential explanation for the underestimation of thickness at Jenny Lake. This does suggest a shortcoming of the Ash3D simulations, however, matching a single distal point should not detract from the overall success of simulating the main dispersal direction of the deposit.

The Ash3D simulations that use the GSDs based on field data produce the simulations with the lowest fit values which indicates the smallest divergence between the observed and modelled

thickness. For example, at Site 73, a distal locality visited for this project, we have a direct measurement of 30 cm of primary tephra (Chapter 2). Only the simulations that use the GSDs based on field data predict >21 cm of tephra at site 73 (Fig. 6.15). This is because the GSDs that are not based on field data over-represent the portion of the total erupted mass that is >250 μm (Fig. 6.5) which means more mass is deposited close to source and less mass is transported to the distal region (>130 km from source) and site 73.

Site 73 is a key locality for comparisons against the Ash3D simulations as it records the primary thickness and the GSD has been measured using laser diffraction (Fig. 2.5) and Dynamic Image Analysis (DIA, Fig. 4.7a). The discrepancy between the simulated and observed GSDs at site 73 (Fig. 6.15e) indicates that the Ash3D model is dispersing coarser grains further than is observed in the field. This could be caused by poor characterisation of the drag coefficient acting on the ash particles. For example, we assume that the 2D aspect ratio (b/l) measured using DIA (Table 4.2) is equivalent to the 3D shape factor from *Wilson and Huang* (1979). But, as with size parameters (Chapter 4, Fig. 4.11), converting from 2D to 3D can overstate the irregularity of the particles and result in higher drag coefficients and lower terminal velocities being calculated. Another explanation for coarse particles reaching further than observed, could be that the umbrella spreading regimes are overestimating the absolute velocity and the distance over which the umbrella winds influence ash dispersion. For instance, the *Costa et al.* (2013) spreading regime predicts a higher proportion of particles >250 μm at site 73 than the *Webster et al.* (2020) formulation because it models higher radial wind-speeds close to source (Fig. 6.3).

6.5.2 Considering the impact of VATDM simplifications

A significant simplification required to simulate the Mazama tephra deposit using Ash3D is that all ash <125 μm aggregates. This assumption is necessary because if the fine ash is not aggregated, the terminal velocity of the individual particles is so low that it cannot overcome the vertical component of atmospheric velocity (turbulence), and therefore, the ash <125 μm is not deposited within the model domain (see Appendix E.4). However, there is very little evidence of aggregation being the main driver for the sedimentation of the distal Mazama tephra. For example, there are no records of accretionary lapilli across the expansive deposit, no definitive evidence of secondary thickening in the deposits, and little to no fine ash is contained in the fall deposits close to source (<130 km; *Young* 1990). This suggests that in addition to aggregation by electrostatic forces (which won't be preserved in the tephra record), other mechanisms resulted in the deposition of the fine-grained distal tephra, such as convective instabilities.

For the Ash3D simulations, we treated the eruption as a single Plinian eruption to avoid uncertainty in the mass attributed to different phases of the eruption (Chapter 3). However, further insight could be gained by separately modelling the Plinian and co-PDC eruption phases. Co-PDC ash has a large source region and tends to be finer grained than that erupted during Plinian erup-

tions, meaning it can therefore be dispersed over large areas. However, substantial difficulties are associated with separating and modelling the two eruptive phases. For example, as determined in Chapter 3, there is no chemical variation in the Mazama Plinian and co-PDC products, which makes identifying the relative proportions in deposits from these phases effectively impossible. Additionally, source conditions and plume rise processes for Plinian plumes are considerably different to those from co-PDC plumes, which can loft from the top of entire PDCs resulting in significant mass flow rates (*Baines and Sparks*, 2005; *Engwell and Eychenne*, 2016).

6.6 Conclusions

Using the Ash3D dispersion model, we simulated the ash disperal following the climactic eruption of Mount Mazama using reanalysis meteorological data. We conclude that, first, that using appropriate wind data is crucial to dispersing the Mazama tephra towards the east and northeast of the vent. Secondly, it is necessary to increase the horizontal diffusion coefficient used by Ash3D and simulate radial winds associated with an umbrella cloud (*Costa et al.*, 2013; *Mastin et al.*, 2014; *Webster et al.*, 2020) to reproduce the off-axis spreading of the tephra deposit. Third, discrepancies between the absolute simulated and observed thicknesses were minimised using GSDs based on the stable distal GSD of the Mazama tephra, however, this still incorporates a significant assumption of particles aggregation <125 μm for which there is little evidence in the field deposits. Finally, the assumption of a single eruptive phase has likely reduced the accuracy of simulations of the Mazama eruption as it is likely a proportion of the distal deposit was from a co-PDC source.

Future work to improve the accuracy of VATDMs for simulating the ash dispersion from large magnitude eruptions should include additional testing of the equations used to simulate the radial spreading of the umbrella cloud region. Our results conclusively showed that it is necessary to include the computation of the horizontal winds within the umbrella region, however, which of the two spreading regimes is the most appropriate, remains unclear (*Costa et al.*, 2013; *Webster et al.*, 2020). Another direction of research required to improve VATDMs is to better understand how fine-ash (<125 μm) is deposited. Currently, the simulated aggregation of fines in Ash3D runs simplifies the computational complexities of modelling wet and dry aggregation or convective instabilities. However, future advancements in understanding the physics of how fine particles are deposited may coincide with increased computational capacity meaning these physical processes will be integrated into VATDMs which will improve forecasts of ash transport and deposition for eruptions of any scale.

CHAPTER 7

CONCLUSIONS AND FUTURE WORK

7.1 Summary

Here I return to the motivating themes of this thesis and discuss how each chapter has contributed to furthering our understanding of the processes that form, transport and deposit ash during large magnitude eruptions. I also examine the new insights gained into the ~7.7 ka climactic Mazama eruption and propose future work that could expand on the outcomes of this thesis.

7.1.1 Sources of uncertainty from remobilised field deposits

Chapter 2 deals with the processes that have remobilised the climactic Mazama tephra deposit and how remobilisation can affect estimates of the total erupted volume. The insight I gained from observing remobilised Mazama tephra in the field (Fig. 2.3) allowed me to scrutinise tephra thickness data reported in the literature (Appendix A.1). Using the localities determined to likely record the primary tephra thickness (tephra that hadn't been remobilised) I produced new isopachs for the Mazama deposit (Fig. 2.6) and showed that including data from over-thickened deposits can introduce >10% error in erupted volume estimates (Fig. 2.8 & Table 2.2). This study shows the importance of recording remobilised tephra deposits and the limitations of constructing isopach maps and estimating the volume of large prehistoric eruptions.

Chapter 2 focuses on the impact of post-depositional processes on the thickness of the Mazama deposits. However, the Grain Size Distribution (GSD) and componentry of the remobilised Mazama deposits are seemingly not always impacted by remobilisation and can be equivalent to primary (non-remobilised) tephra at the same distance from source (Figs. 2.5, & 3.4). This

underscores the utility of studying remobilised tephra deposits as the GSD of remobilised deposits were then used in addition to primary GSDs, to reconstruct the TGSD of the distal deposit in Chapter 5.

7.1.2 Scrutinising methods and applications of grain size analysis in volcanology

A common theme throughout this thesis is the utility of grain size data from tephra deposits for understanding eruption and ash dispersal dynamics. In Chapter 2, I showed that grain size is a tephra property that can remain unchanged by remobilisation. In Chapter 3, the grain size of distal ash is used to infer the eruptive phase that produced large volumes of fine ash during the Mazama eruption (Fig. 3.4). In Chapters 4 and 5, I describe how the GSD of distal tephras stabilises (i.e., does not vary) over large distances from source (Fig. 4.10). And finally, I use the stable distal GSD of the Mazama tephra to inform the GSD input for running the VATDM Ash3D (Chapters 5 & 6) and explore the sensitivity of simulations to the input GSD when simulating tephra transport and deposition (Fig. 6.12).

Given the importance of characterising the grain size of tephra, Chapter 4 provides a thorough review of grain size methods and applications in volcanology (Appendix C.1). I focus on the Camsizer X2 (CX2) instrument and the Dynamic Image Analysis (DIA) measurement principle because these methods are currently less widely used compared to laser diffraction instruments and measurement principles, but can potentially provide more information on particle size and shape characteristics. I discuss the benefits of using image analysis methods to characterise particle size because of the capacity for simultaneous shape characterisation which is extremely valuable when analysing volcanic ash that has characteristically irregular shapes (Fig. 4.12). I also outline the benefits of measuring multiple size parameters using DIA which allows GSDs collected using different instruments to be compared and combined. For example, particle long axis ($x_{Fe}max$) is equivalent to the size parameter measured from cryptotephra shards using optical methods as well as the GSDs collected using laser diffraction using the Fraunhofer approximation (Fig. 4.7c). Similarly, equal area circle diameter (xarea) is the 2D equivalent of volume equivalent sphere diameter that is measured by laser diffraction using Mie scattering theory (Fig. 4.7a), and the minimum particle width ($x_c min$) closely approximates sieve diameter (Fig. 4.4). Very coarse to coarse (>4 mm) tephra samples are typically characterised by sieving in the field and laboratory, therefore, having a method such as DIA that can quantify size according to $x_c min$ is beneficial for easily combining the coarse GSD from sieve data with the fine GSD measured in the laboratory using DIA.

In this thesis, I also discuss the limitations of analysing the grain size of tephra. In Chapter 4, I explain how the heterogeneous nature of tephra (e.g., shape, componentry, density) can affect the methods used to quantify particle size. For example, the density of ash changes according to

the type of particle (glass, crystal, lithic) which can also vary with particle size independently. This means that methods that quantify size as mass or volume distributions cannot be easily combined or compared (Fig 4.8). Moreover, this emphasises that size alone cannot be used to infer the terminal settling velocity of ash particles, and in fact, a measurement of size, shape and density is required to accurately calculate the drag coefficient.

Interpretations of grain size data are also subject to uncertainty. For example in Chapter 5, reconstructing the TGSD of the climactic Mazama eruption is impeded by the uneven distribution of field samples caused by zones of poor tephra preservation (Fig. 5.2). Similarly, the distal Mazama ash cannot be attributed to a distinct eruptive phase (Chapter 3) meaning that any TGSD reconstructed using the distal Mazama tephra is likely the sum of multiple phases of activity which could relate to different fragmentation mechanisms.

7.1.3 Modelling tephra transport and deposition following a large magnitude explosive eruption

This thesis was motivated by a need to improve the accuracy of VATDMs for forecasting ash dispersion following or during the next large magnitude eruption. To work towards this goal I provide new estimates of key Eruption Source Parameters (ESPs) for the climactic Mazama eruption in Chapters 2-5 and use the ESPs to investigate the model sensitivity of Ash3D, a Eulerian VATDM (Chapter 6). I show that the erupted volume estimate of the Mazama eruption is sensitive to the isopachs used (Table 2.2) and uncertainty is also introduced when converting from the bulk erupted volume estimate to the Dense-Rock-Equivalent (DRE) volume. Importantly, the uncertainty in the Mazama ESPs, especially those related to field data, is relevant when estimating the ESPs for any large prehistoric eruption because of the challenges associated with representative sampling and deposit remobilisation and preservation.

Using the ~7.7 ka climactic Mazama eruption as a case study, the sensitivity testing of Ash3D (Chapter 6) shows the importance of the meteorological data, umbrella cloud spreading regime and GSD used to simulate the dispersal of ash from a large magnitude eruption. It also highlights the significant simplifications that are required to model large magnitude eruptions. For example, the deposition of fine-ash (<125 μm) is simulated by artificially aggregating all particles <125 μm into a low-density aggregate class (*Mastin et al.*, 2016) even though there is no evidence for aggregation in the distal Mazama deposits (Fig. 6.5). Similarly, because the distal ash cannot be attributed to a distinct eruptive phase (Chapter 3), the eruption was modelled as a single Plinian phase, ignoring the complexities of the real multi-phase eruption and co-PDC source conditions. However, the Ash3D model testing does provide strong evidence to support the integration of radial umbrella winds with advection-diffusion models (Fig. 6.9). Furthermore, the overall distribution of tephra is not sensitive to the absolute plume height when it is above the region of strong stratospheric winds (Fig. 6.7). This is encouraging because large uncertainties are

associated with estimates of plume height for eruptions that have not been observed using modern satellite remote or ground monitoring techniques (*Biass and Bonadonna*, 2011; *Burden et al.*, 2011).

7.1.4 New insight into the climactic eruption of Mount Mazama

This thesis produced new insight into the already well-studied climactic eruption of Mount Mazama. For example, in Chapter 2 I determine a new estimate of the total erupted volume of the Mazama eruption of 176 km^3 or 61 km^3 DRE. This is larger than the estimate cited in the LaMEVE database (50 km^3) because we have included the volume in the PDC deposits (see section 2.5.4) but is less than the estimate of the pre-eruptive edifice volume of 112 km^3 by *Bacon and Lanphere* (2006) (Table 2.1). The discrepancy between the DRE and pre-collapse edifice volume is likely explained by the thickness versus square root area plots (Fig. 2.8) underestimating the thickness of very proximal deposits (<10 km from source), and the DRE volume not accounting for the volume contained in the caldera collapse deposits.

Investigating the impact of tephra remobilisation on erupted volume estimates (Chapter 2) also provides insight into the secondary tephra hazards that occurred after the climactic Mazama eruption. For example, the rapid accumulation of >3 m of tephra in valleys (Fig. 2.3c) will have caused severe disruption to fluvial networks (*Major et al.*, 2000; *Pierson and Major*, 2014). Furthermore, the GSD of the distal Mazama tephra (Figs. 4.10b & 5.4) combined with the palaeovegetation cover (Fig. 2.10) will have meant that the Mazama deposit was resuspended by surface winds across large areas. These phenomena underline the importance of studying remobilised tephra deposits not only to determine uncertainty in field data, but also the long-lived hazards after an eruption.

In Chapter 3, I report new major element geochemical glass and FeTi oxide data for the main fall deposit and co-PDC units of the climactic Mazama eruption. Whilst the data can not provide a definitive geochemical signature for ash from the co-PDC phase, it does confirm the homogeneity of the Mount Mazama rhyodacite throughout the climactic eruption phases (*Bacon*, 1983; *Bacon and Druitt*, 1988) and provides a geochemical framework of the main eruption sequence (Fig. 3.6). Furthermore, I correlate the presence of high-Ti titanomagnetites in distal Mazama deposits (>500 km from source) to the Upper Pumice Unit (UPU) and co-PDC phases which can be distinguished in proximal sections (~130 km from source, Fig. 3.8).

7.2 Future work

There are numerous avenues of research that could continue to expand on the findings of this thesis. In particular, this work has prompted research questions relating to the eruptive phases

of the climactic Mazama eruption. Similarly, there is still a lot to understand about the processes that deposit fine-grained ash and what is controlling the stable GSD of distal deposits.

7.2.1 Still more to learn from and about the Mazama eruption

The major element glass geochemistry collected in Chapter 3, shows that the rhyodacite erupted during the Plinian and co-PDC phases of the Mazama eruption is extremely homogeneous. Future work measuring the minor and trace element geochemistry of the rhyodacitic glass would help determine if there are any more subtle changes in magma geochemistry that could be used to differentiate the eruptive phases in distal deposits. Moreover, if trace element data confirms the homogeneity of the climactic Mazama rhyodacite, this poses important questions relating to how >60 km^3 of well-mixed magma is produced and stored prior to a large magnitude eruption.

Componentry analyses carried out in Chapter 3, show that the Lower Pumice Unit (LPU) contains a large proportion of holocrystalline particles (Fig. 3.5). I hypothesise that the holocrystalline material is evidence of vent opening during the early phases of the eruption. In general, despite the overlap in rhyodacite geochemistry, the LPU appears distinct from the Upper Pumice Unit (UPU) with unique componentry and dispersal patterns (Fig. E.1). The differences between the LPU and UPU, in addition to the presence of a divider ash layer, could indicate a more prolonged period of repose between the Plinian phases (*Young*, 1990). This requires further investigation including more comprehensive componentry data and detailed mapping of the LPU and divider ash deposits <130 km from source. Ideally this will provide a more thorough understanding of the early stages of the Mazama eruption.

The field and geochemical data available for the climactic Mazama eruption is biased towards the fall deposits (proximal, *Young* 1990; and distal, Chapter 2). I suggest that future work focusing on the PDCs associated with the caldera collapse phase will be beneficial for improving the accuracy of total erupted volume estimates. Also, quantifying the volume of PDCs that has been removed by erosion will provide insight into post-eruptive hazards such as lahars. Understanding the processes that have mobilised Mazama material downstream will also have implications for studies that use the Mazama tephra found in offshore turbidite sequences to investigate the timing of Cascadia subduction zone earthquakes (*Goldfinger et al.*, 2012). Finally, by and large, new studies of the PDCs will increase the major element glass geochemical data available for correlation studies and GSDs from the PDCs could be incorporated into future reconstructions of the Mazama TGSD.

7.2.2 Additional scrutiny of the grain size data from tephra deposits

The utility of grain size data is evident in this thesis, however, some findings require further study. For example, in this thesis, I show that the GSD of tephra can remain unaltered by remobilisation.

However, studies of remobilised tephra from the Younger Toba Tuff (YTT) report that the GSD can be modified by remobilisation (*Gatti et al.*, 2013). This suggests that more work is required to understand fully how different mechanisms of remobilisation (e.g., hillslope, fluvial or aeolian processes) interact with the tephra deposit properties (e.g., GSD, sorting, thickness, compaction, depositional environment). This could include laboratory simulations of tephra remobilisation in addition to enhanced efforts to track tephra properties through time following modern eruptions (e.g., *Manville et al.*, 2000; *Pierson and Major*, 2014; *Cutler et al.*, 2018, 2020).

An important observation in this thesis is the stable GSD of distal tephra deposits (Fig. 4.10). Future studies could potentially use the stable grain size of distal ash deposits to further our understanding of the processes that deposit fine ash and provide insight into the velocity structure of the atmosphere (*Carazzo and Jellinek*, 2013; *Engwell and Eychenne*, 2016; *Osman et al.*, 2020). This could be achieved by studying the settling behavior of fine-ash in the laboratory in addition to observations of ash settling during modern, smaller magnitude eruptions (e.g., *Manzella et al.*, 2015; *Scollo et al.*, 2017; *Freret-Lorgeril et al.*, 2020).

In Chapter 5, I highlight the sensitivity of the Mazama TGSD to the inclusion of proximal data and similar sensitivity studies on the grain size data from Mount St. Helens 1980, Chaiten 2008, and the Campanian Ignimbrite tephra (Appendix D) found similar results. Future work expanding on this study could help determine the statistical significance of different sampling distributions and outline a set of best practises for tephra sampling in anticipation of the next explosive eruption.

7.3 Contributions and wider implications

This thesis has provided: (1) improved estimates of the erupted volume and TGSD of the climactic Mazama eruption, (2) a thorough review and critique of the grain size analysis methods used in volcanology with a focus on Dynamic Image Analysis (DIA), and (3) a sensitivity study using the Ash3D VATDM to simulate the climactic Mazama tephra deposit. Throughout these chapters my analyses have consistently shown that there is inherent uncertainty in the interpretations made from tephra deposits which propagates into uncertainty in the outputs of empirical models of deposit thinning and VATDMs. Importantly, the implications of these findings are relevant when studying volcanic eruptions of all scales, not only when M≥7. More research is required to quantify and propagate the uncertainties that arise from field-based observations through to the models used by volcanologists. Furthermore, effectively communicating the uncertainty in the outputs of models of volcanic activity is key as this data informs policy decisions relating to the risk mitigation strategies required to mitigate the impacts of future large magnitude explosive eruptions.

APPENDIX A - SUPPLEMENTARY MATERIAL FOR CHAPTER 2

A.1 The Mazama Locality Database

See next page

Table A.1: Mazama Locality Database

Site Number	Location	References[a]	Latitude	Longitude	State/ Province	Thickness (cm)	Evidence of Remobilisation[b]	Grainsize (μm)	Mean, mode, median, approx (or NA)
1	Swamp Lake	121	37.950	-119.829	CA	0.5	unk	-	-
2	Simon Young Site 22	133	38.151	-116.731	NV	0.1	unk	-	-
3	Osgood Swamp	35; 54; 133	38.846	-120.042	CA	0.1	unk	-	-
4	Simon Young Site 24	32; 133	39.974	-118.241	NV	5	unk	-	-
5	Blue Lake wetlands, S of Wendover	69	40.500	-114.036	UT	-	S	-	-
6	Juke Box trench, near Wendover	97	40.755	-114.010	UT	0.75	unk	-	-
7	Simon Young Site 21	93; 133	40.790	-112.642	UT	0.1	unk	-	-
8	Pilot Valley Playa	97; 109	41.070	-113.880	UT	-	unk	-	-
9	Great Salt Lake	6; 50; 119; 125	41.479	-112.452	UT	-	unk	-	-
10	Prohibition Creek	90; 97	41.557	-113.638	UT	-	unk	-	-
11	Keg Spring Creek	90; 97	41.602	-113.815	UT	-	unk	-	-
12	Blue Lake	41	41.679	-118.717	NV	-	S	-	-
13	Virgin Creek	32; 114; 133	41.732	-119.135	NV	10	unk	-	-
14	Raft River Mountains	88	41.917	-113.356	UT	-	unk	-	-
15	Night-fire archaeological site, California	61	41.960	-121.798	CA	-	P	-	-
16	Curelom Cirque	61	41.982	-113.736	UT	2	unk	25	mean
17	Independence Lake	13	42.199	-113.668	ID	4	unk	-	-
18	Klamath Falls, Pelican City	J Westgate, pers comm	42.252	-121.793	OR	-	unk	-	-
19	Lake Cleveland	13	42.322	-113.650	ID	4	unk	-	-
20	Upper Klamath Lake	99	42.400	-121.878	OR	-	S	-	-
21	Wildhorse Lake	11; 133	42.629	-118.589	OR	3	B	-	-
22	Paisley Cave	102; 105	42.671	-120.400	OR	-	P	-	-
23	Fish Lake	41; 117; 127	42.737	-118.647	OR	5	P	-	-
24	Summer Lake/Ana River	31	42.876	-120.764	OR	-	P	-	-
25	Rogue River valley	J Westgate, pers comm	42.927	-122.427	OR	-	unk	-	-
26	Antelope Unit	53; 66	42.927	-121.522	OR	223	P	-	-
27	Wineglass	4	42.961	-122.053	OR	-	P	-	-
28	Muir Creek	3; 27; 126; 61	43.046	-122.354	OR	850	P	32000	approx
29	South Chemult	J Westgate, pers comm	43.144	-121.797	OR	-	unk	-	-
30	North Umpqua River Valley	4	43.150	-122.250	OR	-	P	-	-

Table A.1: Mazama Locality Database *cont.*

Site Number	Location	References[a]	Latitude	Longitude	State/ Province	Thickness (cm)	Evidence of Remobilisation[b]	Grainsize (μm)	Mean, mode, median, approx (or NA)
31	North Umpqua River Valley	4	43.150	-122.210	OR	-	P	-	-
32	Connley Cave	8; 61; 116	43.158	-121.019	OR	18	S	32000	approx
33	Huckleberry Springs	53; 66	43.261	-121.499	OR	224	P	-	-
34	Toketee Falls	112	43.263	-122.434	OR	-	P	-	-
35	Crescent	J Westgate, pers comm	43.335	-121.758	OR	-	unk	-	-
36	Route 31, Fort Rock Cave	J Westgate, pers comm	43.354	-121.177	OR	-	unk	-	-
37	Fort Rock Cave	61; 105	43.371	-121.066	OR	-	unk	2000	approx
38	South Ice Cave	53; 66	43.583	-121.088	OR	68	P	-	-
39	Gold Lake	This study	43.636	-122.041	OR	75	P	-	-
40	China Hat Butte	61	43.681	-121.035	OR	-	unk	-	-
41	Offshore turbities, Pacific Ocean	1	43.715	-125.720	-	-	S	-	-
42	Jenny Lake, Wyoming	63	43.751	-110.734	WY	1	P	-	-
43	Grayling Springs archaeological site	85	43.769	-121.633	OR	-	B	177	approx
44	Dusty Mink archaeological site	85	43.770	-121.624	OR	-	B	-	-
45	Pettit Lake	115	43.980	-114.882	ID	6	B	52	median
46	Mount Bachelor	This study	44.006	-121.676	OR	64	P	403	median
47	Tumalo Lake	67	44.022	-121.544	OR	50	P	345	median
48	Lower Decker Lake	130	44.069	-114.889	OR	-	P	-	-
49	Three Creek	67	44.099	-121.628	OR	37	P	-	-
50	Prineville Reservoir	This study	44.133	-120.699	OR	-	S	231	median
51	Simon Young Site 20	93; 133	44.152	-109.182	WY	0.1	unk	-	-
52	Little Lake	68	44.167	-123.585	OR	2	P	-	-
53	Simpson Place Bog	53; 66; 83	44.186	-120.701	OR	45	P	-	-
54	Round Lake	67	44.443	-121.787	OR	14	P	-	-
55	Mitchell	This study	44.554	-120.321	OR	-	B	155	median
56	Three Sheep Rockshelter archaeological site	61	44.559	-121.288	OR	-	unk	-	-
57	Everyone archaeological site	61	44.592	-121.285	OR	-	unk	-	-
58	Day Creek (Forty Day Creek)	53; 66; 104;	44.608	-119.036	OR	59.5	P	-	-
59	Breitenbush Lake	67	44.769	-121.778	OR	17	P	-	-

Table A.1: Mazama Locality Database *cont.*

Site Number	Location	References[a]	Latitude	Longitude	State/ Province	Thickness (cm)	Evidence of Remobilisation[b]	Grainsize (μm)	Mean, mode, median, approx (or NA)
60	West Stayton	101; 133	44.797	-122.850	OR	0.1	unk	-	-
61	Blue Mountains	61	44.821	-119.903	OR	-	unk	-	-
62	McCall Fen	33	44.920	-116.070	ID	15	unk	100	approx
63	Anthony Lake Meadow	53; 66; 133	44.959	-118.232	OR	27	P	-	-
64	Deschutes River	9	45.042	-121.102	OR	200	S	-	-
65 Hubbard	101; 133	45.168	-122.799	OR	0.1	unk	-	-	
66	Kearns Basin	42	45.325	-112.957	MO	0.2	unk	-	-
67	Grande Ronde	This study	45.353	-118.194	OR	40	S	38	median
68	Hurricane Creek	12; 53; 133	45.368	-116.995	OR	26.25	unk	-	-
69	Pole Bridge	This study; 21	45.386	-117.425	OR	300	S	25	median
70	Fivemile Rapids	2; 28	45.627	-121.128	OR	-	unk	-	-
71	Big Eddy archaeological site	28; 61	45.634	-120.916	OR	-	unk	-	-
72	Lost Trail Pass Bog	11; 42; 86; 87	45.692	-113.949	ID	7	P	-	-
73	Andies Prairie	This study	45.703	-118.034	OR	30	P	29	median
74	Hobo Cave	61; 105	45.725	-120.590	OR	-	unk	-	-
75	Wildcat Canyon	25; 61; 105	45.726	-120.183	OR	10	unk	-	-
76	Dick Springs, Tollgate area	12; 53; 104; 133	45.753	-118.158	OR	37	P	-	-
77	Meadowwood, Tollgate area	66; 104	45.756	-118.104	OR	38	P	-	-
78	Cliff's Blowout	122	45.900	-118.987	OR	20	S	-	-
79	Carp Lake	130	45.918	-120.883	WA	2	unk	-	-
80	Juniper Canyon	This study; 122	45.955	-119.032	OR	70	S	24	median
81	Wallula Gap\Spring Gulch	This study; 22	46.001	-118.975	WA	300	S	25	median
82	Joseph Creek	108	46.002	-117.046	WA	-	unk	-	-
83	Burlingame Canyon	128	46.048	-118.657	WA	-	unk	-	-
84	Grande Ronde River Canyon	108	46.066	-117.011	WA	15	unk	-	-
85	Snake River	108	46.092	-116.984	WA	-	unk	-	-
86	Touchet Road	This study	46.101	-118.471	WA	30	S	-	-
87	Warrenton borehole	5	46.103	-123.551	OR	500	B	32	approx
88	Lower Columbia River Valley	98	46.150	-123.030	WA	50	S	32	approx
89	Two Rivers Site	48	46.184	-119.032	WA	12.5	unk	-	-
90	Tenmile Creek	58	46.270	-116.999	WA	12.5	unk	-	-
91	Imnaha Basalt	58	46.441	-117.152	WA	12.5	unk	-	-
92	Steptoe Canyon	58	46.458	-117.186	WA	12.5	unk	-	-

Table A.1: Mazama Locality Database *cont.*

Site Number	Location	References[a]	Latitude	Longitude	State/ Province	Thickness (cm)	Evidence of Remobilisation[b]	Grainsize (μm)	Mean, mode, median, approx (or NA)
93	Smith Canyon	47	46.459	-119.122	WA	9	S	-	-
94	Moscow, Idaho	46; 66	46.468	-116.840	ID	30	P	-	-
95	Dry Creek	15	46.500	-119.630	WA	15	unk	-	-
96	Tucannon River Valley	22	46.508	-117.997	WA	-	S	-	-
97	Seed Cave	124	46.509	-118.618	WA	-	S	-	-
98	Lower Monumental Dam	22	46.544	-118.533	WA	-	unk	-	-
99	Davis Lake	7	46.559	-122.296	WA	6	P	-	-
100	McAdam Junction	19	46.596	-118.217	WA	-	unk	-	-
101	Palouse Falls	This study; 22	46.701	-118.412	WA	-	S	31	median
102	Marys Pond, Montana	42	46.704	-114.351	MO	45	S	-	-
103	Wildcat Lake	11; 42; 83	46.727	-118.158	WA	146	B	-	-
104	Mount Rainier National Park	93; 133	46.916	-121.638	WA	6	P	62	approx
105	Endicott	19	46.935	-117.703	WA	-	S	-	-
106	Sheep Mountain Bog	42	46.952	-113.794	MO	39	S	-	-
107	Mount Rainier, Carbon River	26; 66	46.969	-121.813	WA	5	P	-	-
108	Simon Young Site 11	11; 133	46.973	-118.207	WA	2	unk	-	-
109	Craig	J Westgate, pers comm	47.124	-111.917	MO	-	unk	-	-
110	Lake Superior	118	47.130	-87.820	MI	-	unk	45	mean
111	Bear Swamp	38	47.176	-121.930	WA	-	unk	-	-
112	Simon Young Site 19	93; 133	47.319	-110.496	MO	0.1	unk	-	-
113	Williams Lake Fen	42	47.329	-117.682	WA	46	P	-	-
114	Covington	14	47.383	-122.041	WA	-	P	-	-
115	Arrow Lake	101; 112	47.430	-122.339	WA	-	P	-	-
116	Bow Lake	112	47.438	-122.293	WA	-	P	-	-
117	Simon Young Site 8	133	47.583	-121.949	WA	2.5	unk	-	-
118	Lake Washington	64	47.625	-122.265	WA	-	P	-	-
119	Moss Lake	38; 111	47.695	-121.850	WA	5.5	P	32	median
120	Creston Bog, Washington	29; 83; 133	47.762	-118.500	WA	24	P	-	-
121	Creston	76	47.768	-118.549	WA	5	P	-	-
122	Newman Lake	66	47.773	-117.099	WA	22.5	P	-	-
123	Skykomish River	123	47.809	-121.595	WA	-	unk	-	-
124	Hoh River Valley	56	47.811	-124.202	WA	-	unk	-	-

Table A.1: Mazama Locality Database *cont.*

Site Number	Location	References[a]	Latitude	Longitude	State/ Province	Thickness (cm)	Evidence of Remobilisation[b]	Grainsize (μm)	Mean, mode, median, approx (or NA)
125	Choteau	J Westgate, pers comm	47.818	-112.183	MO	-	unk	17	median
126	Leland Lake	C Goldfinger, pers comm	47.897	-122.881	WA	2	P	-	-
127	Wells Reservoir	24	48.095	-119.823	WA	-	S	-	-
128	Foy Lake	100; 120	48.169	-114.359	MO	48	B	-	-
129	Waits Lake	80	48.184	-117.791	WA	7.5	unk	-	-
130	Methow Valley	J Westgate, pers comm	48.213	-120.125	WA	-	unk	-	-
131	Goose Lake	83; 95	48.276	-118.598	WA	12	unk	-	-
132	Matheson Lake	59	48.361	-123.597	BC	-	P	-	-
133	Dailey Lake Bog	20	48.459	-117.808	WA	165	B	100	approx
134	Portage Inlet, Vancouver Island	18	48.464	-123.421	BC	1.5	P	-	-
135	Galata	J Westgate, pers comm	48.467	-111.352	MO	-	unk	17	median
136	Starvation Flat bog	20	48.470	-117.727	WA	65	B	62	approx
137	Prior Lake	59	48.476	-123.466	BC	-	P	-	-
138	Pike Lake	59	48.490	-123.469	BC	-	P	-	-
139	Rithets Bog, Vancouver Island	71	48.493	-123.386	BC	-	P	-	-
140	Maltby Lake	59	48.497	-123.452	BC	-	unk	-	-
141	Hager Pond	78; 83	48.580	-116.957	ID	10	unk	-	-
142	Hager Lake	91	48.597	-116.972	ID	-	B	-	-
143	Sidney Island	J Westgate, pers comm	48.604	-123.293	BC	-	unk	-	-
144	Skagit River	110	48.625	-121.347	WA	2	B	-	-
145	Mud Lake	77; 83	48.672	-118.766	WA	40	unk	-	-
146	Big Meadow Lake	83; 101	48.727	-117.556	WA	36	unk	-	-
147	Huff Lake	91	48.741	-117.063	WA	-	B	-	-
148	Bonaparte Meadows	77; 83	48.778	-119.061	WA	12	P	75	approx
149	Tepee Lake	79	48.788	-115.101	MO	10	P	-	-
150	Swiftcurrent Lake	75	48.796	-113.662	MO	48	B	15	mean
151	Ryan	J Westgate, pers comm	48.812	-117.933	WA	-	unk	-	-
152	USA border	J Westgate, pers comm	49.004	-119.588	BC	-	unk	17	median
153	Kilpoola Lake	55	49.027	-119.563	BC	30	unk	-	-
154	Chopaka	J Westgate, pers comm	49.035	-119.704	BC	-	unk	-	-
155	Cardston	J Westgate, pers comm	49.038	-113.264	AB	-	unk	15	median

Table A.1: Mazama Locality Database *cont.*

Site Number	Location	References[a]	Latitude	Longitude	State/ Province	Thickness (cm)	Evidence of Remobilisation[b]	Grainsize (μm)	Mean, mode, median, approx (or NA)
156	Osoyoos	J Westgate, pers comm	49.046	-119.512	BC	-	unk	-	-
157	Waterton	J Westgate, pers comm	49.053	-113.839	AB	-	unk	19	median
158	Waterton	J Westgate, pers comm	49.105	-113.878	AB	-	unk	27.2	median
159	Nordans Pond bog	103	49.152	-53.597	NF	-	unk	38	mean
160	Lulu Island	132	49.178	-122.974	BC	1.5	P	-	-
161	Keremos	J Westgate, pers comm	49.191	-119.780	BC	-	unk	-	-
162	Lulu Island	J Westgate, pers comm	49.192	-123.056	BC	3.048	unk	10.3	median
163	Ashnola River Road	J Westgate, pers comm	49.220	-119.952	BC	-	unk	-	-
164	Burnaby Lake	37	49.260	-122.968	BC	-	P	-	-
165	Lake Mike	16	49.274	-122.540	BC	3	P	-	-
166	Olalla	J Westgate, pers comm	49.299	-119.785	BC	-	unk	15.6	median
167	Castlegar Raspberry	J Westgate, pers comm	49.323	-117.680	BC	-	unk	19.2	median
168	Lower Arrow Lake	36	49.343	-117.868	BC	-	P	-	-
169	Twobit Creek	71	49.343	-117.868	BC	8	P	-	-
170	Highway 3	J Westgate, pers comm	49.385	-120.180	BC	-	unk	-	-
171	Raymond	J Westgate, pers comm	49.450	-112.707	AB	-	unk	-	-
172	Princeton	J Westgate, pers comm	49.455	-120.381	BC	-	unk	-	-
173	Connely Creek	J Westgate, pers comm	49.465	-120.602	BC	-	unk	-	-
174	Squeah Lake	51; 82	49.481	-121.406	BC	2	P	-	-
175	Cooley Lake	43	49.491	-117.645	BC	252	B	-	-
176	Rockslide Lake	43	49.551	-117.521	BC	30	S	-	-
177	Maple Leaf Archaeological Site	60; 62	49.566	-114.358	AB	15	P	30	median
178	Pinecrest Lake	J Westgate, pers comm	49.572	-121.411	BC	-	unk	-	-
179	Fraser Canyon	73; 84	49.584	-121.401	BC	-	P	-	-
180	Fort Steele	J Westgate, pers comm	49.632	-115.518	BC	7.5	unk	13	median
181	Crowsnest Pass	34; 60	49.649	-114.708	AB	-	unk	22	median
182	Cypress Hills	44	49.659	-110.293	AB	-	P	-	-
183	Cypress Hills	44	49.660	-110.050	AB	-	P	-	-
184	Stampede Archaeological Site, Elkwater	44; 60; 96	49.667	-110.260	AB	32.5	B	27	median
185	Oldman River	J Westgate, pers comm	49.741	-114.056	AB	-	unk	19	median
186	Cypress Hills	J Westgate, pers comm	49.744	-109.966	SA	-	unk	13.1	median

Table A.1: Mazama Locality Database *cont.*

Site Number	Location	References[a]	Latitude	Longitude	State/ Province	Thickness (cm)	Evidence of Remobilisation[b]	Grainsize (μm)	Mean, mode, median, approx (or NA)
187	Prosser Lake	39	49.751	-120.626	BC	4.25	S	50	approx
188	Oldman River	J Westgate, pers comm	49.769	-114.006	AB	-	unk	-	-
189	Callum Creek	J Westgate, pers comm	49.780	-114.050	AB	-	unk	21	median
190	Friday's Site	60	49.804	-109.722	SA	-	S	26	median
191	Cypress Hills	J Westgate, pers comm	49.827	-109.345	SA	-	unk	13	median
192	Horseshow Bay	J Westgate, pers comm	49.843	-123.093	BC	-	unk	-	-
193	Dennis Ranch	J Westgate, pers comm	49.847	-114.186	AB	-	unk	-	-
194	Livingstone Gap	J Westgate, pers comm	49.849	-114.306	AB	-	unk	27	median
195	The Gap	107	49.870	-114.365	AB	10	unk	-	-
196	Kelowna Bridge	J Westgate, pers comm	49.883	-119.503	BC	-	unk	-	-
197	Township Road, Claresholm	J Westgate, pers comm	49.958	-113.700	AB	-	unk	27	median
198	Claresholm	J Westgate, pers comm	50.015	-113.577	AB	-	unk	19	median
199	Woodsdale	J Westgate, pers comm	50.048	-119.396	BC	-	unk	44	median
200	Medicine Hat	J Westgate, pers comm	50.111	-110.518	AB	24	unk	-	-
201	Island Bluff	J Westgate, pers comm	50.137	-110.588	AB	9	unk	-	-
202	Willow Creek	J Westgate, pers comm	50.138	-113.770	AB	-	unk	27	median
203	Surprise Lake	81; 51	50.146	-125.567	BC	-	unk	-	-
204	near Medicine Hat	J Westgate, pers comm	50.147	-110.480	AB	30.48	S	18.0	median
205	Lavington	71	50.229	-119.100	BC	10	P	-	-
206	Deep Creek	36	50.233	-119.113	BC	-	P	-	-
207	Lytton	J Westgate, pers comm	50.235	-121.579	BC	-	unk	-	-
208	Drynoch Slide Archaeological Site	113; 73	50.253	-121.554	BC	-	unk	-	-
209	Spences Bridge	J Westgate, pers comm	50.359	-121.391	BC	-	unk	-	-
210	Lower Joffre Lake	40; 89	50.366	-122.497	BC	1	P	-	-
211	Cartwright Lake	10	50.372	-114.814	AB	10	S	-	-
212	Chase	51; 70	50.372	-114.814	BC	-	unk	-	-
213	Thompson River	J Westgate, pers comm	50.486	-121.253	BC	-	unk	18	median
214	Westwold	J Westgate, pers comm	50.495	-119.732	BC	-	unk	36	median
215	Fountainview Academy	J Westgate, pers comm	50.531	-121.768	BC	-	unk	-	-
216	Fraser River	J Westgate, pers comm	50.606	-121.847	BC	-	unk	-	-
217	Upper Kananaskis Lake	10	50.621	-115.150	AB	10	unk	-	-
218	Barnhartvale	J Westgate, pers comm	50.645	-120.094	BC	-	unk	15	median

Table A.1: Mazama Locality Database *cont.*

Site Number	Location	References[a]	Latitude	Longitude	State/ Province	Thickness (cm)	Evidence of Remobilisation[b]	Grainsize (μm)	Mean, mode, median, approx (or NA)
219	Kamloops	J Westgate, pers comm	50.655	-120.031	BC	-	unk	-	-
220	Kamloops	J Westgate, pers comm	50.658	-120.102	BC	-	unk	-	-
221	Cobb Lake, Kootenay National Park	51	50.661	-115.876	BC	-	P	-	-
222	Kamloops	J Westgate, pers comm	50.666	-120.183	BC	-	unk	-	-
223	Kamloops	J Westgate, pers comm	50.671	-120.233	BC	-	unk	-	-
224	Pritchard	J Westgate, pers comm	50.699	-119.816	BC	-	unk	-	-
225	Ashcroft	J Westgate, pers comm	50.726	-121.273	BC	-	unk	-	-
226	Canoe Mill	J Westgate, pers comm	50.746	-119.236	BC	-	unk	-	-
227	Dog Lake, Kootenay National Park	51	50.781	-115.929	BC	10	P	-	-
228	Mara Lake	92	50.788	-119.005	BC	9	unk	-	-
229	Jesmond Bog	66; 131; 133	50.820	-120.844	BC	1	P	-	-
230	Pavilion	J Westgate, pers comm	50.829	-121.856	BC	-	unk	-	-
231	Cache Creek	J Westgate, pers comm	50.837	-121.372	BC	-	unk	-	-
232	South Saskatchewan River	30; 66; 133	50.861	-109.970	SA	3	B	62	approx
233	Pavilion	J Westgate, pers comm	50.874	-121.828	BC	-	unk	-	-
234	Empress, Sastkatchewn Outlook	60	50.890	-109.846	SA	4.5	unk	29	median
235	Pavilion	J Westgate, pers comm	50.894	-121.768	BC	-	unk	19	median
236	Fish Creek	J Westgate, pers comm	50.922	-113.953	AB	-	unk	16	median
237	Wasootch	J Westgate, pers comm	50.924	-115.089	AB	-	unk	22	median
238	West Calgary	J Westgate, pers comm	50.954	-115.056	AB	10	unk	17	median
239	Wasootch Creek	J Westgate, pers comm	50.959	-114.921	AB	-	unk	-	-
240	Stoney Trail	J Westgate, pers comm	50.963	-115.124	AB	-	unk	24	median
241	Stoney Creek	J Westgate, pers comm	51.026	-115.002	AB	-	unk	25	median
242	Calgary	60	51.038	-114.092	AB	5	S	-	-
243	McLure	J Westgate, pers comm	51.068	-120.233	BC	-	unk	23.7	median
244	Mount Revelstoke	72	51.081	-118.082	BC	-	P	-	-
245	Frederick Lake	10	51.094	-114.729	AB	10	unk	-	-
246	Bow River	60; 94	51.097	-115.109	AB	-	unk	37	median
247	Tuscany site	96	51.137	-114.274	AB	6	unk	-	-
248	Banff hot springs	J Westgate, pers comm	51.158	-115.534	AB	-	unk	19.2	median

Table A.1: Mazama Locality Database *cont.*

Site Number	Location	References[a]	Latitude	Longitude	State/ Province	Thickness (cm)	Evidence of Remobilisation[b]	Grainsize (μm)	Mean, mode, median, approx (or NA)
249	Banff	J Westgate, pers comm	51.186	-115.576	AB	-	unk	-	-
250	Johnson Lake	10	51.197	-115.485	AB	100	B	-	-
251	Marion Lake	51; 81	51.260	-117.509	BC	-	unk	-	-
252	Copper Lake, Banff National Park	10; 129	51.260	-115.923	AB	35	B	-	-
253	Trans Canada Highway	J Westgate, pers comm	51.289	-116.793	BC	-	unk	-	-
254	Opabin Lake	57; 106	51.341	-116.312	BC	3	unk	-	-
255	Mary Lake	57	51.351	-116.334	BC	6	unk	-	-
256	Lake O'Hara	57; 106	51.356	-116.330	BC	4	unk	-	-
257	Green Lake	40; 89	51.403	-121.231	BC	-	P	-	-
258	Lake Louise	J Westgate, pers comm	51.410	-116.139	AB	-	unk	-	-
259	Dunn Peak	35; 51	51.431	-119.961	BC	-	unk	-	-
260	Downie Creek	J Westgate, pers comm	51.484	-118.467	BC	-	unk	-	-
261	Red Deer River	J Westgate, pers comm	51.648	-115.079	AB	-	unk	23.7	median
262	Maze Peak	J Westgate, pers comm	51.699	-115.408	AB	-	unk	12	median
263	James Pass	60	51.791	-115.469	AB	-	unk	27	median
264	Banff National Park, Saskatchewan Crossing	51; 60; 133	51.967	-116.752	AB	12	P	30	median
265	North Saskatchewan River	J Westgate, pers comm	51.973	-116.487	AB	5.08	unk	-	-
266	Revelstoke	17	52.000	-118.300	BC	-	P	-	-
267	Warsaw Mountain	J Westgate, pers comm	52.000	-118.409	BC	-	unk	37	median
268	Upper North Saskatchewan River	J Westgate, pers comm	52.004	-116.340	AB	7.62	unk	19	median
269	Mica Creek, Chapman	J Westgate, pers comm	52.004	-118.563	BC	5.08	unk	25.4	median
270	Upper North Saskatchewan River	J Westgate, pers comm	52.022	-116.318	AB	5.08	unk	16	median
271	Mica Creek	J Westgate, pers comm	52.076	-118.573	BC	10.16	unk	33.5	median
272	Columbia River Valley	45	52.100	-118.550	BC	-	unk	-	-
273	White Goat	J Westgate, pers comm	52.155	-116.930	AB	-	unk	33.5	median
274	Goldeye Lake Fen	134	52.270	-116.120	AB	2	P	-	-
275	Nordegg Bridge	60	52.462	-116.115	AB	2.5	B	24	median
276	Quesnel Lake	49	52.486	-121.343	BC	1	B	12	mean
277	Quesnel Lake	49	52.613	-120.997	BC	2	B	12	mean

Table A.1: Mazama Locality Database *cont.*

Site Number	Location	References[a]	Latitude	Longitude	State/ Province	Thickness (cm)	Evidence of Remobilisation[b]	Grainsize (μm)	Mean, mode, median, approx (or NA)
278	Boss Hill near Buffalo Lake	60	52.677	-113.146	AB	-	unk	26	median
279	Tonquin Pass	51; 74	53.140	-119.173	BC	2	unk	-	-
280	Rat Creek	J Westgate, pers comm	53.209	-115.496	AB	-	unk	19.2	median
281	Brule Lake	60	53.303	-117.839	AB	2	unk	-	-
282	Upper Pinto Fen	134; 135	53.350	-118.010	AB	-	unk	-	-
283	Muscata Creek Viaduct	J Westgate, pers comm	53.359	-117.587	AB	5.08	unk	31	median
284	Duffield	J Westgate, pers comm	53.419	-114.301	AB	-	unk	-	-
285	Hasse Lake	60	53.488	-114.174	AB	1	unk	-	-
286	Keephills Fen	23	53.495	-114.430	AB	0.1	unk	-	-
287	Roper Rd, Edmonton	J Westgate, pers comm	53.498	-113.408	AB	-	unk	22.1	median
288	Lake Wabamun	J Westgate, pers comm	53.514	-114.520	AB	-	unk	18.0	median
289	Edmonton South	60	53.529	-113.514	AB	0.75	unk	26	median
290	Beverley	133	53.557	-113.354	AB	1.5	unk	16.7	median
291	Lofty Lake	65; 66; 133	54.723	-112.481	AB	0.1	P	-	-
292	GISP2, Greenland	136	73.580	-38.400	-	-	unk	15	approx
293	Camp Century, Greenland	52	77.167	-61.133	-	-	unk	-	-

(a) For references see section A.2

(b) P - primary, S - secondary, B - both and unk - unknown. See Chapter 2 for details.

A.2 References for the Mazama Locality Database

Numbered references that correspond to Table A.1

1. *Adams* (1990)
2. *Ames et al.* (1998)
3. *Arnold and Libby* (1951)
4. *Bacon* (1983)
5. *Baker et al.* (2010)
6. *Balch et al.* (2005)
7. *Barnosky* (1981)
8. *Bedwell* (1970)
9. *Beebee et al.* (2002)
10. *Beierle and Smith* (1998)
11. *Blinman et al.* (1979)
12. *Borchardt et al.* (1973)
13. *Bovet et al.* (2003)
14. *Broecker et al.* (1956)
15. *Brown* (1970)
16. *Brown et al.* (1989)
17. *Buckley and Willis* (1969)
18. *Buckley and Willis* (1970)
19. *Bush et al.* (1979)
20. *Carrara and Trimble* (1992)
21. *Carson* (2001)
22. *Carson and Pogue* (1996)
23. *Chagué-Goff et al.* (1996)
24. *Chatters and Hoover* (1992)
25. *Cole* (1969)
26. *Crandell and Mullineaux* (1967)
27. *Crane* (1956)
28. *Cressman et al.* (1960)
29. *Czamanske and Porter* (1965)
30. *David* (1970)
31. *Davis* (1985)
32. *Davis* (1978)
33. *Doerner and Carrara* (2001)
34. *Driver* (1982)
35. *Duford and Osborn* (1978)
36. *Dyck et al.* (1965)
37. *Dyck et al.* (1966)
38. *Egan et al.* (2016)
39. *Enache and Cumming* (2006)
40. *Filippelli et al.* (2006)
41. *Foit and Mehringer* (2016)
42. *Foit et al.* (1993)
43. *Foit et al.* (2004)
44. *Freeman et al.* (2006)
45. *Fulton* (1971)
46. *Garber* (1970)
47. *Gaylord et al.* (2001)
48. *Gibson* (1984)
49. *Gilbert and Desloges* (2012)
50. *Grey and Bennett* (1972)
51. *Hallett et al.* (1997)
52. *Hammer et al.* (1980)
53. *Harward and Youngberg* (1969)
54. *Haynes et al.* (1967)
55. *Heinrichs et al.* (1999)
56. *Heusser* (1974)
57. *Hickman and Reasoner* (1994)
58. *Hooper et al.* (1985)
59. *James et al.* (2009)
60. *Jensen et al.* (2019)
61. *Kittleman* (1973)
62. *Landals* (1990)
63. *Larsen et al.* (2016)
64. *Leopold et al.* (1982)
65. *Lichti-Federovich* (1970)
66. *Lidstrom* (1971)
67. *Long et al.* (2014)
68. *Long et al.* (1998)
69. *Louderback and Rhode* (2009)
70. *Lowdon and Blake* (1973)
71. *Lowdon and Blake* (1970)
72. *Lowdon et al.* (1971)
73. *Lowdon et al.* (1969)
74. *Luckman et al.* (1986)
75. *MacGregor et al.* (2011)
76. *Mack et al.* (1976)
77. *Mack et al.* (1979)
78. *Mack et al.* (1978a)
79. *Mack et al.* (1983)
80. *Mack et al.* (1978b)

81. *Mathewes* (1973)
82. *Mathewes et al.* (1972)
83. *Matz* (1987)
84. *McCallum and Dyck* (1960)
85. *McFarland* (1989)
86. *Mehringer et al.* (1977a)
87. *Mehringer et al.* (1977b)
88. *Mehringer et al.* (1971)
89. *Menounos* (2002)
90. *Miller et al.* (2013)
91. *Moseley et al.* (1992)
92. *Mothersill* (1991)
93. *Mullineaux* (1974)
94. *Newton* (1991)
95. *Nickman and Leopold* (1985)
96. *Oetelaar and Beaudoin* (2016)
97. *Oviatt et al.* (2018)
98. *Peterson et al.* (2012)
99. *Platt Bradbury et al.* (2004)
100. *Power et al.* (2011)
101. *Powers and Wilcox* (1964)
102. *Preston et al.* (1955)
103. *Pyne-O'Donnell et al.* (2012)
104. *Rai* (1971)
105. *Randle et al.* (1971)
106. *Reasoner and Hickman* (1989)
107. *Reeves and Dormaar* (1972)
108. *Reidel et al.* (1992)
109. *Rey* (2012)
110. *Riedel et al.* (2001)
111. *Rigg and Gould* (1957)
112. *Rubin and Alexander* (1960)
113. *Sanger* (1967)
114. *Sarna-Wojcicki et al.* (1983)
115. *Shapley and Finney* (2015)
116. *Sheets and Grayson* (1979)
117. *Sherrod et al.* (2012)
118. *Spano et al.* (2017)
119. *Spencer et al.* (1984)
120. *Stevens et al.* (2006)
121. *Street et al.* (2012)
122. *Sweeney et al.* (2005)
123. *Tabor et al.* (1963)
124. *Thompson* (1985)
125. *Thompson et al.* (2016)
126. *Valastro et al.* (1968)
127. *Verosub et al.* (1986)
128. *Waitt* (1980)
129. *White and Osborn* (1992)
130. *Whitlock et al.* (2011)
131. *Williams and Goles* (1968)
132. *Williams and D'Auria* (1991)
133. *Young* (1990)
134. *Yu* (2006)
135. *Yu et al.* (2003)
136. *Zdanowicz et al.* (1999)

A.3 Drainage analysis

A.3.1 Methods

For a number of entries in the database of tephra localities (Table A.2), the original publication does not discuss evidence of remobilisation or provide verification that the locality records a primary tephra thickness. Therefore, we analysed the upstream drainage to appraise whether the tephra could have been remobilised downslope. We tested this method on the distal sites visited in this study as we know the extent of remobilisation from field observations (Fig. A.1). 10 m resolution Digital Elevation Models (DEMs) from the USGS National Elevation Dataset were cropped and merged in QGIS (*QGIS*, 2019). Then, using '`TopoToolbox`', MATLAB based software for topographic analysis (*Schwanghart and Kuhn*, 2010; *Schwanghart and Scherler*, 2014), the drainage area above the field sites was determined.

The upstream drainage analysis was repeated for additional sites from the database of localities that had anomalous thickness values. These include Marys Pond, Montana (site 102), where three cores collected by *Foit et al.* (1993) contained between 9-90 cm of "reworked" Mazama tephra. Swiftcurrent Lake, Montana (site 148) and Foy Lake, Montana (site 128), were also analysed due to anomalously thick (48 cm) tephra thicknesses over 800 km from source (*MacGregor et al.*, 2011; *Power et al.*, 2011). For lake core localities the drainage area was calculated from above the outlet of the lake rather than the location of the core.

A.3.2 Results

The upstream drainage analysis of the field localities confirmed that Andies Prairie is likely recording a minimum primary thickness and that due to the upstream drainage, Juniper Canyon and Pole Bridge are overthickened sites where the tephra has been remobilised downslope (section 2.3.1).

However, the drainage analysis of lake core localities gave less coherent results. The tephra thicknesses in Marys Pond, Foy Lake and Swiftcurrent Lake were anomalous for their distance from source. Foy Lake (site 128) contains 48 cm of Mazama tephra, is 835 km from Crater Lake, the upstream drainage covers 9.17 km^2 and the basin slopes are typically less than 20°(Fig. A.2b & e). Swiftcurrent Lake also has a tephra thickness of 48 cm (site 148), is 919 km from Crater Lake, and an upstream drainage area of 81.2 km^2 (Fig. A.2c) which can be split into smaller SW (~36 km^2) and NE (~45 km^2) sub-basins either side of a central topographic divide (*MacGregor et al.*, 2011). The hillslopes in the Swiftcurrent basin are steep (modal slope 30-35°; Fig. A.2f) which is typical of the glacial valleys in the region. The large drainage area and steep slopes of the Swiftcurrent Lake drainage may help explain the overthickening of the Mazama tephra, which was observed to contain up to 25% clastic contamination (*MacGregor et al.*, 2011). However, this reasoning cannot explain the overthickened sequence at Foy Lake (*Power et al.*,

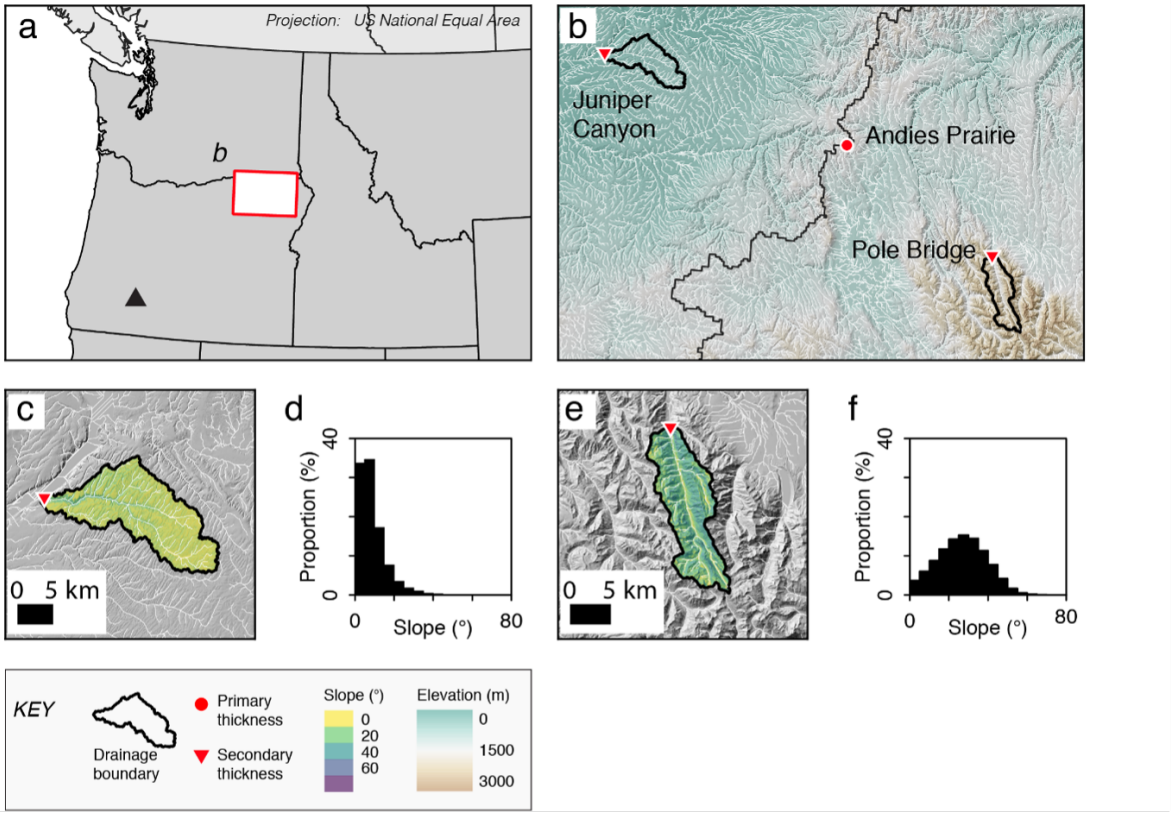

Figure A.1: Drainage area and slope analysis for selected Mazama field localities. a) Map of western USA and Canada with Crater Lake (black triangle) and inset map (red box). b) Digital elevation model of Walla Walla region with Mazama localities shown as red markers. Map projection is Universal Transverse Mercator (UTM). c & e) Slope maps of the upstream drainage area of each locality. Map projection is UTM. d & f) Histograms of slope inclination for each basin.

2011) where the upstream drainage area is small and gently sloping (Fig. A.2b). Similarly, even though the Mazama tephra at Marys Pond ranges in thickness from 9-90 cm (*Foit et al.*, 1993), the drainage basin is extremely small (<1 km^2) and gently sloping. These results suggest other processes must be perturbing tephra accumulation and preservation in lakes rather than simply the characteristics of the upstream drainage area (*McNamara et al.*, 2019).

Our results show that the drainage analysis cannot be used to explain the anomalous thickness of the selected lake localities (Fig. A.2). If hillslope processes were the dominant influence on the amount of tephra accumulating in a lake, we would expect the Swiftcurrent Lake to contain a thicker tephra layer than Foy Lake and Marys Pond due to the large drainage area and steep surrounding slopes.

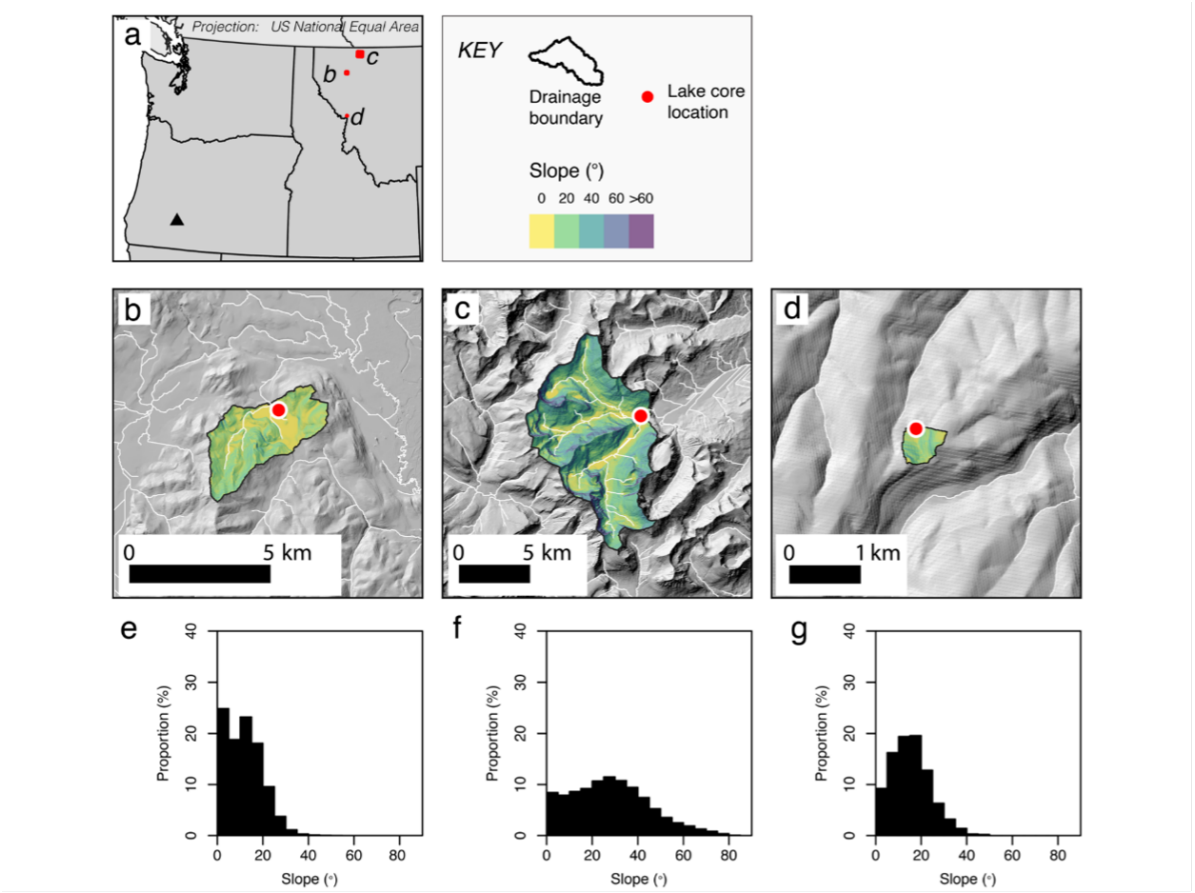

Figure A.2: Drainage area and slope analysis for selected lake core localities. a) Map of western USA and Canada showing Crater Lake (black triangle) and core locations (red dots). b) Slope map of the upstream drainage area of Foy Lake, Montana. c) Slope map of the upstream drainage area of Swiftcurrent Lake, Montana. d) Slope map of the upstream drainage of Marys Pond, Montana. e-g) Histograms of slope inclination for each basin.

A.4 Spline methods

A.4.1 Method - spline fitting parameters

The spline method requires four user defined parameters: tension, roughness, divisions of area and a weighting for each measurement. The tension parameter is used to minimise unrealistic distortions of the model surface and is set between 0 and 1. The roughness value determines the smoothness of the model surface. Low roughness values (0.1) give a very smooth model fit compared to high values of roughness (1000), which strongly reflect local variations in the data. Following the recommendations of previous studies, we set the tension to 0.99 and the roughness to 1.0 (*Inoue*, 1986; *Engwell et al.*, 2015). The size and number of area divisions depends on the total area over which the data are spaced and the spatial density of measurements (*Engwell et al.*, 2015). A coarse area division of 400 km was used for fitting the spline to the Mazama

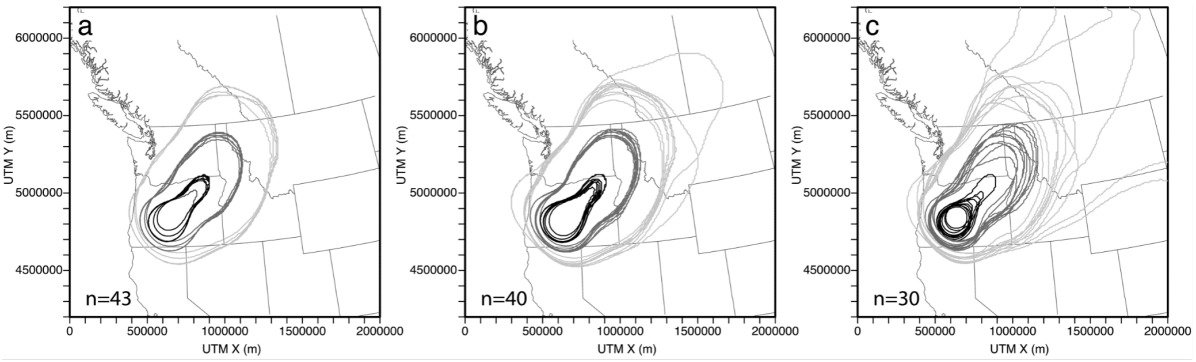

Figure A.3: Sensitivity of cubic B-spline model to number of thickness measurements. a-c) 20 cm (black), 10 cm (dark grey) and 5 cm (light grey) isopachs of spline models for 10 randomly down-sampled thickness data sets where n is the number of measurements.

data because the domain area is 4 million km^2 and the primary thickness data are sparsely distributed.

Applying the spline method enables individual weights to be placed on each measurement, which determines how strongly the model surface is influenced by each point. For example, *Engwell et al.* (2015) used measured uncertainties on Fogo Member A thickness dataset (*Engwell et al.*, 2013) to individually weight each measurement before applying the spline model. Unfortunately, uncertainties in thickness measurements are rarely determined or reported so that these data are not available for the thicknesses amassed in the database of Mazama tephra occurrences. When applying the method, eight inferred thickness measurements were included to approximate the dominant north-western dispersal of the deposit. This is required due to the absence of upwind tephra localities, giving anomalous spline isopachs. Four locations 200 km south east of Crater Lake were assigned 1 cm tephra thickness to represent the rapid decay of tephra thickness upwind. Two sites with inferred 0.01 cm thickness were placed in the western corners of the model domain, and two 0.1 cm thicknesses were placed along the southern edge of the domain to allow closure of the 5 cm isopach. Inferring these sites is similar to the zeros required for the Voronoi tessellation method, which is used to produce Total Grain Size Distributions (TGSDs) of tephra deposits (*Bonadonna et al.*, 2005a).

The cubic B-spline method was also used to fit the proximal thickness data collected by *Young* (1990). The dominantly distal and proximal datasets require separate spline fits due to the different spatial density of measurements; as the density of proximal measurements is greater and the domain size smaller, the grid division was reduced to 40 km. The roughness (1.0), tension (0.99) and weightings (equal) are the same. The fit required inferred upwind thicknesses, which were placed 50 km south east of Crater Lake and assigned 10 cm thickness, as predicted by Young's hand-drawn isopachs (1990).

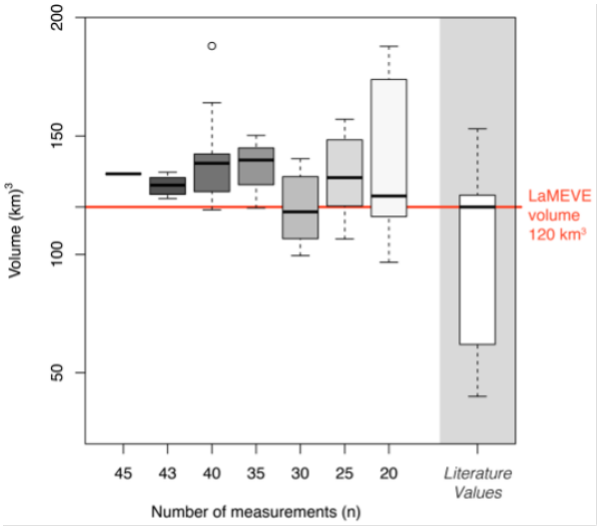

Figure A.4: Range in bulk volumes calculated from isopachs of sub-sampled primary tephra thickness data. Box and whisker plots show the median as a solid line, the box represents the interquartile range and the spread of data corresponds to the whiskers with outliers shown as open circles. The lower number of thickness measurements used (n) results in more varied isopachs which translates into large variability in the volumes calculated from them. When n=15 no closed isopachs could be drawn, so no volume can be estimated. The literature values from Table 2.1 are plotted and the LaMEVE value highlighted in red (*Crosweller et al.*, 2012, ; the LaMEVE database, VOLGRIPA; www.bgs.ac.uk/vogripa/view/controller.cfc?method=lameve).

A.4.2 Sensitivity of isopachs and volume calculations

To examine the sensitivity of the spline interpolation method to individual data points the spline fitting was re-run with randomly sub-sampled primary thickness data. The primary thicknesses were randomly sampled from 45 measurements (n=45) to n=43, n=40 and then in intervals of 5. The random sub-sampling was repeated 10 times for each n value fitting the cubic B-spline model each time. The results show that excluding even a few random data points can alter the extent and shape of the spline isopachs (Fig. A.3). Below n=30, the likelihood of unclosed isopachs increases (Fig. A.3c), and when n=15, no closed isopachs could be drawn.

The volume was calculated for each set of down sampled isopachs using the single exponential fit method (see Chapter 2, section 2.3.4). The range in volume increases as n decreases due to the variability in isopachs drawn for each random sub-sample (Fig. A.4). The variability in the median value (Fig A.4) highlights the sensitivity of the volume calculations to the isopach shape, and reflects the relatively small number of sub-samples (10). No volume calculations were carried out when n≤15 because of the lack of closed isopachs.

Table A.2: Volume estimates using spline surface and truncated integral of log thickness versus square root area plots.

Isopachs	Volume under spline surface (5 cm isopach) (km^3)	Truncated integral distal volume (5 cm isopach) (km^3)
Primary spline	46	82
Mixed spline	63	104

A.5 Volume estimates

A.5.1 Volume under the spline surface

The volume estimates from log thickness versus square root area plots use specific isopachs derived from the spline surface to extrapolate the thickness to the proximal and ultra-distal (>1000 km) areas. However, the spline fit generates a surface so that the volume can be calculated beneath it. The volumes estimated by direct integration below the spline surface are compared to a truncated integral of the corresponding log thickness versus square root area plot in Table A.2. The volume under the spline surface is smaller than the corresponding truncated integral (e.g., 46 km^3 compared to 82 km^3 for the primary spline isopachs). This can be explained by the spline fit not extrapolating to thicker deposits close to the vent, which is in-built to the exponential model.

A.5.2 Burden et al. (2013) method

As discussed in section 2.5.3, isopachs are often not drawn for large prehistoric deposits and log thickness versus true distance from vent plots are favoured (Fig. 2.4). *Burden et al.* (2013) used log thickness and distance data to estimate erupted volumes by assuming the distribution of thickness is not dependent on direction. Using this method, and the exponential fit in Figure 2.4, we calculate a volume of 377 km^3 from the primary data and 510 km^3 from all the data. These values are much larger than other estimates (Table 2.2) due to the absence of upwind data nullifying the assumption that the data distribution is not directional. By including the inferred thicknesses used to fit the spline model in the exponential fit, the volumes calculated by the *Burden et al.* (2013) method are reduced to 208 and 367 km^3 respectively. These values remain large and demonstrate the limitations of this approach for large deposits as seen by *Burden et al.* (2013) for the Santa Maria 1902 deposit.

APPENDIX B

APPENDIX B - SUPPLEMENTARY MATERIAL FOR CHAPTER 3

B.1 Silicate glass compositions

Table B.1 - Major element geochemical data for Mazama glass analysed in Chapter 3

Table B.2 - Major element geochemical data for secondary glass standards analysed in Chapter 3

B.2 FeTi oxide compositions

Table B.3: Major element geochemical data for Mazama FeTi oxides analysed in Chapter 3

Table B.4: Major element geochemical data for secondary FeTi standards analysed in Chapter 3

Table B.1: Major element geochemical data for Mazama glass

Location ID	Analysis ID	SiO_2	TiO_2	Al_2O_3	FeO	MnO	MgO	CaO	Na_2O	K_2O	P_2O_5	Cl	Analytical Total
80	MZ2208JC1_gl01	73.2	0.43	14.06	1.9	0.03	0.44	1.61	5.29	2.78	0.09	0.17	98.21
	MZ2208JC1_gl02	73.18	0.44	14.29	1.92	0.04	0.44	1.51	5.09	2.85	0.05	0.19	98.21
	MZ2208JC1_gl03	72.96	0.43	14.07	1.89	0.06	0.43	1.63	5.41	2.9	0.05	0.16	98.32
	MZ2208JC1_gl04	72.94	0.41	14.36	1.9	0.06	0.45	1.58	5.33	2.72	0.07	0.18	97.86
	MZ2208JC1_gl05	73.05	0.46	14.05	1.87	0.06	0.46	1.69	5.3	2.81	0.08	0.17	98.51
	MZ2208JC1_gl06	73.13	0.41	14.26	1.96	0.03	0.42	1.64	5.24	2.68	0.06	0.17	97.57
	MZ2208JC1_gl07	73.18	0.39	14.12	1.9	0.04	0.38	1.58	5.32	2.85	0.06	0.18	99.13
	MZ2208JC1_gl08	73.24	0.43	14.14	1.96	0.03	0.49	1.61	5.07	2.78	0.08	0.17	98.18
	MZ2208JC1_gl09	73.64	0.45	13.76	1.86	0.05	0.4	1.5	5.3	2.8	0.07	0.17	99.7
	MZ2208JC1_gl10	73.26	0.39	14.21	1.91	0.04	0.47	1.54	5.03	2.94	0.03	0.18	97.5
81	MZ2208SG1_gl01	72.73	0.42	14.43	1.9	0.06	0.46	1.63	5.34	2.82	0.03	0.18	99.87
	MZ2208SG1_gl02	72.97	0.45	14.37	1.91	0.04	0.42	1.59	5.29	2.72	0.07	0.16	98.33
	MZ2208SG1_gl04	72.87	0.45	14.44	1.95	0.04	0.45	1.54	5.13	2.85	0.09	0.19	99.1
	MZ2208SG1_gl05	72.89	0.43	14.39	1.94	0.04	0.43	1.53	5.31	2.78	0.1	0.16	99.21
	MZ2208SG1_gl06	73.01	0.4	14.18	1.91	0	0.47	1.57	5.36	2.82	0.11	0.17	98.97
	MZ2208SG1_gl09	72.78	0.44	14.26	1.93	0.04	0.44	1.53	5.48	2.83	0.09	0.18	99.11
	MZ2208SG1_gl10	73.27	0.41	14.12	1.91	0.05	0.45	1.48	5.21	2.83	0.07	0.19	97.62
101	MZ2308BH1_gl01	73.02	0.44	14.04	1.93	0.04	0.5	1.63	5.3	2.83	0.09	0.18	99.06
	MZ2308BH1_gl02	73.13	0.46	14.18	1.89	0.03	0.41	1.59	5.31	2.73	0.08	0.19	98.86
	MZ2308BH1_gl03	72.95	0.41	14.16	1.93	0.04	0.43	1.71	5.25	2.84	0.1	0.18	99.39
	MZ2308BH1_gl04	72.86	0.4	14.44	1.9	0.04	0.43	1.59	5.16	2.9	0.09	0.19	98.45
	MZ2308BH1_gl05	73.09	0.44	14.17	1.9	0.03	0.43	1.49	5.32	2.9	0.06	0.17	98.95
	MZ2308BH1_gl06	73.01	0.42	14.03	1.94	0.03	0.43	1.63	5.38	2.89	0.04	0.2	97.7
	MZ2308BH1_gl07	72.17	0.37	14.8	1.97	0.06	0.48	1.65	5.43	2.82	0.06	0.18	99.3
	MZ2308BH1_gl09	72.84	0.41	14.33	1.97	0.05	0.41	1.54	5.4	2.79	0.08	0.18	99.99
	MZ2308BH1_gl10	73.15	0.42	14.14	1.88	0.05	0.43	1.69	5.06	2.91	0.1	0.17	98.66
84	MZ2408GR4_gl01	72.59	0.41	14.33	1.98	0.05	0.44	1.64	5.51	2.78	0.08	0.18	98.25
	MZ2408GR4_gl02	72.5	0.44	14.47	1.98	0.05	0.45	1.51	5.58	2.77	0.09	0.16	98.81
	MZ2408GR4_gl03	72.71	0.43	14.22	1.97	0.04	0.5	1.67	5.38	2.81	0.07	0.19	98.48
	MZ2408GR4_gl04	72.59	0.39	14.41	1.92	0.06	0.43	1.75	5.4	2.82	0.07	0.16	99.94

Table B.1: Major element geochemical data for Mazama glass *cont.*

Location ID	Sample ID	SiO_2	TiO_2	Al_2O_3	FeO	MnO	MgO	CaO	Na_2O	K_2O	P_2O_5	Cl	Analytical Total
	MZ2408GR4_gl05	72.98	0.45	14.08	1.92	0.05	0.47	1.65	5.33	2.83	0.07	0.17	99.78
	MZ2408GR4_gl06	72.94	0.43	14.44	1.96	0.05	0.44	1.57	5.1	2.82	0.05	0.19	98.04
	MZ2408GR4_gl07	73.1	0.45	14.08	1.9	0.03	0.49	1.51	5.33	2.85	0.07	0.19	98.4
	MZ2408GR4_gl08	72.96	0.44	14.42	1.92	0.04	0.41	1.55	5.23	2.81	0.05	0.17	98.42
	MZ2408GR4_gl09	73.18	0.44	14.25	1.93	0.06	0.45	1.57	5.17	2.68	0.1	0.18	99.03
	MZ2408GR4_gl10	72.98	0.44	14.37	1.86	0.03	0.43	1.55	5.28	2.83	0.08	0.15	100.43
69	MZ2408PB1_gl01	73.04	0.45	14.22	1.93	0.04	0.44	1.65	5.2	2.77	0.08	0.18	100.47
	MZ2408PB1_gl02	72.79	0.38	14.26	1.98	0.05	0.45	1.65	5.4	2.77	0.1	0.17	100.37
	MZ2408PB1_gl03	73.17	0.44	14.15	1.91	0.06	0.47	1.6	5.14	2.82	0.05	0.19	99.92
	MZ2408PB1_gl04	73.24	0.44	14.18	1.91	0.06	0.41	1.62	5.14	2.76	0.07	0.17	99.54
	MZ2408PB1_gl05	72.74	0.44	14.52	1.89	0.07	0.44	1.7	5.2	2.76	0.07	0.17	100.81
	MZ2408PB1_gl06	73.22	0.41	14.26	1.89	0	0.43	1.53	5.32	2.67	0.08	0.19	100.14
	MZ2408PB1_gl07	72.83	0.38	14.44	1.9	0.04	0.47	1.62	5.35	2.74	0.04	0.19	101.24
	MZ2408PB1_gl08	73.37	0.37	14.05	1.87	0.05	0.44	1.41	5.49	2.68	0.07	0.19	99.67
	MZ2408PB1_gl09	72.61	0.42	14.28	1.98	0.05	0.42	1.56	5.52	2.92	0.07	0.17	99.97
	MZ2408PB1_gl10	72.9	0.44	14.19	1.92	0.07	0.48	1.71	5.25	2.77	0.1	0.17	100.16
73	MZ2408AP1_gl1	73.01	0.39	14.29	1.95	0.05	0.44	1.57	5.17	2.88	0.08	0.17	97.94
	MZ2408AP1_gl2	72.74	0.44	14.09	1.89	0.07	0.44	1.53	5.59	2.93	0.11	0.17	97.26
	MZ2408AP1_gl3	72.67	0.41	14.5	1.88	0.07	0.42	1.68	5.37	2.78	0.04	0.18	97.62
	MZ2408AP1_gl6	72.55	0.42	14.41	1.93	0.06	0.49	1.73	5.43	2.75	0.05	0.18	99.13
	MZ2408AP1_gl7	73.11	0.45	14.38	1.89	0.03	0.44	1.57	5.07	2.81	0.08	0.16	98.58
	MZ2408AP1_gl8	72.74	0.42	14.46	1.92	0.04	0.43	1.61	5.27	2.86	0.07	0.16	98.61
	MZ2408AP1_gl9	72.62	0.42	14.49	1.93	0.06	0.46	1.64	5.28	2.85	0.07	0.18	98.57
	MZ2408AP1_gl10	73.09	0.46	14.3	1.9	0.06	0.4	1.49	5.2	2.84	0.09	0.17	97.34
	MZ2408AP1_gl11	72.66	0.42	14.35	1.91	0.04	0.4	1.68	5.5	2.83	0.05	0.16	98.37
	MZ2408AP1_gl12	72.97	0.4	14.2	1.92	0.04	0.47	1.51	5.38	2.83	0.1	0.18	98.18
	MZ2408AP1_gl13	72.6	0.49	14.26	1.9	0.04	0.39	1.58	5.64	2.84	0.07	0.19	97.99
	MZ2408AP1_gl14	72.53	0.46	14.29	2	0.05	0.45	1.66	5.5	2.8	0.08	0.18	97.68
	MZ2408AP1_gl15	73.7	0.41	13.86	1.9	0.04	0.43	1.43	5.19	2.81	0.06	0.17	98.31
	MZ2408AP4_gl01	73.03	0.43	14.12	1.86	0.06	0.45	1.54	5.46	2.79	0.07	0.19	98.28

Table B.1: Major element geochemical data for Mazama glass *cont.*

Location ID	Sample ID	SiO_2	TiO_2	Al_2O_3	FeO	MnO	MgO	CaO	Na_2O	K_2O	P_2O_5	Cl	Analytical Total
	MZ2408AP4_gl02	72.3	0.4	14.52	1.97	0.04	0.47	1.61	5.63	2.8	0.06	0.19	97.98
	MZ2408AP4_gl03	72.71	0.45	14.12	1.88	0.07	0.43	1.55	5.63	2.89	0.08	0.18	99.28
	MZ2408AP4_gl04	72.71	0.44	14.32	1.96	0.07	0.43	1.63	5.36	2.83	0.07	0.18	98.79
	MZ2408AP4_gl05	72.8	0.41	14.33	1.97	0.07	0.46	1.68	5.34	2.72	0.04	0.17	99.27
	MZ2408AP4_gl06	72.82	0.42	14.27	1.91	0.05	0.46	1.56	5.38	2.87	0.09	0.17	98.32
	MZ2408AP4_gl07	73.05	0.42	14.16	1.92	0.05	0.41	1.46	5.33	2.94	0.08	0.17	98.78
	MZ2408AP4_gl08	72.98	0.43	14.15	2.02	0.05	0.42	1.63	5.33	2.75	0.06	0.18	98.61
	MZ2408AP4_gl09	73.04	0.42	14.05	1.92	0.04	0.44	1.6	5.38	2.85	0.07	0.18	99.62
	MZ2408AP4_gl10	72.94	0.44	14.07	1.93	0.05	0.47	1.62	5.51	2.73	0.06	0.18	98.4
50	MZ69c_10mic	73.05	0.44	14.49	1.95	0.05	0.45	1.43	4.99	2.95	0.05	0.15	98.91
	MZ69c_1mic	72.78	0.46	14.82	1.97	0.07	0.42	1.56	4.86	2.83	0.06	0.17	98.47
	MZ69c_10mic_02	73.18	0.45	14.41	1.96	0.05	0.45	1.62	4.89	2.76	0.06	0.17	98.78
	MZ69c_10mic_03	73.06	0.45	14.33	1.94	0.04	0.44	1.53	5.16	2.83	0.05	0.16	99.23
	MZ69c_10mic_04	73.19	0.45	14.39	1.98	0.06	0.46	1.49	5.1	2.62	0.08	0.17	99.89
	MZ69c_10mic_05	72.86	0.44	14.54	1.95	0.05	0.45	1.58	5.14	2.74	0.05	0.19	98.66
	MZ69c_10mic_06	72.77	0.44	14.35	2	0.05	0.46	1.67	5.1	2.92	0.06	0.17	98.93
	MZ69c_10mic_07	73.24	0.44	14.28	1.99	0.06	0.42	1.51	5.02	2.78	0.08	0.17	100.26
	MZ69c_10mic_08	72.79	0.43	14.42	1.97	0.07	0.44	1.68	5.06	2.89	0.07	0.17	98.12
	MZ69c_10mic_09	72.77	0.4	14.42	1.97	0.03	0.46	1.72	5.29	2.68	0.06	0.19	98.03
	MZ69c_10mic_10	72.77	0.41	14.36	1.9	0.07	0.44	1.52	5.39	2.9	0.05	0.18	98.34
	MZ69_10mic_01	72.75	0.45	14.52	1.99	0.05	0.46	1.66	5.05	2.84	0.05	0.17	99.1
	MZ69_10mic_02	73.1	0.45	14.25	1.94	0.07	0.44	1.65	5.15	2.72	0.05	0.17	99.71
	MZ69_10mic_03	73.3	0.43	14.22	1.98	0.05	0.44	1.63	4.92	2.78	0.08	0.18	97.44
	MZ69_10mic_04	73.28	0.42	14.24	1.96	0.07	0.46	1.54	4.94	2.86	0.07	0.16	99.42
	MZ69_10mic_05	73.58	0.46	13.79	2	0.06	0.45	1.57	5.07	2.77	0.05	0.19	99.38
	MZ69_10mic_07	72.94	0.43	14.49	1.91	0.04	0.45	1.54	5.19	2.78	0.06	0.17	98.12
	MZ69_10mic_08	72.84	0.45	14.57	1.84	0.05	0.45	1.51	5.29	2.79	0.04	0.17	99.55
	MZ69_10mic_09	72.8	0.44	14.49	1.93	0.07	0.44	1.67	5.16	2.74	0.07	0.18	98.98
	MZ71c_10mic_03	72.9	0.41	14.49	2.02	0.04	0.46	1.55	5.08	2.83	0.07	0.15	99.76
	MZ71c_10mic_04	72.84	0.45	14.56	2	0.05	0.46	1.56	5.21	2.63	0.06	0.17	99.88

Table B.1: Major element geochemical data for Mazama glass *cont.*

Location ID	Sample ID	SiO_2	TiO_2	Al_2O_3	FeO	MnO	MgO	CaO	Na_2O	K_2O	P_2O_5	Cl	Analytical Total
	MZ71c_10mic_05	72.86	0.44	14.56	2.03	0.07	0.47	1.61	5.12	2.63	0.03	0.18	99.36
	MZ71c_10mic_07	73.27	0.44	14.31	1.93	0.04	0.44	1.44	4.98	2.92	0.06	0.17	97.18
	MZ71c_10mic_08	73.08	0.44	14.12	1.93	0.06	0.45	1.58	5.23	2.86	0.06	0.18	97.88
	MZ71c_10mic_09	74.28	0.48	13.57	1.95	0.05	0.42	1.34	4.92	2.74	0.06	0.18	99.59
	MZ71_10mic_01	72.94	0.43	14.17	1.95	0.04	0.47	1.6	5.25	2.9	0.06	0.19	99.53
	MZ71_10mic_02	73.17	0.43	14.33	2	0.05	0.46	1.54	5.04	2.76	0.06	0.17	99.29
	MZ71_10mic_03	72.79	0.43	14.43	1.97	0.05	0.45	1.5	5.35	2.8	0.07	0.16	98.63
	MZ71_10mic_04	73.02	0.44	14.14	2.08	0.05	0.47	1.56	5.22	2.76	0.07	0.19	97.8
	MZ71_10mic_05	73.75	0.47	14	1.96	0.06	0.43	1.41	4.87	2.82	0.06	0.17	98.06
55	MZ72_10mic_01	73.14	0.45	14.19	2.01	0.04	0.46	1.54	5.14	2.8	0.06	0.16	98.01
	MZ72_10mic_02	73.27	0.43	14.31	1.97	0.04	0.41	1.56	4.9	2.85	0.08	0.17	97.4
	MZ72_10mic_03	73.35	0.46	14.02	1.9	0.06	0.41	1.44	5.32	2.79	0.07	0.17	97.6
	MZ72_10mic_06	73.15	0.42	14.38	1.93	0.04	0.39	1.49	5.23	2.76	0.04	0.16	99.2
	MZ72_10mic_07	73.25	0.45	14.28	1.91	0.05	0.41	1.46	5.06	2.86	0.08	0.18	99.79
	MZ72_10mic_08	73.1	0.44	14.65	1.91	0.05	0.43	1.37	5.09	2.73	0.05	0.17	99.1
	MZ72_10mic_09	73.38	0.47	13.87	2.04	0.06	0.47	1.41	5.08	2.79	0.12	0.31	98.84
	MZ72_10mic_10	74.11	0.45	13.55	1.96	0.06	0.45	1.38	4.92	2.7	0.11	0.31	98.07
	MZ72_10mic_11	73.82	0.44	13.84	1.95	0.04	0.39	1.36	5.03	2.89	0.07	0.17	100.3
	MZ72_10mic_12	73.7	0.46	13.87	1.91	0.05	0.42	1.55	5.14	2.69	0.05	0.16	96.74
	MZ72_10mic_13	73.13	0.44	14.21	1.9	0.07	0.46	1.6	5.28	2.65	0.07	0.19	99.81
	MZ72_10mic_14	73.28	0.43	14.37	1.98	0.03	0.45	1.41	5.09	2.73	0.07	0.16	99.46
	MZ72_10mic_15	72.99	0.4	14.37	1.97	0.03	0.44	1.72	5.06	2.76	0.09	0.17	99.71
	MZ73_10mic_01	72.81	0.4	14.27	2	0.04	0.46	1.68	5.15	2.93	0.06	0.19	99.72
	MZ73_10mic_02	73.1	0.43	14.29	1.92	0.05	0.44	1.63	4.97	2.95	0.06	0.16	99
	MZ73_10mic_03	73.05	0.42	14.38	1.95	0.08	0.46	1.54	5.03	2.85	0.05	0.18	99.03
	MZ73_10mic_04	73.49	0.45	13.89	2.03	0.06	0.48	1.52	5.08	2.74	0.07	0.19	97.64
	MZ73_10mic_05	73.01	0.44	14.53	1.99	0.06	0.45	1.63	4.9	2.75	0.06	0.17	98.3
	MZ73_10mic_06	73.15	0.42	14.16	1.96	0.04	0.43	1.53	5.27	2.79	0.08	0.16	98.54
	MZ73_10mic_07	73.04	0.42	14.24	2.03	0.07	0.44	1.54	5.14	2.87	0.04	0.17	99.36
	MZ73_10mic_08	73.25	0.42	14.33	1.95	0.07	0.43	1.51	5.03	2.76	0.07	0.18	98.9

Table B.1: Major element geochemical data for Mazama glass *cont.*

Location ID	Sample ID	SiO_2	TiO_2	Al_2O_3	FeO	MnO	MgO	CaO	Na_2O	K_2O	P_2O_5	Cl	Analytical Total
	MZ73_10mic_09	73.04	0.43	14.03	2.2	0.08	0.47	1.66	4.97	2.85	0.06	0.2	99.53
	MZ73_10mic_10	73.62	0.42	14.01	1.92	0.07	0.45	1.47	4.96	2.84	0.07	0.17	98.96
	MZ74_10mic_01	73.05	0.45	14.37	1.9	0.05	0.46	1.65	5.12	2.75	0.04	0.16	98.65
	MZ74_10mic_02	73	0.42	14.46	1.95	0.06	0.44	1.68	5	2.77	0.04	0.17	98.91
	MZ74_10mic_03	72.88	0.42	14.51	1.91	0.04	0.43	1.57	5.14	2.83	0.08	0.18	97.35
	MZ74_10mic_05	73.36	0.46	14.02	2.02	0.03	0.46	1.6	5.04	2.73	0.08	0.19	97.39
	MZ74_10mic_06	72.76	0.44	14.57	1.98	0.07	0.46	1.73	5.12	2.61	0.07	0.19	98.17
	MZ74_10mic_07	73.37	0.46	14.06	2.07	0.04	0.49	1.48	5	2.78	0.06	0.18	97.12
	MZ74_10mic_08	72.72	0.45	14.4	2	0.04	0.44	1.62	5.27	2.8	0.08	0.18	98.87
	MZ74_10mic_09	73.33	0.45	14.32	1.89	0.04	0.43	1.53	5.05	2.71	0.06	0.18	98.34
	MZ74_10mic_10	74.02	0.47	13.74	2	0.04	0.45	1.36	4.97	2.67	0.09	0.18	98.19
46 (LPU)	mz66_mag_gl4	73.65	0.42	13.43	2.51	0.04	0.38	1.38	5.21	2.77	0.04	0.17	98
	mz66_mag_gl5	72.47	0.47	14.18	2.59	0.07	0.45	1.52	5.17	2.86	0.06	0.15	98.22
	mz66_mag_gl7	73.58	0.46	13.75	2.32	0.03	0.44	1.36	5.11	2.72	0.04	0.19	97.42
	mz66_mag_gl8	72.95	0.38	14.26	2.27	0	0.41	1.52	5.14	2.86	0.04	0.17	97.23
	mz66_mag8_gl	72.64	0.47	14.23	2.55	0.03	0.42	1.55	5.2	2.67	0.06	0.18	97.61
	mz66_mag15_gl	72.85	0.42	13.98	2.61	0	0.36	1.4	5.46	2.71	0.05	0.15	98.93
	mz66_mag_gl9	72.61	0.39	13.84	2.52	0.06	0.54	1.76	5.41	2.51	0.12	0.24	97.91
	mz66_mag10_gl	73.06	0.43	14.14	2.33	0.05	0.38	1.37	5.25	2.8	0.03	0.16	97.06
	mz66_mag_gl10	72.63	0.4	14.5	2.37	0.03	0.4	1.4	5.32	2.74	0.05	0.16	97.85
	mz66_mag_gl11	73.5	0.39	14.01	2.26	0.03	0.38	1.71	4.84	2.66	0.05	0.17	97.34
	mz66_mag_gl12	73.03	0.43	13.83	2.52	0.03	0.38	1.56	5.33	2.64	0.09	0.16	97.64
	mz66_mag_gl13	72.4	0.43	14.36	2.77	0	0.37	1.57	5.2	2.67	0.05	0.18	98.21
	mz66_mag_gl14	72.99	0.39	14.07	2.07	0	0.39	1.48	5.47	2.91	0.06	0.17	98.91
	mz66_mag_gl15	72.97	0.41	14.5	2	0	0.41	1.67	5.16	2.67	0.06	0.15	97.05
	mz66_ilm10_gl1	72.33	0.56	14.22	2.56	0.06	0.38	1.58	5.43	2.64	0.06	0.17	98.24
	mz66_ilm10_gl2	72.36	0.69	14.19	2.56	0	0.42	1.45	5.15	2.98	0.04	0.15	98.82
	mz66_mag20_MI	72.41	0.49	14.14	2.83	0	0.38	1.43	5.21	2.88	0.06	0.16	98.54
	mz66_mag14_gl2	75.56	0.43	13.64	2.32	0.04	0.39	1.48	3.04	2.88	0.06	0.16	97.51
	mz66_mag13_MI	73.45	0.47	13.52	2.46	0.04	0.35	1.19	5.06	3.17	0.1	0.19	97.22

Table B.1: Major element geochemical data for Mazama glass *cont.*

Location ID	Sample ID	SiO_2	TiO_2	Al_2O_3	FeO	MnO	MgO	CaO	Na_2O	K_2O	P_2O_5	Cl	Analytical Total
	mz66_mag14_gl1	73.03	0.45	13.95	2.6	0	0.39	1.59	5.15	2.64	0.04	0.16	97.92
	mz65_mag_gl3	72.96	0.43	14.09	2.14	0.03	0.45	1.56	5.34	2.76	0.07	0.16	97.71
	mz65_mag_gl4	73.13	0.5	13.81	2.58	0.03	0.38	1.46	5.17	2.7	0.06	0.17	97.54
	mz65_mag_gl5	73.12	0.43	13.95	2.36	0.05	0.4	1.52	5.31	2.63	0.05	0.18	98.18
	mz65_mag_gl6	73.08	0.39	14.07	2.51	0.03	0.36	1.42	5.24	2.67	0.06	0.17	97.42
	mz65_mag_gl7	73.16	0.45	14.04	2.23	0	0.37	1.53	5.31	2.69	0.06	0.16	99.2
	mz65_mag_gl8	73.11	0.42	14.4	1.99	0	0.39	1.5	5.2	2.77	0.03	0.18	97.32
	mz65_mag_gl9	73.07	0.38	13.99	2.16	0.04	0.46	1.52	5.25	2.93	0.05	0.15	98.75
	mz65_mag_gl10	72.91	0.49	14.17	2.32	0.04	0.41	1.25	5.39	2.79	0.08	0.14	97.34
	mz65_mag_gl11	73.39	0.33	13.88	2.23	0.04	0.44	1.36	5.18	2.92	0.07	0.15	99.51
	mz65_mag_gl14	72.46	0.49	13.93	2.74	0.03	0.41	1.6	5.45	2.67	0.04	0.18	98.63
	mz65_mag19_gl1	73.1	0.44	14.12	2.33	0.03	0.4	1.27	5.28	2.83	0.05	0.15	98.43
	mz65_mag_gl15	72.93	0.41	14.03	2.31	0.06	0.37	1.45	5.34	2.88	0.06	0.15	98.32
	mz65_mag_gl16	72.78	0.39	14.14	2.37	0.04	0.43	1.36	5.26	2.99	0.06	0.18	97.07
	mz65_mag_gl17	72.98	0.41	13.87	2.4	0.03	0.41	1.43	5.47	2.78	0.06	0.16	98.13
	mz65_mag_gl18	72.65	0.42	14.14	2.45	0.06	0.36	1.49	5.63	2.57	0.04	0.18	97.85
	mz65_mag_gl19	73.56	0.4	14	2.02	0	0.4	1.44	5.3	2.64	0.07	0.17	97.06
	mz65_mag_gl20	73.5	0.41	13.91	2.43	0.04	0.38	1.35	5.08	2.69	0.05	0.16	98.21
	mz65_mag_gl21	72.99	0.47	14.08	2.1	0.05	0.39	1.6	5.27	2.84	0.03	0.18	98.04
	mz65_mag_gl22	72.86	0.41	14.28	2.23	0.05	0.38	1.54	5.17	2.84	0.07	0.17	98.97
	mz65_mag_gl24	73.4	0.47	14.26	2.06	0	0.37	1.39	5.2	2.62	0.06	0.17	97.55
	mz65_mag_gl25	72.88	0.45	14.12	2.3	0.03	0.46	1.48	5.43	2.62	0.07	0.15	98.23
46 (DA)	mz64_mag_gl1	72.92	0.43	14.08	2.27	0.06	0.35	1.58	5.41	2.7	0.03	0.17	97.67
	mz64_mag03_gl	72.73	0.42	14.3	2.35	0	0.33	1.72	5.44	2.49	0.06	0.16	99.13
	mz64_mag_gl2	72.88	0.41	14.25	2.48	0.04	0.45	1.23	5.36	2.57	0.05	0.28	98.02
	mz64_mag_gl3	73.11	0.42	13.88	2.34	0	0.37	1.39	5.49	2.76	0.07	0.17	97.88
	mz64_mag_gl4	72.88	0.42	14.27	2.24	0.07	0.36	1.56	5.28	2.72	0.04	0.16	99.23
	mz64_mag_gl5	72.82	0.42	14.09	2.21	0.04	0.4	1.8	5.16	2.82	0.06	0.17	97.94
	mz64_mag_gl5	72.63	0.5	14.19	2.76	0.05	0.38	1.5	5.04	2.73	0.05	0.17	101.8
	mz64_mag_gl6	74.59	0.46	14.35	2.85	0	0.38	1.5	2.78	2.91	0.03	0.15	99.67

Table B.1: Major element geochemical data for Mazama glass *cont.*

Location ID	Sample ID	SiO_2	TiO_2	Al_2O_3	FeO	MnO	MgO	CaO	Na_2O	K_2O	P_2O_5	Cl	Analytical Total
	mz64_mag_gl7	72.47	0.4	14.2	2.47	0.08	0.37	1.56	5.52	2.72	0.05	0.16	100.3
	mz64_mag_gl8	72.6	0.38	14.52	2.28	0.07	0.34	1.55	5.41	2.61	0.08	0.16	98.71
	mz64_mag_gl9	72.7	0.44	14.43	2.12	0.06	0.38	1.55	5.33	2.78	0.05	0.16	99.26
	mz64_mag_gl10	74.11	0.45	13.23	2.73	0	0.35	1.35	4.84	2.74	0.04	0.15	98.06
	mz64_mag_gl11	72.73	0.58	14.35	2.13	0.03	0.36	1.56	5.31	2.74	0.04	0.17	99.56
	mz64_mag_gl12	72.68	0.42	14.31	2.31	0.05	0.37	1.5	5.53	2.62	0.05	0.16	98.47
	mz64_mag_gl13	72.56	0.59	14.13	2.44	0.04	0.41	1.53	5.22	2.85	0.06	0.17	100.01
	mz64_mag_gl14	73.07	0.45	13.71	2.54	0.06	0.44	1.56	5.14	2.81	0.04	0.17	98.43
	mz64_mag_gl15	73.21	0.41	14.24	2.15	0.03	0.36	1.39	5.29	2.72	0.03	0.17	98.32
	mz64_mag_gl16	73.46	0.41	14.06	2.24	0.09	0.4	1.44	5.08	2.57	0.07	0.17	98.37
	mz64_mag_gl17	72.93	0.46	14	2.64	0	0.42	1.47	5.3	2.56	0.03	0.18	99.31
	mz64_mag_gl18	73.39	0.46	13.66	2.4	0.03	0.41	1.52	5.1	2.81	0.05	0.17	99.6
	mz64_mag_gl19	72.73	0.41	14.03	2.74	0.07	0.38	1.49	5.35	2.59	0.06	0.15	99.96
	mz64_mag_MI1	71.97	0.52	14.37	3.06	0.03	0.44	1.74	5.34	2.13	0.13	0.26	98.28
	mz64_mag_gl20	72.81	0.42	14.12	2.45	0.09	0.41	1.54	5.25	2.66	0.08	0.17	99.19
	mz64_mag_gl21	72.49	0.48	14.34	2.56	0.05	0.37	1.44	5.15	2.91	0.06	0.15	99.19
	mz64_mag_gl22	72.8	0.44	14.56	1.96	0.03	0.38	1.58	5.46	2.53	0.08	0.17	98.68
	mz64_mag_gl23	73.79	0.34	13.85	1.91	0.03	0.35	1.31	5.27	2.93	0.06	0.16	97.62
	mz64_mag_gl24	73.16	0.68	13.89	2.34	0.04	0.43	1.39	5.12	2.59	0.06	0.29	97.78
	mz64_mag_gl25	72.31	1.07	13.88	2.76	0.05	0.39	1.61	5.09	2.62	0.06	0.16	99.82
46 (UPU)	mz63_tp3_MI	72.57	0.66	14.14	2.45	0.03	0.44	1.5	5.14	2.88	0.03	0.16	97.05
	mz63_mag14_gl	73.05	0.38	14.13	2.37	0.05	0.46	1.52	5.35	2.49	0.04	0.16	100.75
	mz63_mag18_MI	73.09	0.42	13.72	2.77	0.03	0.4	1.46	4.95	2.91	0.07	0.18	97.88
	mz63_mag_gl1	72.73	0.45	14.05	2.31	0.05	0.45	1.53	5.5	2.72	0.04	0.17	100.38
	mz63_mag17_gl	73.05	0.39	13.87	2.39	0.06	0.45	1.57	5.42	2.57	0.07	0.16	100.51
	mz63_mag_gl2	72.42	0.41	14.31	2.76	0.06	0.41	1.43	5.46	2.47	0.1	0.17	99.38
	mz63_mag_gl3	72.84	0.41	13.93	2.43	0.06	0.45	1.47	5.54	2.64	0.07	0.16	97.77
	mz63_mag_gl5	72.46	0.41	14.15	2.59	0.04	0.44	1.46	5.34	2.89	0.05	0.17	99.38
	mz63_mag_MI1	72.2	0.42	14.36	3.03	0.06	0.44	1.56	5	2.71	0.06	0.16	97.83
	mz63_tp8_gl	72.12	0.56	14.02	2.7	0.07	0.45	1.67	5.36	2.83	0.06	0.16	99.67

Table B.1: Major element geochemical data for Mazama glass *cont.*

Location ID	Sample ID	SiO_2	TiO_2	Al_2O_3	FeO	MnO	MgO	CaO	Na_2O	K_2O	P_2O_5	Cl	Analytical Total
	mz63_mag08_gl	72.7	0.41	14.1	2.51	0.04	0.41	1.39	5.34	2.86	0.07	0.17	98.01
	mz63_mag_gl7	72.63	0.4	14.5	2.27	0.03	0.44	1.54	5.28	2.67	0.04	0.19	97.22
	mz63_mag03_gl	73	0.4	13.92	2.43	0.04	0.46	1.53	5.49	2.49	0.07	0.17	97.68
	mz63_mag04_gl	72.71	0.44	14.35	2.66	0.07	0.46	1.65	4.92	2.52	0.05	0.17	97.54
	mz63_mag_gl8	72.94	0.42	13.96	2.43	0.05	0.47	1.56	5.32	2.64	0.03	0.17	98.84
	mz63_mag_gl9	72.3	0.44	14.23	2.79	0.05	0.42	1.5	5.42	2.61	0.06	0.18	99.39
	mz63_mag_gl10	72.21	0.44	14.09	3	0.07	0.45	1.46	5.32	2.73	0.06	0.16	99.62
	mz63_mag_gl11	72.19	0.46	14.11	2.98	0.05	0.45	1.5	5.35	2.68	0.05	0.18	98.53
	mz63_mag_MI3	72.63	0.42	14.15	2.77	0	0.4	1.6	5.09	2.69	0.07	0.17	98
	mz63_mag_MI4	72.25	0.42	14.57	2.42	0.07	0.39	1.52	5.3	2.82	0.07	0.17	97.61
	mz63_mag_gl13	72.25	0.51	14.44	2.63	0	0.45	1.57	5.4	2.53	0.04	0.17	98.79
	mz63_mag_gl14	73.57	0.47	13.66	2.34	0.03	0.47	1.52	5.07	2.64	0.05	0.17	97.46
	mz63_mag_gl16	72.68	0.41	14.02	2.52	0.06	0.44	1.61	5.18	2.83	0.08	0.17	97.3
	mz63_mag13_MI	72.4	0.43	13.94	2.98	0.06	0.41	1.42	5.33	2.81	0.04	0.18	97.46
	mz62_tp3H_gl	72.96	0.44	14.41	2.1	0.03	0.45	1.5	5.08	2.8	0.07	0.16	98.82
	mz62_mag_gl1	72.7	0.45	14.5	2.28	0	0.44	1.5	5.42	2.46	0.06	0.19	98.46
	mz62_mag_gl2	72.85	0.36	14.37	2.39	0	0.44	1.54	5.41	2.42	0.05	0.17	98
	mz62_mag_gl3	73.91	0.44	13.62	2.2	0.04	0.36	1.37	5.31	2.56	0.03	0.16	98.6
	mz62_mag_gl4	72.73	0.4	14.12	2.59	0	0.4	1.58	5.35	2.59	0.07	0.17	98.88
	mz62_mag_gl5	72.8	0.37	14.29	2.37	0.04	0.41	1.5	5.21	2.8	0.02	0.18	98.11
	mz62_mag_gl7	72.55	0.38	13.94	2.46	0.09	0.44	1.67	5.54	2.71	0.05	0.17	98.85
	mz62_mag_gl8	72.87	0.37	14.18	2.24	0.05	0.39	1.49	5.41	2.78	0.06	0.16	99.56
	mz62_mag_gl9	72.82	0.37	14.13	2.4	0.05	0.33	1.48	5.44	2.71	0.1	0.16	99.31
	mz62_mag10_gl	72.47	0.48	14.2	2.88	0.06	0.45	1.36	5.2	2.68	0.05	0.17	97.94
	mz61_mag01H_gl	72.19	0.39	14.08	2.54	0.04	0.47	1.54	5.83	2.67	0.08	0.17	99.01
	mz61_mag01H_gl	74.4	0.46	14.83	2.58	0.04	0.46	1.79	2.41	2.79	0.04	0.19	97.8
	mz61_mag_gl2	72.89	0.41	14.34	2.16	0.04	0.41	1.29	5.58	2.66	0.05	0.17	99.32
	mz61_mag_gl3	72.79	0.41	14.31	2.28	0.06	0.35	1.5	5.53	2.56	0.03	0.18	97.77
	mz61_mag_gl4	72.6	0.42	14.06	2.41	0.05	0.47	1.39	5.49	2.87	0.06	0.17	99.78
	mz61_mag_gl5	73.37	0.47	14.05	2.19	0.08	0.44	1.37	5.12	2.68	0.06	0.17	98.81

Table B.1: Major element geochemical data for Mazama glass *cont.*

Location ID	Sample ID	SiO_2	TiO_2	Al_2O_3	FeO	MnO	MgO	CaO	Na_2O	K_2O	P_2O_5	Cl	Analytical Total
	mz61_mag_MI	71.64	0.47	14.22	2.96	0.05	0.46	1.63	5.7	2.51	0.06	0.29	98.14
	mz61_mag_gl6	72.94	0.41	14	2.42	0	0.42	1.57	5.31	2.69	0.07	0.16	97.28
	mz61_mag_gl8	73.23	0.42	14.16	2.09	0.03	0.41	1.66	5.18	2.58	0.05	0.18	97.58
	mz61_mag_gl9	72.65	0.47	14.25	2.26	0.04	0.43	1.54	5.23	2.91	0.05	0.17	99.65
	mz61_mag_gl10	73.69	0.51	13.35	2.65	0	0.39	1.36	5.23	2.47	0.07	0.28	99.63
	mz61_mag_gl11	74.09	0.41	13.4	2.06	0.03	0.42	1.43	5.16	2.76	0.06	0.17	98.37
	mz61_mag_gl12	74.56	0.42	13.69	1.91	0.04	0.34	1.27	4.88	2.68	0.04	0.16	97.9
	mz61_mag_gl13	72.86	0.39	14.28	2.17	0.05	0.41	1.51	5.45	2.67	0.03	0.17	98.95
	mz61_mag_gl15	72.77	0.4	14.03	2.09	0.04	0.4	1.64	5.6	2.81	0.06	0.16	97.42
	mz61_mag_gl16	73.27	0.47	13.89	2.14	0.07	0.42	1.4	5.23	2.76	0.04	0.31	98.06
	mz61_mag_gl17	72.65	0.42	14.49	2.29	0.03	0.38	1.41	5.35	2.75	0.05	0.17	97.97
	mz61_mag_MI2	72.48	0.49	14.08	3.18	0.03	0.41	1.43	4.89	2.78	0.06	0.17	97.37
	mz61_mag_gl18	72.49	0.44	14.39	2.44	0.04	0.4	1.57	5.3	2.68	0.08	0.17	97.82
	mz61_mag_gl19	73.02	0.41	13.94	2.64	0.06	0.42	1.41	5.38	2.49	0.06	0.17	97.17
	mz61_mag_gl20	73.05	0.42	13.89	2.48	0.03	0.38	1.29	5.48	2.75	0.06	0.17	97.8
	mz61_mag_gl22	72.39	0.47	14.34	2.65	0.04	0.37	1.56	5.22	2.76	0.04	0.15	99.31
	mz61_mag_gl23	72.96	0.41	14.22	2.11	0.04	0.44	1.51	5.42	2.66	0.06	0.17	98.12
	mz61_mag_gl24	72.74	0.41	14.21	2.68	0.07	0.41	1.53	5.19	2.52	0.06	0.18	98.26
	mz61_mag_gl25	72.59	0.44	14.04	2.31	0	0.53	1.66	5.43	2.6	0.08	0.31	98.78
	mz60_tp3H_gl	70.48	0.64	14.84	2.98	0.06	0.55	1.97	5.72	2.56	0.06	0.14	100.61
	mz60_mag20_MI	72.71	0.4	14.53	2.31	0.04	0.41	1.44	5.27	2.64	0.09	0.15	101.04
	mz60_mag_gl1	73.03	0.39	14.19	2.53	0.03	0.37	1.39	5.12	2.71	0.06	0.17	97.06
	mz60_mag_gl2	72.66	0.41	14.23	2.38	0	0.41	1.47	5.52	2.72	0.03	0.17	98.51
	mz60_mag_gl3	72.72	0.38	14.18	2.5	0.05	0.39	1.42	5.23	2.92	0.03	0.17	98.5
	mz60_mag_gl4	72.23	0.4	14.65	2.44	0.04	0.37	1.56	5.24	2.86	0.03	0.17	98.49
	mz60_mag_gl5	72.4	0.5	13.99	3.03	0.06	0.45	1.48	5.36	2.5	0.05	0.18	99.45
	mz60_mag_gl6	72.79	0.39	14.34	2.46	0.03	0.4	1.45	5.17	2.73	0.06	0.18	99.07
	mz60_mag_gl7	72.32	0.47	13.9	2.96	0.08	0.44	1.37	5.44	2.82	0.04	0.16	98.52
	mz60_mag_gl8	72.98	0.42	14.21	2.34	0	0.41	1.36	5.4	2.63	0.08	0.17	100.71
	mz60_mag_gl9	72.87	0.48	14.07	2.37	0.07	0.44	1.38	5.26	2.77	0.1	0.18	99.34

Table B.1: Major element geochemical data for Mazama glass *cont.*

Location ID	Sample ID	SiO_2	TiO_2	Al_2O_3	FeO	MnO	MgO	CaO	Na_2O	K_2O	P_2O_5	Cl	Analytical Total
	mz60_mag_gl10	72.41	0.45	13.88	3.06	0.03	0.42	1.53	5.45	2.55	0.04	0.18	99.46
	mz60_mag_gl11	73.09	0.37	14.47	1.94	0.05	0.32	1.45	5.19	2.89	0.07	0.15	99.96
	mz60_mag_gl12	72.48	0.45	14.46	2.53	0.04	0.37	1.4	5.47	2.54	0.09	0.17	98.71
	mz60_mag_gl13	72.34	0.39	14.01	2.62	0.05	0.42	1.59	5.69	2.67	0.04	0.17	101.15
	mz60_mag_gl14	72.61	0.44	14.18	2.29	0.03	0.4	1.66	5.47	2.68	0.06	0.18	99.27
	mz60_mag_gl16	73.04	0.44	14.08	2.48	0.04	0.44	1.33	5.24	2.67	0.05	0.19	97.61
	mz60_mag_gl17	71.8	0.43	14.5	2.92	0	0.37	1.63	5.27	2.83	0.06	0.18	98.3
	mz60_mag_gl18	72.97	0.44	14.2	2.4	0	0.45	1.46	5.13	2.71	0.07	0.17	97.91
	mz60_mag_gl19	72.21	0.45	14.6	2.44	0.06	0.42	1.52	5.39	2.68	0.08	0.15	98.27
	mz60_mag_gl20	73.75	0.44	13.79	2.23	0.04	0.38	1.25	5.05	2.83	0.07	0.16	98.29
	mz60_mag_gl21	72.53	0.41	14.37	2.47	0.06	0.45	1.54	5.36	2.59	0.03	0.18	98.15
46 (co-PDC)[a]	mz59_gl13	58.89	1.4	14.95	8.85	0.12	3.56	6.4	3.87	1.52	0.4	0.04	98.16
	mz59_gl03_unk	58.85	1.56	14.54	9.64	0.11	3.22	5.72	4.27	1.67	0.37	0.04	99.38
	mz59_gl08_unk	55.97	1.8	14.9	11.69	0.17	4.25	6.68	3.18	0.89	0.41	0.06	101.12
	mz59_gl09	53.99	2.13	14.43	12.55	0.17	4.47	6.65	3.95	0.93	0.66	0.06	99.98
	mz59_gl10	53.76	2.1	14.75	12.66	0.17	4.38	6.52	3.89	1.05	0.67	0.05	100.65
	mz59_gl12	57.34	1.76	15.06	11.24	0.15	4.29	5.11	3.3	1.21	0.48	0.06	100.28
	mz59_gl14	56.48	2.23	13.42	13.03	0.17	3.4	6.2	3.65	0.78	0.58	0.06	100.29
	mz59_gl16_bas	56.87	1.98	14.58	11.98	0.12	3.95	3.27	4.86	1.77	0.56	0.06	100.63
	mz59_gl17_bas	59.01	1.51	14.33	9.72	0.12	3.47	5.5	4.2	1.73	0.37	0.04	101.02
46 (co-PDC)	mz59_gl01	72.14	0.37	14.32	2.61	0.06	0.42	1.62	5.64	2.58	0.06	0.18	98.78
	mz59_gl02	73.01	0.41	14.22	2.28	0.04	0.45	1.41	5.17	2.78	0.06	0.17	97.97
	mz59_gl05	73	0.39	14.2	2.32	0	0.39	1.43	5.27	2.79	0.05	0.16	97.64
	mz59_gl06	74.47	0.43	13.32	2.13	0.04	0.42	1.37	4.83	2.74	0.08	0.17	97.88
	mz59_gl07	72.09	0.41	14.42	2.51	0.03	0.39	1.56	5.39	2.93	0.09	0.18	98.47
	mz59_gl11	72.91	0.4	14.07	2.3	0.06	0.47	1.45	5.41	2.66	0.09	0.18	98.87
	mz59_gl15	72.02	0.43	14.59	2.78	0.07	0.35	1.5	5.44	2.55	0.09	0.17	100.11
	mz59_gl18	72.59	0.41	14.5	2.5	0.05	0.38	1.42	5.32	2.59	0.08	0.16	99.95
	mz59_gl19	72.39	0.45	14.32	2.23	0.06	0.43	1.47	5.45	2.94	0.09	0.17	98.38
47 (co-PDC)	mzTL_gl2	75.01	0.29	13.48	1.69	0	0.23	1.19	4.47	3.48	0.08	0.08	99.85

Table B.1: Major element geochemical data for Mazama glass *cont.*

Location ID	Sample ID	SiO_2	TiO_2	Al_2O_3	FeO	MnO	MgO	CaO	Na_2O	K_2O	P_2O_5	Cl	Analytical Total
	mzTL_gl3	72.72	0.39	14.41	2.07	0	0.47	1.64	5.16	2.93	0.04	0.17	98.83
	mzTL_gl4	73.42	0.39	13.95	2.14	0.05	0.42	1.49	5.33	2.59	0.05	0.17	97.92
	mzTL_gl5	77.19	0.42	11.66	1.79	0	0.2	0.53	3.9	4.17	0.02	0.12	98.38
	mzTL_gl6	76.82	0.45	11.63	2.07	0.04	0.25	0.89	4.19	3.35	0.05	0.25	99.8
	mzTL_gl7	72.48	0.46	14.3	2.62	0.06	0.39	1.52	5.34	2.61	0.05	0.17	98.64
	mzTL_gl8	76.95	0.37	11.51	1.83	0	0.18	0.63	3.56	4.74	0.03	0.2	99.61
	mzTL_gl9	72.47	0.58	13.8	2.41	0.07	0.59	1.81	5.4	2.36	0.22	0.29	97.96
	mzTL_gl10	73.37	0.44	14.04	2.11	0	0.47	1.48	5.26	2.58	0.08	0.17	98.09
	mzTL_gl11	76.31	0.45	11.78	2	0	0.22	0.59	3.96	4.41	0	0.27	101.26
	mzTL_gl12	73.78	0.45	13.54	2.07	0.04	0.47	1.53	5.33	2.58	0.05	0.16	99.26
	mzTL_gl13	73.12	0.38	14.12	2.06	0	0.43	1.59	5.11	2.96	0.06	0.17	98.74
	mzTL_gl14	73.38	0.42	13.84	2.1	0.05	0.42	1.45	5.37	2.72	0.06	0.18	97.83
	mzTL_gl1	67.99	0.66	15.7	4.07	0.05	0.93	2.53	5.67	2.14	0.14	0.13	98.81
	mzTL_gl15_smll	66.53	0.76	15.75	4.53	0.06	1.13	3.08	5.53	2.2	0.27	0.11	99.35
	mzTL_gl16_smll	64.75	0.91	16.3	4.62	0.04	1.9	3.75	5.37	1.84	0.34	0.2	100

(a) Anomalous compositions found in co-PDC unit at site 46

Table B.2: Major element geochemical data for secondary glass standards

Standard ID	Analysis ID	SiO_2	TiO_2	Al_2O_3	FeO	MnO	MgO	CaO	Na_2O	K_2O	P_2O_5	Cl	F	Analytical Total
KN18	kn18	74.96	0.16	10.45	3.52	0.04	0.01	0.15	5.28	4.57		0.33	0.52	98.81
	kn18	74.85	0.16	10.43	3.48	0.06		0.21	5.33	4.63		0.33	0.54	98.84
	kn18	75.19	0.17	10.38	3.55	0.05		0.12	5.22	4.57		0.32	0.43	99.45
	steen kn18	75.12	0.17	10.38	3.59	0.05	0.02	0.13	5.11	4.59		0.33	0.56	98.33
	steen kn18	75.15	0.18	10.39	3.47	0.06	0.02	0.12	5.26	4.56		0.32	0.49	99.07
	steen kn18	74.79	0.17	10.41	3.57	0.05		0.26	5.26	4.51		0.32	0.68	99.6
	steen kn18	74.87	0.18	10.52	3.52	0.08		0.13	5.31	4.59		0.32	0.52	99.23
	steen kn18	74.94	0.14	10.53	3.53	0.05		0.11	5.3	4.61		0.33	0.5	98.83
	steen kn18	74.66	0.18	10.47	3.56	0.06	0	0.17	5.41	4.52		0.31	0.68	99.42
	steen kn18	74.68	0.18	10.53	3.48	0.07		0.21	5.36	4.64		0.33	0.55	98.84
	steen kn18	74.99	0.16	10.34	3.59	0.08		0.1	5.29	4.59		0.34	0.55	98.46
	steen kn18	74.73	0.16	10.43	3.58	0.06		0.18	5.24	4.66		0.32	0.67	98.48
	steen kn18	74.83	0.17	10.38	3.53	0.06		0.07	5.45	4.63		0.32	0.57	98.71
	steen kn18	74.98	0.18	10.43	3.49	0.05		0.11	5.25	4.66		0.33	0.51	98.84
	steen kn18	75.01	0.18	10.38	3.58	0.06	0.01	0.12	5.14	4.68		0.34	0.51	98.17
	steen kn18	74.56	0.15	10.58	3.57	0.05		0.08	5.51	4.6		0.33	0.58	99.13
	steen kn18	74.99	0.18	10.46	3.56	0.06		0.08	5.24	4.6		0.33	0.52	99.26
	steen kn18	74.86	0.15	10.47	3.51	0.08		0.19	5.32	4.48		0.32	0.64	100.38
	steen kn18	75.18	0.17	10.36	3.53	0.05		0.05	5.29	4.57		0.33	0.5	100.4
	steen kn18	74.98	0.17	10.51	3.45	0.05		0.05	5.31	4.57		0.32	0.61	100.04
	steen kn18	74.78	0.18	10.5	3.5	0.07		0.18	5.32	4.59		0.33	0.58	100.44
	KM_KN18_3	74.56	0.18	10.45	3.55	0.07	0	0.29	5.32	4.55		0.33	0.71	99.37
	KM_KN18_3	75.02	0.22	10.45	3.54	0.05	0.01	0.05	5.24	4.52		0.32	0.58	100.13
	KM_KN18_3	74.89	0.13	10.62	3.54	0.05		0.09	5.3	4.53		0.31	0.56	100.12
	KM_KN18_1	74.79	0.16	10.39	3.6	0.06	0.03	0.08	5.55	4.65		0.33	0.37	99.15
	KM_KN18_1	74.62	0.17	10.55	3.61	0.06	0.03	0.1	5.49	4.58		0.32	0.49	99.29
	KM_KN18_1	74.96	0.2	10.54	3.56	0.05	0.04	0.17	5.1	4.67		0.33	0.43	97.27
	KN_KN18_2	74.93	0.17	10.28	3.58	0.06	0	0.15	5.33	4.6		0.34	0.54	99.21
	KN_KN18_2	74.77	0.17	10.49	3.46	0.05		0.33	5.21	4.48		0.31	0.75	99.87
	KN18__001	74.67	0.16	10.7	3.5	0.06	0.01	0.11	5.28	4.59		0.33	0.58	99.54

Table B.2: Major element geochemical data for secondary glass standards *cont.*

Standard ID	Analysis ID	SiO_2	TiO_2	Al_2O_3	FeO	MnO	MgO	CaO	Na_2O	K_2O	P_2O_5	Cl	F	Analytical Total
	KN18__001	74.68	0.16	10.54	3.61	0.04		0.29	5.21	4.52		0.32	0.64	99.33
	KN18__001	75.1	0.15	10.67	3.53	0.06	0	0.13	4.98	4.47		0.33	0.59	99.65
	KN18__001	74.88	0.19	10.51	3.44	0.03	0	0.09	5.45	4.52		0.32	0.59	99.77
	KN18__001	75.06	0.17	10.6	3.58	0.05	0	0.12	4.89	4.53		0.33	0.67	98.9
	KN18_1micTDI	74.24	0.17	10.89	3.47	0.1	0	0.03	5.5	4.78		0.32	0.51	99.87
	KN18_1micTDI	74.68	0.16	10.79	3.6	0.06	0	0.02	5.24	4.58		0.33	0.53	99.99
	KN18_1micTDI	74.64	0.15	10.59	3.66	0.08	0	0.04	5.31	4.75		0.31	0.49	99.46
	KN18_1micTDI	74.68	0.17	10.86	3.6	0.1	0	0.06	5.33	4.32		0.31	0.58	99.31
	KN18_10mic_end	74.61	0.14	10.55	3.55	0.06	0	0.42	4.9	4.63		0.32	0.85	99.45
	KN18_10mic_end	74.53	0.19	10.49	3.53	0.06	0	0.36	5.18	4.58		0.31	0.75	100.08
	KN18_10mic_end	74.67	0.18	10.61	3.61	0.04	0.01	0.1	5.36	4.5		0.33	0.6	100.06
	KN18_10mic_end	75.08	0.16	10.59	3.58	0.05		0.14	5.06	4.35		0.33	0.65	99.73
	SteenKN18_secstd2	75.38	0.13	10.29	3.72	0.06	0	0.06	5.18	4.34		0.31	0.52	98.62
	SteenKN18_secstd2	74.92	0.16	10.14	3.58	0		0.29	5.42	4.57		0.33	0.6	99.06
	SteenKN18_secstd2	75.15	0.18	10.37	3.65			0.15	5.25	4.54		0.31	0.41	98.73
	SteenKN18_secstd2	74.61	0.19	10.25	3.63	0		0.56	5.46	4.24		0.31	0.73	99.3
	SteenKN18_secstd2	75.07	0.17	10.45	3.66	0.06	0.01	0.07	5.43	4.27		0.35	0.47	98.31
	SteenKN18_secstdend	75.58	0.16	9.97	3.66	0.05		0.21	5.25	4.33		0.33	0.45	98.07
	SteenKN18_secstdend	75.22	0.15	10.4	3.64	0.03		0.18	5.19	4.48		0.32	0.4	99.65
	SteenKN18_secstdend	75.5	0.14	9.99	3.7	0.04	0	0.07	5.26	4.51		0.32	0.48	99.44
	SteenKN18_secstdend	74.83	0.16	10.49	3.69	0.03		0.17	5.15	4.57		0.31	0.6	99.04
	SteenKN18_secstdend	74.73	0.16	10.57	3.59	0.03		0.26	5.37	4.42		0.32	0.53	98.67
	SteenKN18_secstdend	74.96	0.14	10.74	3.65	0.01	0.01	0.08	5.27	4.41		0.3	0.42	98.9
	SteenKN18_secstdend2	74.31	0.14	10.58	3.95	0.07	0.01	0.18	5.24	4.65		0.31	0.57	99.16
	SteenKN18_secstdend2	74.35	0.17	10.44	3.77	0.04		0.61	5.21	4.35		0.31	0.79	98.67
	SteenKN18_secstdend2	75.06	0.17	10.47	3.84	0.03	0	0.08	5.27	4.29		0.32	0.46	99.19
	SteenKN18_secstdend2	74.41	0.15	10.4	3.86	0.07	0	0.34	5.29	4.46		0.31	0.73	99.03
	SteenKN18_secstdend2	75.03	0.14	10.59	4.03	0.05	0.02	0.17	4.61	4.56		0.32	0.49	98.6
	SteenKN18_secstdend2	74.16	0.11	10.64	3.81	0.03		0.24	5.7	4.37		0.33	0.65	99.02
BCR2	bcr2	54.78	2.33	13.55	12.78	0.19	3.6	7.35	3.13	1.86	0.38	0.01	0.03	97

Table B.2: Major element geochemical data for secondary glass standards *cont.*

Standard ID	Analysis ID	SiO_2	TiO_2	Al_2O_3	FeO	MnO	MgO	CaO	Na_2O	K_2O	P_2O_5	Cl	F	Analytical Total
	bcr2	55.2	2.32	13.41	12.75	0.23	3.62	7.08	3.16	1.9	0.35	0.01		97.04
	bcr2	55.06	2.29	13.39	12.77	0.21	3.64	7.25	3.13	1.85	0.34	0.01	0.05	97.34
	bcr2	54.95	2.31	13.48	12.63	0.18	3.7	7.12	3.3	1.88	0.39	0.01	0.04	98
	bcr2	54.98	2.29	13.4	12.63	0.22	3.63	7.2	3.34	1.87	0.39	0.02	0.05	97.53
	bcr2	54.85	2.26	13.47	12.64	0.18	3.67	7.32	3.35	1.86	0.37	0.01	0.03	98.05
	bcr2	54.89	2.28	13.64	12.73	0.19	3.66	7.22	3.13	1.86	0.35	0.01	0.03	97.19
	bcr2	55.15	2.38	13.55	12.62	0.19	3.6	7.19	3.06	1.91	0.34	0.01	0.01	96.83
	bcr2	55.26	2.28	13.58	12.54	0.18	3.75	6.97	3.22	1.86	0.39	0		98.05
	bcr2	55.25	2.27	13.5	12.56	0.21	3.7	7.05	3.28	1.84	0.35	0.03		97.93
	bcr2	55.33	2.29	13.5	12.43	0.19	3.65	7.04	3.34	1.84	0.38	0.01		97.68
	bcr2	55.1	2.31	13.68	12.56	0.18	3.68	7.32	2.97	1.84	0.34	0.01	0	97.44
	bcr2	55.08	2.34	13.55	12.5	0.17	3.64	7.08	3.37	1.88	0.35	0.01	0.03	97.5
Lipari	G1_Lipari_secstd	74.87	0.03	12.99	1.58	0.07	0.04	0.71	4.02	5.23		0.32	0.12	99.18
	G1_Lipari_secstd	75.11	0.08	12.78	1.55	0.06	0.04	0.77	4.01	5.08		0.33	0.18	99.27
	G1_Lipari_secstd	75.13	0.1	13.01	1.59	0.08	0.05	0.76	3.92	4.93		0.33	0.1	99.5
	G1_Lipari_secstd	75.11	0.06	12.62	1.59	0.03	0.04	0.7	4.07	5.37		0.33	0.08	98.26
	G1_Lipari_secstd	75.04	0.09	12.74	1.59	0.04	0.02	0.68	4.19	5.1		0.34	0.14	99.18
	G1_Lipari_secstd	74.99	0.05	12.56	1.64	0.06	0.01	0.74	4.18	5.34		0.33	0.09	99.92
	G1_Lipari_secstdend2	75.05	0.05	13.13	1.62	0.02	0.05	0.59	3.95	5.12		0.35	0.05	97.66
	G1_Lipari_secstdend2	75.02	0.07	13.01	1.65	0.04	0.04	0.62	4.12	5		0.34	0.07	99.18
	G1_Lipari_secstdend2	74.85	0.05	12.85	1.7	0.03	0.03	0.67	4.14	5.23		0.34	0.1	99.11
	G1_Lipari_secstdend2	74.91	0.08	13	1.76	0.01	0.04	0.71	4.03	5.05		0.34	0.09	98.33
	G1_Lipari_secstdend2	74.87	0.08	13.09	1.71	0.05	0.05	0.69	4.02	5.04		0.36	0.08	98.42
	G1_Lipari_secstdend2	74.56	0.06	13.27	1.58	0.05	0.05	0.72	4.31	4.89		0.34	0.16	99.22
KE12	G1_KE12_secstd	71.24	0.29	7.48	8.68	0.19	0.01	0.39	6.87	4.25		0.31	0.25	99.11
	G1_KE12_secstd	71.02	0.29	7.41	8.69	0.22	0.03	0.28	7.24	4.26		0.29	0.25	99.32
	G1_KE12_secstd	71	0.29	7.62	8.64	0.19	0	0.38	7	4.22		0.31	0.33	100.47
	G1_KE12_secstd	70.45	0.32	7.54	8.89	0.19	0.01	0.48	7.22	4.28		0.3	0.3	99.83
	G1_KE12_secstd	71.05	0.3	7.51	8.72	0.19	0.02	0.44	6.87	4.32		0.29	0.28	99.48
	G1_KE12_secstd	71.13	0.28	7.28	8.77	0.14	0.02	0.39	7.03	4.32		0.3	0.36	99.9

Table B.2: Major element geochemical data for secondary glass standards *cont.*

Standard ID	Analysis ID	SiO_2	TiO_2	Al_2O_3	FeO	MnO	MgO	CaO	Na_2O	K_2O	P_2O_5	Cl	F	Analytical Total
	G1_KE12_secstdend	70.77	0.31	7.56	9.03	0.18	0.02	0.4	7.15	3.97		0.3	0.28	98.77
	G1_KE12_secstdend	70.95	0.28	7.46	9.04	0.22	0.01	0.32	6.78	4.22		0.31	0.37	97.81
	G1_KE12_secstdend	70.95	0.28	7.75	8.69	0.19	0.01	0.27	6.99	4.3		0.28	0.26	99.38
	G1_KE12_secstdend	70.95	0.31	7.53	8.76	0.18	0.03	0.32	7.05	4.23		0.31	0.3	99.18
	G1_KE12_secstdend	70.75	0.25	7.5	8.9	0.18		0.32	7.1	4.31		0.3	0.37	98.88
	G1_KE12_secstdend	70.7	0.25	7.62	8.95	0.18	0.02	0.23	7.21	4.21		0.29	0.33	99.93
	G1_KE12_secstdend2	70.39	0.25	7.51	9.21	0.19	0.02	0.32	7.04	4.43		0.29	0.33	99.66
	G1_KE12_secstdend2	70.68	0.28	7.48	9.04	0.16	0.01	0.34	7.04	4.33		0.3	0.32	99.47
	G1_KE12_secstdend2	70.27	0.33	7.57	9.26	0.18	0.02	0.33	7.1	4.27		0.29	0.35	98.79
	G1_KE12_secstdend2	70.79	0.31	7.41	9.21	0.22	0.03	0.37	6.78	4.22		0.31	0.31	99.48
	G1_KE12_secstdend2	70.44	0.32	7.68	9.18	0.15	0	0.37	6.91	4.31		0.3	0.3	98.56
	G1_KE12_secstdend2	70.58	0.28	7.52	9.32	0.16	0.02	0.34	6.86	4.22		0.3	0.37	99.75

Table B.3: Major element geochemical data for Mazama FeTi oxides

Location ID	Sample ID	TiO_2	Al_2O_3	FeO_t	FeO*	Fe_2O_3*	MnO	MgO	SiO_2	Cr_2O_3	$Total_t$	Total*
50	MZ069_tp1_mg	8.36	2.05	81.14	35.28	50.96	0.46	2.16	0.08	-	94.25	99.36
	MZ069_tp2_mg	9.08	2.04	80.76	36.01	49.72	0.51	2.12	0.07	-	94.58	99.56
	MZ069_tp3_mg	8.6	2.07	81.47	35.61	50.97	0.48	2.22	0.07	-	94.91	100.01
	MZ069_tp4_mg	8.67	2.04	81.68	35.79	51	0.49	2.16	0.07	-	95.11	100.22
	MZ069_tp5_mg	8.99	2.04	81.41	36.13	50.32	0.47	2.11	0.05	-	95.07	100.12
	MZ069_mg1	8.71	2.05	81.27	35.62	50.73	0.49	2.22	0.06	-	94.8	99.88
	MZ069_mg2	8.43	2.04	81.99	35.67	51.47	0.47	2.13	0.08	-	95.14	100.3
	MZ069_mg3	8.6	2.08	82.16	35.76	51.56	0.48	2.23	0.04	-	95.59	100.75
	MZ069_mg4	8.62	2.08	81.99	35.78	51.36	0.47	2.2	0.05	-	95.41	100.54
	MZ069_mg5	8.11	2.86	81.02	34.5	51.7	0.43	2.85	0.07	-	95.34	100.53
	MZ071_tp1_mg	9.04	2.04	81.37	36.2	50.2	0.52	2.13	0.1	-	95.2	100.22
	MZ071_tp2_mg	10.82	2.41	79.53	37.89	46.28	0.48	2.1	0.05	-	95.39	100.02
	MZ071_tp3_mg	8.49	2.09	82.01	35.59	51.59	0.5	2.24	0.05	-	95.38	100.55
	MZ071_tp4_mg	8.67	2.06	81.48	35.68	50.89	0.5	2.19	0.06	-	94.96	100.05
	MZ071_tp5_mg	8.79	1.99	81.57	35.72	50.95	0.5	2.25	0.04	-	95.14	100.25
	MZ071_mg1	8.92	2.01	81.57	36.11	50.52	0.47	2.13	0.08	-	95.18	100.25
	MZ071_mg2	11.3	2.89	77.95	37.34	45.13	0.39	2.85	0.07	-	95.45	99.96
	MZ071_mg3	11.69	3.05	77.45	37.57	44.31	0.42	3	0.09	-	95.7	100.14
	MZ071_mg4	8.56	2.04	81.81	35.49	51.48	0.48	2.34	0.06	-	95.29	100.45
	MZ071_mg5	8.65	2.06	81.8	35.77	51.14	0.5	2.18	0.07	-	95.26	100.37
55	MZ073_tp1_mg	8.96	2.05	81.58	36.01	50.64	0.5	2.2	0.04	-	95.33	100.4
	MZ073_tp2_mg	8.93	1.96	81.19	35.83	50.41	0.47	2.22	0.06	-	94.83	99.89
	MZ073_tp3_mg	8.87	2.03	81.89	36.06	50.93	0.49	2.19	0.06	-	95.53	100.63
	MZ073_tp4_mg	8.65	2.03	82	35.8	51.34	0.51	2.2	0.07	-	95.46	100.6
	MZ073_tp5_mg	9	1.99	81.45	36.19	50.3	0.48	2.11	0.09	-	95.12	100.15
	MZ073_mg1	7.41	3.99	80.11	34.15	51.08	0.26	2.77	0.1	-	94.64	99.76
	MZ073_mg2	10.23	2.32	80.27	37.34	47.71	0.44	2.17	0.07	-	95.5	100.28
	MZ073_mg3	11.72	2.98	78.19	37.9	44.77	0.4	2.91	0.08	-	96.28	100.76
	MZ073_mg4	8.84	2.56	81.38	35.54	50.95	0.5	2.63	0.04	-	95.95	101.06
	MZ073_mg5	8.07	2.62	81.75	34.52	52.49	0.46	2.85	0.03	-	95.78	101.04

Table B.3: Major element geochemical data for Mazama FeTi oxides *cont.*

Location ID	Sample ID	TiO_2	Al_2O_3	FeO_t	FeO*	Fe_2O_3*	MnO	MgO	SiO_2	Cr_2O_3	$Total_t$	Total*
	MZ074_tp1_mg	8.7	2.09	82.26	35.99	51.42	0.48	2.19	0.06	-	95.78	100.93
	MZ074_tp2_mg	8.89	1.99	81.84	36.12	50.81	0.53	2.12	0.08	-	95.45	100.54
	MZ074_tp3_mg	9.1	2	81.75	36.28	50.54	0.49	2.17	0.06	-	95.57	100.64
	MZ074_tp4_mg	8.84	2	81.89	35.93	51.08	0.5	2.27	0.07	-	95.57	100.69
	MZ074_tp5_mg	8.79	2.05	81.77	35.96	50.91	0.48	2.14	0.05	-	95.28	100.36
	MZ074_mg1	9.14	2.5	81.26	36.59	49.64	0.46	2.04	0.07	-	95.47	100.45
	MZ074_mg2	8.72	2.04	81.29	35.62	50.75	0.5	2.23	0.06	-	94.84	99.92
	MZ074_mg3	8.76	2.13	81.54	35.93	50.69	0.47	2.15	0.07	-	95.12	100.2
	MZ074_mg4	8.75	2.07	82.02	36.05	51.09	0.5	2.13	0.07	-	95.54	100.66
	MZ074_mg5	8.11	1.68	83.05	35.77	52.55	0.48	1.86	0.07	-	95.25	100.51
46 (LPU)	MZ18066_mag1	8.66	1.99	80.93	35.6	50.39	0.5	2.17	0.05	0	94.3	99.35
	MZ18066_mag3	8.82	2.02	81.14	35.94	50.23	0.46	2.15	0.06	0.04	94.69	99.72
	MZ18066_mag2	8.86	2.07	81.49	36.04	50.5	0.5	2.18	0.06	0.02	95.18	100.23
	MZ18066_mag4	8.94	2.09	81.48	36.42	50.07	0.5	2.12	0.06	0.06	95.25	100.27
	MZ18066_mag5	8.69	1.98	81.75	35.87	50.99	0.49	2.17	0.03	0.04	95.15	100.26
	MZ18066_mag6	8.52	2.08	81.2	35.7	50.56	0.51	2.11	0.06	0.06	94.54	99.59
	MZ18066_mag7	8.74	2.02	80.96	35.75	50.24	0.48	2.18	0.06	0.04	94.48	99.52
	MZ18066_mag8	8.75	2	81.52	35.87	50.73	0.48	2.15	0.06	0.02	94.98	100.07
	MZ18066_mag9	8.92	2.01	81.21	36	50.23	0.48	2.11	0.03	0.02	94.78	99.82
	MZ18066_mag10	8.89	2.04	81.27	36.18	50.12	0.44	2.16	0.06	0.07	94.93	99.96
	MZ18066_mag11	8.79	2.09	81.62	36.02	50.67	0.5	2.13	0.05	0.02	95.2	100.28
	MZ18066_mag12	8.85	2.07	80.77	35.82	49.95	0.5	2.14	0.06	0.03	94.42	99.42
	MZ18066_mag13	9	2.08	81.28	36.08	50.24	0.51	2.21	0.06	0.01	95.15	100.19
	MZ18066_mag14	8.64	2.05	81.04	35.62	50.47	0.48	2.18	0.05	0.02	94.46	99.52
	MZ18066_mag15	8.58	2.01	81.24	35.83	50.46	0.49	2.11	0.07	0.04	94.54	99.59
	MZ18066_mag16	8.97	2.1	81.56	36.25	50.35	0.47	2.16	0.07	0.03	95.36	100.4
	MZ18066_mag17	8.93	2.03	81.41	35.97	50.5	0.49	2.17	0.04	0.01	95.08	100.13
	MZ18066_mag18	7.19	2.05	82.54	34.65	53.22	0.47	1.95	0.04	0.02	94.26	99.6
	MZ18066_mag19	8.29	2.05	81.68	35.45	51.37	0.47	2.11	0.05	0.01	94.66	99.81
	MZ18066_mag20	8.82	2.07	81.05	35.75	50.34	0.5	2.18	0.05	0.01	94.68	99.73

Table B.3: Major element geochemical data for Mazama FeTi oxides *cont.*

Location ID	Sample ID	TiO_2	Al_2O_3	FeO_t	FeO*	Fe_2O_3*	MnO	MgO	SiO_2	Cr_2O_3	$Total_t$	Total*
	MZ18066_tp1_mg	8.98	2.02	80.65	36.03	49.59	0.46	2.17	0.04	0.06	94.38	99.37
	MZ18066_tp2_mg	8.97	2.1	81.64	36.22	50.47	0.48	2.22	0.02	0.05	95.48	100.53
	MZ18066_tp3_mg	8.96	2.05	81.17	36.06	50.14	0.52	2.15	0.04	0.03	94.92	99.95
	MZ18066_tp4_mg	8.91	2.05	81.42	36.15	50.31	0.49	2.11	0.06	0.03	95.07	100.11
	MZ18065_mag01	8.84	2.04	81.55	36.11	50.49	0.48	2.14	0.08	0.02	95.15	100.19
	MZ18065_mag02	8.94	2.11	81.71	36.35	50.41	0.49	2.08	0.04	0.04	95.41	100.46
	MZ18065_tp1_mg	8.97	2.04	81.7	36.38	50.37	0.49	2.12	0.02	0.04	95.38	100.44
	MZ18065_mag03	8.95	1.97	81.29	36.13	50.18	0.45	2.12	0.05	0.02	94.85	99.88
	MZ18065_mag04	8.78	2.08	81.56	36.06	50.57	0.45	2.11	0.05	0.02	95.05	100.11
	MZ18065_mag05	8.43	2.03	81.75	35.68	51.21	0.5	2.08	0.04	0.02	94.85	99.98
	MZ18065_mag06	8.38	2.08	81.75	35.75	51.12	0.49	2.01	0.06	0.04	94.81	99.92
	MZ18065_tp2_mg	8.78	2.07	81.86	36.11	50.84	0.5	2.16	0.04	0.03	95.44	100.52
	MZ18065_tp3_mg	8.86	2.07	81.55	36.09	50.51	0.47	2.17	0.06	0.02	95.2	100.25
	MZ18065_mag07	8.79	2.04	81.24	35.8	50.5	0.51	2.18	0.06	0.03	94.85	99.92
	MZ18065_mag08	8.76	2.08	81.15	35.94	50.25	0.49	2.12	0.05	0.04	94.69	99.74
	MZ18065_mag09	8.82	2.02	81.74	36.06	50.76	0.48	2.09	0.04	0.02	95.21	100.3
	MZ18065_mag10	8.75	2.05	81.76	36.05	50.8	0.49	2.09	0.07	0	95.21	100.3
	MZ18065_mag11	8.92	2.08	81.3	36.12	50.21	0.48	2.15	0.06	0.03	95.02	100.05
	MZ18065_mag12	8.18	2.65	81.53	35.06	51.64	0.52	2.49	0.06	0.01	95.44	100.6
	MZ18065_mag13	8.92	2.05	82.13	36.36	50.86	0.49	2.15	0.05	0.03	95.82	100.91
	MZ18065_mag14	7.37	2.46	82.13	34.54	52.88	0.46	2.29	0.06	0.04	94.81	100.11
	MZ18065_mag15	8.69	2.02	81.04	35.71	50.38	0.48	2.08	0.04	0.02	94.37	99.42
	MZ18065_mag16	8.88	2.1	81.02	36.01	50.02	0.45	2.14	0.03	0.05	94.67	99.69
	MZ18065_mag17	8.69	2.09	81.21	35.75	50.52	0.5	2.18	0.06	0.04	94.77	99.83
	MZ18065_mag18	8.58	2.12	81.72	35.88	50.94	0.49	2.09	0.05	0.02	95.07	100.17
	MZ18065_mag19	8.81	2.07	81.21	35.88	50.37	0.54	2.08	0.04	0.01	94.76	99.8
	MZ18065_mag20	8.88	2.03	81.22	35.94	50.32	0.49	2.14	0.05	0.02	94.83	99.86
	MZ18065_tp4_mg	8.82	2.01	80.9	35.87	50.04	0.46	2.14	0.05	0.05	94.43	99.44
	MZ18065_tp5_mg	8.97	2.09	81.44	36.23	50.25	0.48	2.11	0.04	0.03	95.16	100.2
	MZ18065_tp6_mg	8.92	2.05	80.93	36.04	49.89	0.49	2.09	0.06	0.02	94.56	99.56

Table B.3: Major element geochemical data for Mazama FeTi oxides *cont.*

Location ID	Sample ID	TiO_2	Al_2O_3	FeO_t	FeO*	Fe_2O_3*	MnO	MgO	SiO_2	Cr_2O_3	$Total_t$	Total*
46 (DA)	MZ18064_mag01	8.8	1.99	81.23	35.93	50.34	0.49	2.17	0.07	0.02	94.77	99.81
	MZ18064_mag02	8.86	2.08	82.44	36.37	51.2	0.48	2.2	0.05	0.04	96.15	101.28
	MZ18064_mag03	8.7	2.13	81.64	35.95	50.77	0.51	2.11	0.04	0.02	95.15	100.25
	MZ18064_mag04	8.84	2.09	81.62	36.07	50.62	0.49	2.14	0.05	0.02	95.25	100.32
	MZ18064_mag05	8.67	2	81.07	35.74	50.38	0.49	2.13	0.06	0.03	94.45	99.51
	MZ18064_mag06	8.85	2.13	81.25	35.95	50.34	0.45	2.13	0.07		94.87	99.91
	MZ18064_mag07	8.84	2.07	81.25	36	50.28	0.51	2.13	0.05	0.03	94.88	99.9
	MZ18064_mag08	8.87	2.08	81.22	36	50.26	0.48	2.14	0.03	0.03	94.85	99.88
	MZ18064_mag09	8.64	2.02	81.36	35.69	50.75	0.49	2.22	0.06	0.02	94.81	99.9
	MZ18064_mag10	8.78	2.08	80.74	35.81	49.92	0.47	2.09	0.04	0	94.2	99.2
	MZ18064_tp1_mg	8.97	2.06	81.1	36.08	50.03	0.52	2.13	0.05	0.02	94.85	99.86
	MZ18064_tp2_mg	8.76	1.99	81.36	35.91	50.51	0.48	2.15	0.07	0.02	94.83	99.89
	MZ18064_tp3_mg	9.09	2.1	81.47	36.59	49.88	0.44	2.11	0.06	0.03	95.3	100.3
	MZ18064_tp4_mg	9.09	2.1	81.26	36.42	49.84	0.51	2.11	0.06	0.04	95.17	100.16
	MZ18064_tp5_mg	9.22	1.97	81.19	36.44	49.73	0.5	2.15	0.08	0.05	95.16	100.15
	MZ18064_mag11	8.57	2.08	81.55	35.69	50.97	0.48	2.14	0.04	0.03	94.89	100
	MZ18064_mag12	8.83	2.05	81.61	36.16	50.5	0.48	2.1	0.02	0.05	95.14	100.2
	MZ18064_mag13	8.9	2.08	81.31	36.12	50.22	0.5	2.13	0.07	0.03	95.02	100.05
	MZ18064_mag14	8.05	2.19	82.1	35.73	51.53	0.51	2.12	0.08	0.05	95.1	100.25
	MZ18064_mag15	8.67	2.06	81.32	35.77	50.62	0.51	2.16	0.05	0.04	94.81	99.88
	MZ18064_mag16	8.82	2.06	81.5	35.89	50.68	0.5	2.28	0.08	0.02	95.26	100.34
	MZ18064_mag17	8.27	2.1	81.92	35.52	51.57	0.5	2.14	0.06	0.02	95.01	100.16
	MZ18064_mag18	8.58	2.08	81.71	35.82	51	0.49	2.15	0.05	0.03	95.09	100.2
	MZ18064_mag19	8.86	2.07	81.44	36.03	50.47	0.46	2.17	0.06	0.01	95.07	100.13
	MZ18064_mag20	8.91	2.07	81.42	36.11	50.36	0.46	2.15	0.03	0.03	95.07	100.13
46 (co-PDC)	MZ18059_mag01	8.82	2.11	81.82	36.17	50.73	0.47	2.11	0.05	0.01	95.39	100.48
	MZ18059_mag02	11.01	2.98	78.02	37.72	44.79	0.42	2.86	0.07	0.24	95.6	100.08
	MZ18059_mag03	8.58	2.03	81.51	35.71	50.9	0.47	2.18	0.05	0.03	94.85	99.96
	MZ18059_mag04	11.78	3.1	77.34	38.09	43.61	0.43	2.72	0.06	0.03	95.46	99.83
	MZ18059_mag05	8.78	2.02	81.39	36.03	50.4	0.49	2.04	0.07	0.02	94.81	99.86

Table B.3: Major element geochemical data for Mazama FeTi oxides *cont.*

Location ID	Sample ID	TiO_2	Al_2O_3	FeO_t	FeO*	Fe_2O_3*	MnO	MgO	SiO_2	Cr_2O_3	$Total_t$	Total*
	MZ18059_mag06	8.64	2.11	81.26	35.8	50.52	0.48	2.16	0.08	0.03	94.76	99.83
	MZ18059_mag07	8.28	2.05	81.57	35.39	51.31	0.5	2.14	0.05	0.02	94.61	99.76
	MZ18059_mag08	8.86	2.04	81.06	36.01	50.07	0.48	2.08	0.06	0.02	94.6	99.63
	MZ18059_mag09	8.15	3.54	79.87	34.85	50.03	0.3	2.8	0.08	0.05	94.79	99.81
	MZ18059_mag10	8.55	2.04	81.76	35.77	51.11	0.51	2.16	0.05	0.03	95.1	100.22
	MZ18059_mag11	8.91	2.05	80.82	35.92	49.89	0.5	2.1	0.08	0.01	94.47	99.45
	MZ18059_mag12	6.97	3.17	82	34.67	52.6	0.43	2.12	0.08	0.04	94.81	100.08
	MZ18059_mag13	8.99	2.1	82.03	36.51	50.59	0.47	2.17	0.05	0.04	95.85	100.92
	MZ18059_mag14	8.82	2.05	81.48	36.06	50.48	0.47	2.14	0.08	0.02	95.06	100.12
	MZ18059_mag15	9.01	2.1	81.53	36.34	50.22	0.48	2.14	0.05	0.04	95.35	100.38
	MZ18059_mag16	9.8	3.46	79.14	37.05	46.76	0.4	2.51	0.08	0.14	95.53	100.21
	MZ18059_mag17	8.79	2.04	81.38	35.89	50.55	0.47	2.15	0.05	0.03	94.91	99.97
	MZ18059_mag18	10.21	2.44	80.01	37.16	47.61	0.44	2.35	0.04	0.03	95.52	100.29
	MZ18059_mag19	10.81	3.13	77.91	37.67	44.73	0.38	2.81	0.07	0.23	95.34	99.82
	MZ18059_mag20	8.79	2.14	81.42	35.98	50.5	0.51	2.13	0.07	0.01	95.07	100.13
	MZ18059_mag21	8.82	2.11	81.77	36.05	50.8	0.54	2.17	0.06	0.03	95.5	100.59
	MZ18059_mag22	8.93	1.97	81.93	36.29	50.72	0.5	2.08	0.06	0.02	95.49	100.58
	MZ18059_mag23	8.92	2.1	81.73	36.33	50.45	0.47	2.1	0.05	0.02	95.39	100.44
	MZ18059_mag24	8.85	2.03	81.63	36.3	50.38	0.48	2.13	0.05	0.05	95.22	100.27
	MZ18059_mag25	6.98	3.38	80.64	32.68	53.29	0.33	3.47	0.08	0.02	94.9	100.24
	MZ18059_mag26	8.91	2.05	81.36	36.08	50.32	0.46	2.13	0.05	0.03	94.99	100.03
	MZ18059_mag27	8.89	2.06	80.99	35.96	50.05	0.46	2.15	0.05	0.03	94.63	99.65
	MZ18059_mag28	8.65	2.09	81.91	36.01	51.01	0.52	2.15	0.05	0.03	95.4	100.52
	MZ18059_mag29	10.79	2.95	78.12	37.2	45.47	0.35	2.7	0.05	0.05	95.01	99.55
	MZ18059_mag30	8.78	2.08	81.17	35.82	50.4	0.5	2.14	0.04	0.01	94.72	99.77
	MZ18059_tp1_mg	8.68	2.1	81.1	35.74	50.4	0.48	2.17	0.07	0.02	94.62	99.67
	MZ18059_tp2_mg	8.82	2.08	81.57	36.09	50.54	0.5	2.19	0.05	0.05	95.26	100.32
	MZ18059_tp3_mg	8.7	2	81.94	36	51.06	0.49	2.11	0.06	0.01	95.31	100.43
	MZ18059_tp4_mg	8.84	2.07	82.15	36.36	50.89	0.48	2.1	0.06	0.03	95.73	100.83
	MZ18059_tp5_mg	8.65	2.06	81.92	35.93	51.11	0.51	2.17	0.04	0.03	95.38	100.49

Table B.3: Major element geochemical data for Mazama FeTi oxides *cont.*

Location ID	Sample ID	TiO_2	Al_2O_3	FeO_t	FeO*	Fe_2O_3*	MnO	MgO	SiO_2	Cr_2O_3	$Total_t$	Total*
	MZ18059_tp6_mg	8.94	1.95	81.54	36.11	50.49	0.49	2.16	0.03	0.04	95.15	100.2
	MZ18059_tp7_mg	8.86	2.03	81.35	35.96	50.45	0.5	2.18	0.08	0.02	95.02	100.06
80	MZ17JC1_mag2	8.98	1.98	80.97	36.26	49.69	0.5	2.08	0.08	0.03	94.62	99.6
	MZ17JC1_mag3	8.63	1.84	81.2	35.74	50.52	0.51	2.12	0.1	0.02	94.42	99.48
	MZ17JC1_mag4	6.34	2.11	81.84	33.51	53.7	0.42	2.11	0.18	0.01	93.01	98.38
	MZ17JC1_mag5	8	2.13	80.88	35.07	50.92	0.49	2.12	0.11	0.05	93.78	98.88
67	MZ17BH1_mag2	8.43	2.09	80.45	35.29	50.19	0.5	2.25	0.07	0.07	93.86	98.9
69	MZ17PB1_mag1	8.55	2.09	81.99	35.98	51.13	0.49	2.14	0.06	0.05	95.37	100.47
73	MZ17AP1_mag1	8.87	1.98	80.74	36.24	49.45	0.5	2	0.09	0.08	94.26	99.21
	MZ17AP1_mag2	9.77	1.96	78.58	36.84	46.38	0.5	1.92	0.1	0.11	92.94	97.57
46 (UPU)	MZ18060_mag01	10.3	2.36	79.37	37.6	46.42	0.41	2.26	0.09	0.11	94.9	99.55
	MZ18060_mag02	10.88	2.56	78.98	37.71	45.86	0.38	2.54	0.06	0.12	95.52	100.12
	MZ18060_mag03	11.64	2.88	77.97	38.04	44.38	0.39	2.8	0.06	0.08	95.83	100.27
	MZ18060_mag04	11.9	3.06	76.89	37.85	43.38	0.37	3.04	0.07	0.09	95.41	99.76
	MZ18060_mag05	8.64	2.07	81.69	35.8	50.99	0.46	2.21	0.05	0.02	95.14	100.24
	MZ18060_mag06	8.68	2.01	81.52	35.74	50.87	0.5	2.17	0.04	0.02	94.93	100.03
	MZ18060_mag07	8.89	2.1	81.44	36.01	50.49	0.51	2.2	0.05	0.03	95.22	100.27
	MZ18060_mag08	8.8	2.04	81.58	35.79	50.88	0.47	2.25	0.06	0.01	95.2	100.29
	MZ18060_mag09	9.06	2.05	81.12	35.92	50.24	0.5	2.27	0.06	0.01	95.06	100.09
	MZ18060_mag10	10.87	2.44	79.27	37.84	46.03	0.42	2.4	0.08	0.07	95.55	100.16
	MZ18060_mag11	8.79	2.09	81.34	36.02	50.37	0.47	2.17	0.05	0.04	94.96	100.01
	MZ18060_mag12	11	3.35	77.56	37.11	44.95	0.35	3.18	0.06	0.13	95.62	100.13
	MZ18060_mag13	8.79	2.06	81.41	35.96	50.51	0.51	2.23	0.04	0.04	95.1	100.15
	MZ18060_mag14	8.8	2.11	81.27	35.83	50.5	0.5	2.21	0.07	0.02	94.98	100.04
	MZ18060_mag15	9.08	2.08	81.15	36.18	49.98	0.46	2.17	0.06	0.01	95.01	100.02
	MZ18060_mag16	8.92	2.06	80.97	35.76	50.24	0.52	2.26	0.04	0.02	94.79	99.82
	MZ18060_mag17	9.01	2.02	81.35	36.09	50.3	0.48	2.19	0.06	0.01	95.11	100.15
	MZ18060_mag18	10.81	2.56	79.26	37.81	46.07	0.4	2.4	0.05	0.1	95.58	100.2
	MZ18060_mag19	8.97	2.06	81.23	36.13	50.12	0.49	2.11	0.04	0.02	94.91	99.93
	MZ18060_mag20	8.83	2.1	80.96	35.8	50.18	0.48	2.19	0.05	0.03	94.65	99.67

Table B.3: Major element geochemical data for Mazama FeTi oxides *cont.*

Location ID	Sample ID	TiO_2	Al_2O_3	FeO_t	FeO*	Fe_2O_3*	MnO	MgO	SiO_2	Cr_2O_3	$Total_t$	Total*
	MZ18060_tp1_mg	9.03	2.02	81.18	36.1	50.11	0.5	2.17	0.04	0.02	94.96	99.98
	MZ18060_tp2_mg	9.1	2.04	81.07	36.33	49.72	0.51	2.24	0.07	0.01	95.04	100.02
	MZ18060_tp3_mg	10.68	2.43	79.62	37.88	46.38	0.42	2.26	0.03	0.06	95.5	100.15
	MZ18060_tp4_mg	9.18	2.01	81.21	36.42	49.77	0.52	2.1	0.08	0.03	95.13	100.11
	MZ18060_tp5_mg	8.95	2.09	81.26	36.02	50.28	0.52	2.2	0.07	0.02	95.12	100.16
	MZ18060_tp6_mg	8.83	2.04	80.8	35.6	50.23	0.49	2.26	0.05	0.02	94.49	99.52
	MZ18060_tp7_mg	8.74	2.03	81.21	35.7	50.58	0.47	2.22	0.05	0.02	94.75	99.81
	MZ18060_tp8_mg	10.93	2.39	79.13	37.9	45.82	0.46	2.24	0.06	0.05	95.26	99.85
	MZ18060_tp9_mg	8.94	1.99	81.14	35.9	50.28	0.52	2.21	0.06	0.02	94.88	99.92
	MZ18060_tp10_mg	9.04	2.04	80.76	36.01	49.73	0.48	2.22	0.08	0.02	94.63	99.61
	MZ18061_mag01	11.14	2.59	78.88	37.97	45.47	0.44	2.49	0.06	0.08	95.68	100.23
	MZ18061_mag02	10.01	2.42	79.74	36.65	47.88	0.5	2.6	0.06	0.1	95.43	100.23
	MZ18061_mag03	8.93	2.03	81.54	35.92	50.7	0.5	2.24	0.02	0.02	95.27	100.35
	MZ18061_mag04	10.86	3.51	77.94	37.01	45.48	0.36	3.08	0.08	0.03	95.86	100.42
	MZ18061_mag05	9.48	2.82	79.95	36.6	48.18	0.49	2.26	0.07	0.06	95.12	99.95
	MZ18061_mag06	8.99	2.08	81.31	36.12	50.21	0.48	2.23	0.04	0.04	95.17	100.2
	MZ18061_mag07	9.92	2.21	80.13	36.52	48.46	0.46	2.45	0.05	0.02	95.24	100.09
	MZ18061_mag08	8.64	2.02	81.52	35.8	50.81	0.49	2.17	0.05	0.03	94.91	100
	MZ18061_mag09	8.6	1.97	81.03	35.44	50.67	0.49	2.23	0.04	0.03	94.39	99.47
	MZ18061_mag10	8.82	2.06	81.24	36.07	50.2	0.48	2.12	0.05	0.04	94.82	99.85
	MZ18061_mag11	9.03	2.09	81.77	36.43	50.38	0.5	2.12	0.06	0.04	95.61	100.65
	MZ18061_mag12	10.22	2.81	78.96	37.16	46.45	0.39	2.43	0.04	0.12	94.97	99.62
	MZ18061_mag13	8.82	2.05	80.87	35.66	50.25	0.48	2.25	0.06	0.01	94.55	99.58
	MZ18061_mag14	9.01	2.09	81.4	36.12	50.32	0.5	2.22	0.07	0.02	95.3	100.34
	MZ18061_mag15	9.01	2.07	81.29	36.15	50.16	0.48	2.14	0.05	0.02	95.06	100.08
	MZ18061_mag16	11.12	2.71	78.64	37.72	45.47	0.42	2.54	0.04	0.06	95.53	100.09
	MZ18061_mag17	11.48	2.66	78.64	38.26	44.87	0.46	2.57	0.06	0.1	95.96	100.46
	MZ18061_mag18	9.19	3.25	79.41	35.95	48.3	0.39	2.73	0.07	0.11	95.15	99.98
	MZ18061_mag19	8.57	2.02	81	35.54	50.52	0.45	2.17	0.05	0.03	94.29	99.35
	MZ18061_mag20	8.96	2.09	81.26	36.02	50.28	0.51	2.14	0.04	0.01	95.01	100.05

Table B.3: Major element geochemical data for Mazama FeTi oxides *cont.*

Location ID	Sample ID	TiO_2	Al_2O_3	FeO_t	FeO*	Fe_2O_3*	MnO	MgO	SiO_2	Cr_2O_3	$Total_t$	Total*
	MZ18061_tp1_mg	8.94	2.03	81.57	36.08	50.56	0.52	2.23	0.04	0.04	95.37	100.43
	MZ18061_tp2_mg	8.71	2.08	81.66	35.78	50.99	0.51	2.24	0.06	0.02	95.28	100.39
	MZ18061_tp3_mg	9.22	2.08	80.95	36.29	49.62	0.5	2.2	0.05	0.04	95.04	100.01
	MZ18061_tp4_mg	8.9	2.06	81.09	35.97	50.14	0.48	2.19	0.07	0.04	94.82	99.84
	MZ18061_tp5_mg	8.82	2.02	81.47	35.85	50.69	0.49	2.24	0.03	0.03	95.11	100.18
	MZ18061_mag21	7.42	2.13	82.43	34.49	53.28	0.44	2.33	0.04	0.03	94.82	100.15
	MZ18061_mag22	8.52	2.02	81.36	35.54	50.91	0.51	2.18	0.06	0.03	94.68	99.78
	MZ18061_mag23	10.94	2.71	78.72	37.66	45.63	0.41	2.49	0.07	0.07	95.41	99.98
	MZ18061_mag24	8.78	2.02	81.5	35.93	50.65	0.5	2.23	0.06	0.05	95.13	100.2
	MZ18061_mag25	10.37	2.51	79.44	37.04	47.11	0.35	2.72	0.05	0.1	95.54	100.26
	MZ18062_mag01	13.06	2.77	76.98	39.87	41.24	0.51	2.32	0.07	0.09	95.8	99.93
	MZ18062_mag02	8.57	2.04	81.81	35.66	51.28	0.46	2.21	0.06	0	95.14	100.28
	MZ18062_mag03	11.15	2.75	78.58	37.67	45.46	0.43	2.64	0.05	0.06	95.67	100.22
	MZ18062_mag04	8.95	2.03	81.39	36.11	50.32	0.51	2.15	0.04	0.03	95.09	100.13
	MZ18062_mag05	9.02	2.15	81.17	36.23	49.94	0.48	2.15	0.03	0.05	95.05	100.05
	MZ18062_mag06	9	2.07	81.28	36.09	50.21	0.48	2.18	0.05	0.02	95.08	100.11
	MZ18062_mag07	12.65	2.92	76.87	39.2	41.86	0.48	2.51	0.09	0.06	95.59	99.78
	MZ18062_mag08	8.68	2.14	81.64	35.89	50.84	0.5	2.17	0.02	0.04	95.18	100.27
	MZ18062_mag09	8.7	2.09	81.49	35.9	50.67	0.49	2.15	0.06	0.02	95.01	100.08
	MZ18062_mag10	8.69	2.04	81.45	35.87	50.66	0.45	2.15	0.06	0.03	94.87	99.94
	MZ18062_mag11	12.12	3.09	76.54	37.95	42.89	0.45	3	0.07	0.08	95.36	99.65
	MZ18062_mag12	9.03	2.06	81	35.97	50.04	0.47	2.17	0.06		94.78	99.79
	MZ18062_mag12	8.79	2.01	81.51	35.87	50.73	0.51	2.26	0.07	0.03	95.2	100.28
	MZ18062_mag13	8.87	2.09	81.57	35.89	50.77	0.49	2.29	0.04	0.03	95.39	100.47
	MZ18062_mag14	8.3	2.27	82.13	36.22	51.01	0.34	1.94	0.06	0.1	95.13	100.24
	MZ18062_mag15	10.58	2.55	79.35	37.67	46.33	0.44	2.31	0.06	0.09	95.39	100.03
	MZ18062_mag16	8.7	2.09	81.39	35.71	50.77	0.49	2.24	0.05	0.03	94.98	100.06
	MZ18062_mag17	11.88	2.93	77.95	38.02	44.38	0.47	2.91	0.06	0.03	96.22	100.67
	MZ18062_mag18	8.07	2.07	82.02	35.26	51.97	0.45	2.16	0.05	0.02	94.83	100.04
	MZ18062_mag19	8.64	2.02	81.19	35.67	50.58	0.47	2.13	0.09	0.01	94.55	99.61

Table B.3: Major element geochemical data for Mazama FeTi oxides *cont.*

Location ID	Sample ID	TiO_2	Al_2O_3	FeO_t	FeO*	Fe_2O_3*	MnO	MgO	SiO_2	Cr_2O_3	$Total_t$	Total*
	MZ18062_mag20	11.61	3.03	76.76	37.46	43.67	0.41	3.03	0.06	0.1	95	99.37
	MZ18062_tp1_mg	12.11	3.03	77.01	38.21	43.11	0.4	2.97	0.06	0.1	95.68	99.99
	MZ18062_tp2_mg	11.52	1.26	80.22	39.48	45.28	0.46	1.58	0.07	0.11	95.22	99.76
	MZ18062_tp3_mg1	8.78	2.03	81.55	35.97	50.66	0.48	2.21	0.08	0.04	95.17	100.24
	MZ18062_tp3_mg2	8.73	2.11	81.05	35.69	50.4	0.51	2.23	0.06	0.03	94.73	99.78
	MZ18062_tp4_mg	9.17	2.07	81.07	36.46	49.58	0.48	2.14	0.05	0.09	95.07	100.04
	MZ18062_tp5_mg	11.95	2.81	77.88	38.2	44.09	0.45	2.77	0.06	0.04	95.94	100.36
	MZ18062_tp6_mg	9.03	2.09	81.11	35.9	50.24	0.49	2.32	0.04	0.02	95.1	100.13
	MZ18062_tp7_mg	10.99	2.62	78.71	37.77	45.5	0.43	2.51	0.08	0.09	95.42	99.98
	MZ18062_tp8_mg	9.07	2.06	81.49	36.36	50.15	0.47	2.13	0.06	0.04	95.32	100.34
	MZ18062_mag21	8.81	2.07	81.22	35.8	50.48	0.5	2.22	0.07	0.02	94.89	99.95
	MZ18062_mag22	8.66	2.06	81.6	35.83	50.86	0.49	2.22	0.07	0.04	95.14	100.24
	MZ18063_mag01	8.74	2.09	81.48	35.82	50.74	0.5	2.2	0.05	0.02	95.08	100.16
	MZ18063_mag02	8.68	2.05	81.24	35.73	50.57	0.49	2.16	0.05	0.01	94.68	99.75
	MZ18063_mag03	9.11	2.06	81.88	36.41	50.53	0.51	2.13	0.05	0	95.74	100.8
	MZ18063_mag04	8.94	2.08	81.81	36.02	50.88	0.51	2.26	0.04	0.01	95.65	100.75
	MZ18063_mag05	8.88	2.04	81.85	36.15	50.79	0.49	2.16	0.07	0.01	95.51	100.6
	MZ18063_mag06	8.86	1.98	81.73	36	50.81	0.49	2.15	0.05	0.01	95.27	100.36
	MZ18063_mag07	8.79	2.11	81.53	35.99	50.6	0.5	2.15	0.06	0.01	95.16	100.22
	MZ18063_mag08	9	2.02	80.9	36.01	49.89	0.53	2.13	0.04	0.03	94.65	99.65
	MZ18063_mag09	8.78	2	81.68	35.96	50.8	0.51	2.13	0.06	0.03	95.18	100.27
	MZ18063_mag10	8.84	2.1	80.63	35.7	49.92	0.5	2.2	0.06	0.02	94.35	99.35
	MZ18063_mag11	8.58	2.15	81.7	35.85	50.95	0.46	2.13	0.04	0.02	95.07	100.17
	MZ18063_mag12	8.6	2.08	81.82	35.76	51.19	0.48	2.22	0.06	0.01	95.26	100.39
	MZ18063_mag13	8.7	2.02	80.54	35.54	50.02	0.48	2.15	0.05	0.02	93.97	98.98
	MZ18063_mag14	8.94	2.11	81.19	36.04	50.18	0.49	2.16	0.04	0.03	94.95	99.98
	MZ18063_mag15	8.86	2.11	81.68	36.15	50.6	0.5	2.15	0.08	0.01	95.39	100.45
	MZ18063_mag16	8.76	2.04	81.22	35.81	50.46	0.5	2.19	0.08	0.03	94.81	99.87
	MZ18063_mag17	8.46	2	81.63	35.68	51.06	0.48	2.07	0.06	0.01	94.7	99.82
	MZ18063_mag18	8.69	2.12	81.36	35.61	50.85	0.5	2.26	0.04	0.02	94.99	100.08

Table B.3: Major element geochemical data for Mazama FeTi oxides *cont.*

Location ID	Sample ID	TiO_2	Al_2O_3	FeO_t	FeO*	Fe_2O_3*	MnO	MgO	SiO_2	Cr_2O_3	$Total_t$	Total*
	MZ18063_mag19	8.69	2.02	81.76	35.88	50.99	0.48	2.18	0.04	0.03	95.2	100.31
	MZ18063_mag20	8.69	2.09	81.48	35.86	50.69	0.49	2.15	0.06	0.02	94.97	100.05
	MZ18063_tp1_mg	8.89	2.06	80.94	35.8	50.17	0.5	2.25	0.05	0.04	94.74	99.77
	MZ18063_tp2_mg	9	2.01	80.97	36.04	49.93	0.47	2.16	0.03	0.01	94.65	99.65
	MZ18063_tp3_mg	9.18	2.03	80.82	36.27	49.51	0.5	2.2	0.07	0.05	94.84	99.8
	MZ18063_tp4_mg	8.97	2.03	81.33	36	50.37	0.49	2.17	0.03	0.01	95.03	100.07
	MZ18063_tp5_mg	8.67	2.05	81.42	35.82	50.68	0.51	2.18	0.05	0.04	94.92	100
	MZ18063_tp6_mg	9.02	2	80.94	35.91	50.04	0.53	2.2	0.04	0.03	94.74	99.75
	MZ18063_tp7_mg	8.7	2.1	81.21	35.84	50.42	0.51	2.17	0.07	0.05	94.8	99.84
	MZ18063_tp8_mg	8.92	2.12	81.55	36.09	50.51	0.48	2.19	0.04	0.02	95.32	100.38
	MZ18063_tp9_mg	8.54	2.07	81.87	35.8	51.2	0.48	2.2	0.06	0.04	95.27	100.4
	MZ18063_tp10_mg	9	2	81.55	36.12	50.49	0.48	2.2	0.04	0.03	95.31	100.37
47 (co-PDC)	TL484_mag01	11.14	2.83	77.85	37.46	44.89	0.4	2.77	0.05	0.09	95.13	99.62
	TL484_mag02	10	2.45	79.31	36.8	47.24	0.44	2.35	0.07	0.04	94.66	99.39
	TL484_mag03	9.9	2.71	79.74	37.22	47.25	0.38	2.43	0.06	0.16	95.38	100.12
	TL484_mag04	11.26	3.21	77.44	37.97	43.86	0.41	2.66	0.07	0.14	95.17	99.56
	TL484_mag05	7.77	4.15	79.74	34.84	49.9	0.2	2.9	0.09	0.15	95.01	100.01
	TL484_mag06	9.68	3.38	79.13	36.42	47.47	0.36	2.81	0.09	0.09	95.53	100.29
	TL484_mag07	11.42	1.45	79.76	40.14	44.03	0.3	1.25	0.06	0.27	94.51	98.92
	TL484_mag08	11.09	3.11	77.48	37.23	44.73	0.4	3.02	0.06	0.14	95.28	99.76
	TL484_mag09	7.72	2.88	81.11	34.53	51.77	0.45	2.55	0.06	0.05	94.81	100
	TL484_mag10	10.19	2.06	80.36	37.62	47.5	0.41	2.1	0.05	0.1	95.26	100.01
	TL484_mag12	10.93	3.1	77.96	37.33	45.15	0.45	2.66	0.06	0.05	95.2	99.72
	TL484_mag14	9.37	4.02	77.02	36.38	45.17	0.3	3.38	0.07	0.59	94.76	99.28
	TL484_mag16	8.68	2.09	81.16	35.68	50.55	0.5	2.2	0.05	0.03	94.71	99.77
	TL484_mag17	10.98	2.34	79.19	37.98	45.81	0.53	2.21	0.06	0.07	95.39	99.98
	TL484_mag18	10.89	2.61	78.38	37.46	45.47	0.42	2.52	0.07	0.08	94.97	99.53
	TL484_mag19	11.11	3.22	78.48	38.01	44.97	0.38	2.65	0.06	0.09	95.99	100.5
50	MZ069_tp1_il	40.32	0.27	52.84	30.25	25.11	0.49	3.1		-	97.02	99.55
	MZ069_tp2_il	39.98	0.3	53.32	30.05	25.85	0.5	3.04	0.01	-	97.15	99.73

Table B.3: Major element geochemical data for Mazama FeTi oxides *cont.*

Location ID	Sample ID	TiO_2	Al_2O_3	FeO_t	FeO*	Fe_2O_3*	MnO	MgO	SiO_2	Cr_2O_3	$Total_t$	Total*
	MZ069_tp3_il	40.24	0.25	53.08	29.87	25.8	0.51	3.25		-	97.33	99.91
	MZ069_tp4_il	39.82	0.24	52.86	29.67	25.78	0.48	3.2	0.04	-	96.64	99.22
	MZ069_tp5_il	40.2	0.3	53.3	30.11	25.76	0.49	3.11		-	97.4	99.99
	MZ069_il1	40.26	0.25	53.15	30.1	25.62	0.48	3.15		-	97.29	99.85
	MZ069_il2	40.02	0.26	53.73	30.02	26.35	0.5	3.07		-	97.58	100.22
	MZ069_il3	39.92	0.29	54.12	30.03	26.78	0.5	3.04	0.04	-	97.91	100.58
	MZ069_il4	39.98	0.32	53.69	30.09	26.22	0.46	3.05	0.03	-	97.53	100.15
	MZ069_il5	40.09	0.27	53.46	29.99	26.09	0.5	3.14	0.02	-	97.48	100.1
	MZ071_tp1_il	40.47	0.26	53.25	30.21	25.6	0.49	3.21	0.03	-	97.71	100.28
	MZ071_tp2_il	43.65	0.29	50.27	32.97	19.22	0.56	3.21		-	97.98	99.89
	MZ071_tp3_il	39.74	0.31	53.88	29.61	26.97	0.49	3.17	0.02	-	97.61	100.3
	MZ071_tp4_il	39.71	0.29	53.73	29.8	26.6	0.46	3.09	0.04	-	97.32	99.99
	MZ071_tp5_il	40.13	0.3	53.43	30.03	26	0.47	3.15	0.02	-	97.5	100.09
	MZ071_il1	41.51	0.37	51.71	30.7	23.34	0.32	3.54	0.01	-	97.46	99.8
	MZ071_il2	40.03	0.28	53.68	30.05	26.26	0.48	3.09	0.03	-	97.59	100.22
	MZ071_il3	39.87	0.31	53.56	30.06	26.11	0.48	2.98		-	97.2	99.82
	MZ071_il4	40.43	0.29	52.94	30.26	25.2	0.51	3.14	0.01	-	97.32	99.84
	MZ071_il5	39.93	0.31	53.96	29.96	26.67	0.52	3.06	0.02	-	97.8	100.47
55	MZ073_tp1_il	39.97	0.28	53.8	30.01	26.44	0.45	3.07		-	97.57	100.23
	MZ073_tp2_il	40.47	0.25	53.12	30.15	25.53	0.52	3.24	0.03	-	97.63	100.18
	MZ073_tp3_il	40.33	0.27	52.97	29.97	25.55	0.5	3.27	0.03	-	97.37	99.93
	MZ073_tp4_il	40.33	0.29	53.88	30.41	26.09	0.48	3.03	0.03	-	98.04	100.66
	MZ073_tp5_il	40.15	0.29	53.29	30.19	25.67	0.48	3.07	0.02	-	97.3	99.86
	MZ073_il1	40.12	0.27	53.49	30.19	25.89	0.48	3.04	0.01	-	97.41	100
	MZ073_il2	40.46	0.28	53.14	30.22	25.47	0.46	3.2		-	97.54	100.09
	MZ073_il3	40.25	0.29	53.56	30.23	25.93	0.49	3.08	0.01	-	97.68	100.27
	MZ073_il4	40.36	0.26	53.6	30.09	26.13	0.52	3.2	0.02	-	97.96	100.57
	MZ073_il5	40.09	0.31	53.72	30.27	26.06	0.48	3	0.04	-	97.64	100.24
	MZ074_tp1_il	40.18	0.27	53.08	29.88	25.78	0.52	3.23	0.02	-	97.3	99.88
	MZ074_tp2_il	40.12	0.28	54.07	30.21	26.52	0.48	3.03	0.02	-	98	100.66

Table B.3: Major element geochemical data for Mazama FeTi oxides *cont.*

Location ID	Sample ID	TiO_2	Al_2O_3	FeO_t	FeO*	Fe_2O_3*	MnO	MgO	SiO_2	Cr_2O_3	$Total_t$	Total*
	MZ074_tp3_il	40.21	0.28	53.1	30.21	25.44	0.54	3.06	0.04	-	97.23	99.78
	MZ074_tp4_il	40.06	0.29	53.25	29.8	26.05	0.49	3.24	0.03	-	97.36	99.95
	MZ074_tp5_il	39.72	0.28	53.5	29.52	26.64	0.49	3.22	0.02	-	97.23	99.9
	MZ074_il1	40.28	0.29	53.53	30.2	25.92	0.49	3.12	0.01	-	97.72	100.32
	MZ074_il2	40.1	0.31	53.64	30.16	26.09	0.5	3.04	0.02	-	97.61	100.22
	MZ074_il3	39.82	0.29	53.86	29.95	26.57	0.49	3.02	0.01	-	97.49	100.16
	MZ074_il4	39.66	0.28	53.99	29.78	26.9	0.45	3.06	0.02	-	97.46	100.17
	MZ074_il5	39.93	0.29	53.53	29.94	26.22	0.5	3.09	0.03	-	97.37	99.99
46 (LPU)	MZ18066_tp1_il	39.85	0.34	52.91	29.89	25.59	0.52	3.1	0.02	-	96.74	99.29
	MZ18066_tp2_il	40.39	0.26	53.64	30.56	25.65	0.5	2.97	0.01	-	97.77	100.33
	MZ18066_tp3_il	40.29	0.28	53.09	30.29	25.34	0.48	3.09	0.03	-	97.26	99.8
	MZ18066_tp4_il	40.22	0.27	53.41	30.32	25.67	0.47	3.02	0.01	-	97.4	99.98
	MZ18066_il1	40.15	0.3	53.45	30.27	25.76	0.45	3.07	0.01	-	97.43	100
	MZ18066_il2	40.3	0.29	53.72	30.59	25.71	0.47	2.94		-	97.72	100.29
	MZ18066_il3	40.33	0.29	53.89	30.49	26	0.48	3	0.01	-	98	100.59
	MZ18066_il4	40.11	0.29	53.46	30.35	25.68	0.49	2.95		-	97.3	99.86
	MZ18066_il5	41.47	0.11	53.49	33.6	22.11	1.13	1.46		-	97.66	99.87
	MZ18066_il6	40.09	0.28	53.69	30.19	26.12	0.48	3.04	0.01	-	97.59	100.22
	MZ18066_il7	40.45	0.28	53.75	30.55	25.78	0.49	3.01		-	97.98	100.56
	MZ18066_il8	40.38	0.23	53.19	30.49	25.23	0.48	3.04		-	97.32	99.85
	MZ18066_il9	40.67	0.26	53.32	30.83	25	0.46	2.99	0.01	-	97.71	100.21
	MZ18066_il10	40.18	0.26	53.2	30.5	25.23	0.51	2.91	0.01	-	97.07	99.6
	MZ18065_tp1_il	40.63	0.28	52.96	30.52	24.93	0.53	3.12	0.01	-	97.53	100.02
	MZ18065_tp2_il	40.17	0.28	53.62	30.1	26.14	0.5	3.09		-	97.66	100.28
	MZ18065_tp3_il	40.33	0.3	52.91	30.17	25.27	0.5	3.14		-	97.18	99.69
	MZ18065_tp4_il	40.23	0.29	53.78	30.35	26.03	0.49	3	0.01	-	97.8	100.39
	MZ18065_tp5_il	40.56	0.29	53.26	30.52	25.27	0.52	3.08		-	97.71	100.25
	MZ18065_tp6_il	40.47	0.26	52.61	30.22	24.88	0.49	3.23	0.03	-	97.09	99.58
	MZ18065_il01	40.56	0.32	53.35	30.66	25.22	0.49	3		-	97.72	100.24
	MZ18065_il02	39.89	0.25	53.39	30.15	25.83	0.45	2.97		-	96.95	99.52

Table B.3: Major element geochemical data for Mazama FeTi oxides *cont.*

Location ID	Sample ID	TiO_2	Al_2O_3	FeO_t	FeO*	Fe_2O_3*	MnO	MgO	SiO_2	Cr_2O_3	$Total_t$	Total*
	MZ18065_il03	40.39	0.24	53.2	30.59	25.13	0.5	2.95	0.01	-	97.29	99.8
	MZ18065_il04	40.7	0.26	52.92	30.77	24.61	0.48	3.04		-	97.4	99.86
	MZ18065_il05	40.28	0.28	53.93	30.59	25.94	0.51	2.93	0.01	-	97.94	100.54
46 (DA)	MZ18064_tp1_il	40.09	0.24	53.49	30.14	25.95	0.48	3.06		-	97.36	99.95
	MZ18064_tp2_il	39.94	0.28	53.59	30.21	25.98	0.45	2.97	0.01	-	97.24	99.85
	MZ18064_tp3_il	40.39	0.25	53.65	30.55	25.66	0.49	2.98		-	97.76	100.32
	MZ18064_tp4_il	40.6	0.26	53.47	30.82	25.18	0.5	2.95		-	97.78	100.3
	MZ18064_tp5_il	40.54	0.31	52.89	30.59	24.78	0.49	3.07	0.02	-	97.32	99.81
	MZ18064_il01	39.43	0.31	54.27	29.93	27.05	0.47	2.88		-	97.36	100.06
	MZ18064_il02	40.27	0.3	53.63	30.6	25.59	0.5	2.88		-	97.58	100.14
	MZ18064_il03	40.67	0.3	53.32	30.77	25.06	0.47	3.03	0.01	-	97.8	100.31
	MZ18064_il04	40.47	0.27	52.98	30.49	25	0.51	3.04	0.02	-	97.29	99.8
	MZ18064_il05	40.67	0.32	53.22	30.81	24.91	0.5	3	0.02	-	97.73	100.23
46 (co-PDC)	MZ18059_tp1_il	40.3	0.25	53.18	30.24	25.5	0.47	3.12	0.01	-	97.33	99.89
	MZ18059_tp2_il	40.18	0.33	53.6	30.39	25.8	0.48	2.99	0.02	-	97.6	100.18
	MZ18059_tp3_il	39.83	0.3	53.8	29.94	26.52	0.49	3.04		-	97.46	100.1
	MZ18059_tp4_il	40.15	0.28	53.28	30.13	25.73	0.5	3.13	0.03	-	97.37	99.94
	MZ18059_tp5_il	40.32	0.28	52.83	30.27	25.07	0.49	3.12	0.01	-	97.05	99.56
	MZ18059_tp6_il	39.92	0.27	53.61	29.83	26.43	0.51	3.15		-	97.46	100.11
	MZ18059_tp7_il	40.17	0.28	53.22	30.08	25.72	0.53	3.11		-	97.31	99.88
	MZ18059_il01	40.16	0.3	53.78	30.22	26.19	0.47	3.06	0.01	-	97.78	100.41
	MZ18059_il02	40.23	0.31	53.33	30.46	25.42	0.46	2.99		-	97.32	99.88
	MZ18059_il03	40.89	0.27	53.11	30.95	24.63	0.5	3.02		-	97.79	100.27
80	MZ17JC1_mag1	39.78	0.31	53.59	30.22	25.97	0.48	2.89	0.03	-	97.08	99.69
67	MZ17BH1_mag1	39.93	0.3	53.47	29.99	26.1	0.47	3.11	0.03	-	97.31	99.91
46 (UPU)	MZ18060_tp1_il	40.79	0.29	53.5	30.7	25.34	0.5	3.11		-	98.19	100.73
	MZ18060_tp2_il	40.19	0.31	52.68	30.23	24.94	0.51	3.21	0.02	-	96.92	99.41
	MZ18060_tp3_il	43.59	0.23	50.63	32.96	19.63	0.48	3.3		-	98.23	100.19
	MZ18060_tp4_il	40.68	0.29	53.88	30.73	25.72	0.47	3.03		-	98.35	100.92
	MZ18060_tp5_il	40.47	0.28	53	30.18	25.36	0.51	3.21	0.01	-	97.48	100.02

Table B.3: Major element geochemical data for Mazama FeTi oxides *cont.*

Location ID	Sample ID	TiO_2	Al_2O_3	FeO_t	FeO*	Fe_2O_3*	MnO	MgO	SiO_2	Cr_2O_3	$Total_t$	Total*
	MZ18060_tp6_il	40.42	0.29	52.96	30.39	25.08	0.46	3.1	0.01	-	97.24	99.75
	MZ18060_tp7_il	40.32	0.3	53.49	30.34	25.73	0.49	3.06		-	97.66	100.24
	MZ18060_tp8_il	43.49	0.31	50.39	32.6	19.77	0.5	3.4	0.02	-	98.11	100.09
	MZ18060_tp9_il	40.73	0.31	53.35	30.56	25.32	0.52	3.14		-	98.05	100.58
	MZ18060_tp10_il	40.5	0.29	53.74	30.51	25.81	0.49	3.07	0.01	-	98.1	100.68
	MZ18061_tp1_il	40.54	0.27	53.5	30.41	25.66	0.5	3.13		-	97.94	100.51
	MZ18061_tp2_il	40.74	0.29	52.88	30.4	24.98	0.48	3.25	0.02	-	97.66	100.16
	MZ18061_tp3_il	40.21	0.29	52.67	30.29	24.88	0.47	3.13	0.09	-	96.86	99.36
	MZ18061_tp4_il	40.58	0.3	53.39	30.46	25.49	0.49	3.13	0.01	-	97.9	100.46
	MZ18061_tp5_il	40.66	0.29	53.28	30.52	25.3	0.49	3.16	0.02	-	97.9	100.44
	MZ18061_il01	40.59	0.29	53.86	30.64	25.8	0.49	3.03	0.02	-	98.28	100.86
	MZ18061_il02	41.45	0.28	52.81	31.34	23.87	0.45	3.13	0.01	-	98.13	100.53
	MZ18061_il03	37.2	0.4	56.65	28.8	30.94	0.31	2.47		-	97.03	100.12
	MZ18061_il04	40.83	0.23	53.26	30.79	24.98	0.52	3.07		-	97.91	100.42
	MZ18061_il05	40.9	0.27	53.35	30.77	25.09	0.5	3.1		-	98.12	100.63
	MZ18062_tp1_il	44.56	0.38	49.04	32.39	18.5	0.42	4.14	0.06	-	98.6	100.45
	MZ18062_tp2_il	41.83	0.23	52.92	33.09	22.04	0.45	2.29		-	97.72	99.93
	MZ18062_tp3_il	40.77	0.28	52.51	30.42	24.55	0.47	3.27		-	97.3	99.76
	MZ18062_tp4_il	40.46	0.27	53.08	30.52	25.08	0.46	3.06	0.03	-	97.36	99.88
	MZ18062_tp5_il1	44.58	0.37	49.82	32.84	18.87	0.46	3.83	0.01	-	99.07	100.96
	MZ18062_tp5_il2	44.35	0.35	49.01	32.26	18.61	0.47	4.03	0.02	-	98.23	100.09
	MZ18062_tp6_il	40.46	0.32	53.26	30.33	25.49	0.5	3.15		-	97.69	100.25
	MZ18062_tp7_il	43.73	0.3	50.54	32.52	20.03	0.48	3.58	0.02	-	98.65	100.66
	MZ18062_tp8_il	40.31	0.3	53.61	30.53	25.65	0.47	2.96		-	97.65	100.22
	MZ18063_tp1_il	40.88	0.32	53.33	30.8	25.04	0.52	3.07	0.01	-	98.13	100.64
	MZ18063_tp2_il	40.76	0.24	53.75	30.79	25.52	0.49	3.03		-	98.27	100.83
	MZ18063_tp3_il	40.72	0.3	53.42	30.59	25.37	0.47	3.12	0.01	-	98.04	100.58
	MZ18063_tp4_il	40.39	0.37	52.38	30.37	24.45	0.47	3.16	0.06	-	96.83	99.27
	MZ18063_tp5_il	40.61	0.3	53.68	30.51	25.74	0.48	3.1		-	98.17	100.74
	MZ18063_tp6_il	40.67	0.27	53.21	30.76	24.95	0.46	3.01		-	97.62	100.12

Table B.3: Major element geochemical data for Mazama FeTi oxides *cont.*

Location ID	Sample ID	TiO_2	Al_2O_3	FeO_t	FeO*	Fe_2O_3*	MnO	MgO	SiO_2	Cr_2O_3	$Total_t$	Total*
	MZ18063_tp7_il	40.56	0.35	53.29	30.53	25.3	0.49	3.09		-	97.78	100.32
	MZ18063_tp8_il	40.67	0.3	53.08	30.45	25.15	0.45	3.19		-	97.69	100.21
	MZ18063_tp9_il	41.12	0.28	52.65	30.89	24.18	0.49	3.16	0.01	-	97.71	100.13
	MZ18063_tp10_il	41.56	0.26	53.82	31.44	24.86	0.51	3.05		-	99.2	101.68
47 (co-PDC)	TL484_mag11	40.61	0.3	53.59	30.83	25.29	0.49	2.94	0.03	-	97.96	100.49
	TL484_mag13	42.59	0.29	51.18	32	21.32	0.48	3.31	0.02	-	97.87	100.01
	TL484_mag15	43.64	0.35	50.67	32.49	20.2	0.42	3.58	0.02	-	98.68	100.7
	TL484_mag20	41.04	0.3	53.54	30.93	25.13	0.51	3.12	0.02	-	98.53	101.05

Table B.4: Major element geochemical data for secondary FeTi standards

Secondary Standard	Analysis ID	TiO_2	Al_2O_3	MgO	SiO_2	FeO*	Fe_2O_3*	Fe_3O_4*	MnO	Cr_2O_3	Total*
Hematite	hemfull_ss	0	0.02			-	99.58	-	0.02	0	99.53
	hemfull_ss	0.03	0.03	0		-	99.85	-	0	0	99.95
	hemfull_ss	0.01	0.02			-	100.31	-	0.01	0	100.29
	hem_ss_end	0	0.02	0.01	0.01	90.1	-	-	0.01	0	90.15
	hem_ss_end	0	0	0.03	0	89.29	-	-	0	0	89.26
	hem_ss_end	0	0.04	0	0	89.17	-	-	0	0	89.14
	hem_ss_end	0	0.02	0.01	0.01	89.35	-	-	0	0	89.36
	hem_ss_end	0		0	0	89.2	-	-	0	0	89.16
	hem_ss_end	0		0	0	89.5	-	-	0	0	89.55
	hem_ss_end	0.02		0	0	88.27	-	-	0	0.01	88.28
	hem_ss_end	0	0		0	88.38	-	-	0	0.01	88.36
	hem_ss_end	0.01	0.03	0	0	88.7	-	-	0		88.72
	hem_ss_end	0	0.02			88.55	-	-	0	0	88.54
	hem_ss_end	0			0.02	88.45	-	-	0.01	0	88.46
	hem_ss_end	0.01		0		88.01	-	-	0	0.01	87.98
	hem_ss_end	0	0.03			88.14	-	-	0		88.12
	hem1_ss	0.01	0	0	0	-	101.18	-	0	0.01	101.16
	hem1_ss	0	0	0	0.01	-	100.85	-	0	0	100.79
	hem1_ss	0	0	0.01	0	-	101.02	-	0.01	0	101.01
	hem1_ss	0	0.03	0	0.01	-	101.06	-	0	0	101.07
	hem1_ss	0.01	0	0.01	0	-	100.83	-	0.01	0	100.79
	hem1_ss	0	0	0	0	-	100.57	-	0.01	0	100.5
	hem_ss	0.01	0.01		0.01	88.18	-	-	0.03	0.01	88.23
	hem_ss	0		0		88.75	-	-	0	0	88.74
	hem_ss	0			0.02	88.92	-	-	0.01		88.89
	hem_ss	0	0.02	0.01	0.01	88.45	-	-	0.01	0.02	88.52
	hem_ss	0	0.01			88.27	-	-	0	0	88.24
	hem_ss	0.02			0.02	88.65	-	-	0	0	88.66
Hematite 2	hemfull2_ss	0	0.31	0.01	0	-	100.6	-	0	0	100.93
	hemfull2_ss	0.01	0.29	0.01		-	100.15	-	0	0	100.38

Table B.4: Major element geochemical data for secondary FeTi standards *cont.*

Secondary Standard	Analysis ID	TiO_2	Al_2O_3	MgO	SiO_2	FeO*	Fe_2O_3*	Fe_3O_4*	MnO	Cr_2O_3	Total*
	hemfull2_ss	0	0.33	0.01	0	-	100.2	-	0	0	100.53
	hem_2ss_end	0	0.29	0	0.04	88.91	-	-	0	0	89.27
	hem_2ss_end	0	0.03	0	0.02	89.54	-	-	0	0	89.54
	hem_2ss_end	0	0.13		0.03	89.47	-	-	0.01	0	89.59
	hem_2ss_end	0.01	0.04		0.05	89.08	-	-	0	0	89.15
	hem_2ss_end	0	0.4		0.08	88.88	-	-	0	0	89.37
	hem_2ss_end	0	0.46	0.01	0.07	88.83	-	-	0	0	89.42
	hem2_ss_end	0	0.5		0.14	88.85	-	-	0	0	89.4
	hem2_ss_end	0	0.03	0	0.04	88.98	-	-	0	0.01	89.05
	hem2_ss_end	0.02	0.07	0	0.07	89.5	-	-	0	0	89.65
	hem2_ss_end	0	0.01	0	0.08	89.41	-	-	0	0.02	89.51
	hem2_ss_end	0	0.04	0	0.05	89.06	-	-	0	0	89.15
	hem2_ss_end	0.02	0.01	0	0.01	89.67	-	-	0	0.01	89.72
	hem2_ss	0.01	0.39		0.04	88.36	-	-	0	0.01	88.8
	hem2_ss	0	0.5	0.02	0.07	88.3	-	-	0	0	88.88
	hem2_ss	0.01	0.41		0.09	88.32	-	-	0.01	0	88.83
	hem2_ss	0	0.41		0.08	88.24	-	-	0	0.01	88.72
	hem2_ss	0	0.38		0.06	87.84	-	-	0	0.01	88.26
	hem2_ss	0.01	0.32		0.1	88.69	-	-	0.01	0	89.13
K22 Ilmenite	k22_ss	53.17	0.52	13.15	0.05	29.65	-	-	0.27	1.86	98.64
	k22_ss	53.24	0.58	13.24	0.08	29.72	-	-	0.24	1.86	98.99
	k22_ss	53.27	0.52	13.19	0.05	29.6	-	-	0.22	1.86	98.8
	k22_ss	53.56	0.52	13.45	0.05	29.59	-	-	0.23	1.86	99.26
	k22_ss_end	53.32	0.51	13.16	0.02	29.81	-	-	0.23	0	97.04
	k22_ss_end	53.5	0.51	13.15	0.04	29.83	-	-	0.26	0	97.35
	k22_ss_end	53.67	0.53	13.23	0.04	29.58	-	-	0.24	0	97.37
	k22_ss_end	53.53	0.54	13.31	0.05	29.85	-	-	0.22	0	97.52
	k22_ss_end	53.55	0.5	13.4	0.03	29.75	-	-	0.22	0	97.48
	k22_ss_end	53.39	0.54	13.52	0.04	29.71	-	-	0.25	0	97.46
	k22ilm_ss	53.6	0.54	12.48	0.05	30.01	-	-	0.24	1.83	98.79

Table B.4: Major element geochemical data for secondary FeTi standards *cont.*

Secondary Standard	Analysis ID	TiO_2	Al_2O_3	MgO	SiO_2	FeO*	Fe_2O_3*	Fe_3O_4*	MnO	Cr_2O_3	Total*
	k22ilm_ss	53.56	0.44	12.53	0.05	30.27	-	-	0.23	1.88	98.97
	k22ilm_ss	53.58	0.49	12.65	0.05	29.92	-	-	0.24	1.94	98.89
	k22ilm_ss	53.58	0.49	12.73	0.03	29.94	-	-	0.28	1.92	99.02
	k22ilm_ss	53.51	0.6	12.77	0.06	29.69	-	-	0.24	1.95	98.86
	k22ilm_ss	53.79	0.53	12.84	0.05	29.97	-	-	0.23	1.95	99.38
	k22ilm_ss_end	53.04	0.56	12.62	0.05	29.98	-	-	0.24	1.9	98.43
	k22ilm_ss_end	53.41	0.44	12.58	0.07	29.82	-	-	0.23	1.9	98.45
	k22ilm_ss_end	53.3	0.42	12.77	0.06	30.12	-	-	0.22	1.91	98.81
	k22ilm_ss_end	52.98	0.42	12.58	0.07	30.1	-	-	0.25	1.91	98.33
	k22ilm_ss_end	53.35	0.52	12.81	0.05	29.77	-	-	0.25	1.84	98.63
	k22ilm_ss	54.12	0.48	12.99	0.07	29.81	-	-	0.22	1.94	99.66
	k22ilm_ss	53.69	0.46	13.11	0.04	29.37	-	-	0.22	1.9	98.81
	k22ilm_ss	54.03	0.48	12.96	0.05	29.35	-	-	0.24	1.91	99.06
	k22ilm_ss	53.89	0.49	13.19	0.07	29.52	-	-	0.24	1.89	99.32
	k22ilm_ss	53.95	0.57	13.22	0.04	29.18	-	-	0.25	1.92	99.16
	k22ilm_ss	53.77	0.49	13.34	0.06	29.44	-	-	0.25	1.86	99.25
Magnetite	mag_ss	0.27	0.18	0.08	0	-	-	100.31	0.06	0	100.85
	mag_ss	0.31	0.19	0.1	0.02	-	-	99.77	0.04	0	100.42
	mag_ss	0.27	0.19	0.1	0	-	-	100.02	0.05	0	100.61
	mag_ss	0.3	0.18	0.11		-	-	100.16	0.04	0	100.77
	mag_ss	0.24	0.17	0.08	0.01	-	-	100.55	0.04	0	101.08
	mag_ss_end	0.27	0.15	0.09	0	92.58	-	-	0.05	0	93.24
	mag_ss_end	0.27	0.19	0.1	0.01	92.55	-	-	0.04	0	93.14
	mag_ss_end	0.3	0.17	0.1	0.01	92.22	-	-	0.04	0	92.85
	mag_ss_end	0.28	0.17	0.12		92.74	-	-	0.02	0	93.31
	mag_ss_end	0.32	0.18	0.1		91.95	-	-	0.03	0	92.5
	mag_ss_end	0.31	0.16	0.09	0	92.53	-	-	0.05	0	93.1
	hem2_ss	0	0.47	0	0.11	-	101.14	-	0	0	101.71
	hem2_ss	0.02	0.47	0	0.09	-	100.22	-	0	0	100.81
	hem2_ss	0.03	0.5	0	0.03	-	100.66	-	0	0.01	101.19

Table B.4: Major element geochemical data for secondary FeTi standards *cont.*

Secondary Standard	Analysis ID	TiO_2	Al_2O_3	MgO	SiO_2	FeO*	Fe_2O_3*	Fe_3O_4*	MnO	Cr_2O_3	Total*
	hem2_ss	0	0.33	0	0.09	-	101.22	-	0	0	101.63
	hem2_ss	0	0.39	0	0.05	-	100.61	-	0.01	0	101.03
	hem2_ss	0.02	0.28	0	0.02	-	100.81	-	0	0	101.09
	mag_ss	0.3	0.11	0.11	0.01	-	-	100.95	0.03	0.01	101.53
	mag_ss	0.25	0.18	0.1		-	-	100.27	0.03	0.01	100.85
	mag_ss	0.29	0.17	0.08	0.01	-	-	100.48	0.04	0.03	101.11
	mag_ss	0.26	0.16	0.07		-	-	100.4	0.06	0.02	100.96
	mag_ss	0.3	0.16	0.08	0	-	-	100.95	0.02	0.02	101.54
	mag_ss	0.27	0.19	0.09	0	-	-	100.12	0.05	0.03	100.76
	mag_ss_end	0.22	0.21	0.07	0	92.58	-	-	0.04	0.04	93.18
	mag_ss_end	0.22	0.18	0.08	0	92.71	-	-	0.04	0.03	93.26
	mag_ss_end	0.25	0.21	0.07	0	93.12	-	-	0.05	0.04	93.75
	mag_ss_end	0.25	0.22	0.08		92.86	-	-	0.06	0.04	93.49
	mag_ss_end	0.28	0.19	0.11	0.01	92.98	-	-	0.03	0.04	93.64
	mag_ss_end	0.29	0.2	0.1		92.86	-	-	0.05	0.02	93.53
	mag_ss	0.39	0.15	0.08	0.01	-	-	99.33	0.04	0.02	100.01
	mag_ss	0.25	0.15	0.1		-	-	99.31	0.05	0	99.85
	mag_ss	0.3	0.19	0.08	0.03	-	-	98.98	0.02	0.02	99.61
	mag_ss	0.28	0.16	0.09	0.02	-	-	99.33	0.05	0.04	99.98
	mag_ss	0.29	0.17	0.08	0.02	-	-	99.44	0.05	0.02	100.06
	mag_ss	0.22	0.11	0.09	0.01	-	-	99.63	0.03	0.03	100.15

APPENDIX C

APPENDIX C - SUPPLEMENTARY MATERIAL FOR CHAPTER 4

C.1 Review of grain size methods in volcanology

C.1.1 Coarse sieving

The GSD of coarse (>125 μm) unconsolidated tephra is typically measured by sieving. The tephra is passed through a series of nested sieves where the aperture size typically decreases on the logarithmic ϕ or Krumbein scale (*Krumbein*, 1934) in whole-ϕ, half-ϕ or quarter-ϕ increments where

$$\phi = -log_2 d \tag{C.1}$$

and d is the length of the side of the square aperture in mm. The ϕ-scale is widely used in sedimentology and volcanology instead of an arithmetic or linear scale to avoid emphasis of this mass-based measure on the coarse sediment (*Blott and Pye*, 2001). Manual or mechanical shaking, with or without the addition of water, is used to segregate the tephra into the individual sieve fractions. The minimum particle 'size' (diameter for a sphere) within a sieve fraction is equal to d. The GSD is then reported as the percentage of the analysed mass (weight percent) retained in each sieve fraction.

Sieving is a low cost and established method that is often the only available tool for measuring very coarse size fractions particularly whilst in the field (*Folk and Ward*, 1957; *Walker*, 1971; *Fairbridge and Bourgeois*, 1978). However, sieving does have limitations. Firstly, the sieve size is only equal to the particle size for spheres. Anisotropic particle shapes mean that clasts do

not always pass through the sieve mesh according to the same dimension. For example, flat or elongated particles can be sorted according to their largest or smallest dimension which can vary substantially (e.g., needle like particles in Katla SILK layers; *Saxby et al.*, 2018, 2020). This means that sieving sorts by both size and shape (*Komar and Cui*, 1984). Agitation of delicate tephra when sieving can also lead to clast breakage and alteration of the GSD and particle shape during analysis (*Cox et al.*, 2017) so the reproducibility of the GSD depends on the method and duration of agitation. The amount of material sieved affects the ease of GSD measurement, particularly for coarse material where large quantities of material are required to ensure a representative aliquot (*Swineford and Swineford*, 1946; *Sarocchi et al.*, 2011; *Román-Sierra et al.*, 2013). Interpretations of GSDs produced by sieving also depend on the sieve interval. Ideally, sieve intervals should be quarter- or half-ϕ, because larger intervals present difficulties in computing statistics, especially for fractions >2 mm (-1 ϕ; *Hails et al.*, 1973). The grain size range typically covered by sieves is from 125 mm to 20 µm (Table 4.1). However, sieving below 125 µm is challenging as fine sieves are prone to overloading, and fine material can form coarser aggregates or loft when agitated meaning that the particles do not pass into the correct sieve fraction and can be lost. For this reason, other methods are preferred for measuring particles <125 µm.

C.1.2 Particle sedimentation

An alternative method of grain size analysis uses rates of particle sedimentation; this method measures the velocities of particles settling in a fluid of known viscosity and density and can cover a wide range of particle sizes (~50-5000 µm; Table 4.1; *Gibbs et al.*, 1971). From the measured settling velocities, the diameters of dense equivalent spheres that would have the same settling velocities are calculated using an empirical equation (*Gibbs et al.*, 1971). A variant is the pipette method, which uses water as the fluid and has been used with volcanic tephra (*Watanabe et al.*, 1999; *Wiesner et al.*, 2004). Another sedimentation method is the Roller apparatus (*Roller*, 1931; *Riley et al.*, 2003), an air elutriation device that separates particles according to their settling velocities in air. As with sieving, however, sedimentation methods of grain size analysis indirectly measure the effects of grain shape, and specifically for these methods, variations in particle density (*Sanford and Swift*, 1971; *Komar and Cui*, 1984; *Beuselinck et al.*, 1998). Moreover, the settling behaviour of fine material (<125 µm) is poorly described by existing settling laws because of aggregation, Brownian motion (<10 µm) and complex flow and depositional regimes (*Rose and Durant*, 2009; *Brown et al.*, 2012; *Engwell and Eychenne*, 2016; *Saxby et al.*, 2018).

C.1.3 Laser diffraction

Laser diffraction is the most common method used in volcanology to characterise the GSD of fine material (e.g., *Horwell*, 2007; *Buckland et al.*, 2018; *Genareau et al.*, 2019). The sample is dispersed in a liquid (commonly distilled water) to form a suspension that passes by three lasers

with different wavelengths. The diffraction of the laser beams by the suspended particles is used to calculate particle size by inverting the measured scattering pattern. The GSD is then output as a volume distribution; combining laser diffraction data with sieve data thus requires estimates of particle density. This method is rapid (<2 mins per analysis) and instruments such as the Mastersizer 3000 by Malvern Panalytical (formerly Malvern Instruments Ltd) can measure a particle size range of 0.01-3500 µm (*Panalytical*, 2020). However, the mathematical model chosen to resolve the laser scattering can introduce errors. For example, Mie scattering theory assumes spherical particles and requires an assumption of refractive index. Tephra is very rarely close to spherical, however, and the refractive index is not routinely measured. Moreover, as tephra is commonly a mixture of crystals, lithics and glass, one refractive index will not be representative of the whole sample. An alternative mathematical model used to resolve the laser scattering is the Fraunhofer theory, which assumes particles are flat discs and that the particles only cause diffraction, thus it does not require an assumption of refractive index (*Beuselinck et al.*, 1998; *Cyr and Tagnit-Hamou*, 2001). However, the Fraunhofer approximation can overestimate the proportion of very fine particles (<10 µm) due to this simplification (*Cyr and Tagnit-Hamou*, 2001).

C.1.4 Electrozone sensing

Another method of characterising the GSD of fine material is electrozone sensing, or the Coulter counter method, which has a measurement range of ~0.4-1600 µm. This requires that particles are suspended in an electrically conductive fluid. The suspended particles are counted as they pass through an aperture of known diameter which generates a pulse in electrical resistivity that is measured and related to an equivalent sphere diameter based on the calibration curve of the instrument (*Figueiredo*, 2006). The resulting GSD can be output either as a number (particle count) or volume (converted from equivalent sphere diameter) distribution. This method has been used to measure the GSD of volcanic ash (e.g., *Sparks et al.*, 1983; *Carey et al.*, 1988; *Brand et al.*, 2016) and has the benefit of being non-optical and therefore not affected by variations in particle opacity or reflectivity. However, similar to particle sedimentation methods, electrozone sensing methods quantify size as an equivalent sphere diameter and provide no information about particle shape.

C.1.5 Grain size analysis from image analysis

Image analysis is a flexible method for characterising the grain size and shape of coarse- and fine-grained materials. Here we focus on the application of image analysis to determine the GSD for fine-grained materials, but there are a number of studies that use image analysis to determine the GSD of coarse and consolidated volcanic material (e.g., *Capaccioni et al.*, 1997; *Sarocchi et al.*, 2011; *Jutzeler et al.*, 2012). The grain size of fine ash can be characterised using Scanning Electron Microscope (SEM) images, most commonly collected in Secondary Electron

mode (SE, e.g., *Horwell et al.*, 2003; *Riley et al.*, 2003; *Coltelli et al.*, 2008; *Liu et al.*, 2015). This method allows simultaneous classification of particle shape and componentry (lithic, glass or crystal). However, particle imaging using the SEM may require some sample preparation, such as sieving, to ensure the particles are imaged at the optimal resolution. Furthermore, large particles may be underrepresented if small sample volumes are used. There is also an assumption of 3D shape required to convert from 2D images to a GSD in terms of volume % (*Sahagian and Proussevitch*, 1998). Whilst SEM methods can provide excellent particle information, such as shape and the proportion of different components, the time required for these analyses (hours to days) exceeds that of other methods such as laser diffraction (~minutes per analysis). This may be a disadvantage for some applications of grain size data, for example, if being analysed for rapid assessments of tephra hazard during an eruption.

Other image analysis methods use optical imagery. For example, the Morphologi G3 particle analyser by Malvern Panalytical scans and rapidly images particles that have been dispersed onto a glass plate; size and shape are measured using the built-in software. Similar to SEM analyses, this method requires that the sample is sieved prior to analysis to ensure optimal particle dispersion and image resolution (*Leibrandt and Le Pennec*, 2015; *Buckland et al.*, 2018; *Freret-Lorgeril et al.*, 2019). Studies of cryptotephra (non-visible tephra layers) also quantify grain size using optical imaging methods; size is typically measured along the longest particle axis (e.g., *Palais et al.*, 1992; *Zdanowicz et al.*, 1999; *Stevenson et al.*, 2015). Here chemical and physical tephra extraction (*Dugmore et al.*, 1992; *Cooper et al.*, 2019) is required before tephra shards are counted and imaged using an optical microscope. However, part of the tephra extraction process involves removing very fine material by wet sieving (<20 μm) and only a small number of particles are measured (~100; *Stevenson et al.*, 2015). These aspects of the sample handling, combined with the different size parameterisation, make cryptotephra GSDs difficult to compare with GSDs from other methods (*Cashman and Rust*, 2020).

C.1.6 In situ methods

In situ methods of particle size analysis utilise a variety of the measurement principles used by laboratory methods such as diffraction and image analysis (Table 4.1). As with laboratory methods of size analysis, the grain size range and definition of size is unique to each in situ method and instrument. Ground-based radar systems such as the PLUDIX instrument (*Scollo et al.*, 2005; *Bonadonna et al.*, 2011) measure the settling velocity of particles from ~1000-10 000 μm. The settling velocity is converted into a PSD by assuming spheres with variable densities (*Bonadonna et al.*, 2011); thus size is quantified as an equivalent sphere diameter. Optical disdrometers, such as the Parsivel^2, also quantify size as the volume equivalent sphere diameter according to the manufacturers specifications (*Kozono et al.*, 2019; *OTT*, 2020), however, studies of rainfall found that the measured size of non-spherical particles is closer to the maximum

horizontal diameter (Table 4.1; *Adachi et al.*, 2013). In situ high resolution 2D imaging of active tephra fall can measure particles from 62-2000 µm; the images can be used to determine multiple size descriptors including minimum and maximum particle lengths and area equivalent measures (*Miwa et al.*, 2020). Finally, the methods used to determine PSDs from satellite infrared measurements typically assume that the particles are dense spheres with a constant refractive index and that the scattering can be resolved using Mie theory; thus the 'size' reported refers to a sphere diameter (*Wen and Rose*, 1994; *Pavolonis et al.*, 2013; *Kylling et al.*, 2014; *Stevenson et al.*, 2015). Note that the term 'effective radius' that is used in remote sensing refers to a log-normal PSD that contains a range of particle sizes rather than a single particle size (*Stevenson et al.*, 2015).

C.2 Grain size statistics and distribution fitting

C.2.1 Definitions of parameters and probability density functions

The Folk and Ward (FW; 1957) graphical statistics are calculated using interpolated values from the cumulative distribution function (Fig. B1b). The parameters are calculated using the formulas below:

$$\mu_{FW} = \frac{\phi_{16} + \phi_{50} + \phi_{84}}{3} \tag{C.2}$$

$$\sigma_{FW} = \frac{\phi_{84} - \phi_{16}}{4} + \frac{\phi_{95} + \phi_5}{6.6} \tag{C.3}$$

$$Sk = \frac{\phi_{16} + \phi_{84} - 2\phi_{50}}{2\left(\phi_{84} - \phi_{16}\right)} + \frac{\phi_5 + \phi_{95} - 2\phi_{50}}{2\left(\phi_{95} - \phi_5\right)} \tag{C.4}$$

$$K = \frac{\phi_{95} - \phi_5}{2.44\left(\phi_{75} - \phi_{25}\right)} \tag{C.5}$$

where μ_{FW} denotes the Folk and Ward mean, σ_{FW} is the standard deviation or sorting, Sk is the skewness and K is Kurtosis. ϕ_y is the value in ϕ where y denotes the percentile of the cumulative distribution, e.g., ϕ_{50} is the median grain size (Fig. C.1b). The values of sorting, skewness and Kurtosis then correspond to a qualitative classification according to the categories in Table C.1.

FW parameters assume that the GSD is log-normally distributed (normal on the ϕ-scale). However, GSDs can also be fit to probability density functions (PDFs) directly. When working with grain size data on the ϕ scale the GSD can be fit using a normal distribution which has the PDF:

Table C.1: Descriptive terminology corresponding to the Folk and Ward parameters calculated for grain size data on the ϕ scale.

Sorting (σ_{FW})		Skewness (Sk)		Kurtosis (K)	
Very well sorted	<0.35	Very fine skewed	+0.3 to +1.0	Very platykurtic	<0.67
Well sorted	0.35-0.50	Fine skewed	+0.1 to +0.3	Platykurtic	0.67-0.90
Moderately well sorted	0.50-0.70	Symmetrical	+0.1 to -0.1	Mesokurtic	0.90-1.11
Very well sorted	0.70-1.00	Coarse skewed	-0.1 to -0.3	Leptokurtic	1.11-1.15
Poorly sorted	1.00-2.00	Very coarse skewed	-0.3 to -1.0	Very leptokurtic	1.50-3.00
Very poorly sorted	2.00-4.00			Extremely leptokurtic	>3.00
Extremely poorly sorted	>4.00				

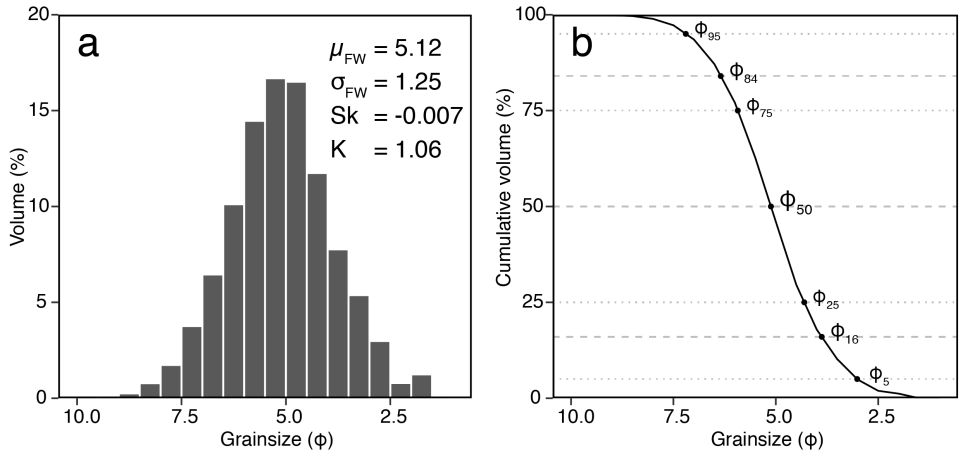

Figure C.1: Example of the FW parameters calculated for distal Mazama sample AP1. a) The Grain Size Distribution measured using the CX2 quantified as the volume percent in each half-ϕ size fraction. b) Cumulative Grain Size Distribution represented as the percentage coarser than the nominal grain size fraction with the interpolated values required for calculating the FW statistics plotted as black circles.

$$f_{norm}(\phi) = \frac{1}{\sigma_\phi \sqrt{2\pi}} exp\left[-\frac{1}{2}\left(\frac{\phi - \mu_\phi}{\sigma_\phi}\right)^2\right] \tag{C.6}$$

where ϕ is the grain size in ϕ units, μ_ϕ denotes the mean and μ_σ is the standard deviation. This can be extended to facilitate the fitting of mixture models where the PDF is described as the sum of multiple normal distributions multiplied by their mixing proportion. For example, the PDF for a bimodal distribution which is the sum of two normal distributions is:

$$f_{bi-norm}(\phi) = p_1 \frac{1}{\sigma_{\phi 1} \sqrt{2\pi}} exp\left[-\frac{1}{2}\left(\frac{\phi - \mu_{\phi 1}}{\sigma_{\phi 1}}\right)^2\right] \quad + \quad p_2 \frac{1}{\sigma_{\phi 2} \sqrt{2\pi}} exp\left[-\frac{1}{2}\left(\frac{\phi - \mu_{\phi 2}}{\sigma_{\phi 2}}\right)^2\right] \tag{C.7}$$

where p_1 and p_2 are the mixing proportions of each population. When fitting a normal distribution to GSDs on the ϕ-scale, it must be remembered that the mean and standard deviation relate to the logarithm of the data and that the GSD is log-normal in linear space. This is an important distinction because when data follows a log-normal distribution the mean, mode and median are not equal. Furthermore, data visualisation of GSDs on the ϕ-scale can be distorted (Fig. C.1a).

It can be preferrable to fit log-normal PDFs directly to grain size data and to work in metric units as is standard procedure in engineering and aerosol science (*Dartevelle et al.*, 2002). To fit a log-normal function, the grain size data cannot be on the ϕ-scale because d must be greater than 0 (Eq. C.8). Therefore, the GSD must either be output using a linear bin configuration or exponentiated from the ϕ scale ($d = 2^{-\phi}$). The PDF of a log-normal distribution is:

$$f_{lnorm}(d) = \frac{1}{d\sigma' \sqrt{2\pi}} exp\left[-\frac{(-ln(d) - \mu')^2}{2\sigma'^2}\right] \quad \text{for d > 0} \tag{C.8}$$

where d is the grain size in mm, μ' denotes the mean of the natural logarithm of the data and σ' is the standard deviation of the natural logarithm of the data. Using these parameters, the mean (μ), median (Md) and mode (Mo) can also then be calculated:

$$\mu_L = exp\left[\mu' + \frac{1}{2}\sigma'^2\right] \tag{C.9}$$

$$Md_L = exp\left[\mu'\right] \tag{C.10}$$

$$Mo_L = exp\left[\mu' - \sigma'^2\right] \tag{C.11}$$

where the μ_L is the mean, Md_L is the median and Mo_L is the mode of the log-normal distribution in mm units. Mixture models of log-normal distributions can also be used to describe GSDs where the PDF is the sum of the PDF of each sub-population multiplied by the mixing proportion:

$$f_{bi-lnorm}(d) = p_1 \frac{1}{d\sigma_1' \sqrt{2\pi}} exp\left[-\frac{(-ln(d)-\mu_1')^2}{2\sigma_1'^2}\right] \quad + \quad p_2 \frac{1}{d\sigma_2' \sqrt{2\pi}} exp\left[-\frac{(-ln(d)-\mu_2')^2}{2\sigma_2'^2}\right] \tag{C.12}$$

Grain Size Distributions can also be described using a Weibull distribution which has the PDF:

$$f_{Weibull}(d) = \frac{k}{\lambda}\left(\frac{d}{\lambda}\right)^{k-1} exp\left[-\left(\frac{d}{\lambda}\right)^{k}\right] \quad \text{for d} \geq 0 \tag{C.13}$$

where d is particle diameter in mm, k is the shape parameter and λ is the scale parameter. Similar to the log-normal distribution, the Weibull distribution cannot be fit to grain size data on the ϕ-scale so the GSD must be quantified in mm. GSDs can also be fit with mixtures of Weibull PDF, for example the PDF of a bimodal Weibull distribution is:

$$f_{bi-Weibull}(d) = p_1 \frac{k_1}{\lambda_1}\left(\frac{d_1}{\lambda_1}\right)^{k_1-1} exp\left[-\left(\frac{d_1}{\lambda_1}\right)^{k_1}\right] \quad + \quad p_2 \frac{k_2}{\lambda_2}\left(\frac{d_2}{\lambda_1}\right)^{k_2-1} exp\left[-\left(\frac{d_2}{\lambda_2}\right)^{k_2}\right] \tag{C.14}$$

where p_1 and p_2 are the mixing proportions, k_1 and k_2 are the scale parameters, and λ_1 and λ_2 are the scale parameters.

The mean, median and mode of the Weibull distribution can be calculated from the shape and scale parameters using the equations:

$$\mu_W = \lambda \cdot \Gamma\left(\frac{1}{k}+1\right) \tag{C.15}$$

$$Md_W = \lambda(\ln 2)^{\frac{1}{k}} \tag{C.16}$$

$$Mo_W = \lambda\left(1-\frac{1}{k}\right)^{\frac{1}{k}} \tag{C.17}$$

where the μ_W is the mean, Γ is the gamma function, Md_W is the median and Mo_W is the mode in mm units.

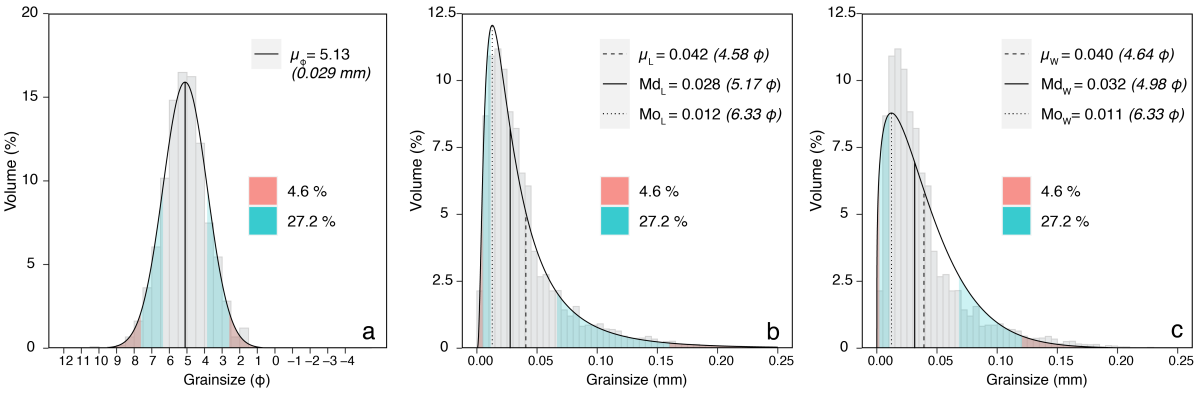

Figure C.2: Simulated grain size data for distal Mazama sample AP1 fit with a) normal; b) log-normal and c) Weibull probability density functions. The coloured segments correspond to >1 standard deviation, so the blue shaded area contains 27.2% of the distribution (±1 to 2σ) and the red shaded area contains 4.6% of the distribution (>2σ).

C.2.2 Methods of fitting distributions

GSDs are reported as histograms, in other words, the individual particle sizes are not known the proportion of the total mass or volume of particles is known within a grain size range. This is why graphical parameters and the method of moments have been favoured (*Folk and Ward*, 1957; *Blott and Pye*, 2001) as they can be easily calculated from binned data. An alternative approach is to find the best fit parameters of a chosen function (e.g., log-normal or Weibull) using least squares regression, typically by fitting the cumulative density function (e.g., *Macías-García et al.*, 2004). Another method is to simulate measurements of individual particle sizes based on the proportion within each grain size bin, which facilitates the use of maximum likelihood estimation methods.

For this contribution we have used the latter approach of simulating data based on the measured GSD (Fig. C.2). We chose this approach because we found that the least squares regression approach was more sensitive to the grain size bin configuration than maximum likelihood estimates. We simulate the grain size data by assuming that the weight or volume percent within each grain size bin is equivalent to the number or frequency of measurements (n). We then generate a uniform distribution of grain size measurements, where the number of measurements is equal to m and the absolute value ranges between the minimum and maximum size of the bin. This simulated dataset can then be used to fit a range of PDFs.

We fit log-normal and Weibull distributions to the simulated data using the '`fitdistrplus`' package in R (*Delignette-Muller and Dutang*, 2015). An example of a normal, log-normal and Weibull distribution fit to a unimodal Grain Size Distribution (distal Mazama) is shown in Figure B2. We fit bimodal distributions using the '`mixfit`' function from the '`mixR`' R package (*Yu*, 2018) with example fits shown in Figure C.3 (distal MSH).

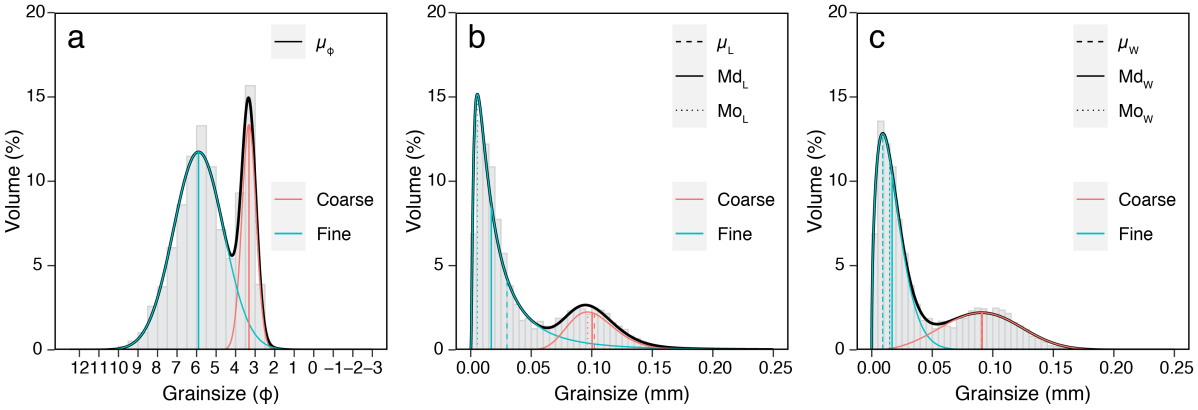

Figure C.3: Simulated grain size data for distal Mount St. Helens sample SB fit with bimodal a) normal; b) log-normal and c) Weibull probability density functions. The coarse and fine sub-populations are indicated by the coloured PDFs with the mode, mean and median of each population also indicated by corresponding lines. The solid black line is the bimodal distribution according to Eqs. C.7, C.12 and C.14

In Chapter 4, we report the FW parameters and the parameters of bimodal normal distributions fit to data on the ϕ-scale (Eq. C.7) to allow comparisons with previously published grain size statistics. This also avoids any confusion that might arise from comparing Weibull parameters determined by different fitting methods (e.g., DECOLOG; *Eychenne et al.*, 2015).

C.3 Further specifications on the Camsizer X2

C.3.1 Further information regarding the Dynamic Image Analysis procedure

The Dynamic Image Analysis (DIA) procedure used by the CX2 has been extensively tested and calibrated as certified by the International Organisation for Standardisation (ISO 13322-2). Uniquely the CX2 (*MRB*, 2020) has been designed to optimise the use of DIA. For example, to ensure optimal images are collected for the size and shape analysis, the concentration of particles per image is moderated. For the X-fall and X-jet dispersion modules, samples are fed by a vibrating feeding chute that ensures a steady stream of sample is fed into the imaging module and the CX2 software has been programmed to moderate the frequency of the vibrations to reach an optimal obscuration of the cameras. When using the X-flow dispersion module, the user adds small amounts of the sample until the images have a set concentration or obscuration. Both the automatic sample feeder and obscuration limits ensures that the images are not overcrowded with particles that would increase the chances of overlapping particles. Furthermore, the automatic feeder minimises user error which would be introduced if the sample was fed manually.

The basic camera images the whole width of the particle beam and every particle within each image is analysed. The zoom camera analyses a smaller area of the particle beam that is then

scaled to match that of the basic camera. Not all particles within a sample will be imaged and analysed, for example, the first particles that pass through the cameras field of view initiate the measurement and are omitted whilst the sample feeder is calibrated according to the software specifications. Whilst there can be some variability within the absolute number of particles analysed for repeated measurements, CX2 analyses are highly reproducible when at least 30 000 images have been processed per analysis (*MRB*, 2020). Typically this number of images ensures that at least ~105-108 particles are analysed per analysis (see Supplementary Data).

C.3.2 Simplified user guidelines for practical use of the CX2

Here we provide Figure C.4, a flow chart that can be used to decide on pre-analysis sample prep and the choice of dispersion module. If sieve analysis is to be combined with CX2 data, the sieve data can be input into the CX2 software, which has a function to combine sieve and CX2 analyses. If two separate CX2 analyses are being combined (e.g., X-fall and X-jet), we recommend combining them according to their relative weight or volume percent, which must be quantified separately. After deciding on the best dispersion mechanism and whether pre-analysis sieving is required, the sample is ready to be analysed using the CX2. The next step is to set the acquisition parameters in the taskfile or use an existing taskfile. The most important parameters to set are the size and shape parameters to be measured, the grain size increments for the data to be output in, the size range of measurement and whether a velocity adaption file is necessary. Specific to the X-jet dispersion method is inputting the air pressure used in the analysis.

C.3.3 Additional method limitations

The CX2 protocol and software is generally flexible but this adaptability facilitates the introduction of user error and potential bias. As outlined in the methodology (see Chapter 4 section 4.3), a 'task file' is required to initiate the appropriate dispersal conditions (e.g., air pressure, velocity adaption, grain size bins) however, if designed incorrectly, the task file can introduce systematic errors in the GSD. For example, the CX2 underestimated the volume of particles in the dense sieve fractions of the Mazama tephra samples (Fig.4.8e-f in Chapter 4). This is because the velocity adaption file (Fig.e C.5) cannot account for particles within a narrow grain size range (~ half-ϕ sieve fraction) being dispersed at different speeds. We see this in Figure C.5a where the scatter in particle velocities around 200 μm cannot be captured by a user-fitted curve. The Mazama sample is an extreme case because of the dense magnetite crystals falling much faster relative to the glassy particles of the same size, however it revealed the limitations of the velocity adaption.

Another detriment in the need to design appropriate task files for CX2 analysis is the iterative approach necessary to find the optimal conditions. For example, when designing a task file to use with the X-jet module (compressed air dispersion) the air pressure must be sufficient to

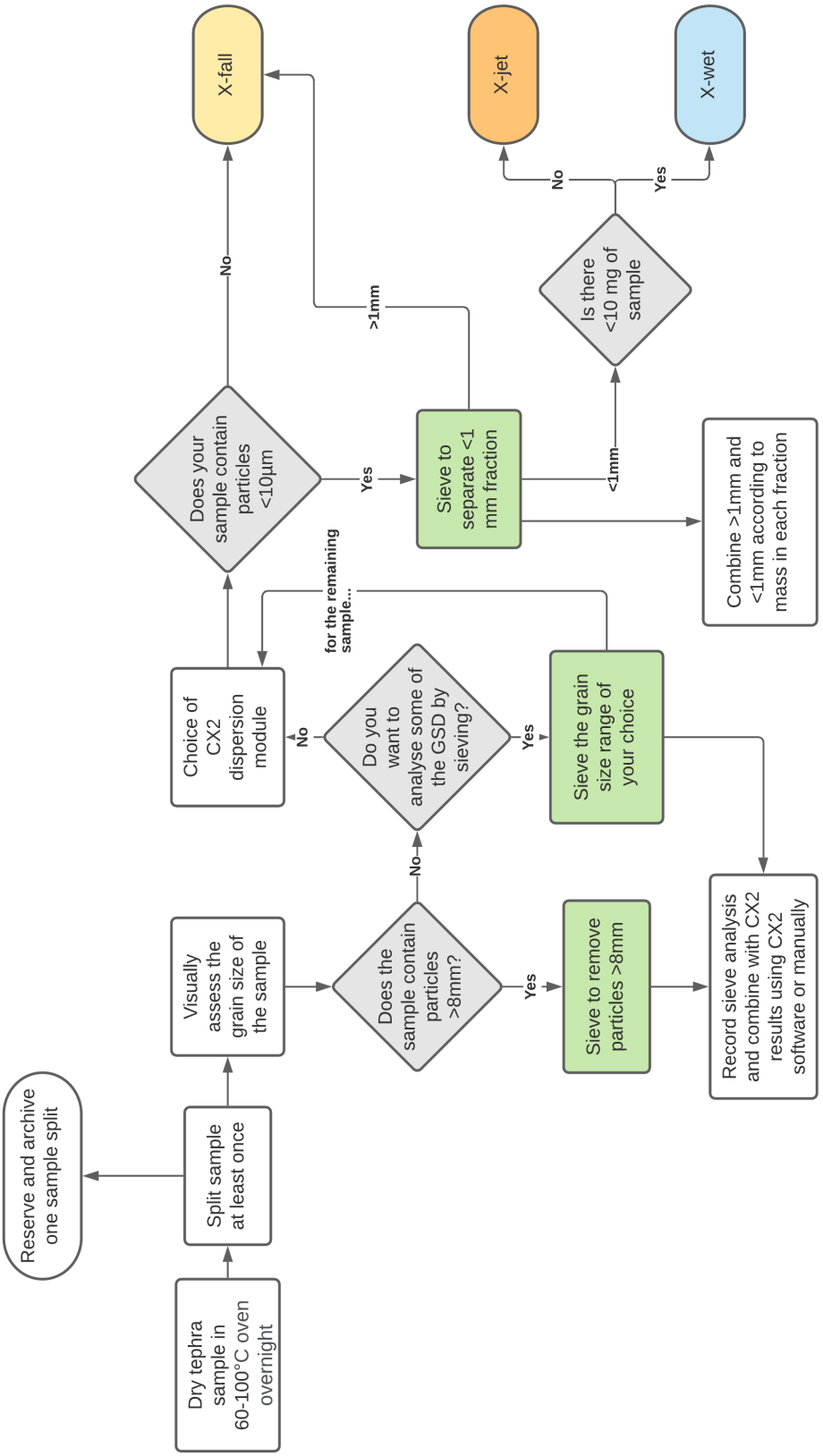

Figure C.4: Flow chart for sample preparation and CX2 dispersion mechanism choice.

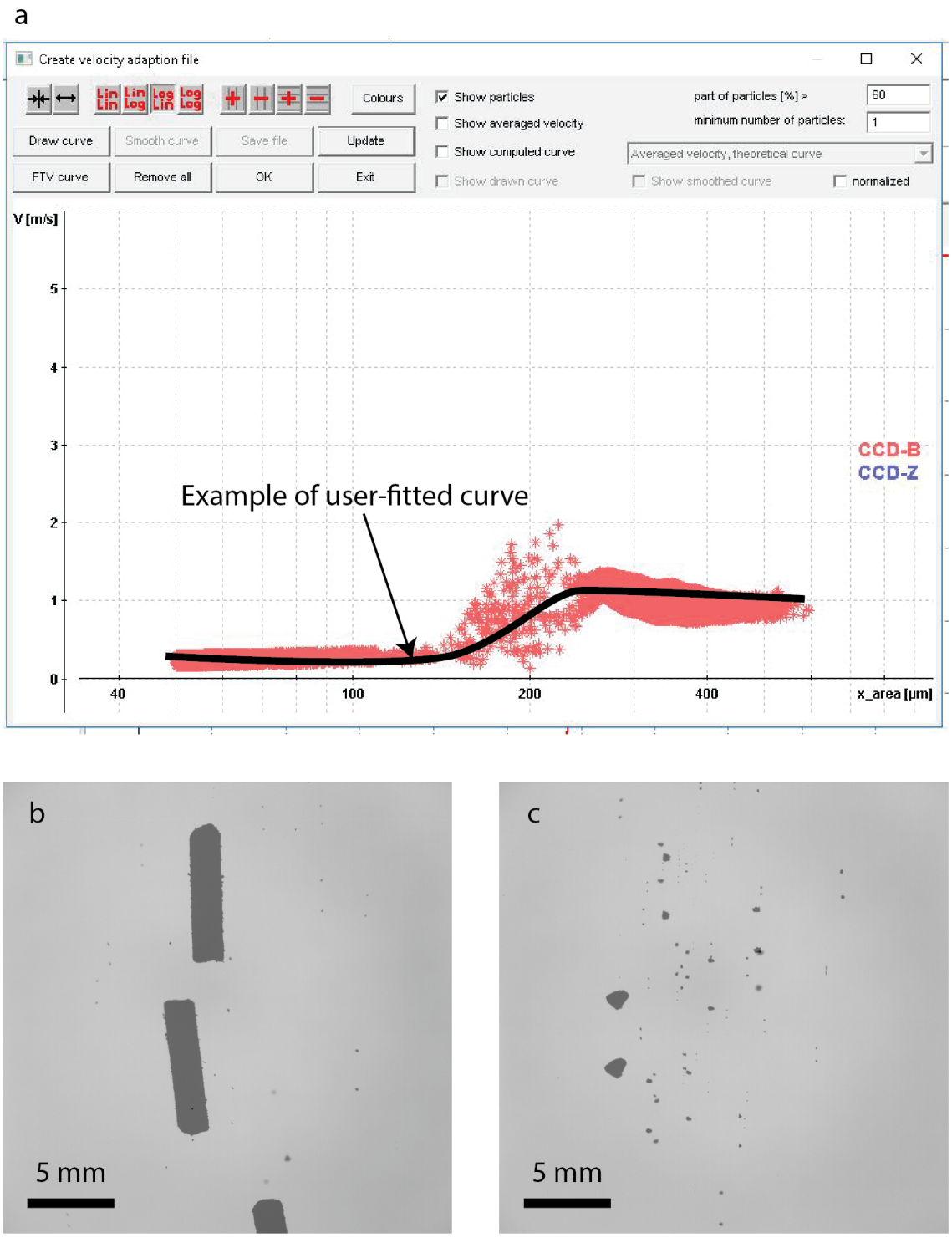

Figure C.5: The CX2 velocity adaption. a) A screenshot of the particle size (x-axis) versus particle velocity (y-axis) data calculated by the CX2 software from the double exposure images. b) An example of a double exposure image of the rod-shaped particles. c) An example of a double exposure image of Mount St. Helens ash.

break-up particle aggregates, but not so high that is breaks particles (*MRB*, 2020). However, this threshold can only be assessed by running multiple analyses to observe when the GSD stabilises and clearly this is only possible with large quantities of the sample, especially for the X-jet and X-flow analyses where the sample is non-recoverable. For volume limited samples, we use an existing task file designed for a sample of similar properties, but this may be difficult if you are working with an unfamiliar sample.

C.4 Information on the natural samples used in method testing and comparisons

C.4.1 The Mazama ~7.7 ka tephra

The climactic eruption of Mount Mazama formed modern day Crater Lake, Oregon, USA. The caldera forming eruption occurred ~ 7700 yr BP (*Bacon and Lanphere*, 2006; *Egan et al.*, 2015) and the distal ash has been recorded >2000 km from source in the Greenland ice sheet (*Hammer et al.*, 1980; *Zdanowicz et al.*, 1999). Recent estimates of the total erupted volume from the climactic eruption range from ~150-180 km^3 and the area that experienced ~1 cm of tephra fallout >1.7 million km^2. The tephra has been extensively studied and sampled by multiple disciplines, but the availability of grain size data varies across the deposit.

For this study we used 18 samples (Table C.2) from 120-1300 km from source to test the capabilities of the CX2. The most proximal sample used is from site 46 which in close proximity to Mount Bachelor. The tephra record at this locality records the full fallout sequence (Young 1990) and evidence of co-pyroclastic density current (co-PDC) fallout (see Fig. 4.3 and Chapter 3). The distal samples were collected for this study (see Chapter 2 and by other authors including J. Westgate (*pers.comms*) and *Jensen et al.* (2019).

C.4.2 Hverfjall Fires ~2.5 ka tephra

The Hverfjall Fires refers to a period of fissure activity from the Krafla volcanic system in northern Iceland in that initiated ~2500 BP (*Þórarinsson*, 1952; *Mattsson and Höskuldsson*, 2011; *Liu et al.*, 2017). The activity was concentrated on the southern end of the fissure, in the Mývatn region, that formed both magmatic cones (Jarðbaðshólar cone complex) and hydromagmatic cones (Hverfjall tuff ring) (*Mattsson and Höskuldsson*, 2011; *Liu et al.*, 2017).

The Hverfall samples analysed in this study are from the hydromagmatic fallout sampled 1.5 and 3.5 km from source. Both samples have been previously analysed by *Liu et al.* (2017) with grain size measured using sieving and laser diffraction. Grain shape and the proportion of different components was determined from SEM images (*Liu et al.*, 2017).

Table C.2: Sample names, Global Volcano Program (GVP) volcano name and the sampling location information for the natural samples used in the method development and testing.

Sample	GVP Volcano Name	Latitude	Longitude	Distance from source (km)	Reference(s)
Mazama ~7.7 ka[a]					
Mount Bachelor (46_UPU)	Crater Lake	44.006 N	121.676 W	123	Appendix A.1
Mount Bachelor (46_LPU)	Crater Lake	44.006 N	121.676 W	123	Appendix A.1
Juniper Canyon (80)	Crater Lake	45.955 N	119.032 W	413	*Sweeney et al.* (2005); Appendix A.1
Spring Gulch (81)	Crater Lake	46.001 N	118.975 W	420	*Carson and Pogue* (1996); Appendix A.1
Andies Prairie (73)	Crater Lake	45.703 N	118.034 W	444	Appendix A.1
Pole Bridge (69)	Crater Lake	45.386 N	117.425 W	459	Carson 2001; *Carson* (2001); Appendix A.1
Palouse Falls (101)	Crater Lake	46.701 N	118.412 W	508	*Carson and Pogue* (1996); Appendix A.1
UA3377 (181)	Crater Lake	49.649 N	114.708 W	937	*Driver* (1982); *Jensen et al.* (2019); Appendix A.1
UA2932 (177)	Crater Lake	49.466 N	114.358 W	946	*Landals* (1990); *Jensen et al.* (2019); Appendix A.1
UA2820 (246)	Crater Lake	51.097 N	115.109 W	1052	*Newton* (1991); *Jensen et al.* (2019); Appendix A.1
UA3379 (264)	Crater Lake	51.967 N	116.752 W	1086	*Westgate and Dreimanis* (1967); *Jensen et al.* (2019); Appendix A.1
UA3378 (263)	Crater Lake	51.791 N	115.469 W	1106	*Jensen et al.* (2019); Appendix A.1
UA2816 (275)	Crater Lake	52.462 N	116.115 W	1154	*Jensen et al.* (2019); Appendix A.1
UA2825 (184)	Crater Lake	49.667 N	110.260 W	1173	*Freeman et al.* (2006); *Jensen et al.* (2019); Appendix A.1
UA2704 (190)	Crater Lake	49.804 N	109.722 W	1214	*Jensen et al.* (2019); Appendix A.1
UA2963 (278)	Crater Lake	52.677 N	113.146 W	1274	*Jensen et al.* (2019); Appendix A.1
UA2703 (234)	Crater Lake	50.890 N	109.846 W	1280	*Jensen et al.* (2019); Appendix A.1
UA1573 (289)	Crater Lake	53.529 N	113.514 W	1341	*Jensen et al.* (2019); Appendix A.1
Hverfjall Fires ~2.5 ka					
HV2.3	Krafla	65.594 N	16.861 W	1.5	*Liu et al.* (2017)
HV6.3	Krafla	65.633 N	16.844 W	3.5	*Liu et al.* (2017)
Mount St. Helens 1980					
DZ20-25[b]	St. Helens	47.006 N	120.591 W	152	*Durant et al.* (2009)
Ellensburg (EB)	St. Helens	46.997 N	120.545 W	153	*Meredith* (2019)
Moses Lake (ML)	St. Helens	47.130 N	119.278 W	245	*Meredith* (2019)
DZ21-8[b]	St Helens	47.137 N	119.258 W	248	*Durant et al.* (2009)
Walla Walla (WW)	St. Helens	46.065 N	118.333 W	298	*Meredith* (2019)
Ritzville (RV)	St. Helens	47.127 N	118.380 W	309	*Meredith* (2019)
DAVIS 11**	St. Helens	47.130 N	118.347 W	312	*Durant et al.* (2009)
Starbuck (SB)	St. Helens	46.520 N	118.129 W	314	*Meredith* (2019)
Campanian Ignimbrite ~39 ka					
SGM	Campi Flegrei	40.65 N	15.43 E	110	*Engwell et al.* (2014)
RC9-189	Campi Flegrei	36.98 N	19.68 E	645	*Engwell et al.* (2014)
Phillipon Tenaghi	Campi Flegrei	40.97 N	24.22 E	850	*Engwell et al.* (2014)
Franchi Cave	Campi Flegrei	37.51 N	22.96 E	850	*Engwell et al.* (2014)
Caciulastesti	Campi Flegrei	43.94 N	23.94 E	880	*Engwell et al.* (2014)
Dragnesti-OLT	Campi Flegrei	44.16 N	24.54 E	940	*Engwell et al.* (2014)
Bordusani	Campu Flegrei	45.104 N	26.961 E	1145	This study
Boschevo	Campi Flegrei	51.4 N	39 E	2300	*Engwell et al.* (2014)
Kostenki	Campi Flegrei	51.4 N	39 E	2300	*Engwell et al.* (2014)

(a) Sample numbers referred to locality numbers in Appendix A.1.

(b) Samples not analysed in this study, but the GSD from *Durant et al.* (2009) was used for comparison.

C.4.3 Mount St. Helens 1980 tephra

The 18 May 1980 eruption of Mount Saint Helens (MSH) produced a subaerial tephra deposit dominantly to the east of the volcano. The eruption began with a directed lateral blast and flank collapse, which was followed by series of sub-Plinian and Plinian phases that erupted dominantly dacite (*Sarna-Wojcicki et al.*, 1981; *Carey and Sigurdsson*, 1982; *Durant et al.*, 2009). The bulk total erupted volume is estimated to be ~1.3 km^3 (*Pyle*, 1989) and the deposit has been extensively studied from physical volcanology, petrology and modelling perspective (e.g., *Carey and Sigurdsson*, 1982; *Armienti et al.*, 1988; *Muñoz et al.*, 2004; *Durant et al.*, 2009; *Saunders et al.*, 2012; *Muir et al.*, 2012; *Eychenne et al.*, 2015; *Brand et al.*, 2016; *Meredith*, 2019).

A new set of MSH May 1980 distal tephra samples were selected for analysis using the CX2 (*Meredith*, 2019). The samples range from 153-314 km from source and three sample locations have been matched with corresponding sample locations previously analysed with laser diffraction by *Durant et al.* (2009; Table C.2) and (*Eychenne et al.*, 2015).

C.4.4 Campanian Ignimbrite ~39 ka tephra

The Campanian Ignimbrite eruption occurred ~39 ka from the Campi Flegrei caldera complex in Italy. It is the largest eruption to occur in Europe in the past 200 kyr with an estimated bulk erupted volume of >300 km3 (*Pyle et al.*, 2006). The fallout from the Campanian ignimbrite eruption has a large offshore record (*Engwell et al.*, 2014; *Smith et al.*, 2016) and a number of studies have used dispersion models to reconstruct the deposit (*Costa et al.*, 2012; *Marti et al.*, 2015).

7 of the 8 distal samples analysed in this study were first analysed for grain size by *Engwell et al.* (2014) using laser diffraction (Table C.2). One new distal Campanian Ignimbrite sample is reported in this study, which was collected near Bordusani, Romania (Table C.2). All distal samples are from >500 km from source and are dominated by platy glass fragments. We also analysed individual sieve fractions from one proximal sample (110 km) from the San Gregorio Magno (SGM) lacustrine basin (*Engwell et al.*, 2015). The proximal sample has previously been analysed by sieving and laser diffraction (S Engwell pers. comm.; *Engwell et al.* 2014) and contains a large portion of elongated tube pumice.

C.5 Additional results from CX2 method testing

Here we present the results from additional method testing. Figure C.6 shows that the size and shape of delicate particles can be affected by sieving (*Cox et al.*, 2017). The static image analysis revealed that sieving increased the sphericity (ψR) and decreased the equivalent circle diameter (d_c) and that the effects where the most significant for the sieve meshes between 32-125 µm.

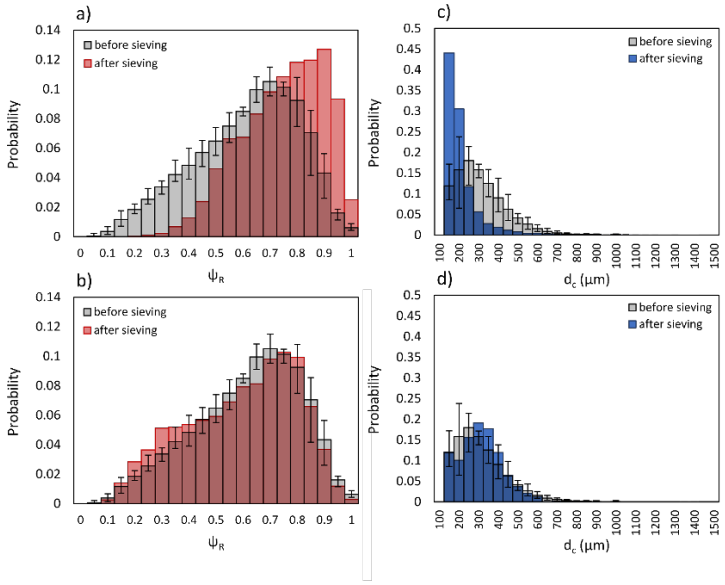

Figure C.6: The impact of sieving on particle size and shape. Sphericity (ψR) and equivalent circle diameter (d_c) distribution of 24,856 particles of Katla SILK-LN ash (KSL; *Saxby et al.* 2020) before and after being passed through a) 3 sieves with mesh sizes between 32-125 µm; and b) 2 sieves with mesh sizes of 125 and 500 µm. Also shown are distributions of area-equivalent circle diameter d_c for the same particles before and after being passed through c) 3 sieves with mesh sizes between 32-125 µm; and d) 2 sieves with mesh sizes of 125 and 500 µm. Error bars show error in distributions before sieving, from 5 repeat data collections on subsets of the same sample. Data and analysis by *Cox et al.* (2017).

Table C.3: Fixed shape particle information and GSD statistics.

	Manufacturer $x_F e$max (µm)	Manufacturer $x_c$min (µm)	CX2 $x_F e$max (Md, µm)	CX2 $x_c$min (Md, µm)	Manufacturer b/l	CX2 b/l
Disc	3200	1000	3700	3200	0.31	0.72
Rod	6200	1800	6400	1800	0.29	0.32

Particles with fixed shapes were analysed with the CX2; rod and disc shaped beads (see Chapter

4, Figs. 4.5 & 4.6). The CX2 Grain Size Distributions (GSDs) vary significantly depending on the size parameter used, as shown in Figure C.7 and in the distribution statistics in Table C.3. This emphasises one key limitation of the CX2 that arises particles being imaged at different orientations to the imaging module . In the case of the disc shaped particles it is rare that the particles are ever precisely orientated in the particle stream so that the true minimum dimension ($x_c$min) is captured (Fig. C.7c). This is reflected in the flat distribution of $x_c$min values measured for the fixed shape particles (see Fig. 4.6 in the main text). This has implications for the size and shape parameters calculated by the CX2 and is related to the challenges of converting from 2D images to 3D volume data.

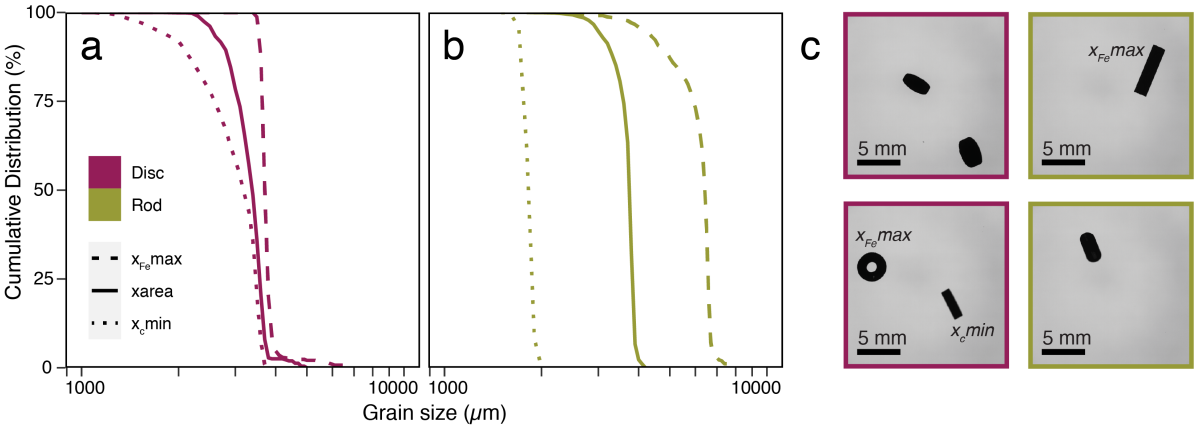

Figure C.7: Comparing the size parameters for fixed size and shape particles. a-b) Cumulative Grain Size Distributions showing the three size parameters (differentiated by the line pattern). c) CX2 X-fall images of falling particles illustrating the impact of particle orientation relative to the captured image.

For spherical particles we would expect sphericity, symmetry and aspect ratio to equal 1. We observed from optical images of the ballotini, however, that some particles deviate from perfect spheres which explains why the distribution of SPHT, Symm and b/l measured on the sieved ballotini samples range between ~0.9-1 (Fig. C.8). Importantly we do not observe a significant trend between SPHT and size suggesting that this parameter is not sensitive to particle size. The only trend observed is between grain size and aspect ratio which we attribute to the increasing proportion of non-spherical particles in the coarsest ballotini sieve fraction (see Figs. 4.3 and C.8).

Comparisons of sieve analysis and CX2 data highlights the importance of particle density for grain size analysis. Varied particle densities mean that mass-based GSDs (sieving) and volume-based GSDs (CX2) can diverge (see Fig. 4.8). However, what we show in Figure C.9 is that where the changes in particle density are less significant, CX2 and sieving GSDs can be in close agreement.

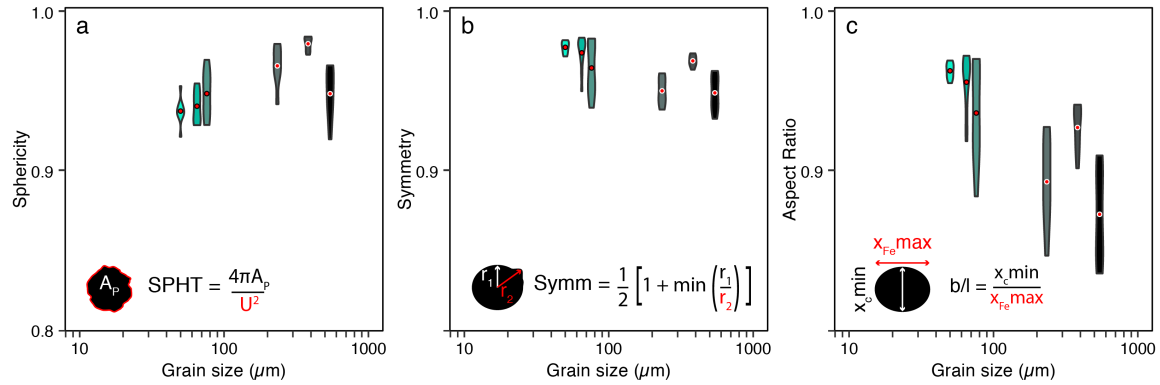

Figure C.8: Shape parameters indicating the deviation of ballotini from perfect spheres. Violin plots show the distribution of the shape parameters for the median grain size where the colour corresponds to the grain size (see Chapter 4, Fig. 4.3a). The red dot corresponds to the mean value of the shape parameter. a) Sphericity (SPHT), b) Symmetry (Symm) and c) Aspect ratio (b/l).

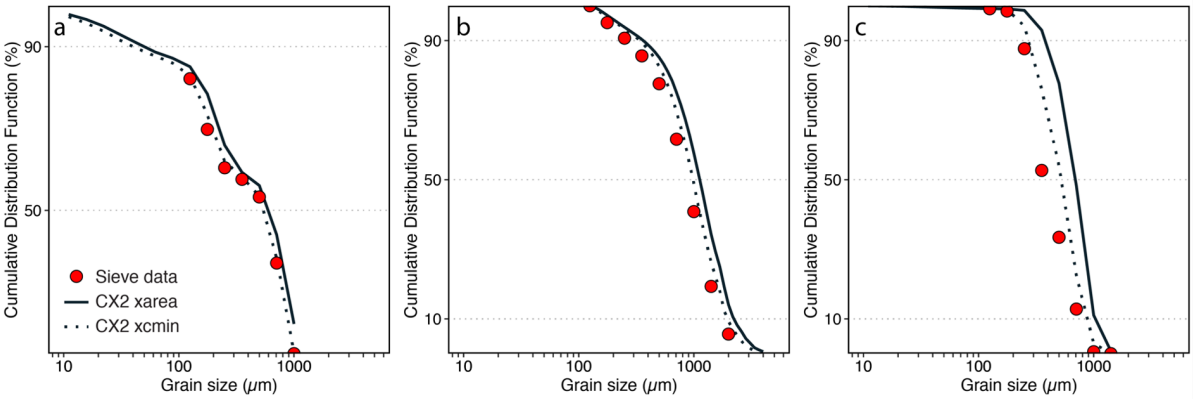

Figure C.9: Comparing sieve data (red dots) with CX2 GSDs (black lines). a) Mount Saint Helens sample SB; b) Surtsey 1963, Iceland and c) climactic Mazama sample (MZ46 low).

APPENDIX D

APPENDIX D - SUPPLEMENTARY MATERIAL FOR CHAPTER 5

D.1 Sensitivity analysis of TGSDs

I repeated the jack-knife resampling analysis on three additional grain size data sets to investigate the sensitivity of TGSDs to the inclusion of proximal data. Here I briefly introduce the data sets and present the results of the jack-knife resampling. In the future, this work and the results of Chapter 5 will be contribute to a more detailed study on the sensitivity of TGSDs to the distribution of field data. The grain size datasets and the scripts used to fit the mixture models to are all shared in a GitHub repository at: https://github.com/HannahBuckland/Grain-size-scripts.

D.1.1 Grain size datasets

D.1.1.1 Mount St. Helens May 1980

For background on the May 18th, 1980 eruption of Mount St. Helens (MSH) please see Appendix C, section C.4.3.

The grain size characteristics of the MSH fallout deposit were characterised by USGS scientists soon after the eruption from May 19th-22nd 1980 (*Sarna-Wojcicki et al.*, 1981). Five transects perpendicular to the deposit axis allowed for systematic sample collection from 160 to 630 km from the vent (Fig. D.1b). The TGSD has previously been estimated using a weighted sector approach (*Carey and Sigurdsson*, 1982) and Voronoi tesselation (*Rose and Durant*, 2009). All reconstructions produce bimodal TGSDs and often the MSH 1980 deposit is cited as an example

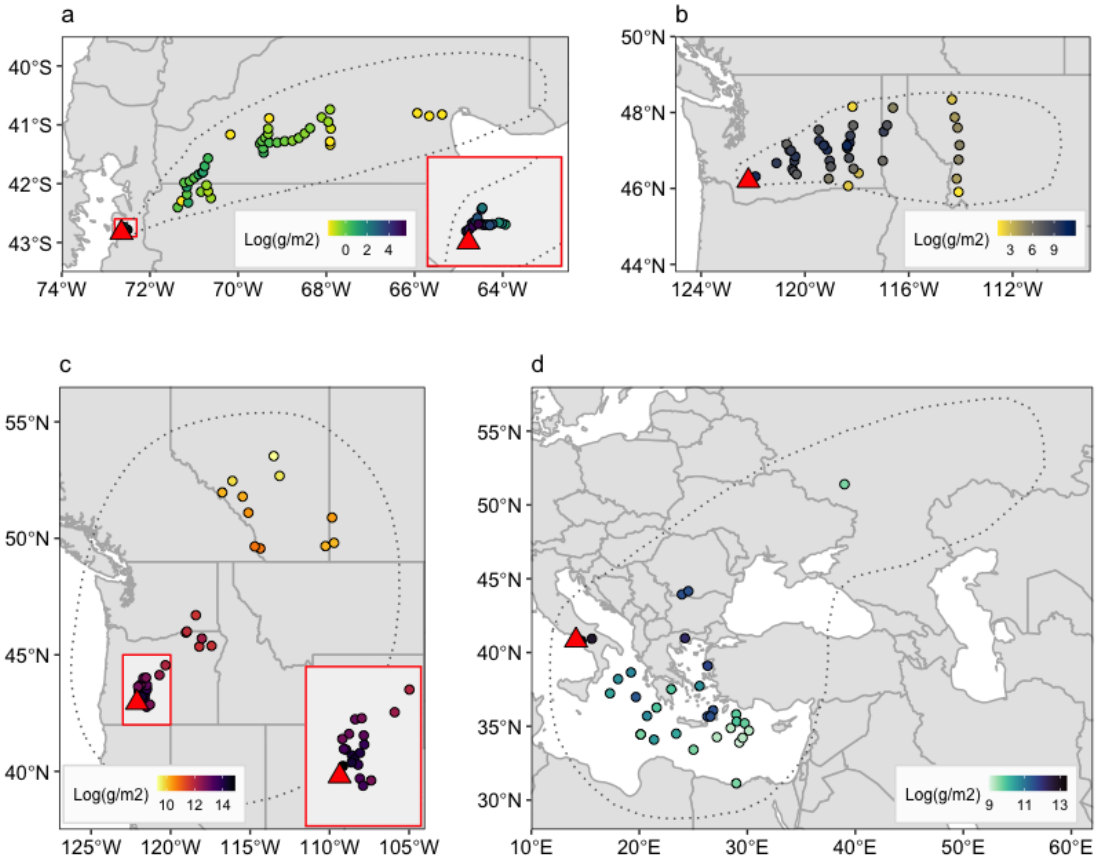

Figure D.1: Maps of the deposits analysed for TGSD sensitivity. Points are colour coded according to the logarithm of the mass accumulation of tephra at that location. The zero-mass line used in the TGSD calculations is shown for each deposit as a dotted line. a) Chaitén (*Watt et al.*, 2009; *Alfano et al.*, 2016), b) Mount St. Helens (*Sarna-Wojcicki et al.*, 1981; *Carey and Sigurdsson*, 1982; *Meredith*, 2019), c) Mount Mazama (*Young* 1990, Chapters 2-5) and d) Campanian Ignimbrite (*Rosi et al.*, 1999; *Engwell et al.*, 2014).

of a very fine-grained TGSD. The dataset used here in the jack-knife resampling analysis also includes additional GSDs collected by *Meredith* (2019, Appendix C).

D.1.1.2 Chaiten 2008

Chaitén, an Andean volcano in southern Chile, erupted on the 2nd of May 2008 with minimal precursory activity in part due to limited monitoring (*Watt et al.*, 2009; *Alfano et al.*, 2011b). The eruption was characterised by an explosive phase from May 2-8 where the eruption column reached ~15-30 km. The tephra deposit from the main explosive phase (May 2-8) was dispersed to the east of the volcano (Fig. D.1a), across Chile and reached the Atlantic coast of Argentina,

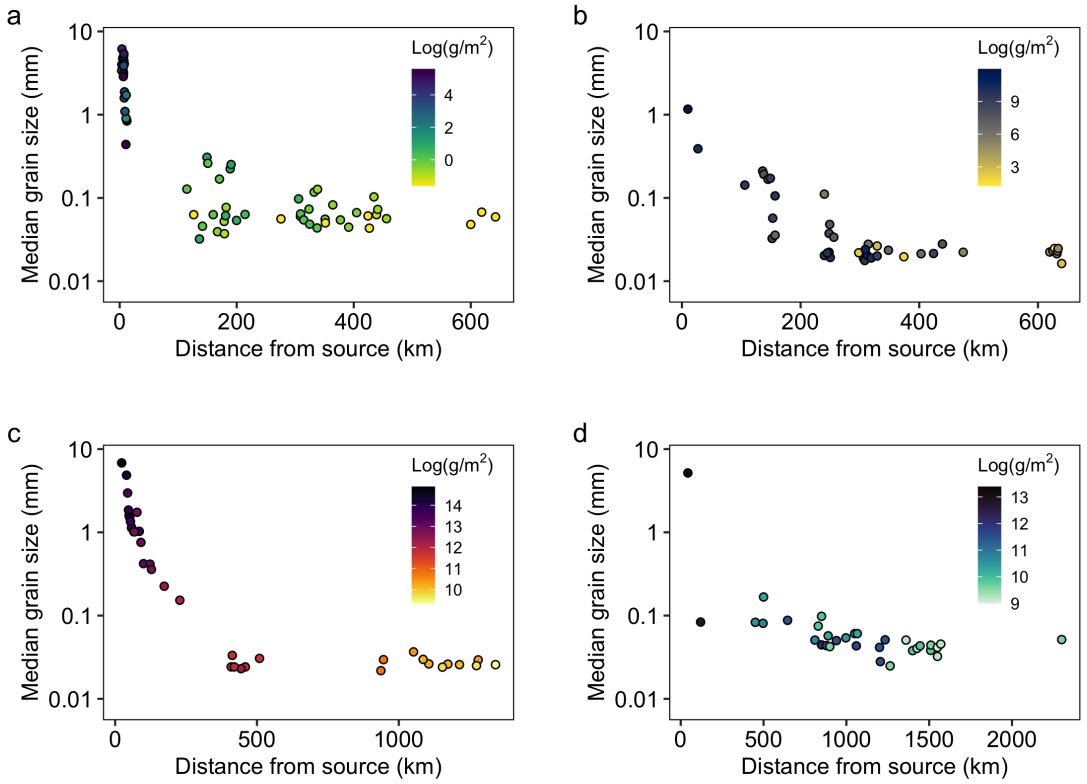

Figure D.2: Trends in median grain size with distance from source. The colour of the points shows the logarithm of the mass accumulation of tephra at each locality (as in Fig. D.1). a) Chaitén, b) Mount St. Helens, c) Mount Mazama and d) Campanian Ignimbrite (data sources as in Fig. D.1).

covering an area >2x10^5 km^2 (*Watt et al.*, 2009; *Alfano et al.*, 2011b). Tephra mapping and sampling was carried out soon after the eruption from ~3-25 km (*Alfano et al.*, 2011b) and 115-640 km from source (*Watt et al.*, 2009; *Durant et al.*, 2012) to characterise the proximal and distal deposits (Fig. D.2a).

Here I focus on the deposit associated with the most explosive period of activity on the 6th of May (Layer β; *Alfano et al.* 2011b). The TGSD of this layer has been assessed using a weighted sector approach (*Watt et al.*, 2009) and by *Osores et al.* (2013). Furthermore, *Alfano et al.* (2016) assessed the sensitivity of the TGSD of Layer β by adding synthetic data points in areas where sampling was not achieved (Dataset B in *Alfano et al.* 2016). Using the Voronoi tessellation method *Alfano et al.* (2016) found that the TGSD was most sensitive to the inclusion of synthetic data in medial areas and where the settling regime of particles was changing. Here I use the Chaitén grain size data without the synthetic data point as the aim is to assess the sensitivity of TGSDs derived

purely from field data. However, we recognise the significance of the sensitivity analysis already carried out on this dataset by *Alfano et al.* (2016).

D.1.1.3 Campanian Ignimbrite Tephra ~39 ka

For background on the ~39 ka Campanian Ignimbrite eruption of the Campi Flegrei caldera complex, please see Appendix C, section C.4.4.

The grain size data for the Campanian Ignimbrite tephra is mostly from the distal deposit >450 km from source (Figs. D.1d & D.2d). The GSDs have been measured from tephra contained in offshore cores and from terrestrial sections collected by various authors (*Pyle et al.*, 2006; *Engwell et al.*, 2014). We also include one GSD from the Plinian fall deposit of the Campanian Ignimbrite eruption reported by *Rosi et al.* (1999) in order to demonstrate the sensitivity of the TGSD to including a single locality <50 km from source. The TGSD of the Plinian and co-PDC phases has been reconstructed from distal deposits using the Voronoi tesselation technique by *Marti et al.* (2016), however, here we treat the deposit as one phase for illustrative purposes.

D.1.2 Methods

To reconstruct the TGSD of each tephra deposit, I applied the Voronoi tessellation method (*Bonadonna et al.*, 2005a) to the complete grain size data sets (Fig. D.3). To investigate the sensitivity of this calculation I used jack-knife resampling or leave-one-out analysis, following the methodology outlined in the main text in section 5.3. All the grain size data has been processed in full ϕ units for continuity throughout. Additionally, all the TGSDs were fit with bimodal normal distributions (in ϕ units, see Appendix C.2, Eq. C.7) which allows reporting of the the coarse and fine modes.

D.1.3 Results

The complete TGSDs reconstructed for tephra deposits are shown in panel i of Figure D.4 (Table 5.1). Additionally, the finest (panel ii) and coarsest (panel iii) TGSDs reconstructed from the jack-knifed datasets are also shown in Figure D.4. The results using the full Mazama grain size dataset (Dataset A in Chapter 5) are plotted for comparison. The median grain size (Md) of each TGSD, and the coarse and fine modes of the bimodal TGSDs are reported in Table D.1.

The TGSD that is the most susceptible to variability by the exclusion of a single point is the Campanian data set (Fig. D.1d). This is because there is only one location that has a coarse GSD (Md > 1000 μm; Fig. D.2d) that is associated with the Plinian fallout <50 km from source (*Rosi et al.*, 1999). Including this locality introduces a coarse mode ~-2.6 ϕ in the TGSD (Table D.1). Whilst the sensitivity to a single point is important to note, it is unlikely this dataset would be used to infer a meaningful TGSD for the Campanian Ignimbrite eruption. In other words, this

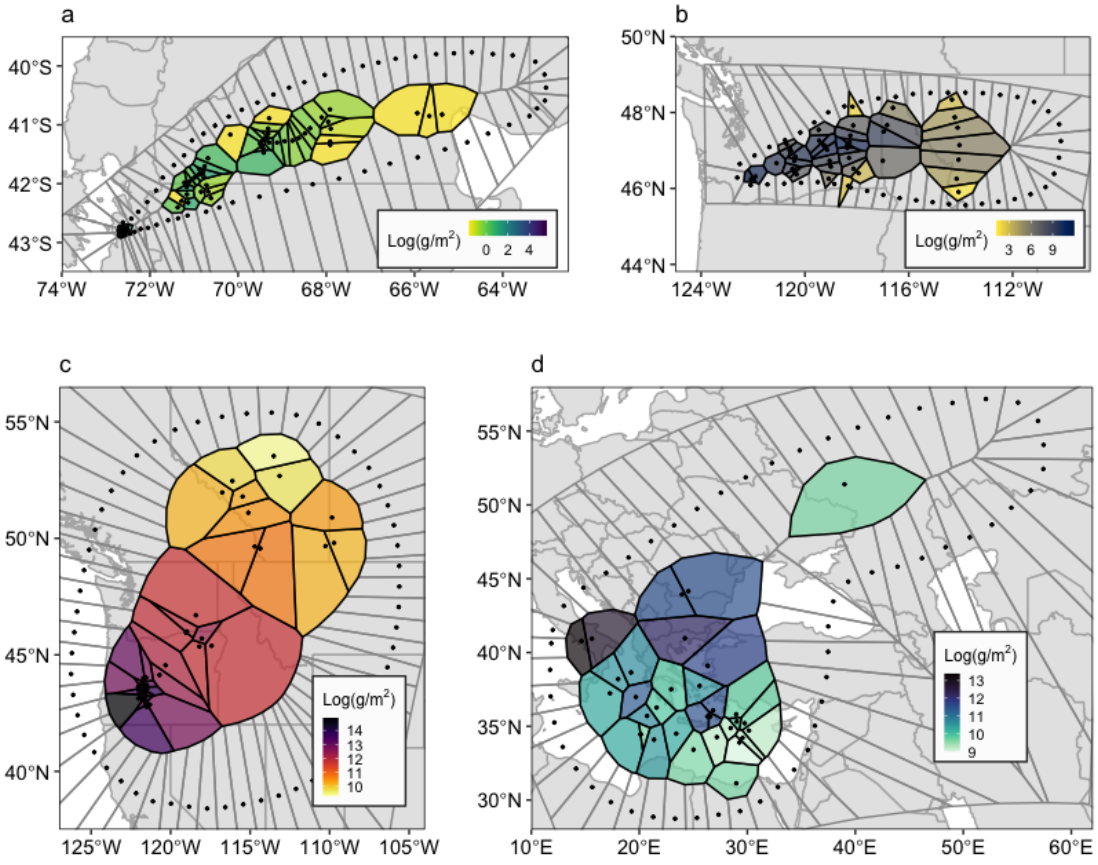

Figure D.3: Maps of the spatial Voronoi tessellation method used to reconstruct the TGSDs. The Voronoi cells are coloured according to the logarithm of the mass accumulation recorded at the tephra locality associated with each cell. Maps are for a) Chaitén, b) Mount St. Helens, c) Mount Mazama and d) Campanian Ignimbrite (data sources as in Fig. D.1).

distribution of field sampling clearly will not represent the full range of particle sizes produced by the eruption.

Excluding the Campanian dataset, the jack-knife analysis that exhibits the largest range in the Md of the computed TGSD is the May 18th eruption of Mount St. Helens (Fig. D.1b). This is an important observation because the MSH grain size data was collected systematically along transects soon after the eruption. However, it appears that reconstructing the TGSD is still sensitive to one locality 10 km from source (Table D.1).

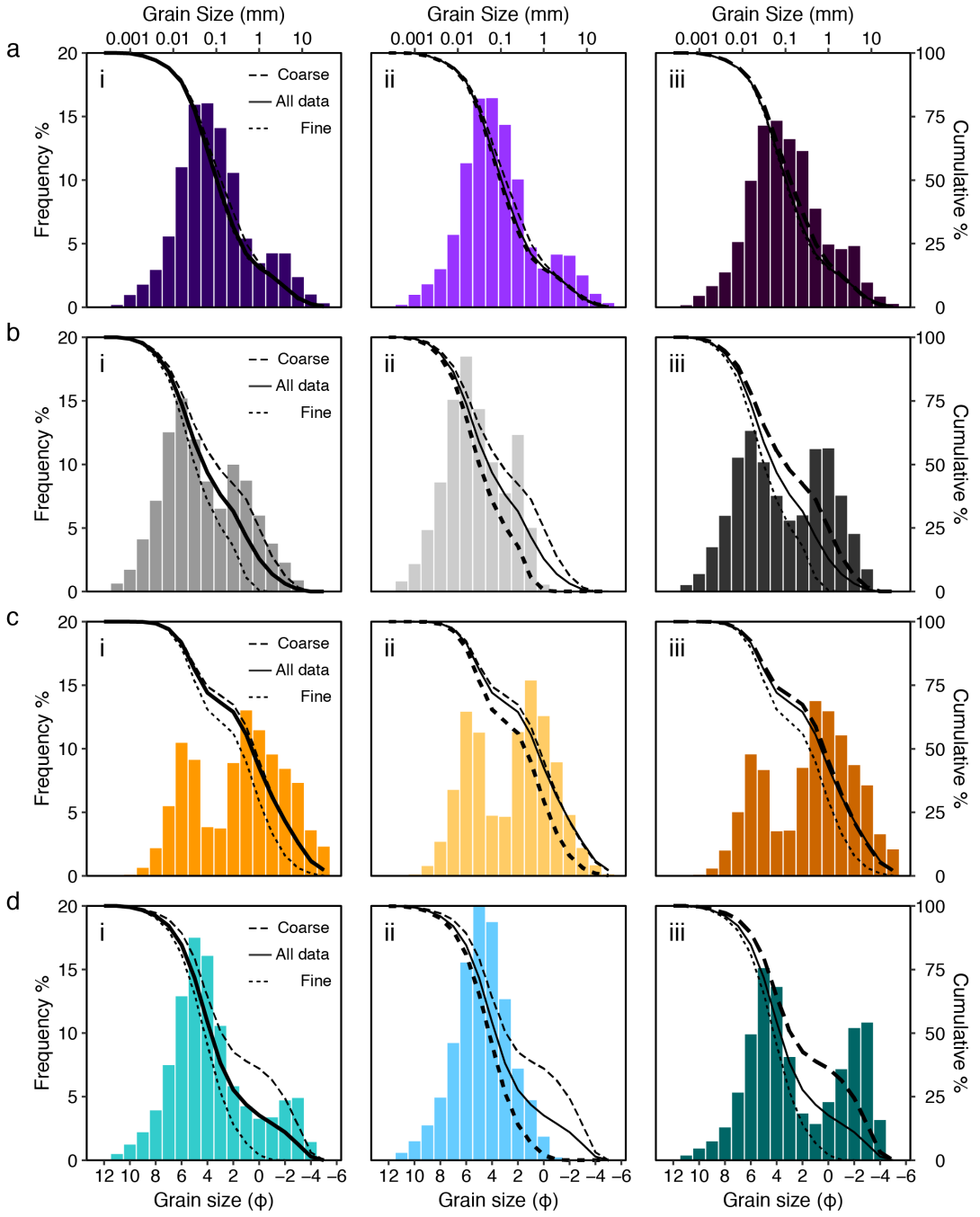

Figure D.4: End-members TGSD sensitivity analysis. The TGSDs calculated using all the data available are show in panel i. The finest and coarsest TGSDs from the leave one out validation are show as frequency plots in panels ii and iii. All three TGSDs are shown for each deposit as cumulative distributions (solid line is full dataset, the dashed line is the finest TGSD and the dashed line is the coarsest TGSD). The datasets used are a) Chaitén, b) Mount St. Helens, c) Mount Mazama and d) the Campanian Ignimbrite (data sources as in Fig. D.1).

Table D.1: Grain size statistics of jack-knife resampled TGSDs. Values are reported in ϕ units.

	Subset	Voronoi Md (ϕ)	Bimodal (Y/N)	Coarse mode (ϕ)	Coarse proportion	Fine mode (ϕ)	Fine proportion
Chaiten	Full	3.27	Y	-2.44	0.12	3.65	0.88
	Finest	3.35	Y	-2.50	0.12	3.73	0.88
	Coarsest	2.96	Y	-2.38	0.10	3.28	0.90
Mount St. Helens	Full	4.27	Y	0.63	0.38	5.69	0.62
	Finest	4.99	Y	1.39	0.18	5.50	0.82
	Coarsest	3.29	Y	-0.35	0.43	5.50	0.57
Mazama (Dataset A)	Full	0.57	Y	-0.78	0.71	5.44	0.29
	Finest	1.46	Y	0.00	0.62	5.39	0.38
	Coarsest	0.35	Y	-0.80	0.73	5.44	0.27
Campanian	Full	3.73	Y	-2.66	0.15	4.17	0.85
	Finest	2.91	N	-	-	-	-
	Coarsest	4.23	Y	-2.55	0.35	4.23	0.65

APPENDIX E

APPENDIX E - SUPPLEMENTARY MATERIAL FOR CHAPTER 6

E.1 Umbrella cloud spreading regime derivation

This section contains the formulas used to derive the different spreading regimes used in Ash3D. For the full derivations please see *Sparks et al.* (1997); *Costa et al.* (2013) and *Webster et al.* (2020). The conservation equation of volume for an expanding cylindrical umbrella cloud with time varying radius R and average cloud thickness h is given by:

$$\frac{d}{dt}\left(\pi R^2 h\right) = q, \tag{E.1}$$

where q is the volume flow rate into the umbrella cloud. And it is assumed that the velocity of the cloud front u_R scales linearly with the cloud average thickness (h):

$$u_R = \frac{dR}{dt} = \lambda N h \tag{E.2}$$

where N is the Brunt-Väisälä frequency and λ is an empirical constant reflecting cloud shape.

The spreading of the umbrella cloud is driven by a horizontal pressure gradient between plume and the ambient atmosphere (*Sparks et al.*, 1997) which is given by:

$$\frac{dP}{dr} = (\rho_c - \rho_a) g \frac{h}{R}, \tag{E.3}$$

where ρ_c is the density of the umbrella cloud, ρ_a is the ambient air density at the neutral buoyancy level and g is is gravitational acceleration.

By accounting for the conservation of mass and momentum using Eqs. E.1 & E.3, *Sparks et al.* (1997) then derive the following formula for the radius of the umbrella cloud (R) fed by a steady column with respect to time (t):

$$R = \left(\frac{3\lambda N q}{2\pi}\right)^{\frac{1}{3}} t^{\frac{2}{3}}, \tag{E.4}$$

Finally, by taking the derivative of Eq. E.3 with respect to time (*Costa et al.*, 2013; *Mastin et al.*, 2014), the velocity of the cloud's outer margin (u_R) with respect to time is given by:

$$u_R = \frac{2}{3}\left(\frac{3\lambda N q}{2\pi}\right)^{\frac{1}{3}} t^{-\frac{1}{3}} \tag{E.5}$$

E.2 Inversion modelling using Tephra2

E.2.1 Motivation and rationale

Numerical tephra dispersion models are another way by which field data can be related to ESPs. Running numerical models in reverse (inversion) allows the user to solve for the best estimates of ESPs given the observed field data (*Connor and Connor*, 2006). This approach has been applied to the Bronze Age eruption of Santorini (*Johnston et al.*, 2012) which informed estimates of erupted mass, plume height and the seasonality of the prehistoric eruption. Here we use a similar approach to evaluate the the Eruption Source Parameters (ESPs) of the climactic Mazama eruption of Crater Lake, Oregon. The aim is to provide another estimate of the plume height and erupted volume to supplement the estimates from field data (Chapter 2). We use the thickness of the proximal (<130 km) Plinian fall deposit collected by *Young* (1990) with the Tephra2 model in inversion mode to bracket key ESPs for use in Chapter 6. We only performed preliminary runs using this approach because the opportunity to collaborate with L. Mastin at the USGS, and use the Ash3D VATDM, arose during the final year of this thesis. However, the inversion modelling with Tephra2 was a valuable exercise which highlighted some of the limitations of using simple advection-diffusion models to model large magnitude (M>7) eruptions (see sections E.2.5 and 6.2).

E.2.2 Tephra2 a semianalytical ash dispersion model

Tephra2 is a semi-analytical advection diffusion model that computes tephra dispersal and deposition (*Suzuki* 1983; *Armienti et al.* 1988; *Bonadonna et al.* 2005b; *Connor and Connor* 2006 and references therein). The forward model computes tephra accumulation (kgm^{-2}) across a grid, given a set of input parameters. The inversion technique for Tephra2 (*Connor and Connor*, 2006) uses a downhill simplex method to determine an optimal set of ESPs given the field data, that are then used for the forward solution. The downhill simplex method is based on a simplex, which can be thought of as the parameter space where the number of dimensions is equal to the number

of input parameters (n_i), the number of vertices equals n_i+1 (*Nelder and Mead*, 1965; *Connor and Connor*, 2006), and all the parameters are related by a function. The algorithm then moves the vertices into the simplex (parameter space) to find the minimum of the function (*Nelder and Mead*, 1965; *Magill et al.*, 2015).

One disadvantage of the downhill simplex method is that multiple minima may exist in the parameter space. In the Tephra2 inversion, some of these minima will be geologically unrealistic solutions, but the algorithm cannot identify these "fake" minima (*Connor and Connor*, 2006; *Johnston et al.*, 2012; *Magill et al.*, 2015; *Biass*, 2018). To overcome this artefact of the method, we use the "batch" approach outlined by *Biass* (2018) which reduces a wide range of plume height and total erupted mass values into smaller domains and performs the inversion over each domain. This enables the identification of false minima and narrows the range of two key input parameters. The batch runs, reduce the initial range of erupted mass and plume height, meaning you can then you can run multiple inversions where the "seed" value is varied (*Magill et al.*, 2015; *Biass*, 2018). The seed value determines the starting point for the downhill simplex algorithm and in some cases the inversion is extremely sensitive to this number.

For each iteration of the inversion, the forward model solution calculates the tephra accumulation at each input point (field measurement). The residual between the computed and observed tephra accumulation at each point is then used to calculate a root mean square error (RMSE) value:

$$RMSE = \sqrt{\frac{\sum_{i=1}^{n} (x_{obs_i} - x_{comp_i})^2}{n}}, \tag{E.6}$$

where n is the number of field measurements, x_obs is the observed and x_comp is the computed accumulation at location i. Low RMSE values indicate a better fit that high RMSE values when comparing runs with the same input data. However, the absolute RMSE value is strongly dependent on the number of observations and the magnitude of the residuals so cannot be compared between runs that use different subsets of field sites. This is where the normalised root mean square error (NRMSE) value is beneficial (*Connor and Connor*, 2006). The NRMSE is the RMSE divided by the range in observed values.

E.2.3 Model inputs

The input mass accumulation data is based on detailed mapping of the Plinian fallout by *Young* (1990; Fig. E.1). *Young* (1990) reported tephra thickness at individual localities, contours of deposit density and isomass maps (Fig. E.1). However, the mass accumulation (kgm^{-2}) at each locality is not provided. Therefore, we converted the thickness at each locality to mass accumulation using the density contours (Fig. E.1) which leads to some mass accumulation data not fitting the isomass lines (Fig. E.1). However, as the construction of the isomass contours will have involved some interpretation by *Young* (1990), we felt it was best to work with the reported thickness

Table E.1: Eruption Source Parameter estimates from *Young* (1990) for the Plinian phase of the climactic Mazama eruption.

Unit	Volume (km^3)[a]	Mass (kg)	Plume height (km; asl)[a]
Plinian Lower Pumice Unit (LPU)	5.17-5.26	8.4 x 10^{12}	42.4-45.3
Plinian Upper Pumice Unit (UPU)	17.14	3.1 x 10^{13}	42.9-58.0
Total Plinian fall	21.59-22.40	4.2 x 10^{13}	42.4-58.0

(a) Ranges in volume and plume height arise from splitting the LPU into two lobes, and different plume heights estimated from maximum pumice and maximum lithic isopleths.

data and assign a level of uncertainty to each individual value. Here for simplicity, we only use Tephra2 to invert the Upper Plinian Unit (UPU) because the multiple lobes of the Lower Plinian Unit (LPU) would require multiple wind-fields (Fig. E.1)

The meteorological data used in the inversion is reanalysis wind data obtained from the European Centre for Medium Range Weather Forecasts (ECMWF) ERA5 dataset (*Hersbach et al.*, 2020). Monthly averaged wind profiles at Crater Lake (42.93°N, 122.12°W) were downloaded for the 40-year period between 01/01/1979 and 31/12/2019 from the Copernicus Climate Change Service (C3S) Climate Data Store (Fig. E.2). We then determined qualitatively that between the months of August and November is when the dominant wind directions are most likely to disperse a tephra deposit towards the north and east of Crater Lake. This supports pollen records that suggest that the Mazama eruption occurred during autumn (*Mehringer et al.*, 1977b). Subsequently, we downloaded 6 hourly reanalysis wind profiles for the period between August to November 2010 and ran Tephra2 in forward mode using each wind profile, outputting the RMSE for each run (Eq. E.6). The wind profile with the lowest RMSE was then used for all subsequent inversion modelling. The best-fit wind profile determined using this approach is from the 02 August 2010 at 06:00 UTC which interestingly is characterised by extremely low wind speeds (Fig. E.2).

The ranges of the input parameters (Table E.2) used in the inversion are based on the estimates from empirical models (Table E.1) and the ranges used in other studies using the Tephra2 model (*Bonadonna et al.*, 2005b; *Connor and Connor*, 2006; *Johnston et al.*, 2012; *Magill et al.*, 2015; *Biass et al.*, 2017; *Crummy et al.*, 2019). Two important empirical parameters in Tephra2 are the diffusion coefficient and the fall-time threshold. The diffusion coefficient can integrate the effects of plume and atmospheric processes that are not directly computed in the Tephra2 model (*Bonadonna et al.*, 2005b; *Volentik et al.*, 2010). For example in some cases, very large diffusion coefficients are necessary to reproduce the effect of gravitational spreading of a plume (*Bonadonna and Phillips*, 2003; *Volentik et al.*, 2010). The fall-time threshold is related to the terminal settling velocity and accounts for whether particles follow linear or power-law diffusion laws (*Bonadonna et al.*, 2005b). The α and β parameters are used in a beta probability density

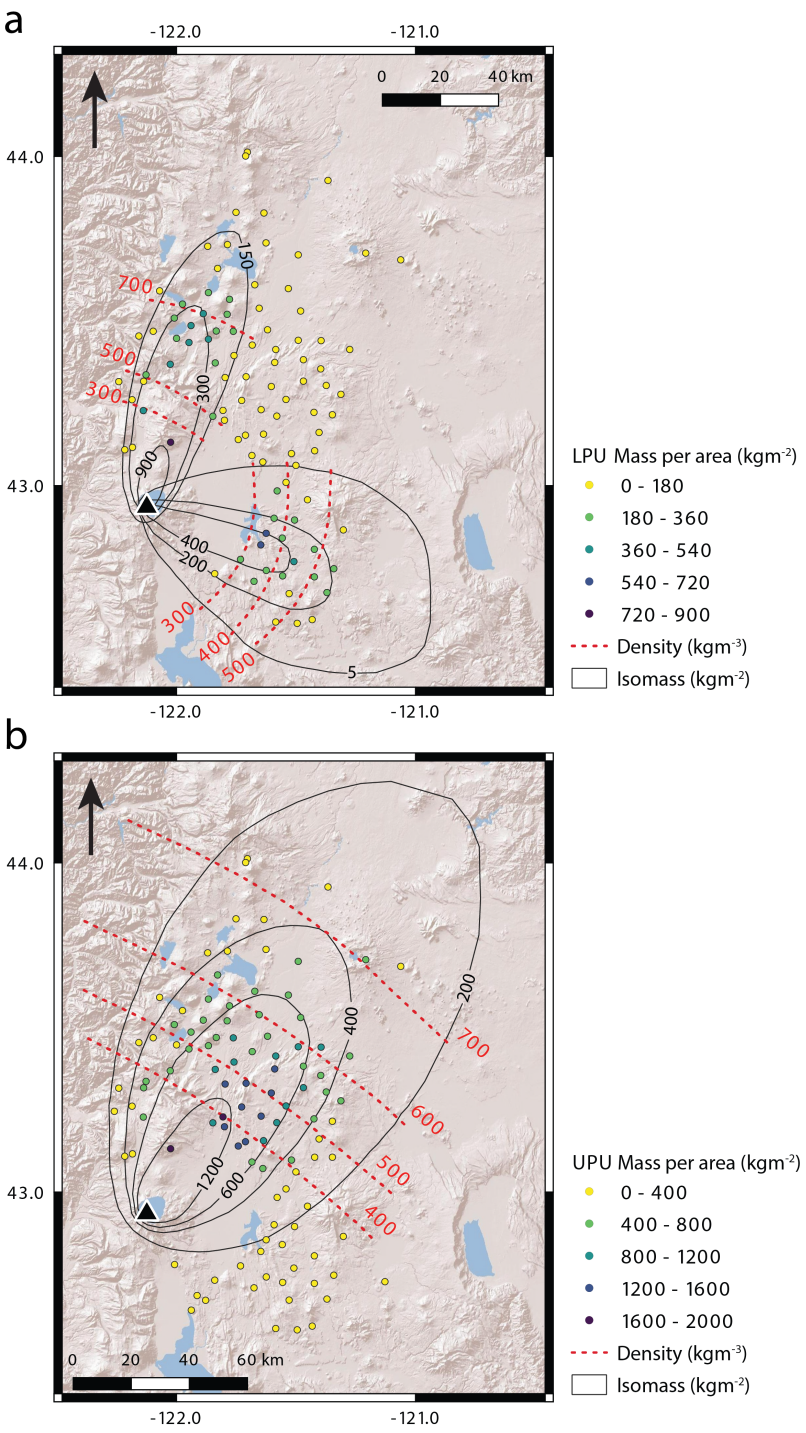

Figure E.1: Mass accumulation (filled circles) calculated from the thickness and density contours (dashed red lines) reported for the a) Lower Pumice Unit and b) Upper Pumice Unit by *Young* (1990). The isomass contours (solid black lines) are from *Young* (1990).

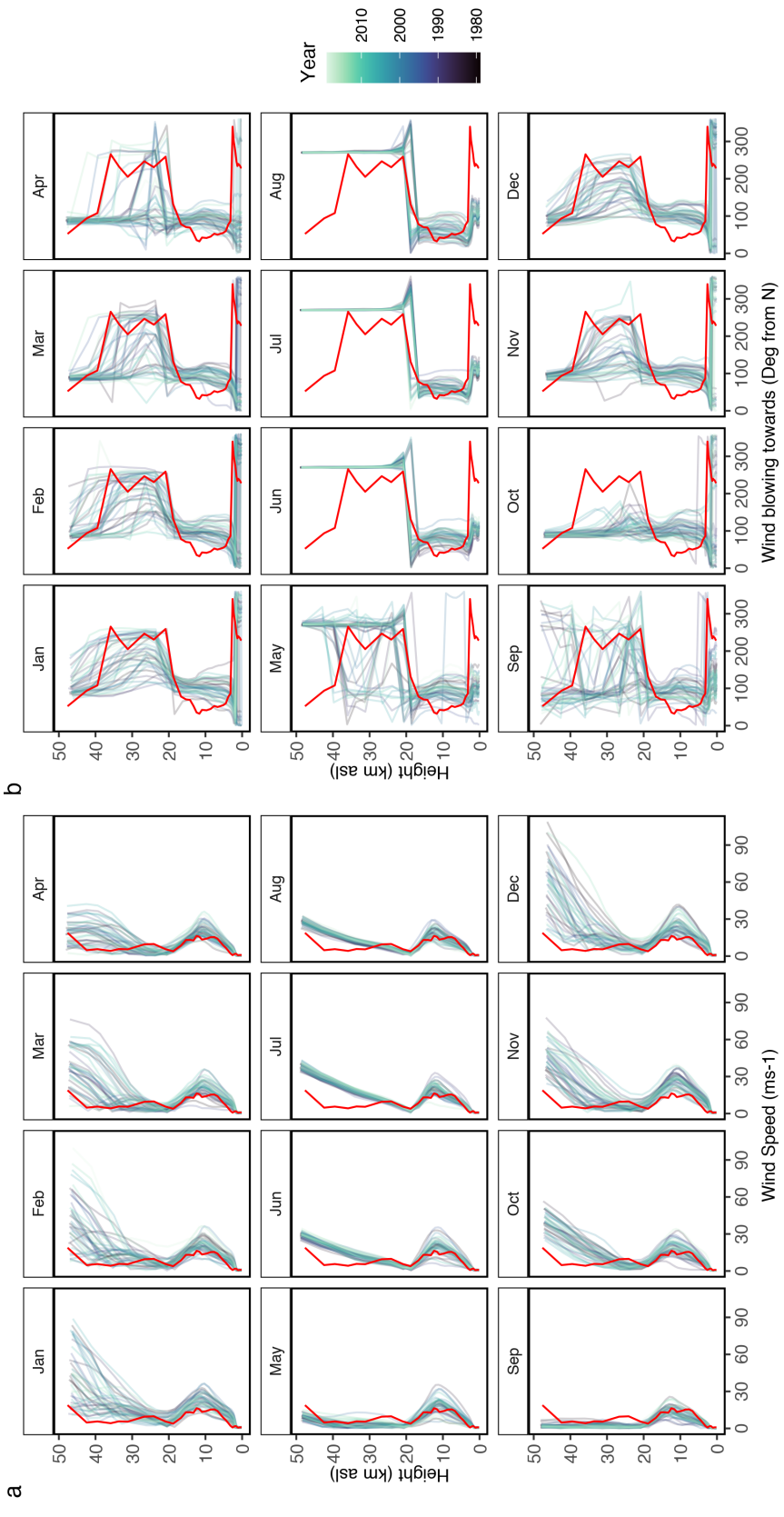

Figure E.2: Reanalysis wind data used in Tephra2 Inversion Modelling. Monthly average wind profiles for Crater Lake, Oregon, USA from the ECMWF ERA5 data set (*Hersbach et al.*, 2020) for the 40 year period from 1979-2019 are shown in blue shades. The best-fit wind profile for 02 August 2010 06:00 UTC is shown in red. Panels show a) average wind speed and b) average wind direction (given as the direction the wind is blowing towards).

Table E.2: Ranges of input parameters used in the Tephra2 inversion of the Upper Plinian Unit of the climactic Mazama eruption.

Input Parameter	Upper Plinian Unit (UPU) range
Plume height (km; asl)	30-48
Erupted mass (x 10^{10} kg)	1-1000
Median grain size; Md (ϕ)	-1-0
Standard deviation; σ (ϕ)	1-3
Lithic density (kgm^{-3})	2600
Pumice density (kgm^{-3})	600
Fall-time threshold (s)	1-10000
Diffusion coefficient (ms^{-1})	0.001-10000
Eddy constant	0.04
Alpha (α)	3
Beta (β)	0.001-3

function to describe the mass distribution in the plume:

$$P(x) = \frac{(1-x)^{\beta-1} x^{\alpha-1}}{B(\alpha,\beta)} \tag{E.7}$$

where x is a dimensionless height normalised to the plume height, and α and β change the shape of the distribution (*Magill et al.*, 2015; *Biass et al.*, 2016). When $\alpha = \beta$ the mass is distributed uniformly and $\alpha > \beta$ means the mass is concentrated towards the top of the plume .

The grain size data used in the inversion (Table E.2; Md and σ) are based on field data collected by *Young* (1990). The raw sieve data (see Appendix D) and the mass accumulation data (Fig. E.1) were used to estimate a Total Grain Size Distribution (TGSD) for the Plinian fallout using the Voronoi tessellation method (*Bonadonna et al.*, 2005a; *Biass and Bonadonna*, 2014). It must be noted that the grain size parameters (Table E.2) do not represent a TGSD for the whole Mazama eruption or the Plinian phase because the calculation does not incorporate the distal tephra as we cannot determine the quantity of fine ash associated with discrete phases of the eruption (Plinian or caldera collapse).

E.2.4 Results

Here we present the preliminary results of inversion modelling using Tephra2 with the batch approach (*Biass*, 2018). For each of the plume height and erupted mass domains, the input parameters that best reproduce the tephra deposit are reported. The input parameters of the ten batch domains that produce the lowest RMSE value are listed in Table E.3. Using the post-processing MATLAB package by *Biass* (2018), we visualise the plume height and erupted mass parameter space in Figure E.3.

Table E.3: Results from the batch Tephra2 inversion modelling. Input parameter combinations that produce the ten lowest RMSE values from batch inversion modelling using Tephra2.

ID	RMSE	Plume height (m)	Mass (kg)	Alpha	Beta	Diffussion coefficient (ms^{-1})	Fall Time threshold	Md (ϕ)	σ (ϕ)
1	457.03	36940	2.26 x 10^{13}	3.00	0.26	8438	6243	0.99	3.00
2	467.49	37214	2.19 x 10^{13}	3.00	0.59	8196	469	0.49	3.00
3	469.88	36000	2.14 x 10^{13}	3.00	0.15	8212	0	0.20	3.00
4	472.27	38000	2.23 x 10^{13}	3.00	0.62	7651	0	0.42	3.00
5	477.44	40000	2.24 x 10^{13}	3.00	0.85	10000	5797	0.00	3.00
6	478.86	35000	2.13 x 10^{13}	3.00	0.00	1657	2	0.00	3.00
7	478.92	39000	2.26 x 10^{13}	3.00	0.31	8767	466	0.24	3.00
8	484.70	33000	1.98 x 10^{13}	3.00	0.19	10000	5325	0.00	3.00
9	487.66	34000	2.09 x 10^{13}	3.00	0.55	9	21	0.00	3.00
10	490.56	41429	2.28 x 10^{13}	3.00	0.83	166	903	0.01	3.00

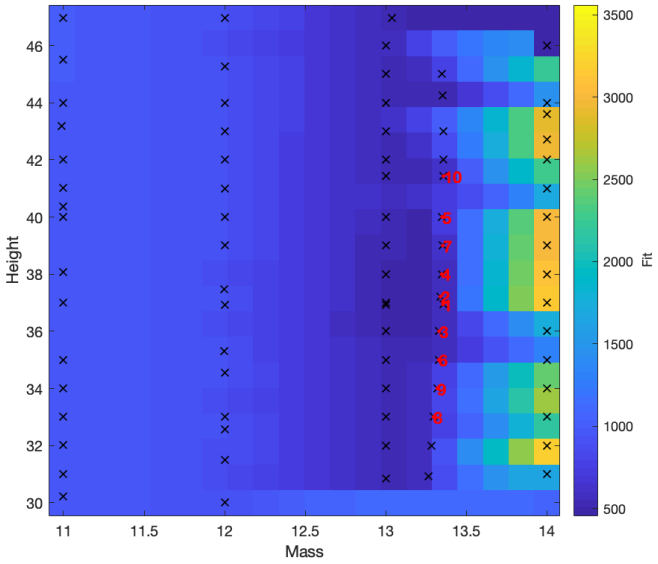

Figure E.3: Plume height and erupted volume parameter space explored using the Tephra2 inversion model. The colour indicates the RMSE (fit on colourbar) value across the parameter space. The ten batch domains that produced the lowest RMSE values are plotted with the associated input parameters (red points numbered with the ID from Table E.3).

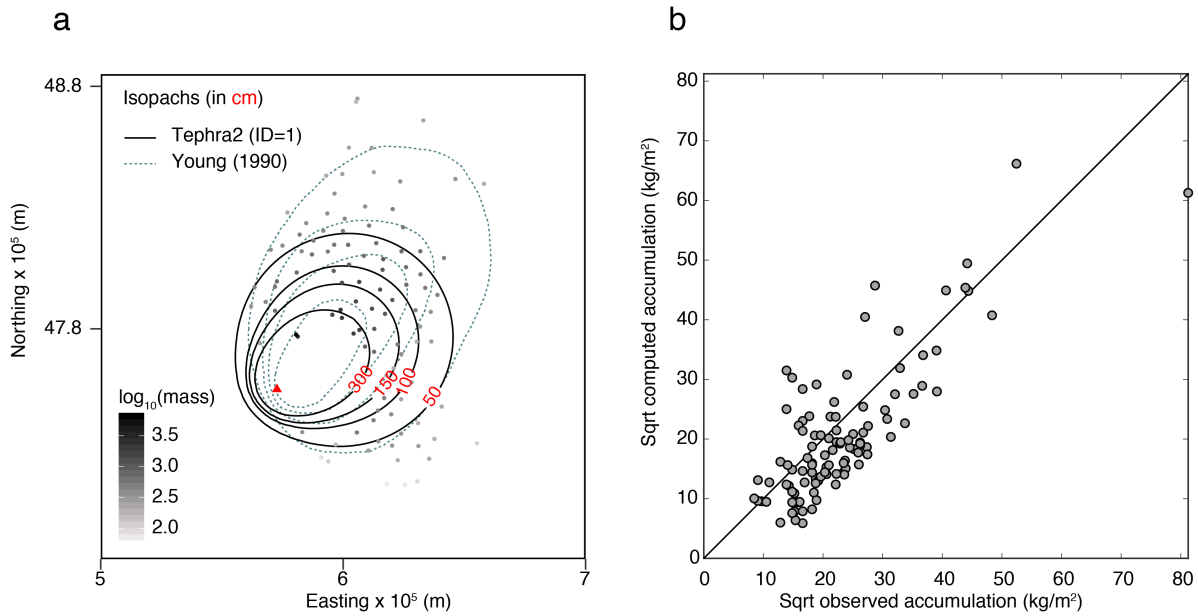

Figure E.4: Tephra2 modelling of the Upper Plinian Unit from the climactic Mazama eruption. Input parameters are equivalent to run ID=1 from Table E.3. a) Isopach map of Tephra2 output and isopachs from *Young* (1990). Isopach intervals are: 50, 100, 150 and 300 cm. b) Plot of the square root of the observed mass versus the square root of the modelled thicknesses.

The batch runs show that the erupted mass of the UPU likely is between 10^{13} and 10^{14} kg, which supports the estimate from the tephra deposit by *Young* (1990, Table E.2). However, the plume height remains uncertain as the best-fit parameters range from 33-41 km asl (Table E.2).

In Figure E.4, we compare the deposit produced by Tephra2 using the best-fit input parameters determined by the batch inversion (ID=1 from Table E.3). We see that the overall dispersal direction is towards to the northeast of the vent, however, the isopachs lack the elongation of the mapped deposit (Fig. E.4a).

E.2.5 Discussion of Tephra2 limitations

The preliminary inversion modelling using Tephra2 of the climactic Mazama eruption demonstrated some of the limitations of using VATDMs to reproduce the ash dispersion and deposition from a large magnitude eruption. First, the Tephra2 model uses wind data for a single site (in this case Crater Lake, Oregon, USA). This is inappropriate for a deposit on the scale of the Mazama eruption because the area impacted by the tephra exceeds 1 million km^2 over which the winds are changing direction and speed causing unique patterns of tephra deposition. Therefore, assuming that the wind profile at Crater Lake is representative of the winds across whole deposit is inappropriate. Second, the approach used to find the best-fit wind file is biased by the absence of up-wind data. In this instance, this meant that the best-fit wind profile was close to a no-wind

case (Figs. E.2 & E.4) which did not reproduce the elongation of the deposit towards the north and east of the vent. Third, Tephra2 currently does not include an approximation of umbrella cloud spreading and is purely an advection-diffusion model. The diffusion coefficient can be increased to account for enhanced spreading (*Bonadonna et al.*, 2005b; *Volentik et al.*, 2010), however, this cannot be directly related to equations that govern umbrella cloud spreading (e.g., sections E.1 & 6.2) and is applied uniformly across the model domain rather than dominantly close to source. The combination of these factors are why in the main text (Chapter 6), we focus using the Ash3D model in collaboration with L. Mastin to model the Mazama eruption because it uses 3D time dependant wind fields and incorporates umbrella spreading regimes.

E.3 Inventory of Ash3D Simulations

See Table E.4 for the input parameters used in the individual Ash3D simulations.

E.4 Adjusting the Grain Size Distribution in Ash3D

Here we demonstrate why it is necessary to simulate the aggregation of particles <125 μm in Ash3D (Fig. E.5). When the particles <125 μm are not combined into an artificial aggregate class, they do not deposit within the model domain because their low terminal settling velocities are less than the atmospheric turbulence (Fig. E.5a).

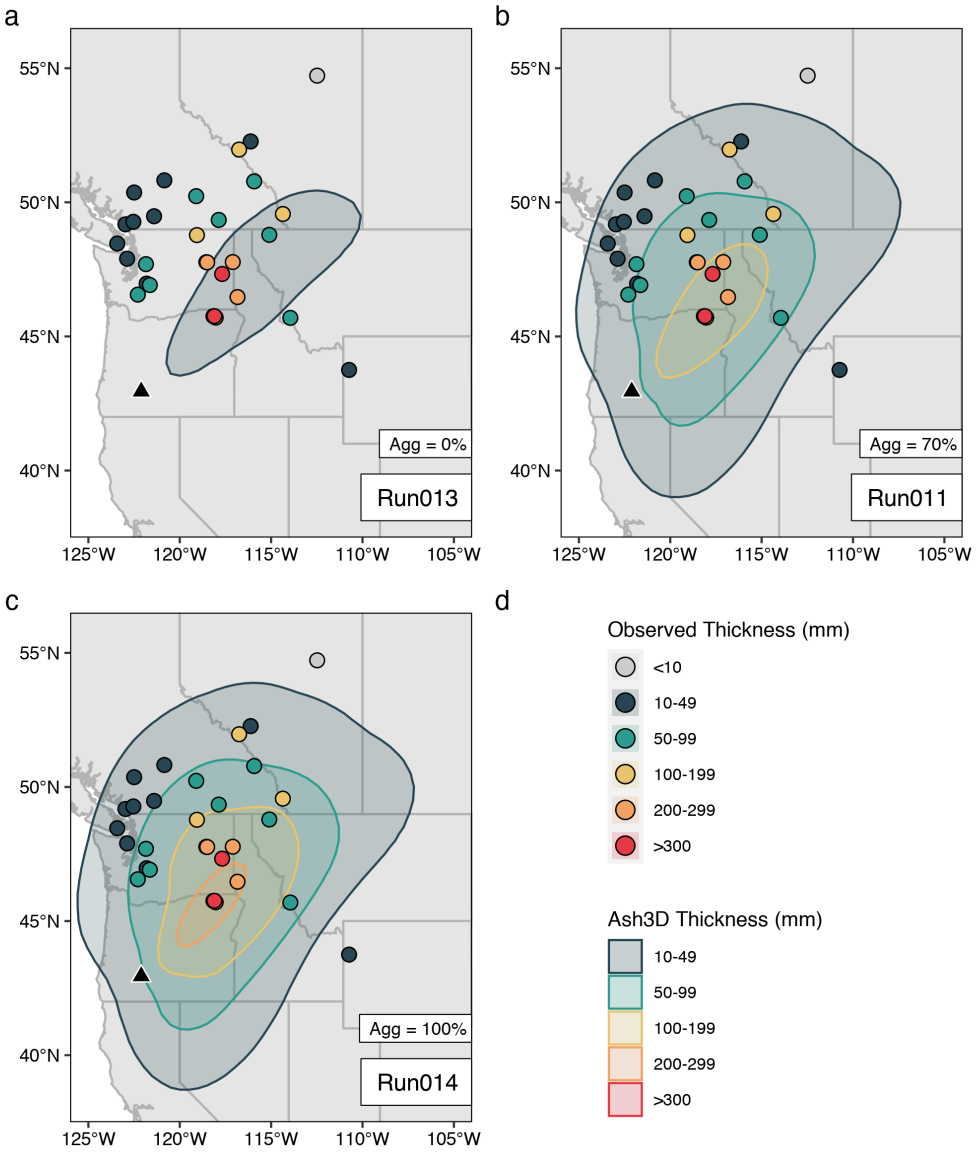

Figure E.5: The impact of simulating the aggregation of particles <125 µm in Ash3D. The percentage of the particles <125 µm aggregation in each panel (Agg) is a) 0% b) 70% and c) 100%. The colour of the filled circles (observed) and shaded isopachs (simulated) correspond to intervals of ash thickness in mm.

Table E.4: Input parameters in the Ash3D Simulations in Chapter 6

Run	DRE volume (km^3)	GSD	Diffusion coefficient (K; m^2s^{-1})	Top of umbrella height (km)	Umbrella spreading regime	% of fines aggregated	Deposit density (ρ_d; kgm^{-3})	Notes
Run001	40	M16_N	0	30	*Costa et al.* (2013)	100	1000	
Run002	40	M14	0	30	*Costa et al.* (2013)	100	1000	
Run003	40	M16_FS	0	30	*Costa et al.* (2013)	100	1000	
Run004	40	M16_N	1000	30	*Costa et al.* (2013)	100	1000	Like Run001 but with K = 1000 m^2s^{-1}
Run005	40	M14	1000	30	*Costa et al.* (2013)	100	1000	Like Run002 but with K = 1000 m^2s^{-1}
Run006	40	M16_FS	1000	30	*Costa et al.* (2013)	100	1000	Like Run003 but with K = 1000 m^2s^{-1}
Run007	40	M16_N	1000	40[a]	None	100	1000	Like Run004 with no umbrella spreading
Run008	40	M16_N	1000	30	*Webster et al.* (2020)	100	1000	Like Run004 but with Webster spreading formulation
Run009	40	B21_U	1000	30	*Costa et al.* (2013)	90	1000	Using unimodal GSD from field data and only aggregating 90% of mass <125 μm
Run010	40	B21_U	1000	30	*Costa et al.* (2013)	80	1000	Using unimodal GSD from field data and only aggregating 80% of mass <125 μm
Run011	40	B21_U	1000	30	*Costa et al.* (2013)	70	1000	Using unimodal GSD from field data and only aggregating 70% of mass <125 μm
Run012	40	B21_U	1000	30	*Costa et al.* (2013)	60	1000	Using unimodal GSD from field data and only aggregating 60% of mass <125 μm
Run013	40	B21_U	1000	30	*Costa et al.* (2013)	0	1000	Using unimodal GSD from field data with NO aggregation
Run014	40	B21_U	1000	30	*Costa et al.* (2013)	100	1000	Like Run004 but using unimodal GSD from field data and only aggregating 100% of mass <125 μm
Run015	40	B21_U	1000	30	*Costa et al.* (2013)	100	1000	Like Run014 but with μ_{agg}=2.6
Run016	40	B21_U	1000	30	*Costa et al.* (2013)	100	1000	Like Run014 but with μ_{agg}=2.8
Run017	40	B21_U	1000	30	*Costa et al.* (2013)	100	1000	Like Run014 but with μ_{agg}=3.0
Run018	40	B21_U	1000	30	*Costa et al.* (2013)	100	1000	Like Run014 but with μ_{agg}=3.2
Run019	40	M16_FS	1000	30	*Costa et al.* (2013)	100	700	Like Run006 but with ρ_d = 700kgm^{-3}
Run020	40	M16_FS	1000	25	*Costa et al.* (2013)	100	1000	Like Run006 but with umbrella height = neutral buoyancy height (25 km)

Table E.4: Input parameters in the Ash3D Simulations in Chapter 6 *cont.*

Run	DRE volume (km^3)	GSD	Diffusion coefficient (K; m^2s^{-1})	Top of umbrella height (km)	Umbrella spreading regime	% of fines aggregated	Deposit density (ρ_d; kgm^{-3})	Notes
Run021	40	M16_FS	1000	15	*Costa et al.* (2013)	100	1000	Like Run006 but with umbrella height = tropopause (15 km)
Run022	40	M16_FS	1000	25	*Costa et al.* (2013)	100	700	Like Run020 but with ρ_d = 700 kgm^{-3}
Run023	40	M16_FS	1000	15	*Costa et al.* (2013)	100	700	Like Run021 but with ρ_d = 700 kgm^{-3}
Run024	40	M16_FS	3000	30	*Costa et al.* (2013)	100	700	Like Run019 but with K = 3000 m^2s^{-1}
Run025	40	M14	1000	30	*Costa et al.* (2013)	100	700	Like Run005 but with ρ_d = 700 kgm^{-3}
Run026	40	M16_FS	1000	30	*Costa et al.* (2013)	100	700	Like Run006 but with ρ_d = 700 kgm^{-3}
Run027	40	M16_N	1000	40[a]	None	100	700	Like Run007 but with ρ_d = 700 kgm^{-3}
Run028	40	M16_N	1000	30[a]	None	100	700	Like Run058 but with ρ_d = 700 kgm^{-3}
Run029	40	M16_N	1000	30	*Webster et al.* (2020)	100	700	Like Run008 but with ρ_d = 700 kgm^{-3}
Run030	40	B21_U	1000	30	*Costa et al.* (2013)	80	700	Like Run010 but with ρ_d = 700 kgm^{-3}
Run032	40	B21_U	1000	30	*Costa et al.* (2013)	70	700	Like Run011 but with ρ_d = 700 kgm^{-3}
Run033	40	B21_U	1000	30	*Costa et al.* (2013)	60	700	Like Run012 but with ρ_d = 700 kgm^{-3}
Run034	40	B21_U	1000	30	*Costa et al.* (2013)	0	700	Like Run013 but with ρ_d = 700 kgm^{-3}
Run035	40	B21_U	1000	30	*Costa et al.* (2013)	100	700	Like Run014 but with ρ_d = 700 kgm^{-3}
Run036	40	B21_U	1000	30	*Costa et al.* (2013)	100	700	Like Run015 but with ρ_d = 700 kgm^{-3}
Run037	40	B21_U	1000	30	*Costa et al.* (2013)	100	700	Like Run016 but with ρ_d = 700 kgm^{-3}
Run038	40	B21_U	1000	30	*Costa et al.* (2013)	100	700	Like Run017 but with ρ_d = 700 kgm^{-3}
Run039	40	B21_U	1000	30	*Costa et al.* (2013)	100	700	Like Run018 but with ρ_d = 700 kgm^{-3}
Run045	40	B21_U	1000	30	*Costa et al.* (2013)	50	1000	Using unimodal GSD from field data and only aggregating 50% of mass <125 µm
Run052	40	B21_U	1000	30	*Costa et al.* (2013)	50	700	Like Run045 but with ρ_d = 700 kgm^{-3}
Run054	40	B21_B	1000	30	*Costa et al.* (2013)	100	1000	Like Run004 but using bimodal GSD from field data and aggregating 100% of the mass <125 µm
Run055	40	B21_B	1000	30	*Costa et al.* (2013)	100	700	Like Run054 but using ρ_d = 700kgm^{-3}
Run056	40	M16_N	0	30	*Costa et al.* (2013)	100	700	Like Run001 but using ρ_d = 700kgm^{-3}
Run057	40	M16_N	1000	30	*Costa et al.* (2013)	100	700	Like Run004 but using ρ_d = 700kgm^{-3}
Run058	40	M16_N	1000	30[a]	None	100	1000	Like Run004 with no umbrella spreading

Table E.4: Input parameters in the Ash3D Simulations in Chapter 6 *cont.*

Run	DRE volume (km^3)	GSD	Diffusion coefficient (K; m^2s^{-1})	Top of umbrella height (km)	Umbrella spreading regime	% of fines aggregated	Deposit density (ρ_d; kgm^{-3})	Notes
Run059	40	B21_U	1000	30	*Costa et al.* (2013)	90	700	Like Run009 but with ρ_d = 700 kgm^{-3}

(a) When no umbrella spreading, plume height is the top of the plume

BIBLIOGRAPHY

Abella, S. E., The effect of the Mt. Mazama ashfall on the planktonic diatom community of Lake Washington, *Limnology and Oceanography*, *33*(6), 1376–1385, 1988.

Adachi, A., T. Kobayashi, H. Yamauchi, and S. Onogi, Detection of potentially hazardous convective clouds with a dual-polarized C-band radar., *Atmospheric Measurement Techniques Discussions*, *6*(2), 2013.

Adams, J., Paleoseismicity of the Cascadia Subduction Zone: Evidence from turbidites off the Oregon-Washington Margin, *Tectonics*, *9*(4), 569–583, doi: 10.1029/TC009i004p00569, 1990.

Adams, J., A. Beaudoin, O. Davis, P. Delacourt, H. Delacourt, and P. Richard, North America during the last 150,000 years, 1997.

Alfano, F., C. Bonadonna, P. Delmelle, and L. Costantini, Insights on tephra settling velocity from morphological observations, *Journal of Volcanology and Geothermal Research*, *208*(3), 86–98, doi: 10.1016/j.jvolgeores.2011.09.013, 2011a.

Alfano, F., C. Bonadonna, A. C. M. Volentik, C. B. Connor, S. F. L. Watt, D. M. Pyle, and L. J. Connor, Tephra stratigraphy and eruptive volume of the May, 2008, Chaitén eruption, Chile, *Bulletin of Volcanology*, *73*(5), 613–630, doi: 10.1007/s00445-010-0428-x, 2011b.

Alfano, F., C. Bonadonna, S. Watt, C. Connor, A. Volentik, and D. M. Pyle, Reconstruction of total grain size distribution of the climactic phase of a long-lasting eruption: the example of the 2008–2013 Chaitén eruption, *Bulletin of Volcanology*, *78*(7), 46, doi: 10.1007/s00445-016-1040-5, 2016.

Allan, A. S. R., D. J. Morgan, C. J. N. Wilson, and M.-A. Millet, From mush to eruption in centuries: assembly of the super-sized Oruanui magma body, *Contributions to Mineralogy and Petrology*, *166*(1), 143–164, doi: 10.1007/s00410-013-0869-2, 2013.

Allan, A. S. R., S. J. Barker, M.-A. Millet, D. J. Morgan, S. M. Rooyakkers, C. I. Schipper, and C. J. N. Wilson, A cascade of magmatic events during the assembly and eruption of a super-sized magma body, *Contributions to Mineralogy and Petrology*, *172*(7), 49, doi: 10.1007/s00410-017-1367-8, 2017.

Ames, K. M., D. E. Dumond, J. R. Galm, and R. Minor, Prehistory of the southern Plateau, *Handbook of North American Indians*, *12*, 103–119, 1998.

Annen, C., From plutons to magma chambers: Thermal constraints on the accumulation of eruptible silicic magma in the upper crust, *Earth and Planetary Science Letters*, *284*(3), 409–416, doi: 10.1016/j.epsl.2009.05.006, 2009.

Annen, C., J. D. Blundy, and R. S. J. Sparks, The Genesis of Intermediate and Silicic Magmas in Deep Crustal Hot Zones, *Journal of Petrology*, *47*(3), 505–539, doi: 10.1093/petrology/egi084, 2006.

Armienti, P., G. Macedonio, and M. T. Pareschi, A numerical model for simulation of tephra transport and deposition: Applications to May 18, 1980, Mount St. Helens eruption, *Journal of Geophysical Research: Solid Earth*, *93*(B6), 6463–6476, doi: 10.1029/JB093iB06p06463, 1988.

Arnold, J. R., and W. F. Libby, Radiocarbon Dates, *Science*, *113*(2927), 111–120, 1951.

Aubry, T. J., et al., The Independent Volcanic Eruption Source Parameter Archive (IVESPA, version 1.0): A new observational database to support explosive eruptive column model validation and development, *Journal of Volcanology and Geothermal Research*, p. 107295, doi: 10.1016/j.jvolgeores.2021.107295, 2021.

Bachmann, O., and G. W. Bergantz, Rhyolites and their Source Mushes across Tectonic Settings, *Journal of Petrology*, *49*(12), 2277–2285, doi: 10.1093/petrology/egn068, 2008.

Bacon, C. R., Eruptive history of Mount Mazama and Crater Lake Caldera, Cascade Range, U.S.A., *Journal of Volcanology and Geothermal Research*, *18*(1), 57 – 115, doi: https://doi.org/10.1016/0377-0273(83)90004-5, 1983.

Bacon, C. R., and T. H. Druitt, Compositional evolution of the zoned calcalkaline magma chamber of Mount Mazama, Crater Lake, Oregon, *Contributions to Mineralogy and Petrology*, *98*(2), 224–256, doi: 10.1007/BF00402114, 1988.

Bacon, C. R., and M. A. Lanphere, Eruptive history and geochronology of Mount Mazama and the Crater Lake region, Oregon, *Geological Society of America Bulletin*, *118*(11-12), 1331–1359, doi: https://doi.org/10.1130/B25906.1, 2006.

Bagheri, G. H., C. Bonadonna, I. Manzella, and P. Vonlanthen, On the characterization of size and shape of irregular particles, *Powder Technology*, *270*, 141–153, doi: 10.1016/j.powtec.2014.10.015, 2015.

Baines, P., and R. Sparks, Dynamics of giant volcanic ash clouds from supervolcanic eruptions, *Geophysical Research Letters*, *32*(24), 2005.

Baker, D., C. Peterson, E. Hemphill-Haley, and D. Twichell, Latest Pleistocene and Holocene (2–16ka) sedimentation in the Columbia River Estuary, Oregon, USA, *Marine Geology*, *273*(1), 83 – 95, doi: https://doi.org/10.1016/j.margeo.2010.02.005, 2010.

Balch, D. P., A. S. Cohen, D. W. Schnurrenberger, B. J. Haskell, B. L. Valero Garces, J. W. Beck, H. Cheng, and R. L. Edwards, Ecosystem and paleohydrological response to Quaternary climate change in the Bonneville Basin, Utah, *Palaeogeography, Palaeoclimatology, Palaeoecology*, *221*(1), 99–122, doi: 10.1016/j.palaeo.2005.01.013, 2005.

Barberi, F., R. Cioni, M. Rosi, R. Santacroce, A. Sbrana, and R. Vecci, Magmatic and phreatomagmatic phases in explosive eruptions of Vesuvius as deduced by grain-size and component analysis of the pyroclastic deposits, *Journal of Volcanology and Geothermal Research*, *38*(3), 287–307, doi: 10.1016/0377-0273(89)90044-9, 1989.

Barker, S. J., A. R. V. Eaton, L. G. Mastin, C. J. N. Wilson, M. A. Thompson, T. M. Wilson, C. Davis, and J. A. Renwick, Modeling Ash Dispersal From Future Eruptions of Taupo Supervolcano, *Geochemistry, Geophysics, Geosystems*, *20*(7), 3375–3401, doi: 10.1029/2018GC008152, 2019.

Barnosky, C. W., A record of late Quaternary vegetation from Davis Lake, southern Puget Lowland, Washington, *Quaternary Research*, *16*(2), 221 – 239, doi: https://doi.org/10.1016/0033-5894(81)90046-6, 1981.

Bebbington, M., S. J. Cronin, I. Chapman, and M. B. Turner, Quantifying volcanic ash fall hazard to electricity infrastructure, *Journal of Volcanology and Geothermal Research*, *177*(4), 1055–1062, doi: 10.1016/j.jvolgeores.2008.07.023, 2008.

Beckett, F. M., C. S. Witham, M. C. Hort, J. A. Stevenson, C. Bonadonna, and S. C. Millington, Sensitivity of dispersion model forecasts of volcanic ash clouds to the physical characteristics of the particles, *Journal of Geophysical Research: Atmospheres*, *120*(22), 11,636–11,652, doi: 10.1002/2015JD023609, 2015.

Beckett, F. M., C. S. Witham, S. J. Leadbetter, R. Crocker, H. N. Webster, M. C. Hort, A. R. Jones, B. J. Devenish, and D. J. Thomson, Atmospheric Dispersion Modelling at the London VAAC: A Review of Developments since the 2010 Eyjafjallajökull Volcano Ash Cloud, *Atmosphere*, *11*(4), 352, doi: 10.3390/atmos11040352, 2020.

Bedwell, S. F., Prehistory and environmnent of the pluvial Fort Rock Lake area of south central Oregon, PhD Thesis, 1970.

Beebee, R. A., J. E. O'Connor, and G. E. Grant, Geology and geomorphology of the Lower Deschutes River Canyon, Oregon., *Oregon Department of Geology and Mineral Industries. Special Paper 36: 91-108*, 2002.

Beierle, B., and D. G. Smith, Severe drought in the early Holocene (10,000–6800 BP) interpreted from lake sediment cores, southwestern Alberta, Canada, *Palaeogeography, Palaeoclimatology, Palaeoecology*, *140*(1), 75 – 83, doi: https://doi.org/10.1016/S0031-0182(98)00044-3, 1998.

Beuselinck, L., G. Govers, J. Poesen, G. Degraer, and L. Froyen, Grain-size analysis by laser diffractometry: comparison with the sieve-pipette method, *CATENA*, *32*(3), 193–208, doi: 10.1016/S0341-8162(98)00051-4, 1998.

Biass, S., Tephra2 Inversion, https://e5k.github.io/codes/utilities/2018/06/06/inversion/, 2018.

Biass, S., and C. Bonadonna, A quantitative uncertainty assessment of eruptive parameters derived from tephra deposits: the example of two large eruptions of Cotopaxi volcano, Ecuador, *Bulletin of Volcanology*, *73*(1), 73–90, doi: 10.1007/s00445-010-0404-5, 2011.

Biass, S., and C. Bonadonna, TOTGS, https://github.com/e5k/TOTGS/tree/v2.1, 2014.

Biass, S., C. Bonadonna, L. Connor, and C. Connor, TephraProb: a Matlab package for probabilistic hazard assessments of tephra fallout, *Journal of Applied Volcanology*, *5*(1), 10, doi: 10.1186/s13617-016-0050-5, 2016.

Biass, S., A. Todde, R. Cioni, M. Pistolesi, N. Geshi, and C. Bonadonna, Potential impacts of tephra fallout from a large-scale explosive eruption at Sakurajima volcano, Japan, *Bulletin of Volcanology*, *79*(10), 73, doi: 10.1007/s00445-017-1153-5, 2017.

Blake, D. M., T. M. Wilson, and C. Gomez, Road marking coverage by volcanic ash: an experimental approach, *Environmental Earth Sciences*, *75*(20), 1348, doi: 10.1007/s12665-016-6154-8, 2016.

Blake, D. M., T. M. Wilson, J. W. Cole, N. I. Deligne, and J. M. Lindsay, Impact of Volcanic Ash on Road and Airfield Surface Skid Resistance, *Sustainability*, *9*(8), 1389, doi: 10.3390/su9081389, 2017.

Blinman, E., P. J. Mehringer Jr, and J. C. Sheppard, Pollen influx and the deposition of Mazama and Glacier Peak tephra, in *Volcanic activity and human ecology*, pp. 393–425, Academic Press, 1979.

Blong, R., N. Enright, and P. Grasso, Preservation of thin tephra, *Journal of Applied Volcanology*, *6*(1), 10, doi: 10.1186/s13617-017-0059-4, 2017.

Blong, R. J., *The time of darkness : local legends and volcanic reality in Papua New Guinea*, Australian National University Press, 1982.

Blott, S. J., and K. Pye, GRADISTAT: a grain size distribution and statistics package for the analysis of unconsolidated sediments, *Earth Surface Processes and Landforms*, *26*(11), 1237–1248, doi: 10.1002/esp.261, 2001.

Bonadonna, C., and A. Costa, Estimating the volume of tephra deposits: A new simple strategy, *Geology*, *40*(5), 415–418, doi: 10.1130/G32769.1, 2012.

Bonadonna, C., and A. Costa, Plume height, volume, and classification of explosive volcanic eruptions based on the Weibull function, *Bulletin of Volcanology*, *75*(8), 742, doi: 10.1007/s00445-013-0742-1, 2013.

Bonadonna, C., and J. C. Phillips, Sedimentation from strong volcanic plumes, *Journal of Geophysical Research: Solid Earth*, *108*(B7), doi: 10.1029/2002JB002034, 2003.

Bonadonna, C., G. G. J. Ernst, and R. S. J. Sparks, Thickness variations and volume estimates of tephra fall deposits: the importance of particle Reynolds number, *Journal of Volcanology and Geothermal Research*, *81*(3), 173–187, doi: 10.1016/S0377-0273(98)00007-9, 1998.

Bonadonna, C., C. B. Connor, B. F. Houghton, L. Connor, M. Byrne, A. Laing, and T. K. Hincks, Probabilistic modeling of tephra dispersal: Hazard assessment of a multiphase rhyolitic eruption at Tarawera, New Zealand, *Journal of Geophysical Research: Solid Earth*, *110*(B3), doi: 10.1029/2003JB002896, 2005a.

Bonadonna, C., J. C. Phillips, and B. F. Houghton, Modeling tephra sedimentation from a Ruapehu weak plume eruption, *Journal of Geophysical Research: Solid Earth*, *110*(B8), doi: 10.1029/2004JB003515, 2005b.

Bonadonna, C., R. Genco, M. Gouhier, M. Pistolesi, R. Cioni, F. Alfano, A. Hoskuldsson, and M. Ripepe, Tephra sedimentation during the 2010 Eyjafjallajökull eruption (Iceland) from deposit, radar, and satellite observations, *Journal of Geophysical Research: Solid Earth*, *116*(B12), doi: 10.1029/2011JB008462, 2011.

Bonadonna, C., A. Folch, S. Loughlin, and H. Puempel, Future developments in modelling and monitoring of volcanic ash clouds: outcomes from the first IAVCEI-WMO workshop on Ash Dispersal Forecast and Civil Aviation, *Bulletin of Volcanology*, *74*(1), 1–10, 2012.

Bonadonna, C., R. Cioni, M. Pistolesi, C. Connor, S. Scollo, L. Pioli, and M. Rosi, Determination of the largest clast sizes of tephra deposits for the characterization of explosive eruptions: a study of the IAVCEI commission on tephra hazard modelling, *Bulletin of Volcanology*, *75*(1), 680, doi: 10.1007/s00445-012-0680-3, 2013.

Bonadonna, C., S. Biass, and A. Costa, Physical characterization of explosive volcanic eruptions based on tephra deposits: Propagation of uncertainties and sensitivity analysis, *Journal of Volcanology and Geothermal Research*, *296*, 80–100, doi: 10.1016/j.jvolgeores.2015.03.009, 2015.

Bonadonna, C., et al., Tephra fallout in the eruption of Soufrière Hills Volcano, Montserrat, *Geological Society, London, Memoirs*, *21*(1), 483–516, doi: 10.1144/GSL.MEM.2002.021.01.22, 2002.

Bond, A., and R. S. J. Sparks, The Minoan eruption of Santorini, Greece, *Journal of the Geological Society*, *132*(1), 1–16, doi: 10.1144/gsjgs.132.1.0001, 1976.

Borchardt, G. A., J. A. Norgren, and M. E. Harward, Correlation of Ash Layers in Peat Bogs of Eastern Oregon, *GSA Bulletin*, *84*(9), 3101–3108, doi: 10.1130/0016-7606(1973)84<3101:COALIP>2.0.CO;2, 1973.

Bovet, P. M., N. Bowerman, D. Cadol, D. Clark, and E. Leonard, A paleoenvironmental record of the late Pleistocene and Holocene inferred from organic carbon analysis of glacial lakes sediments in the Albion range, Idaho, in *XVI INQUA Congress*, 2003.

Boygle, J., Variability of tephra in lake and catchment sediments, Svínavatn, Iceland, *Global and Planetary Change*, *21*(1), 129–149, doi: 10.1016/S0921-8181(99)00011-9, 1999.

Brand, B. D., S. Bendaña, S. Self, and N. Pollock, Topographic controls on pyroclastic density current dynamics: Insight from 18 May 1980 deposits at Mount St. Helens, Washington (USA), *Journal of Volcanology and Geothermal Research*, *321*, 1–17, doi: 10.1016/j.jvolgeores.2016.04.018, 2016.

Brazier, S., A. N. Davis, H. Sigurdsson, and R. S. J. Sparks, Fall-out and deposition of volcanic ash during the 1979 explosive eruption of the soufriere of St. Vincent, *Journal of Volcanology and Geothermal Research*, *14*(3), 335–359, doi: 10.1016/0377-0273(82)90069-5, 1982.

Broecker, R. W. S., J. L. Kulp, and C. S. Tucek, Lamont Natural Radiocarbon Measurements III, *Science*, *124*(3223), 630–630, doi: 10.1126/science.124.3223.630-b, 1956.

Bronk Ramsey, C., R. A. Housley, C. S. Lane, V. C. Smith, and A. M. Pollard, The RESET tephra database and associated analytical tools, *Quaternary Science Reviews*, *118*, 33–47, doi: 10.1016/j.quascirev.2014.11.008, 2015.

Brown, R. E., Interrelationships of geologic formations and processes affecting ecology as exposed at Rattlesnake Spring, Hanford project., *Tech. rep.*, Battelle-Northwest, Richland, Wash. Pacific Northwest Lab., 1970.

Brown, R. J., C. Bonadonna, and A. J. Durant, A review of volcanic ash aggregation, *Physics and Chemistry of the Earth, Parts A/B/C*, *45*, 65–78, 2012.

Brown, S. K., M. Auker, and R. Sparks, Populations around Holocene volcanoes and development of a Population Exposure Index, in *Global Volcanic Hazards and Risk*, edited by S. C. Loughlin, S. Sparks, S. K. Brown, S. F. Jenkins, and C. Vye-Brown, pp. 223–232, Cambridge University Press, 2015.

Brown, T. A., D. E. Nelson, R. W. Mathewes, J. S. Vogel, and J. R. Southon, Radiocarbon dating of pollen by accelerator mass spectrometry, *Quaternary Research*, *32*(2), 205 – 212, doi: https://doi.org/10.1016/0033-5894(89)90076-8, 1989.

Brown, W. K., and K. H. Wohletz, Derivation of the Weibull distribution based on physical principles and its connection to the Rosin–Rammler and lognormal distributions, *Journal of Applied Physics*, *78*(4), 2758–2763, doi: 10.1063/1.360073, 1995.

Buckland, H. M., J. Eychenne, A. C. Rust, and K. V. Cashman, Relating the physical properties of volcanic rocks to the characteristics of ash generated by experimental abrasion, *Journal of Volcanology and Geothermal Research*, *349*, 335–350, doi: 10.1016/j.jvolgeores.2017.11.017, 2018.

Buckland, H. M., K. V. Cashman, S. L. Engwell, and A. C. Rust, Sources of uncertainty in the Mazama isopachs and the implications for interpreting distal tephra deposits from large magnitude eruptions, *Bulletin of Volcanology*, *82*(3), 23, doi: 10.1007/s00445-020-1362-1, 2020.

Buckland, H. M., J. Saxby, M. Roche, P. Meredith, A. C. Rust, K. V. Cashman, and S. L. Engwell, Measuring the size of non-spherical particles and the implications for grain size analysis in volcanology, *Journal of Volcanology and Geothermal Research*, *415*, 107,257, doi: 10.1016/j.jvolgeores.2021.107257, 2021.

Buckley, J. D., and E. H. Willis, Isotopes' Radiocarbon Measurements VII, *Radiocarbon*, *11*(1), 53–105, doi: 10.1017/S0033822200064444, 1969.

Buckley, J. D., and E. H. Willis, Isotopes' radiocarbon measurements VIII, *Radiocarbon*, *12*(1), 87–129, 1970.

Burden, R. E., J. C. Phillips, and T. K. Hincks, Estimating volcanic plume heights from depositional clast size, *Journal of Geophysical Research: Solid Earth*, *116*(B11), doi: 10.1029/2011JB008548, 2011.

Burden, R. E., L. Chen, and J. C. Phillips, A statistical method for determining the volume of volcanic fall deposits, *Bulletin of Volcanology*, *75*(6), 707, doi: 10.1007/s00445-013-0707-4, 2013.

Bursik, M., et al., Estimation and propagation of volcanic source parameter uncertainty in an ash transport and dispersal model: application to the Eyjafjallajokull plume of 14–16 April 2010, *Bulletin of Volcanology*, *74*(10), 2321–2338, 2012.

Bush, J. H., B. D. Cochran, R. M. Breckenridge, and W. D. Hall, *Palouse-Cheney tract of the channeled scablands, Eastern Washington: a one-day field trip from Moscow, Idaho*, vol. 10, Idaho Dept. of Lands, Bureau of Mines and Geology, 1979.

Cabaniss, H. E., P. M. Gregg, and E. B. Grosfils, The Role of Tectonic Stress in Triggering Large Silicic Caldera Eruptions, *Geophysical Research Letters*, *45*(9), 3889–3895, doi: 10.1029/2018GL077393, 2018.

Calder, E. S., R. S. J. Sparks, and M. C. Gardeweg, Erosion, transport and segregation of pumice and lithic clasts in pyroclastic flows inferred from ignimbrite at Lascar Volcano, Chile, *Journal of Volcanology and Geothermal Research*, *104*(1), 201–235, doi: 10.1016/S0377-0273(00)00207-9, 2000.

Capaccioni, B., L. Valentini, M. B. L. Rocchi, G. Nappi, and D. Sarocchi, Image analysis and circular statistics for shape-fabric analysis: applications to lithified ignimbrites, *Bulletin of Volcanology*, *58*(7), 501–514, doi: 10.1007/s004450050158, 1997.

Carazzo, G., and A. M. Jellinek, Particle sedimentation and diffusive convection in volcanic ash-clouds, *Journal of Geophysical Research: Solid Earth*, *118*(4), 1420–1437, doi: https://doi.org/10.1002/jgrb.50155, 2013.

Carazzo, G., E. Kaminski, and S. Tait, The route to self-similarity in turbulent jets and plumes, *Journal of Fluid Mechanics*, *547*, 137–148, doi: 10.1017/S002211200500683X, 2006.

Carey, S., and R. Sparks, Quantitative models of the fallout and dispersal of tephra from volcanic eruption columns, *Bulletin of Volcanology*, *48*(2-3), 109–125, 1986.

Carey, S. N., and H. Sigurdsson, Influence of particle aggregation on deposition of distal tephra from the MAy 18, 1980, eruption of Mount St. Helens volcano, *Journal of Geophysical Research: Solid Earth*, *87*(B8), 7061–7072, doi: 10.1029/JB087iB08p07061, 1982.

Carey, S. N., H. Sigurdsson, and R. S. J. Sparks, Experimental studies of particle-laden plumes, *Journal of Geophysical Research: Solid Earth*, *93*(B12), 15,314–15,328, doi: 10.1029/JB093iB12p15314, 1988.

Carn, S. A., V. E. Fioletov, C. A. McLinden, C. Li, and N. A. Krotkov, A decade of global volcanic SO 2 emissions measured from space, *Scientific Reports*, *7*(1), 44,095, doi: 10.1038/srep44095, 2017.

Carrara, P. E., and D. A. Trimble, A Glacier Peak and Mount Saint Helens J volcanic ash couplet and the timing of deglaciation in the Colville Valley area, Washington, *Canadian Journal of Earth Sciences*, *29*(11), 2397–2405, doi: 10.1139/e92-187, 1992.

Carson, R. J., Where the Rockies meet the Columbia Plateau: Geologic field trip from the Walla Walla Valley to the Wallowa Mountains, Oregon, *Oregon Department of Geology and Mineral Industries*, *63*(1), 2001.

Carson, R. J., and K. R. Pogue, *Flood basalts and glacier floods: Roadside geology of parts of Walla Walla, Franklin, and Columbia Counties, Washington*, vol. Information Circular 90, Washington State Department of Natural Resources, Division of Geology and Earth Resources, 1996.

Casadevall, T. J., The 1989–1990 eruption of Redoubt Volcano, Alaska: impacts on aircraft operations, *Journal of Volcanology and Geothermal Research*, *62*(1), 301–316, doi: 10.1016/0377-0273(94)90038-8, 1994.

Cashman, K., and A. Rust, Introduction: Part 2: Volcanic Ash: Generation and Spatial Variations, in *Volcanic ash: Hazard observation*, pp. 5–22, Elsevier Inc., 2016.

Cashman, K. V., and S. J. Cronin, Welcoming a monster to the world: Myths, oral tradition, and modern societal response to volcanic disasters, *Journal of Volcanology and Geothermal Research*, *176*(3), 407–418, doi: 10.1016/j.jvolgeores.2008.01.040, 2008.

Cashman, K. V., and A. C. Rust, Far-travelled ash in past and future eruptions: combining tephrochronology with volcanic studies, *Journal of Quaternary Science*, *35*(1-2), 11–22, doi: 10.1002/jqs.3159, 2020.

Cashman, K. V., R. S. J. Sparks, and J. D. Blundy, Vertically extensive and unstable magmatic systems: A unified view of igneous processes, *Science*, *355*(6331), doi: 10.1126/science.aag3055, 2017.

Castro, M., and D. Andronico, Operazioni di base per la misura della distribuzione granulometrica di particelle vulcaniche tramite il CAMSIZER, *Rapporti Tecnici 79*, Instituto Nazionale di Geofisica e Vulcanologia, Catania, 2008.

Chagué-Goff, C., F. Goodarzi, and W. S. Fyfe, Elemental Distribution and Pyrite Occurrence in a Freshwater Peatland, Alberta, *The Journal of Geology*, *104*(6), 649–663, doi: 10.1086/629860, 1996.

Chatters, J. C., and K. A. Hoover, Response of the Columbia River fluvial system to Holocene climatic change, *Quaternary Research*, *37*(1), 42 – 59, doi: https://doi.org/10.1016/0033-5894(92)90005-4, 1992.

Cimarelli, C., M. A. Alatorre-Ibargüengoitia, U. Kueppers, B. Scheu, and D. B. Dingwell, Experimental generation of volcanic lightning, *Geology*, *42*(1), 79–82, doi: 10.1130/G34802.1, 2014.

Cioni, R., M. Pistolesi, A. Bertagnini, C. Bonadonna, A. Hoskuldsson, and B. Scateni, Insights into the dynamics and evolution of the 2010 Eyjafjallajökull summit eruption (Iceland) provided by volcanic ash textures, *Earth and Planetary Science Letters*, *394*, 111–123, doi: 10.1016/j.epsl.2014.02.051, 2014.

Clark, E. E., *Indian legends of the Pacific Northwest*, Univ of California Press, 1953.

Cole, D., Excavation; in area 6 ol site 35 GM 9, the Wildcat Canyon site: Oregon Univ. Museum, *Nat. History*, 1969.

Coltelli, M., L. Miraglia, and S. Scollo, Characterization of shape and terminal velocity of tephra particles erupted during the 2002 eruption of Etna volcano, Italy, *Bulletin of Volcanology*, *70*(9), 1103–1112, doi: 10.1007/s00445-007-0192-8, 2008.

Connor, C. B., B. E. Hill, B. Winfrey, N. M. Franklin, and P. C. L. Femina, Estimation of Volcanic Hazards from Tephra Fallout, *Natural Hazards Review*, *2*(1), 33–42, doi: 10.1061/(ASCE) 1527-6988(2001)2:1(33), 2001.

Connor, L. J., and C. B. Connor, Inversion is the key to dispersion: understanding eruption dynamics by inverting tephra fallout, in *Statistics in Volcanology*, vol. 1, edited by H. M. Mader, S. G. Coles, C. B. Connor, and L. J. Connor, p. 231, Geological Society of London, 2006.

Constantinescu, R., A. Hopulele-Gligor, C. B. Connor, C. Bonadonna, L. J. Connor, J. M. Lindsay, S. Charbonnier, and A. C. M. Volentik, The radius of the umbrella cloud helps characterize large explosive volcanic eruptions, *Communications Earth & Environment*, *2*(1), 1–8, doi: 10.1038/s43247-020-00078-3, 2021.

Cooper, C. L., I. P. Savov, and G. T. Swindles, Standard chemical-based tephra extraction methods significantly alter the geochemistry of volcanic glass shards, *Journal of Quaternary Science*, *34*(8), 697–707, doi: 10.1002/jqs.3169, 2019.

Cooper, K. M., Time scales and temperatures of crystal storage in magma reservoirs: implications for magma reservoir dynamics, *Philosophical Transactions of the Royal Society A: Mathematical, Physical and Engineering Sciences*, *377*(2139), 20180,009, doi: 10.1098/rsta.2018.0009, 2019.

Costa, A., A. Folch, G. Macedonio, B. Giaccio, R. Isaia, and V. Smith, Quantifying volcanic ash dispersal and impact of the Campanian Ignimbrite super-eruption, *Geophysical Research Letters*, *39*(10), 2012.

Costa, A., A. Folch, and G. Macedonio, Density-driven transport in the umbrella region of volcanic clouds: Implications for tephra dispersion models, *Geophysical Research Letters*, *40*(18), 4823–4827, 2013.

Costa, A., V. C. Smith, G. Macedonio, and N. E. Matthews, The magnitude and impact of the Youngest Toba Tuff super-eruption, *Frontiers in Earth Science*, *2*, doi: 10.3389/feart.2014.00016, 2014.

Costa, A., L. Pioli, and C. Bonadonna, Assessing tephra total grain-size distribution: Insights from field data analysis, *Earth and Planetary Science Letters*, *443*, 90–107, doi: 10.1016/j.epsl.2016.02.040, 2016.

Costa, A., Y. J. Suzuki, and T. Koyaguchi, Understanding the plume dynamics of explosive super-eruptions, *Nature Communications*, *9*(1), 654, doi: 10.1038/s41467-018-02901-0, 2018.

Cox, L., J. Wood, J. Fan, and Y. Huang, Experimental Separation of Non-spherical Ash Particles by Terminal Velocity, *Master of Engineering*, University of Bristol, 2017.

Crandell, D. R., and D. R. Mullineaux, Volcanic hazards at Mount Rainier, Washington, *Tech. rep.*, US Geological Survey, 1967.

Crane, H., University of Michigan Radiocarbon Dates I, *Science*, *124*, 664 – 672, 1956.

Cressman, L. S., D. L. Cole, W. A. Davis, T. M. Newman, and D. J. Scheans, Cultural Sequences at the Dalles, Oregon: A Contribution to Pacific Northwest Prehistory, *Transactions of the American Philosophical Society*, *50*(10), 1–108, 1960.

Crosweller, H. S., et al., Global database on large magnitude explosive volcanic eruptions (LaMEVE), *Journal of Applied Volcanology*, *1*(1), 4, doi: 10.1186/2191-5040-1-4, 2012.

Crummy, J. M., I. P. Savov, S. C. Loughlin, C. B. Connor, L. Connor, and C. Navarro-Ochoa, Challenges of determining frequency and magnitudes of explosive eruptions even with an unprecedented stratigraphy, *Journal of Applied Volcanology*, *8*(1), 3, doi: 10.1186/s13617-019-0083-7, 2019.

Cutler, N. A., R. T. Streeter, J. Marple, L. R. Shotter, J. S. Yeoh, and A. J. Dugmore, Tephra transformations: variable preservation of tephra layers from two well-studied eruptions, *Bulletin of Volcanology*, *80*(11), 77, doi: 10.1007/s00445-018-1251-z, 2018.

Cutler, N. A., R. T. Streeter, S. L. Engwell, M. S. Bolton, B. J. L. Jensen, and A. J. Dugmore, How does tephra deposit thickness change over time? A calibration exercise based on the 1980 Mount St Helens tephra deposit, *Journal of Volcanology and Geothermal Research*, *399*, 106,883, doi: 10.1016/j.jvolgeores.2020.106883, 2020.

Cyr, M., and A. Tagnit-Hamou, Particle size distribution of fine powders by LASER diffraction spectrometry. Case of cementitious materials, *Materials and Structures*, *34*(6), 342–350, doi: 10.1007/BF02486485, 2001.

Czamanske, G. K., and S. C. Porter, Titanium Dioxide in Pyroclastic Layers from Volcanoes in the Cascad Range, *Science*, *150*(3699), 1022–1025, doi: 10.1126/science.150.3699.1022, 1965.

Dacre, H. F., et al., Evaluating the structure and magnitude of the ash plume during the initial phase of the 2010 Eyjafjallajökull eruption using lidar observations and NAME simulations, *Journal of Geophysical Research: Atmospheres*, *116*(D20), 2011.

Daggitt, M. L., T. A. Mather, D. M. Pyle, and S. Page, AshCalc–a new tool for the comparison of the exponential, power-law and Weibull models of tephra deposition, *Journal of Applied Volcanology*, *3*(1), 7, doi: 10.1186/2191-5040-3-7, 2014.

Dartevelle, S., G. G. J. Ernst, J. Stix, and A. Bernard, Origin of the Mount Pinatubo climactic eruption cloud: Implications for volcanic hazards and atmospheric impacts, *Geology*, *30*(7), 663–666, doi: 10.1130/0091-7613(2002)030<0663:OOTMPC>2.0.CO;2, 2002.

Dashtgard, S. E., M. K. Gingras, and S. G. Pemberton, Grain-size controls on the occurrence of bioturbation, *Palaeogeography, Palaeoclimatology, Palaeoecology*, *257*(1), 224–243, doi: 10.1016/j.palaeo.2007.10.024, 2008.

David, P. P., Discovery of Mazama ash in Saskatchewan, Canada, *Canadian Journal of Earth Sciences*, *7*(6), 1579–1583, doi: 10.1139/e70-150, 1970.

Davis, J. O., Quaternary tephrochronology of the Lake Lahontan area, Nevada and California, PhD Thesis, University of Nevada, 1978.

Davis, J. O., Correlation of late Quaternary tephra layers in a long pluvial sequence near Summer Lake, Oregon, *Quaternary Research*, *23*(1), 38 – 53, doi: https://doi.org/10.1016/0033-5894(85)90070-5, 1985.

Dean, W. E., T. S. Ahlbrandt, R. Y. Anderson, and J. Platt Bradbury, Regional aridity in North America during the middle Holocene, *The Holocene*, *6*(2), 145–155, doi: 10.1177/095968369600600202, 1996.

Delignette-Muller, M. L., and C. Dutang, fitdistrplus: An R Package for Fitting Distributions, *Journal of Statistical Software*, *64*(4), 1–34, 2015.

Dioguardi, F., and D. Mele, A new shape dependent drag correlation formula for non-spherical rough particles. Experiments and results, *Powder Technology*, *277*, 222–230, doi: 10.1016/j.powtec.2015.02.062, 2015.

Dioguardi, F., D. Mele, P. Dellino, and T. Dürig, The terminal velocity of volcanic particles with shape obtained from 3D X-ray microtomography, *Journal of Volcanology and Geothermal Research*, *329*, 41–53, doi: 10.1016/j.jvolgeores.2016.11.013, 2017.

Doerner, J. P., and P. E. Carrara, Late Quaternary Vegetation and Climatic History of the Long Valley Area, West-Central Idaho, U.S.A., *Quaternary Research*, *56*(1), 103–111, doi: 10.1006/qres.2001.2247, 2001.

Driver, J. C., Early prehistoric killing of bighorn sheep in the Southeastern Canadian Rockies, *Plains Anthropologist*, *27*(98), 265–271, 1982.

Druitt, T. H., and C. R. Bacon, Lithic breccia and ignimbrite erupted during the collapse of Crater Lake Caldera, Oregon, *Journal of Volcanology and Geothermal Research*, *29*(1), 1 – 32, doi: https://doi.org/10.1016/0377-0273(86)90038-7, 1986.

Druitt, T. H., and C. R. Bacon, Petrology of the zoned calcalkaline magma chamber of Mount Mazama, Crater Lake, Oregon, *Contributions to Mineralogy and Petrology*, *101*(2), 245–259, 1989.

Duford, J. M., and G. D. Osborn, Holocene and latest Pleistocene cirque glaciations in the Shuswap Highland, British Columbia, *Canadian Journal of Earth Sciences*, *15*(6), 865–873, doi: 10.1139/e78-098, 1978.

Dugmore, A., R. Streeter, and N. Cutler, The role of vegetation cover and slope angle in tephra layer preservation and implications for Quaternary tephrostratigraphy, *Palaeogeography, Palaeoclimatology, Palaeoecology*, *489*, 105–116, doi: 10.1016/j.palaeo.2017.10.002, 2018.

Dugmore, A. J., and A. J. Newton, Thin tephra layers in peat revealed by X-radiography, *Journal of Archaeological Science*, *19*(2), 163–170, doi: 10.1016/0305-4403(92)90047-7, 1992.

Dugmore, A. J., A. J. Newton, D. E. Sugden, and G. Larsen, Geochemical stability of fine-grained silicic Holocene tephra in Iceland and Scotland, *Journal of Quaternary Science*, *7*(2), 173–183, doi: 10.1002/jqs.3390070208, 1992.

Dugmore, A. J., A. J. Newton, K. T. Smith, and K.-A. Mairs, Tephrochronology and the late Holocene volcanic and flood history of Eyjafjallajökull, Iceland, *Journal of Quaternary Science*, *28*(3), 237–247, doi: 10.1002/jqs.2608, 2013.

Durant, A. J., R. A. Shaw, W. I. Rose, Y. Mi, and G. G. J. Ernst, Ice nucleation and overseeding of ice in volcanic clouds, *Journal of Geophysical Research: Atmospheres*, *113*(D9), doi: 10.1029/2007JD009064, 2008.

Durant, A. J., W. I. Rose, A. M. Sarna-Wojcicki, S. Carey, and A. C. M. Volentik, Hydrometeor-enhanced tephra sedimentation: Constraints from the 18 May 1980 eruption of Mount St. Helens, *Journal of Geophysical Research: Solid Earth*, *114*(B3), doi: 10.1029/2008JB005756, 2009.

Durant, A. J., G. Villarosa, W. I. Rose, P. Delmelle, A. J. Prata, and J. G. Viramonte, Long-range volcanic ash transport and fallout during the 2008 eruption of Chaitén volcano, Chile, *Physics and Chemistry of the Earth, Parts A/B/C*, *45-46*, 50–64, doi: 10.1016/j.pce.2011.09.004, 2012.

Dyck, W., J. G. Fyles, and W. Blake, Geological Survey of Canada radiocarbon dates IV, *Radiocarbon*, *7*, 24–46, 1965.

Dyck, W., J. Lowdon, J. G. Fyles, and W. Blake, Geological Survey of Canada radiocarbon dates V, *Radiocarbon*, *8*, 96–127, 1966.

Dürig, T., L. S. Schmidt, J. D. L. White, and M. H. Bowman, DendroScan: an open source tool to conduct comparative statistical tests and dendrogrammatic analyses on particle morphometry, *Scientific Reports*, *10*(1), 21,682, doi: 10.1038/s41598-020-78698-0, 2020.

Egan, J., R. Staff, and J. Blackford, A high-precision age estimate of the Holocene Plinian eruption of Mount Mazama, Oregon, USA, *The Holocene*, *25*(7), 1054–1067, doi: 10.1177/0959683615576230, 2015.

Egan, J., W. J. Fletcher, T. E. H. Allott, C. S. Lane, J. J. Blackford, and D. H. Clark, The impact and significance of tephra deposition on a Holocene forest environment in the North Cascades, Washington, USA, *Quaternary Science Reviews*, *137*, 135–155, doi: 10.1016/j.quascirev.2016.02.013, 2016.

Enache, M. D., and B. F. Cumming, The Morphological and Optical Properties of Volcanic Glass: A Tool to Assess Density-induced Vertical Migration of Tephra in Sediment Cores, *Journal of Paleolimnology*, *35*(3), 661–667, doi: 10.1007/s10933-005-3604-9, 2006.

Engwell, S., R. Sparks, and W. Aspinall, Quantifying uncertainties in the measurement of tephra fall thickness, *Journal of Applied Volcanology*, *2*(1), 5, doi: 10.1186/2191-5040-2-5, 2013.

Engwell, S. L., and J. Eychenne, Contribution of fine ash to the atmosphere from plumes associated with pyroclastic density currents, in *Volcanic Ash: Hazard Observation*, pp. 67–85, Elsevier, 2016.

Engwell, S. L., R. S. J. Sparks, and S. Carey, Physical characteristics of tephra layers in the deep sea realm: the Campanian Ignimbrite eruption, *Geological Society, London, Special Publications*, *398*(1), 47–64, doi: 10.1144/SP398.7, 2014.

Engwell, S. L., W. P. Aspinall, and R. S. J. Sparks, An objective method for the production of isopach maps and implications for the estimation of tephra deposit volumes and their uncertainties, *Bulletin of Volcanology*, *77*(7), 61, doi: 10.1007/s00445-015-0942-y, 2015.

Eychenne, J., and J.-L. Le Pennec, Sigmoidal particle density distribution in a subplinian scoria fall deposit, *Bulletin of Volcanology*, *74*(10), 2243–2249, doi: 10.1007/s00445-012-0671-4, 2012.

Eychenne, J., J.-L. Le Pennec, L. Troncoso, M. Gouhier, and J.-M. Nedelec, Causes and consequences of bimodal grain-size distribution of tephra fall deposited during the August 2006 Tungurahua eruption (Ecuador), *Bulletin of Volcanology*, *74*(1), 187–205, doi: 10.1007/s00445-011-0517-5, 2012.

Eychenne, J., K. Cashman, A. Rust, and A. Durant, Impact of the lateral blast on the spatial pattern and grain size characteristics of the 18 May 1980 Mount St. Helens fallout deposit, *Journal of Geophysical Research: Solid Earth*, *120*(9), 6018–6038, doi: 10.1002/2015JB012116, 2015.

Eychenne, J., A. C. Rust, K. V. Cashman, and W. Wobrock, Distal Enhanced Sedimentation From Volcanic Plumes: Insights From the Secondary Mass Maxima in the 1992 Mount Spurr

Fallout Deposits, *Journal of Geophysical Research: Solid Earth*, *122*(10), 7679–7697, doi: 10.1002/2017JB014412, 2017.

Fairbridge, R. W., and J. Bourgeois, *The Encyclopedia of sedimentology*, *Encyclopedia of earth sciences series ; v. 6*, vol. Section: xvi, Dowden, Hutchinson & Ross ;, Stroudsburg, Pa., 1978.

Fenner, C. N., Tuffs and other volcanic deposits of Katmai and Yellowstone Park, *Eos, Transactions American Geophysical Union*, *18*(1), 236–239, doi: https://doi.org/10.1029/TR018i001p00236, 1937.

Fero, J., S. N. Carey, and J. T. Merrill, Simulating the dispersal of tephra from the 1991 Pinatubo eruption: Implications for the formation of widespread ash layers, *Journal of Volcanology and Geothermal Research*, *186*(1), 120–131, doi: 10.1016/j.jvolgeores.2009.03.011, 2009.

Fierstein, J., and W. Hildreth, The plinian eruptions of 1912 at Novarupta, Katmai National Park, Alaska, *Bulletin of Volcanology*, *54*(8), 646–684, doi: 10.1007/BF00430778, 1992.

Fierstein, J., and M. Nathenson, Another look at the calculation of fallout tephra volumes, *Bulletin of Volcanology*, *54*(2), 156–167, doi: 10.1007/BF00278005, 1992.

Figueiredo, M. M., Electrozone Sensing in Particle Size Analysis, in *Encyclopedia of Analytical Chemistry*, American Cancer Society, 2006.

Filippelli, G. M., C. Souch, B. Menounos, S. Slater-Atwater, A. J. T. Jull, and O. Slaymaker, Alpine lake sediment records of the impact of glaciation and climate change on the biogeochemical cycling of soil nutrients, *Quaternary Research*, *66*(1), 158 – 166, doi: https://doi.org/10.1016/j.yqres.2006.03.009, 2006.

Fisher, R. V., Maximum size, median diameter, and sorting of tephra, *Journal of Geophysical Research (1896-1977)*, *69*(2), 341–355, doi: https://doi.org/10.1029/JZ069i002p00341, 1964.

Foit, F. F., and P. J. Mehringer, Holocene tephra stratigraphy in four lakes in southeastern Oregon and northwestern Nevada, USA, *Quaternary Research*, *85*(2), 218 – 226, doi: https://doi.org/10.1016/j.yqres.2015.12.008, 2016.

Foit, F. F., P. J. Mehringer, and J. C. Sheppard, Age, distribution, and stratigraphy of Glacier Peak tephra in eastern Washington and western Montana, United States, *Canadian Journal of Earth Sciences*, *30*(3), 535–552, doi: 10.1139/e93-042, 1993.

Foit, F. F. F., D. G. Gavin, and F. S. Hu, The tephra stratigraphy of two lakes in south-central British Columbia, Canada and its implications for mid-late Holocene volcanic activity at Glacier Peak and Mount St. Helens, Washington, USA, *Canadian Journal of Earth Sciences*, *41*(12), 1401–1410, doi: 10.1139/e04-081, 2004.

Folch, A., A review of tephra transport and dispersal models: Evolution, current status, and future perspectives, *Journal of Volcanology and Geothermal Research*, *235-236*, 96–115, doi: 10.1016/j.jvolgeores.2012.05.020, 2012.

Folch, A., A. Costa, and S. Basart, Validation of the FALL3D ash dispersion model using observations of the 2010 Eyjafjallajökull volcanic ash clouds, *Atmospheric Environment*, *48*, 165–183, 2012.

Folk, R. L., and W. C. Ward, Brazos River bar [Texas]; a study in the significance of grain size parameters, *Journal of Sedimentary Research*, *27*(1), 3–26, doi: 10.1306/74D70646-2B21-11D7-8648000102C1865D, 1957.

Fontijn, K., et al., Synchronisation of sedimentary records using tephra: A postglacial tephrochronological model for the Chilean Lake District, *Quaternary Science Reviews*, *137*, 234–254, doi: 10.1016/j.quascirev.2016.02.015, 2016.

Ford, M. T., A. L. Grunder, and R. A. Duncan, Bimodal volcanism of the High Lava Plains and Northwestern Basin and Range of Oregon: Distribution and tectonic implications of age-progressive rhyolites, *Geochemistry, Geophysics, Geosystems*, *14*(8), 2836–2857, doi: 10.1002/ggge.20175, 2013.

Francis, P., and D. Rothery, Remote Sensing of Active Volcanoes, *Annual Review of Earth and Planetary Sciences*, *28*(1), 81–106, doi: 10.1146/annurev.earth.28.1.81, 2000.

Francis, P. N., M. C. Cooke, and R. W. Saunders, Retrieval of physical properties of volcanic ash using Meteosat: A case study from the 2010 Eyjafjallajökull eruption, *Journal of Geophysical Research: Atmospheres*, *117*(D20), 2012.

Freeman, A. K., et al., Radiocarbon age estimates from the SCAPE Project 2000–2005, *Plains Anthropologist*, *51*(199), 451–486, 2006.

Freret-Lorgeril, V., F. Donnadieu, J. Eychenne, C. Soriaux, and T. Latchimy, In situ terminal settling velocity measurements at Stromboli volcano: Input from physical characterization of ash, *Journal of Volcanology and Geothermal Research*, *374*, 62–79, doi: 10.1016/j.jvolgeores.2019.02.005, 2019.

Freret-Lorgeril, V., et al., Ash sedimentation by fingering and sediment thermals from wind-affected volcanic plumes, *Earth and Planetary Science Letters*, *534*, 116,072, doi: 10.1016/j.epsl.2020.116072, 2020.

Fries, C., Volumes And weights of pyroclastic material, lava, and water erupted by Paricutin volcano, Michoacan, Mexico, *Eos, Transactions American Geophysical Union*, *34*(4), 603–616, doi: 10.1029/TR034i004p00603, 1953.

Froggatt, P. C., Review of methods of estimating rhyolitic tephra volumes; applications to the Taupo volcanic zone, New Zealand, *Journal of Volcanology and Geothermal Research*, *14*(3), 301 – 318, doi: https://doi.org/10.1016/0377-0273(82)90067-1, 1982.

Fulton, R. J., *Radiocarbon geochronology of southern British Columbia*, Department of Energy, Mines and Resources, 1971.

GabbroSoft, GabbroSoft, https://www.gabbrosoft.org/spreadsheets/, 2011.

Ganser, G. H., A rational approach to drag prediction of spherical and nonspherical particles, *Powder Technology*, *77*(2), 143–152, 1993.

Garber, L., Influence of volcanic ash on the genesis and classification of two spodsols in Idaho, Master's thesis, University of Idaho, Moscow, 1970.

Gardner, J. E., R. M. E. Thomas, C. Jaupart, and S. Tait, Fragmentation of magma during Plinian volcanic eruptions, *Bulletin of Volcanology*, *58*(2), 144–162, doi: 10.1007/s004450050132, 1996.

Gardner, J. E., S. Carey, and H. Sigurdsson, Plinian eruptions at Glacier Peak and Newberry volcanoes, United States: Implications for volcanic hazards in the Cascade Range, *GSA Bulletin*, *110*(2), 173–187, doi: 10.1130/0016-7606(1998)110<0173:PEAGPA>2.3.CO;2, 1998.

Gatti, E., and C. Oppenheimer, Utilization of distal tephra records for understanding climatic and environmental consequences of the Youngest Toba Tuff, *Climates, Landscapes and Civilizations, Geophys. Monogr. Ser*, *198*, 63–74, doi: https://doi.org/10.1029/2012GM001216, 2012.

Gatti, E., A. J. Durant, P. L. Gibbard, and C. Oppenheimer, Youngest Toba Tuff in the Son Valley, India: a weak and discontinuous stratigraphic marker, *Quaternary Science Reviews*, *30*(27-28), 3925–3934, doi: https://doi.org/10.1016/j.quascirev.2011.10.008, 2011.

Gatti, E., M. Saidin, K. Talib, N. Rashidi, P. Gibbard, and C. Oppenheimer, Depositional processes of reworked tephra from the Late Pleistocene Youngest Toba Tuff deposits in the Lenggong Valley, Malaysia, *Quaternary Research*, *79*(2), 228–241, doi: https://doi.org/10.1016/j.yqres.2012.11.006, 2013.

Gaylord, D. R., F. F. Foit, J. K. Schatz, and A. J. Coleman, Smith Canyon dune field, Washington, U.S.A: relation to glacial outburst floods, the Mazama eruption, and Holocene paleoclimate, *Journal of Arid Environments*, *47*(4), 403 – 424, doi: https://doi.org/10.1006/jare.2000.0731, 2001.

Gelman, S. E., F. J. Gutiérrez, and O. Bachmann, On the longevity of large upper crustal silicic magma reservoirs, *Geology*, *41*(7), 759–762, doi: 10.1130/G34241.1, 2013.

Genareau, K., K. L. Wallace, P. Gharghabi, and J. Gafford, Lightning Effects on the Grain Size Distribution of Volcanic Ash, *Geophysical Research Letters*, *46*(6), 3133–3141, doi: 10.1029/2018GL081298, 2019.

Gertisser, R., and S. Self, The great 1815 eruption of Tambora and future risks from large-scale volcanism, *Geology Today*, *31*(4), 132–136, doi: 10.1111/gto.12099, 2015.

Geyer, A., and J. Martí, The new worldwide collapse caldera database (CCDB): A tool for studying and understanding caldera processes, *Journal of Volcanology and Geothermal Research*, *175*(3), 334–354, doi: 10.1016/j.jvolgeores.2008.03.017, 2008.

Ghiorso, M. S., and B. W. Evans, Thermodynamics of Rhombohedral Oxide Solid Solutions and a Revision of the FE-TI Two-Oxide Geothermometer and Oxygen-Barometer, *American Journal of Science*, *308*(9), 957–1039, doi: 10.2475/09.2008.01, 2008.

Ghiorso, M. S., and K. B. Prissel, ENKI Cloud App: Implementation of the Fe-Ti Oxide Geothermooxybarometer of Ghiorso and Evans, 2008, 2020.

Gibbs, A., M. Charman, W. Schwarzacher, and A. C. Rust, Immersion freezing of supercooled water drops containing glassy volcanic ash particles, *GeoResJ*, *7*, 66–69, doi: 10.1016/j.grj.2015.06.002, 2015.

Gibbs, R. J., M. D. Matthews, and D. A. Link, The relationship between sphere size and settling velocity, *Journal of Sedimentary Research*, *41*(1), 7–18, doi: 10.1306/74D721D0-2B21-11D7-8648000102C1865D, 1971.

Gibson, E. C., A Report of Archaeological Investigations at the Two Rivers Site (45BN14), at the Confluence of the Snake and Columbia Rivers., *Tech. rep.*, Professional Analysts Eugene, OR, 1984.

Gilbert, R., and J. R. Desloges, Late glacial and Holocene sedimentary environments of Quesnel Lake, British Columbia, *Geomorphology*, *179*, 186 – 196, doi: https://doi.org/10.1016/j.geomorph.2012.08.010, 2012.

Gilman, B., B. Moser, and others, *Ashen Sky: The Letters of Pliny the Younger on the Eruption of Vesuvius*, Getty Publications, 2007.

Goldfinger, C., et al., Turbidite event history—Methods and implications for Holocene paleoseismicity of the Cascadia subduction zone, *USGS Numbered Series 1661-F*, U.S. Geological Survey, Reston, VA, 2012.

Gouhier, M., J. Eychenne, N. Azzaoui, A. Guillin, M. Deslandes, M. Poret, A. Costa, and P. Husson, Low efficiency of large volcanic eruptions in transporting very fine ash into the atmosphere, *Scientific Reports*, *9*(1), 1–12, doi: 10.1038/s41598-019-38595-7, 2019.

Grey, D. C., and R. Bennett, A preliminary limnological history of Great Salt Lake, in *The Great Salt Lake and Utah's Water Resources*, pp. 3–18, 1972.

Griggs, A. J., S. M. Davies, P. M. Abbott, M. Coleman, A. P. Palmer, T. L. Rasmussen, and R. Johnston, Visualizing tephra deposits and sedimentary processes in the marine environment: The potential of X-ray microtomography, *Geochemistry, Geophysics, Geosystems*, *16*(12), 4329–4343, doi: 10.1002/2015GC006073, 2015.

Gudmundsson, M. T., et al., Ash generation and distribution from the April-May 2010 eruption of Eyjafjallajökull, Iceland, *Scientific Reports*, *2*(1), 572, doi: 10.1038/srep00572, 2012.

Hadley, D., G. L. Hufford, and J. J. Simpson, Resuspension of relic volcanic ash and dust from Katmai: still an aviation hazard, *Weather and forecasting*, *19*(5), 829–840, doi: https://doi.org/10.1175/1520-0434(2004)019<0829:RORVAA>2.0.CO;2, 2004.

Hails, J. R., B. S. Thompson, and L. Cummings, An Appraisal of the Significance of Sieve Intervals in Grain Size Analysis for Environmental Interpretation, *Journal of Sedimentary Research*, *43*(3), 1973.

Hallett, D. J., L. V. Hills, and J. J. Clague, New accelerator mass spectrometry radiocarbon ages for the Mazama tephra layer from Kootenay National Park, British Columbia, Canada, *Canadian Journal of Earth Sciences*, *34*(9), 1202–1209, doi: https://doi.org/10.1139/e17-096, 1997.

Hammer, C. U., H. B. Clausen, and W. Dansgaard, Greenland ice sheet evidence of post-glacial volcanism and its climatic impact, *Nature*, *288*(5788), 230–235, doi: https://doi.org/10.1038/288230a0, 1980.

Harward, M., and C. Youngberg, Soils from Mazama ash in Oregon identification, distribution and properties, in *Pedology and Quaternary Research Symposium University of Alberta, Edmonton Alberta, Canada*, pp. 163–178, University of Alberta, University of Alberta, 1969.

Haynes, C., D. C. Grey, P. E. Damon, and R. Bennett, Arizona radiocarbon dates VII., *Radiocarbon*, *9*(1), 1–14, doi: https://doi.org/10.1017/S0033822200000424[Opensinanewwindow], 1967.

Heiken, G., Morphology and Petrography of Volcanic Ashes, *GSA Bulletin*, *83*(7), 1961–1988, doi: 10.1130/0016-7606(1972)83[1961:MAPOVA]2.0.CO;2, 1972.

Heinrichs, M., I. Walker, R. Mathewes, and R. Hebda, Holocene chironomid-inferred salinity and paleovegetation reconstruction from Kilpoola Lake, British Columbia, *Géographie physique et Quaternaire*, *53*(2), 211–221, doi: https://doi.org/10.7202/004878ar, 1999.

Hersbach, H., et al., The ERA5 global reanalysis, *Quarterly Journal of the Royal Meteorological Society*, *146*(730), 1999–2049, doi: 10.1002/qj.3803, 2020.

Heusser, C. J., Quaternary vegetation, climate, and glaciation of the Hoh River Valley, Washington, *Geological Society of America Bulletin*, *85*(10), 1547–1560, doi: https://doi.org/10.1130/0016-7606(1974)85<1547:QVCAGO>2.0.CO;2, 1974.

Hickman, M., and M. A. Reasoner, Diatom responses to late Quaternary vegetation and climate change, and to deposition of two tephras in an alpine and a sub-alpine lake in Yoho National Park, British Columbia, *Journal of Paleolimnology*, *11*(2), 173–188, doi: 10.1007/BF00686864, 1994.

Hildreth, W., *Quaternary magmatism in the Cascades: Geologic perspectives*, US Geological Survey, 2007.

Hobbs, P. V., L. F. Radke, J. H. Lyons, R. J. Ferek, D. J. Coffman, and T. J. Casadevall, Airborne measurements of particle and gas emissions from the 1990 volcanic eruptions of Mount Redoubt, *Journal of Geophysical Research: Atmospheres*, *96*(D10), 18,735–18,752, doi: 10.1029/91JD01635, 1991.

Holasek, R. E., S. Self, and A. W. Woods, Satellite observations and interpretation of the 1991 Mount Pinatubo eruption plumes, *Journal of Geophysical Research: Solid Earth*, *101*(B12), 27,635–27,655, doi: 10.1029/96JB01179, 1996.

Hooper, P., G. Webster, and V. Camp, Geologic map of the Clarkston 15-minute quadrangle, *Geologic Map*, Washington and Idaho: Washington Division of Geology and Earth Resources=], 1985.

Hooper, P., G. Binger, and K. Lees, Ages of the Steens and Columbia River flood basalts and their relationship to extension-related calc-alkalic volcanism in eastern Oregon, *GSA Bulletin*, *114*(1), 43–50, doi: 10.1130/0016-7606(2002)114<0043:AOTSAC>2.0.CO;2, 2002.

Hopkins, J. L., M.-A. Millet, C. Timm, C. J. N. Wilson, G. S. Leonard, J. M. Palin, and H. Neil, Tools and techniques for developing tephra stratigraphies in lake cores: A case study from the basaltic Auckland Volcanic Field, New Zealand, *Quaternary Science Reviews*, *123*, 58 – 75, doi: https://doi.org/10.1016/j.quascirev.2015.06.014, 2015.

Horwell, C., Grain-size analysis of volcanic ash for the rapid assessment of respiratory health hazard, *Journal of Environmental Monitoring*, *9*(10), 1107–1115, doi: 10.1039/B710583P, 2007.

Horwell, C. J., and P. J. Baxter, The respiratory health hazards of volcanic ash: a review for volcanic risk mitigation, *Bulletin of Volcanology*, *69*(1), 1–24, doi: 10.1007/s00445-006-0052-y, 2006.

Horwell, C. J., L. P. Braña, R. S. J. Sparks, M. D. Murphy, and V. L. Hards, A geochemical investigation of fragmentation and physical fractionation in pyroclastic flows from the Soufrière

Hills volcano, Montserrat, *Journal of Volcanology and Geothermal Research*, *109*(4), 247–262, doi: 10.1016/S0377-0273(00)00319-X, 2001.

Horwell, C. J., R. S. J. Sparks, T. S. Brewer, E. W. Llewellin, and B. J. Williamson, Characterization of respirable volcanic ash from the Soufrière Hills volcano, Montserrat, with implications for human health hazards, *Bulletin of Volcanology*, *65*(5), 346–362, doi: 10.1007/s00445-002-0266-6, 2003.

Houghton, B. F., C. J. N. Wilson, J. Fierstein, and W. Hildreth, Complex proximal deposition during the Plinian eruptions of 1912 at Novarupta, Alaska, *Bulletin of Volcanology*, *66*(2), 95–133, doi: 10.1007/s00445-003-0297-7, 2004.

Inman, D. L., Measures for describing the size distribution of sediments, *Journal of Sedimentary Research*, *22*(3), 125–145, doi: 10.1306/D42694DB-2B26-11D7-8648000102C1865D, 1952.

Inoue, H., A least-squares smooth fitting for irregularly spaced data: Finite-element approach using the cubic B-spline basis, *Geophysics*, *51*(11), 2051–2066, doi: https://doi.org/10.1190/1.1442060, 1986.

Jackson, M. D., J. Blundy, and R. S. J. Sparks, Chemical differentiation, cold storage and remobilization of magma in the Earth's crust, *Nature*, *564*(7736), 405–409, doi: 10.1038/s41586-018-0746-2, 2018.

James, M. R., S. J. Lane, and J. S. Gilbert, Volcanic plume electrification: Experimental investigation of a fracture-charging mechanism, *Journal of Geophysical Research: Solid Earth*, *105*(B7), 16,641–16,649, doi: 10.1029/2000JB900068, 2000.

James, T., E. J. Gowan, I. Hutchinson, J. J. Clague, J. V. Barrie, and K. W. Conway, Sea-level change and paleogeographic reconstructions, southern Vancouver Island, British Columbia, Canada, *Quaternary Science Reviews*, *28*(13), 1200 – 1216, doi: https://doi.org/10.1016/j.quascirev.2008.12.022, 2009.

Jashemski, W. F., and F. G. Meyer, *The Natural History of Pompeii*, Cambridge University Press, 2002.

Jellinek, A. M., and D. J. DePaolo, A model for the origin of large silicic magma chambers: precursors of caldera-forming eruptions, *Bulletin of Volcanology*, *65*(5), 363–381, doi: 10.1007/s00445-003-0277-y, 2003.

Jenkins, S., C. Magill, J. McAneney, and R. Blong, Regional ash fall hazard I: a probabilistic assessment methodology, *Bulletin of Volcanology*, *74*(7), 1699–1712, doi: 10.1007/s00445-012-0627-8, 2012.

Jensen, B. J. L., A. B. Beaudoin, M. A. Clynne, J. Harvey, and J. W. Vallance, A re-examination of the three most prominent Holocene tephra deposits in western Canada: Bridge River, Mount St. Helens Yn and Mazama, *Quaternary International*, *500*, 83–95, doi: 10.1016/j.quaint.2019.03.017, 2019.

Johnson, B., et al., In situ observations of volcanic ash clouds from the FAAM aircraft during the eruption of Eyjafjallajökull in 2010, *Journal of Geophysical Research: Atmospheres*, *117*(D20), 2012.

Johnston, E. N., J. C. Phillips, C. Bonadonna, and I. M. Watson, Reconstructing the tephra dispersal pattern from the Bronze Age eruption of Santorini using an advection–diffusion model, *Bulletin of Volcanology*, *74*(6), 1485–1507, doi: 10.1007/s00445-012-0609-x, 2012.

Johnston, E. N., R. S. J. Sparks, J. C. Phillips, and S. Carey, Revised estimates for the volume of the Late Bronze Age Minoan eruption, Santorini, Greece, *Journal of the Geological Society*, *171*(4), 583–590, doi: 10.1144/jgs2013-113, 2014.

Jones, T. J., K. McNamara, J. Eychenne, A. C. Rust, K. V. Cashman, B. Scheu, and R. Edwards, Primary and secondary fragmentation of crystal-bearing intermediate magma, *Journal of Volcanology and Geothermal Research*, *327*, 70–83, doi: 10.1016/j.jvolgeores.2016.06.022, 2016.

Jonkers, L., M. A. Prins, G.-J. A. Brummer, M. Konert, and B. C. Lougheed, Experimental insights into laser diffraction particle sizing of fine-grained sediments for use in palaeoceanography, *Sedimentology*, *56*(7), 2192–2206, doi: 10.1111/j.1365-3091.2009.01076.x, 2009.

Jutzeler, M., A. A. Proussevitch, and S. R. Allen, Grain-size distribution of volcaniclastic rocks 1: A new technique based on functional stereology, *Journal of Volcanology and Geothermal Research*, *239-240*, 1–11, doi: 10.1016/j.jvolgeores.2012.05.013, 2012.

Kalnay, E., et al., The NCEP/NCAR 40-Year Reanalysis Project, *Bulletin of the American Meteorological Society*, *77*(3), 437–472, doi: 10.1175/1520-0477(1996)077<0437:TNYRP>2.0.CO;2, 1996.

Kaminski, E., and C. Jaupart, The size distribution of pyroclasts and the fragmentation sequence in explosive volcanic eruptions, *Journal of Geophysical Research: Solid Earth*, *103*(B12), 29,759–29,779, doi: 10.1029/98JB02795, 1998.

Kaminski, E., S. Tait, and G. Carazzo, Turbulent entrainment in jets with arbitrary buoyancy, *Journal of Fluid Mechanics*, *526*, 361–376, doi: 10.1017/S0022112004003209, 2005.

Kandlbauer, J., and R. S. J. Sparks, New estimates of the 1815 Tambora eruption volume, *Journal of Volcanology and Geothermal Research*, *286*, 93–100, doi: 10.1016/j.jvolgeores.2014.08.020, 2014.

Karlstrom, L., H. M. Wright, and C. R. Bacon, The effect of pressurized magma chamber growth on melt migration and pre-caldera vent locations through time at Mount Mazama, Crater Lake, Oregon, *Earth and Planetary Science Letters*, *412*, 209–219, doi: 10.1016/j.epsl.2014.12.001, 2015.

Kauahikaua, J. P., and B. Camara, Most recent eruptions of Hualalai Volcano, Hawai'i: Geological evidence from the historical record, doi: 10.1130/0-8137-2345-0.25, 2000.

Kavanagh, J. L., S. L. Engwell, and S. A. Martin, A review of laboratory and numerical modelling in volcanology, *Solid Earth*, *9*(2), 531–571, doi: 10.5194/se-9-531-2018, 2018.

Kittleman, L., Mineralogy, Correlation, and Grain-Size Distributions of Mazama Tephra and Other Postglacial Pyroclastic Layers, Pacific Northwest, *GSA Bulletin*, *84*(9), 2957–2980, doi: 10.1130/0016-7606(1973)84<2957:MCAGDO>2.0.CO;2, 1973.

Klawonn, M., B. F. Houghton, D. A. Swanson, S. A. Fagents, P. Wessel, and C. J. Wolfe, From field data to volumes: constraining uncertainties in pyroclastic eruption parameters, *Bulletin of Volcanology*, *76*(7), 839, doi: 10.1007/s00445-014-0839-1, 2014.

Klemetti, E., Let's Return the Cascade Volcanoes to Their Original Names, https://www.discovermagazine.com/planet-earth/lets-return-the-cascade-volcanoes-to-their-original-names, 2021.

Klug, C., K. Cashman, and C. Bacon, Structure and physical characteristics of pumice from the climactic eruption of Mount Mazama (Crater Lake), Oregon, *Bulletin of Volcanology*, *64*(7), 486–501, doi: 10.1007/s00445-002-0230-5, 2002.

Komar, P. D., and B. Cui, The analysis of grain-size measurements by sieving and settling-tube techniques, *Journal of Sedimentary Research*, *54*(2), 603–614, doi: 10.1306/212F8481-2B24-11D7-8648000102C1865D, 1984.

Koyaguchi, T., and M. Ohno, Reconstruction of eruption column dynamics on the basis of grain size of tephra fall deposits: 1. Methods, *Journal of Geophysical Research: Solid Earth*, *106*(B4), 6499–6512, doi: https://doi.org/10.1029/2000JB900426, 2001.

Koyaguchi, T., and M. Tokuno, Origin of the giant eruption cloud of Pinatubo, June 15, 1991, *Journal of Volcanology and Geothermal Research*, *55*(1), 85–96, doi: 10.1016/0377-0273(93)90091-5, 1993.

Kozono, T., M. Iguchi, T. Miwa, M. Maki, T. Maesaka, and D. Miki, Characteristics of tephra fall from eruptions at Sakurajima volcano, revealed by optical disdrometer measurements, *Bulletin of Volcanology*, *81*(7), 41, doi: 10.1007/s00445-019-1300-2, 2019.

Krumbein, W. C., Size frequency distributions of sediments, *Journal of Sedimentary Research*, *4*(2), 65–77, doi: 10.1306/D4268EB9-2B26-11D7-8648000102C1865D, 1934.

Kueppers, U., D. Perugini, and D. B. Dingwell, "Explosive energy" during volcanic eruptions from fractal analysis of pyroclasts, *Earth and Planetary Science Letters*, *248*(3), 800–807, doi: 10.1016/j.epsl.2006.06.033, 2006.

Kylling, A., M. Kahnert, H. Lindqvist, and T. Nousiainen, Volcanic ash infrared signature: porous non-spherical ash particle shapes compared to homogeneous spherical ash particles, *Atmospheric Measurement Techniques*, *7*(4), 919–929, doi: https://doi.org/10.5194/amt-7-919-2014, 2014.

Lacroix, A., *La Montagne Pelée et ses éruptions*, vol. 1, Masson, 1904.

Landals, A., The Maple Leaf Site: implications of the analysis of small-scale bison kills, in *Hunters of the recent past*, pp. 122–151, 1990.

Larsen, D. J., M. S. Finkenbinder, M. B. Abbott, and A. R. Ofstun, Deglaciation and postglacial environmental changes in the Teton Mountain Range recorded at Jenny Lake, Grand Teton National Park, WY, *Quaternary Science Reviews*, *138*, 62 – 75, doi: https://doi.org/10.1016/j.quascirev.2016.02.024, 2016.

Larsen, G., and J. Eiríksson, Late Quaternary terrestrial tephrochronology of Iceland—frequency of explosive eruptions, type and volume of tephra deposits, *Journal of Quaternary Science*, *23*(2), 109–120, doi: 10.1002/jqs.1129, 2008.

Larsen, G., A. J. Newton, A. J. Dugmore, and E. G. Vilmundardóttir, Geochemistry, dispersal, volumes and chronology of Holocene silicic tephra layers from the Katla volcanic system, Iceland, *Journal of Quaternary Science*, *16*(2), 119–132, doi: 10.1002/jqs.587, 2001.

Leadbetter, S., M. Hort, S. Löwis, K. Weber, and C. Witham, Modeling the resuspension of ash deposited during the eruption of Eyjafjallajökull in spring 2010, *Journal of Geophysical Research: Atmospheres*, *117*(D20), 2012.

Lechner, P., A. Tupper, M. Guffanti, S. Loughlin, and T. Casadevall, Volcanic Ash and Aviation—The Challenges of Real-Time, Global Communication of a Natural Hazard, in *Observing the Volcano World: Volcano Crisis Communication*, edited by C. J. Fearnley, D. K. Bird, K. Haynes, W. J. McGuire, and G. Jolly, Advances in Volcanology, pp. 51–64, Springer International Publishing, Cham, 2018.

Leibrandt, S., and J.-L. Le Pennec, Towards fast and routine analyses of volcanic ash morphometry for eruption surveillance applications, *Journal of Volcanology and Geothermal Research*, *297*, 11–27, doi: 10.1016/j.jvolgeores.2015.03.014, 2015.

Leopold, E. B., R. Nickmann, J. I. Hedges, and J. R. Ertel, Pollen and Lignin Records of Late Quaternary Vegetation, Lake Washington, *Science*, *218*(4579), 1305–1307, doi: 10.1126/science.218.4579.1305, 1982.

Lichti-Federovich, S., The pollen stratigraphy of a dated section of Late Pleistocene lake sediment from central Alberta, *Canadian Journal of Earth Sciences*, *7*(3), 938–945, doi: 10.1139/e70-089, 1970.

Lidstrom, J. W., A new model for the formation of Crater Lake Caldera, Oregon, PhD Thesis, Oregon State University, 1971.

Liu, E. J., K. V. Cashman, F. M. Beckett, C. S. Witham, S. J. Leadbetter, M. C. Hort, and S. Guðmundsson, Ash mists and brown snow: Remobilization of volcanic ash from recent Icelandic eruptions, *Journal of Geophysical Research: Atmospheres*, *119*(15), 9463–9480, doi: https://doi.org/10.1002/2014JD021598, 2014.

Liu, E. J., K. V. Cashman, and A. C. Rust, Optimising shape analysis to quantify volcanic ash morphology, *GeoResJ*, *8*, 14–30, 2015.

Liu, E. J., K. V. Cashman, A. C. Rust, and A. Höskuldsson, Contrasting mechanisms of magma fragmentation during coeval magmatic and hydromagmatic activity: the Hverfjall Fires fissure eruption, Iceland, *Bulletin of Volcanology*, *79*(10), 68, doi: 10.1007/s00445-017-1150-8, 2017.

Long, C. J., C. Whitlock, P. J. Bartlein, and S. H. Millspaugh, A 9000-year fire history from the Oregon Coast Range, based on a high-resolution charcoal study, *Canadian Journal of Forest Research*, *28*(5), 774–787, doi: 10.1139/x98-051, 1998.

Long, C. J., M. J. Power, T. A. Minckley, and A. L. Hass, The impact of Mt Mazama tephra deposition on forest vegetation in the Central Cascades, Oregon, USA, *The Holocene*, *24*(4), 503–511, doi: 10.1177/0959683613520258, 2014.

Louderback, L. A., and D. E. Rhode, 15,000 Years of vegetation change in the Bonneville basin: the Blue Lake pollen record, *Quaternary Science Reviews*, *28*(3), 308–326, doi: 10.1016/j.quascirev.2008.09.027, 2009.

Lowdon, J., and W. Blake, Geological Survey of Canada radiocarbon dates IX, *Radiocarbon*, *12*(1), 46–86, 1970.

Lowdon, J., and W. Blake, Geological Survey of Canada Radiocarbon dates XIII, *Geological Survey of Canada*, *73-7*, 1973.

Lowdon, J., R. Wilmeth, and W. Blake, Geological Survey of Canada radiocarbon dates VIII, *Radiocarbon*, *11*(1), 22–42, 1969.

Lowdon, J., I. Robertson, and W. Blake, Geological Survey of Canada radiocarbon dates XI, *Radiocarbon*, *13*(2), 255–324, 1971.

Lowe, D. J., Tephrochronology and its application: A review, *Quaternary Geochronology*, *6*(2), 107 – 153, doi: https://doi.org/10.1016/j.quageo.2010.08.003, 2011.

Lowe, D. J., A. G. Hogg, J. D. Green, and J. A. T. Boubee, Stratigraphy and chronology of late Quaternary tephras in Lake Maratoto, Hamilton, New Zealand, *New Zealand Journal of Geology and Geophysics*, *23*(4), 481–485, doi: 10.1080/00288306.1980.10424118, 1980.

Luckman, B. H., M. S. Kearney, R. H. King, and A. B. Beaudoin, Revised 14C age for St. Helens Y tephra at Tonquin Pass, British Columbia, *Canadian Journal of Earth Sciences*, *23*(5), 734–736, doi: 10.1139/e86-072, 1986.

MacGregor, K. R., C. A. Riihimaki, A. Myrbo, M. D. Shapley, and K. Jankowski, Geomorphic and climatic change over the past 12,900yr at Swiftcurrent Lake, Glacier National Park, Montana, USA, *Quaternary Research*, *75*(1), 80 – 90, doi: https://doi.org/10.1016/j.yqres.2010.08.005, 2011.

Machida, H., Volcanoes and tephras in the Japan area, *Global Environmental Research - English Edition*, *6*(2), 19–28, 2002.

Mack, R. N., V. M. Bryant, and R. Fryxell, Pollen Sequence from the Columbia Basin, Washington: Reappraisal of Postglacial Vegetation, *The American Midland Naturalist*, *95*(2), 390–397, 1976.

Mack, R. N., N. W. Rutter, V. M. Bryant, and S. Valastro, Reexamination of postglacial vegetation history in northern Idaho: Hager Pond, Bonner Co., *Quaternary Research*, *10*(2), 241 – 255, doi: https://doi.org/10.1016/0033-5894(78)90104-7, 1978a.

Mack, R. N., N. W. Rutter, S. Valastro, and J. Vaughn M. Bryant, Late Quaternary Vegetation History at Waits Lake, Colville River Valley, Washington, *Botanical Gazette*, *139*(4), 499–506, doi: 10.1086/337025, 1978b.

Mack, R. N., R. Okazaki, and S. Valastro, Bracketing dates for two ash falls from Mount Mazama, *Nature*, *279*(5710), 228–229, doi: doi:10.1038/279228a0, 1979.

Mack, R. N., N. W. Rutter, and S. Valastro, Holocene vegetational history of the Kootenai River Valley, Montana, *Quaternary Research*, *20*(2), 177 – 193, doi: https://doi.org/10.1016/0033-5894(83)90076-5, 1983.

Macías-García, A., E. M. Cuerda-Correa, and M. A. Díaz-Díez, Application of the Rosin–Rammler and Gates–Gaudin–Schuhmann models to the particle size distribution analysis of agglomerated cork, *Materials Characterization*, *52*(2), 159–164, doi: 10.1016/j.matchar.2004.04.007, 2004.

Magill, C., K. Mannen, L. Connor, C. Bonadonna, and C. Connor, Simulating a multi-phase tephra fall event: inversion modelling for the 1707 Hoei eruption of Mount Fuji, Japan, *Bulletin of Volcanology*, *77*(9), 81, doi: 10.1007/s00445-015-0967-2, 2015.

Mahony, S. H., N. H. Barnard, R. S. J. Sparks, and J. C. Rougier, VOLCORE, a global database of visible tephra layers sampled by ocean drilling, *Scientific Data*, *7*(1), 330, doi: 10.1038/s41597-020-00673-1, 2020.

Major, J. J., T. C. Pierson, R. L. Dinehart, and J. E. Costa, Sediment yield following severe volcanic disturbance—A two-decade perspective from Mount St. Helens, *Geology*, *28*(9), 819–822, doi: 10.1130/0091-7613(2000)28<819:SYFSVD>2.0.CO;2, 2000.

Mana, S., E. DiMaggio, and K. Fontijn, East African Rift Tephra Database [EARThD]: a compilation documenting and analyzing explosive volcanism in East Africa, *2018*, V23I–0162, 2018.

Manga, M., A. Patel, and J. Dufek, Rounding of pumice clasts during transport: field measurements and laboratory studies, *Bulletin of Volcanology*, *73*(3), 321–333, doi: 10.1007/s00445-010-0411-6, 2011.

Manville, V., K. A. Hodgson, B. F. Houghton, J. R. H. Keys, and J. D. L. White, Tephra, snow and water: complex sedimentary responses at an active snow-capped stratovolcano, Ruapehu, New Zealand, *Bulletin of Volcanology*, *62*(4), 278–293, doi: 10.1007/s004450000096, 2000.

Manzella, I., C. Bonadonna, J. C. Phillips, and H. Monnard, The role of gravitational instabilities in deposition of volcanic ash, *Geology*, *43*(3), 211–214, doi: 10.1130/G36252.1, 2015.

Marti, A., A. Folch, A. Costa, and S. Engwell, A novel approach to reconstruct the plinian and co-ignimbrite phases of large eruptions-Campanian Ignimbrite, in *BSC Doctoral Symposium (2nd: 2015: Barcelona)*, pp. 81–82, Barcelona Supercomputing Center, 2015.

Marti, A., A. Folch, A. Costa, and S. Engwell, Reconstructing the plinian and co-ignimbrite sources of large volcanic eruptions: A novel approach for the Campanian Ignimbrite, *Scientific Reports*, *6*, 21,220, 2016.

Mason, B. G., D. M. Pyle, and C. Oppenheimer, The size and frequency of the largest explosive eruptions on Earth, *Bulletin of Volcanology*, *66*(8), 735–748, doi: 10.1007/s00445-004-0355-9, 2004.

Mastin, L. G., and A. R. Van Eaton, Comparing Simulations of Umbrella-Cloud Growth and Ash Transport with Observations from Pinatubo, Kelud, and Calbuco Volcanoes, *Atmosphere*, *11*(10), 1038, doi: 10.3390/atmos11101038, 2020.

Mastin, L. G., M. J. Randall, H. F. Schwaiger, and R. P. Denlinger, User's guide and reference to Ash3d—A three-dimensional model for Eulerian atmospheric tephra transport and deposition, *USGS Numbered Series 2013-1122*, U.S. Geological Survey, Reston, VA, 2013.

Mastin, L. G., A. R. V. Eaton, and J. B. Lowenstern, Modeling ash fall distribution from a Yellowstone supereruption, *Geochemistry, Geophysics, Geosystems*, *15*(8), 3459–3475, doi: https://doi.org/10.1002/2014GC005469, 2014.

Mastin, L. G., A. R. Van Eaton, and A. J. Durant, Adjusting particle-size distributions to account for aggregation in tephra-deposit model forecasts, *Atmospheric Chemistry and Physics*, *16*(14), 9399–9420, doi: https://doi.org/10.5194/acp-16-9399-2016, 2016.

Mastin, L. G., et al., A multidisciplinary effort to assign realistic source parameters to models of volcanic ash-cloud transport and dispersion during eruptions, *Journal of Volcanology and Geothermal Research*, *186*(1-2), 10–21, 2009.

Mathewes, R. W., A palynological study of postglacial vegetation changes in the University Research Forest, southwestern British Columbia, *Canadian Journal of Botany*, *51*(11), 2085–2103, doi: 10.1139/b73-271, 1973.

Mathewes, R. W., C. E. Borden, and G. E. Rouse, New Radiocarbon Dates from the Yale Area of the Lower Fraser River Canyon, British Columbia, *Canadian Journal of Earth Sciences*, *9*(8), 1055–1057, doi: 10.1139/e72-089, 1972.

Matthews, N. E., V. C. Smith, A. Costa, A. J. Durant, D. M. Pyle, and N. J. G. Pearce, Ultra-distal tephra deposits from super-eruptions: Examples from Toba, Indonesia and Taupo Volcanic Zone, New Zealand, *Quaternary International*, *258*, 54–79, doi: 10.1016/j.quaint.2011.07.010, 2012.

Mattsson, H. B., and \. A. Höskuldsson, Contemporaneous phreatomagmatic and effusive activity along the Hverfjall eruptive fissure, north Iceland: Eruption chronology and resulting deposits, *Journal of Volcanology and Geothermal Research*, *201*(1), 241–252, doi: 10.1016/j.jvolgeores.2010.05.015, 2011.

Matz, S. E., The effects of the Mazama tephra-falls: a geoarchaeological approach, Master's thesis, Oregon State University, 1987.

McCallum, K. J., and W. Dyck, University of Saskatchewan Radiocarbon Dates II, *Radiocarbon*, *2*, 73–81, doi: 10.1017/S1061592X00020615, 1960.

McFarland, J. R., An analysis of two post-Mazama prehistoric flaked stone scatters in the upper Deschutes River basin of central Oregon, Master's thesis, 1989.

McNamara, K., K. V. Cashman, A. C. Rust, K. Fontijn, F. Chalié, E. L. Tomlinson, and G. Yirgu, Using Lake Sediment Cores to Improve Records of Volcanism at Aluto Volcano in the Main Ethiopian Rift, *Geochemistry, Geophysics, Geosystems*, *19*(9), 3164–3188, doi: 10.1029/2018GC007686, 2018.

McNamara, K., A. C. Rust, K. V. Cashman, A. Castruccio, and A. M. Abarzúa, Comparison of lake and land tephra records from the 2015 eruption of Calbuco volcano, Chile, *Bulletin of Volcanology*, *81*(2), 10, doi: 10.1007/s00445-019-1270-4, 2019.

Mehringer, P. J., W. P. Nash, and R. H. Fuller, A Holocene volcanic ash from northwestern Utah, *Proc. Utah Acad. Sci., Arts Lett*, *48*, 46–51, 1971.

Mehringer, P. J., S. F. Arno, and K. L. Petersen, Postglacial history of lost trail pass bog, Bitterroot Mountains, Montana, *Arctic and Alpine Research*, *9*(4), 345–368, 1977a.

Mehringer, P. J., E. Blinman, and K. L. Petersen, Pollen influx and volcanic ash, *Science*, *198*(4314), 257–261, 1977b.

Mele, D., P. Dellino, R. Sulpizio, and G. Braia, A systematic investigation on the aerodynamics of ash particles, *Journal of Volcanology and Geothermal Research*, *203*(1), 1–11, doi: 10.1016/j.jvolgeores.2011.04.004, 2011.

Mele, D., A. Costa, P. Dellino, R. Sulpizio, F. Dioguardi, R. Isaia, and G. Macedonio, Total grain size distribution of components of fallout deposits and implications for magma fragmentation mechanisms: examples from Campi Flegrei caldera (Italy), *Bulletin of Volcanology*, *82*(4), 31, doi: 10.1007/s00445-020-1368-8, 2020.

Menounos, B. P., Climate fine-sediment transport linkages Coast Mountains British Columbia, PhD Thesis, University of British Columbia, 2002.

Meredith, P., Using the May 18, 1980 ash fallout deposit of Mount Saint Helens to compare methods of particle size analysis, Master's thesis, University of Bristol, 2019.

Miffre, A., G. David, B. Thomas, P. Rairoux, A. M. Fjaeraa, N. I. Kristiansen, and A. Stohl, Volcanic aerosol optical properties and phase partitioning behavior after long-range advection characterized by UV-Lidar measurements, *Atmospheric Environment*, *48*, 76–84, doi: 10.1016/j.atmosenv.2011.03.057, 2012.

Miller, D. M., C. G. Oviatt, and J. P. Mcgeehin, Stratigraphy and chronology of P rovo shoreline deposits and lake-level implications, L ate P leistocene L ake B onneville, eastern G reat B asin, USA, *Boreas*, *42*(2), 342–361, 2013.

Miura, T., T. Koyaguchi, and Y. Tanaka, Measurements of electric charge distribution in volcanic plumes at Sakurajima Volcano, Japan, *Bulletin of Volcanology*, *64*(2), 75–93, doi: 10.1007/s00445-001-0182-1, 2002.

Miwa, T., Y. Iriyama, M. Nagai, and F. Nanayama, Sedimentation process of ashfall during a Vulcanian eruption as revealed by high-temporal-resolution grain size analysis and high-speed camera imaging, *Progress in Earth and Planetary Science*, *7*(1), 3, doi: 10.1186/s40645-019-0316-8, 2020.

Moore, B. N., Deposits of Possible Nuée Ardente Origin in the Crater Lake Region, Oregon, *The Journal of Geology*, *42*(4), 358–375, doi: 10.1086/624174, 1934.

Moore, C., The distal terrestrial record of explosive rhyolitic volcanism: an example from Auckland, New Zealand, *Sedimentary Geology*, *74*(1), 25–38, doi: 10.1016/0037-0738(91)90033-A, 1991.

Mori, T., T. Hashimoto, A. Terada, M. Yoshimoto, R. Kazahaya, H. Shinohara, and R. Tanaka, Volcanic plume measurements using a UAV for the 2014 Mt. Ontake eruption, *Earth, Planets and Space*, *68*(1), 49, doi: 10.1186/s40623-016-0418-0, 2016.

Moseley, R. K., R. J. Bursik, and P. J. Mehringer, *Paleoecology of Peatlands at Huff and Hager Lakes, Idaho Panhandle National Forest: FY92 Year-end Summary*, US Forest Service, 1992.

Mothersill, J. S., Dating of paleomagnetic logs by tephra layers, Mara Lake, Canada, *Studia Geophysica et Geodaetica*, *35*(4), 302–313, doi: 10.1007/BF01613976, 1991.

Mothes, P. A., and M. L. Hall, The plinian fallout associated with Quilotoa's 800 yr BP eruption, Ecuadorian Andes, *Journal of Volcanology and Geothermal Research*, *176*(1), 56–69, doi: 10.1016/j.jvolgeores.2008.05.018, 2008.

MRB, M., CAMSIZER X2 - particle size & shape analyzer - Microtrac, https://www.microtrac.com/products/particle-size-shape-analysis/dynamic-image-analysis/camsizer-x2/function-features, 2020.

Mueller, S. B., S. J. Lane, and U. Kueppers, Lab-scale ash production by abrasion and collision experiments of porous volcanic samples, *Journal of Volcanology and Geothermal Research*, *302*, 163–172, doi: 10.1016/j.jvolgeores.2015.07.013, 2015.

Mueller, S. B., P. M. Ayris, F. B. Wadsworth, U. Kueppers, A. S. Casas, P. Delmelle, J. Taddeucci, M. Jacob, and D. B. Dingwell, Ash aggregation enhanced by deposition and redistribution of salt on the surface of volcanic ash in eruption plumes, *Scientific Reports*, *7*(1), 45,762, doi: 10.1038/srep45762, 2017.

Muir, D. D., J. D. Blundy, and A. C. Rust, Multiphase petrography of volcanic rocks using element maps: a method applied to Mount St. Helens, 1980–2005, *Bulletin of Volcanology*, *74*(5), 1101–1120, doi: 10.1007/s00445-012-0586-0, 2012.

Mullineaux, D., Pumice and other pyroclastic deposits erupted in Mount Rainier National Park, Washington., *US Geol. Surv. Bull.*, *1326*, doi: https://doi.org/10.3133/b1326, 1974.

Muñoz, O., H. Volten, J. W. Hovenier, B. Veihelmann, W. J. v. d. Zande, L. B. F. M. Waters, and W. I. Rose, Scattering matrices of volcanic ash particles of Mount St. Helens, Redoubt, and Mount Spurr Volcanoes, *Journal of Geophysical Research: Atmospheres*, *109*(D16), doi: 10.1029/2004JD004684, 2004.

Nel, P., and M. Righarts, Natural disasters and the risk of violent civil conflict, *International Studies Quarterly*, *52*(1), 159–185, 2008.

Nelder, J. A., and R. Mead, A Simplex Method for Function Minimization, *The Computer Journal*, *7*(4), 308–313, doi: 10.1093/comjnl/7.4.308, 1965.

Newhall, C., S. Self, and A. Robock, Anticipating future Volcanic Explosivity Index (VEI) 7 eruptions and their chilling impacts, *Geosphere*, *14*(2), 572–603, doi: https://doi.org/10.1130/GES01513.1, 2018.

Newhall, C. G., and S. Self, The volcanic explosivity index (VEI) an estimate of explosive magnitude for historical volcanism, *Journal of Geophysical Research*, *87*(C2), 1231, doi: 10.1029/JC087iC02p01231, 1982.

Newton, A. J., A. J. Dugmore, and B. M. Gittings, Tephrabase: tephrochronology and the development of a centralised European database, *Journal of Quaternary Science*, *22*(7), 737–743, 2007.

Newton, B., Bow corridor project: summary of the 1988-1989 research, *Occasional Paper 33*, Archaeological Survey of Alberta, 1991.

Nickman, R. J., and E. B. Leopold, A postglacial pollen record from Goose Lake, Okanogan County, Washington: evidence for early Holocene cooling, *Tech. rep.*, Office for Public Archaeology, Institute for Environmental Studies, University of Washington, Seattle, 1985.

Oetelaar, G. A., and A. B. Beaudoin, Evidence of cultural responses to the impact of the Mazama ash fall from deeply stratified archaeological sites in southern Alberta, Canada, *Quaternary International*, *394*, 17 – 36, doi: https://doi.org/10.1016/j.quaint.2014.08.015, 2016.

Osborn, G., Compositional variability of Mazama tephra magnetites, *Canadian Journal of Earth Sciences*, *22*(4), 642–643, 1985.

Osman, S., F. Beckett, A. Rust, and E. Snee, Sensitivity of Volcanic Ash Dispersion Modelling to Input Grain Size Distribution Based on Hydromagmatic and Magmatic Deposits, *Atmosphere*, *11*(6), 567, doi: 10.3390/atmos11060567, 2020.

Osores, M. S., A. Folch, E. Collini, G. Villarosa, A. Durant, G. Pujol, and J. G. Viramonte, Validation of the FALL3D model for the 2008 Chaitén eruption using field and satellite data, *Andean Geology*, *40*(2), 262–276, doi: 10.5027/andgeoV40n2-a05, 2013.

OTT, OTT Parsivel2 - Laser Weather Sensor, https://www.ott.com/download/operating-instructions-present-weather-sensor-ott-parsivel2-without-screen-heating-1/, 2020.

Oviatt, C., G., J. S. Pigati, D. B. Madsen, D. E. Rhode, and J. Bright, Juke Box trench: A valuable archive of late Pleistocene and Holocene stratigraphy in the Bonneville basin, Utah, *Miscellaneous Publication 18-1*, Utah Geological Survey, 2018.

Palais, J. M., M. S. Germani, and G. A. Zielinski, Inter-hemispheric Transport of Volcanic Ash from a 1259 A.D. Volcanic Eruption to the Greenland and Antarctic Ice Sheets, *Geophysical Research Letters*, *19*(8), 801–804, doi: 10.1029/92GL00240, 1992.

Panalytical, M., Mastersizer 3000 | World's Leading Particle Size Analyzer | Malvern Panalytical, https://www.malvernpanalytical.com/en/products/product-range/mastersizer-range/mastersizer-3000, 2020.

Panebianco, J. E., M. J. Mendez, D. E. Buschiazzo, D. Bran, and J. J. Gaitán, Dynamics of volcanic ash remobilisation by wind through the Patagonian steppe after the eruption of Cordón Caulle, 2011, *Scientific Reports*, *7*, 45,529, doi: https://doi.org/10.1038/srep45529, 2017.

Papale, P., Strain-induced magma fragmentation in explosive eruptions, *Nature*, *397*(6718), 425–428, doi: 10.1038/17109, 1999.

Paredes-Mariño, J., B. Scheu, C. Montanaro, A. Arciniega-Ceballos, D. B. Dingwell, and D. Perugini, Volcanic ash generation: Effects of componentry, particle size and conduit geometry on size-reduction processes, *Earth and Planetary Science Letters*, *514*, 13–27, doi: 10.1016/j.epsl.2019.02.028, 2019.

Parfitt, E. A., A study of clast size distribution, ash deposition and fragmentation in a Hawaiian-style volcanic eruption, *Journal of Volcanology and Geothermal Research*, *84*(3), 197–208, doi: 10.1016/S0377-0273(98)00042-0, 1998.

Pavolonis, M. J., A. K. Heidinger, and J. Sieglaff, Automated retrievals of volcanic ash and dust cloud properties from upwelling infrared measurements, *Journal of Geophysical Research: Atmospheres*, *118*(3), 1436–1458, doi: 10.1002/jgrd.50173, 2013.

Perrotta, A., and C. Scarpati, Volume partition between the plinian and co-ignimbrite air fall deposits of the Campanian Ignimbrite eruption, *Mineralogy and Petrology*, *79*(1), 67–78, doi: 10.1007/s00710-003-0002-8, 2003.

Peterson, C., R. Minor, E. B. Gates, S. Vanderburgh, and K. Carlisle, Correlation of tephra marker beds in latest Pleistocene and Holocene fill of the submerged lower Columbia River valley, Washington and Oregon, USA, *Journal of Coastal Research*, *28*(6), 1362–1380, 2012.

Pettijohn, F. J., *Sedimentary rocks*, vol. 1, Harper & Row New York, 1949.

Petäjä, T., et al., In-situ observations of Eyjafjallajökull ash particles by hot-air balloon, *Atmospheric Environment*, *48*, 104–112, doi: 10.1016/j.atmosenv.2011.08.046, 2012.

Pieri, D., C. Ma, J. J. Simpson, G. Hufford, T. Grindle, and C. Grove, Analyses of in-situ airborne volcanic ash from the February 2000 eruption of Hekla Volcano, Iceland, *Geophysical Research Letters*, *29*(16), 19–1–19–4, doi: 10.1029/2001GL013688, 2002.

Pierson, T. C., and J. J. Major, Hydrogeomorphic Effects of Explosive Volcanic Eruptions on Drainage Basins, *Annual Review of Earth and Planetary Sciences*, *42*(1), 469–507, doi: 10.1146/annurev-earth-060313-054913, 2014.

Pioli, L., C. Bonadonna, and M. Pistolesi, Reliability of Total Grain-Size Distribution of Tephra Deposits, *Scientific Reports*, *9*(1), 10,006, doi: 10.1038/s41598-019-46125-8, 2019.

Platt Bradbury, J., S. M. Colman, and R. L. Reynolds, The History of Recent Limnological Changes and Human Impact on Upper Klamath Lake, Oregon, *Journal of Paleolimnology*, *31*(2), 151–165, doi: 10.1023/B:JOPL.0000019233.12287.18, 2004.

Pouget, S., M. Bursik, C. G. Johnson, A. J. Hogg, J. C. Phillips, and R. S. J. Sparks, Interpretation of umbrella cloud growth and morphology: implications for flow regimes of short-lived and long-lived eruptions, *Bulletin of Volcanology*, *78*(1), 1, doi: 10.1007/s00445-015-0993-0, 2016.

Power, M. J., C. Whitlock, and P. J. Bartlein, Postglacial fire, vegetation, and climate history across an elevational gradient in the Northern Rocky Mountains, USA and Canada, *Quaternary Science Reviews*, *30*(19), 2520 – 2533, doi: https://doi.org/10.1016/j.quascirev.2011.04.012, 2011.

Powers, H. A., and R. E. Wilcox, Volcanic Ash from Mount Mazama (Crater Lake) and from Glacier Peak, *Science*, *144*(3624), 1334–1336, doi: 10.1126/science.144.3624.1334, 1964.

Prata, A., and A. Tupper, *Aviation hazards from volcanoes: the state of the science*, Springer, 2009.

Prata, A. J., Infrared radiative transfer calculations for volcanic ash clouds, *Geophysical Research Letters*, *16*(11), 1293–1296, doi: 10.1029/GL016i011p01293, 1989.

Prata, A. J., and I. F. Grant, Retrieval of microphysical and morphological properties of volcanic ash plumes from satellite data: Application to Mt Ruapehu, New Zealand, *Quarterly Journal of the Royal Meteorological Society*, *127*(576), 2153–2179, doi: 10.1002/qj.49712757615, 2001.

Prata, A. J., and A. T. Prata, Eyjafjallajökull volcanic ash concentrations determined using Spin Enhanced Visible and Infrared Imager measurements, *Journal of Geophysical Research: Atmospheres*, *117*(D20), doi: 10.1029/2011JD016800, 2012.

Press, T. N. A., *Volcanic Eruptions and Their Repose, Unrest, Precursors, and Timing*, The National Academies of Sciences, Engineering and Medicine, Washington, DC, 2017.

Preston, R. S., E. Person, and E. Deevey, Yale natural radiocarbon measurements II, *Science*, *122*(3177), 954–960, 1955.

Pye, K., The nature, origin and accumulation of loess, *Quaternary Science Reviews*, *14*(7), 653–667, doi: 10.1016/0277-3791(95)00047-X, 1995.

Pyle, D. M., The thickness, volume and grainsize of tephra fall deposits, *Bulletin of Volcanology*, *51*(1), 1–15, 1989.

Pyle, D. M., Sizes of volcanic eruptions, in *The Encyclopedia of Volcanoes*, vol. 1, edited by H. Sigurdsson, B. Houghton, S. McNutt, H. Rymer, and J. Stix, pp. 257–264, Academic Press, 2000.

Pyle, D. M., Chapter 1 - Field Observations of Tephra Fallout Deposits, in *Volcanic Ash*, edited by S. Mackie, K. Cashman, H. Ricketts, A. Rust, and M. Watson, pp. 25–37, Elsevier, 2016.

Pyle, D. M., G. D. Ricketts, V. Margari, T. H. van Andel, A. A. Sinitsyn, N. D. Praslov, and S. Lisitsyn, Wide dispersal and deposition of distal tephra during the Pleistocene 'Campanian Ignimbrite/Y5' eruption, Italy, *Quaternary Science Reviews*, *25*(21), 2713–2728, doi: 10.1016/j.quascirev.2006.06.008, 2006.

Pyne-O'Donnell, S. D. F., et al., High-precision ultra-distal Holocene tephrochronology in North America, *Quaternary Science Reviews*, *52*, 6 – 11, doi: https://doi.org/10.1016/j.quascirev.2012.07.024, 2012.

QGIS, D. T., QGIS geographic information system, *Open Source Geospatial Foundation Project*, 2019.

Rai, D., Stratigraphy and genesis of soils from volcanic ash in the Blue Mountains of eastern Oregon, PhD Thesis, Oregon State University, 1971.

Rampino, M. R., and S. Self, Climate-Volcanism Feedback and the Toba Eruption of $\sim$74,000 Years Ago, *Quaternary Research*, *40*(3), 269–280, doi: 10.1006/qres.1993.1081, 1993.

Randle, K., G. G. Goles, and L. R. Kittleman, Geochemical and petrological characterization of ash samples from cascade range volcanoes, *Quaternary Research*, *1*(2), 261 – 282, doi: https://doi.org/10.1016/0033-5894(71)90046-9, 1971.

Reasoner, M. A., and M. Hickman, Late Quaternary environmental change in the Lake O'Hara region, Yoho National Park, British Columbia, *Palaeogeography, Palaeoclimatology, Palaeoecology*, *72*, 291 – 316, doi: https://doi.org/10.1016/0031-0182(89)90149-1, 1989.

Reeves, B. O., and J. F. Dormaar, A partial Holocene pedological and archaeological record from the southern Alberta Rocky Mountains, *Arctic and Alpine Research*, *4*, 325–336, doi: https://doi.org/10.1080/00040851.1972.12003652, 1972.

Reidel, S., P. Hooper, G. Webster, and V. Camp, Geologic map of southeasten Asotin County, Washington, *Geologic Map GM-40*, Washington Division of Geology and Earth Resources, 1992.

Rey, K., Insights into the Early Transgressive History of Lake Bonneville from Stratigraphic Investigation of Pilot Valley Playa, UT/NV, USA, Master's thesis, Brigham Young University - Provo, 2012.

Riedel, J. L., P. T. Pringle, and R. L. Schuster, Deposition of Mount Mazama tephra in a landslide-dammed lake on the upper Skagit River, Washington, USA, *Special Publication-International Association of Sedimentologists*, *30*, 285–298, 2001.

Rigg, G. B., and H. R. Gould, Age of Glacier Peak eruption and chronology of post-glacial peat deposits in Washington and surrounding areas, *American Journal of Science*, *255*(5), 341–363, 1957.

Riley, C. M., W. I. Rose, and G. J. S. Bluth, Quantitative shape measurements of distal volcanic ash, *Journal of Geophysical Research: Solid Earth*, *108*(B10), doi: 10.1029/2001JB000818, 2003.

Roller, P. S., *Separation and Size Distribution of Microscopic Particles: An Air Analyzer for Fine Powders*, U.S. Government Printing Office, 1931.

Román-Sierra, J., J. J. Muñoz-Perez, and M. Navarro-Pons, Influence of sieving time on the efficiency and accuracy of grain-size analysis of beach and dune sands, *Sedimentology*, *60*(6), 1484–1497, doi: 10.1111/sed.12040, 2013.

Rose, W. I., and A. J. Durant, Fine ash content of explosive eruptions, *Journal of Volcanology and Geothermal Research*, *186*(1), 32–39, doi: 10.1016/j.jvolgeores.2009.01.010, 2009.

Rose, W. I., G. J. S. Bluth, D. J. Schneider, G. G. J. Ernst, C. M. Riley, L. J. Henderson, and R. G. McGimsey, Observations of Volcanic Clouds in Their First Few Days of Atmospheric Residence: The 1992 Eruptions of Crater Peak, Mount Spurr Volcano, Alaska, *The Journal of Geology*, *109*(6), 677–694, doi: 10.1086/323189, 2001.

Rosi, M., L. Vezzoli, A. Castelmenzano, and G. Grieco, Plinian pumice fall deposit of the Campanian Ignimbrite eruption (Phlegraean Fields, Italy), *Journal of Volcanology and Geothermal Research*, *91*(2), 179–198, doi: 10.1016/S0377-0273(99)00035-9, 1999.

Rosi, M., M. Paladio-Melosantos, A. Di Muro, R. Leoni, and T. Bacolcol, Fall vs flow activity during the 1991 climactic eruption of Pinatubo Volcano (Philippines), *Bulletin of Volcanology*, *62*(8), 549–566, doi: 10.1007/s004450000118, 2001.

Rosin, P., and E. Rammler, The laws governing the finesness of powdered coal, *Journal of the Institute of Fuel*, *7*, 29–36, 1933.

Rossi, E., C. Bonadonna, and W. Degruyter, A new strategy for the estimation of plume height from clast dispersal in various atmospheric and eruptive conditions, *Earth and Planetary Science Letters*, *505*, 1–12, doi: 10.1016/j.epsl.2018.10.007, 2019.

Rossi, E., G. Bagheri, F. Beckett, and C. Bonadonna, The fate of volcanic ash: premature or delayed sedimentation?, *Nature Communications*, *12*(1), 1303, doi: 10.1038/s41467-021-21568-8, 2021.

Rougier, J., R. S. J. Sparks, K. V. Cashman, and S. K. Brown, The global magnitude–frequency relationship for large explosive volcanic eruptions, *Earth and Planetary Science Letters*, *482*, 621–629, doi: 10.1016/j.epsl.2017.11.015, 2018.

Rubin, M., and C. Alexander, U. S. Geological Survey Radiocarbon Dates V, *Radiocarbon*, *2*, 129–185, doi: 10.1017/S1061592X00020652, 1960.

Sahagian, D. L., and A. A. Proussevitch, 3D particle size distributions from 2D observations: stereology for natural applications, *Journal of Volcanology and Geothermal Research*, *84*(3), 173–196, doi: 10.1016/S0377-0273(98)00043-2, 1998.

Sanford, R. B., and D. J. P. Swift, Comparison of Sieving and Settling Techniques for Size Analysis, Using a Benthos Rapid Sediment Analyzer, *Sedimentology*, *17*(3-4), 257–264, doi: 10.1111/j.1365-3091.1971.tb01778.x, 1971.

Sanger, D., Prehistory of the Pacific Northwest Plateau as Seen from the Interior of British Columbia, *American Antiquity*, *32*(2), 186–197, doi: 10.2307/277903, 1967.

Sarna-Wojcicki, A. M., S. Shipley, R. B. Waitt Jr, D. Dzurisin, and S. H. Wood, Areal distribution, thickness, mass, volume, and grain size of air-fall ash from the six major eruptions of 1980, *US Geol Surv Prof Paper*, *1250*, 577–600, 1981.

Sarna-Wojcicki, A. M., D. E. Champion, and J. O. Davis, Holocene volcanism in the conterminous United States and the role of silicic volcanic ash layers in correlation of latest-Pleistocene and Holocene deposits, *Late Quaternary environments of the United States*, *2*, 52–77, 1983.

Sarocchi, D., R. Sulpizio, J. L. Macías, and R. Saucedo, The 17 July 1999 block-and-ash flow (BAF) at Colima Volcano: New insights on volcanic granular flows from textural analysis, *Journal of Volcanology and Geothermal Research*, *204*(1), 40–56, doi: 10.1016/j.jvolgeores.2011.04.013, 2011.

Saunders, K., J. Blundy, R. Dohmen, and K. Cashman, Linking Petrology and Seismology at an Active Volcano, *Science*, *336*(6084), 1023–1027, doi: 10.1126/science.1220066, 2012.

Saxby, J., F. Beckett, K. Cashman, A. Rust, and E. Tennant, The impact of particle shape on fall velocity: Implications for volcanic ash dispersion modelling, *Journal of Volcanology and Geothermal Research*, *362*, 32–48, doi: 10.1016/j.jvolgeores.2018.08.006, 2018.

Saxby, J., A. Rust, K. Cashman, and F. Beckett, The importance of grain size and shape in controlling the dispersion of the Vedde cryptotephra, *Journal of Quaternary Science*, *Special Issue: Intav Tephra*(n/a), doi: 10.1002/jqs.3152, 2019.

Saxby, J., A. Rust, F. Beckett, K. Cashman, and H. Rodger, Estimating the 3D shape of volcanic ash to better understand sedimentation processes and improve atmospheric dispersion modelling, *Earth and Planetary Science Letters*, *534*, 116,075, doi: 10.1016/j.epsl.2020.116075, 2020.

Scarpati, C., and A. Perrotta, Stratigraphy and physical parameters of the Plinian phase of the Campanian Ignimbrite eruption, *Bulletin*, *128*(7-8), 1147–1159, 2016.

Scarpati, C., D. Sparice, and A. Perrotta, A crystal concentration method for calculating ignimbrite volume from distal ash-fall deposits and a reappraisal of the magnitude of the Campanian Ignimbrite, *Journal of Volcanology and Geothermal Research*, *280*, 67 – 75, doi: https://doi.org/10.1016/j.jvolgeores.2014.05.009, 2014.

Schellenberg, B., et al., Remote sensing and identification of volcanic plumes using fixed-wing UAVs over Volcán de Fuego, Guatemala, *Journal of Field Robotics*, *36*(7), 1192–1211, doi: 10.1002/rob.21896, 2019.

Schwaiger, H. F., R. P. Denlinger, and L. G. Mastin, Ash3d: A finite-volume, conservative numerical model for ash transport and tephra deposition, *Journal of Geophysical Research: Solid Earth*, *117*(B4), doi: https://doi.org/10.1029/2011JB008968, 2012.

Schwanghart, W., and N. J. Kuhn, TopoToolbox: A set of Matlab functions for topographic analysis, *Environmental Modelling & Software*, *25*(6), 770–781, doi: 10.1016/j.envsoft.2009.12.002, 2010.

Schwanghart, W., and D. Scherler, Short Communication: TopoToolbox 2 – MATLAB-based software for topographic analysis and modeling in Earth surface sciences, *Earth Surface Dynamics*, *2*(1), 1–7, doi: https://doi.org/10.5194/esurf-2-1-2014, 2014.

Scollo, S., M. Coltelli, F. Prodi, M. Folegani, and S. Natali, Terminal settling velocity measurements of volcanic ash during the 2002–2003 Etna eruption by an X-band microwave rain gauge disdrometer, *Geophysical Research Letters*, *32*(10), doi: 10.1029/2004GL022100, 2005.

Scollo, S., C. Bonadonna, and I. Manzella, Settling-driven gravitational instabilities associated with volcanic clouds: new insights from experimental investigations, *Bulletin of Volcanology*, *79*(6), 39, 2017.

Scott, W. E., R. P. Hoblitt, R. C. Torres, S. Self, M. M. L. Martinez, and T. Nillos, Pyroclastic flows of the June 15, 1991, climactic eruption of Mount Pinatubo, *Fire and mud: Eruptions and lahars of Mount Pinatubo, Philippines*, pp. 545–570, 1996.

Self, S., The effects and consequences of very large explosive volcanic eruptions, *Philosophical Transactions of the Royal Society A: Mathematical, Physical and Engineering Sciences*, *364*, doi: doi:10.1098/rsta.2006.1814, 2006.

Shapley, M. D., and B. P. Finney, Lake morphometry controls the remobilization and long-term geochemical imprint of distal tephra deposition, *Journal of Paleolimnology*, *53*(3), 309–320, doi: 10.1007/s10933-015-9826-6, 2015.

Sheets, P. D., and D. K. Grayson, *Volcanic activity and human ecology*, Academic Press, 1979.

Sheldrake, T., Long-term forecasting of eruption hazards: A hierarchical approach to merge analogous eruptive histories, *Journal of Volcanology and Geothermal Research*, *286*, 15–23, doi: 10.1016/j.jvolgeores.2014.08.021, 2014.

Sheridan, M. F., Particle-size characteristics of Pyroclastic Tuffs, *Journal of Geophysical Research (1896-1977)*, *76*(23), 5627–5634, doi: https://doi.org/10.1029/JB076i023p05627, 1971.

Sherrod, D. R., D. E. Champion, and J. P. McGeehin, Age and duration of volcanic activity at Diamond Craters, southeastern Oregon, *Journal of Volcanology and Geothermal Research*, *247-248*, 108 – 114, doi: https://doi.org/10.1016/j.jvolgeores.2012.08.008, 2012.

Sigurdsson, H., The History of Volcanology, in *The Encyclopedia of Volcanoes (Second Edition)*, edited by H. Sigurdsson, pp. 13–32, Academic Press, Amsterdam, 2015.

Sigurdsson, H., and S. Carey, Plinian and co-ignimbrite tephra fall from the 1815 eruption of Tambora volcano, *Bulletin of Volcanology*, *51*(4), 243–270, doi: 10.1007/BF01073515, 1989.

Sigurdsson, H., S. Cashdollar, and S. R. J. Sparks, The Eruption of Vesuvius in A. D. 79: Reconstruction from Historical and Volcanological Evidence, *American Journal of Archaeology*, *86*(1), 39–51, doi: 10.2307/504292, 1982.

Smith, R. L., Ash-flow magmatism, in *Ash-Flow Tuffs*, Geological Society of America, 1979.

Smith, V. C., R. Isaia, S. L. Engwell, and P. G. Albert, Tephra dispersal during the Campanian Ignimbrite (Italy) eruption: implications for ultra-distal ash transport during the large caldera-forming eruption, *Bulletin of Volcanology*, *78*(6), 45, doi: 10.1007/s00445-016-1037-0, 2016.

Spano, N., C. Lane, S. Francis, and T. Johnson, Discovery of Mount Mazama cryptotephra in Lake Superior (North America): Implications and potential applications, *Geology*, *45*(12), 1071, doi: 10.1130/G39394.1, 2017.

Sparks, R., M. Bursik, G. Ablay, R. Thomas, and S. Carey, Sedimentation of tephra by volcanic plumes. Part 2: controls on thickness and grain-size variations of tephra fall deposits | SpringerLink, *Bulletin of Volcanology*, *54*, 685–695, doi: https://doi.org/10.1007/BF00430779, 1992.

Sparks, R. S. J., Grain size variations in ignimbrites and implications for the transport of pyroclastic flows, *Sedimentology*, *23*(2), 147–188, doi: https://doi.org/10.1111/j.1365-3091.1976.tb00045.x, 1976.

Sparks, R. S. J., and K. V. Cashman, Dynamic Magma Systems: Implications for Forecasting Volcanic Activity, *Elements*, *13*(1), 35–40, doi: 10.2113/gselements.13.1.35, 2017.

Sparks, R. S. J., and G. P. L. Walker, The significance of vitric-enriched air-fall ashes associated with crystal-enriched ignimbrites, *Journal of Volcanology and Geothermal Research*, *2*(4), 329–341, doi: 10.1016/0377-0273(77)90019-1, 1977.

Sparks, R. S. J., L. Wilson, and G. Hulme, Theoretical modeling of the generation, movement, and emplacement of pyroclastic flows by column collapse, *Journal of Geophysical Research: Solid Earth*, *83*(B4), 1727–1739, doi: https://doi.org/10.1029/JB083iB04p01727, 1978.

Sparks, R. S. J., L. Wilson, H. Sigurdsson, and G. P. L. Walker, The pyroclastic deposits of the 1875 eruption of Askja, Iceland, *Philosophical Transactions of the Royal Society of London. Series A, Mathematical and Physical Sciences*, *299*(1447), 241–273, doi: 10.1098/rsta.1981.0023, 1981.

Sparks, R. S. J., S. Brazier, T. C. Huang, and D. Muerdter, Sedimentology of the Minoan deep-sea tephra layer in the Aegean and Eastern Mediterranean, *Marine Geology*, *54*(1), 131–167, doi: 10.1016/0025-3227(83)90011-7, 1983.

Sparks, R. S. J., M. Bursik, S. Carey, J. Gilbert, L. Glaze, H. Sigurdsson, and A. Woods, *Volcanic plumes*, Wiley, 1997.

Spencer, R. J., et al., Great Salt Lake, and precursors, Utah: The last 30,000 years, *Contributions to Mineralogy and Petrology*, *86*(4), 321–334, doi: 10.1007/BF01187137, 1984.

Spera, F. J., and J. A. Crisp, Eruption volume, periodicity, and caldera area: Relationships and inferences on development of compositional zonation in silicic magma chambers, *Journal of Volcanology and Geothermal Research*, *11*(2), 169–187, doi: 10.1016/0377-0273(81)90021-4, 1981.

Stevens, L. R., J. R. Stone, J. Campbell, and S. C. Fritz, A 2200-yr record of hydrologic variability from Foy Lake, Montana, USA, inferred from diatom and geochemical data, *Quaternary Research*, *65*(2), 264–274, doi: 10.1016/j.yqres.2005.08.024, 2006.

Stevenson, J. A., S. C. Millington, F. M. Beckett, G. T. Swindles, and T. Thordarson, Big grains go far: understanding the discrepancy between tephrochronology and satellite infrared measurements of volcanic ash, *Atmospheric Measurement Techniques*, *8*(5), 2069–2091, doi: 10.5194/amt-8-2069-2015, 2015.

Stewart, C., D. M. Johnston, G. S. Leonard, C. J. Horwell, T. Thordarson, and S. J. Cronin, Contamination of water supplies by volcanic ashfall: A literature review and simple impact modelling, *Journal of Volcanology and Geothermal Research*, *158*(3), 296–306, doi: 10.1016/j.jvolgeores.2006.07.002, 2006.

Stohl, A., et al., Determination of time-and height-resolved volcanic ash emissions and their use for quantitative ash dispersion modeling: the 2010 Eyjafjallajökull eruption, *Atmospheric Chemistry and Physics*, *11*(9), 4333–4351, 2011.

Stothers, R. B., The Great Tambora Eruption in 1815 and Its Aftermath, *Science*, *224*(4654), 1191–1198, doi: 10.1126/science.224.4654.1191, 1984.

Street, J. H., R. S. Anderson, and A. Paytan, An organic geochemical record of Sierra Nevada climate since the LGM from Swamp Lake, Yosemite, *Quaternary Science Reviews*, *40*, 89 – 106, doi: https://doi.org/10.1016/j.quascirev.2012.02.017, 2012.

Sun, D., J. Bloemendal, D. K. Rea, Z. An, J. Vandenberghe, H. Lu, R. Su, and T. Liu, Bimodal grain-size distribution of Chinese loess, and its palaeoclimatic implications, *CATENA*, *55*(3), 325–340, doi: 10.1016/S0341-8162(03)00109-7, 2004.

Suzuki, T., A theoretical model for dispersion of tephra, *Arc volcanism: physics and tectonics*, *95*, 95–103, 1983.

Suzuki, Y. J., and T. Koyaguchi, A three-dimensional numerical simulation of spreading umbrella clouds, *Journal of Geophysical Research: Solid Earth*, *114*(B3), doi: 10.1029/2007JB005369, 2009.

Sweeney, M. R., A. J. Busacca, and D. R. Gaylord, Topographic and climatic influences on accelerated loess accumulation since the last glacial maximum in the Palouse, Pacific Northwest, USA, *Quaternary Research*, *63*(3), 261 – 273, doi: https://doi.org/10.1016/j.yqres.2005.02.001, 2005.

Swineford, A., and F. Swineford, A comparison of three sieve shakers, *Journal of Sedimentary Research*, *16*(1), 3–13, doi: 10.1306/D426923D-2B26-11D7-8648000102C1865D, 1946.

Tabor, R., V. Frizzell Jr, D. Booth, R. Waitt Jr, J. Whetten, and R. Zartman, Geologic map of the Skykomish River 30 A 60 minute quadrangle, Washington, *Geologic Map Map I-1963*, US Geological Surey., 1963.

Taylor, P. W., Myths, Legend and Volcanic Activity: an example from Northern Tonga, *The Journal of the Polynesian Society*, *104*(3), 323–346, 1995.

Thompson, R. S., Paleoenvironmental Investigations at Seed Cave (Windust Cave H-45FR46), Franklin County, Washington., *Tech. rep.*, Eastern Washington University Cheney Archaeological and Historical Services, 1985.

Thompson, R. S., C. G. Oviatt, J. S. Honke, and J. P. McGeehin, Chapter 11 - Late Quaternary Changes in Lakes, Vegetation, and Climate in the Bonneville Basin Reconstructed from Sediment Cores from Great Salt Lake, in *Developments in Earth Surface Processes*, *Lake Bonneville*, vol. 20, edited by C. G. Oviatt and J. F. Shroder, pp. 221–291, Elsevier, 2016.

Thorarinsson, S., On the rate of lava- and tephra production and the upward migration of magma in four icelandic eruptions, *Geologische Rundschau*, *57*(3), 705–718, doi: 10.1007/BF01845358, 1968.

Thorarinsson, S., The Application of Tephrochronology in Iceland, in *Tephra Studies*, edited by S. Self and R. S. J. Sparks, NATO Advanced Study Institutes Series, pp. 109–134, Springer Netherlands, Dordrecht, doi: 10.1007/978-94-009-8537-7_8, 1981.

Thorsteinsson, T., T. Jóhannsson, A. Stohl, and N. I. Kristiansen, High levels of particulate matter in Iceland due to direct ash emissions by the Eyjafjallajökull eruption and resuspension of deposited ash, *Journal of Geophysical Research: Solid Earth*, *117*(B9), doi: 10.1029/2011JB008756, 2012.

Tomlinson, E. L., et al., Geochemistry of the Phlegraean Fields (Italy) proximal sources for major Mediterranean tephras: Implications for the dispersal of Plinian and co-ignimbritic components of explosive eruptions, *Geochimica et Cosmochimica Acta*, *93*, 102–128, doi: 10.1016/j.gca.2012.05.043, 2012.

Turcotte, D. L., Fractals and fragmentation, *Journal of Geophysical Research: Solid Earth*, *91*(B2), 1921–1926, doi: 10.1029/JB091iB02p01921, 1986.

Valastro, S., E. M. Davis, and C. T. Rightmire, University of Texas at Austin Radiocarbon Dates VI, *Radiocarbon*, *10*(2), 384–401, doi: 10.1017/S0033822200010985, 1968.

Van Eaton, A. R., J. D. Muirhead, C. J. N. Wilson, and C. Cimarelli, Growth of volcanic ash aggregates in the presence of liquid water and ice: an experimental approach, *Bulletin of Volcanology*, *74*(9), 1963–1984, doi: 10.1007/s00445-012-0634-9, 2012.

Venzke, E., Global Volcanism Program, Volcanoes of the World v. 4.10.1 (29 Jun 2021), *Smithsonian Institution*, *v. 4.10.1*, doi: https://doi.org/10.5479/si.GVP.VOTW4-2013, 2013.

Verosub, K. L., P. J. Mehringer, and P. Waterstraat, Holocene secular variation in western North America: Paleomagnetic record from Fish Lake, Harney County, Oregon, *Journal of Geophysical Research: Solid Earth*, *91*(B3), 3609–3623, doi: 10.1029/JB091iB03p03609, 1986.

Visher, G. S., Grain size distributions and depositional processes, *Journal of Sedimentary Research*, *39*(3), 1074–1106, 1969.

Volentik, A. C. M., C. Bonadonna, C. B. Connor, L. J. Connor, and M. Rosi, Modeling tephra dispersal in absence of wind: Insights from the climactic phase of the 2450BP Plinian eruption of Pululagua volcano (Ecuador), *Journal of Volcanology and Geothermal Research*, *193*(1), 117–136, doi: 10.1016/j.jvolgeores.2010.03.011, 2010.

Vriend, M., and M. A. Prins, Calibration of modelled mixing patterns in loess grain-size distributions: an example from the north-eastern margin of the Tibetan Plateau, China, *Sedimentology*, *52*(6), 1361–1374, doi: 10.1111/j.1365-3091.2005.00743.x, 2005.

Waitt, R. B., About Forty Last-Glacial Lake Missoula Jökulhlaups through Southern Washington, *The Journal of Geology*, *88*(6), 653–679, doi: 10.1086/628553, 1980.

Waitt, R. B., *In the path of destruction - eyewitness chronicles of Mount St. Helens*, Washington State University Press, 2015.

Waitt, R. B., V. L. Hansen, A. M. Sarna-Wojcicki, and S. H. Wood, Proximal air-fall deposits of eruptions (of Mount St. Helens) between May 24 and August 7, 1980 - stratigraphy and field sedimentology., *U.S. Geological Survey Professional Paper*, *1250*, 617–628, 1981.

Walker, G. P. L., Grain-Size Characteristics of Pyroclastic Deposits, *The Journal of Geology*, *79*(6), 696–714, doi: 10.1086/627699, 1971.

Walker, G. P. L., The Taupo pumice: Product of the most powerful known (ultraplinian) eruption?, *Journal of Volcanology and Geothermal Research*, *8*(1), 69 – 94, doi: https://doi.org/10.1016/0377-0273(80)90008-6, 1980.

Walker, G. P. L., Plinian eruptions and their products, *Bulletin Volcanologique*, *44*(3), 223, doi: 10.1007/BF02600561, 1981a.

Walker, G. P. L., The Waimihia and Hatepe plinian deposits from the rhyolitic Taupo Volcanic Centre, *New Zealand Journal of Geology and Geophysics*, *24*(3), 305–324, doi: 10.1080/00288306.1981.10422722, 1981b.

Wastegård, S., B. Wohlfarth, D. A. Subetto, and T. V. Sapelko, Extending the known distribution of the Younger Dryas Vedde Ash into northwestern Russia, *Journal of Quaternary Science*, *15*(6), 581–586, doi: 10.1002/1099-1417(200009)15:6<581::AID-JQS558>3.0.CO;2-3, 2000.

Watanabe, K., K. Ono, K. Sakaguchi, A. Takada, and H. Hoshizumi, Co-ignimbrite ash-fall deposits of the 1991 eruptions of Fugen-dake, Unzen Volcano, Japan, *Journal of Volcanology and Geothermal Research*, *89*(1), 95–112, doi: 10.1016/S0377-0273(98)00126-7, 1999.

Watson, E. J., G. T. Swindles, I. T. Lawson, and I. P. Savov, Do peatlands or lakes provide the most comprehensive distal tephra records?, *Quaternary Science Reviews*, *139*, 110–128, doi: 10.1016/j.quascirev.2016.03.011, 2016.

Watt, S. F. L., D. M. Pyle, T. A. Mather, R. S. Martin, and N. E. Matthews, Fallout and distribution of volcanic ash over Argentina following the May 2008 explosive eruption of Chaitén, Chile, *Journal of Geophysical Research: Solid Earth*, *114*(B4), doi: 10.1029/2008JB006219, 2009.

Webley, P., and L. Mastin, Improved prediction and tracking of volcanic ash clouds, *Journal of Volcanology and Geothermal Research*, *186*(1-2), 1–9, 2009.

Webley, P. W., B. J. B. Stunder, and K. G. Dean, Preliminary sensitivity study of eruption source parameters for operational volcanic ash cloud transport and dispersion models—A case study of the August 1992 eruption of the Crater Peak vent, Mount Spurr, Alaska, *Journal of Volcanology and Geothermal Research*, *186*(1-2), 108–119, 2009.

Webster, H. N., B. J. Devenish, L. G. Mastin, D. J. Thomson, and A. R. Van Eaton, Operational Modelling of Umbrella Cloud Growth in a Lagrangian Volcanic Ash Transport and Dispersion Model, *Atmosphere*, *11*(2), 200, doi: 10.3390/atmos11020200, 2020.

Weibull, W., A statistical distribution function of wide applicability, *Journal of Applied Mechanics*, pp. 293–297, 1951.

Wells, R. E., and R. McCaffrey, Steady rotation of the Cascade arc, *Geology*, *41*(9), 1027–1030, doi: 10.1130/G34514.1, 2013.

Wen, S., and W. I. Rose, Retrieval of sizes and total masses of particles in volcanic clouds using AVHRR bands 4 and 5, *Journal of Geophysical Research: Atmospheres*, *99*(D3), 5421–5431, doi: https://doi.org/10.1029/93JD03340, 1994.

Wentworth, C. K., A scale of grade and class terms for clastic sediments, *The Journal of Geology*, *30*(5), 377–392, 1922.

Westgate, J. A., and A. Dreimanis, Volcanic ash layers of recent age at Banff National Park, Alberta, Canada, *Canadian Journal of Earth Sciences*, *4*(1), 155–161, doi: 10.1139/e67-006, 1967.

Westgate, J. A., and M. P. Gorton, Correlation Techniques in Tephra Studies, in *Tephra Studies*, edited by S. Self and R. S. J. Sparks, pp. 73–94, Springer Netherlands, Dordrecht, 1981.

White, J. M., and G. Osborn, Evidence for a Mazama-like tephra deposited ca. 10 000 BP at Copper Lake, Banff National Park, Alberta, *Canadian Journal of Earth Sciences*, *29*(1), 52–62, 1992.

White, J. T., C. B. Connor, L. Connor, and T. Hasenaka, Efficient inversion and uncertainty quantification of a tephra fallout model, *Journal of Geophysical Research: Solid Earth*, *122*(1), 281–294, doi: 10.1002/2016JB013682, 2017.

Whitlock, C., C. E. Briles, M. C. Fernandez, and J. Gage, Holocene vegetation, fire and climate history of the Sawtooth Range, central Idaho, USA, *Quaternary Research*, *75*(1), 114 – 124, doi: https://doi.org/10.1016/j.yqres.2010.08.013, 2011.

Wickham, H., *ggplot2: Elegant Graphics for Data Analysis*, Springer-Verlag New York, 2016.

Wiesner, M. G., A. Wetzel, S. G. Catane, E. L. Listanco, and H. T. Mirabueno, Grain size, areal thickness distribution and controls on sedimentation of the 1991 Mount Pinatubo tephra layer in the South China Sea, *Bulletin of Volcanology*, *66*(3), 226–242, doi: 10.1007/s00445-003-0306-x, 2004.

Williams, H., *The Geology of Crater Lake National Park, Oregon: With a Reconnaissance of the Cascade Range Southward to Mount Shasta*, vol. 540, Carnegie Institution, 1942.

Williams, H., and G. Goles, Volume of the Mazama ash-fall and the origin of Crater Lake Caldera, in *Andesite conference guidebook*, vol. 62, pp. 37–41, Bull. Oreg. Dep. Geol. Mineral. Ind, 1968.

Williams, H. F. L., and J. D'Auria, A Mazama tephra marker bed in the Fraser Lowland, British Columbia, *Canadian Journal of Earth Sciences*, *28*(1), 150–153, doi: 10.1139/e91-014, 1991.

Williams, S. N., and S. Self, The October 1902 plinian eruption of Santa Maria volcano, Guatemala, *Journal of Volcanology and Geothermal Research*, *16*(1), 33–56, doi: 10.1016/0377-0273(83)90083-5, 1983.

Wilson, C. J., and B. L. Charlier, The Life and Times of Silicic Volcanic Systems, *Elements*, *12*(2), 103–108, doi: 10.2113/gselements.12.2.103, 2016.

Wilson, C. J. N., and W. Hildreth, Hybrid fall deposits in the Bishop Tuff, California: A novel pyroclastic depositional mechanism, *Geology*, *26*(1), 7–10, doi: 10.1130/0091-7613(1998)026<0007:HFDITB>2.3.CO;2, 1998.

Wilson, C. J. N., S. Blake, B. L. A. Charlier, and A. N. Sutton, The 26.5 ka Oruanui Eruption, Taupo Volcano, New Zealand: Development, Characteristics and Evacuation of a Large Rhyolitic Magma Body, *Journal of Petrology*, *47*(1), 35–69, doi: 10.1093/petrology/egi066, 2006.

Wilson, C. J. N., G. F. Cooper, K. J. Chamberlain, S. J. Barker, M. L. Myers, F. Illsley-Kemp, and J. Farrell, No single model for supersized eruptions and their magma bodies, *Nature Reviews Earth & Environment*, pp. 1–18, doi: 10.1038/s43017-021-00191-7, 2021.

Wilson, L., and T. C. Huang, The influence of shape on the atmospheric settling velocity of volcanic ash particles, *Earth and Planetary Science Letters*, *44*(2), 311–324, doi: 10.1016/0012-821X(79)90179-1, 1979.

Wilson, T. M., J. W. Cole, C. Stewart, S. J. Cronin, and D. M. Johnston, Ash storms: impacts of wind-remobilised volcanic ash on rural communities and agriculture following the 1991 Hudson eruption, southern Patagonia, Chile, *Bulletin of Volcanology*, *73*(3), 223–239, doi: 10.1007/s00445-010-0396-1, 2011.

Wilson, T. M., C. Stewart, V. Sword-Daniels, G. S. Leonard, D. M. Johnston, J. W. Cole, J. Wardman, G. Wilson, and S. T. Barnard, Volcanic ash impacts on critical infrastructure, *Physics and Chemistry of the Earth, Parts A/B/C*, *45*, 5–23, 2012.

WMO, VAAC Operational Dispersion Model Configuration Snap Shot Version 3, *Tech. Rep. 3*, 2018.

Wohletz, K. H., M. F. Sheridan, and W. K. Brown, Particle size distributions and the sequential fragmentation/transport theory applied to volcanic ash, *Journal of Geophysical Research: Solid Earth*, *94*(B11), 15,703–15,721, doi: 10.1029/JB094iB11p15703, 1989.

Woods, A. W., and K. Wohletz, Dimensions and dynamics of co-ignimbrite eruption columns, *Nature*, *350*(6315), 225, 1991.

Wotzlaw, J.-F., I. N. Bindeman, R. A. Stern, F.-X. D'Abzac, and U. Schaltegger, Rapid heterogeneous assembly of multiple magma reservoirs prior to Yellowstone supereruptions, *Scientific Reports*, *5*(1), 14,026, doi: 10.1038/srep14026, 2015.

Wright, H. M., C. R. Bacon, J. A. Vazquez, and T. W. Sisson, Sixty thousand years of magmatic volatile history before the caldera-forming eruption of Mount Mazama, Crater Lake, Oregon, *Contributions to Mineralogy and Petrology*, *164*(6), 1027–1052, doi: 10.1007/s00410-012-0787-8, 2012.

Young, S. R., Physical volcanology of Holocene airfall deposits from Mt Mazama, Crater Lake, Oregon., PhD Thesis, University of Lancaster, 1990.

Yu, Y., *mixR: Finite Mixture Modeling for Raw and Binned Data*, https://CRAN.R-project.org/package=mixR, 2018.

Yu, Z., Holocene Carbon Accumulation of Fen Peatlands in Boreal Western Canada: A Complex Ecosystem Response to Climate Variation and Disturbance, *Ecosystems*, *9*(8), 1278–1288, doi: 10.1007/s10021-006-0174-2, 2006.

Yu, Z., D. H. Vitt, I. D. Campbell, and M. J. Apps, Understanding Holocene peat accumulation pattern of continental fens in western Canada, *Canadian Journal of Botany*, *81*(3), 267–282, doi: 10.1139/b03-016, 2003.

Zdanowicz, C., G. Zielinski, and M. Germani, Mount Mazama eruption: Calendrical age verified and atmospheric impact assessed, *Geology*, *27*(7), 621–624, doi: 10.1130/0091-7613(1999)027<0621:MMECAV>2.3.CO;2, 1999.

Þórarinsson, S., *Hverfjall*, vol. Náttúrufrædingurinn, 22 ed., 1952.